CARBON NANOMATERIALS OF GRAPHITE-LIKE STRUCTURE AND THEIR COMPOSITES

PHYSICS, CHEMISTRY AND TECHNOLOGY

NATIONAL ACADEMY OF SCIENCES OF UKRAINE

CHUIKO INSTITUTE OF SURFACE CHEMISTRY OF THE NAS OF UKRAINE
INSTITUTE OF MACROMOLECULAR CHEMISTRY OF THE NAS OF UKRAINE

TARAS SHEVCHENKO NATIONAL UNIVERSITY OF KYIV

НАЦІОНАЛЬНА АКАДЕМІЯ НАУК УКРАЇНИ

ІНСТИТУТ ХІМІЇ ПОВЕРХНІ ім. О.О. ЧУЙКА НАН УКРАЇНИ
ІНСТИТУТ ХІМІЇ ВИСОКОМОЛЕКУЛЯРНИХ СПОЛУК НАН УКРАЇНИ

КИЇВСЬКИЙ НАЦІОНАЛЬНИЙ УНІВЕРСИТЕТ
імені ТАРАСА ШЕВЧЕНКА

Ю.І. СЕМЕНЦОВ
М.Т. КАРТЕЛЬ
С.Г. НЕДІЛЬКО
Ю.А. ХИЖНИЙ
К.О. ІВАНЕНКО

ВУГЛЕЦЕВІ НАНОМАТЕРІАЛИ З ГРАФІТОПОДІБНОЮ СТРУКТУРОЮ ТА ЇХНІ КОМПОЗИТИ:

ФІЗИКА, ХІМІЯ ТА ТЕХНОЛОГІЯ

Науковий редактор М.Т. КАРТЕЛЬ

ПРОЄКТ
«УКРАЇНСЬКА НАУКОВА КНИГА»
ІНОЗЕМНОЮ МОВОЮ

КИЇВ
АКАДЕМПЕРІОДИКА
2022

YURII I. SEMENTSOV
MYKOLA T. KARTEL'
SERHII G. NEDILKO
YURII A. KHYZHNYI
KATERYNA O. IVANENKO

CARBON NANOMATERIALS OF GRAPHITE-LIKE STRUCTURE AND THEIR COMPOSITES: PHYSICS, CHEMISTRY AND TECHNOLOGY

Scientific editor M.T. KARTEL'

PROJECT
«UKRAINIAN SCIENTIFIC BOOK»
IN A FOREIGN LANGUAGE

KYIV
AKADEMPERIODYKA
2022

https://doi.org/10.15407/akademperiodyka.473.456
UDC 544.023-126-032.36+620.168-032.36+542.97+620.3-032.3+544.7+544.6
C21

Reviewers:

L.A. BULAVIN, Dr. Sci. (Phys. & Math.), Prof.,
Academician of the National Academy of Sciences of Ukraine,
Head of the Department of Taras Shevchenko National University of Kyiv

V.M. OGENKO, Dr. Sci. (Chem.), Prof.,
Correspondent member of the National Academy of Sciences of Ukraine,
Head of the Department of the Vernadsky Institute of General and Inorganic Chemistry of the NAS of Ukraine

Yu.V. SAVELYEV, Dr. Sci. (Chem.), Prof.,
Institute of Macromolecular Chemistry of the NAS of Ukraine,
Head of department of Chemistry heterochain polymers
and interpenetrating polymer networks

Approved for publication by the Scientific Council of the Chuiko Institute of Surface Chemistry of the National Academy of Sciences of Ukraine (August 13, 2021, Protocol No. 10)

The publication was funded within the framework of the Targeted Complex Program of the NAS of Ukraine "Scientific Bases of Functioning and Providing for Conditions for the Development of the Scientific and Publishing Complex of the NAS of Ukraine"

C21 **Carbon** nanomaterials of graphite-like structure and their composites: physics, chemistry and technology / Yurii I. Sementsov, Mykola T. Kartel', Serhii G. Nedilko, Yurii A. Khyzhnyi, Kateryna O. Ivanenko; NAS of Ukaine, Chuiko Institute of Surface Chemistry, Institute of Macromolecular Chemistry; Taras Shevchenko National University of Kyiv. — Kyiv: Akademperiodyka, 2022. — 456 p.

ISBN 978-966-360-473-2

The book considers the patterns of formation of the structure and properties of sp^2-hybridized carbon nanoformations: nanotubes (CNTs), expanded graphite (EG), graphene nanoparticles and composite materials (CM) with their participation with carbon, polymer and ceramic matrices, including EG-CNTs composite, as well as the mechanism of influence of low content of nanosized fillers on the functional and operational characteristics of the created nano-CM. It is experimentally confirmed that the mechanism of strengthening of low-filled matrices of low consists in creation by a grid of CNTs of layers of the matrix in a nanosized state with the increased characteristics. The monograph is intended for specialists in the field of physical and chemical material science.

UDC 544.023-126-032.36+620.168-032.36+542.97+620.3-032.3+544.7+544.6

ISBN 978-966-360-473-2

CONTENT

CHAPTER 6 OPTICAL PROPERTIES OF CARBON MATERIALS

INTRODUCTION

It is generally known that the properties of materials are determined by the nature of the interatomic interaction, the peculiarities of the structure, and its change under the influence of various factors. The transition to nanoscale systems, for which the number of atoms or molecules on the surface becomes commensurate with their number in the volume, increases the interaction energy due to "surface tension" (surface energy) without significant changes in the structure of the bulk phase, and the properties of the nanosystem as a whole are actually determined by surface characteristics. In this case, the density of structural defects decreases significantly or they are absent at all, and, in this case, the specific characteristics of the nanosystem become high, approaching the theoretically possible level. Thus, nanoscale materials are a unique object for study by chemistry, physics, and surface technology with the undeniable perspective of creating materials with unique properties.

Nanoscale carbon materials such as fullerenes, single-wall, double-wall and multi-wall nanotubes, nanofibers, nanoonions, nanotroids, nanodiamonds, etc. have special electronic, optical, and mechanical properties. Their physical and chemical characteristics differ significantly from the related properties of macrocrystalline materials of similar structures. Thus, although carbon nanotubes (CNTs) and nanofibers (CNFs) are constructed of graphene layers like graphite, their electrical conductivity, chemical reactivity, and ability to form intercalated compounds differ significantly.

Among the carbon nanosized materials (CNM), a prominent place is occupied by:

- CNTs, which at a diameter of (1—50) nm and a length of several tens of micrometers form a new class of quasi-one-dimensional nanoobjects and have unique properties.
- Expanded graphite (EG), which is a nanosized cluster-assembled system, best realizes the properties of graphene in the production of material on the industrial scale.

• Graphene nanoparticles with a thickness of up to tens of layers, which are of unconditional interest thanks to their unique optical and electronic properties.

The most productive method of obtaining CNTs is the method of catalytic chemical vapor deposition (CCVD). Under the conditions of using an effective catalyst, the carbon crystallizes in the form of CNTs, the structure and quality of which are largely determined by the catalyst used and also depend on the nature of the carbon source and technological modes. Optimization of these factors is fundamentally important because it determines the selectivity of the structural forms that are formed.

The results of developments in the field of synthesis and production of CNTs, as well as composite materials based on them, indicate that these materials in the near future will be more widely used in known and new areas [1, 2]. This is due to a set of unique characteristics of CNTs. Single-wall CNTs have a modulus of elasticity of about 1TPa and tensile strength 100 times higher than that of steel, at a density ratio of 1: 6 [3]. This makes multiwall CNTs ideal fillers for composites based on polymer and other matrices, given the possibility of chemical functionalization of the surface layer of the tube without its complete destruction. Their high specific thermal conductivity, ~2 kW/(m · K) along the tube, allows one to create effective thermally conductive composite materials (CM) for heat dissipation from chips and other elements of electronic equipment. The high electrical conductivity of CNTs justifies their choice when creating conductive composites with polymers. CNTs and CNFs are among the promising materials for energy storage devices such as chemical power sources, supercapacitors, fuel cells, hydrogen absorbers, etc. [3—11]. The energy capacity is determined by the structure of the carbon material, in particular, the specific surface area, volume, and size of mesopores formed by the outer surfaces of CNT, the ability of nanosized packets of graphene layers in CNFs to reversible intercalation–deintercalation. In the area of environmentally friendly energy, it is important to create materials that can reversibly absorb hydrogen.

Large-scale production of CNTs, within the CCVD method, allows producing CNTs in the form of agglomerates of intertwined tubes, with sizes of 20—500 μm. It is known that CNTs are highly effective fillers in the sense that a continuous mesh of CNTs is formed in the polymer matrix at a concentration of only 0.1 mass% provided that they are homogeneous [12, 13]. At the same time, the properties change significantly: the composite acquires high electrical and thermal conductivity; the modulus of elasticity, conditional yield strength, wear resistance, etc. increase. This necessitates the study of the characteristics of CNT agglomerates and the search for an effective method for their dispersion and separation.

Natural graphite in the form of EG has the ability to become a durable material without binders, which allows it to be used as a basis for sealing, electrical,

antifriction, and structural materials. It is an effective filler for polymers and rubbers, etc. Consumer properties of CM based on EG, including physical and mechanical characteristics, are determined by the peculiarities of its crystal structure and phase composition, as well as the energy between the EG particles that arises in the process of material formation. It is possible to regulate the structural state of the surface and volume of EG particles within certain limits by changing the conditions of oxidative and thermal treatments of natural graphite. Chemical modification of the surface of EG particles, in particular, molecules of thermosetting organic compounds, allows enhancing the interparticle interaction. The resulted creation of a continuously distributed carbon structure in the graphite matrix qualitatively changes the physical and mechanical characteristics of CM [14]. A significant increase in the strength characteristics of CM is achieved by introducing highly modular components, CNFs or CNTs, into the EG-carbon or EG-polymer systems.

Graphene is a single graphite plane in which sp^2-hybridized carbon atoms form a hexagonal lattice. Graphene can be represented as a "building block" for graphite, CNTs, EG, and other carbon materials. Investigation of graphene both in terms of possible large-scale production and the range of physicochemical properties is at an early stage, although the number of publications in recent years is growing exponentially [15—17] and requires further consistent and thorough studies, especially against the background of the results achieved in the physical chemistry of EG and CNTs.

The promising objects for the use of nanosized carbon materials are CM with polymer matrices and nanocarbon fillers, products made of them, characterized by high strength, wear resistance, and small weight; polymers suitable for painting; radiation protection materials; antistatic; coatings that provide lightning protection; electrical and mechanical voltage sensors; electrically conductive ceramics; nanoelectronics; information storage and display devices; materials for endoprosthesis; anticorrosive coatings; coatings that provide high heat dissipation; coatings for protection against ultraviolet radiation, shielding, and non-reflecting electromagnetic radiation in the radio frequency and infrared bands; adsorption materials; catalysts; electrochemical devices for generating and storing energy such as chemical power sources, supercapacitors, fuel cells; materials that accumulate hydrogen and other energy substances, etc.

Thus, a comprehensive study of physicochemical processes of directed formation of the structure and properties of a new class of nanosized carbon materials CNT, CNF, EG, graphene nanoparticles, and composite materials based on them to create the large-scale production of them is an urgent task, which is covered in this monograph within the capabilities of the authors.

REFERENCES

1. A.P. Shpak, Yu.A. Kunitskii, V.L. Karbovskii, *Cluster and nanostructured materials* (Akademperiodika, Kyiv, 2001), vol. 1. [in Rassian].
2. M. Inagaki, K. Kaneko and T. Nishizawa, Carbon. **42** (8-9), 1401 (2004).
3. M.M.J. Treacy, T.W. Ebbesen and J.M. Gibson, Nature. **381**, 678 (1996).
4. S.H. Yoon, C.-W. Park, H. Yang, Y. Korai, I. Mochida, R.T.K. Baker and N.M. Rodriguez, Carbon. **42** (1), 21 (2004).
5. W. Li, C. Liang, W. Zhou, J. Qiu, H. Li, G. Sun and Q. Xin, Carbon. **42** (2), 436 (2004).
6. T. Liu, T.V. Sreekumar, S. Kumar, R.H. Hauge and R.E. Smalley, Carbon. **41** (12), 2440 (2003).
7. P.X. Hou, S.-T. Xu, Z. Ying, Q.-H. Yang, C. Liu and H.-M. Cheng, Carbon. **41** (13), 2471 (2003).
8. H.F. Yang and R.T. Yang, Carbon. **40** (3), 437 (2002).
9. Y.Y. Fan, B. Liao, M. Liu, Y.L. Wei, M.Q. Lu and H.M. Cheng, Carbon. **37** (10), 1649 (1999).
10. E. Frackowiak and F. Beguin, Carbon. **40** (10), 1775 (2002).
11. B.K. Gupta and O.N. Srivastava, in: *Hydrogen Materials Science and Chemistry of Carbon Nanomaterials. NATO Science Series II: Mathematics, Physics and Chemistry*, ed. by T.N. Veziroglu, S.Yu. Zaginaichenko, D.V. Schur, B. Baranowski, A.P. Shpak and V.V. Skorokhod (Springer, Dordrecht, 2004), vol. 172, pp. 177—184. https://doi.org/10.1007/1-4020-2669-2_18
12. W. Bauhofer and J.Z. Kovacs. Comp. Sci. Technol. **69** (10), 1486 (2009).
13. L. Bokobza, Polymer. **48** (17), 4907 (2007).
14. Yu.I. Sementsov, S.L. Revo, K.O. Ivanenko and S. Hamamda, *Expanded graphite and its composites,* ed. by M.T. Kartel (Akademperiodika, Kyiv, 2019).
15. S. Yang, S. Brüller, Z.-S. Wu, Z. Liu, K. Parvez, R. Dong, F. Richard, P. Samorì, X. Feng and K. Müllen, J. Am. Chem. Soc. **137** (43), 13927 (2015).
16. V. Dhand, K. Y. Rhee, H.J. Kim and D.H. Jung, Journal of Nanomaterials. **2013**, 763953, (2013). https://doi.org/10.1155/2013/763953.
17. E.D. Graifer, V.G. Makotchenko, A.S. Nazarov S.J. Kim and V.E. Fedorov, Russian Chemical Reviews. **80** (8), 751 (2011).

CHAPTER 1

SHORT REMARKS ON LATTICE AND ELECTRONIC STRUCTURES OF GRAPHITE, GRAPHITIC, AND SOME OTHERS CARBON FORMS

We have shown above that particles of graphite in the form of scales are the main components of expanded graphite. In addition, the expanded graphite may contain particles of amorphous graphite, graphene of various numbers of layers, carbon nanotubes, etc. (Fig. 1.1). Their cumulative effect determines mechanical, electrical, optical, and other properties of expanded graphite. Therefore, below, we briefly consider the basic characteristics of the spatial and electronic structure of some of the above-mentioned entities.

It is well known that the carbon atom possesses four electrons in the valence shell (outer shell) and the electron configuration of $1s^2 2s^2 2p^2$. Since this energy shell can hold eight electrons, each carbon atom is able to share its electrons with up to four various atoms. As a result, the carbon electronic configuration allows it a possibility to combine with other chemical elements and with itself as well. So, it can form many different compounds of varying sizes and morphology. Alone carbon atoms form a great variety of crystalline and disordered structures because they can form three types of atom orbitals hybridizations, sp^3, sp^2, and sp^1 (Fig. 1.2) [1, 2].

1.1. Crystal lattice and electronic structure of graphite

Let us start with a short description of the carbon forms' electronic structure with a review of the graphite electronic structure. In the three-fold configuration, the sp^2-graphite case, three of four valence electrons enter trigonally directed orbitals, which form σ bonds in a plane. The fourth electron lies in a $p\pi$, which lies normal to the σ bonding plane. This π orbital forms a weaker π bond with π orbital on one or more neighboring atoms. Graphite has four valence electrons, three of which form tight bonds with neighboring atoms in the layer. The fourth electron is considered to be in

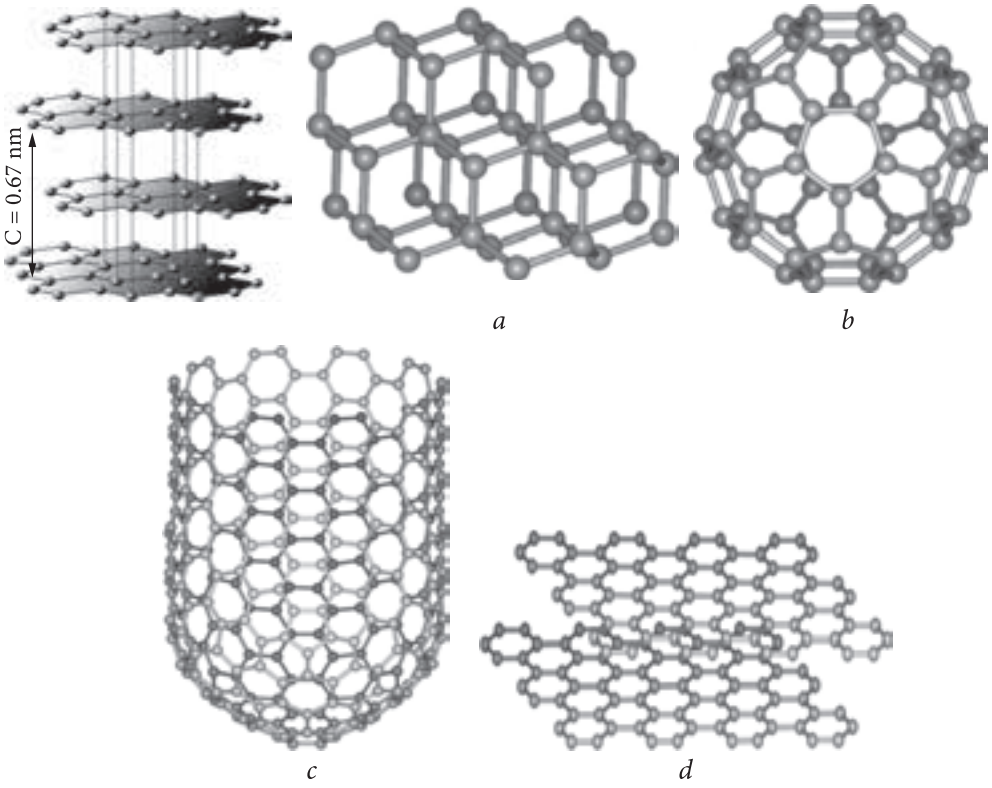

Fig. 1.1. Illustrations of the lattices of different modifications of carbon materials (WiKi): *a* — diamond; *b* — C_{60} fullerene; *c* — nanotube; *d* — graphene layers

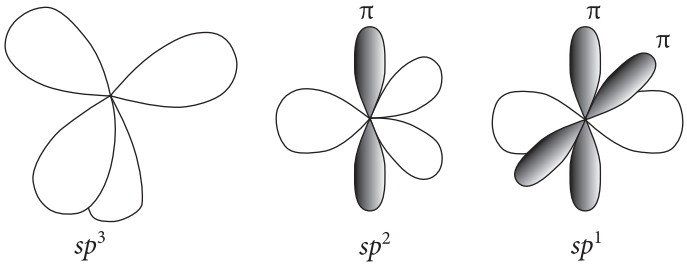

Fig. 1.2. The sp^3, sp^2, and sp^1 hybridized bonding [1, 2]

the $2P_z$ state with its axis of symmetry which is perpendicular to the lattice plane. It can be assumed that graphite has only one conduction electron that is electron in the $2p_z$ state, as the electrons forming bonds in the plane do not take part in the electrical properties of graphite. A single graphite plane is a zero-bandgap semiconductor, and in three dimensions it is an anisotropic metal [2].

There are many works devoted to the electronic band structure of graphite study, e.g. developed by [1], where the group theory and perturbation methods were used

to calculate the bands' characteristics. An excellent summary of the structure and electronic properties of graphite and graphite intercalation compounds has been given by M.S. Dresselhaus and G. Dresselhaus [2], and many aspects of the summary relevant to our research are briefly reviewed below.

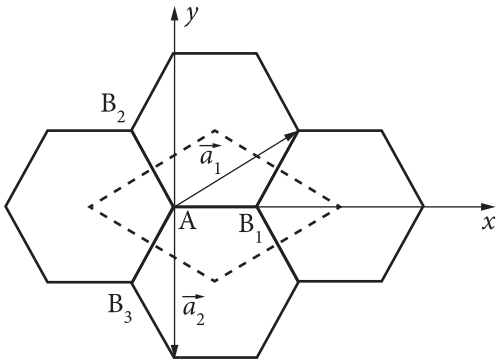

Fig. 1.3. The unit cell in the hexagonal layer of graphite [2]

The unit cell in the hexagonal layer of graphite contains two atoms: A and B (Fig. 1.3). The hexagonal spacing in the layer (1.42 Å) is small compared with the spacing of the lattice planes (d = 3.37 Å). The fact indicates that in many cases in the first approximations, the interaction between layers can be neglected, and thus graphite may be treated as a 2D crystal structure [2].

Because of the large anisotropy of the crystal structure, most models for the electronic structure start from a 2D approximation, treating the intraplanar interaction between the 2*s*, $2p_x$, and $2p_y$ atomic orbitals as being able to form the strongly coupled bonding and antibonding trigonal orbitals. These trigonal orbitals give rise to three bonding and three antibonding σ-bands in the 2D graphite band structure. In these models, the weakly coupled p_z atomic wavefunctions give rise to two π-bands, which are degenerated by symmetry at the six Brillouin zone corners at point P, through which the Fermi level passes. The points P, Q, and Γ of the 2D zone correspond to HKH, LML, and AΓA, respectively, of the 3D zone shown in Fig. 1.4. A large number of calculations of the 2D graphite electronic structure were made many years ago [3—9]. The degenerate π-bands at point P are of particular interest since the Fermi level goes through this P-point degeneracy, and the E (**k**) relation away from the P-point is linear in **k** for the π-bands. The three antibonding σ-bands lie far above the π-bands in energy, and the three antibonding σ-bands lie far below at the P-point. 3D band models confirm that (1) the Fermi surface is located near the Brillouin zone edges HKH and H′K′H′ (shown in Fig. 1.4), and (2) the width of the π-bands in the vicinity of the Brillouin zone edges is much less than the separation between the π-bands and the bonding and antibonding σ-bands. Therefore, 2D band models have been extensively applied to the qualitative interpretation of many experimental data on graphite [2].

Graphite, however, is a 3D solid with AB stacking of the graphite layers, giving rise to four carbon atoms per unit cell as shown in Fig. 1.3. Although the interlayer interaction is small, it has a profound effect on the four π-bands near the Brillouin zone edges, causing a band overlap that is responsible for the semimetallic properties of graphite, whereas the 2D model gives a zero-gap

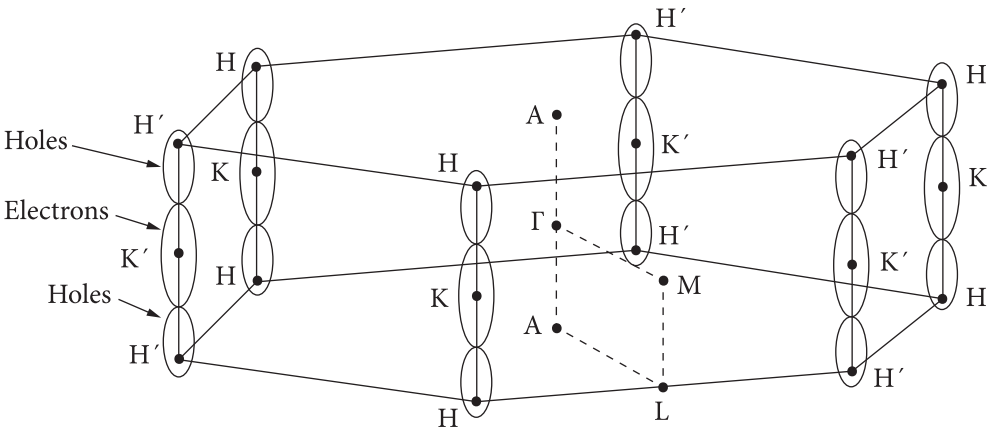

Fig. 1.4. Graphite Brillouin zone showing several high symmetry points and a schematic version of the graphite electron and hole Fermi surfaces located along the HK axes [2]

semiconductor for graphite. Detailed models for the dispersion relations for the four π-bands have been developed in [1, 10, 11]. In particular, the Slonczewski — Weiss — McClure (SWMcC) band model has been applied extensively to explain the transport, quantum oscillatory, optical, and magnetic-optical properties dependent on the electronic structure near the Fermi level [2]. An excellent summary of the electronic properties is given in [12].

Whereas the 2D band models give in-plane dispersion relations for two π-bands for a planar graphite unit cell, the 3D SWMcC model gives 3D dispersion relations for four π-bands corresponding to the full graphite unit cell containing four crystallographically distinct atoms based on the ABAB stacking sequence (Fig. 1.3). The effect of different stacking arrangements of the graphite layers (AAA, ABAB, ABCABC) on the electronic structure has been considered in [13, 14], where each stacking arrangement was shown to result in somewhat different energy levels near E_F. It should be emphasized that the mathematical form of the three-dimensional SWMcC model is general and is based on the space group symmetry of graphite. The basic SWMcC model has also been extended to include explicitly the spin-orbit interaction [15]. The SWMcC model gives a phenomenological treatment of the electronic structure based on crystal symmetry. The most general form of the hamiltonian consistent with crystal symmetry is developed for **k** values in the vicinity of the Brillouin zone edges. In the k_z direction, a Fourier expansion is made, and rapid convergence is obtained owing to the weak interplanar binding. In the layer planes, a $\mathbf{k} \cdot \mathbf{p}$ expansion is made since the extent of the Fermi surface in the basal planes is small compared with Brillouin zone dimensions. Each of the seven parameters (γ_0, $\ldots\gamma_5$, Δ) of the SWMcC model can be identified with overlap and transfer integrals within the framework of the tight- binding approximation, but in practice, they are evaluated experimentally [2].

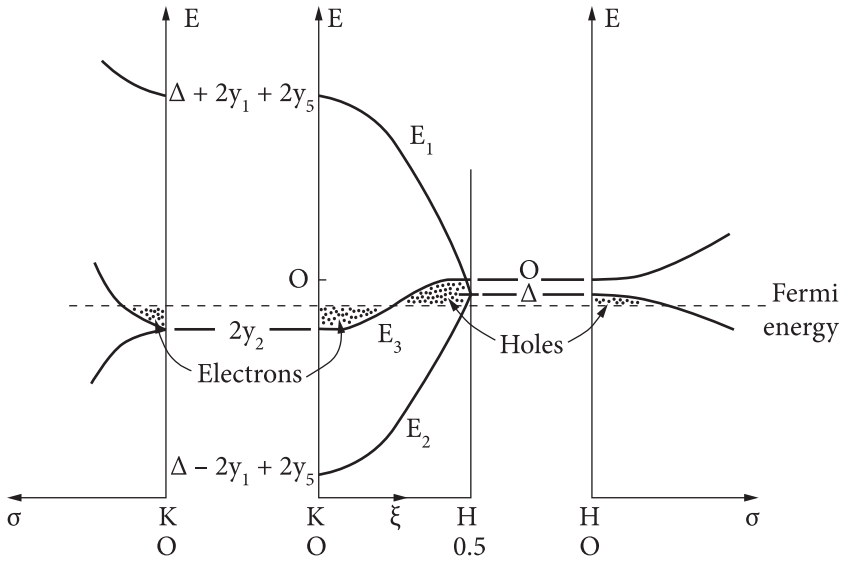

Fig. 1.5. Electronic energy bands near the HK axis in 3D graphite as obtained from the SWMcC band model. Along the HK axis (center of the figure), the E_3 band is doubly degenerate. This degeneracy is lifted as you move away from the axis, as ~~is~~ illustrated in the left-hand figure for **k** vectors of the **c**-axis, but in the $\xi = 0$ plane. For $\mathbf{k} \perp \mathbf{c}$-axis and in the plane $\xi = 1/2$ (at the Brillouin zone hexagonal boundary), the four π-bands occur in doubly degenerate pairs, as illustrated in the right-hand figure [2]

The eigenvalues of the SWMcC hamiltonian yield the energy dispersion relations which are schematically illustrated in Fig. 1.5. Along the Brillouin zone edge HKH, two of the four solutions are doubly degenerate and were labeled by E_3. The remaining two solutions are non-degenerate and are denoted by E_1 and E_2. The degeneracy of the two E_3 levels increases as we move away from the zone edge, and this is indicated on the left-hand side of Fig. 1.5 with reference to the plane defined by $\xi = 0$. At the H point ($\xi = 1/2$), the levels E_1 and E_2 are degenerate, and the double degeneracy of these levels is maintained throughout the planes $\xi = \pm 1/2$, as shown on the right-hand side of Fig. 1.5.

It is of interest to note that whereas 2D graphite is a zero-gap semiconductor, 3D graphite is semimetallic with a band overlap of $2\gamma_2$ (~0.040 eV) and a bandwidth along the Brillouin zone edge of $4\gamma_1$ (~1.56 eV) [2].

First-principles 3D calculations of the electronic band structure of graphite have also been carried out using a variety of methods [16—19], and they have resulted in good agreement with the widely used phenomenological SWMcC model. These calculations have been extended to consider the effect of pressure on the graphite electronic structure [20], and to treat low-stage graphite intercalation compounds [2, 21—25].

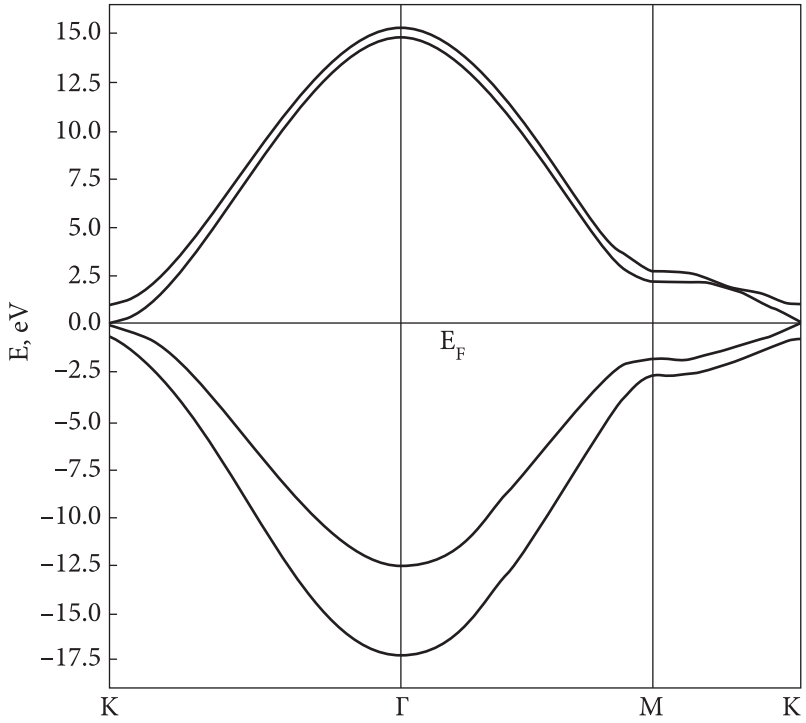

Fig. 1.6. Graphite π-bands along several high symmetry directions calculated in [26] using a 3D Fourier expansion of E (**k**). The Fourier expansion coefficients are evaluated by fitting E (**k**) to the SWMcC model along the HK axis and by comparing the calculated frequency-dependent dielectric function ε(ω) with the optical reflectivity measurements [2]

Since the Fermi surface of the intercalation compounds occupies a much larger volume of the Brillouin zone than for pristine graphite, the extension of the SWMcC model [26] to yield dispersion relations for the π-bands throughout the Brillouin zone is of particular interest. Using symmetry requirements to specify the form of the hamiltonian, a 3D Fourier expansion was used for the basis functions. The band parameters of the model were evaluated using (1) Fermi surface data in the vicinity of the Brillouin zone edges HKH and H′K′H′, (2) fits to the optical data below 6 eV, and (3) the requirement that the dispersion relations reduce to those of the SWMcC model in the vicinity of the Brillouin zone edges [2]. The resulting dispersion relations for the π-bands along several high symmetry directions are shown in Fig. 1.6. An extension of this 3D Fourier expansion model to describe dispersion relations in graphite intercalation compounds was described in [27].

Graphite is one of the classical semimetals that has been a prototype material for Fermi surface studies. A large variety of quantum oscillatory phenomena has been observed in graphite and the results are summarized in the

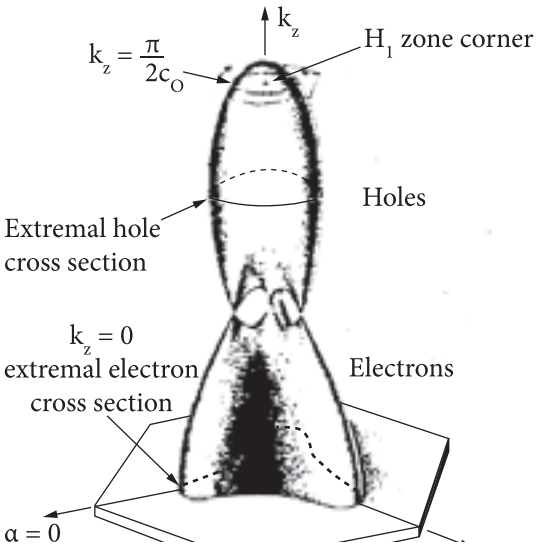

Fig. 1.7. Fermi surface model for graphite illustrating the three types of extremal constant energy orbits: majority electrons, majority holes, and minority holes [2]

review articles [12, 28]. Graphite is also a material for which the one electron energy band structure is well understood [2]. Measurements that have been of particular importance to the determination of the one-electron energy band model are DHVA frequencies for majority electron, majority and minority hole carrier pockets, the magnetoreflection K- and H-point interband transitions and the modulated infrared reflectivity spectrum.The Fermi surface of pure graphite consists of two sets of three elongated, trigonally warped hole and electron carrier pockets (Fig. 1.7). These carrier pockets have threefold symmetry with respect to the vertical edges HKH, and H′K′H′ of the hexagonal graphite Brillouin zone. The Fermi surfaces are highly anisotropic, with a length in the *c*-direction about 13 times the width perpendicular to that direction. Thus, within experimental error, the Θ dependence of the experimentally determined cross-sectional areas cannot be distinguished easily from the cosΘ dependence, characteristic of a cylindrical Fermi surface and a 2D solid, except for measurements in the range 90° > Θ > 80°.

The main Fermi surface results for graphite are expressed in terms of the de Haas-van Alphen frequencies for the **H**||**c** axis, which are 6.5, 4.9, and 0.33 T for the majority electron, majority hole, and minority hole surfaces, respectively [29—34]. The minority hole frequency is associated with the intersection of the hole Fermi surface with the Brillouin zone boundary at $\pm\pi/2c_0$. Several interpretations of the quantum oscillatory phenomena in graphite intercalation compounds have been made in terms of graphitic constant energy surfaces [2].

The values reported for the *c*-axis electrical conductivity σ_c^0 in pristine graphite vary considerably according to the type of graphite (single crystal, kish graphite, and HOPG), and the quality of the sample as measured by the residual resistance ratio defined as ρ_a(300 K)/ρ_a(4.2 K) [35—38]. A typical value for σ_c^0 in pristine graphite is ~10 $(\Omega\,\mathrm{cm})^{-1}$. There has been considerable disagreement with regard to the interpretation of these *c*-axis measurements. Recent experimental and theoretical works on the temperature dependence and the relation between

σ_c^0 and the residual resistance have shown that the dominant mechanism for *c*-axis conduction in pristine graphite is band conduction rather than hopping [37, 38]. These studies have further shown that stacking faults associated with extended main plane dislocations rather than the electron-phonon interaction dominate room temperature scattering processes for *c*-axis conduction in samples with high in-plane residual resistance ratios ρ_a (300 K) / ρ_a (4.2K). It has also been found that the extended main plane dislocations that dominate *c*-axis scattering become denser through the intercalation process [2, 39].

1.2. Crystal lattice and electronic properties of intercalation graphite

The most important structural characteristic of graphite intercalation compounds is the occurrence of separate graphite and intercalant layers due to the very strong intraplanar binding and the very weak interplanar binding. Thus, the graphite layers retain the basic properties of pristine graphite, and the intercalant layers behave similarly to the parent intercalant material. These layers can in addition exhibit various types of ordering, the most important of which is the stage ordering along the *c*-direction. The stage index, *n*, denotes the number of graphite planes between adjacent layers and it is readily determined from XRD measurements. The 3D and 2D schemes of the intercalation graphite lattice are shown in Fig. 1.8.

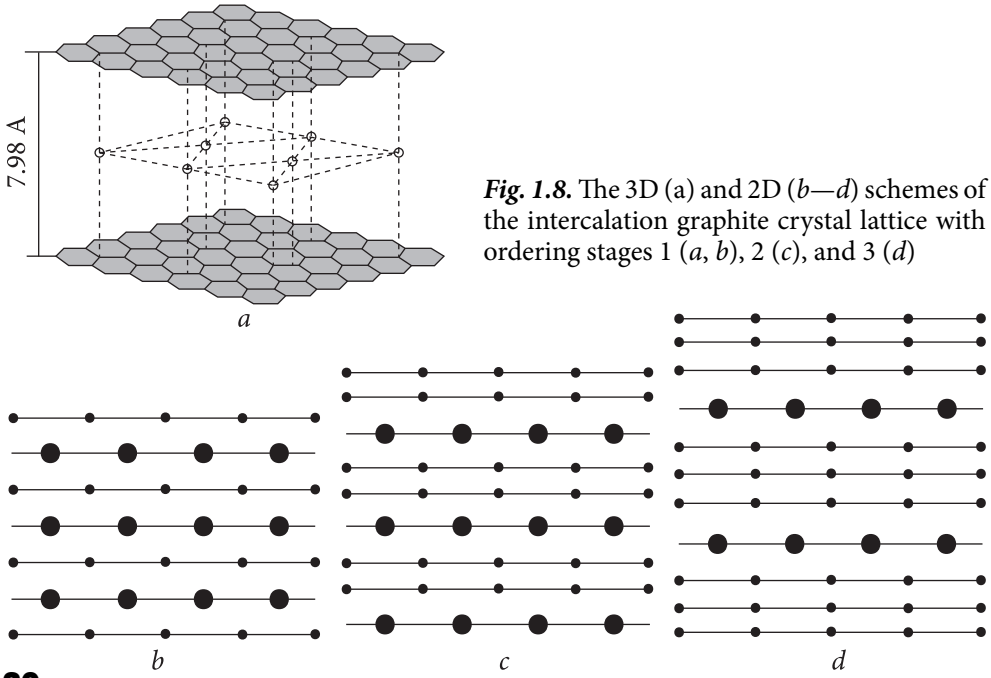

Fig. 1.8. The 3D (a) and 2D (*b*—*d*) schemes of the intercalation graphite crystal lattice with ordering stages 1 (*a*, *b*), 2 (*c*), and 3 (*d*)

Other types of ordering prevalent in graphite intercalation compounds include the stacking order of the graphite layers, in-plane ordering in the graphite and intercalant layers as well as the interlayer correlation between these layers, commensurate and incommensurate molecular ordering, and interlayer intercalant stacking order. In the following, these types of ordering are described and examples of intercalation compounds exhibiting each ordering type are given.

The graphite layers themselves exhibit definite stacking arrangements in the intercalation compounds. There are two basic types of graphite stacking arrangements: type I where the graphite layer arrangement about the intercalant layer is the same (A‖A) and type II where it is different (A‖B). In some cases, the stacking arrangement is temperature-dependent, and in other cases, more than one stacking arrangement can coexist at the same temperature.

An example of the type I stacking is found in stage I alkali metal compounds with the intercalants K, Rb, and Cs, where the stacking arrangement is A‖A‖A, while for stage 2 compounds, the stacking arrangement is AB‖BC‖CA‖AB, where the vertical line denotes an intercalant layer and A, B and C denote graphite layers [40]. For higher stage compounds, the graphite layers between two intercalant layers will alternate ABAB or ACAC, or BCBC in accordance with the usual stacking sequence in pristine graphite. A rhombohedral form of graphite also occurs, exhibiting the ABCABC stacking arrangement and corresponding to the space group R32/m [41]. For these compounds, the insertion of an intercalant layer results in a rhombohedral slippage across intercalant layers, though adjacent graphite layers retain their usual hexagonal ABAB stacking sequence. An example of the AB‖BA‖AB stacking sequence is found in graphite—SO_3 compounds. In the case of graphite—HNO_3 [42], an AB‖BA‖AB stacking has also been reported though [43] reported an AB‖BC‖CA stacking arrangement for this system.

Examples of the type II graphite layer stacking arrangement A‖B can be found in a number of acceptor compounds. E.g., the stage 2 graphite—SbF_5 compound exhibits the hexagonal type II arrangement AB‖AB‖AB [42] while for stage 4 graphite—$MoCl_5$ both the hexagonal A‖BABA‖BA and rhombohedral A‖BCAB‖ABCA‖B stacking arrangements have been reported [44]. For some intercalants such as H_2SO_4, both type I and type II graphite stacking arrangements were observed. E.g., for stage 2 graphite—H_2SO_4, both A‖AB‖BA‖AB‖B and A‖BA‖BA‖BA stacking arrangements have been reported in [42]. On the other hand, one cannot rule out the possibility of intercalation compounds (e.g., with large intercalant layer thickness d_i) where there is no stacking correlation between graphite layers on either side of the intercalant layer (or intercalant sandwich for the large molecular intercalants).

It is also of interest to point out that the intercalation process can be used to stabilize the hexagonal graphite stacking arrangement. E.g., when metastable

rhombohedral graphite is intercalated and subsequently desorbed, the stable hexagonal stacking remains [42].

The basic symmetry within the graphite interior layers remains unaffected by intercalation. Not only is the ABAB hexagonal stacking preserved but also the spacing between graphite layers in the intercalation compounds is essentially the same as in pristine graphite $c_0 = 3.35$ Å [45]. Small variations in interplanar spacing are expected for graphite layers adjacent to the intercalant layer (graphite bounding layers) because of the different charge distributions at this interface, but such variations in interplanar spacing have only been explored for a few cases. In this connection, Table 1.1 gives data on several donor and acceptor intercalants for the stage index dependence of the distance between graphite layers d_s where an intercalant layer is sandwiched. More succinctly, d_s is called the intercalant sandwich thickness.

Thus, the repeat distance, as measured by (00*l*) XRD, to a good approximation, is related to c_0 and d_s by the equation

$$I_c = d_s + (n - 1)\, c_0, \tag{1.1}$$

where $d_s \approx d_i + c_0$ (Table 1.2).

The intercalant layer thickness d_i must be greater than the Burgers vector for the stacking fault to occur, or $d_i \geq a_0/\sqrt{3}$. Na and Li fail to satisfy this criterion (Table 1.2) and would not be expected to stage in an A‖A configuration by the mechanism outlined here. This mechanism suggests a domain size that is inversely proportional to the stage index. The pairing of the Burgers vectors results in the stacking arrangement A‖AB‖BC‖CA for stage 2 compounds, in agreement with experimental observations on compounds with intercalants such as K, Rb, Cs, HNO_3. It should be mentioned in this connection that rhombohedral graphite, having the stacking sequence ABCABC is metastable and can be transformed into the commonly occurring hexagonal graphite by heating to high temperature or by undergoing intercalation-desorption cycles with an intercalant such as potassium [54].

The data in Table 1.1 show that for most *donor* compounds the intercalant sandwich distance d_s *increases* from stage 1 to stage 2 but it *decreases* for most *acceptor* compounds. For both donors and acceptors, d_s is in most cases essentially independent of the stage for $n \geq 2$. These conclusions are in agreement with preliminary results for the charge distribution of the graphite bounding layers as calculated from (00*l*) XRD intensity measurements, showing that for donor compounds the bounding layer charge distribution shifts towards the intercalanlayer and thus decreases the bonding between the graphite boundary layer and the graphite interior layer, whereas the acceptors show the opposite effect, namely an increase in bonding between the bounding layer and the interior layer [55]. Also consistent with these conclusions are EXAFS (extended

Table 1.1. **Metal sandwich thickness for some compounds of low stage [2]**

Intercalant	Metal sandwich thickness d_s, Å			References
	Stage 1	Stage 2	Stage 3	
K	5.35	5.39	5.40	[46]
Rb	5.65	5.70	5.70	[47]
Cs	5.94	6.01	—	[47]
Li	3.706	3.71	3.70	[48]
HNO_3	7.84	7.79	7.79	[49]
SO_3	7.96	7.90	7.90	[50]
$HClO_4$	7.94	7.77	7.60	[49]
Cl_2O_7	7.98	7.78	7.70	[50]
$SbCl_5$	9.42	9.36	9.36	[51]
SbF_5	8.46	8.41	8.41	[51]
Br_2	—	7.04	7.04	[52]
$AlCl_3$	9.54	9.48	—	[49]
$FeCl_3$	9.37	9.45	9.51	[49]
AsF_5	—	8.15	—	[53]

Table 1.2. **Intercalant layer thickness d_i for various intercalants [2]**

Intercalant	Thickness d_i, Å	Intercalant	Thickness d_i, Å	Intercalant	Thickness d_i, Å
K	2.05	HNO_3	4.44	$AlCl_3$	6.13
Rb	2.35	$SbCl_5$	6.01	$FeCl_3$	6.10
Cs	2.66	SbF_5	5.06	$NiCl_2$	5.98
Li	0.35	Br_2	3.69	AsF_5	4.80

X-ray absorption fine structure) measurements on graphite-K samples [56]. These experiments are sensitive to the carbon-potassium distances and confirm the d_s increase in from stage 1 to stage 2 compounds.

The in-plane ordering in the graphitic planes is the same as in pristine graphite, with approximately the same in-plane lattice constant a_0 = 2.46 Å, or the nearest neighbor carbon-carbon distance of 1.42 Å [41]. A small in-plane expansion due to intercalation has, however, been found for graphite-K donor compounds by [57], with an approximately linear dependence of the nearest-neighbor carbon-carbon distance on reciprocal stage ($1/n$) given by

$$d_{C\text{-}C} = (1.4203 + 0.0113/n)\ \text{Å}. \quad (1.2)$$

The work [58] on other donor stage 1 compounds yielded a relation between d_{C-C} and the ionic radius r and the valence Z of the metal ($Z = 1$ for alkali metals, 2 for alkaline earths and 3 for lanthanide metals):

$$d_{C-C} = (1.420 + 0.032\ 66Z/r)\ \text{Å} \quad \text{for } C_8X; \tag{1.3}$$

$$d_{C-C} = (1.420 + 0.019\ 58Z/r)\ \text{Å} \quad \text{for } C_6X. \tag{1.4}$$

For all the donor intercalants examined, K, Cs, Li, Ba, Sr, Eu, and Yb, intercalation resulted in a lattice expansion. The dependence of d_{C-C} on $1/n$ is consistent with a sharing between graphite layers of the lattice strain resulting from intercalation. The observed dependence of d_{C-C} on Z is also consistent with the expected increase in strain associated with increased intercalant layer charge, though the larger increase in d_{C-C} for C_8X as compared with C_6X structures has not yet been clarified.

Raman scattering experiments suggest that a small in-plane contraction occurs in a number of acceptor compounds [59, 60] in contrast with the in-plane expansion reported for donor compounds. (Similar Raman data will be discussed in detail below in Chapter 6). Such a contraction in acceptor compounds has recently been verified by direct XRD measurement in $NiCl_2$ [61], AsF_5 [62], $FeCl_3$, and $AlCl_3$ [63] compounds, and the contraction was shown to be much smaller in acceptor compounds than the expansion in donor compounds of the same stage.

Although a great deal less is known about the structure of a large number of molecular intercalation compounds, it is well established that well-staged compounds can be prepared and that the intercalant layers are closely related to layer planes in the parent crystalline materials. The molecular intercalants tend to occupy relatively large volumes, resulting in large intercalant sandwich thicknesses d_s (Table 1.1), which have been measured for many compounds and summarized in several review articles [42, 64, 65]. The intercalant in most cases retains its molecular identity, though in other cases, changes occur upon intercalation. E.g., halogens (Br_2, ICl and IBr) and some metal chlorides such as $FeCl_3$ and $AlCl_3$ are believed to maintain their molecular identity, while highly reactive acid intercalants such as HNO_3, AsF_5, $SbCl_5$, and H_2SO_4 are believed to transform upon intercalation [42, 64].

Phase transitions in intercalation graphites. Graphite intercalation compounds exhibit many different ordered structures or phases (see Chapter 2). Various types of transitions between these phases have been reported, including structural transitions associated with changes in stage, interlayer ordering, and plane ordering as well as magnetic and superconducting transitions. Structural phase transitions have been induced by variation of the temperature, pressure, and, in some cases, the intercalant vapor pressure. To date, only a few of the observed phases have been completely interpreted, and correspondingly few transi-

tions between these phases have been carefully studied. Complete phase diagrams as a function of temperature and intercalant density have not yet been determined for even the simplest compounds (e.g., graphite-alkali metal compounds) [2].

One class of phase transitions is represented by the stage change $n \leftrightarrow n-1$. Such transitions have been documented on a *static* basis using (00*l*) XRD data showing that changes in growth conditions can produce a transition from one distinct stage to another, as predicted by a growth diagram, such as shown for alkali metal compounds with K. During the stage changing, both stages are in equilibrium. Dynamically, transitions between stages $n \leftrightarrow n-1$ have been identified on the basis of stable regions in the intercalation isotherms [52, 66] and in dilatation-time plots [67]. Thermodynamic changes associated with the stage transition $n \leftrightarrow n-1$ have been measured and both entropy and enthalpy changes were determined for a number of stage transitions in compounds containing the donor intercalants K, Rb and Cs, as well as the acceptor H_2SO_4 [68, 69]. The kinetics and thermodynamics associated with the stage transition were discussed. Those studies showed that the staging transition is of the first order and exhibits hysteresis during intercalation-deintercalation cycles [2].

Another type of phase transition relevant to *c*-axis ordering relates to the intercalant interlayer stacking ordering observed in low stage alkali metal compounds. A simple example of such a phase transition has been observed in [70] for C_6Li where a reversible transition is found between the low temperature phase exhibiting αβγ intercalant layer stacking order (for $T < 220$ K) and another phase above ~220 K with either random interlayer stacking order, or αα stacking order as suggested in [71] for the room temperature intercalant arrangement. A similar reversible transition has also been reported on the basis of electron diffraction studies by [72] for stage 1 C_8Rb from the low-temperature phase in which the interlayer stacking sequence is αβγδ to a higher temperature phase above ~300 K which lacks this stacking order. The observation of αβγδ intercalantant stacking order at 290 K, and αβ intercalant stacking at 721 K on C_8Rb has been reported in [73]. The disappearance of a well-defined superlattice pattern above 747 K was interpreted in terms of the onset of a liquid-like or highly disordered intercalant arrangement [73]. Phase transitions associated with changes in interlayer intercalant stacking order are also found in stage 2 alkali metal compounds, but in these cases the interlayer stacking transition is also accompanied by a change in the in-plane intercalant ordering, as discussed below [2].

The transitions associated with a commensurate to incommensurate ordering relative to the graphite layer provide another class of transitions. Such transitions have been observed in connection with structural transitions of adsorbed rare gases on graphite. E.g., epitaxial monolayers of solid krypton on a graphite surface exhibit a second-order phase transition from a commensurate p $(\sqrt{3} \times \sqrt{3})$ R30° structure to a denser incommensurate structure as the krypton

vapor pressure is increased above a critical value [74, 75]. Commensurate-incommensurate transitions have also been observed in stage 2 alkali metal compounds as described below, but they are also reported to be accompanied by a change in intercalant interlayer stacking order [2].

Another example of a commensurate ↔ incommensurate phase transition that may occur in intercalated graphite is the charge density wave transition. Arising from a strong electron-phonon interaction, charge density waves form incommensurate superlattices whose periodicity is governed by Fermi surface wave vectors rather than reciprocal lattice vectors. In [23], it has been pointed out that the stage 1 Fermi surface in C_8K is theoretically favorable for the occurrence of charge density waves. From the experimental side, several tentative identifcations of observed phenomena with charge density wave transitions have been made but in no case has the evidence been compelling. Certain phase transitions in graphite-Br_2 and in graphite-Cs compounds observed by electron diffraction [76] were tentatively identified with charge density waves, though no clear connection of the transition with the Fermi wave vector was demonstrated. There were identified sideband XRD reflections with a static distortion wave (SDW), associated with the lattice strain introduced by an incommensurate intercalant [77, 78]. However, they were careful to distinguish their mechanism for superlattice formation from a Fermi surface instability which gives rise to charge density waves (CDW). In addition, certain DHVA frequencies observed in graphite-Br_2 were attributed to CDW-induced orbits [79].

The phase transitions involving changes of in-plane ordering provide a second main category of phase transitions in graphite intercalation compounds, and such phase transitions have been both considered theoretically and observed experimentally. The theoretical work [80] for interacting adsorbed rare gas overlays on graphite surfaces shows phase diagrams as a function of adsorbate concentration with many in-plane structures commonly found in intercalated graphite. These phase diagrams indicate that coexisting phases occur at most temperatures and adsorbate concentrations.

In the intercalation compounds, phase transitions from one in-plane intercalant arrangement to another have received considerable attention to donor compounds, particularly to the series of phase transitions occurring in the stage 2 alkali metal compounds with K, Rb, and Cs [77, 81—87]. In addition to the structural changes discussed in those references, XRD measurements of in-plane intercalant density have been made in [88], which when combined with the suggested superlattice structure, imply the stoichiometry of the intercalation compound. Since the adsorbed phases on graphite are very sensitive to the adsorbate concentration [89], it seems likely that the same is true for intercalant layers. In the intercalation compounds, both the in-plane order and the interplanar (stacking) order are expected to be sensitive to the in-plane intercalant

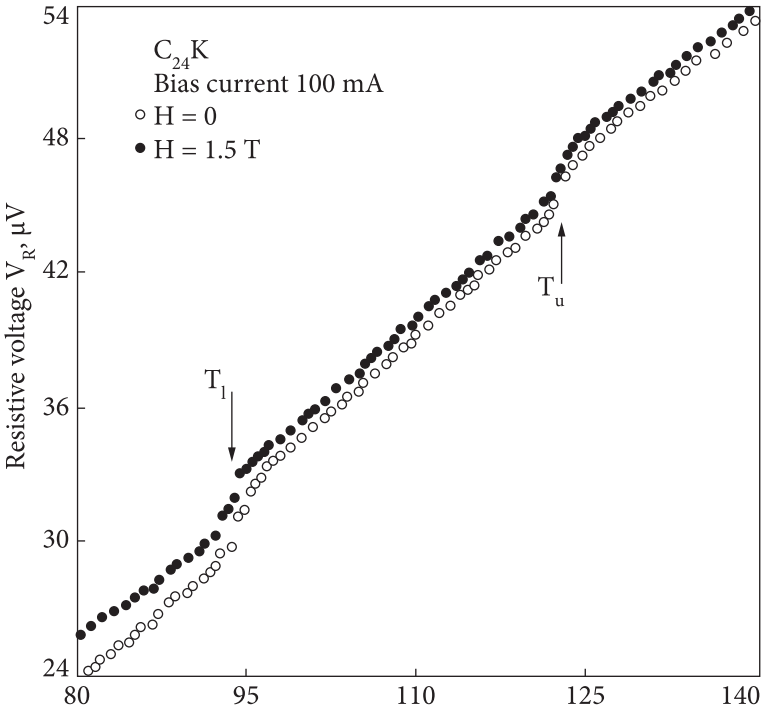

Fig. 1.9. Measurements of resistivity versus temperature for stage 2 graphite-K at zero magnetic field (open circles) and for H =1.5 T (closed circles). The transition temperatures of T_l = 95 K and T_u = 124 K are indicated [93]

density. Some of the differences in structure reported by other researchers may be related to the fact that though the compounds are of the same stage, the in-plane densities may differ. E.g., stage 1 graphite-K was observed with an in-plane p ($\sqrt{3} \times \sqrt{3}$) R30° structure which corresponds to C_6K stoichiometry [90], the usual p (2 × 2) R0° strcture corresponding to C_8K [91], and a high temperature presumably mixed and/or incommensurate $C_{10}K$ purple phase [92].

Because of the found variety of in-plane phase transitions, the stage 2 alkali metal compounds have provided an important means to study the physics of phase transitions. An overview of these transitions is provided by the temperature- dependent resistivity measurements on stage 2 compounds with K, Rb, and Cs (Fig. 1.9), revealing similar resistivity anomalies and defining lower and upper transition temperatures T_l and T_u respectively for each of the compounds [93, 94].

For the case of Cs, single crystal XRD measurements give evidence to p (2 × 2) and p (3 × 3) ordered structures below 50 K, while for 50 K < T < T_l, a ring pattern, modulated by 12 sidebands, was reported and interpreted in terms of an in-plane incommensurate ordering [70, 88], though c-axis intercalant interplanar AαABβBCγC ordering and commensurate in-plane ordering were also reported

for this temperature range [46, 82]. Above T_l, short-range *c*-axis correlation and long-range orientational order were reported by [95]. Also, for the Cs compound, a second-order transition at T_u, similar to that shown for potassium, was found [95]. An intercalant melting temperature of $T = 608$ K was also reported in [84].

The transition temperatures associated with structural transitions can also be obtained by studying anomalies in transport and other properties of intercalated graphite. Phase changes are often accompanied by changes in scattering mechanisms which give rise to changes in transport properties. In alkali metal donor compounds, resistivity anomalies at T_l and T_u, which yielded transition temperatures in good agreement with values obtained from structural studies, were observed [93, 94]. A summary of their results for donor compounds with stages $n = 2$, 3, and 4 is given in Table 1.3. For $n \geq 2$ the stage dependence of the transition temperatures is weak, in general. These authors, however, found no resistivity anomalies for stage 1 alkali metal compounds, where the phase transitions, as observed by electron diffraction, involve only a change in interlayer intercalant stacking order and no change in the close-packed in-plane arrangement [2].

Phase transitions in molecular acceptor compounds have also been studied. In most cases, they give rise to larger changes in the pertinent observances than do donor compounds. Also, in them, phase transitions have been detected by more diverse techniques than for the donor compounds. On the other hand, dffraction studies on donor compounds have yielded more detailed information than for the acceptors.

The acceptor system that has received more attention in this connection is the graphite-HNO_3 system. By measuring the intensity of (*hkl*) XRD reflections [43], the authors could draw a number of conclusions concerning the unit cell dimensions, appropriate space group, the in-plane intercalant ordering, stacking order of the graphite layers, and interlayer intercalant correlation. In the low

Table 1.3. **Phase transition found for various donor and acceptor compounds [2]**

Intercalant	Stage	Transition temperature, K	Metod	References
K	3	87, 112	Resistivity	[96]
K	4	92, 250	"	[94]
K	5	~200, ~230	"	[97]
Rb	4	~220	"	[97]
Cs	5	~190, ~230	"	[97]
HNO_3	1,2,3	253	Thermal expansion	[98]
	2,3,4	~250	XRD	[43]
	1	~250	Resistivity	[99]

temperature phase ($T < 252$ K), they found the basic intercalant in-plane structure to be commensurate with the graphite layers and to exhibit some interlayer intercalant correlation in the *c*-direction. Above 252 K, both the interlayer correlation and the in-plane ordering were found to disappear. For $T > 252$ K, the HNO_3 intercalant was described as liquid-like [43], and the phase transformation was classified as an order-disorder transformation. The transition to a liquid-like state is also consistent with motional narrowing effects observed in the proton NMR line [100, 101], giving rise to sharp, discontinuous jumps in the spin-lattice relaxation time T_1, and in the spin-spin relaxation time T_2. Closely related to these discontinuous changes in T_1 and T_2 is the large increase in the ESR linewidth of the line as T was lowered below 250 K [102].

The anomaly in the thermal expansion and the corresponding to the discontinuous decrease in the *c*-axis lattice constants of 0.044, 0.048, and 0.052 Å for stages $n = 1$, 2, and 3, respectively, are also associated with this order-disorder transition in graphite-HNO_3, as the sample was cooled through the transition temperature, which showed little stage dependence [98]. The larger *c*-axis spacing above the transition temperature might be necessary to stabilize the large molecular intercalant in the liquid zone. An anomalous peak in the thermoelectric power at the transition temperature was found in [99] and attributed to the additional scattering of holes. In addition, large anomalies were later reported to be near 250 K in the electrical resistivity, magnetoresistance, and Hall effect [103]. Using the differential scanning calorimetry technique, the authours of [104] acquired additional information about the thermodynamics of this order-disorder transition. They showed that there are in fact two distinct anomalies closely spaced in temperature, the exothermic peaks occurring at 250 ± 1 K and 254 ± 1 K and the endothermic peaks at $T_1 = 252.0 \pm 0.2$ K and $T_2 = 261.5 \pm 0.2$ K, both peaks being associated with the first-order transitions. Their analysis yielded values for the change in enthalpy and entropy of $\Delta H_1 = 370 \pm 3$ cal/mol, $\Delta H_2 = 46 \pm 1$ cal/mol, $\Delta S_1 = 1.43 \pm 0.01$ cal/mol K, and $\Delta S_2 = 0.16 \pm 0.01$ cal/mol K, where it was noted that $\Delta S_1 = R\ln 2$ within experimental error. The low-temperature resistivity and Hall effect measurements on graphite-HNO_3 compounds have identified an additional sharp anomaly slightly below 30 K, which they attributed to a structural phase transition between two ordered phases [97]. The explicit identification of the structure of the low-temperature phase awaits further diffraction studies. As for the graphite-AsF_5 system, a broad phase transition is observed at 200 K for stage 1 and near 220 K for stage 2 compounds using susceptibility, electron spin resonance, and resistivity measurements [105—107]. A sharp phase transition was also observed in the graphite—AsF_5 system at low temperature (21 K) as a resistivity anomaly [107]. A phase transition has also been found in the graphite—H_2SO_4 system at 199 K as a result of the resistivity anomaly in [108].

Electronic structure of graphite intercalation compounds. A major simplification is made in treating the electronic structure of graphite intercalation compounds by recognizing the strong similarity of the structural and electronic properties of graphite intercalation compounds to those of their parent constitutive materials, the graphite host and the intercalant [1, 2]. The physical basis for this identification arises from the strong *intralayer* binding in both graphitic and intercalant layers and the relatively weak *interlayer* binding between graphite-intercalant and graphite-graphite layers in the intercalation compounds. A close relationship between the graphite intercalation compounds and their parent materials implies that in the dilute intercalant concentration limit, the electronic structure is closely related to that of pristine graphite.

Several first-principles band structure calculations have been carried out for graphite intercalation compounds, but all have so far focused on stage 1 compounds. The restriction to stage 1 is brought about by the complexity of the problem for higher stage compounds. This complexity can be appreciated from the following example. For the simplest intercalation compound, stage 1 C_6Li, there are six carbon atoms and one Li atom per unit cell, assuming αAαAα interlayer graphite (A) and intercalant (α) stacking order. Thus, C_6Li has 39 occupied orbitals out of a total of 70 orbitals, considering all $1s^2 2s_2 2p^6$ levels for both C and Li atoms. The unit cell for stage 2 graphite-(1.5)Li with the same in-plane superlattice p ($\sqrt{3} \times \sqrt{3}$) R30°, and assuming CAαABαBCαCA *c*-axis interlayer stacking order, contains 36 carbon atoms and three lithium atoms, which to the same $1s^2 2s^2 2p^6$ levels gives 390 orbitals, 225 of which are occupied. Because of the large number of orbitals that are involved in the higher stage compounds, the first efforts toward first principles band calculations have been made for stage 1 compounds with small unit cells [2].

The band structure for the simplest graphite intercalation compound, the first stage C_6Li with a p ($\sqrt{3} \times \sqrt{3}$) R30° in-plane superlattice, was first calculated by [109—111], assuming an αα interlayer intercalant stacking. This material is amenable to any of the standard band calculational methods, and excellent results for E (**k**) are expected using current techniques. From the basic calculation for αα intercalant stacking, it could be possible to calculate E (**k**) for other stacking sequences (such as αβα or αβ) using perturbation theory. For their treatment, the authors [111] used a modified KKR method based on an ionic potential for $C_6^- Li^+$ and obtained the energy bands along high symmetry directions shown in Fig. 1.10, which refers to the hexagonal Brillouin zone in Fig. 1.4. It is worth noting that the bands in Fig. 1.10 derived from folding of the graphite π-bands (dashed lines) remain highly graphitic in the intercalation compound. The band labelled 1^+ in Fig. 1.10 is derived from the Li *s*-band. Since the Li 1^+ band lies above the Fermi level throughout the Brillouin zone, it is concluded that the Li intercalant is fully ionized (fractional charge transfer $f = 1$) with one electron/Li atom transferred to the graphite bands. It is also of interest to note the very

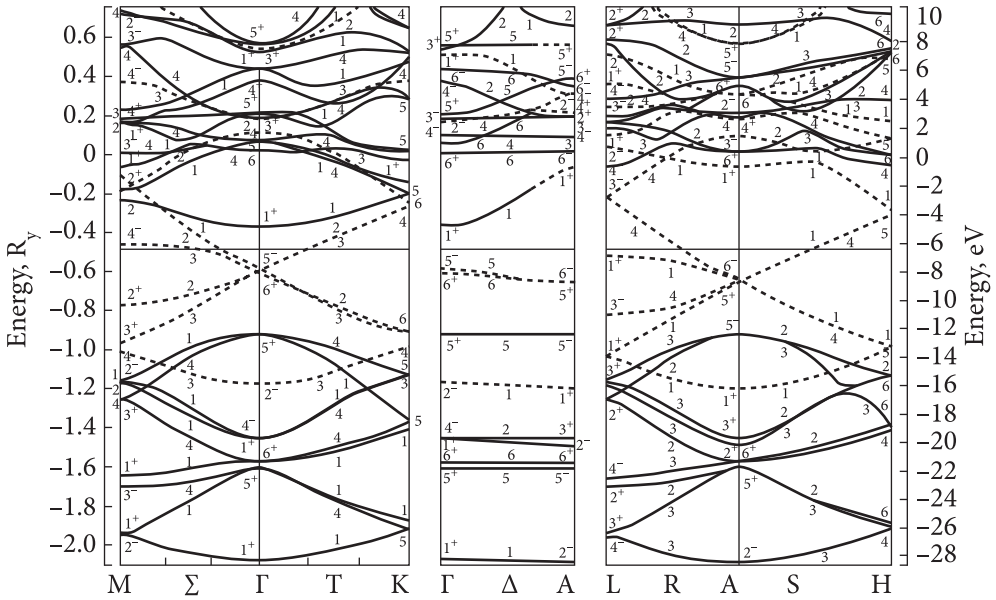

Fig. 1.10. Band structure of C_6Li by [111] based on an ionic crystal potential ($C_6^-Li^+$). Carbon π-bands are represented by dashed lines; σ-bands are represented by solid lines. Dispersion relations are shown along M-Σ-Γ-T-K ($k_z = 0$ plane), Γ-Δ-A (the k_z direction), and L-R-A-S-H ($k_z = \pi/I_c$ plane). Note that the Li *s*-bands lie above the Fermi level [2]

weak dispersion of the graphite π-bands along k_z, and the greater dispersion for the lithium 1^+ band along k_z.

The data of [111] about high symmetry directions evaluated coeffcients for an LCAO interpolation expansion were used to obtain energy bands throughout the Brillouin zone [112]. These LCAO-derived energy bands were then used to calculate the Fermi surface. Effective masses and de Haas-van Alphen cross-sectional areas for six principal orbits on the Fermi surface thus obtained are given in Table 1.4 for the two bands which give rise to the Fermi surface.

As the Li 1^+ band lies above the Fermi level and is only weakly hybridized with the graphite π-bands, the Fermi surfaces are of primarily graphite π-band character.

Experimental confirmation of the one-electron energy dispersion relations calculated by [111] has come from angle-resolved photoemission energy distributions measured in [113], where Γ-point energies in excellent agreement with the [111] calculations were obtained [2]. For the graphite bands that are not zone-folded, there is a clear indication of the levels in the intercalation compound with those in the graphite host.

The extension of these first principles calculations to higher stage compounds has not yet been carried out. For the higher stage compounds, phenom-

enological models have been developed, and application of these models have been made to the interpretation of experimental results. The first principles calculations for stage 1 compounds discussed above provide strong evidence for the predominantly graphite π-band nature of the occupied states. This fact coupled with strong experimental evidence that the structural, electronic and lattice properties of the intercalation compounds are largely graphitic in character suggests that a phenomenological model for the electronic structure should be based on the graphite π-bands, with appropriate perturbations introduced to account for the intercalant-graphite bounding layer interaction. Various phenomenological models based on this idea have been proposed to discuss experimental results on graphite intercalation compounds [2].

A phenomenological model which makes direct contact with both the SWMcC model and the first principles band calculations for stage 1 alkali compounds has been discussed in [114]. This phenomenological model, which gives E (**k**) throughout the Brillouin zone, makes use of the 3D Fourier expansion of the graphite π-bands, previously developed by [115] to account for the optical properties of pristine graphite (see also Chapter 6). The superlattice periodicity appropriate to the intercalation compound is added to the basic graphite symmetry through suitable zone folding of the Brillouin zone for pristine graphite. The effect of the intercalant layer is treated by substitution of an intercalant layer Hamiltonian for one appropriate to a graphite layer. The interaction between graphite bounding layers and the intercalant layer is treated as a perturbation dependent on the band parameters related to the overlap between the graphite π-band p_z orbitals and orbitals on the intercalant layer. These band parameters can be evaluated by comparison with either first principles calculations or experimental Fermi surface, optical and magnetic-optical data [2].

It can be noted that the dispersion of the energy bands along k_z is very small (Fig. 1.11), which arises from the confinement of carriers within the n contiguous graphite layers between two consecutive intercalant layers. Such a

Table 1.4. **Frequencies and masses from the band calculation for C_6Li [111]**

Band	Orbit		Carrier type	DHVA frequency (10^4 T)	m/m_0
	Plane	Centre			
1 Lower	$k_z = 0$	Γ	Electron	0.40	0.98
2 Upper	$k_z = 0$	Γ	"	0.21	0.32
3 Lower	$k_z = \pi/I_c$	H	Hole	0.54	0.64
4 Upper	$k_z = \pi/I_c$	A	Electron	0.48	0.47
5 Lower	$k_x = 2\pi/3A_0$	L	"	0.20	0.71
6 Lower	$k_y = 0$	M	Hole	0.55	2.13

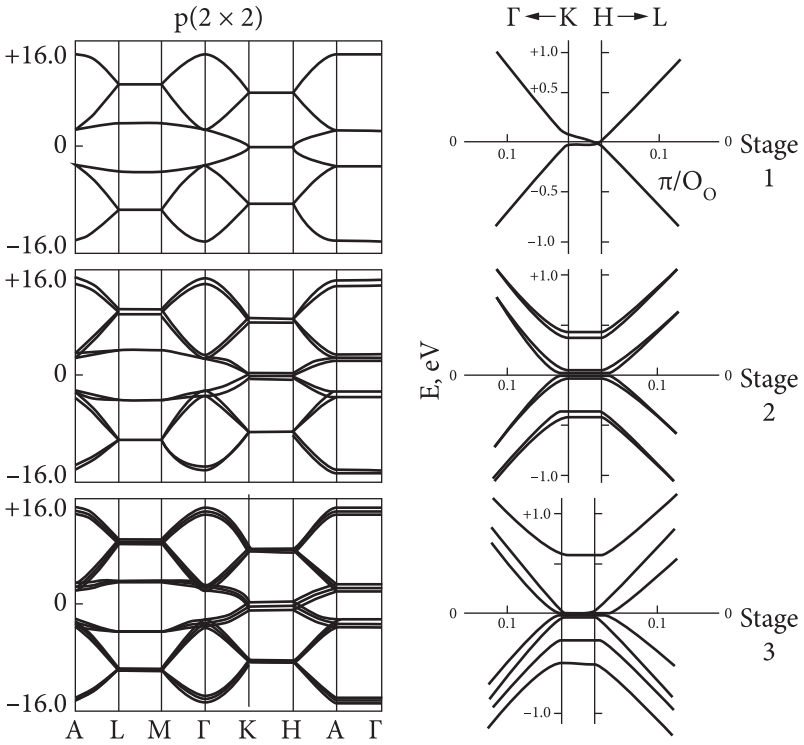

Fig. 1.11. Electronic energy levels derived by zone folding of the SWMcC dispersion relations for a p (2 × 2) superlattice [2, 55]

carrier confinement was also considered in connection with a phenomenological model for E (**k**) based on a single set of n contiguous layers bounded by two intercalant layers [116]. Though the original graphite SWMcC bands display a larger dispersion in the k_z-direction than do the bands in Fig. 1.11 for the intercalation compound, the same number of states is in both cases contained in an energy interval comparable to the bandgaps in the intercalation compound.

The first principles calculations for the stage 1 compounds C_6Li and C_8K yield screening of the intercalant layer by the graphite bounding layers directly by mapping the z-dependence of the charge density from the wave functions of the electron orbitals. For the phenomenological models used to calculate the dispersion relations for the higher stage compounds, this screening effect is treated as part of the intercalant-graphite bounding layer interaction. This interaction is explicitly evaluated from comparison with a first principles calculation for stages $n = 1$ and $n = 2$ (if available), or from a non-linear Thomas — Fermi screening calculation as described below. It is then argued that for a given intercalant, the intercalant-graphite bounding layer sandwich for higher stage compounds has approximately the same interactions as for the stage 2 compound.

The effect of screening of the intercalant by the surrounding graphite layers has been explicitly considered by [117, 118] who applied the Thomas — Fermi model to calculate the screen charge distribution ρ (z) as a function of distance z from the intercalant layer for a dilute compound. Their results are expressed in a simple analytical form [2]:

$$\rho(z) = 3z_0^3 (z + z_0)^{-4}, \tag{1.5}$$

where the characteristic screening length z_0 is related to the Fermi velocity v_F and the transverse dielectric constant $\varepsilon_\perp$ by

$$z_0^3 = \left(\frac{\varepsilon_\perp}{6e^2} \hbar v_F \right) \frac{c}{\pi \rho_0}, \tag{1.6}$$

where ρ_0 is the two 2D charge density at $z = 0$. Using values for $\rho_0 = 6.4 \times 10^{14}$ cm^{-2} and $\varepsilon_\perp = 3.4$, a characteristic length of $z_0 = 4.0$ Å is obtained [118], which corroborates a number of experimental results that show the intercalant layer to be effectively screened by a single graphite bounding layer. In principle, a self-consistent band calculation accounts for these screening effects directly [2]. On the other hand, the Thomas — Fermi treatment of the screening phenomenon has been applied to modeling the electrical conductivity [117, 118], the dielectric response [118], and the magnetic susceptibility of intercalated graphite [119].

Several interpretations of the quantum oscillatory phenomena in graphite intercalation compounds have been made in terms of graphitic constant energy surfaces [2]. Many of the observed DHVA frequencies in both donor and acceptor compounds are greater by several orders of magnitude than those in pristine graphite. This observation is interpreted as a large increase in the Fermi surface cross-sectional areas resulting from the transfer of charge from the intercalant to the graphite layers. The large increase in carrier density thus obtained is consistent with the large increase observed in the low frequency electrical conductivity and the observation of metallic plasma edges in the optical reflectivity. Since in most cases, accurate measurements have not been reported for large angles ($\Theta \sim 90°$), the anisotropy data do not distinguish between an open cylindrical 2D Fermi surface, and the highly elongated ellipsoid-like closed Fermi surfaces that occur in pristine graphite [2].

Very small cyclotron effective masses were observed comparable to ones in pristine graphite for some of the DHVA frequencies, while for other electron and hole orbits, large effective masses were reported. The cases where small effective masses were found include $m^*/m_0 = 0.075$ for the δ orbit in $C_{48}K$ by [120]. Some small effective masses in the graphite-$FeCl_3$ system have also been reported in [121]. Thus, small masses have been found for both donor and acceptor compounds. In contrast, higher effective masses in the range

$0.1 < m^*/m_0 < 1.2$ were reported for graphite–HNO_3 compounds [122]. Because of the wide range of effective mass values reported, systematic measurements of the masses associated with each of the DHVA frequencies are needed for application to the transport properties.

Application of the first principles calculations is possible only for the measurements on C_8K, where, as shown below, good agreement is obtained between experiment and the theoretical model. For C_8K a single DHVA frequency of 2875 T has been identified experimentally. On the basis of the Fermi surface for C_8K calculated in [123], this high DHVA frequency is identified with the large cylindrical pieces of Fermi surfaces located about the edges HKH of the Brillouin zone, which have a calculated DHVA frequency of 3030 T, in good agreement with the experimental value. Although the Fermi surface calculation explains this high DHVA frequency quantitatively, no DHVA frequencies have been observed corresponding to the more spherical (3D) pieces of Fermi surface given by the calculation about the Γ- and A-points in the Brillouin zone [2].

Conductivity of graphite intercalation compounds. The most widely studied property of graphite intercalation compounds is their electrical conductivity, mainly due to two distinguishing characteristics: the high in-plane conductivity σ_a and the large anisotropy of the in-plane to *c*-axis conductivity (σ_a/σ_c) that can be produced by intercalation [124, 125]. The ability to prepare intercalation compounds with room temperature conductivities comparable to that of copper but with one-fourth the mass density offers attractive commercial applications. A detailed review of the transport properties of graphite intercalation compounds was given in [126].

Electrical conductivity studies have been made on a wide variety of donor and acceptor compounds, and some typical values for stage 1 compounds are given in Table 1.5. The large electrical anisotropy, resulting from the high in-plane conductivity σ_a relative to the low *c*-axis conductivity σ_c, makes accurate measurement of the conductivity tensor in the intercalant compounds diffcult and a variety of special techniques have been developed to make measurements of improved reliability [107, 124, 127—129]. For the donor compounds, the electrical anisotropy is not large enough to invalidate the use of the conventonal four-point method, and thus the four-point method is commonly used. For the acceptor compounds, the high anisotropy in the conductivity prevents unevenly injected current from becoming uniformly distributed over the sample, and the injected current tends to be concentrated in those layers where the current lead makes good electrical contact, so that the effective conducting cross-sectional area is less than the geometrical area. For this reason, contactless radiofrequency (r.f.) measurements have been developed, utilizing eddy currents generated by the r.f. magnetic fields. Similar arguments can be made in support of the use of r.f. contactless methods for the measurement of other transport properties in

acceptors such as magnetoresistance and Hall effect. Additional complications are associated with the tendency of the samples to cleave, exfoliate, form microcracks and desorb. The use of multistage and poorly characterized samples sometimes made it diffcult to compare measurements by different workers. In Table 1.5 values for σ_a using the r.f. contactless method are quoted for acceptor compounds, where available [2].

The most widely studied aspects of the conduction behaviour is the large increase in the in-plane conductivity with increasing concentration for both donor and acceptor intercalants. An order of magnitude increase in σ_a is obtained for many intercalants, but the largest increases are found in strong acid acceptor intercalants, especially AsF_5 which has been reported by [137, 138] to have a room temperature value for $\sigma_a = 6.2 \cdot 10^5\ \Omega^{-1} \cdot cm^{-1}$ greater than or comparable to that in copper, $\sigma = 5.8 \cdot 10^5\ \Omega^{-1} \cdot cm^{-1}$. The large increase in σ_a can be inerpreted in terms of physics in the following way. Graphite, the host material, has a high in-plane mobility: room temperature mobility = 13000 $cm^2/V \cdot s$ as compared to Cu with 35 $cm^2/V \cdot s$ and to Si with 1600 $cm^2/V \cdot s$ [12, 143]. Despite its high carrier mobility, graphite has a modest conductivity because of its low carrier concentration, with a room temperature value of $\sim 2 \times 10^{-4}$ carriers/atom (or $\sim 2 \times 10^{19}\ cm^{-3}$). The intercalation process provides a mechanism for injection of carriers (electrons for donors and holes for acceptors) from the intercalant layer, which has a relatively low carrier mobility, to the graphite layers, which have a high carrier mobility. A similar transfer of carriers from a low

Table 1.5. **Room temperature in-plane conductivity σ_a for a number of stage 1 donor and acceptor compounds[a] [2]**

Intercalant	σ_a ($\Omega^{-1}cm^{-1}$)	References	Intercalant	σ_a ($\Omega^{-1}cm^{-1}$)	References
Pristine graphite	2.5×10^4	[12]	HNO_3	1.6×10^5	[124, 135, 136]
K	1.1×10^5		AsF_5	4.7×10^5	[137, 138]
Rb	1.0×10^5	[108, 124, 126, 130, 131]	SbF_5	5.0×10^5	[139—141]
			H_2SO_4	2.3×10^5	[108, 124, 135]
Cs	1.0×10^5				
Li	2.4×10^5	[108, 132]	$SbCl_5$ (stage 3)	1.3×10^5	[139, 141]
Br_2 (stage 2)	2.2×10^5	[124, 133, 134]	$FeCl_3$	1.1×10^5	[142]
ICl	3.5×10^5	[124, 134]	$AlCl_3$	1.6×10^5	[124]

[a] For HOPG, $\sigma_a = 2.5 \times 10^4\ \Omega^{-1}cm^{-1}$ and for OFHC copper, $\sigma = 5.8 \times 10^5\ \Omega^{-1}cm^{-1}$ [12]. Conductivity values are given for stage 1 compounds unless otherwise indicated. It should be noted that the maximum conductivity does not usually occur at stage 1. Representative values for ¼*a* are listed, with some scatter found among values reported by the various authors.

mobility doped region ($GaAl_xAs_{1-x}$) to a high mobility undoped region (GaAs) also occurs in the superlattice semiconductor layer materials grown by molecular beam epitaxy [144, 145].

Because of release of carriers from the intercalant layer, this layer becomes charged, positively for donors and negatively for acceptors. The released charge gives rise to a charge density in the graphite layers that falls off rapidly with distance measured from the intercalant layer. The screening length is approximately the thickness of a single graphite layer, the graphite bounding layer (see the Raman spectroscopy data in Chapter 6), the Fermi — Thomas screen calculation [117, 118], along with other data. We thus assume that the graphite bounding layers (adjacent to the intercalant layers) have a high current density due to their high carrier density and that the current density on the graphite interior layers is much lower and can be approximated by some average value [2].

In modelling the conductivity, one thus assumes that the graphite bounding layers make the major contribution to the in-plane conductivity. Though smaller in magnitude, the contribution from the graphite interior layers can be significant in some cases, particularly for alkali metal compounds. For most intercalants, the conductivity in the intercalant layer is negligibly small for several reasons: (1) the mobile electron and hole carrier density tends to be low; (2) the carrier mobility is relatively low, and (3) ionic mobilities tend to be very low. This interpretation assumes that the Fermi level lies below the intercalant conduction band but above the intercalant valence levels as shown explicitly by the energy band calculation for C_6Li [24—26]. As for C_8K, it is however clear that the electrons associated with the 1^+ potassium *s*-band will make a significant contribution to the conductivity.

The in-plane conductivity for very dilute alkali metal compounds (e.g., stage 15 graphite-K) has been measured in [108]. Taking into account the threefold to fourfold increase in conductivity relative to graphite, the authors concluded that the intercalant is present in an ordered array and not as a statistical distribution even in such dilute compounds This observation together with XRD results on dilute compounds support a layered model for graphite intercalation compounds over a wide intercalant concentration range [2].

Contributions from graphite interior layers are significant when the charge transfer to them is appreciable and the carrier mobility in the graphite interior layers is significantly higher than that in the graphite bounding layers. The experimental conductivity data (e.g. in [108]) show that the maximum conductivity is found in alkali metal donor compounds with K, Rb, and Cs at a higher stage ($n = 3$ to 5) than for the acceptor compounds where the maxima in most cases occur for $n = 2$. These results suggest that the contribution from the graphite interior layers is greater for the graphite-alkali metal compounds with K, Rb, and Cs than for the acceptor compounds of the comparable stage with

intercalants such as AsF_5, SbF_5, HNO_3, and Br_2. This conclusion is also in agreement with magnetoreflection results on the stage dependence of the Fermi level and with the oscillator strengths of infrared modes [2].

The phenomenological conductivity model suggests that maximum enhancement of the in-plane electrical conductivity of graphite intercalation compounds is achieved when the charge density transferred to the graphite layers from the intercalant is maximized along with minimizing the intercalant thickness d_i and maximizing the mobility in the graphite bounding layers. Although the charge transfers to the graphite bounding layers tend to be significantly higher for the alkali metal donor compounds than for typical acceptor compounds, the mobility in the graphite bounding layers tends to be lower for the alkali metal donor compounds, presumably due to the greater coupling to the intercalant and consequently more effective carrier scattering.

Whereas the addition of both donor and acceptor intercalants to graphite increases the in-plane conductivity σ_a, the behavior of the *c*-axis conductivity σ_c is very different: *donor* intercalation tends to *increase* σ_c while *acceptor* intercalation tends to *decrease* σ_c [124, 126]. Typical values of σ_c for a number of donor and acceptor compounds are given in Table 1.6.

The experimental difficulties associated with measurements of *c*-axis conductivity in pristine graphite and intercalation compounds have limited the amount and accuracy of available data. For all donor intercalants that have been studied, the *c*-axis conductivity σ_c increases upon intercalation relative to σ_c^0 for the graphite host. E.g., σ_c/σ_c^0 is ~230 for C_8K, and ~2170 for C_6Li. The large increase in σ_c for stage 1 compounds implies a strong overlap of the graphite p_z-orbital with the potassium *s*-orbital and some overlap between consecutive

Table 1.6. **The c-axis conductivity σ_c and anisotropy ratio σ_a/σ_c for several donor and acceptor compounds**

Intercalant	Stage	σ_c, $\Omega^{-1}cm^{-1}$	σ_a/σ_c	References
HOPG	∞	8.3	3.0×10^3	[38]
K	1	1.94×10^3	56	[130]
K	2	1.97×10^2	1.97×10^2	[130]
Li	1	1.8×10^4	14	[132]
Br_2	2	1.6	1.4×10^5	[124]
HNO_3	1	1.8	1.7×10^5	[124]
$AlCl_3$	1	6.1	2.6×10^4	[124]
H_2SO_4	1	0.90	1.8×10^5	[124]
$FeCl_3$	1	1.1×10^5	1.1×10^4	[136]
AsF_5	2	10	2.7×10^6	[137]

intercalant layers, in addition to the large increase in the carrier density. Furthermore, an inspection of the Fermi surface for C_8K indicates that there will be a significant contribution to the *c*-axis conduction from the spherical carrier pocket and a rather smaller contribution from the cylindrical carrier pockets which have very large effective masses in the *c*-direction (2D carriers). The Fermi surface for C_6Li also suggests orbits where *c*-axis conduction can occur effectively. It should be noted that the anisotropy ratio for C_6Li is the lowest for any of the intercalation compounds (Table 1.6).

On the other hand, measurements of σ_c at room temperature for acceptor compounds typically show a significant decrease in σ_c relative to σ_c^0 for the graphite host [124, 137], the magnitude of σ_c/σ_c^0 depending strongly on intercalant species. This decrease in σ_c for acceptor compounds is attributed to the high electrical impedance across the intercalant layer, arising from the low overlap between the graphite p_z-orbitals and the molecular orbitals of the intercalant. Due to the increase in σ_a by the order of magnitude and the decrease in σ_c by the order of magnitude for typical acceptor compounds upon intercalation, the anisotropy ratio over 10^6 can be achieved [137]. The values for the anisotropy ratio σ_a/σ_c are given in Table 1.6 for several donor and acceptor compounds.

The transport of charged carriers across the intercalant layer may involve a tunnelling process in the case of acceptor compounds, though the lack of correlation between the decrease in (σ_c/σ_c^0) and the intercalant thickness casts some doubt on the tunnelling mechanism for *c*-axis conduction. Furthermore, the observation that (σ_c/σ_c^0) is approximately an order of magnitude greater at 77K than at 295K led to conclude that *c*-axis conduction is driven by a band conduction mechanism in acceptor compounds, rather than by a hopping mechanism [124]. The studies of spin diffusion using the electron spin resonance (ESR) technique have led to suggestion about diffusion mechanism for *c*-axis conduction in intercalation compounds [102].

Graphite intercalated with certain dopants is capable to exhibit superconductivity properties [2]. The alkali metal-graphite intercalation compounds [144, 145] are the most well studied [146, 147], and the C_8K system among them is the most easily fabricated [148]. This system exhibits a transition temperature near 0.14 K [146, 147]. If the alkali metal concentration increases, the temperature of the transition increases up to 5 K in C_2Na [149]. Superconductivity in C_6Yb and C_6Ca with $T_c \approx 6.5$ and 11.5 K, respectively, has been observed in ambient conditions [150]. The newly discovered C_6Yb system was investigated in [146], where calculations rely on the density functional theory (DFT) techniques applied in the local density approximation (LDA). It was found that in addition to the expected charge transfer from the intercalant atoms to the graphene sheets, resulting from the occupation of the π-bands, in all of those (and only those) compounds that superconduct, an interlayer state, which is well-separated from

the carbon sheets, also becomes occupied. The authors showed that the energy of the interlayer band is controlled by combination of its occupancy and the separation between the carbon layers.

1.3. Structure and properties of some carbon nanostructured forms related to EG

Nanostructured forms of carbon have a number of structural and property features when compared with bulk ones, which have been discussed above. Similar forms can be presented as constituents of EG, and therefore some characteristics of more important of them (in our opinion) will be briefly considered below.

Some remarks about graphene. Graphene is one of the allotropic forms formed by carbon atoms. Graphene is a monoatomic layer of carbon atoms with a hexagonal structure of their arrangement (Fig. 1.12). It was discovered in the form of really accessible material in 2004.

The graphene structure is similar to a separate atomic layer in the structure of graphite: carbon atoms form a cellular structure with an interatomic distance of 0.142 nm. Graphene tends to bend without buttress, but it can be resistant on a substrate. Moreover, graphene has been obtained without substrate, almost in a free suspended state stretched on the buttress.

Single-layer and bilayer graphene systems can exhibit a remarkable diversity of phenomena, including observations of a room-temperature unconventional quantum Hall effect [151—153] predictions of the quantum spin Hall effect [154], broken spin [155, 156] or pseudospin [153] symmetries, and finite size effects, which can be used for various purposes [155—161].

However, the absence of electronic bandgap in graphene, which makes its volt-ampere characteristic (the dependence of the channel conductivity on the voltage on shutter) symmetric with respect to zero voltage, and makes it difficult to obtain two states that could be considered logical "0" and "1" is an impediment of the emergence of serial electronic and optoelectronic devices based on graphene, which could, in the long run, replace the silicon-based devices massively.

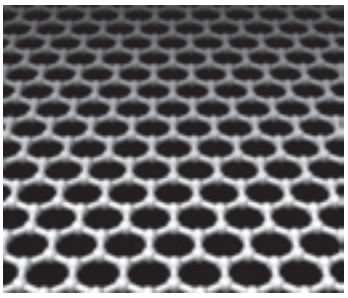

Fig. 1.12. Schematic representation of the single-layer graphene sheet [WiKi]

Another graphene feature is its band structure with the dispersion law, which in the form is similar to the law of relativistic quantum particles dispersion. Elementary excitations in graphene are described by equations analogous to the Dirac equation. By its electronic properties, graphene differs from 3D graphite. It can be characterized

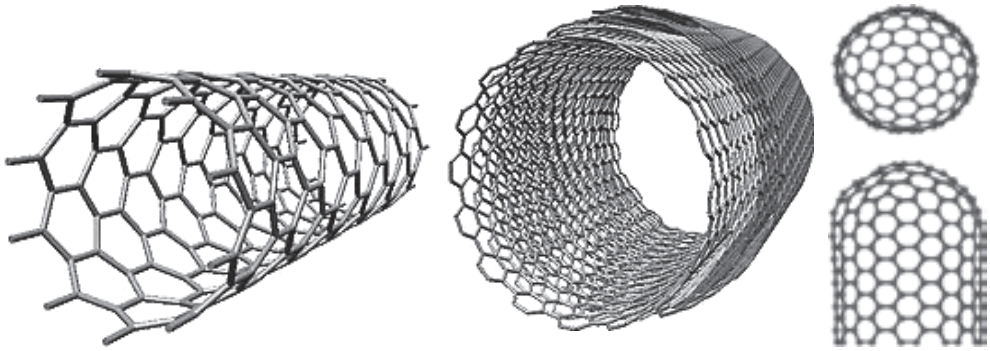

a *b* *c*

Fig. 1.13. Schematic representation of SWCNT (*a*), MWCNT (*b*), and CNT with a closed surface (*c*) [163]

as a semi-metal, or as a superconductor with a zero bandgap. The conduction band and the valence zone of graphene intersect, but this occurs not in the center of the Brillouin zone, but in special points at its edges. These are six points and they are pairwise equivalent and called as Dirac points. As a result, the zones are non-parabolic and the charge carrier effective mass is of zero. The dispersion law near the Dirac points is given by the equation:

$$E = v_F \sqrt{k_x^2 + k_y^2}, \quad N_B = \frac{4(n^2 + nm + m^2)}{N_r}, \tag{1.7}$$

where E is the energy of excitation, v_F is the Fermi rate, k_x and k_x are wave vector components.

Theoretically, graphene has a zero density of states at the Dirac points, which correspond to the Fermi level at zero temperature, so graphene should not conduct an electric current. However, in practice, it has conductivity comparable with the value of $4e^2/h$, where e is the elementary electric charge, h is the Planck constant. The reason for the conductivity is still unclear. It is possible that charge carriers join graphene from the substrate, or the cause of the charge carriers is a distorted surface of the material where charge carriers are redistributed and uncontrolled impurities may be present. That is why in certain cases, controlled impurities are introduced to increase the graphene conductivity.

The graphene bandgap is also attempted to induce in other ways: by mechanical processing, oxidation, the addition of defects and stresses, etc. As a result, they deal, e.g., with graphene nano-types (this area arises from additional quantization in one direction), hydrogenated graphene (graphpan), fluoride graphene, etc. However, in general, to date, the task of functionalization is yet not been satisfactorily resolved.

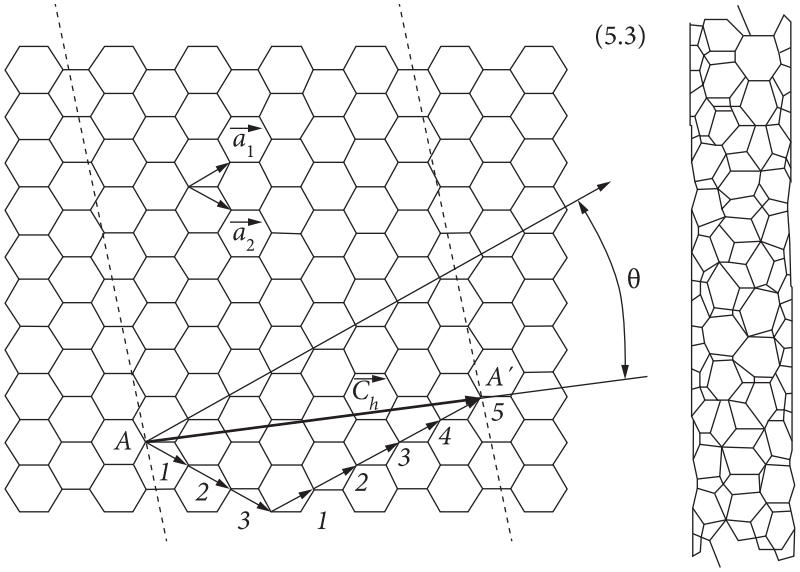

Fig. 1.14. The scheme of the SWCNT (5,3) formation with a chiral vector $\mathbf{C}_h = 5\mathbf{a}_1 + 3\mathbf{a}_2$, which determines the possible curling of a 2D graphene sheet into a tubular form [163]

Some remarks concerning carbon nanotubes. Carbon nanotubes are long-hollow cylindrical structures with a diameter of one to several dozen nanometers and a length of several centimeters, consisting of one or more hexagonal graphite plates (graphene sheets) rolled into a tube and usually end with a hemispherical head, which can be regarded as half the fullerene molecule [162]. The CNTs can also have open ends after oxidation, which may be relevant precisely for the case of carbonaceous material such as EG. Depending on the number of layers, the CNTs are divided into one-wall (SWCNT) and multi-wall (MWCNT) (Fig. 1.13).

The ideal SWCNT can be represented as a graphene sheet (hexagonal layer of carbon atoms) rolled into a cylinder without any seams [162].

Since the microscopic structure of SWCNT is closely related to graphene, the tubes are usually designated in terms of graphene lattice vectors. The SWCNT can be obtained geometrically by curling of graphene strip (Fig. 1.14). Its structure is determined by the vector ($\mathbf{C}_h$), which is denoted by a chiral vector (*AA*' in Fig. 1.14), connecting two crystallographically equivalent points (*A* and *A')* of graphene sheet [163]. Thus, the SWCNT geometry is completely determined by a pair of indices (*n, m*) denoting the relative position $\mathbf{C}_h = n\mathbf{a}_1 + m\mathbf{a}_2$ of the graphene strip pair atoms, which in the course of tube formation superimposed on each other ($\mathbf{a}_1$ and $\mathbf{a}_2$ — base vectors of the hexagonal layer (Fig. 1.14).

The number of carbon atoms in an elementary cell N_B can be expressed as a function of chirality indices *n* and *m*:

$$N_B = \frac{4\left(n^2 + nm + m^2\right)}{N_r}. \qquad (1.8)$$

If for a particular nanotube (n, m) the difference in the chirality indices is multiple 3, then such a nanotube is a metal, and in all other cases it is a semiconductor. The all of chair type (n = m) CNTs, zigzaging with n multiples of 3, and chiral ones, for which n—m is multiple 3, are of metal type.

Electronic band structure and conductivity of carbon nanotubes: influence of defects and adsorbed functional molecules. Carbon nanotubes are known for their particular electronic properties due to the nature of the connections of the electronic shells of carbon atoms in their structure. CNTs are characterized by σ and π bonds and their sp^2 hybridization. In the latter, the (s, p_x, p_y) orbitals combine to form binding and antibinding σ and σ* orbitals in the plane, and in the lateral interaction with adjacent p_z orbitals — to form delocalized binding and antibinding π and π* orbitals. The π bonds are perpendicular to the nanotube surface are responsible for the interaction between the SWCNT in a beam similar to the interaction between carbon layers in pure graphite. The σ bonds firmly connect carbon atoms to the surface of carbon hexagons and thus determine the binding energy and elastic properties of the tube (Fig. 1.15, *a*).

The energy levels associated with the σ bonds in the plane lie far from the Fermi-energy level (Fig. 1.15, *b*), so they do not affect the electronic properties of CNT. On the other hand, binding and antibinding π-bonds cross the Fermi level at points of high symmetry of the Brillouin zone. Therefore, the above described properties of electronic bonds define graphene and some carbon nanotubes as metallic or quasimetallic [164]. Depending on the CNT chirality indices ***n*** and ***m***, the forbidden band of SWCNT can vary from 0 to 2 eV. The bandgap of semiconductor nanotubes has an inverse relationship with their diameter: the width of the bandgap is about 1.8 eV for thin tubes, while it is approximately 0.18 eV for the thickest ones [165].

As in the case of bulk crystalline solids, in carbon nanotubes, the appearance of "own" defects, which are formed in the places of transformation of part of the hexagons into penta- and heptagon rings, may occur (Fig. 1.16, *a*) [163].

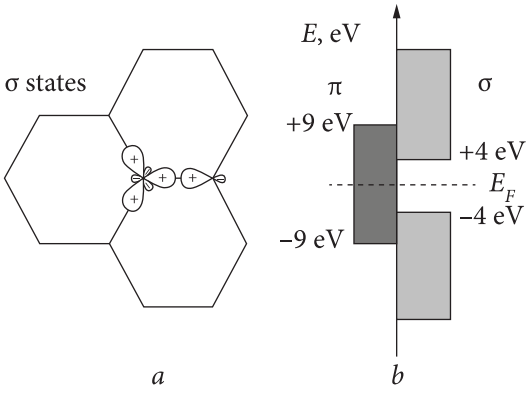

Fig. 1.15. The scheme of formation of a hexagonal carbon surface by σ bonds (*a*) and the scheme of energy zones formed by binding and anti-binding π and σ orbitals (*b*) [163]

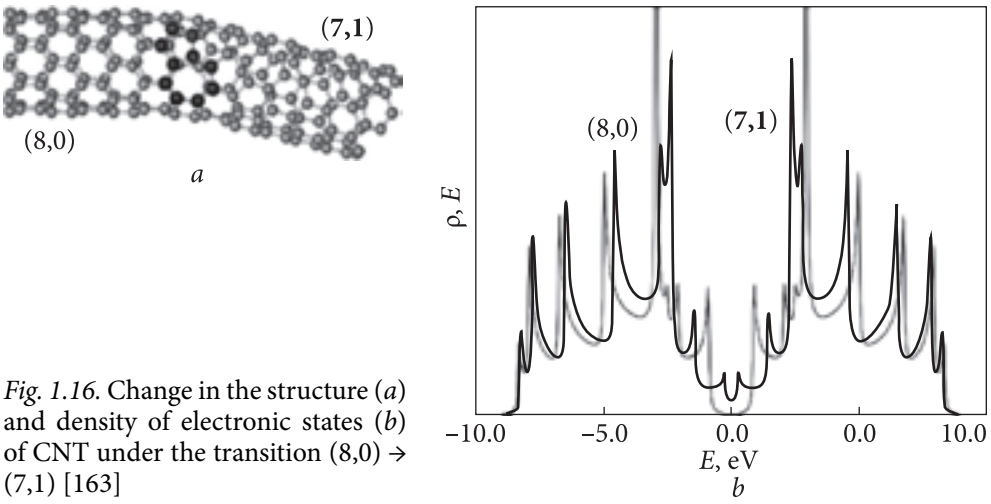

Fig. 1.16. Change in the structure (*a*) and density of electronic states (*b*) of CNT under the transition (8,0) → (7,1) [163]

Defects can also be of external origin: imported accidentally as a result of the manufacturing process, or specially incorporated to modify the CNT properties. The appearance of the defects leads to bending of the tube, changes in the chirality vector and its diameter, changes in the relation with adjacent tubes in the bunch, changes in the distribution of the electronic states density and so on (Fig. 1.16, *b*), and hence the change in the tube properties.-

Defects, impurities, and limitations in size influence the electronic structure of carbon nanomaterials, in particular, they affect the energy distribution of valence electrons. Thus, by means of X-ray emission spectroscopy of the electronic structure of CNTs with 5 and 10 walls, made using Fe (33%), Co (11%) and Ni (30%), unlike the nanotubes washed away from the catalysts and large CNT with over 200 walls, the presence of mixed π + σ states was found, which were formed due to distortions of the surface when the graphene sheet was bent in a tube. In addition, the difference between the forms of the emission bands of nanotubes of different chirality was revealed, and it was established that the electronic structure of nanotubes depends on the diameter and on the method of their production. As the CNT diameter increases, the curvature of their surface decreases, the angles between σ-bonds become closer to the angles in the graphite, and the difference between the energies of the π- and σ-states decreases [163]. In the high-energy region of the emission bands in MWCNT purified from Ni and Fe, the *ppσ* hybrid states are produced, to which the pp-states are mixed, when coagulating a graphene sheet in a nanotube. Moreover, the intensity of energy interactions in the CNT axis direction is the same, both inside and on the surface, but it is smaller than that in the middle of the radial direction.

Atoms of metals are introduced into the walls of nanotubes at places of defect formation, when a part of hexagonal rings is converted into five- and seven-

cornered ones. As a result, the degree of hybridization changes in the places of the bends due to the approach of the pentagon angles to the values, which are characteristic for the sp^3-hybridization. If diameters are greater than 70 nm, the curvature of the surface decreases with increasing diameter to such an extent that the overlapping πp_z-orbitals will remain unchanged with further increase in the nanotube diameter.

Structural defects also arise in large numbers as a result of the processes of CNT functionalization. Oxidation is the most common method of chemical treatment of carbon nanotubes, with a view to their purification and functionalization. As a result, various oxygen-containing groups, such as hydroxyl, aldehyde, ketone, etheric, carboxylic, anhydride, and lactone, are formed on the surface of carbon nanotubes [166].

Carboxylic, hydroxyl, carbonyl and lactone groups are most often fixed on the surface of oxidized CNTs. Oxygen-containing reagents most often use oxygen-containing acids and mixtures of them based on HNO_3 [167—170], $HNO_3 + H_2SO_4$ [171, 172], $HClO_4$ [173], H_2SO_4 [174], $HNO_3 + K_2Cr_2O_7$ [175], $H_2SO_4 + KMnO_4$ [176], $H_2SO_4 + H_2O_2$ [177].

When oxidized in a widely used mixture of concentrated nitric and sulfuric acids (3 : 1), sulfur-containing functional groups are often formed [178, 179]. It is believed that due to the oxidation of multiwall CNT with concentrated acid HNO_3, in addition to the end opening and the appearance of oxygen-containing groups, aromatic polycyclic compounds, fulvic acids, which can both be removed by alkaline washing and reverse adsorption, are formed on the surface [168].

Different physical and chemical methods are used to intensify liquid-phase functionalization. In particular, the work [180] showed the possibility of effective carboxylation of CNT in a mixture of nitric and sulfuric acids (3:1) at room temperature under the action of cavitation caused by the influence of ultrasound on the reaction mass. The activity of hydrogen peroxide with respect to CNT increases with UV irradiation [181].

Carbon dioxide [182, 183], water vapor [184], air oxygen [168, 185—187], ozone [188—191] or nitric acid vapor [192, 193] are used as oxidants in the cases of the CNT gas-phase functionalization.

CO_2 contributes to selective oxidation of CNT. In particular, with this process, it is possible to separate arrays of parallel oriented nanotubes from the substrate.

Occasionally, CNT pre-treated with acids are oxidized in air [194]. In this method of functionalization, a certain number of hydroxyl and carbonyl groups are formed on the surface of CNT, and effective removal of residual amorphous phase almost always takes place.

The most effective oxidation of multi-wall CNT occurs in nitric acid vapor. At the same time, despite the considerable degree of functionalization, the structure of the output CNT is preserved [192].

The methods of mechano-chemical oxidation of carbon nanotubes are separateinot own group. Such treatment contributes to the formation of a minimum number of oxygen-containing groups on the CNT surface and a noticeable shortening of the tubes takes place [187]. In addition to the described influence on the structure, there is also the adherence of a significant number of OH groups to the surface under mechanochemical treatment of CNT in water-alcohol KOH solutions [195, 196].

Oxidizing functionalization by any of the above noted methods can lead to the opening of the ends and shortening of individual tubes [197]. The characterisrics and number of groups formed on the nanotube surface depend on the oxidant nature and the process conditions. For single wall CNTs it was shown in [198] that under boiling in nitric acid and in the treatment of alkaline solutions of potassium permanganate, carboxyl, hydroxyl and carbonyl groups are formed only in the places of the primary surface defects. New defects arise when a mixture of HNO_3 and H_2SO_4 acids are used as an oxidizer, and the process is activated by ultrasound. In this case, hydroxyl groups electrophilic joining the aromatic rings forming the surface of nanotubes can occur. With prolonged oxidation, the destruction of the graphene layer begins around the formed active centers, which leads to a shortening of the CNT.

The trends of the oxidation processes depend on the structural features of CNT (curvature of the carbon surface, in particular) [199]. However, information on systematic research in this area is practically unknown.

The ends and defects of lateral surfaces are the most reactive areas on the surface of carbon nanotubes [200]. It was shown for dual-wall CNT by means of spectroscopic studies that the attachment of functional groups occurs exclusively in the outer wall defects and, moreover, mainly near the tube ends [201]. Practically, the internal layer of CNT is not affected by functionalization. It can be assumed that this is true for multi-wall CNTs. The affinity of the CNTs surface to various solvents and polymeric matrices increases [202], as well as their structural and physical (mechanical and electrical) properties change with the oxidative functionalization of CNTs. Thus, the exact correlation between the occurrence of CNT oxidation in concentrated nitric acid and the change in interatomic bonds was shown in [203]. It is interesting that the surface defects are grouped around active oxidation centers, but not randomly distributed along the nanotubes. Destruction of the integrity of the CNT outer layer can takes place at the early stages of oxidation process. As a result, the mechanical properties of individual nanotubes may get worse. The positive effect of CNT with a high degree of functionalization on the strength properties of polymer composites is due primarily to the interaction of functional surface groups with the molecule matrices and often due to formation of chemical bonds between them.

Information on the effect of oxidation on the conducting properties of multi-wall CNTs is contradictory. On the one hand, the violation of the integrity of the graphene layers during formation of functional groups should lead to a decrease in electrical conductivity, as shown in [204, 205], but, on the other hand, it was often reported about opposite effects. E.g., it was shown in [206] that the increase in conducting properties is due to the crosslinking of functionalized sections of CNT in plasma oxidation, which results in the formation of an integral system instead of the initially separated CNT. The increase in electrical conductivity during oxidation by various reagents is also associated with the appearance of additional conducting zones near the Fermi level in the presence of oxygen-containing groups [207, 208]. The best way to improve conductance properties of CNTs is treatment by ozone. It wass reported that ozone causes a bond breakage in separate layers of multi-wall CNTs, resulting in the formation of interband bonds between carbon atoms in the state of sp^3-hybridization [209]. It was believed that this facilitates the transition of electrons to the inner walls.

Oxidation processing in different ways can affect the properties of CNTs which differ in shape and number of walls and geometric parameters. This had been confirmed in [206], where it was shown that the ratio of the number of oxygen-containing functional groups and the change in the properties after functionalization to a greater extent is due not to the oxidant nature, but to the structure of carbon nanotubes.

Above, we have paid considerable attention to the description of different effects on the structure, morphology and properties of graphene and carbon nanotubes. This was done in order to show that these characteristics are quite sensitive to the effects of defects due to structural disturbances incorporated and adsorbed on their surface impurities. In particular, the effect of adsorbed functional groups (used in oxidization of carbon nanomaterials) is significant.

We have already noted that the same carbon forms (nanotubes, pieces of graphene, etc.) are also pesent in the composition of expanded graphite, the procedure for which obtaining is associated with the use of similar or the same reagents, as well as with the processes of functionalization. Moreover, it is obvious that tubes and pieces of graphene in EG should be much deformed, crushed and even partially disintegrated and contain attached and adsorbed residues of the chemical reagents used in the EG production.

In this case, the phenomena described above regarding the influence of various factors and, in particular, the adsorption of molecular groups should be considered as inherent to expanded graphite. That is why, the mechanisms of adsorption of different types of molecular groups (from two up to nine atoms) on the surface of carbon materials are related to graphene and CNT as components of EG.

1.4. Theoretical studies (computer modelling) of simple molecular groups adsorption on the surface of graphene and carbon nanotubes

Study of the molecule interaction with the surface of carbon nanomaterials is important not only from the viewpoint of elucidation of mechanisms and characteristics of adsorption, and the influence of adsorbed molecules on the structure and surface morphology, electronic structure and electrical conductivity of carbonaceous material. These data are also important in terms of clarifying graphite intercalation mechanisms, and, moreover, the results of such studies are also important for assessing the prospects for the use of a carbon material, in particular EG, as a sensor of molecular compounds, such as gases, or to remove them from a specific environment, in particular from atmosphere [210]. The importance of this estimation becomes more significant when the study concerns the adsorption of molecules that have a strong toxic effect on the human body. The hydrogen halide molecules HX (X = Cl, Br, F) and simple inorganic molecules containing heavy metal ions: Cr, W, and Mo are such metals [211]. The mechanisms of such molecules adsorption by carbon nanoparticles are considered in this section.

Computational studies of boron- and nitrogen-doped single-wall carbon nanotubes with adsorbed hydrogen halide molecules HX (X = F, Cl, Br). Hydrogen halide gases HX (X = F, Cl, Br) are widely used in industry as reagents (see e.g. [126]) and are produced as byproducts in many industrial processes [213—216]. At the same time, they are very toxic and harmful for biological organisms even at low concentrations [212, 217].

Theoretical modeling of adsorption of molecules on the CNT surface is a powerful tool since it can predict several important physical and chemical properties of the materials [218—221]. Adsorption of several types of molecules of industrially-important gases on the B- or N-CNTs was treated so far in the first-principles electronic structure calculations. In particular, such studies were reported for carbon monoxide CO [222, 223—225], nitrogen dioxide NO_2 [218, 222, 223], chlorine Cl_2 [27], formaldehyde HCOH [221], methanol CH_3OH and ammonia NH_3 [223, 226]. Here we show the results of such computational studies of B- and N-CNTs considering adsorption of hydrogen halide molecules HX (X = F, Cl, Br) on their surfaces.

The results of a DFT-based calculations of the electronic structures of undoped, B- and N-doped single-wall CNTs with adjacent placed HX (X = F, Cl, Br) molecules are presented here. Three types of adsorbents were considered in calculations, namely CNT(3,3), CNT(5,5), and graphene sheets. Relaxed geometries, binding energies of the adsorbate molecules to the CNTs and charge

states of the molecules were obtained in geometry-optimized calculations carried out by the Gaussian 03 program package [227].

It should be noted that most of modern synthesis procedures for carbon nanotubes allow one to produce only mixes of CNTs with high dispersion of chirality index (m, n) [228]. Technologies of synthesis of CNTs monodisperse by (m, n) index (or procedures for selection of already synthesized CNTs by their structure) appeared only in the recent years and are still very complicated and expensive [229]. Materials of available CNT-based gas sensors are in fact "mixes" of CNTs with high dispersion of chirality index (m, n) since these materials were produced by conventional synthesis methods without preliminary selection by the CNT structure (see e.g. [222, 230—232]). It is therefore obvious that studies of a set of CNTs with various (m, n) indexes are desirable for prediction of properties of real working materials of CNT-based gas sensors. However, studies of such a set require extensive computing resources and make analysis of results very complicated. So, researchers generally limit themselves to consideration of gaseous adsorption of the CNTs with some single case of (m, n) index (see e.g. [218, 221]), or graphene [222] reasonably regarding such limitation as being sufficient for adequate prediction of properties of gas sensing materials. In this work, we consider simultaneously three several types of adsorbents which represent various cases of carbon surface curvature, namely low-diameter nanotubes CNT(3,3), nanotubes with larger diameter CNT(5,5) and graphene sheetsl which can be considered as a model approximation for large-diameter nanotubes.

The electronic structures of undoped single-wall CNT(3,3) and CNT(5,5) were calculated for the first time relatively long ago and may be considered now as well-studied by various calculation methods [233—236]. The electronic structures of low-diameter (i.e. with low values of *m* and *n*) B- or N-doped CNT(n, m) are also well-studied. In particular, such calculations were reported for the B(N)-doped metallic-type CNT(5,5) [237—239] and also for semiconductor-type CNT(4,5) [240], B(N)–CNT(5,7) [241], N–CNT(6,0) [242] and for many other B(N)-doped CNTs with higher values of (n,m) index. The electronic structures of B(N)-doped graphene sheets have been studied recently in the molecular cluster approach by the DFT-based methods [243, 244]. The results on the electronic structure of B(N)–CNT(3,3) calculations were presented for the first time in the work [210].

The carbon nanotubes and graphene sheets were modeled there in calculations by molecular clusters, since the current computational capabilities are insufficient to perform *ab initio* calculations for the full-length carbon nanotubes as well as for the entire variety of nanotube structures. For this reason, in computational studies of molecular adsorption on the CNT surface, only fragments (clusters) of CNTs are usually considered. The clusters of CNT(3,3) comprised 78 carbon atoms, or in

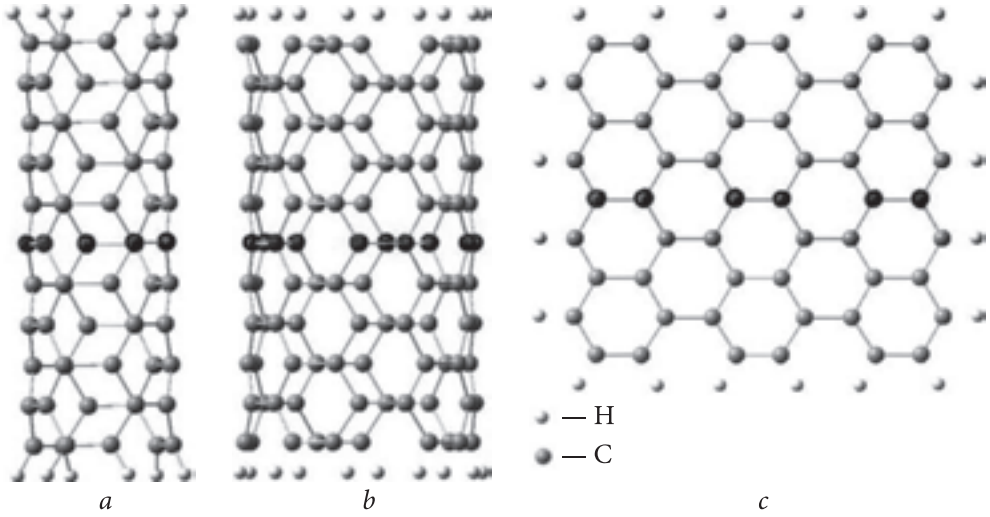

Fig. 1.17. Clusters of undoped CNT(3,3) (*a*), CNT(5,5) (*b*) and graphene sheet (*c*) with geometry-optimized structures. Carbon atoms colored in black lie in plane where the density contours of electronic wavefunction were calculated [210]

other words, 13 C_6 rings along the nanotube axis were taken. In order to compensate the effects of dangling C–C bonds, 12 outermost C atoms of the clusters were replaced by H atoms providing $C_{66}H_{12}$ formula of the cluster (Fig. 1.17, *a*).

Such replacement is a widely used approximation in computational modeling of CNTs within molecular cluster approach [245—247]. In order to model B(N) impurities, one carbon atom from the central C_6 ring of the cluster was substituted by B or N atom. Before geometry optimization, the HX (X = F, Cl, Br) molecules were put at 1.5 Å distance from the CNT surface in the vicinity of the B(N) atom, and the H-X bond was initially oriented parallel to the CNT axis. Clusters with $C_{110}H_{20}$ and $C_{54}H_{20}$ formulas were constructed to model CNT(5,5) and graphene sheets, respectively (Fig. 1.17, *b, c*). Modeling of B(N) dopants and starting geometries of HX adsorbates for CNT(5,5) and graphene clusters was analogous to the CNT(3,3) case.

The geometry-optimized calculations were performed with Gaussian 09 (build E01 software package [227]) with B3LYP nonlocal exchange-correlation density functional (DFT level) [227, 248, 249]. The basis set and approximation for the exchange-corellation potential using split-valence double-zeta 6-31G* basis set used for C and H atoms are typical for recent computational studies of molecular adsorption on CNTs [245].

The binding energies were obtained as the difference of the calculated total energies using an expression like $E_b = E_{CNT–B(N)–HX} – E_{CNT–B(N)} – E_{HX}$. The calculated E_b value should be negative at a stable adsorption configuration. The

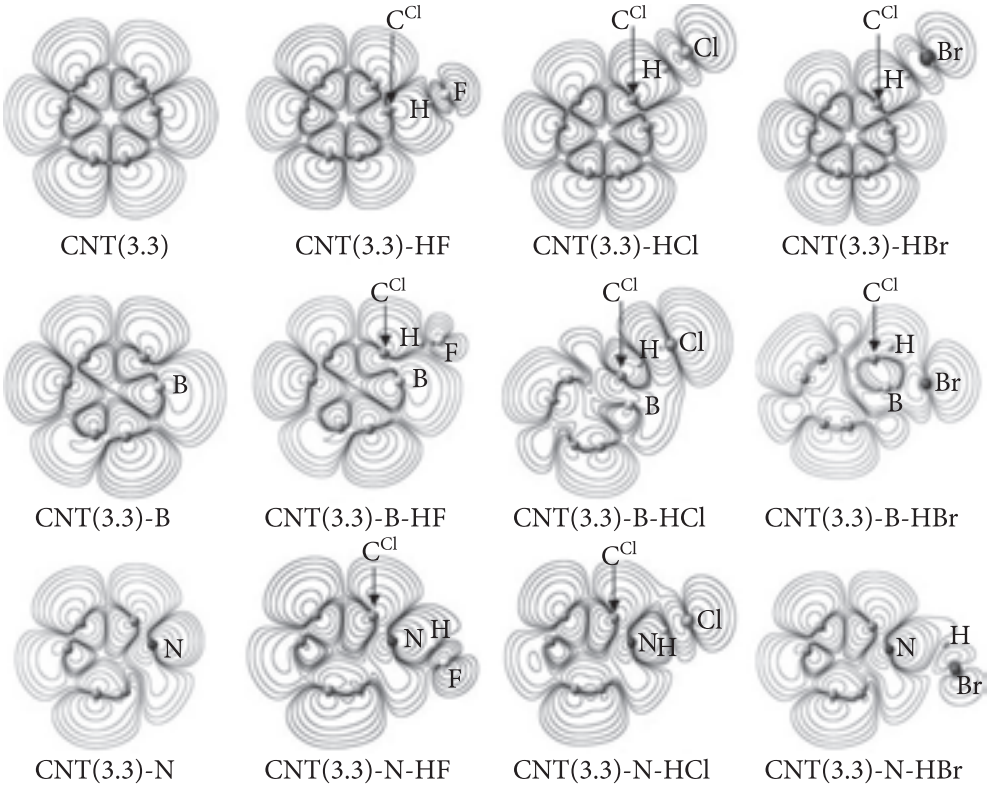

Fig. 1.18. Density contours of the electronic wave-functions of undoped (upper raw), B-doped (medium raw) and N-doped (lower raw) CNT(3,3) clusters in pristine configuration (left column) and with adsorbed hydrogen halide molecules (three other columns). All shown atoms are in plane of the figure (deviations are less than ~0.0001 Å). The C atom of nanotube closest to H atom of the adsorbate is denoted as C^{cl} [210]

charge states of HX (X = F, Cl, Br) adsorbates are obtained as an algebraic sum of calculated Mulliken charges of H and X atoms. Negative charge of the adsorbate molecule means transfer of negative electronic charge from the CNT to the molecule. For all studied adsorption cases (with few exceptions indicated in captions of Figs. 1.18—1.20, the density contour plots of the electronic wave-functions were calculated in plains which contained the H, X and B(N) nuclei together with the C nuclei from the central regions of clusters (they are (colored in blue in Fig. 1.17). Contour plots were calculated for molecular orbitals (MOs) which clearly demonstrate the character of chemical bonds. These MOs were chosen as the highest occupied (HOMO) for CNT(3,3) clusters and the next below HOMO for CNT(5,5) and graphene clusters.

Clusters of undoped CNT(3,3), CNT(5,5) and graphene were considered in calculations as electrically neutral, i.e. no additional electron charge was as-

Table 1.7. **Calculated binding energies, charges of adsorbate molecules HX (X = F, Cl,**

Type of doping	Type of adsorbate	Configuration	Binding energy E_b (eV/kJ*mol^{-1})	Charge state of HX adsorbate, e
Undoped	HF	CNT(3,3)—HF	−0.19664 (−18.9736)	−0.038
		CNT(5,5)—HF	−0.15972 (−15.4107)	−0.033
		GR–HF	−0.1231 (−11.8727)	−0.024
	HCl	CNT(3,3)—HCl	−0.1356 (−13.0861)	−0.071
		CNT(5,5)—HCl	−0.1422 (−13.7186)	−0.046
		GR—HCl	−0.0707 (−6.8231)	−0.033
	HBr	CNT(3,3)—HBr	−0.1536 (−14.8217)	−0.068
		CNT(5,5)—HBr	−0.16345 (−15.7705)	−0.044
		GR—HBr	−0.0868 (−8.3755)	−0.031
B-doped	HF	CNT(3,3)—B—HF	−0.5950 (−57.4076)	−0.03
		CNT(5,5)—B—HF	−0.4963 (−47.8908)	−0.018
		GR—B—HF	−2.5311 (−244.21629)	−0.003
	HCl	CNT(3,3)—B—HCl	−0.8800 (−84.9076)	−0.503
		CNT(5,5)—B—HCl	−0.3764 (−36.3147)	−0.137
		GR—B—HCl	−2.3824 (−229.8698)	−0.12
	HBr	CNT(3,3)–B–HBr	−2.1342 (−205.9240)	−0.112
		CNT(5,5)–B–HBr	−0.3622 (−34.9500)	−0.14
		GR–B–HBr	−2.3907 (−230.6682)	−0.125
N-doped	HF	CNT(3,3)–N–HF	−0.1703 (−16.4300)	0.007
		CNT(5,5)–N–HF	−0.4126 (−39.8151)	0.02
		GR–N–HF	−0.2116 (−2.4200)	0.021
	HCl	CNT(3,3)–N–HCl	−0.0603 (−5.8190)	−0.064
		CNT(5,5)–N–HCl	Geometry optimization unconverged (no ad	
		GR–N–HCl	−0.06534 (−6.3046)	−0.001
	HBr	CNT(3,3)–N–HBr	−0.0942 (−9.0919)	0.013
		CNT(5,5)–N–HBr	−0.1868 (−18.0225)	−0.009
		GR–N–HBr	−0.0716 (−6.9086)	0.005

R_{H-X} — inter-nuclear distance in adsorbed HX molecule; $(R_{H-X})^{free}$ — inter-nuclear distance shortest distance from a carbon atom of the adsorbent to the H atom of HX.

signed. At the same time, additional charges equal to −1*e* and 1*e* were assigned to clusters describing the B- and N-doped clusters respectively. By such additional charging of clusters, we modeled a local type of charge compensation for deficiency (excess) of one electron caused by non-isovalent substitutional doping of the nanotube by Boron (Nitrogen) atoms. In fact, we model a very common situation when an extra electron introduced into a real CNT by the

Br) and internuclear distances

	R_{H-X} (Å)/$(R_{H-X})^{free}$	$(R_{C-H}$ (Å))^{min}
	0.9567 (0.94927) + 0.78	2.07545
	0.95255/0.94927 + 0.35	2.07033
	0.95178/0.94927 + 0.26	2.24942
	1.3404/1.32057 + 1.50	2.18253
	1.33027/1.32057 + 0.73	2.36785
	1.32667/1.32057 + 0.46	2.48136
	1.4578 /1.44006 + 1.23	2.20396
	1.44780 /1.44006 + 0.54	2.36396
	1.44429/1.44006 + 0.29	2.46213
	0.9729/0.94927 + 2.49	1.90231
	0.96624/0.94927 + 1.79	2.00599
	0.9598/0.94927 + 1.11	2.6819
	2.027/1.32057 + 53.49	1.15766
	1.37235/1.32057 + 3.92	1.96542
	1.35292/1.32057 + .45	2.56420
	2.7779/1.44006 + 92.90	1.0962
	1.4933/1.44006 + 3.70	1.98348
	1.47253/1.44006 + 2.25	2.78799
	0.9555/0.94927 + 0.66	2.53622
	0.95049/0.94927 + 0.13	3.73704
	0.95008/0.94927 + 0.09	3.92233
	1.3519/1.32057 + 2.37	2.66707
sorption configurations found)		
	1.32000/1.32057 – 0.04	5.16923
	1.4392/1.44006 – 0.06	3.88017
	1.43967/1.44006 – 0.03	3.08926
	1.43913/1.44006 – 0.06	4.17118

in free HX molecule; $(R_{C-H})^{min}$ — the

N_C impurity is captured by an additional compensating defect created somewhere far from the N_C site at the stage of synthesis (such compensating defects were not modeled explicitly in our clusters). Correspondingly, additional compensating defects can provide a lacking electron in the B_C case.

It should be noted that the lengths of real carbon nanotubes usually exceed their diameters by several orders of magnitude. So, a section of the CNT modeled in a cluster must be long enough to guarantee a negligible influence of side surfaces on the central region of the section where the B(N) impurities and adsorbed HX molecules are situated. To examine this property, supplementary geometry-optimized calculations of undoped CNT(3,3), CNT(5,5) and graphene clusters were carried out. As the calculations showed, the addition of two extra carbon rings to both sides of CNT(3,3) and CNT(5,5) clusters only slightly (within ~0.8% of magnitude) changes the C—C distances in the central regions of clusters. Analogous slight changes in core region were observed when two extra carbon strips were added to the opposite sides of graphene cluster.

The following characteristic size parameters of undoped CNT(3,3) cluster were obtained in geometry-optimized calculations: distance along the nanotube axis between outermost C_6 rings was ~12.3 Å, distance between the edging H_6 rings (cluster length) was ~14.1 Å, averaged distance between "contralateral" C nuclei of the central C_6 ring (cluster diameter) was ~4.2 Å. Analogously, the length and diameter of undoped CNT(5,5) cluster were obtained as ~14.2 Å and ~7.0 Å, respectively. Characteristic dimension of undoped graphene cluster (the maximal internuclear distances between H nuclei located on the opposite sides) was obtained as ~11.74 × 3.6 Å.

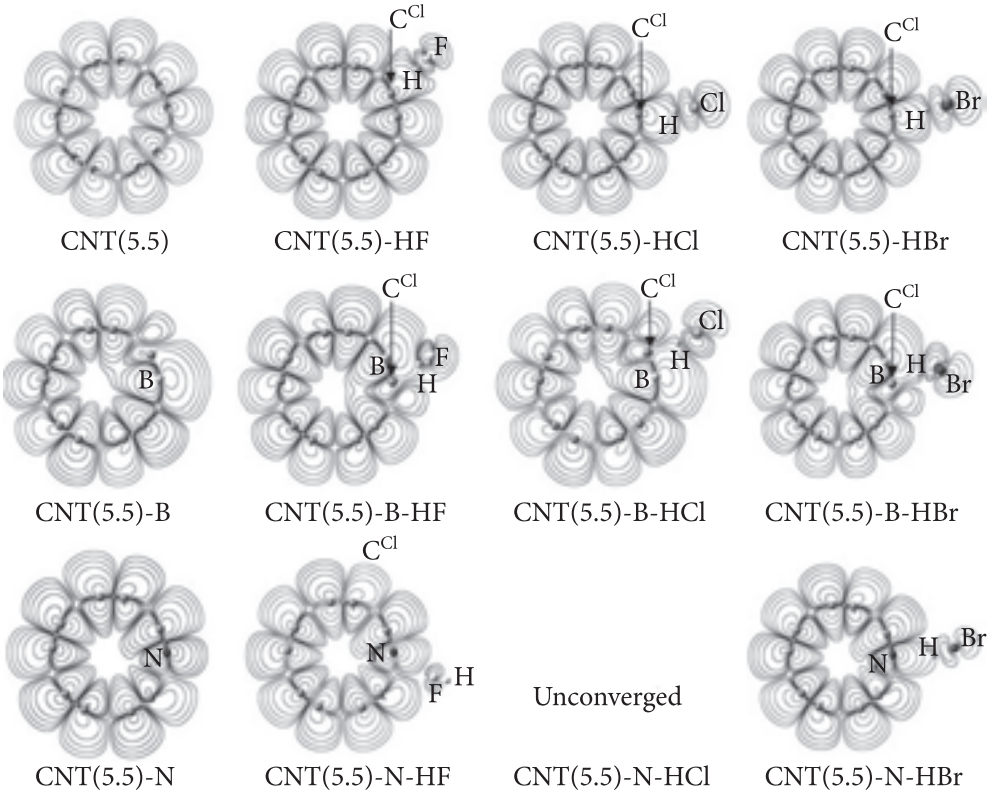

Fig. 1.19. Density contours of the electronic wave-functions for HX adsorption configurations on CNT(5,5) clusters. All shown atoms are in plane of the figure, excluding CNT(5,5)—N—HF case, for which the H atom is situated ~0.21 Å below the plane [210]

The calculated binding energies, charges of adsorbed HX molecules and relaxed-geometry inter-nuclear distances are listed in Table 1.7.

Corresponding density contour plots of the electronic wave-functions calculated for CNT(3,3), CNT(5,5), and graphene clusters are given in Figs. 1.18, 1.19, and 1.20, respectively.

It is worth noting that internuclear distances R_{C-C} (not shown in Table 1.7), obtained in calculations for undoped CNT(3,3) cluster, are different for various pairs of near carbon atoms. For the core region of the cluster (3 medial C_6 rings) where the influence of side surfaces is minimal, these distances can be grouped into three sets with the following average values and standard deviations: $R^1_{C-C} = 1.42468 \pm 0.00007$ Å, $R^2_{C-C} = 1.44307 \pm 0.0002$ Å and $R^3_{C-C} = 1.4820 \pm 0.0002$ Å. The existence of different R_{C-C} values is an inherent structural property of low-diameter CNTs [126]. The first-principles electronic structure calculations of armchair-type single-walled CNTs of low diameter (m or n indexes are not

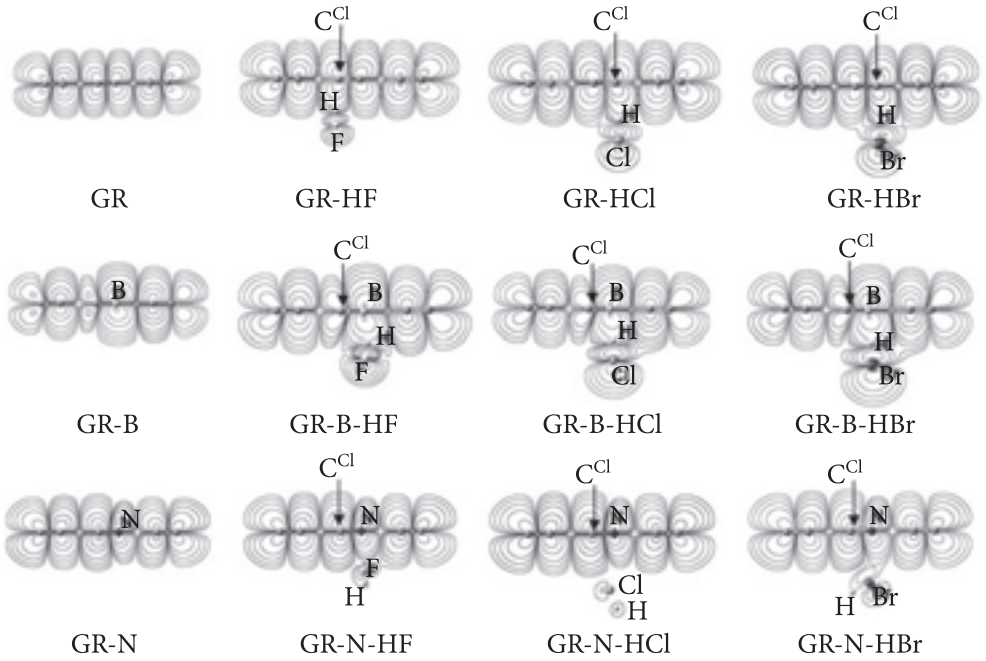

Fig. 1.20. Density contours of the electronic wave functions for HX adsorption configurations on graphene clusters. All shown atoms are in plane of the figure, excluding CRAPH—N—HBr case for which the H atom is situated ~0.39 Å above the plane and CRAPH—B—HCl, where Cl is ~0.10 Å below the plane [210]

greater than 5) reflect this feature: they usually provide two or more values of R_{C-C} [233, 237, 245, 247].

As the Table 1.7 data show, the calculations provide relatively low values of binding energies for adsorbed HX molecules and un-doped clusters: they range from –0.07 to –0.19 eV. The internuclear distances in adsorbed molecules R_{H-X} are only slightly changed with respect to corresponding distances in free molecules (the difference does not exceed 1.5%. For all considered cases of adsorption on un-doped clusters, the "axis" of HX molecule is settled practically perpendicular to the carbon surface (this feature is well illustrated by upper rows in Figs. 1.18—1.20). The shortest R_{C-H} distance exceeds 2 Å for all studied HX cases.

For all adsorption configurations, calculations indicate lower binding energies and higher $(R_{C-H})_{min}$ distances for undoped graphene clusters in comparison with CNT(3,3) and CNT(5,5) (Table 1.7).

The values of E_b obtained for undoped CNT(3,3) and CNT(5,5) fall into the region of binding energies typical for hydrogen bonds (0.1—0.6 eV [250]), however, are close to its lower limit. The E_b value in GRAPH–HCl and GRAPH–HBr cases are even slightly below this lower limit and fall into the region of the van der

Waals bonds (0.01—0.1 eV [251]). Relatively low values of E_b and slight changes of internuclear distances in adsorbed molecules indicate the absence of covalent bonding between HX (X = F, Cl, Br) adsorbates and undoped carbon nanotubes.

Contour plots of the electronic wave function clearly illustrate the absence of covalent binding between undoped clusters and HX molecules (see upper rows in Figs. 1.18—1.20). As the figures show, contours of the wavefunction between the C atoms of the clusters demonstrate antibinding ppπ^* bonds. Such character of the bonds at HOMO and several MOs below HOMO is a well-known general property of CNTs [126].

Adsorbed HX molecules only slightly disturb the wavefunction of undoped CNT(3,3), CNT(5,5), and graphene clusters. In particular, one can see that for all studied HX cases, wavefunction contours around C^{cl} atom are only slightly different from corresponding contours in undoped clusters without adsorbates (compare the left with all other plots in upper rows of Figs. 1.18—1.20). Such very slight disturbances of nanotube wavefunctions by adsorbates are typical for a physisorption mechanism of adsorption.

Physisorption mechanism of adsorption on un-doped clusters is illustrated by dependence of the binding energy on tube-molecule distance presented in Fig. 1.21 for HCl adsorption cases on CNT(3,3) (among all studied cases, HCl on CNT(3,3) are selected since they most remarkably illustrate the influence of the B(N)-doping on adsorption properties). As Fig. 1.21 shows (curve *1*), the binding energy curve has only slightly distinguishable (very shallow) minimum, which is typical for physisorption.

Calculations also give small charges for HX molecules adsorbed on undoped clusters: they are in –0.02…–0.07 *e* range (Table 1.7). So, only insignificant changes in conductivity of undoped carbon nanotubes should be expected after adsorption of HF, HCl, and HBr. An example of evident correlation between low values of calculated binding energies and adsorbate charges and insignificant changes in resistivity of CNT based materials observed in experiment can be found in recent work [222] where adsorption of NO_2, CO, and C_2H_4 molecules on a CNT surface was studied. It was shown that when the calculated binding energies of adsorbates does not exceed |–0.25| eV, and their charges are less than |–0.1| *e*, the changes in resistivity of CNT-based materials are very low and these materials are not perspective for elaboration of effective gas sensors of corresponding molecules [222].

At the moment, adsorption of several types of molecules on CNTs has been examined in such complex computational and experimental studies and these studies generally confirmed that if calculations reveal only physisorption of some molecules, the CNT-based materials will be not perspective for creation of gas sensors of these molecules (see [230] and references therein).

So, we have reasons to consider undoped carbon nanotubes as less perspective materials for elaboration of gas sensors of hydrogen halides HX (X = F, Cl, Br).

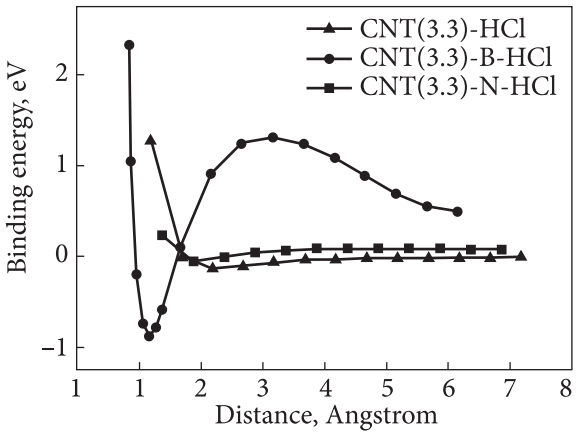

Fig. 1.21. Dependence of the binding energy on tube-molecule distance for adsorption of HCl molecules on CNT(3,3) clusters. Indicated distance is the internuclear distance between the closest atoms of the molecule and the nanotube [210]

As for B-doped CNT, calculations revealed different situation for adsorption of HX molecules on the boron-doped carbon nanotubes. In this case, the binding energies with adsorbate molecules range from –0.36 to –2.53 eV (Table 1.7) and are generally higher by an order of magnitude than corresponding energies of adsorption on undoped clusters. The E_b values for CNT(3,3) and CNT(5,5) fall into the region of hydrogen bonds (0.1—0.6 eV, [250]) or are slightly above this region (–0.87 eV, for CNT(3,3)—B—HCl), while the –2.13 eV value observed in CNT(3,3)—B—HBr case is typical for molecules with covalent bonds [252]. Despite the E_b value in the CNT(3,3)—B—HCl case is lower than typical binding energies of covalent bonds, Fig. 1.21 demonstrates a well-defined minimum in the energy-distance relationship (curve *2*).

For all of adsorption cases, CNT(5,5) reveals lower binding energies relatively to CNT(3,3) clusters (compare corresponding raws in Table 1.7). The B-doped graphene clusters reveal binding energies typical for covalent bonds (ranging from –2.53 for GRAPH—B—HF to –2.38 for GRAPH—B—HCl (Table 1.7)).

As the Table 1.7 data show, in each case of HX adsorption on B-doped CNT(3,3) and CNT(5,5), the H atom of adsorbate is located closer to one of the C atoms of the nanotube (C^{cl}), than to the impurity atom B, i.e. $(R_{C-H})^{min} < (R_{B-H})^{min}$. In the CNT(3,3)—B—HBr case, the $(R_{C-H})^{min}$ distance is even almost twice shorter than the $(R_{B-H})^{min}$ distance. Contour plots in Fig. 1.18 (medium raw) clearly illustrate the bonding character of the electronic wavefunction between C^{cl} and H atoms for all cases of adsorption on CNT(3,3). So, it is arguable that C^{cl} and H atoms create chemical bonds in all studied cases of adsorption on the B-doped CNT(3,3) and CNT(5,5) clusters.

For the B-doped graphene, on contrary, $(R_{C-H})^{min} > (R_{B-H})^{min}$ and the H atoms of the adsorbates create chemical bonds with the B dopant atoms. Corresponding density plots confirm this feature (Fig. 1.20, medium raw).

The most significant elongations of H–X distances are obtained for the CNT(3,3)—B—HBr and CNT(3,3)—B—HCl cases (~53 and ~93%, respectively). In contrast, adsorption of HX molecules on B-doped graphene clusters, despite high binding energies, does not lead to significant changes of internuclear distances in the adsorbates (the relative change does not exceed + 2.5%).

As Fig. 1.18 shows, perturbations of the electronic wavefunction of the B-doped CNT(3,3) nanotube due to adsorption of HX molecules increase in the HF—HCl—HBr sequence. Only slight distorsions occur in the HF case (compare two left pictures in the medium raw of Fig. 1.18). Such slight disturbances of the electronic wavefunction correlate with very low value of calculated charge of HF adsorbate (Table 1.7). In contrast, adsorption of HBr leads to significant changes in the electronic wavefunction of the B-doped CNT(3,3). In particular, the bonding σ-type character of wavefunction is observed between B and C^{cl} atoms in the CNT(3,3)—B—HBr case, whereas corresponding bond in B-doped CNT(3,3) without adsorbates has the $pp\pi^*$ character (compare two edge pictures in the medium raw of Fig. 1.18). From the viewpoint of perturbations of the nanotube wavefunction, adsorption of HCl can be considered as an intermediate case between HF and HBr.

An evident correlation between degree of disturbance of the adsorbent electronic wavefunction and calculated charge of HX adsorbate is also observed for the B-doped graphene clusters. In the GRAPH—B—HF case, in contrast to GRAPH—B—HCl and GRAPH—B—HBr, the disturbance is slight (Fig. 1.20, medium raw) and the calculated HF charge is only –0.03 *e*. In contrast, GRAPH—B—HCl and GRAPH—B—HBr cases demonstrate a higher degree of disturbance and HX charges.

Analysis of the set of works [218, 221, 222, 224, 225] where the results of computational modeling of adsorption of several types of molecules on B-doped CNTs were analyzed from the viewpoint of potential application of the B—CNT-based materials to gas detection allowed us to make the following outline. If the calculated binding energies fall in the range –0.70…–2.74 eV and charges of the adsorbates are in the range |0.121|—|0.328| *e*, we should consider B—CNT-based materials as suitable for elaboration of corresponding molecules detection.

As the calculations showed, the HCl and HBr adsorption on B-doped CNT(3,3) and graphene is characterized by binding energies and adsorbate charges in the above ranges. The CNT(5,5)—B—HCl and CNT(5,5)—B—HBr cases reveal slightly lower E_b values, however calculated charges of adsorbates also fall within the mentioned above range. So, we can assume that materials based on B-doped CNTs will be suitable for elaboration of effective sensors of hydrogen halide gases HCl and HBr. However, we cannot make such assumption for HF as the charge of the adsorbate for all clusters was calculated to be smaller than |–0.03| *e* despite high values of E_b (reaching –2.53 eV in the GR—B—HF

case). Additionaly, first of all, experimental studies are obviously required in order to estimate potential of B—CNT-based materials for detection of HF gases.

Regarding N-doped clusters, we should note that for all studied adsorptions cases, calculations give relatively low values of binding energies (not exceeding –0.41 eV, Table 1.7), small adsorbate charges (not exceeding |0.05| *e*), slight changes (not exceeding 2.5%) in the internuclear distances in adsorbates, and relatively high internuclear distances between adsorbates and nanotubes (above 2 Å). Although in some cases (CNT(3,3)—N—HF, CNT(5,5)—N—HF, GRAPH—N—HF and CNT(5,5)—N—HBr), the values of E_b can be formally attributed to the energy range of weak hydrogen bonds (see above), the rest of adsorption cases reveal binding energies typical for van der Waals' interaction (0.01—0.1 eV range of binding energies [252]), i.e. physisorption. The geometry optimization calculations were unconverged in the CNT(5,5)—N—HF case, i.e. no adsorbed states were found. The weakness of bonding between the N-doped clusters and HX molecules is also illustrated by contour plots in lower rows of Figs. 1.18—1.20. As the figures show, adsorption of each studied HX leads to only slight distortions in the electronic wavefunction of N-doped CNT(3,3), if compared, for instance, with changes of the cluster wavefunction in the B-doped cases. Fig. 1.21 also demonstrates physisorption for the CNT(3,3)—N—HCl case: the energy-distance curve has a very shallow minimum (curve *3*).

As it was stated above, in case of physisorption of molecules, CNT-based materials have low potential for gas detection. So, our calculations indicate that N-doped CNTs are less promising materials for detection of hydrogen halide gases HX (X = F, Cl, Br).

Study of the M^{VI} metals oxoanions (M^{VI} = Cr, Mo, W) adsorption by carbon nanostructures. Removal of heavy metals from environment is a topical technological problem. One of the most efficient methods of such removal is adsorption of heavy metals on artificial adsorbents [253, 254]. Search for novel economically efficient adsorbent materials for the heavy metal removal is an important research task of modern materials science [255, 256].

Oxoanions of hexavalent Cr, Mo, and W are very harmful to living organisms. Hexavalent chromium, Cr(VI), is a cancerogen [257] and is able to modify the DNA transcription process in living cells leading to chromosomal aberrations [258—260]. Acute exposure to Cr (VI) compounds causes nausea, diarrhea, kidney, liver, and gastric damage, internal hemorrhage, lung cancer, ulcer formation, and respiratory problems [260—263]. Biological objects can also suffer from harmful effects of molecules containing Mo(VI) [264, 265] and W(VI) ions [266].

The removal of molecules which comprise oxoanions of hexavalent Cr, Mo and W is of particular importance since these compounds are widely-spread industrial pollutants. The main industries that contribute to water pollution

by Cr(VI) are mining, leather production, textile dyeing, electroplating, metal finishing, wood manufacturing, nuclear power plants, electrical and electronic equipment, catalysis [258, 262, 267—269]. Modern industrial procedures can produce up to hundreds of mg/L of Cr(VI) discharge into the inland surface and potable waters, while the regulated tolerance values are 0.1 and 0.05 mg/L, respectively [259, 263, 269—271]. The Mo(VI)-containing residuals are produced in multiple industries, in particular in production of nickel-based alloys, lubricants, glass, ink and pigments, electronic components [264]. Tungsten is a widely used resource in many industrial and manufacturing applications that can produce W(VI)-containing wastes [266].

The properties of CNTs as adsorbent materials of Cr(VI) compounds were intensively studied within the last decade [255, 272—277]. The CNT-based materials have been recognized as perspective adsorbents of Cr(VI) compounds [255, 273, 275—278]. However to the best of our knowledge, no specific studies of adsorption capabilities of carbon nanomaterials with respect to Mo(VI) or W(VI) compounds have been presented in literature so far.

From the viewpoint of this book content, it is interesting to note that sulphate anions, which are important participants in the processes of intercalation of graphite, belong to MA of the XO_4^{2-} type as well. Thus, the study of adsorption mechanisms of MA of the XO_4^{2-} type by carbon nanostructured materials is of interest in terms of studying the features of intercalation of graphite and the formation of expanded graphite on their basis.

In spite of intensive experimental studies, there is a considerable lack of understanding of M(VI)-on-CNTs adsorption mechanisms at the single-molecule level. This lack can be successfully overcome by the first-principles electronic structure calculations. Currently, the study of only M(II) heavy metals (Pb, Zn, Hg, Cd, Ni) adsorption on CNTs has been studied in the DFT-based computational [279—283]. Moreover, in all these studies except [279] the calculations were carried out *in vacuo*, so their results can be considered only as a rough approximation for adsorption properties in aqueous solutions.

Both *in vacuo* and *in aqua* calculations were applied in the work [284] to reveal the mechanisms of: a) adsorption of CrO_4^{2-}, MoO_4^{2-}, and WO_4^{2-} oxoanions on pristine and B(N)-doped carbon nanostructures; b) adsorption of CrO_4^{2-} anions on CNTs functionalized by oxygen-containing surface groups (OSG); c) adsorption of two other compounds of hexavalent chromium, dichromate $Cr_2O_7^{2-}$ and hydrogen chromate $HCrO_4^-$, on pristine and B(N)-doped carbon nanostructures.

Along with CrO_4^{2-}, the dichromate $Cr_2O_7^{2-}$ and hydrogen chromate $HCrO_4^-$ anions are a wide-spread kind of Cr(VI) compounds which usually exist in aqueous solutions in wide range of concentrations [255, 274, 276]. The $HCrO_4^-$ anions prevail at $1 < pH < 7$, whereas Cr(VI) exists predominantly as CrO_4^{2-} at $pH > 7$ in Cr(VI)-containing aqueous solutions [285—287]. Consequently, con-

sidering these three kinds of chromate anions in calculations, clarification of the mechanisms of Cr(VI) uptake by carbon adsorbents is a necessary step.

Four kinds of carbon nanostructures were modeled in the calculations: single-walled CNT(3,3) and CNT(5,5), multi-walled carbon nanotube (MWCNT) wall fragment with outer layer of (37,37) chirality, and graphene sheets. The two former CNTs were considered to study the adsorption mechanisms of oxoanions on low-diameter CNTs, whereas graphene sheets can be considered as a model for large-diameter CNTs. The diameter of the MWCNT was about ~5.1 nm which is the most common value of the CNT diameter in commercially available mixtures of carbon nanotubes [274]. Doping of CNT-based materials with non-isovalent impurities of B or N can substantially change their adsorption capabilities [288—290], so here we consider the B(N)-doped carbon nanostructures in order to examine the possibility of tuning the adsorption properties of the materials with respect to anions of M^{VI} metals.

One of the most perspective ways of improvement of the adsorption capabilities of the CNT-based materials with respect to Cr(VI) compounds is their functionalization by oxygen-containing surface groups (OSG) [272, 274—276, 278, 291]. In order to analyze the influence of OSG-functionalization on adsorption properties of carbon nanotubes with respect to chromate anions, adsorption of CrO_4^{2-} on CNT(5,5) functionalized with —COOH, $—COO^-$, —OH, and $—NH_3^+$ functional groups were considered in the work [284].

Consideration of adsorption in water provides results well suitable the water purification task, whereas in vacuum computations might have significance for the case of toxic anions removal from air, which is also an important technological problem [292—294].

The analysis of the calculation results and available literature data allowed us to predict several important issues which can advance elaboration of efficient adsorbent materials for removal of toxic hexavalent metals from surrounding media.

In computational studies of molecular adsorption on the CNT surface, only fragments (clusters) of CNTs were usually considered taking into account the reason noted in the previous section. The clusters were chosen to be sufficiently large to make negligible the effect of the cluster edges on the central region where molecules are intensely adsorbed. Correspondingly, only several types of the CNT structures are usually considered. These selected types have to be a largest possible way representing possible variations of the CNT surfaces.

So, the following set of carbon nanostructures which covers the full range of possible curvatures of the CNT surfaces was considered to analyze the adsorption properties of real CNT mixtures with respect to the M^{VI} oxoanions: CNT(3,3), CNT(5,5), MWCNT and graphene sheets.

The narrowest possible nanotubes are CNT(3,3) and CNT(5,5) having diameters ~0.4 and ~0.7 nm, respectively. However, such nanotubes are conve-

nient objects of calculations, since their clusters will have sufficient length for modeling of molecular adsorption even with comparatively small number of atoms. A single-layered graphene sheet is commonly used to model the surface of large-diameter CNTs (with correspondingly low surface curvature). Consideration of both low-diameter CNTs and graphene is a widely spread approach in prediction of the adsorption properties of real CNT mixtures by computational techniques (see [284] and references in [210] and [284]).

In order to complement these edge cases of the CNT surface curvatures by an intermediate one, we have additionally considered a fragment of the hexa-layered multi-walled carbon nanotube which can be denoted using formal rules as MWCNT(17,17)@(21,21)@(25,25)@(29,29)@(33,33)@(37,37) and will be mentioned in the following text as MWCNT. The outer diameter of such MWCNT is ~5.1 nm, which corresponds to the average CNT diameter in commercially available mixtures [274].

In our calculations, the clusters of CNT(3,3) comprised 23 C_6 rings of armchair carbon nanotube (3,3). The dangling C-C bonds in the cluster were capped with H atoms, resulting in the $C_{126}H_{12}$ formula. Replacement of the edge C atoms with H atoms is a widely used approximation in computational studies of CNTs within the molecular cluster approach [219]. Clusters with 21 C_{10} and 2 H_{10} rings were constructed to model a CNT(5,5) providing the $C_{210}H_{20}$ formula. The $C_{266}H_{46}$ (size, x by y) clusters were used to model a single-layered graphene (GR) sheet. Approximate lengths of both CNT clusters were ~26.5 Å. The dimensions of GR cluster were ~24.1×30.8 Å. Detailed structures of CNT(3,3), CNT(5,5), and GR clusters have been described above, where a proof for a weak influence of the cluster edges on their central regions was also provided using supplementary calculations. It was shown there for low-diameter CNTs that CNT fragments of at least 30 Å length can guarantee a sufficiently weak influence of the edges on the central part. However, construction of MWCNT cluster of such length would require ~6800 carbon atoms. Such a number is too large for efficient DFT-based calculations of adsorption geometries, inasmuch as hundreds of combinations of adsorbents and adsorbates that have to be studied. For this reason, we have constructed a conical section of MWCNT which comprises the hexagonal part of the nanotube outer surface (Fig. 1.22). This part has transverse dimension of ~29.0 Å; the distance between inner and outer walls of MWCNT is ~15.2 Å. All dangling C-C bonds of MWCNT cluster were capped with H atoms providing the $C_{546}H_{126}$ formula.

Under geometry optimization calculations, the H atoms of MWCNT were fixed (frozen). As our geometry optimizations showed, the structure of MWCNT cluster was not stable without such freezing, i.e. the carbon sheets constituting the conical part of the multi-walled tube moved apart. Normally,

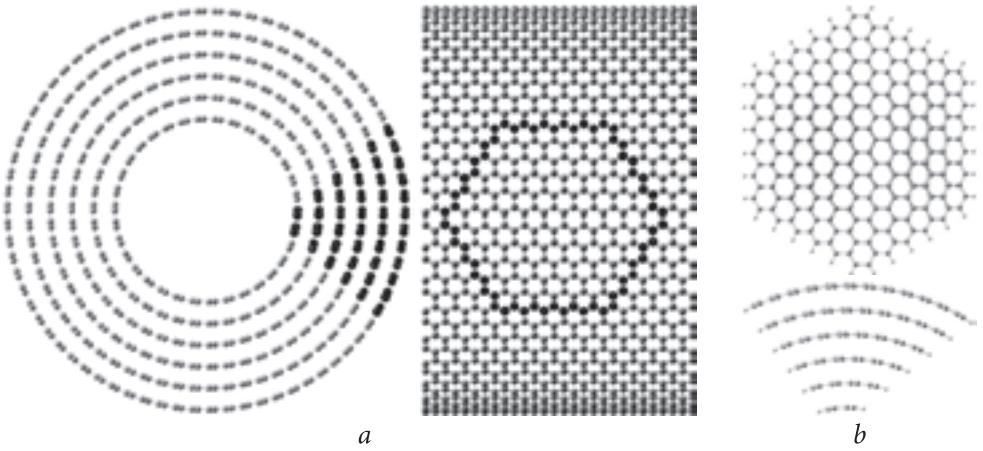

Fig. 1.22. Scheme of selection of MWCNT cluster from six-wall carbon nanotube (edge atoms of the cluster are marked by black shadows) (*a*); structure of selected MWCNT cluster given in two projections (*b*) [295]

a coaxial structure of MWCNTs prevents such decomposition. The freezing of the edge hydrogen atoms was applied in studies of molecular adsorption on the outer layer of MWCNT of 2 nm diameter [296]. Such freezing obviously provides some limitations to geometric optimization of the whole cluster. On the other hand, it leaves the atomic positions in the cluster core to be optimized providing (as it was also shown in [296]) an adequate treatment of molecular adsorption properties.

It was found that geometry optimization of undoped MWCNT cluster resulted in a little bulging of the outer carbon layers of the cluster (several deeper layers were also bulged, but to a lower extent). However, despite the bulging, the cluster preserved the curvature of the outer surface (after optimization, corresponding curvature radius decreased only by ~10%). This feature indicates that freezing of outer atoms provides a reasonable approximation in modeling of adsorption on middle-diameter MWCNT.

When the B_C or N_C substitutional impurities were modeled, one C atom from the central cluster region was replaced with either B or N. The oxygen-containing surface groups were located above several central atoms of the clusters of studied systems.

Calculations were performed using Gaussian software package and approaches as have been described above, while correlation-consistent polarized valence double-zeta (cc-pVDZ) basis sets [297] were applied for Cr and O atoms. Mo and W atoms were represented by cc-pVDZ-PP basis sets with pseudopotentials [298, 299].

The similar combination of basis sets is generally utilized in computational studies of adsorption of molecules with d-metals on the CNT surfaces (see e.g.

[300, 301]). The basis set superposition error (BSSE) correction of total energies was taken into account [302]. All other settings were Gaussian 09 defaults, that is, no additional keywords were specified. Effects of water solvent on the studied adsorption cases were optionally considered with the PCM [303].

If there is a $-2e$ charge of "free" $M^{VI}O_4^{2-}$ (M^{VI} = Cr, Mo, W) anion, additional –2e charges were assigned to the clusters of undoped adsorbent and chromate anion. Consequently, additional charges of –3e or –1e were assigned to the B- or N-doped clusters, respectively. In summary, all systems were treated as close-shell, i.e. with no un-paired electrons.

Under the geometry optimization studies, several starting positions of $M^{VI}O_4^{2-}$ (M^{VI} = Cr, Mo, W) anions with respect to the carbon surface were considered for each adsorption case. In all the cases, the anions were initially put in such a way that the shortest C/B/N—O distance lied between 1.5 and 2.2 Å. Using such initial geometry, it was ensured the binding of the anion particularly to the dopant atoms, not at just some other site of the doped CNT or graphene [284].

It is worth to remember some designation and terms. Particularly, the binding energy E_b of anion to adsorbents, both *in vacuo* and *in aqua* was obtained as the difference of the calculated total energies using formulae:

$$E_b = E_{ads—anion} - E_{ads} - E_{anion}, \tag{1.9}$$

where $E_{ads—anion}$ is total energy of the optimized adsorption system "adsorbent with anion", E_{ads} is total energy of the optimized adsorbent and E_{anion} is a total energy of optimized anion calculated within the same approximations. Then, the differences in charge density on the $M^{VI}O_4^{2-}$ (M^{VI} = Cr, Mo, W), $Cr_2O_7^{2-}$ and $HCrO_4^-$ anions (in respect to the isolated anion) in adsorbed state was defined as $\Delta q = -2e - q$ ($\Delta q = -e - q$ for $HCrO_4^-$). It should be recalled if the calculated value of Δq is negative, the electronic charge is transferred from the anion to the adsorbent.

Adsorption of the $M^{VI}O_4^{2-}$ (M^{VI} = Cr, Mo, W) anions on undoped and B(N)-doped carbon materials. The binding energies E_b and charge differences Δq for adsorption configurations of $M^{VI}O_4^{2-}$ (M^{VI} = Cr, Mo, W) oxoanions on pristine and B(N)-doped carbon nanostructures found *in vacuo* are presented in Fig. 1.23. For convenience, corresponding E_b, and Δq values as well as characteristic inter-nuclear distances of these configurations are also listed in Table 1.8.

Single adsorption configurations were found in each case except for the adsorption on undoped graphene. In all cases, the binding energies are negative and fall within –0.7…–7.5 eV range. The E_b values of such type are typical for the chemisorption mechanism of adsorption [252]. As Fig. 1.23 shows for all anions, doping with B substantially decreases (by ~1.5—2.5 eV), while doping with N increases (by ~2—4 eV) the absolute values of binding energies relatively to the corresponding adsorption cases on undoped nanostructures.

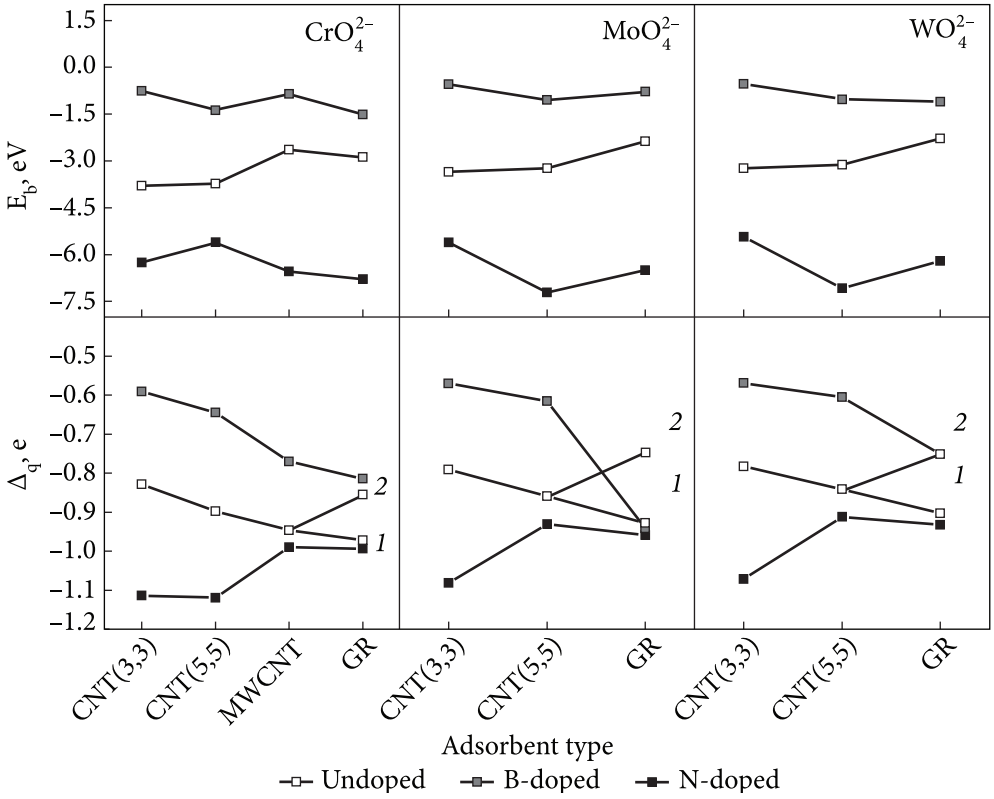

Fig. 1.23. Dependences of the binding energies (upper plots) and charge differences of adsorbed $M^{VI}O_4^{2-}$ (M^{VI} = Cr, Mo, W) anions (lower plots) on the type of adsorbent and type of adsorbent doping (calculated for *in vacuo*) [295]

This result indicates that aliovalent doping with B or N can be an efficient tool for tuning the adsorption properties of the CNT-based materials with respect to $M^{VI}O_4^{2-}$ (M^{VI} = Cr, Mo, W) anions in gaseous phase. At the same time, the E_b values are much less dependent on the adsorbent type if compared with their dependence on type of doping. This means that adsorption characteristics described here will be in great measure similar for all variety of the CNT diameters, and also that it is a less important question whether the CNTs are single- or multi-walled for such kind of adsorption.

All three anions CrO_4^{2-}, MoO_4^{2-} and WO_4^{2-} have very similar dependencies of both E_b, and Δq on type of doping and type of the adsorbent structure. This feature is quite expected since Cr, Mo and W metals are isoelectronic and the valence properties of $M^{VI}O_4^{2-}$ anions are determined by interplaying 3*d* (4*d* or 5*d*) orbitals of the M^{VI} cation and 2*p* orbitals of the oxygen ligands. At that, the cationic *d* orbitals are localized at the central core of the anion, so creation of the chemical

Table 1.8. **Binding energies E_b (eV), charge differences Δq (e) of $M^{VI}O_4^{2-}$ (M^{VI} = Cr, Mo, W) anions adsorbed on undoped and B(N)-doped carbon nanostructures, and the shortest internuclear distances R^{min} between anions and adsorbents (Å) calculated in vacuo [295]**

Type of anion	Type of doping	Configuration	E_b	Δq	R^{min} (bond type)
CrO_4^{2-}	Undoped	CNT(3,3)—CrO_4^{2-}	–3.79083	–0.82911	1.4161 (C—O)
		CNT(5,5)—CrO_4^{2-}	–3.7329	–0.89742	1.43652 (C—O)
		MWCNT—CrO_4^{2-}	–2.63828	–0.94642	1.45463 (C—O)
		GR—CrO_4^{2} 1	–2.89096	–0.97239	1.4678 (C—O)
		GR—CrO_4^{2} 2	–2.87873	–0.85541	3.14651 (C—O)
	B-doped	CNT(3,3)—B—CrO_4^{2-}	–0.76203	–0.59076	1.44814 (B—O)
		CNT(5,5)—B—CrO_4^{2-}	–1.36138	–0.64461	1.47594 (B—O)
		MWCNT—B—CrO_4^{2-}	–0.85638	–0.77058	1.50932 (B—O)
		GR—B—CrO_4^{2-}	–1.50437	–0.81477	1.51794 (B—O)
	N-doped	CNT(3,3)—N—CrO_4^{2-}	–6.25441	–1.11372	1.48069 (N—O)
		CNT(5,5)—N—CrO_4^{2-}	–5.62802	–1.1197	1.51974 (N—O)
		MWCNT—N—CrO_4^{2-}	–6.54564	–0.99018	1.39640 (C—O)
		GR—N—CrO_4^{2-}	–6.79154	–0.99407	1.40748 (C—O)
MoO_4^{2-}	Undoped	CNT(3,3)—MoO_4^{2-}	–3.35158	–0.79101	1.42157 (C—O)
		CNT(5,5)—MoO_4^{2-}	–3.23772	–0.85944	1.44191 (C—O)
		GR—MoO_4^{2-} 1	–2.37352	–0.92825	1.47396 (C—O)
		GR—MoO_4^{2-} 2	–2.34263	–0.74623	3.10782 (C—O)
	B-doped	CNT(3,3)—B—MoO_4^{2-}	–0.5478	–0.57013	1.45440 (B—O)
		CNT(5,5)—B—MoO_4^{2-}	–1.05357	–0.61563	1.47825 (B—O)
		GR—B—$MoOO_4^{2-}$	–0.78632	–0.94201	1.55429 (C—O)
	N-doped	CNT(3,3)—N—MoO_4^{2-}	–5.61597	–1.08153	1.48592 (N—O)
		CNT(5,5)—N—MoO_4^{2-}	–7.21026	–0.9307	1.40001 (C—O)
		GR—N—MoO_4^{2-}	–6.49465	–0.9589	1.42121 (C—O)
WO_4^{2-}	Undoped	CNT(3,3)—WO_4^{2-}	–3.23703	–0.78278	1.42612 (C—O)
		CNT(5,5)—WO_4^{2-}	–3.12088	–0.84121	1.44547 (C—O)
		GR—WO_4^{2-} 1	–2.27914	–0.90331	1.48033 (C—O)
		GR—WO_4^{2-} 2	–2.36037	–0.75135	3.10519 (C—O)
	B-doped	CNT(3,3)—B—WO_4^{2-}	–0.53325	–0.56991	1.45440 (B—O)
		CNT(5,5)—B—WO_4^{2-}	–1.01168	–0.60518	1.47534 (B—O)
		GR—B—WO_4^{2-}	–1.10752	–0.75158	1.52304 (B—O)
	N-doped	CNT(3,3)—N—WO_4^{2-}	–5.42915	–1.07195	1.50997 (N—O)
		CNT(5,5)—N—WO_4^{2-}	–7.07997	–0.91222	1.4075 (C—O)
		GR—N—WO_4^{2-}	–6.21075	–0.93246	1.42828 (C—O)

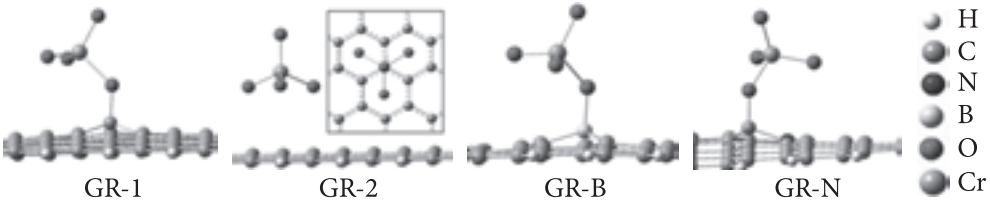

Fig. 1.24. Geometry-optimized structures of CrO_4^{2-} anions adsorbed on graphene *in vacuo* [295]

bonds to outer atoms is determined mainly by the oxygen 2*p* orbitals which have very common energy and spatial structure for all three $M^{VI}O_4^{2-}$ anions [304].

So, our results indicate that one would expect quite similar absorption characteristics for the three anions also for other types of adsorbents; for this reason we have limited the set of anions to only CrO_4^{2-} in studies of adsorption on the functionalized carbon nanostructures presented below.

The optimized geometries of CrO_4^{2-} adsorbed on pristine and doped graphene (Fig. 1.24) illustrate typical peculiarities of adsorption configurations (i.e. all other configurations possess geometries analogous to one of these four, despite different anions and adsorbent structures).

Fig. 1.24 shows that in the case of configuration 1 (this kind of atomic configuration is the most common among all adsorption cases presented in Table 1.8), the chemical bond between the O atom of the anion and C atom of the adsorbent is created (the internuclear distance $R_{C\text{-}O}^{min}$ is ~1.47 Å, which is a typical value for C—O covalent bonding [305]). In configuration 2, three O atoms are located at approximately equal distance from the carbon surface, i.e. one of the faces of the CrO_4^{2-} tetrahedron is parallel to the graphene surface. Here, each of the three O atoms is located about ~2.80 Å above the center of C_6 "honeycomb" of graphene surface and all three O atoms have approximately the same local surrounding (within 0.01 Å accuracy of nuclear coordinates). Within this accuracy, the structure is characterized by the C_3 symmetry axis perpendicular to the graphene plane and containing one C atom of the adsorbent, the Cr atom, and the "upper" O atom of the CrO_4^{2-} anion.

In the GR—B—CrO_4^{2-} case, one O atom of the anion creates a covalent bond to the B dopant atom of the adsorbent (Fig. 1.24) and such kind of bonding is common for all cases of adsorption on the B-doped adsorbents presented in Table 1.8. The situation is different for the N-doped adsorbents: one O atom of the anion can create bond either with N atom or with C atom which is the nearest neighbour to N (Fig. 1.24). Creation of covalent O—C bonds is observed for adsorption of CrO_4^{2-} and MoO_4^{2-} on CNT(3,3)—N and CNT(5,5)—N and for WO_4^{2-} on CNT(3,3)—N (Table 1.8). The O—N covalent bonds are created in all other adsorption cases on the N-doped adsorbents. As

Fig. 1.23 shows, creation of O—N bonds provides the highest absolute values of binding energies.

Fig. 1.23 also shows that a substantial value (ranging from ~ –0.5 to ~ –1e) of the electronic charge is transferred from the anion to the adsorbent in all adsorption configurations. Such substantial values give a reason to speak about a significant change of the adsorbent conductivity due injection of additional electronic charge after $M^{VI}O_4^{2-}$ adsorption. As it was proved by experimental and computational studies (see [210] and references therein), if the injected charge is of an order of 1e per adsorbed molecule, the electrical resistivity of the CNTs mixes can substantially depend on the number of adsorbed molecules and therefore the mixes of such type carbon materials the can be considered as perspective materials for various uses, e.g. for elaboration of gas sensors.

Fig. 1.23 shows lower values of Δq transferred to the B-doped adsorbents as compared with the pristine ones, whereas higher values of charge transfer are observed for the N-doped adsorbents. This picture is well consistent with tendencies in binding energies: the higher absolute value of E_b implies stronger covalent bonding and therefore higher absolute value of Δq transferred. At the same time, the Δq values are clearly dependent on the adsorbent type. The higher is the diameter of pristine or B-doped adsorbent (to remind, in some approximation, the graphene sheet can be considered a high-diameter SWCNT) the higher is the value of transferred charge. However, this tendency is not preserved for the N-doped adsorbents, for which configurations with O-C bonds have substantially lower $|\Delta q|$ than those having O-N bonds. The adsorption configurations 2 of un-doped graphene also have substantially lower $|\Delta q|$ than their configuration 1 counterparts.

For all configurations, except 2, the closest interatomic distances between adsorbents and $M^{VI}O_4^{2-}$ anions increase monotonically with increase of the adsorbent diameter (Table 1.8). However, this decrease is not very significant (in all cases, it is below ~7.5%).

Since our results reveal the chemisorption mechanisms, they indicate that the CNT-based materials can efficiently interact with CrO_4^{2-}, MoO_4^{2-} and WO_4^{2-} anions in gaseous media (from air). However, the situation is quite different for water environment.

In fact, the adsorbtion parameters obtained *in aqua* for the same combinations of adsorbents and $M^{VI}O_4^{2-}$ anions are given in the Table 1.9 for the *in aqua* adsorption cases.

So, we can conclude that un-doped CNTs could be less-efficient materials for adsorption of $M^{VI}O_4^{2-}$ anions in water. The efficiency can be improved if the materials would contain a valuable amount of low-diameter CNTs or they would be doped by aliovalent impurities like B or N. Both ways of improvement are expensive and hardly realizable for massive production of CNT mixtures [306, 307]. So, another mechanisms should be proposed to explain a

substantial uptake of Cr (VI) anions by CNT-based materials from water solutions observed in experiments [276, 308—311] and these mechanisms will be examined below.

Table 1.9. **Binding energies E_b (eV), charge differences Δq (e) of $M^{VI}O_4^{2-}$ (M^{VI} = Cr, Mo, W) anions adsorbed on undoped and B(N)-doped carbon nanostructures, and the shortest internuclear distances R^{min} between anions and adsorbents (Å) calculated in aqua [295]**

Type of anion	Type of doping	Configuration	E_b	Δq	R^{min} (bond type)
CrO_4^{2-}	Undoped	CNT(3,3)—CrO_4^{2-}	0.051836	–0.58393	1.47456 (C—O)
		CNT(5,5)—CrO_4^{2-}	0.679748	–0.67025	1.49594 (C—O)
		MWCNT—CrO_4^{2-}	0.03715	0.00886	4.22942 (C—O)
		GR—CrO_4^{2-}	Unconverged		
	B-doped	CNT(3,3)—B—CrO_4^{2-}	–0.75355	–0.30906	1.52525 (B—O)
		CNT(5,5)—B—CrO_4^{2-}	–0.51729	–0.38881	1.54467 (B—O)
		MWCNT—B—CrO_4^{2-}	0.487069	–0.34024	1.76103 (B—O)
		GR—B—CrO_4^{2-}	0.469333	–0.4068	1.60073 (B—O)
	N-doped	CNT(3,3)—N—CrO_4^{2-}	–2.5076	–0.6844	1.34220 (C—O)
		CNT(5,5)—N—CrO_4^{2-}	–0.04731	–0.00579	3.00821 (C—O)
		MWCNT—N—CrO_4^{2-}	0.362179	–0.74208	1.47368 (C—O)
		GR—N—CrO_4^{2-}	0.550818	–0.76429	1.48531 (C—O)
MoO_4^{2-}	Undoped	CNT(3,3)—MoO_4^{2-}	0.107118	–0.58258	1.47454 (C—O)
		CNT(5,5)—MoO_4^{2-}	0.761901	–0.65894	1.49558 (C—O)
		GR—MoO_4^{2-}	Unconverged		
	B-doped	CNT(3,3)—B—MoO_4^{2-}	–0.77034	–0.33025	1.52940 (B—O)
		CNT(5,5)—B—MoO_4^{2-}	–0.51831	–0.39701	1.54668 (B—O)
		GR—B—MoO_4^{2-}	0.492639	–0.43349	1.59292 (B—O)
	N-doped	CNT(3,3)—N—MoO_4^{2-}	–2.32348	–0.67003	1.35715 (C—O)
		CNT(5,5)—N—MoO_4^{2-}	–0.09081	–0.74556	1.44646 (C—O)
		GR—N—MoO_4^{2-}	–0.049	–0.0097	3.02454 (N—O)
WO_4^{2-}	Undoped	CNT(3,3)—WO_4^{2-}	0.176553	–0.58886	1.47833 (C—O)
		CNT(5,5)—WO_4^{2-}	0.817554	–0.65263	1.50302 (C—O)
		GR—WOO_4^{2-}	Unconverged		
	B-doped	CNT(3,3)—B—WO_4^{2-}	–0.72484	–0.34951	1.52665 (B—O)
		CNT(5,5)—B—WO_4^{2-}	–0.51958	–0.40576	1.54901 (B—O)
		GR—B—WO_4^{2-}	0.429102	–0.4245	1.60290 (B—O)
	N-doped	CNT(3,3)—N—WO_4^{2-}	–0.08849	–0.00707	3.11305 (N—O)
		CNT(5,5)—N—WO_4^{2-}	–0.01017	–0.73594	1.4535 (C—O)
		GR—N—WO_4^{2-}	0.614163	–0.73917	1.49695 (C—O)

These data show that much lower absolute values of binding energies are observed for all studied combinations relatively to corresponding cases *in vacuo*. The E_b values of all adsorption cases on MWCNT and graphene are positive indicating that adsorption of $M^{VI}O_4^{2-}$ anions by such adsorbents is energetically unfavorable. Positive are also the energies of adsorption cases on all undoped adsorbents. Only the B- and N-doped CNT(3,3) and CNT(5,5) reveal negative E_b values and these values are below –2 eV for adsorption of CrO_4^{2-} and MoO_4^{2-} on CNT(3,3). All three anions reveal no stable adsorption configurations on undoped graphene *in aqua* (geometry optimization was not convergent).

These results allowed us to conclude that undoped CNTs could be less-efficient materials for adsorption of $M^{VI}O_4^{2-}$ anions in water. The efficiency can be improved if the materials would contain a valuable amount of small-diameter CNTs or they would be doped by aliovalent impurities like B or N. Both ways of improvement are expensive and hardly realizable for massive production of CNT mixtures [306, 307]. So, another mechanisms should be proposed to explain a substantial uptake of Cr(VI) anions by CNT-based materials from water solutions observed in experiments [276, 308—311]. These mechanisms are examined in the following subsections.

REFERENCES

1. J.C. Slonczewski and P.R. Weiss, Phys. Rev. **109**, 272 (1958).
2. M.S. Dresselhaus and G. Dresselhaus, Advances in Physics. **51** (1), 1 (2002).
3. P. R. Wallace, Phys. Rev. **71**, 622 (1947).
4. Coulson, C. A., Nature, Lond., **159**, 265 (1947).
5. F. J. Corbato, Ph.D. Thesis, MIT, Cambridge, Massachusetts, 1956.
6. F. J. Corbato, in: *Proceedings of the Third Conference on Carbon* (Pergamon Press, New York, 1959), p. 173.
7. F. Bassani and G. Pastori Parravicini, Nuovo Cim. B. **50**, 95 (1967).
8. E. Doni and G. Pastori Parravicini, Nouvo Cim. B. **64**, 117 (1969).
9. G.S. Painter and D.E. Ellis, Phys. Rev. B. **1**, 4747 (1970).
10. J.W. McClure, Phys. Rev. **108**, 612 (1957).
11. J.W. McClure, Phys. Rev. **119**, 606 (1960).
12. I.L. Spain, in: *Chemistry and Physics of Carbon*, edited by P. L. Walker (Marcel Dekker, New York, 1973), vol. 8, pp. 105, 110.
13. J.W. McClure, Carbon, **7**, 425 (1969).
14. L. Samuelson, I. P. Batra and C. Roetti, Solid St. Commun. **33**, 817 (1980).
15. G. Dresselhaus and M.S. Dresselhaus, Phys. Rev. A. **140**, 401 (1965).
16. L. G. Johnson and G. Dresselhaus, Phys. Rev. B. **7**, 2275 (1973).
17. G. Dresselhaus, S.Y. Leung, M. Shayegan and T.C. Chieu, Synth. Metals. **2**, 321 (1980).
18. W. van Haeringen, and H.-G. Junginger, Solid St. Commun. **7**, 1723 (1969).
19. H. Nagayoshi, M. Tsukada, K. Nakao, and Y. Uemura, J. Phys. Soc. Japan. **35**, 396 (1973).
20. H. Nagayoshi, K. Nakao and Y. Yemura, J. Phys. Soc. Japan. **41**, 1480 (1976).

21. A. Zunger, Phys. Rev. B. **17**, 626 (1978).
22. H. Nagayoshi, J. Phys. Soc. Japan, **43**, 760 (1977).
23. T. Inoshita, K. Nakao and H. Kamimura, J. Phys. Soc. Japan. **43**, 1237 (1977).
24. N. A. W. Holzwarth and S. Rabii, Mater. Sci. Engng. **31**, 195 (1977).
25. N. A. W. Holzwarth, L. A. Girifalco and S. Rabii, Phys. Rev. B. **18**, 5206 (1978).
26. N. A. W. Holzwarth, S. Rabii and L. A. Girifalco, , Phys. Rev. B. **18**, 5190 (1978).
27. T. Ohno, K. Nakao and H. Kamimura, J. Phys. Soc. Japan. **47**, 1125 (1979).
28. J. W. McClure, in: *Proceedings of the International Conference on Semimetals and Narrow Gap Semiconductors*, edited by D. L. Carter and R. T. Bate (Pergamon Press, New York, 1971), p. 127.
29. D. E. Soule, J. W. McClure and L. B. Smith, Phys. Rev. A. **134**, 453 (1964).
30. D. E. Soule, IBM Jl Res. Dev. **8**, 268 (1964).
31. S. Williamson, S. Foner and M. S. Dresselhaus, Phys. Rev. A. **140**, 1429 (1965).
32. J. A. Woollam, Physics Lett. A. **32**, 115 (1970).
33. J. D. Cooper, J. Woore and D. A. Young, Nature, Lond. **225**, 721 (1970).
34. W. W. Toy, M. S. Dresselhaus and G. Dresselhaus, Phys. Rev. B. **15**, 4077 (1977).
35. I. L. Spain, in: *Proceedings of the International Conference on Semimetals and Narrow Gap Semiconductors*, edited by D. L. Carter and R. T. Bate (Pergamon Press, New York, 1971), p. 177.
36. D. Z. Tsang and M. S. Dresselhaus, Carbon. **14**, 43 (1976).
37. S. Ono, J. Phys. Soc. Japan. **40**, 498 (1976).
38. T. Tsuzuku, Carbon. **17**, 293 (1979).
39. N.H. Saito and T. Tsuzuku, Carbon. **11**, 469 (1973).
40. D.E. Nixon and G. S. Parry, J. Phys. D. **1**, 291 (1968).
41. R.W.G. Wyckoff, *Crustal Structures* (Interscience, New York, 1964), Vol. 1.
42. A. Herold, in: *Physics and Chemistry of Materials with Layered Structures*, edited by F. Lévy (Reidel, Dordrecht, 1979), vol. 6, p. 323.
43. D.E. Nixon, G. S. Parry and A. R. Ubbelohde, Proc. R. Soc. A. **291**, 324 (1966).
44. A.W. Syme-Johnson, Acta crystallogr. **23**, 770 (1967).
45. G.R. Hennig, in: *Progress in Inorganic Chemistry*, edited by F.A. Cotton (Interscience, New York, 1959), vol. 1, p. 125.
46. G.S. Parry, Mater. Sci. Engin. **31**, 99 (1977).
47. C. Underhill, T. Krapchev and M. Dresselhaus, Synth. Metals. **2**, 47 (1980).
48. D. Guerard, G. M. T. Foley, M. Zanini and J. E. Fischer, Nuovo Cim. B. **38**, 410 (1977).
49. W. Rudorff and W. F. Siecke, Chem. Ber. **91**, 1348 (1958).
50. H. Fuzellier, J. Melin and A. Herold, Carbon. **15**, 45 (1977).
51. J. Melin and A. Herold, Carbon. **13**, 357 (1975).
52. T. Sasa, Y. Takahashi and T. Mukaibo, Bull. chem. Soc. Japan. **45**, 2250 (1972).
53. R.S. Markiewicz, H.R. Hart Jr., L.V. Interrante and J.S. Kasper, Synth. Metals. **2**, 331 (1980).
54. M. Crespin, D. Tchoubor, L. Gatineau, F. Beguin and R. Setton, Carbon. **15**, 303 (1977).
55. S.Y. Leung and G. Dresselhaus, Phys. Rev B. **24**, 3490 (1981).
56. N. Caswell, S.A. Solin, T.M. Hayes and S.J. Hunter, Physica B, **99**, 463 (1980).
57. D.E. Nixon and G.S. Parry, J. Phys. C. **2**, 1732 (1969).
58. D. Guerard, C. Zeller and A. Herold, C. R. hebd. Seanc. Acad. Sci., Paris C, **283**, 437 (1976).

59. C. Underhill, S.Y. Leung, G. Dresselhaus and M.S. Dresselhaus, Solid St. Commun. **29**, 769 (1979).
60. G.M. Gualberto, C. Underhill, S.Y. Leung and G. Dresselhaus, Phys. Rev. B. **21**, 862 (1980).
61. S. Flandrois, J. Masson, J.-C. Rouillou, J. Gualtier and C. Hauw, Synth. Metals. **3** (1-2), 1-13 (1981).
62. R.S. Markiewicz, J.S. Kasper and L.V. Interrante, Synth Metals. **2**, 363 (1980).
63. T. Krapchev, R. Ogilvie and M.S. Dresselhaus, in: *Extended Abstracts of the 15th Biennial Conference on Carbon* (University of Pennsylvania, 1981).
64. L.B. Ebert, A. Rev. Mater. Sci. **6**, 181 (1976).
65. E. Stumpp, Mater. Sci. Engng. **31**, 53 (1977).
66. J.G. Hooley, in: *Preparation and Crystal Growth of Materials with Layered Structures*, edited by R.M.A. Leith (Reidel, Dordrecht, 1977), p. 1;
67. E. R. Falardeau, L. R. Hanlon and T. E. Thompson, Inorg. Chem. **17**, 301 (1978).
68. S. Aronson, F.J. Salzano and D. Bellafiore, J. Chem. Phys. **49**, 434 (1986).
69. S. Aronson, C. Frishberg and G. Frankl, Carbon, **9**, 715 (1971).
70. N. Kambe, M.S. Dresselhaus, G. Dresselhaus, S. Basu, A. R. McGhie and J. E. Fischer, Mater. Sci. Engng. **40**, 1 (1979).
71. D. Guerard and A. Herold, Carbon. **13,** 337 (1975).
72. N. Kambe, G. Dresselhaus and M.S. Dresselhaus, Phys. Rev. B. **21,** 3491 (1980).
73. W.D. Ellenson, D. Semmingsen, D. GueArard, D.G. Onn and J.E. Fischer, Mater. Sci. Engng. **31,** 137 (1977).
74. M.D. Chinn and S.C. Fain Jr., Phys. Rev. Lett. **39,** 146 (1977).
75. P. W. Stephens, P. Hwiney, R. J., Birgeneau and P. M. Horn, Phys. Rev. Lett. **43,** 47 (1979).
76. D. D. L. Chung, Ph.D. Thesis, MIT, Cambridge, Massachusetts, 1977.
77. R. Clarke, N. Caswell, S. A. Solin and P. M. Horn, Phys. Rev. Lett. **43**, 2018 (1979).
78. R. Clarke, N. Caswell, S. A. Solin and P. M. Horn, Physica B. **99,** 457 (1980).
79. I. Rosenman, F. Batallan and G. Furdin, Phys. Rev. B. **20,** 2373 (1979).
80. S. Postlund and A. N. Berker, Phys. Rev. B. **21,** 5410 (1980).
81. G. S. Parry and D. E. Nixon, Nature, London, **216**, 909 (1967).
82. G. S. Parry, D.E. Nixon, K. M. Lester and B. C. Levene, J. Phys. C. **2**, 2156 (1969).
83. J. B. Hastings, W. D. Ellenson and J. E. Fischer, Phys. Rev. Lett., **42**, 1552 (1979).
84. R. Clarke, N. Caswell and S.A. Solin, Phys. Rev. Lett. **42**, 61 (1979).
85. H. Zabel, S.C. Moss, N. Caswell, and S.A. Solin, Phys. Rev. Lett. **43**, 2022 (1979).
86. N. Kambe, G. Dresselhaus and M.S. Dresselhaus, Phys. Rev. B. **21**, 3491 (1980).
87. A.N. Berker, N. Kambe, G. Dresselhaus and M.S. Dresselhaus, Phys. Rev. Lett. **45**, 1452 (1980).
88. S.Y. Leung, C. Underhill, G. Dresselhaus, T. Krapchev, R. Ogilvie and M.S. Dresselhaus, Solid St. Commun. **32**, 635 (1979).
89. J.J. Lander and J.M. Morrison, Surf. Sci. **6**, 235 (1967).
90. E.L. Evans and J.M. Thomas, J. Solid St. Chem. **14**, 99 (1975).
91. W. Rudorff and E. Schulze, Z. Anorg. Allg. Chem. **277**, 156 (1954).
92. S. Aronson, F. J. Salzano and D. Bellafiore, J. Chem. Phys. **49**, 434 (1986).
93. D.G. Onn, G.M.T. Foley and J.E. Fischer, Mater. Sci. Engng. **31**, 271 (1977).
94. D.G. Onn, G.M.T. Foley and J.E. Fischer, Phys. Rev. B. **19**, 6474 (1979).
95. R. Clarke, N. Caswell, S.A. Solin and P.M. Horn, Physica B. **99**, 457 (1980).
96. H. Suematsu, K. Higuchi and S. Tanuma, J. Phys. Soc. Japan. **48**, 1541 (1980).

97. E. McRae, D. Billaud, J. F. Mareche and A. Herold, Physica B. **99**, 489 (1980).
98. M. Bottomley, G. S. Parry and A. R. Ubbelhode, Proc. R. Soc. A. **278**, 291 (1963).
99. A. R. Ubbelohde, Carbon. **6**, 177 (1968).
100. A. Avogadro, G. Bellodi, G. Borghesi, G. Samoggia and M. Villa, Nuovo Cim. B. **38**, 403 (1977).
101. A. Avogadro and M. Villa, J. Chem. Phys. **66**, 2359 (1977).
102. S.K. Khanna, E.R. Falardeau, A.J. Heeger and J.E. Fischer, Solid St. Commun. **25**, 1059 (1978).
103. K. Kawamura, T. Saito and T. Tsuzuku, Carbon. **13**, 452 (1975).
104. A. Dworkin and A.R. Ubbelohde, Carbon. **16**, 292 (1978).
105. B.R. Weinberger, J. Kaufer, A.J. Heeger, E.R. Falardeau and J.E. Fischer, Solid St. Commun. **27**, 163 (1978).
106. B.R. Weinberger, J. Kaufer, A.J. Heeger, J.E. Fischer, M. Moran and N.A.W. Holzwarth, Phys. Rev. Lett. **41**, 1417 (1978).
107. C. Zeller, L.A. Pendrys and F.L. Vogel, J. Mater. Sci. **14**, 2241 (1979).
108. E. McRae, D. Billaud, J.F. Mareche and A. Herold, Physica B. **99,** 489 (1980).
109. N.A.W. Holzwarth and S. Rabii, Mater. Sci. Engng. **31**, 195 (1977).
110. N.A.W. Holzwarth, L.A. Girifalco and S. Rabii, Phys. Rev. B. **18**, 5206 (1978).
111. N.A.W. Holzwarth, S. Rabii and L.A. Girifalco, Phys. Rev. B. **18**, 5190 (1978).
112. J.C. Slater and G. F. Koster, Phys. Rev. **94**, 1498 (1954).
113. W. Eberhardt, I.T. McGovern, E.W. Plummer and J.E. Fischer, Phys. Rev. Lett. **44**, 200 (1980).
114. G. Dresselhaus, S.Y. Leung, M. Shayegan and T.C. Chieu, Synth. Metals. **2**, 321 (1980).
115. L.G. Johnson and G. Dresselhaus, Phys. Rev. B. **7**, 2275 (1973).
116. N.A.W. Holzwarth, Phys. Rev. B. **21**, 3665 (1980).
117. L. Pietronero, S. StraÈssler, H.R. Zeller and M.J. Rice, Phys. Rev. Lett. **41**, 763 (1978).
118. L. Pietronero and S. StraÈssler, Solid. St. Commun. **32**, 1337 (1979).
119. S.A. Safran and F.J. Di Salvo, Phys. Rev. **20**, 4889 (1979).
120. H. Suematsu, S. Tanuma and K. Higuchi, Physica B. **99**, 420 (1980).
121. J.A. Woollam, E. Haugland, M.B. Dowell, N. Kambe, E. Mendez, F. Hakimi, G. Dresselhaus and M. S. Dresselhaus, in: *Extended Abstracts of the 14th Biennial Conference on Carbon* (Pennsylvania State University, 1979), p. 320.
122. G. Batallan, I. Rosenman, C. Simon, G. Furdin and H. Fuzellier, Physica B. **99**, 411 (1980).
123. T. Inoshita, K. Nakao and H. Kamimura, J. Phys. Soc. Japan. **43**, 1237 (1977).
124. A.R. Ubbelohde, Proc. R. Soc. A. **327**, 289 (1972).
125. A.R. Ubbelohde, Carbon. **14**, 1 (1976).
126. R.M. Fischer, D.J. Smith, L.A. Freeman, S.J. Pennycook and A. Howie, in: *Extended Abstracts of the 14th Biennial Conference on Carbon* (Pennsylvania State University, 1979), p. 318.
127. E. McRae and A. Herold, Mater. Sci. Engng. **31**, 249 (1977).
128. C. Zeller, G.M.T. Foley and F.L. Vogel, J. Mater. Sci. **13**, 1114 (1978).
129. C. Zeller, A. Denenstein and G.M.T. Foley, Rev. scient. Instrum. **50**, 602 (1979).
130. J.J. Murray and A.R. Ubbelohde, Proc. R. Soc. A. **312**, 371 (1969).
131. D. Guerard, P. Lagrange and A. Herold, Mater. Sci. Engng. **31**, 29 (1977).

132. S. Basu, C. Zeller, P. Flanders, C.D. Fuerst, W.D. Johnson and J.E. Fischer, Mater. Sci. Engng. **38**, 275 (1979).
133. T. Sasa, Y. Takahashi and T. Mukaibo, Bull chem. Soc. Japan. **43**, 34 (1970).
134. P. Pfluger, P. Oelhafen, H.U. Kunzi, R. Jeker, E. Hauser, K.P. Ackerman, M. Muller, and H.-J. Guntherodt, Physica B. **99**, 395 (1980).
135. A. R. Ubbelohde, Proc. R. Soc. A. **309**, 297 (1969).
136. F.L. Vogel, *Molecular Metals*, edited by W. E. Hateld (Plenum Press, New York, 1979), p. 261.
137. G.M.T. Foley, C. Zeller, E.R. Falardeau and F. L. Vogel, Solid St. Commun. **24**, 371 (1977).
138. F.L. Vogel, G.M.T. Foley, C. Zeller, E.R. Falardeau and J. Gan, Mater. Sci. Engng. **31**, 261 (1977).
139. H. Fuzellier, J. Melin and A. Herold, Carbon. **15**, 45 (1977).
140. T.E. Thompson, E.R. Falardeau and L.R. Hanlon, Carbon. **15**, 39 (1977).
141. L. Streifinger, H.P. Boehm, R. SchloÈgl and R. Pentenreider, Carbon. **17**, 195 (1979).
142. J.B. Perrachon, C. Zeller and F.L. Vogel, in: *Extended Abstracts of the 14th Biennial Conference on Carbon* (Pennsylvania State University, 1979), p. 304.
143. C. Kittel, Solid St. Commun. **25**, 519 (1978).
144. R. Dingle, in: *Festkorperprobleme* (Advances in Solid State Physics), edited by H.J. Queisser (PergamonVieweg, Braunschweig, 1975), vol. XV, p. 21.
145. L. Esaki and L. L. Chang, Thin Solid Films. **36**, 285 (1976).
146. G. Csányi, P.B. Littlewood, A.H. Nevidomskyy, C.J. Pickard and B.D. Simons, Nature Physics. **1**, 42 (2005).
147. Y. Koike, H. Suemetsu, K. Higuchi and S. Tanuma, Physica B+C. **99**, 503 (1980).
148. N.B. Hannay, T.H. Geballe, B.T. Matthias, K. Andres, P. Schmidt and D. MacNair, Phys. Rev. Lett. **14**, 225 (1965).
149. I.T. Belash, A.D. Bronnikov, O.V. Zharikov and A.V. Palnichenko, Solid State Commun. **64,** 1445 (1987).
150. T. Weller, M. Ellerby, S.S. Saxena, R. Smith and N. Skipper, Nature Phys. **1**, 39 (2005).
151. K. Novoselov, A. Geim, S. Morozov, D. Jiang, M. Katsnelson, I. Grigorieva, S. Dubonos and A. Firsov, Nature (London), **438**, 197, (2005).
152. K. Novoselov, E. McCann, S. Morozov, V. Fal'ko, M. Katnelson, U. Zeitler, D. Jiang, F. Schedin and A. Geim, Nat. Phys. **2**, 177 (2006).
153. Y. Zhang, Y. Tan, H. Stormer and P. Kim, Nature (London). **438**, 201 (2005).
154. C. L. Kane and E. J. Mele, Phys. Rev. Lett. **95**, 226801 (2005).
155. K. Nomura and A. H. MacDonald, Phys. Rev. Lett. **96**, 256602 (2006).
156. Y.-W. Son, M. Cohen and S. Louie, Nature (London). **444**, 347 (2006).
157. M. Katsnelson, K. Novoselov and A. Geim, Nat. Phys. V. **2**, 620 (2006).
158. L. Brey and H. Fertig, Phys. Rev. B. **73**, 235411 (2006).
159. K. Kusakabe and M. Maruyama, Phys. Rev. B. **67**, 092406 (2003).
160. N. M. R. Peres, F. Guinea and A. H. C. Neto, Phys. Rev. B. **73**, 125411 (2006).
161. Z. Luo, P.M. Vora, E.J. Mele, A.T. C. Johnson and J.M. Kikkawa. Appl. Phys. Lett. **94**, 111909 (2009).
162. R. Saito, G. Dresselhaus and M. S. Dresselhaus, *Physical Properties of Carbon Nanotubes* (Imperial College Press, London, 1998).
163. J.-C. Charlier, X. Blasé and S. Roche, Rev. Mod. Phys. **79**, 677 (2007).
164. S. Reich, C. Thomsen and J. Maultzsch, *Carbon nanotubes: basic concepts and physical properties* (John Wiley & Sons, New York, 2008).

165. J.A. Elliott, J.K.W. Sandler, A.H. Windle, R.J. Young and M.S.P. Shaffer, Phys. Rev. Lett. **92**, 095501 (2004).
166. T.P. Diychkova and A.G. Tkachev, *Methods of carbon nanotubes functionalization and modification* (Edition house "Spectrum", Moscow, 2013).
167. I.D. Rosca, F. Watari, M. Uo and T. Akasaka, Carbon. **43**, 3124 (2005).
168. Z. Wang, M.D. Shirley, S.T. Meikle et al. Carbon. **47**, 73 (2009).
169. N.V. Glebova and A.A. Nechitailov, Technical Physics Letters. **36** (10), 878 (2010).
170. I. Mazov, V.L. Kuznetsov, I.A. Simonova, A.I. Stadnichenko, A.V. Ishchenko, A.I. Romanenko, E.N. Tkachev and O.B. Anikeeva, Applied Surface Science. **258**. 6272 (2012).
171. G. Ovejero, J. L. Sotelo, M. D. Romero, A. Rodríguez, M. A. Ocaña, G. Rodríguez and J. García, Ind. Eng. Chem. Res. **45**, 2206 (2006).
172. A.G. Osorio, I.C.L. Silveira, V.L. Bueno and C.P. Bergmann, Applied Surface Science. **255**, 2485 (2008).
173. K. Hernadi, A. Siska, L. Thiên-Nga, L. Forró, I. Kiricsi, Solid State Ionics. **141–142**, 203 (2001).
174. Y.T. Kim and T. Mitani, Appl. Phys. Lett. **89**, 033107 (2006).
175. M.W. Wang, J. Wang, J.W. Qu. Advanced Material Research. **197–198**, 571 (2011).
176. Y. Lian, Y. Maeda, T. Wakahara, T. Akasaka, S. Kazaoui, N. Minami, T. Shimizu, N. Choi and H. Tokumoto, J. Phys. Chem. B. **108** (26), 8848 (2004).
177. V. Datsyuk, M. Kalyva, K. Papagelis, J. Parthenios, D. Tasis, A. Siokou, I. Kallitsisa and C. Galiotis, Carbon. **46** (6), 833 (2008).
178. T. Lin, V. Bajpai, T. Ji, L. Dai, Aust. J. Chem. **56**, 635 (2003).
179. M.N. Kirikova, PhD dissertation, Lomonosov Moscow State University, 2009.
180. C. M. Ng and S. Manickam, Chemical Physics Letters. **557**, 97 (2013).
181. O. Martín, H.R. Gutierrez, A. Maroto-Valiente, M. Terrones, T. Blanco and J. Baselga, Materials Chemistry and Physics. **140** (2–3), 499 (2013).
182. K. Imasaka, J. Suehiro, Y. Kanatake, Y. Kato and M. Hara, Nanotechnology. **17** (14), 3421 (2006).
183. J.-Q. Huang, Q. Zhang, M.-Q. Zhao and F. Wei, Carbon. **48**, 1441 (2010).
184. M. Ran, W. Sun, Y. Liu, W. Chu and C. Jiang, Journal of Solid State Chemistry. **197**, 517 (2013).
185. P.M. Ajayan, T.W. Ebbesen, T. Ichihashi, S. Iijima, K. Tanigaki and H. Hiura, Nature. **362** (6420), 522 (1993).
186. V. Yao, S. X. C. Lordi, E. Ma, E. Dujardin, A. Krishnan, M.M.J. Treacy and T.W. Ebbesen, J. Mater. Res. **13** (9), 2432 (1998).
187. A. Solhy, B. F. Machado, J. Beausoleil, Y. Kihn, F. Gonçalves, M.F.R. Pereira, J.J.M. Órfão, J.L. Figueiredo, J.L. Faria and P. Serp, Carbon. **46** (9), 1194 (2008).
188. F. Cataldo, Fullerenes, Nanotubes, and Carbon Nanostructures. **16**, 1 (2008).
189. J. M. Simmons, B. M. Nichols, S. E. Baker, M.S. Marcus, O.M. Castellini, C.-S. Lee, R.J. Hamers and M.A. Eriksson, J. Phys. Chem. B. **110** (14), 7113 (2006).
190. K. Peng, L.-Q. Liu, H. Li, H. Meyer and Z. Zhang, Carbon. **49** (1), 70 (2011).
191. L.-C. Tang, H. Zhang, J.-H. Han, X.-p. Wu and Z. Zhang, Composites Science and Technology. **72** (1), 7 (2011).
192. W. Xia, C. Jin, S. Kundu and M. Muhler, Carbon. **47**, 919 (2009).
193. R. W. Gosselink, R. Berg, W. Xia, M. Muhler, K.P.de Jong and J.H. Bitter, Carbon. **50** (12), 4424 (2012).

194. D. Dutta, R. Dubey, J. Yadav, T.C. Shami and K.U.B. Rao, New Carbon Materials. **26** (2), 98 (2011).
195. Yu.V. Tamarkina, I.B. Frolova, M.I. Chernyshova and V.O. Kucherenko, in: *Third National Conference "Current problems of chemistry research and perspectives" Conference Proceedings* (ZhDU Publishing House. I. Franko, Zhytomyr, 2019), pp. 157-159.
196. L. Chen, H. Xie, Y. Li and W. Yu, Thermochimica Acta. **477**, 21 (2008).
197. K.J. Ziegler, Z. Gu, H. Peng et al., J. Am. Chem. Soc. **127** (5), 1541 (2005).
198. J. Zhang, H. Zou, Q. Qing, Y. Yang, Q. Li, Z. Liu, X. Guo and Z. Du, J. Phys. Chem. B. **107** (12), 3712 (2003).
199. W. Zhou, Y. H. Ooi, R. Russo P. Papanek, D.E. Luzzi, J.E.Fischer, M.J.Bronikowski, P.A.Willis and R.E. Smalley, Chem. Phys. Lett. **350**, 6 (2001).
200. A. Hirsch and O. Vostrowsky, Top Curr Chem. **245**, 193 (2005).
201. V. Leon, R. Parret, R. Almairac, L. Alvarez, M.-R. Babaa, B.P. Doyle, P. Ienny, P. Parent, A. Zahab and J-L. Bantignies, Carbon. **50**, 4987 (2012).
202. J. Chen, Q. Chen and Q. Ma, Journal of Colloid and Interface Science. **370**, 32 (2012).
203. N. Lachman, X. Sui, T. Bendikov, H. Cohen and H.D. Wagner, Carbon. **50**, 1734 (2012).
204. P. Singjai, S. Changsarn and S. Thongtem, Materials Science and Engineering: A. **443**, 42 (2007).
205. I. Mazov, V. L. Kuznetsov, I. A. Simonova, A.I. Stadnichenko, A.V. Ishchenko, A.I. Romanenko, E.N. Tkachev and O.B. Anikeeva, Applied Surface Science. **258**, 6272 (2012).
206. S.I. Cha, T.K. Kim, K.H. Lee, C.B. Mo, Y.J. Jeong and S.H. Hong, Carbon. **46**, 482 (2008).
207. C.H. Lau, R. Cervini, S.R. Clarke, M.G. Markovic, J.G. Matisons, S.C. Hawkins, C.P. Huynh and G.P. Simon, J. Nanopart. Res. **10**, 77 (2008).
208. S. Piccozi, S. Santucci, L. Lozzi, C. Cantalini, C. Baratto, G. Sberveglieri, I. Armentano, J. M. Kenny, L. Valentini and B. Delley, J. Vac. Sci. Technol. **22**, 1466 (2004).
209. S. Agrawal, M. Raghuveer, H. Li and G. Ramanath, Appl. Phys. Lett. **90**, 19 3104 (2007).
210. Yu. Hizhnyi, S.G. Nedilko, V. Borysiuk and V. A. Gubanov, International Journal of Quantum Chemistry. **115** (20), 1475 (2015).
211. Borysiuk V.I. PhD dissertation, Taras Shevchenko National University of Kyiv, 2018.
212. B. Anderson, A. Peyster, S.C. Gad, P.J.B. Hakkinen, M. Kamrin, B. Locey, H.M. Mehendale, C. Pope, L. Shugart and P. Wexler, *Encyclopedia of Toxicology*, 2nd ed. (Academic Press, Oxford, 2005).
213. E. Aylón, R. Murillo, A. Fernández-Colino, A. Aranda, T. García, M.S. Callén and A.M. Mastral, J. Anal. Appl. Pyrolysis. **79**, 210 (2007).
214. W.J. Hall and P.T. Williams, J. Anal. Appl. Pyrolysis. **77**, 75 (2006).
215. F. Barontini and V. Cozzani, J. Anal. Appl. Pyrolysis. **77**, 41 (2006).
216. J.P.B. Karama, A. Béré, J. Lemonon, T. Daho, A. Dissa, Y. Rogaume and J. Koulidiati, J. Anal. Appl. Pyrolysis. **101**, 209 (2013).
217. D.M. Stavert, D.C. Archuleta, M.J. Behr and B.E. Lehnert, Fundam. Appl. Toxicol. **16**, 636 (1991).
218. L. Bai and Z. Zhou, Carbon. **45**, 2105 (2007).
219. Z. Zhou, X. Gao, J. Yan and D. Yan, Carbon. **44**, 939 (2006).
220. F. Villalpando-Páez, A.H. Romero, E. Muñoz-Sandoval, L.M. Martinez, H. Terrones and M. Terrones, Chem. Phys. Lett. **386**, 137 (2004).
221. R. Wang, D. Zhang, Y. Zhang and C. Liu, J. Phys. Chem. B. **110**, 18267 (2006).

222. J.-J. Adjizian, R. Leghrib. A.A. Koos, I. Suarez-Martinez, A. Crossley, P. Wagner, N. Grobert, E. Llobet and C.P. Ewels, Carbon. **66**, 662 (2014).
223. W. An and C.H. Turner, Chem. Phys. Lett. **482,** 274 (2009).
224. J.A. Talla, Phys. B Condens. Matter. **407**, 966 (2012).
225. J.A. Talla, Chem. Phys. **392,** 71 (2012).
226. T. Vikramaditya and K. Sumithra, J. Comput. Chem. **35,** 586 (2014).
227. M. J. Frisch, G. W. Trucks, H. B. Schlegel, G. E. Scuseria, M. A. Robb, J. R. Cheeseman, J. A. Montgomery, Jr., T. Vreven, K. N. Kudin, J. C. Burant, J. M. Millam, S. S. Iyengar, J. Tomasi, V. Barone, B. Mennucci, M. Cossi, G. Scalmani, N. Rega, G. A. Petersson, H. Nakatsuji, M. Hada, M. Ehara, K. Toyota, R. Fukuda, J. Hasegawa, M. Ishida, T. Nakajima, Y. Honda, O. Kitao, H. Nakai, M. Klene, X. Li, J. E. Knox, H. P. Hratchian, J. B. Cross, V. Bakken, C. Adamo, J. Jaramillo, R. Gomperts, R. E. Stratmann, O. Yazyev, A. J. Austin, R. Cammi, C. Pomelli, J. W. Ochterski, P. Y. Ayala, K. Morokuma, G. A. Voth, P. Salvador, J. J. Dannenberg, V. G. Zakrzewski, S. Dapprich, A. D. Daniels, M. C. Strain, O. Farkas, D. K. Malick, A. D. Rabuck, K. Raghavachari, J. B. Foresman, J. V. Ortiz, Q. Cui, A. G. Baboul, S. Clifford, J. Cioslowski, B. B. Stefanov, G. Liu, A. Liashenko, P. Piskorz, I. Komaromi, R. L. Martin, D. J. Fox, T. Keith, M. A. Al-Laham, C. Y. Peng, A. Nanayakkara, M. Challacombe, P. M. W. Gill, B. Johnson, W. Chen, M. W. Wong, C. Gonzalez, and J. A. Pople, *Gaussian 03* (Gaussian, Inc., Wallingford, CT, 2003).
228. G. Hong, Y. Chen, P. Li and J. Zhang, Carbon. **50**, 2067 (2012).
229. J.R. Sanchez-Valencia, T. Dienel, O. Gröning, I. Shorubalko, A. Mueller, M. Jansen, K. Amsharov, P. Ruffieux and R. Fasel, Nature. **512**, 61 (2014).
230. Y. Wang and J.T.W. Yeow, J. Sens. **2009**, 493904 (2009).
231. R. Leghrib, A. Felten, J.J. Pireaux and E. Llobet, Thin Solid Films, **520,** 966 (2011).
232. L. Valentini, I. Armentano, J.M. Kenny, C. Cantalini, L. Lozzi and S. Santucci, Appl. Phys. Lett. **82**, 961 (2003).
233. K. Kato and S. Saito, Phys. E Low-Dimens. Syst. Nanostructures. **43,** 669 (2011).
234. G. Bertoni and L. Calmels, Micron. **37**, 486 (2006).
235. U. Borštnik, M. Hodošček, D. Janežič and I. Lukovits, Chem. Phys. Lett. **411,** 384 (2005).
236. A. Ito, Y. Natsume, S. Ohmori and K. Tanaka, Nano Lett. **2**, 629 (2002).
237. V.G. Boutko, A.A. Gusev, T.N. Shevtsova and Yu G. Pashkevich, Low Temp. Phys. **37**, 1021 (2011).
238. K. Wang, C. Shi, N. Zhao, X. Du and J. Li, Chem. Phys. Lett. **469,** 145 (2009).
239. F. Buonocore, Philos. Mag. **87**, 1097 (2007).
240. R.A. Espejel-Morales, S. López-Moreno, A.G. Calles and J.L. Morán-López, Eur. Phys. J. D. **67,** 1 (2013).
241. P.N. D'yachkov, D.Z. Kutlubaev and D.V. Makaev, Phys. Rev. B. **82,** 035426 (2010).
242. M.D. Esrafili, Comput. Theor. Chem. **1015,** 1 (2013).
243. L. Zhang and Z. Xia, J. Phys. Chem. C. **115,** 11170 (2011).
244. G. Fazio, L. Ferrighi and C. Di Valentin, J. Catal. **318**, 203 (2014).
245. A.S. Ghasemi, Research Journal of Applied Sciences, Engineering and Technology **5** (6), 1892 (2013).
246. A. Galano, Chem. Phys. **327**, 159 (2006).
247. I.K. Petrushenko and N.A. Ivanov, Mod. Phys. Lett. B. **27,** 1350210 (2013).
248. A.D. Becke, J. Chem. Phys. **98,** 5648 (1993).

249. C. Lee, W. Yang and R.G. Parr, Phys. Rev. B. **37,** 785 (1988).
250. V.I. Minkin, Pure Appl. Chem. **71** (10), (1999).
251. J.N. Israelachvili, *Intermolecular and Surface Forces*, 2nd ed. (Academic Press, London, 1991).
252. S. Owen, C. Ahmed, C. Martin and R. Woodward, *Chemistry for the IB Diploma* (Cambridge University Press, 2011).
253. K.R. Kunduru, M. Nazarkovsky, S. Farah, R.P. Pawar, A. Basu and A.J Domb, in: *Water Purification*, edited by A.M. Grumezescu (Academic Press, 2017), pp. 33-74.
254. K.K. Yadav, J.K. Singh, N. Gupta, V. Kumar, JMES. **8** (2), 740 (2017).
255. M. Anjum, R. Miandad, M. Waqas, F. Gehany and M.A. Barakat, Arab. J. Chem. **12** (8), 4897 (2019), doi:10.1016/j.arabjc.2016.10.004.
256. I. Mohmood, C. B. Lopes, I. Lopes, I. Ahmad, A. C. Duarte and E. Pereira, Environ. Sci. Pollut. Res., **20**, 1239 (2013).
257. M. Ghashghaee and V. Farzaneh, Iranian Journal of Toxicology. **10** (6), 15 (2016).
258. A. Tytłak, P. Oleszczuk and R. Dobrowolski, Environ. Sci. Pollut. Res., **22**, 5985 (2015).
259. P.K. Pandey, S.K. Sharma and S.S. Sambi, Int. J. Environ. Sci. Technol. **7**, 395 (2010).
260. T. Dula, K. Siraj and S.A. Kitte, ISRN Environmental Chemistry. **2014**, 438245, (2014), https://doi.org/10.1155/2014/438245.
261. B. Salunkhe and S.J. Raut, Int. J. Chem. Sci. **10** (2), 1133 (2012).
262. M. A. Shouman, N.A. Fathy, S.A. Khedr and A.A. Attia, Adv. Phys. Chem. **2013**, 159712 (2013), DOI: 10.1155/2013/159712.
263. D. Satapathy, G. S. Natarajan and S.J. Patil, J. Chin. Chem. Soc. **52**, 35 (2005).
264. M.I.E. Halmi and S.A. Ahmad, J. Biochem. Microbiol. Biotechnol. **2**, 1 (2014).
265. C.-W. Wang, C. Liang and H.-J. Yeh, Chemosphere. **147**, 82 (2016).
266. S. Datta, S. E. Vero, G. M. Hettiarachchi and K. Johannesson, Curr.Pollut. Rep. **3**, 55 (2017).
267. M. Dakiky, M. Khamis, A. Manassra and M. Mer'eb, Adv. Environ. Res. **6**, 533 (2002).
268. J. Romero-GonzÅlez, J.R. Peralta-Videa, E. Rodrıguez, S.L. Ramirez and J.L. Gardea-Torresdey, J. Chem. Thermodyn. **37**, 343 (2005).
269. R. Yavuz, İ. Orbak and N. Karatepe, J. Environ. Sci. Health Part A. **41**, 1967 (2006).
270. R. Gottipati, Ph.D. dissertation, National Institute of Technology Rourkela, 2012.
271. S. Yang, J. Li, D. Shao, J. Hu and X. Wang, J. Hazard. Mater. **166**, 109 (2009).
272. X. Ren, C. Chen, M. Nagatsu and X. Wang, Chem. Eng. J. **170**, 395 (2011).
273. C. Jung, J. Heo, J. Han, N. Her, S.J. Lee, J. Oh and Y. Yoon, Sep. Purif. Technol. **106**, 63 (2013).
274. Y. Xu, A. Rosa, X. Liu and D. Su, New Carbon Mater. **26**, 57 (2011).
275. J. Hu, C. Chen, X. Zhu and X. Wang, J. Hazard. Mater. **162**, 1542 (2009).
276. F.A. Ihsanullah Al-Khaldi, B. Abu-Sharkh, A. M. Abulkibash, M. I. Qureshi, T. Laoui and M.A. Atieh, Desalination and Water Treatment. **57** (16), 7232 (2016).
277. K. Pillay, E. M. Cukrowska and N.J. Coville, J. Hazard. Mater. **166**, 1067 (2009).
278. V. K. Gupta, O. Moradi, I. Tyagi, S. Agarwal, H. Sadegh, R. Shahryari-Ghoshekandi and A. Garshasbi, Crit. Rev. Environ. Sci. Technol. **46**, 93 (2016).
279. D. Iannazzo, A. Pistone, I. Ziccarelli, C. Espro, S. Galvagno, S.V. Giofré and L. Legnani, Environmental Science and Pollution Research. **24** (17), 14735 (2017).
280. I. Shtepliuk, N.M. Caffrey, T. Iakimov, V. Khranovskyy, I.A. Abrikosov and R. Yakimova, Scienti reports. **7** (1), 3934 (2017).

281. P.E. Diaz-Flores, F. López-Urı, M. Terrones and J.R. Rangel-Mendez, Journal of colloid and interface science. **334** (2), 124 (2009).
282. O.A. Oyetade, A.A. Skelton, V.O. Nyamori, S.B. Jonnalagadda and B.S. Martincigh, Separation and Purification Technology. **188**, 174 (2017).
283. A.S. Deb, V. Dwivedi, K. Dasgupta, S. M. Ali and K. T. Shenoy, Chemical Engineering Journal. **313**, 899 (2017).
284. Y. Hizhnyi, S. Nedilko, V. Borysiuk and A. Shyichuk, Nanoscale Res. Lett. **12**, 71 (2017).
285. A.K. Sengupta and D. Clifford, Environ. Sci. Technol. **20**, 149 (1986).
286. A.K. Sengupta, S. Subramonian and D. Clifford, J. Environ. Eng. **114**, 137 (1988).
287. D. Zhao, A.K. SenGupta and L. Stewart, Ind. Eng. Chem. Res. **37**, 4383 (1998).
288. C. Cazorla, Coord. Chem. Rev. **300**, 142 (2015).
289. T.M. Radchenko, V.A. Tatarenko, I.Y. Sagalianov and Y.I. Prylutskyy, Phys. Lett. A. **378**, 2270 (2014).
290. U. Ritter, N.G. Tsierkezos, Y.I. Prylutskyy, L.Y. Matzui, V.O. Gubanov, M.M. Bilyi and M.O. Davydenko, J. Mater. Sci. **47**, 2390 (2012).
291. A. Abbas, A.M. Al-Amer, T. Laoui, M.J. Al-Marri, M.S. Nasser, M. Khraisheh and M.A. Atieh, Sep. Purif. Technol. **157**, 141 (2016).
292. B. Saha and C. Orvig, Coord. Chem. Rev. **254**, 2959 (2010).
293. J. Kotaś and Z. Stasicka, Environ. Pollut. **107**, 263 (2000).
294. A.K. Shanker, C. Cervantes, H. Loza-Tavera and S. Avudainayagam, Environ. Int. **31**, 739 (2005).
295. Y. Hizhnyi, S. Nedilko, V. Borysiuk, A. Shyichuk, International Journal of Quantum Chemistry. **118** (20), e25715 (2018).
296. I. Vasiliev, M. L. del Puerto, M. Jain, A. Lugo-Solis and J.R.J. Chelikowsky, Mol. Struct. THEOCHEM. **914**, 115 (2009).
297. T. H. J. Dunning, Chem. Phys. **90**, 1007 (1989).
298. K. A. Peterson, D. Figgen, M. Dolg and H. J. Stoll, Chem. Phys. **126**, 124101 (2007).
299. D. Figgen, K. A. Peterson, M. Dolg and H. J. Stoll, Chem. Phys. **130**, 164108 (2009).
300. I. Kumari, S. Gupta and N. Goel, Comput.Theor. Chem. **1091**, 107 (2016).
301. H.-J. Zhai, S. Li, D.A. Dixon and L.-S. Wang, J. Am. Chem. Soc. **130**, 5167 (2008).
302. S. Miertuљ, E. Scrocco and J. Tomasi, Chem. Phys. **55**, 117 (1981).
303. S.F. Boys and F. Bernardi, Mol. Phys. **19**, 553 (1970).
304. I. Seidu, M. Krykunov and T.J. Ziegler, Chem. Theory Comput. **11**, 4041 (2015).
305. W.M. Haynes, editor, *CRC Handbook of Chemistry and Physics* (CRC press, Boca Raton, 2014).
306. F. Mercuri, M. Baldoni and A. Sgamellotti, Nanoscale. **4**, 369 (2012).
307. C. P. Ewels and M. J. Glerup, Nanosci. Nanotechnol. **5**, 1345 (2005).
308. C.-G. Lee and S.-B. Kim, Water Environ. Res. **88**, 2111 (2016).
309. E. M. Verdugo, Y. Xie, J. Baltrusaitis and D. M. Cwiertny, *RSC Adv.*, **6**, 99997 (2016).
310. M. H. Dehghani, M.M. Taher, A.K. Bajpai, B. Heibati, I. Tyagi, M. Asif and V. K. Gupta, Chem. Eng. J., **279**, 344 (2015).
311. E.M. Elsehly, N.G. Chechenin, A.V. Makunin, H.A. Motaweh, E.A. Vorobyeva, K.A. Bukunov and A.B. Priselkova, Chin. J. Chem. Eng. **24**, 1695 (2016).
312. D. Tasis, N. Tagmatarchis, A. Bianco and M. Prato, Chem. Rev. **106**, 1105 (2006).
313. V. Georgakilas, N. Tagmatarchis, D. Pantarotto, A. Bianco, J.P. Briand and M. Prato, Chem. Commun. **24**, 3050 (2002).

CHAPTER 2

EXPANDED GRAPHITE AND SOLID MATERIALS BASED ON IT

Nowadays, one of the most promising areas of nanotechnology is the synthesis and application of carbon nanomaterials. Among these materials, expanded graphite (EG) occupies a prominent place, which best realizes the unique properties of graphene in the production of the material on an industrial scale.

The phenomenon of thermal expansion of graphite has been known since the late 19th century, when an increase in the volume of the carbon sample, i.e. its expansion, was observed after interaction with Bronsted acids and heating. But only in the mid-60s of the 20th century, the stage of the recent history of research and industrial use of EG began.

Intensive development as used in industry for the production of sealing materials and seals [1—4], research-modeling of the structure and properties of EG [1, 5], development of new hybrid materials for electrodes of chemical current sources [6, 7], obtaining composite carbon-carbon materials [8, 9], synthesis of graphene nanoparticles and materials from them [10—14], reinforcement of polymeric materials [12, 15—17], etc. are going on today.

Practical application of EG in the world practice began in the 60s of last century, while in the USSR, and then in independent Ukraine, industrial technology did not exist until the beginning of the 21st century.

Expanded (exfoliated) graphite [1, 2], or thermographite [18, 19], is a group of materials with a graphite-like structure, obtained by rapid heating (thermal shock) at temperatures of 800—1100 °C of graphite intercalation compounds (GIC) or their hydrolyzed forms. The decomposition and evaporation of the intercalant lead to a strong expansion along the axis perpendicular to the graphene planes. This effect is observed for GIC with various intercalants such as acids, metal chlorides, halogens, etc., but it is most pronounced for graphite salts with anions of

mineral acids, the molecules of which easily form gaseous products and allow one to obtain EG powder with a specific surface area of 50—100 m^2/g.

Natural graphite in the state of EG acquires the ability to form into a solid material without binders, which allows it to be used as a basis for a wide class of carbon materials: sealing, electrical, antifriction, structural, polymer, and rubber fillers [18, 19].

Thus, in particular, both GIC and EG are used to create effective current sources that have a long term of operation and are intended for the manufacture of various microelectronics products. They are also used as catalysts of chemical reactions and coolants, in the manufacture of explosion-proof membranes, sound-proof materials, fillers for filters, various kinds of membranes, diamagnetic suspensions and screens, sensors of magnetic field and temperature, nonmetallic heaters of any form, etc.

In addition to practical use, these materials, due to the peculiarities of their structure, represent significant scientific interest as objects of research for fundamental phenomena. For example, they have inherent negative magnet resistance and two-dimensional electronic structure, which allows conducting an experimental study of the physical properties of low-dimensional systems.

Consumer properties of composite materials (CM) on the basis of EG, including physical-mechanical characteristics, are determined by the peculiarities of their crystalline structure and phase composition, as well as the strength of bonds between EG particles arising in the process of material formation and adjusting the structural state of the surface and volume of EG particles in certain limits by changing the conditions of oxidative and thermal treatments of natural graphite [19—21].

Chemical modification of the surface of EG particles, in particular, by thermosetting organic compounds, allows enhancing interparticle interaction and creating a continuous distributed carbon structure in the graphite matrix, which qualitatively changes the physical and mechanical characteristics of CM. A significant increase in the strength characteristics of CM is achieved by introducing into the system of EG-carbon or EG-polymer highly modular components, namely carbon fiber or carbon nanotubes/nanofibers [22].

Modification of EG surface with metals, nonmetals, or their oxides during the reaction of its formation also opens wide possibilities for regulating the physicochemical properties of composite materials based on EG [23, 24].

The process of obtaining EG is multi-stage, so the purposeful formation of its structure and properties requires a thorough study of physicochemical processes starting from the purification of natural graphite, its intercalation in the cleanest, energy- and resource-saving way, in particular by electrochemical (anodic) oxidation in sulfuric acid to obtain graphite intercalated with sulfuric acid (GIC-H_2SO_4), hydrolysis of GIC-H_2SO_4, drying, heat treatment by rapid heating, followed by compaction via rolling or pressing [1, 2].

2.1. Graphite intercalated compounds: methods of obtaining and purifying

Graphitized carbon and its products, as well as metals and their alloys, polymers, ceramics, etc., hold a special place among materials widely used in industry. In all their diversity one can distinguish two large classes: synthetic graphitized carbon materials obtained by hydrocarbon pyrolysis and materials fabricated from natural graphite [1, 25].

Natural graphite occurs in the Earth's crust in the form of individual deposits accompanied by other minerals such as quartz, feldspar, glist, pyrite, calcium carbonate minerals, complex and aluminum silicates, etc. The content of graphite in the deposits can vary from a few fractions of a percent up to 10—20%. Deposits with a graphite content of 5% or more are considered minable. Graphite is extracted from an ore mineral by the flotation method as described, for example, in [26]. Basically, flotation concentrates with 94—97% wt. of carbon are mass-produced. The dispersed graphite raw material with a content of high-ash admixtures of (4—15)% wt. represents more than 90% of the overall production and is widely used foremost in metallurgy, refractory materials manufacturing, oil and gas extraction, etc. But it should be noted that even these industries eventually increase their demands for the purity of graphite. For example, the refractory materials industry uses raw materials with graphite content of at least 97% wt. Therefore, the task of optimizing the processes of chemical cleaning of the flotation concentrate or the second-stage cleaning of the low-ash raw graphite is quite important [27].

The chemical content of ash admixtures is different but could be approximated as listed in Table 2.1.

The content of microelements is even more variable depending on the deposit and can include the following elements (Table 2.2).

The dispersity is a second important feature of natural graphite. Since graphite ore processing by flotation is associated with wet grinding, the main part of the graphite scale in aggregates is dispersed. Thus, the content of the

Table 2.1. **The chemical content of ash admixtures in the graphite deposits**

SiO_2, % wt.	Al_2O_3, % wt.	Fe_2O_3, % wt.	CaO, % wt.	MgO, % wt.	S, % wt.
50—65	11—20	6—20	1—4	1—5	0.5—3.0

Table 2.2. **The content of microelements in the graphite raw material**

Cu, ppm	Ti, ppm	Mn, ppm	Mo, ppm
5—35	25—110	15—65	5—35

most valuable fraction (≥200 μm) in the froth-floated slurry does not exceed 25% wt. The most common brands of natural graphite produced are 500 μm (32 mesh), 315 μm (50 mesh), 200 μm (80 mesh), 160 μm (100 mesh), et al.

Graphite sublimates at temperatures above 3000 °C, however, the study of graphite in a liquid state requires even more critical conditions [28]. Therefore, the exfoliated (expanded) graphite technology is the only possibility to obtain a solid material of natural graphite on an industrial scale.

Intercalated compounds can be formed from carbon materials with a graphite-like (layered) structure both synthetic as artificial graphite or pyrolytic graphite and natural graphite with different orders of structure perfection. However, the natural macrocrystalline (flake) graphite of high purity is generally used for the production of expanded graphite on an industrial scale. It demonstrates the maximum effect of thermal exfoliation during the formation of the graphite intercalation compounds (GICs) with Bronsted acids.

The current technologies for the Bronsted-acid-assisted production of GICs, which are thermally expanded under heating, are based on the concept of oxidation and intercalation reactions shown in the schematic diagram:

$$C_n + HA \xrightarrow{O_x\,(I)} C_n^+ A^- \cdot xHA \xrightarrow{R(II)} \mathrm{RGIC}, \tag{2.1}$$

where C_n is a graphene layer fragment in the graphite matrix; C_{24} is the minimal fragment of the layer that is necessary for the formation of stoichiometric GIC (defined empirically); *HA* is the Bronsted acid (H_2SO_4, HNO_3, H_3PO_4); O_x is the oxidizing substance (HNO_3, $K_2Cr_2O_7$, $KMnO_4$, $(NH_4)_2S_2O_8$, H_2O_2, O_3, CrO_3, anodic oxidation); *R* is a chemical reagent (H_2O, NH_4OH, etc.), and RGIC is the residual compound of graphite intercalation.

The process of the first stage (I) is the oxidation process of graphite with GIC formation. The process of the second stage (II) is the GIC treatment with the formation of RGIC as a final product. Process (II) is needed to stabilize the characteristics of the obtained graphite compounds in time and to add specific properties, for example, the desired pH value of the aqueous extract. Structural features of EG are defined by the conditions of GIC obtaining and transformation, ie by the conditions of (I) process, the content of the final product obtained by (II) process, and by the thermal decomposition of RGIC.

Process (I) is a conjugation of oxidation reactions of the graphite matrix [C] and the formation of the product of inclusion of intercalants (HNO_3, H_2SO_4, $HClO_4$, H_3PO_4, $H_4P_2O_7$, etc.) in the presence of oxidant O_x [26]:

$$[\mathrm{nC}] \xrightarrow{[\mathrm{Ox}]} C_n^+, \tag{2.2}$$

$$C_n^+ + A^- + \mathrm{m}HA \longrightarrow [C_n^+ A^- \times \mathrm{m}HA]. \tag{2.3}$$

The structural features of EG are determined by the GIC structure (process (I)), the state of the product obtained in process (II), and the conditions of thermal decomposition. The direction and depth of processes (2.2) and (2.3) determine the result: obtaining GIC, peroxidation (up to the formation of graphite oxide) and "wet combustion" of carbon, and so on. Prediction of properties of the final product of oxidation and intercalation reactions is possible under conditions when the real values of oxidation potentials are known. In this regard, the determination of thermodynamic conditions of these reactions has always been given much attention [28, 29]. An experimental study of oxidation potentials by two- or three-electrode methods, *HA* — [O_x] media, and GIC potentials by direct potentiometric in situ was carried out in detail in [29]. Experimentally determined values of Red/Ox-potentials of the model system with pyrolytic graphite of a high degree of structure perfection as a matrix on the scale of the hydrogen electrode are given in Table 2.3 [29].

One of the characteristic features of GIC is the presence of some stages of intercalation [1—3, 18]. In the n stage compound, each pair of intercalant layers is separated by n number of graphene layers. The intercalation compounds of stage 1 graphite are more graphene-concentrated, and the EG formed from them best realizes the unique properties of graphene. The composition of GIC with sulfuric acid (graphite bisulfate) can be described by the gross formula $C^{+}_{24n} \cdot HSO^{-}_{4} \times 2{,}5\ H_2SO_4$ [1, 2]. Table 2.3 shows the potentials of graphite bisulfate stages 1—5 in reactions with 94 wt.% H_2SO_4 and in the presence of various oxidants [28, 29] or anodic oxidation [30, 31].

Of course, in the case of the intercalant inclusion between graphene planes, the period of identity (Ic) of the crystal structure in the direction of the *c*-axis increases (Chapter 1).

For the implementation of each stage of GIC, there are values of potentials that indicate the correspondence of the action of chemical (or electrochemical) oxidation. It has been established in [29] that the potential for the formation of E_{GIC} is

Table 2.3. **Potentials for the formation of graphite bisulfate E_{GIC}**

Stage number (n)	$H_2SO_4 + [K_2Cr_2O_7]$		$H_2SO_4 + [KMnO_4]$		H_2SO_4, electrochem. [30]	H_2SO_4, electrochem. [31]
	E_{Hg/Hg_2SO_4}, V experiment	E_{H_2}, V	E_{Hg/Hg_2SO_4}, V experiment	E_{H_2}, V	E_{Hg/Hg_2SO_4}, V	E_{H_2}, V
1	1.02—1.30	1.63—1.91	1.02—1.50	1.63—2.11	0.83—1.33	1.44—1.94
2	0.70—0.85	1.31—1.46	0.80—0.90	1.41—1.50	0.55—0.83	1.16—1.44
3	0.62—0.65	1.23—1.26	0.60—0.65	1.21—1.26	0.48—0.55	1.09—1.16
4	0.61	1.22	0.60	1.21	—	—
5	0.50	1.11	0.50	1.11	—	—

a quantitative characteristic that determines the number of stages, for the implementation of which, obviously, you need to choose an oxidant with $E_{H_2} \geq E_{GIC}$. The thermodynamic conditions for the GIC formation with one stage or another are determined by the potential of the reaction medium, but its implementation involves the use of the stoichiometric amount of oxidant in the synthesis.

The study of the kinetic dependences of the potential E(t) of graphite samples shows [3, 29] their stepwise nature. The sections parallel to the abscissa axis correspond to the mixture potential for two stages, (n) and (n + 1), and the intervals on the slopes of these dependences correspond to the degree (n). The potential of the last horizontal "section" characterizes the potential of the oxidant solution. This behavior of E (t) is a confirmation of the domain model of the GIC structure.

The depth of oxidation of the graphite matrix depends on the potential of the oxidant solution. Its certain value can lead to re-oxidation of the first degree, amorphization of the product structure, and the effect on the kinetics of intercalant inclusion. Thus, the minimum time of formation of GIC I degree for the system [Graphite—H_2SO_4—$KMnO_4$], then with $K_2Cr_2O_7$, and so on. Thus, the main regularity of the process of GIC formation is that the Red/Ox potential of the oxidant determines the thermodynamics and kinetics of the inclusion process.

The well-known industrial technologies for producing exfoliated graphite use nitric and sulfuric acids as intercalants, $K_2Cr_2O_7$ and $(NH_4)_2S_2O_8$ as oxidizers due to their ability to expand.

The graphite — H_2SO_4/HNO_3 system:

$$C_n + 3H_2SO_4 + HNO_3 \rightarrow C_{24}^{+}HSO_4^{-} \cdot 2H_2SO_4 + H_2O + NO_2 + C_{n-24}. \qquad (2.5)$$

The graphite — $H_2SO_4/K_2Cr_2O_7$ system:

$$C_n + 25H_2SO_4 + K_2Cr_2O_7 \rightarrow 6C_{24}^{+}HSO_4^{-} \cdot 2{,}5H_2SO_4 + Cr_2(SO_4)_3 + \\ + K_2SO_4 + 7H_2O + C_{n-144}. \qquad (2.6)$$

The graphite-$H_2SO_4/(NH_4)_2S_2O_8$ system:

$$C_n + 5H_2SO_4 + (NH_4)_2S_2O_8 \rightarrow \\ \rightarrow 2C_{24}^{+}HSO_4^{-} \cdot 2H_2SO_4 + (NH_4)_2SO_4 + C_{n-48}. \qquad (2.7)$$

The stage of GIC is defined by the sequence of filling of the interlayer spaces in the graphite lattice by the doping substance (intercalant). An intercalant fills the whole interlayer space in the most saturated GIC of stage 1. GIC of stages 2 and 3 is formed if an intercalant occupies each second or third position of the interlayer space, respectively.

The process of obtaining graphite nitrate via the treatment of graphite by fuming nitric acid can be expressed as:

$$C_n + 5HNO_3 \rightarrow C_{24}^{+}NO_3^{-} \cdot 3HNO_3 + NO_2 + H_2O + C_{n-24}. \quad (2.8)$$

The processes of chemical intercalation and their features depending on the types of *HA*, O_x (I), and *R*(II) in (2.1) have been studied sufficiently [1, 5—14].

Anodic Oxidation Method. Electrochemical intercalation or anodic oxidation is the greenest, resource- and energy-saving method of producing GICs under well-controlled conditions [18, 28, 29, 32], which allows reaching the specific characteristics of EG, including regulation of the structural and chemical state of its surface [33, 34].

The chemical composition of GIC with sulfur acid can be expressed by the following empirical formula: $C_{24i}^{+} \cdot HSO_4^{-} \cdot 2{,}5H_2SO_4$ [2], where *i* is the GIC stage number. The value of electric power calculated by the Faraday laws [35] as required for the graphite matrix oxidation to obtain stage 1 GIC H_2SO_4 is equal to 93 A · h/kg; to obtain 1 + 2 stage GIC — 62 A · h/kg; to obtain stage 2 GIC — 46.5 A · h/kg. These values are i good agreement with the data listed in [36]. So, one can speculate that the electrical consumption will vary from 0.372 to 0.744 kW · h at the voltage of 4—8 V to treat 1 kg of graphite to obtain stage 1 GIC.

A number of studies are devoted to obtaining GICs by anodic oxidation of graphite in sulfur and nitric acids [18,19, 32, 36—42]. Electrolytic cells of laboratory size with a charge of graphite up to 100 g were used for the studies [18, 28, 29, 32—40]. The difficulties in creating an effective electrochemical reactor for the anodic treatment of dispersed carbon powders consist in a proper electric contact supply throughout particles and the necessity of using corrosion- and acid-resistant materials for the reactor vessel and electrodes, removal of gases formed during the side reaction of water electrolysis, compensation for the increase in the volume of the solid reaction mass due to the increase in the interlayer distance of graphene planes in the GICs formed. It is worth noting that the equipment schemes for GICs industrial production presented in the literature [36] are too complicated and have rather theoretical than practical meanings.

The periodical regime involves loading the graphite material in the reactor filled with acid, intercalation process, draining the spent electrolyte, GIC unloading, and further processing. The results of the process study in the laboratory cells are given in [18, 37, 38]. Anodic oxidation of powders is performed in three ways:

- on a horizontal anode in a vertical column with free powder backfilling, with a horizontal cathode;
- on a horizontal anode in a vertical column with powder bias against the anode by the piston, with a horizontal cathode;

• on a vertical anode with powder bias against the anode by the piston, with a vertical cathode.

All the variants include an acid bath, furthermore, sometimes flushing of acid through the graphite. The sulfuric acid of 50% concentration has been used in [39] while both sulfuric and nitric acids of 93 and 55% concentration respectively have been used in [37, 38]. The authors of [18] recommend using an anode current density of 50 mA/cm^2 and an H_2SO_4 content of ~30—50%. Thus, the power consumption for obtaining intercalated graphite of high quality is limited by 60—400 A · h/kg.

The authors of [43] analyzed the processes of periodic intercalation of graphite with sulfuric acid in electrochemical reactors of different designs: a flow reactor with freeloading of graphite; a reactor with vertical electrodes; a cassette reactor with a vertical arrangement of electrodes; a horizontal cassette reactor in different modes. In [44] the principles of construction of a new electrochemical reactor are offered.

The main disadvantage of batch reactors is the need to stop the process, so the work was continued in order to create an efficient electrochemical reactor of continuous operation [45]. One of the elements of solving the problem is the arrangement of continuous movement of the pulp "graphite-acid" in the gap between the anode plate and the separator to ensure close contact of the mixture with the current discharge. Thus, the possibility of moving graphite material with the help of a piston and an auger has been established. The authors [46] propose a device that uses the principle of pushing a graphite-electrolyte mixture with a piston or auger and a cathode made in such a way that it can perform oscillational and rotational movements, which should eliminate jamming, occurring due to expanding graphite during its oxidation. The authors [29, 47—49] have proposed forced transportation of the working mixture through the gap, which expands between the anode plate and the porous diaphragm. The main disadvantages of this method are the need to use graphite only one brand (or particle size) because the effect of the expansion of graphite particles because of intercalation depends on their sizes. In the case of a smaller dispersion of particles, jamming can occur, and in the case of a larger one, contact violation in the electrical circuit takes place.

Therefore, in [49], a suspension was previously obtained by holding graphite in 80—98% wt. nitric acid till the formation of intercalation compounds of graphite 2 or 3 stages, and subsequent anodic oxidation led to the production of stage 1 GIC. Thus, compensation for the effect of increasing the suspension volume of the due to anodic oxidation is achieved. This process is implemented in a device comprising a carousel-type reactor with a cylindrical body, an annular anode in the form of a chute mounted in the housing coaxially with it, and cathodes made in the form of blades radially mounted on an axial vertical shaft and mounted in the chute anode, with the possibility of their longitudi-

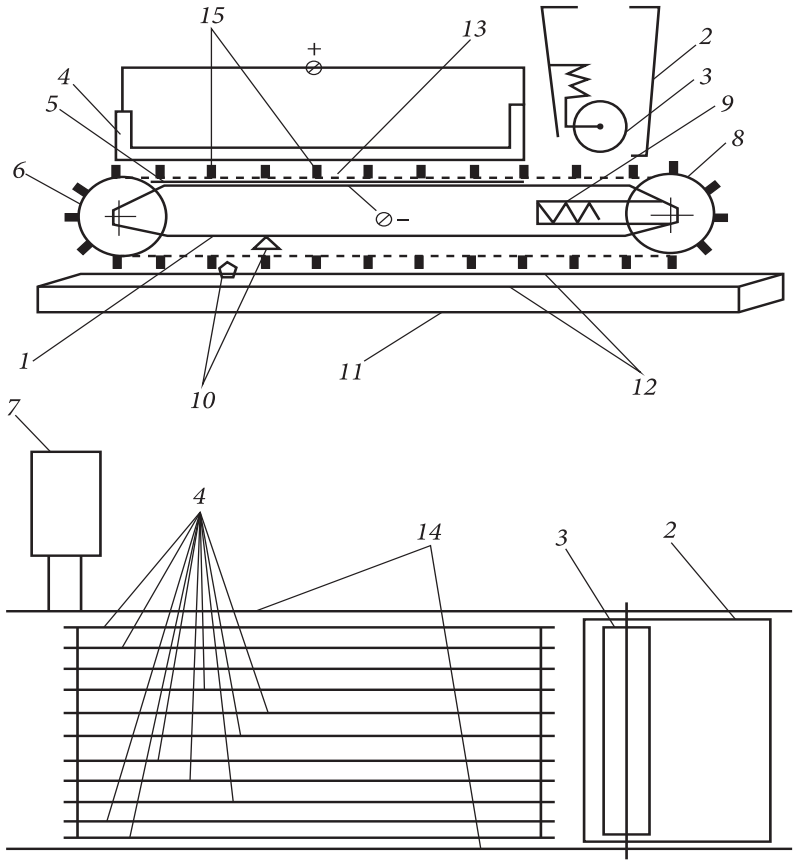

Fig. 2.1. Schematic diagram of the reactor for intercalation of graphite: *1* — reactor frame; *2* — loading hopper; *3* — leveling roll; *4* — component anode; *5* — perforated cathode; *6* — drive drum; *7* — drive drum drive; *8* — tension drum; *9* — device of the tension drum; *10* — flushing collectors; *11* — receiving tray; *12* — restrictive walls; *13* — movable membrane (separator); *14* — limiting boards; *15* — cross-sections

nal movement in the reaction chambers [47]. While in [29] a large amount of concentrated acid was required, in [46—49] almost only wetted ("semi-dry") mixtures of graphite with solutions are used.

The continuous movement of graphite mixture along the separator (or compatible with it) over time leads to clogging of the separator pores because in graphite raw materials of any dispersion there is always a very small fraction ("tail" in the particle size distribution), which can enter the pores and cause a short circuit between the electrodes. The disadvantages of these devices are not only the complexity of the design and low productivity but also the insufficient efficiency of cleaning the separator from GIC. No scrapers allow you to completely clean the separator if it is clogged with a fine fraction of graphite.

The following is a description of the simple design of the reactor, which allows the achievement of high productivity at low energy costs and preserves the consumer properties of thermally expanded graphite obtained from the thus synthesized GIC. The problem is solved by taking into account the fact that according to [44] the method for obtaining GIC includes: mixing graphite with 30—94% sulfuric acid at the ratio of 0.5—1.0 cm^3 of solution per 1 g of graphite; transporting the mixture through the zone of electrochemical treatment; transmitting a direct current with a density of 25—42 mA/cm^2 through the mixture layer.

According to the proposed technical solution [50, 51] (Fig. 2.1), a mixture of graphite with sulfuric acid is loaded into the hopper (2) with a leveling device (3), which by means of roll presses and levels the mixture. The loading hopper (2) is located above the movable membrane (separator) (13), made in the form of a closed conveyor belt with fixed transverse profiles (15). The membrane (13) is moved along the cathode (5) surface at a speed of (1—18) cm/min. The anode (4) has the shape of knife electrodes located with a gap (10—25) mm from each other at a distance of 4—14 mm from the separator surface. Next, during the separator passage along the cylindrical surface of the drum (6), there occurs a partial detachment of the GIC mixture from its surface. At the beginning of the reverse movement, the mixture falls on the receiving tray (11), where the remnants of the adhered intercalated graphite are washed off by jets of water from washing collectors (nozzles) (10) located on both sides of the separator. The roll (3) evens and adjusts the thickness of the mixture layer of graphite with a sulfuric acid solution. The membrane (13) is fixed on the drive (6) and tension drums (8) with a device (9) that stretches the membrane.

The device for unloading GIC is made in the form of an inclined receiving tray (11), from which water flows from the flushing collectors to wash the GIC on the suction filter.

To test the method, graphite (brand GSM-2, GOST 17022-81), sulfuric acid (DSTU 4204), and the device according to the scheme in Fig. 2.1 were used. Fig. 2.2 shows a 3D diagram of the electrochemical reactor and a photograph of production tests.

The ability to thermally expand the GIC obtained was determined by the expanded coefficient (K_c^{1000}, cm^3/g). For this purpose, water-washed and dried GIC samples were used. In a quartz beaker placed in a mine furnace heated to 1000 °C, a suspended 1 g sample of GIC was added and kept for 60 s until completely swollen. The beaker with the expanded graphite was removed from the furnace. After cooling, the EG was moved to the measuring cylinder, and its volume (V) was determined. The coefficient of thermal expansion for each sample was calculated as an average of three measurements by the formula:

$$K_c^{1000} = V/m. \quad (2.9)$$

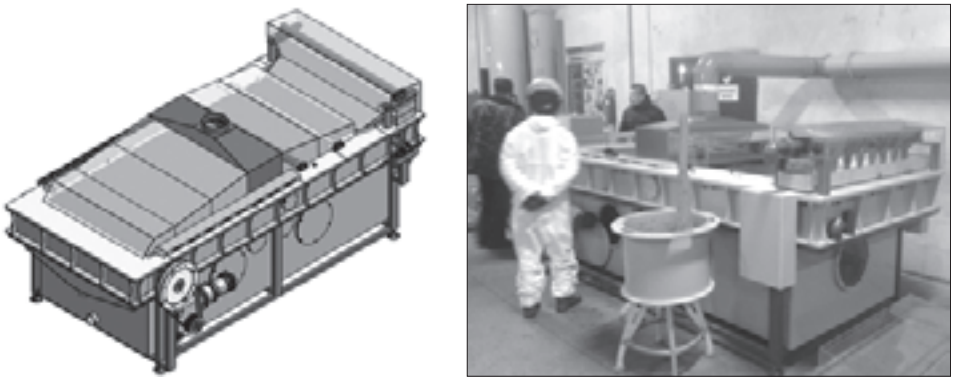

a *b*

Fig. 2.2. 3D diagram of the electrochemical reactor (*a*). Stage of testing an electrochemical reactor with a production capacity of 10 kg/h (*b*)

The possibilities of the anodic oxidation process according to the above scheme are confirmed by examples of its specific implementation, the results of which are given in Table 2.4.

Example 1 (Table 2.4): natural graphite is mixed with a 30% aqueous solution of sulfuric acid (1 cm^3 of acid solution per 1 g of graphite). The graphite suspension is placed in a loading hopper 2 with a roll 3, which equalizes and adjusts the thickness of the graphite suspension layer. A gap is established between the knife electrodes of anode 4 with an interval of 18 mm from each other, and the distance from the knife electrodes to the membrane surface is 14 mm. On turning on drive drum drive 7, drive drum 6 makes the conveyor belt (membrane) 13 start moving with a speed of 1 cm/min. The graphite slurry is moved from the loading hopper to conveyor belt 13, where roll 3 distributes the graphite slurry along its surface in a uniform 14 mm thick layer. When the graphite suspension layer reaches anode 4, a direct electric current is switched on, maintaining its density at 42 mA/cm^2.

Next, new portions of the suspension are added to the loading hopper, ensuring continuity of the process of obtaining GIC. After 100 min, the initial portion of the graphite suspension, which during electrolysis is converted into a suspension of GIC, reaches drive drum 6.

When moving diaphragm 13 along the cylindrical surface of drive drum 6, the GIC suspension peels off from its surface and enters the receiving tray 11 with limiting walls 12. Jets of water from flushing collectors 10 wash away the remnants of GIC and the entire product of electrochemical treatment in the receiving tray 11, and then — on the suction filter. After washing and drying, we obtain GIC, the expansion coefficient of which is 143 cm^3/g. The amount of electricity consumed is 35.0 A · h/kg.

The following examples 2—6 were conducted as described in example 1, except for changing the process parameters. Table 2.4 provides specific data on the process conditions, as well as on the expanded coefficient for the product obtained.

In examples 7 and 8, GICs were obtained as described in example 1, except that the process parameters were changed (Table 2.4). In example 7, the distance between the knife electrodes of the anode (30 mm) is greater than the values stated in the claims [50, 51]. In this example, the resulting product contains particles of unoxidized graphite and has a low expanded coefficient. In example 8, the distance between the knife electrodes of the anode (8 mm) is less than the values stated in the claims. The resulting product contains particles of peroxidized graphite and has unsatisfactory consumer properties. In example 9 (according to the prototype [48]), 200 g of natural graphite was mixed with 100 cm^3 of 55% aqueous solution of sulfuric acid (the ratio of the acid volume to the graphite mass is 1 cm^3/g). The resulting mixture was pushed into the gap between the anode and the porous membrane 13. Through the graphite, a direct current was delivered with a density of 30 mA/cm^2. The amount of electricity consumed was 37.5 A · h/kg. After washing and drying, GIC was obtained with an expanded coefficient of 105 cm^3/g.

Thus, we have developed a scheme and created a reactor for electrochemical oxidation of dispersed natural graphite of continuous action with a production

Table 2.4. **Expanded coefficient of EG depending on the parameters of oxidation process**

Example	Ratio of acid volume to graphite mass, cm^3/g	Mass content of acid, % wt.	Distance between separator and anode, mm	Current density, mA/cm^2	Thickness of graphite suspension layer, mm	Speed of conveyor belt-separator, cm/min	Distance between knife electrodes, mm	Electricity consumption, A · h/kg	Expanded coefficient at 1000 °C, cm^3/g
1	1	30	14	42	14	2.0	18	36.5	143
2	1	55	7	40	8	3.6	18	30	200
3	1	94	7	25	8	1.1	18	60	290
4	0.5	55	4	40	5	6.5	18	33	210
5	0.85	55	9	35	9	2.1	25	40	250
6	0.75	94	4	40	5	2.7	10	60	405
7	0.5	55	4	40	5	6.5	30	33	100
8	0.5	55	4	40	5	6.5	8	33	130
9 (p)	1	55	—	30	—	—	—	37.5	105

capacity of 10 kg/h. The operating modes were optimized to ensure the stable quality of oxidized graphite, satisfactory for obtaining functional products from thermally expanded graphite. The method of obtaining intercalated graphite and the device for its implementation are suitable for use in enterprises producing sealing materials and products from EG for equipment used in the nuclear and chemical industries, thermal power, metallurgy, and the like.

Chemical and electrochemical purification of natural graphite. Natural graphite of 50 mesh 75—80% fraction content and ≤1% wt. of the ash content is used for obtaining EG for sealing materials and goods for the fuel and energy complex, petrochemical industry, etc. [32]. The goods for nuclear power plants use materials made from EG of so-called "nuclear cleanliness", in which the carbon content should not be below 99.85% wt. That is why the problem of optimization of oxidation and purification processes of natural graphite to produce EG of a given purity is very important.

Chemical processing is based on the fact that graphite is quite inert and, unlike ash impurities, does not react with most chemicals. The most common methods of chemical purification are:

- decomposition of impurities by hydrofluoric acid silicates;
- sintering of flotation concentrates with soda and caustic soda followed by the disintegration of sulfuric acid;
- thermal removing the impurities, which includes the blow-off of the graphite by halogenated gases at high temperatures.

It is considered reasonable to use the sintering of graphite with caustic soda within 300—500 °C followed by treatment under standard conditions with 5% sulfuric acid for most medium and refractory ores. If a deep purification is necessary (up to 0.2% wt. ash or less), the third purification stage by 3.5% solution of hydrofluoric acid or ammonium difluoride solution in sulfuric acid is implemented. On this basis, the study for the possibility of purification has been provided by:

- standard scheme of graphite purification from various manufacturers;
- alkaline purification in a “soft” mode and a reduced temperature of the graphite-alkali mixture;
- graphite purification by ammonium difluoride, eliminating the labor-intensive and energy-intensive process of the alkali treatment;
- graphite purification after chemical oxidation;
- graphite purification after anodic oxidation, and oxidation with a change in polarity.

The samples of the flotation concentrate (90—97% wt. of carbon) and low-ash graphite (carbon content ≥ 99% wt.) from different manufacturers in Ukraine, China, India, and Madagascar have been studied.

Purification with alkaline and ammonium difluoride. The mid-ash graphite by Xiang Yang (China) company (the carbon content by passport was not lower

than 94% wt.; the ash content was equal to 4.16% wt. according to our estimates) was processed by the standard mode. The costs and ash content of the product obtained are shown in Table 2.5.

Thus, after an alkaline purification of graphite by Xiang Yang (China) with the original ash content above 4% wt., we can get graphite of a "nuclear" purity at a cost of the ammonium difluoride about 50 kg per ton of the raw graphite.

The mid-ash graphite by Titan Metals And Minerals Limited (India), with the carbon content by passport not below 94.6% (the ash content was 3.6% according to our estimates) after the treatment with alkali (40% NaOH) was heated at 140—160 °C in a sand bath for 2 h and washed with hot water (60—70 °C) supplemented with 55% sulfuric acid, and after exposure to 10 min "cold", washing to pH ≥ 6, and drying at 150—200 °C provides an ash content of 0.62% wt. Thus, the graphite studied is purified by the alkaline treatment to the ash content below 1% at the sintering temperature of 140—160 °C instead of the traditional 300—500 °C.

Purification without alkali. The possibility of purification of high-ash graphite by ammonium difluoride without complicated and energy-intensive procedures of an alkali treatment has been studied. The results of the purification of the Madagascar graphite flotation concentrate with an ammonium difluoride solution in sulfuric acid are summarized in Table 2.6.

The data of Table 2.6 clearly show that by using a sufficient amount of ammonium difluoride, namely 4 parts by weight of difluoride to 1 part by weight of ash, it is possible to obtain graphite with ash content below 1% for the Madagascar deposit of the flotation concentrate.

After purification. Table 2.7 shows the results of checking the possibility of graphite after purification during the chemical oxidation of sulfuric acid with hydrogen peroxide as an oxidant. The ash content in the source graphite was 0.76% wt. (carbon content of not less than 99.0%, Xiang Yang manufacturer, China).

Table 2.5. **Costs and ash content for the product obtained**

Raw graphite: manufacturer, carbon content,% wt., dispersity	Caustic soda used, t/t	Sintering temperature, °C	Sulfuric acid (94%) used, t/t	Ammonium difluoride used, t/t	Water used, m^3/t	Ash content,%
Xiang Yang, China, 94%, 50 mesh	0.115	320—330	0.23	0.019	21.5	0.50
	0.115	320—330	0.23	0.048	28	0.11
Titan Metals and Minerals Limited, India, 94.6%, 50 mesh	0.572	140—160	1.11	—	—	0.62

Chemical treatment of the graphite with a carbon content of ≥99.0% during oxidation by sulfuric acid using hydrogen peroxide as an oxidant leads to deterioration of EG quality (bulk density is increasing, i.e. decreasing in the strength of rolled products, etc. [27]). In addition, the ash content is almost unchanged, despite the

Table 2.6. **Costs and ash content for graphite obtained**

Raw graphite: manufacturer, carbon content,% wt.	Sulfuric acid (94%) used, t/t	Ammonium difluoride used, t/t	Water used, t/t	Reaction temperature, °C	Reaction duration, h	Ash content obtained,%	Initial ash content, %
«B», 90.5% C, Madagascar	0.6	0.2	2.4	20	16	1.32	9.0
«C», 94.3% C, Madagaskar	0.6	0.2	2.4	20	16	0.84	5.1

Table 2.7. **Costs and features of graphite used**

Process	Sulfuric acid (94%) used, t/t	Hydrogen peroxide (50%) used, t/t	Ammonium difluoride used, t/t	Water used, t/t	Intercalant content,%	EG pour density at 1000 °C, g/dm^3	Ash content, %
Chemical oxidation	1.48	0.067	—	27.8	13.5	4.4	0.72
Chemical oxidation and after purification	1.48	0.067	0.037	27.8	11.5	9.6	0.35

Table 2.8. **Purification of the graphite flotation concentrate after electrochemical**

# of sample, family	Source graphite: manufacturer, the carbon content,%, dispersity	Anodic treatment
88	Qing Dao, China 94.5% C, 50 mesh	Vertical tube cell [24] with acid excess, ρ_{acid}=1.45 g/cm^3, V_{acid}/m_g = 3.4 cm^3/g, Q = 80 A · h/kg
92	Madagascar «C» 94.3% C	Vertical tube cell [24] with acid excess, ρ_{acid}=1.45 g/cm^3, V_{acid}/m_g = 3.4 cm^3/g, Q = 80 A · h/kg
171	CNMIEC, China A90	Horizontal cell of 12 × 12 cm [24], ρ_{acid}=1.45 g/cm^3, V_{acid}/m_g = 0.7 cm^3/g
320	Xiang Yang, China, 94% C 50 mesh	Horizontal cell of 12 × 12 cm with down cathode [24], ρ_{acid} = 1.43 g/cm^3, V_{acid}/m_g = 0.9 cm^3/g, polarity reversal

rather high content of ammonium difluoride. It may also indicate the presence of insoluble impurities in the ammonium difluoride solution in the sulfuric acid.

Purification of graphite from different fields after an anodic treatment. An anodic treatment of graphite in aqueous solutions of sulfuric acid, which can be realized in different schemes is the greenest and less expensive method of graphite oxidation to produce intercalation compounds enabled for thermal expansion [43—45, 50, 51]. Therefore, an optimal combination of processes of graphite electrochemical and chemical intercalation after treatment of both the flotation concentrate and low-ash graphite of different fields has been considered. An attempt to purify graphite by an anodic treatment at the polarity reversal has been made. In this procedure, the intercalation and deintercalation processes should lead to a "buildup" of the graphite lattice and to simplifying the access to chemical contaminants "encapsulated" in the graphite matrix. The schemes and conditions of the anodic treatment are described above in [43—45, 50, 51]. Usually, after anodic treatment with ~80 A · h/kg, the graphite mixture was extracted on a filter, and sulfuric acid and ammonium difluoride were added in appropriate amounts. Tables 2.7—2.9 briefly summarize the methods, modes, settings, and processing of source materials from different fields (ρ_{acid} is the density of the acid, V_{acid} is its volume, m_g is the mass of the graphite materials).

As follows from Table 2.8, it is possible afterpurification of the flotation concentrate of graphite from various manufacturers with ammonium diftuoride in corresponding amount, to the ash content of below 1% wt. after the anodic treatment in the electrochemical cell of the design proposed. A comparison of the ash content reached for graphite of grade "C" (Madagascar) (sample 92, Tables 2.6, 2.8) reveals that the ash content became almost three times lower after the anodic treatment than before it. The ammonium difluoride used is less also

oxidation (ECHO)

Ammonium difluoride per graphite weight, g/g	Water volume per graphite weight, cm^3/g	Reaction temperature, °C	Reaction time, h	Ash content obtained, %	Initial ash content, %
0.16	2.4	60	2	0.72	5.5
0.16	3.0	80	1.5	0.3	5.1
0.10	2.0	70 20	2 + 12	1.48	6.57
0.10	5.0	80	1.5	0.4	5.3; 3.3 (after oxidation)

Table 2.9. **Purification of low-ash graphite after electrochemical oxidation (ECHO)**

# of sample family	Source graphite: manufacturer, carbon content, %, dispersity	Anodic treatment
91	Qing Dao, China, 99%C, 50 mesh	Vertical tube cell [24] with acid excess, ρ_{acid} = 1.45 g/cm^3, V_{acid}/m_g = 3.4 cm^3/g
149.1	Xiang Yang, China, 99% C, 50 mesh	Horizontal cell of 12 × 12 cm [24], ρ_{acid} = 1.44 g/cm^3, V_{acid}/m_g = 0.85 cm^3/g
149.2	Xiang Yang, China, 99% C, 50 mesh	Horizontal cell of 12 × 12 cm in size [24], ρ_{acid} = = 1.44 g/cm^3, V_{acid}/m_g = 0.85 cm^3/g
158	Xiang Yang, China, 99% C, 50 mesh	Horizontal cell of 12 × 12 cm [24], ρ_{acid} = 1.44 g/cm^3, V_{acid}/m_g = 0.75 cm^3/g
315	Qing Dao Gu Yu Graphite Co. Ltd, China, 99% C	Horizontal cell of 12 × 12 cm with down cathode [24], ρ_{acid} = 1.44 g/cm^3, V_{acid}/m_g = 0.85 cm^3/g
316	Qing Dao Gu Yu Graphite Co. Ltd, China, 99%C	Horizontal cell of 12 × 12 cm with down cathode [24], ρ_{acid} = 1.44 g/cm^3, V_{acid}/m_g = 0.85 cm^3/g
312	Xiang Yang, China, 99% C, 50 mesh	Horizontal cell of 12 × 12 cm with down cathode (electrodes made of stainless steel) [24], ρ_{acid} = = 1.83 g/cm^3 (strong acid), V_{acid}/m_g = 0.75 cm^3/g
314	GSL-2 Zavalie Graphite Plant, Ukraine, 99.8%C, 80 mesh	Horizontal cell of 12 × 12 cm with down cathode (electrodes from stainless steel) [24], ρ_{acid} = = 1.83 g/cm^3 (strong acid), V_{acid}/m_g = 0.8 cm^3/g
298	Xiang Yang, China, 99% C, 50 mesh	Cell of a quasi-continuous propulsion with a down cathode [29], ρ_{acid} = 1.45 g/cm^3, V_{acid}/m_g = 0.75 cm^3/g
308	Xiang Yang, China, 99% C, 50 mesh	Quasi-continuous drum-type reactor with propulsion, anode assembly and down cathode [29], ρ_{acid} = 1.445 g/cm^3, V_{acid}/m_g = 0.65 cm^3/g
318	Xiang Yang, China, 98% C, 1500 mesh	Horizontal cell of 12 × 12 cm with down cathode (electrodes from stainless steel) [24], ρ_{acid} = = 1.83 g/cm^3 (strong acid), V_{acid}/m_g = 1.08 cm^3/g
319	Xiang Yang, China, 98% C, 1500 mesh	Horizontal cell of 12 × 12 cm with down cathode [24], ρ_{acid} = 1.43 g/cm^3, V_{acid}/m_g = 1.2 cm^3/g, the polarity reversal

at significantly less time, but at higher temperatures. It should be noted that the effectiveness of this technique for flotation concentrates from different fields is somewhat different.

Analyzing the data in Table 2.9, one can see that the ash content is decreased by 2—5 times at a reasonable cost of ammonium difluoride (2.5 mass parts per 100 mass parts of graphite) for low-ash graphite from different fields with a dispersion of 50 mesh after the anodic treatment in sulfuric acid solu-

Ammonium difluoride per graphite weight, g/g	Water volume per graphite weight, cm^3/g	Reaction temperature, °C	Reaction time, h	Ash content obtained,%	Initial ash content,%
0.04	2.4	80	1.5	0.09	0.40 (after oxidation)
0.02	2.5	70	3	0.16	0.72
0.05	2.5	70	2.5	0.12	0.72
0.04	2.0	70	2 4	0.3 0.25	0.7
0.05	2.5	80	1.5	0.15	0.58 (after oxidation)
0.05	2.5	20	20	0.13	0.58 (after oxidation)
0.10	4.0	20	3	0.7	1.53 (after oxidation)
0.10	4.0	20	2	0.69	0.79 (after oxidation)
0.04	2.5	80	1.5	0.26	0.7
0.05	2.7	70	2	0.38	0.74
0.033	2.5	80	2	0.17	0.71 (after oxidation)
0.10	4.0	80	2	0.07	0.65 (after oxidation)

tions (50—55%) in the horizontal cell (samples 149, 158, 315, 316) and the cells of quasi-continuous mode (samples ## 298, 308), but it is impossible to reach an "atomic purity," i.e. 0.1% wt. and *less* for the ash. Less than 0.1% wt. could be obtained in a vertical cell with an excess of acid (sample # 91), however, the intercalation process parameters decreased in this case [43]. The anodic treatment of low-ash graphite samples in the concentrated sulfuric acid (## samples 312, 314), which provides high levels of the intercalated graphite [43], unfortu-

nately, increases the ash content (likely due to the electrodes-electrolyte reaction), and after treatment by ammonium difluoride substantially returns the original graphite purity. The ash content below 0.1% wt. was achieved in the graphite samples with a carbon content of 98% wt., dispersion of 1500 mesh (samples 318, 319), an increase in the reaction of the ammonium difluoride to 10 mass parts per 100 mass parts of graphite and further anodic treatment by the polarity reversal (sample 319).

Table 2.10 demonstrates the change in the ash content of the flotation concentrate of natural graphite of different fields and different batches from the same origin after anodic treatment with the polarity reversal. In other words, the intercalation → deintercalation → intercalation processes have been provided without chemical purification with ammonium difluoride in sulfuric acid. Thus, for samples of three series 321, 326, and 330 by Xiang Yang (China) with 50 mesh, the ash content decreased from 5.3% to 3.4 ± 0.4%, that is, by nearly 40%, while for sample # 323 by Qing Dao Gu Yu Graphite Co Ltd (China), 90% C (grade 590) it is almost doubled. However, an anodic treatment of sample #331 by Madagascar "C", 94.3% C with a polarity reversal almost does not change its

Table 2.10. **Effect of anode treatment on ash flotation concentrate of natural graphite from different fields (without chemical purification by ammonium difluoride solution in sulfuric acid)**

# of sample, family	Source graphite: manufacturer, carbon content, %, dispersity	Anodic treatment	Ash content obtained,%	Initial ash content, %
321	Xiang Yang, China, 94% C, 50 mesh	Horizontal cell of 12 × 12 cm with down cathode [24], ρ_{acid} = = 1.43 g/cm^3, V_{acid}/m_g=1.0 cm^3/g	2.6	5.3
323	Qing Dao Gu Yu Graphite Co. Ltd, China, 90% C, (grade 590)	Horizontal cell of 12 × 12 cm with down cathode [24], ρ_{acid} = = 1.43 g/cm^3, V_{acid}/m_g = 1.0 cm^3/g	6.3	11.8
326	Xiang Yang, China, 94% C, 50 mesh	Horizontal cell of 12 × 12 cm with down cathode [24], ρ_{acid} = = 1.43 g/cm^3, V_{acid}/m_g = 1.1 cm^3/g	3.6	5.3
330	Xiang Yang, China, 94% C, 50 mesh	Horizontal cell of 12 × 12 cm with down cathode [27], ρ_{acid} = = 1.43 g/cm^3, V_{acid}/m_g = 1.0 cm^3/g	3.9	5.3
331	Madagascar «C», 94.3% C	Horizontal cell of 12 × 12 cm with down cathode [27], ρ_{acid} = = 1.43 g/cm^3, V_{acid}/m_g = 1.1 cm^3/g	5.07	5.1

ash content. Thus, on the basis of studies of the chemical and electrochemical purification of the flotation concentrate and the low-ash graphite from different fields the following conclusions can be made.

1. The effectiveness of all the above flotation concentrates and low-ash graphite purification methods depends essentially on the geological origin of the graphite raw material. So, we can obtain graphite of an "atomic" purity using ammonium difluoride (about 50 kg per 1 t of original graphite) after an alkaline purification of the graphite with an initial ash content above 4% wt. by Xiang Yang (China). There is a possibility to purify the mid-ash graphite from Titan Metals and Minerals Ltd (India) with an ash content of 3.6% to the ash content of less than 1% by an alkaline treatment at the sintering temperature of 140—160 °C instead of the traditional 300—500 °C. Besides, one can produce graphite of below 1% of the ash content from the flotation concentrate of the Madagascar field (the initial ash content 5.1%) using a sufficient amount of ammonium difluoride (namely, 4 mass parts of difluoride to 1 part of the ash) without alkaline processing, etc. So, it is necessary to provide the search and optimization for the purification procedures for each origin of the natural graphite.

2. It is shown that the combination of an anodic treatment to produce graphite capable of thermal expansion with purification of flotation concentrates from a number of fields with ammonium difluoride in sulfuric acid allows one to obtain oxidized graphite with the ash content below 1% wt., which is suitable for the production of sealing power equipment without further alkali treatment.

3. Graphite of high purity (ash content of 0.07% wt.) suitable for use in chemical power sources has been obtained by anodic treatment with a polarity reversal of graphite of 1500 mesh and the carbon content of 98% wt. (Xiang Yang, China) and with further treatment by ammonium difluoride in sulfuric acid.

4. The polarity reversal during the anode purification of both the flotation concentrate and the low-ash graphite may be an additional effective method for natural graphite purification.

2.2. The exfoliated graphite: formation, structural features of the solid material, and application

This subsection presents the results of studies of structural and phase transformations in products prior to the EG, the effects of heating conditions, expansion and chemical modification on the structure, physical properties of bulk EG; some aspects of the formation of strong features of low-density materials from the EG at the main stages of their preparation are considered.

2.2.1. The structural transition of graphite — H_2SO_4 residual intercalation compounds

Previous measurements of the temperature of the structural transition of residual compounds at atmospheric pressure, conducted by the differential thermal analysis have shown that, according to [18], it is within 100—400 °C. According to the thermogravimetric analysis, the region of maximum weight loss rate is 200—250 °C. Therefore, to study the structural changes that occur during the thermal expansion of graphite bisulfate crystals, they were washed in a distilled water up to pH 6—7 of the wash water with a further thermal treatment performed at atmospheric pressure and the final heating temperature of 100, 250, 400, 1000 °C. Exposure at the finite temperature continued until the termination of the sample weight loss. Thus, the different states of samples were achieved, which were defined as the residual compounds of graphite bisulfate [52].

As shown by the structural study, the source materials (UT highly oriented pyrolytic graphite and the natural graphite of Zavalevsky field brand GAK-2) have a perfect crystalline structure close to the structure of monocrystal graphite, which made it possible to generalize the results of experiments carried out with each of these materials. Intercalation with sulfuric acid was carried out by the method of Ref. [53] in stoichiometric oxidation conditions. The process of the graphite samples' intercalation and the different states of residual compounds were controlled by a DRON-3M diffractometer with CoKα radiation (λ = 0.17902 nm). Electron microscopy analysis was performed on a «Tesla» BS-540 unit with a maximum acceleration voltage of 120 kV and a resolution of 0.7 nm. Thinning of samples was performed as described in [54]. A comparison mode with the original quasi-single crystal allowed us to exclude from consideration the structural features that are not related to the processes of inclusion and deintercalation [55].

As shown in [56], the main feature of the XRD pattern of the residual graphite bisulfate compounds in the initial state (i.e., after heat treatment at 100 °C) is a substantial broadening of (002) diffraction reflections of graphite and the presence of additional peaks. After the sample treatment at temperatures up to 400 °C, the intensity of the additional diffraction reflections is redistributed, and the (002) peak width of the graphite matrix is reduced as well. Such a change of diffraction patterns indicates the restructuring of the residual compounds that apparently ends at 1000 °C. In electron diffraction, removed from the original part of the sample (Fig. 2.3, *a*), there are non-periodically arranged reflexes that do not belong to the graphite matrix. Analysis of the dark-field and brightfield images (Fig. 2.3 *b*, *c*) by [57], indicates that the structure comprises a thin plate formation of phases different from the matrix, but such that it has a specific crystal structure matching. These formations can be characterized as fields enriched with the intercalant or its residues. The areas of structural inho-

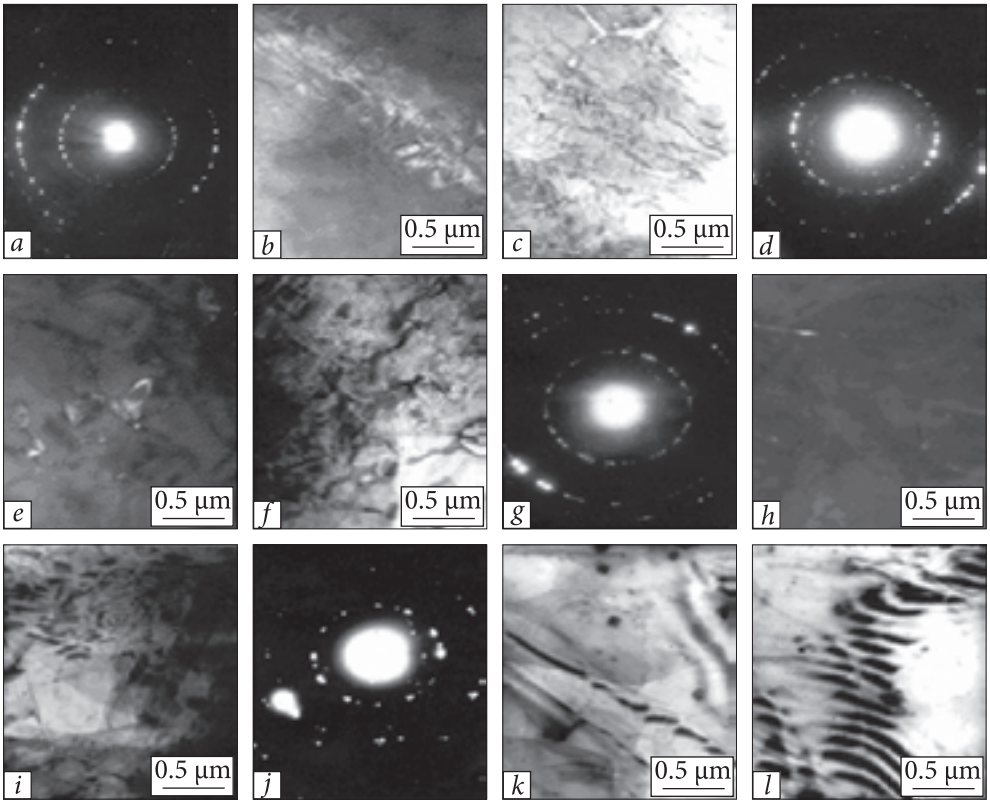

Fig. 2.3. Electron-diffraction patterns and corresponding dark- and bright-field images from samples of the residual compounds of graphite bisulfate (GIC—H_2SO_4) heat-treated at 100 (*a*, *b*, *c*), 250 (*d*, *e*, *f*), 400 (*g*, *h*, *i*), and 1000 °C (*j*, *k*, *l*)

mogeneities (bright regions) are elongated and curved, both with alternating dark and light bands and without them. This may be due to the fact that the structures of these areas are similar, but differ in the degree of order, including a fully disordered state. The structural inhomogeneities in the form of lamellar precipitates are obviously the cause of the elastic bending of the crystal, as evidenced by the series of distinct reflexes along certain directions in the pattern (Fig. 2.3, *a*). Besides, there are distinct phase formations of two types, probably, the intercalant residues. The precipitates of structural inhomogeneities of the round form with a distinct orientation are detected in the areas with an obvious texture matrix.

Analysis of changes in diffraction patterns as well as the pictures of microdiffraction and corresponding bright- and darkfield images of the samples after treatment at 250 and 400 °C (Fig. 2.3 *g*—*i*) and during heating up to 400 °C (*in situ*) [58] revealed the following regularities in the structure of the residual compounds.

Heat treatment of samples at 250 °C leads to structural changes in the bundle type, which affects mainly the most disordered regions of structural inhomogeneities and results in the conversion of the areas into a more ordered structure.

At the same time, along with deintercalation increases the likelihood of the intercalant phases' formation. Heating up to 400 °C leads to the dynamic development of the processes of structural and phase transformations. It is quite possible that all areas of structural irregularities identified in the original sample change; besides, the intercalant residues phases are formed. The greatest variety of characteristic quantities and phases of the intercalant residues and regions of structural inhomogeneities is inherent to these samples. Increasing the heating temperature to 1000 °C causes deeper structural transformations of disordered phase formations and the phases of the intercalant residues. This is reflected, above all, in the change in the type of diffraction patterns. The additional reflections in the small-angle region disappeared; the peak width at half-height of the graphite matrix decreased. However, heating and aging of samples, even at 1000 °C, do not lead to a complete deintercalation. At least two phases of residues intercalant with different dispersity are formed as a result of the transformation of areas of structural inhomogeneities. Moreover, a finely divided phase having a pronounced texture matrix may be defined as O=C=S based on the received sets of d/n. The regions with an ordered distribution of the intercalant remain as well.

Thus, the residual compounds of graphite bisulfate (precursor of exfoliated graphite) are heterogeneous systems at all stages of heat treatment, including high temperature and rapid heating, to obtain EG. They include graphite crystals with structural inhomogeneities caused by the intercalant residues' distribution with different degrees of order, as well as at least two phases with different particle intercalant residues. The treatment temperature determines the qualitative composition and the quantitative ratio of phase formations.

2.2.2. Changes in the electronic properties due to the structural transition

Structural transformations in residual graphite bisulfate compounds at a bulk compression have been studied via the resistance and thermopower measurements in the temperature range of 200–1200 °C by the procedure described in [59].

Two variants of the structural transition have been considered: the "free" expansion (sample is placed on the substrate) and expansion into a limited volume (sample is in the shape limiting the change of its volume). The excess argon pressure is created in a high-temperature chamber [60]. Electrical conductivity and thermopower are measured by the standard four-probe method [61]. Temperature dependence of the electrical conductivity (σ) and thermoelectric power

(*S*) in the free expansion model have been studied under a pressure of 5, 10, and 20 MPa. Electrical conductivity increases with heating to a certain temperature and then decreases abruptly by several tens of times and thereafter linearly decreases with a constant temperature coefficient (Fig. 2.4). Thermopower is reduced from 30—50 μV/K to 15—20 μV/K with heating, then quickly reduces to close to zero or negative values. The temperatures of jumps in the conductivity and thermopower, i.e. the temperatures of the structural transition, recorded by changing σ (T^{σ}_{tr}) and *S* (T^{s}_{tr}), differ significantly (Fig. 2.4). The results at different pressures are shown in Table 2.11. Thus, the increase in pressure leads to a shift of the structural transition temperature to higher values and to an expansion of the temperature range (ΔT^{σ}, ΔT^{s}). Note that σ(*T*) and *S*(*T*) demonstrate an inflection point at about 200 °C, which corresponds to the beginning of intensive weight loss of residual compounds at normal pressure.

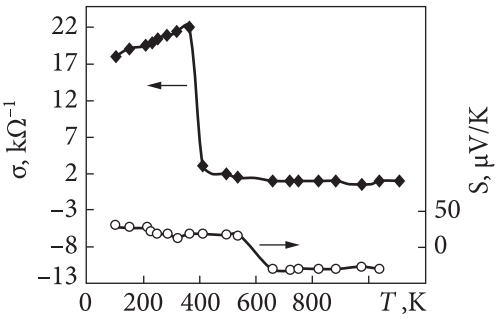

Fig. 2.4. Temperature dependences of the electric conductivity (*σ*) and thermopower (*S*) for "free" expansion model of graphite bisulfate under a pressure of 10 MPa

The temperature dependence of the of structural transition, which is registered by the conductivity jump under pressure (Fig. 2.5), is linear according to [62]; the value of Δ*H*, determined from the slope of the line, is 70 ± 2 kJ/mol, which is virtually identical to Δ*H* of the intercalated graphite-bromine compound. In this case, the proximity of Δ*H* values may indicate that the activation energy of the process is determined by the thermal expansion properties of the graphite matrix rather than by the individual characteristics of the intercalant.

The structural transition of the residual compounds due to expansion into a limited volume has been examined under a pressure of 10 MPa. Monotonic change in *σ* (*T*) and *S* (*T*) occurs with increasing temperature up to 1200 °C

Table 2.11. **The effect of pressure on temperature of the structural transition of the residual compounds of graphite bisulfate**

Pressure, MPa	T^{σ}_{tr},°C	ΔT^{σ}_{tr},°C	T^{s}_{tr},°C	ΔT^{s}_{tr},°C
5	290	65	500	65
10	330	100	555	100
20	345	110	575	110

N o t e: ΔT is the temperature range of the structural transition.

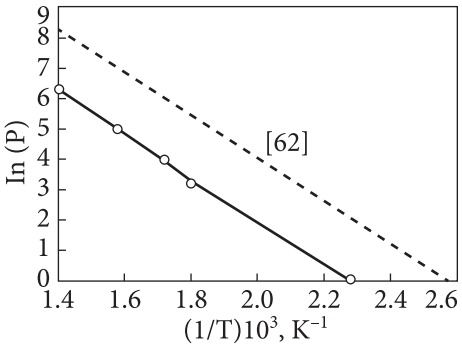

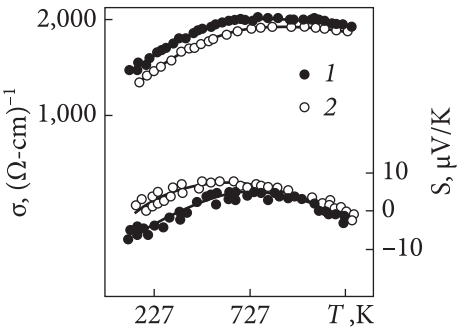

Fig. 2.5. Temperature dependence of the structural transition on the pressure of graphite bisulfate recorded at the conductivity jump

Fig. 2.6. Temperature dependences of the electrical conductivity and thermopower of the residual compounds of graphite bisulfate for expansion in a limited volume under a pressure of 10 MPa: *1* — heating; *2* — cooling

(Fig. 2.6). Conductivity increases up to 700 °C and then slightly decreased in the whole temperature range. Upon cooling, σ (*T*) curve (Fig. 2.7) reproduces the form of the whole heating dependence, but the electric conductivity takes smaller values, and the inflection point corresponds to 900 °C.

Thus, the change in the electronic properties following the structural transition of the residual compounds under heating is caused by the changes in the sample geometry. With changing the sample sizes due to expanding in a limited volume, the properties change monotonically. Hysteresis of the temperature dependences σ (*T*) and *S* (*T*) indicates the quasi-continuous microregions of the "phase" transformations in the heterogeneous system (residual compounds of graphite bisulfate) almost over the whole temperature range. Reduction in the conductivity and switching thermopower in the region of positive values indicates that such conversion (intercalant losses, formation of new phases, etc.) leads to a decrease in the total concentration of charge carriers and growth of the relative concentration of positive carriers.

2.2.3. Nanoscale elements of the EG structure

Experimentally, we have determined [21] such characteristics of EG structure as the lattice parameter along the C–d_{002} axis and the content of turbostratic defects γ (defects due to azimuthal disorientation of the graphene layers, which leads to an increase in the interlayer distance from d_{002} (min) = = 0.335 nm to d_{002} (max) = 0.344 nm) defined as

$$\gamma = \frac{d_{002} - 0{,}335}{d_{002}(\max) - d_{002}(\min)}. \qquad (2.10)$$

The coherent scattering domain size in the basal L_a plane along the C–L_c axis are listed in Table 2.12. As seen (Table 2.12), the structural characteristics depend on the method of intercalation and the treatment temperature.

It should be noted that the concentration of turbostratic defects in the oxidized graphite (OG), i.e., graphite intercalated with sulfuric acid with further hydrolysis, is lower than in EG. The rapid heating of the oxidized graphite results in the crushing of crystallites in the basis plane (L_a decreases) and crystallite growth along the C axis. Besides, the effective sizes of these parameters are getting close. However, these data do not provide complete information concerning the interpretation of the known properties of EG. Thus, the inability to obtain a rolled or extruded EG with a density greater than 2.0 g/cm^3 (XRD density of the perfect hexagonal graphite is 2.24 g/cm^3), the presence of high concentrations of turbostratic defects indicates the possible existence of a nanoporous structure, which is responsible in a certain way for the properties of EG and materials on its basis. Therefore, the next step was to study the properties of the crystal structure of an exfoliated graphite in a view of possible nanoscale elements [64].

Samples of exfoliated graphite were made by the persulfate method [53, 55]. Powder samples possess a worm-like structure with a large surface area of 35—70 m^2/g, 1—5 mm long, with an average effective diameter of 0.3 mm (Fig. 2.7). A ribbon of exfoliated graphite was made by rolling its powder on a rolling mill.

The centers of annihilation of hydrogen-type atoms of positronium (P_s) in as-prepared samples (powdered and rolled in the form of a ribbon) were studied by the method of positron annihilation [65] (angular correlation of annihilated photons (ACAP)). ACAP was recorded using a standard geometry with a long-slit spectrometer and the ^{22}Na radioactive isotope (about 1 mKu of activity) as a positron source. The half-width of the angular expansion of the spectrometer, measured for a narrow component of the ACAP spectrum and connected with the own annihilation of the delocalized P_s in single-crystal quartz, is

Table 2.12. **Structural parameters of the natural graphite and its products**

Sample	Material	d_{002}, nm	γ	L_a, nm	L_c, nm
1	Natural graphite	0.3354	0,008	110	40
2	Oxidized graphite	0,3355	0.15	65	10
3	EG, hydrolysis, $^*T_{tr}$ = 400 °C	0.3359	0.185	23	23
4	EG, hydrolysis, $^*T_{tr}$ = 800 °C	0.3360	0.19	21	22
5	EG, hydrolysis, $^*T_{tr}$ = 1000 °C	0.3356—0.3362	—	—	—
6	EG, without hydrolysis, $^*T_{tr}$ = 1800 °C, [63]	0.338—0.3343	—	—	—

* T_{tr} is the temperature of obtaining exfoliated graphite.

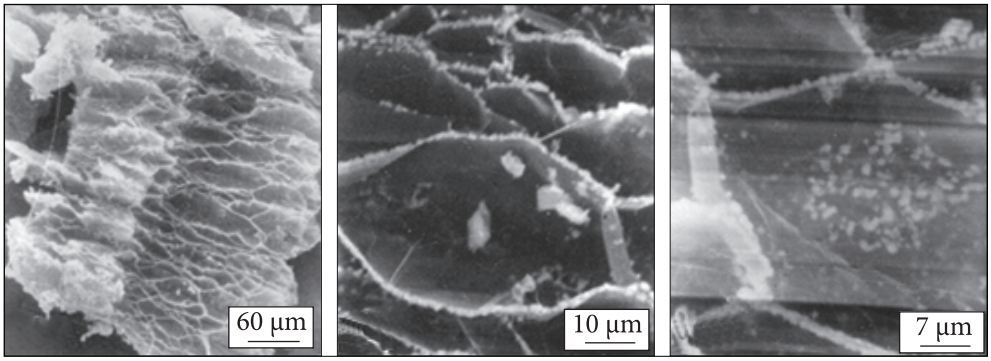

Fig. 2.7. SEM images of exfoliated graphite surface

Table 2.13. **Intensity of the positronium component I_{Ps} and pore size (R) along different directions in pressed samples and EG powder**

Orientation or state	Pore size, nm	I_{Ps},%
Perpendicular to the surface	> 4	0.6
In parallel surfaces	1.4	0.6
EG powder	0.7	0.6

σ_{ang} = 0.39 mrad. It is used to determine the dispersion, σ^2_{Ps}, and the momentum of P_s in the middle of nanopores [66]:

$$\sigma_1^2 = \sigma_{Ps}^2 + \sigma_{ang}^2. \tag{2.11}$$

where σ^2_1 is the dispersion of the narrowest component of ACAP, which can be defined by its decomposition in three Gaussian:

$$N(\theta) = \Sigma A_i \exp(-\theta^2/2\sigma_i^2). \tag{2.12}$$

Nanopore size has been defined in [66]:

$$R = 1.66/\sigma_1 - 0.166 \text{ nm}. \tag{2.13}$$

The certain intensity of the positronium component (relative area of the narrow component in the ACAP spectrum) and the nanopore size for various states and orientations of exfoliated graphite are listed in Table 2.13.

The results obtained indicate that all EG samples contain nanopores with an average size of about 0.7 nm. ACAP spectra for compacted samples of EG with different orientations show that nanopores in pressed EG are anisotropic, ie, have an elongated shape with a long axis oriented perpendicular to the EG ribbon surface. The parameter of anisotropy (the length ratio of the long and short axes) is ~3. The same structure of anisotropic nanopores (the length ratio

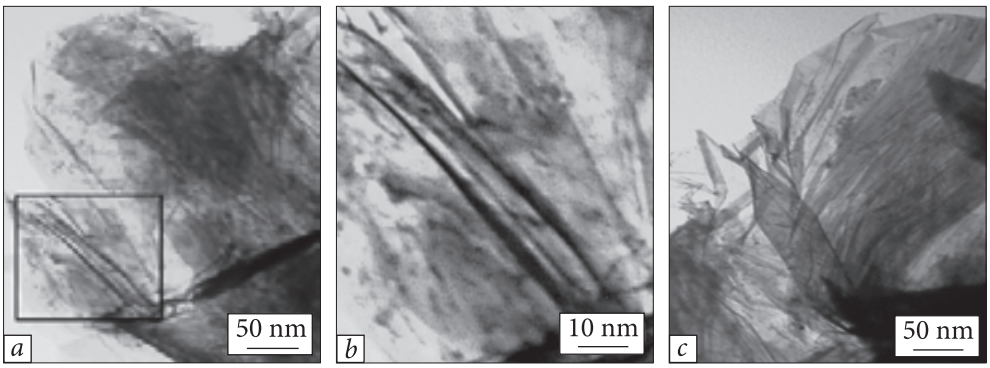

Fig. 2.8. TEM micrographs of the exfoliated graphite flake

of the axes is 1.9) was observed by the method of positron annihilation in PEEK (polyaryl-ether-ether-ketone) polymers [67].

Thus, EG samples in the form of powder or ribbon contain isotropic oriented nanopores, where the hydrogen-type atom of positronium (e^+e^-) is formed and makes a contribution to the narrow spectral component of ACAP spectrum at the annihilation. This feature of the positron annihilation is inherent only to the EG samples. Positronium was not observed in the other forms and modifications of carbon materials such as crystalline graphite, fullerites, or nanotubes. The capture of positrons by nanopores in EG can be explained by the polarization of atoms in the inner surface of nanopores due to broken symmetry, which leads to the expulsion of the electron density in the volume of nanopores and formation of a potential well for positrons. The smallest size of the nanopore (~0.7 nm) is sufficient for the formation and distribution of the hydrogen-type positronium atoms. Obviously, the change in nanopore size of s will occur in discrete steps, equal to the interlayer distance in graphite (0.335 nm). The hypothesis can be offered on the basis of the data, according to which defects are formed with a certain structure similar to that of linear dislocations caused by excess of graphene layers, which is shown in Fig. 2.8. In the first case, the length of the oriented nanopore, which is equal to 4 nm (Table 2.13), may correspond to the length of the linear defect or dislocation, and in the second case — to the width of the belt graphene layer, which is depicted in Fig. 2.9 [68].

The EG flake microstructure was studied using an EMB-100AK electron microscope in addition to the method of positron annihilation. The accelerat-

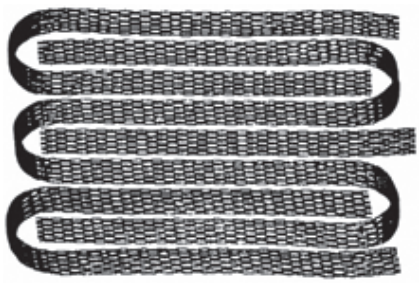

Fig. 2.9. Possible equilibrium structure of graphene layers [68]

ing voltage of 100 kV was used, which provided a resolution up to 0.7 nm [69]. The microstructure pattern of the flake is presented in Fig. 2.8. The separate fragments can be seen as folded formations of cylindrical shape. Sizes of nanostructured fragments that can be separated are in the range of a few to hundreds of nanometers. Quite a unique picture is shown in Fig. 2.8 *a*. Exceptionally good view of images makes it possible to talk about the existence of convolution of the graphene plane. Moreover, the outer diameter of the cross-section of the convolution can be estimated as ~2 nm for thin parts and ~20 nm for thick ones.

Raman spectroscopy (RS) is widely used to determine the structure of carbon materials. This method makes it possible to identify and explore different structural modifications of the carbon materials such as natural graphites of different genesis, shungites, fullerites, nanotubes, thermolysis products of organometallic and organic compounds, synthetic and natural diamonds, etc. [70—74].

The results for EG microporous structure obtained with RS study (diameter of cylindrical pores or slits ~2.6 nm) are in good agreement with the results of adsorption on EG [75, 76]. According to the results of experiments on the adsorption of CO_2, the authors of [74] characterized the EG microstructure mainly as slit pores with dimensions of 0.77–0.92 nm. In Ref. [76], the analysis of results on low-temperature nitrogen adsorption has shown the presence of mesopores with the effective radii of 1.2; 2.0, and 22.5...25 nm.

A more detailed description of the experiments and results on optical and in particular Raman spectroscopy of EG and its possible components can be found in Chapter 6.

These data are in good agreement with the results of low-temperature nitrogen adsorption-desorption on EG samples obtained by various methods [1], given in Table 2.14 and Fig. 2.10.

As follows from these data, the sizes and size distribution of pores are different, but their sizes lie in the range from below 1 nm to 100 nm.

Table 2.14. **Characteristics of porosity of EG samples depending on technological parameters of their production**

Sample	S_{BET}, m^2/g	R_P, nm	S_{nano}, m^2/g	S_{meso}, m^2/g	S_{macro}, m^2/g	V_{nano}, cm^3/g	V_{meso}, cm^3/g	V_{macro}, cm^3/g	V_P, cm^3/g
1, (EG^{100})	32.3	3.0922E + 01	10.7	20.5	1.1	0.004	0.045	0.041	0.09
3, (EG_{exo}, foil)	13.4	3.1600E + 01	1.1	11.1	1.2	—	0.039	0.041	0.08
6, (EG^{250})	51.0	2.8121E + 01	13.9	35.2	1.8	0.005	0.074	0.062	0.141

1, chemically oxidized with a coefficient of expansion of 100 at 450 °C; 3, electrochemically (anodic) oxidized; 6, chemically oxidized with a coefficient of expansion of 250 at 450 °C.

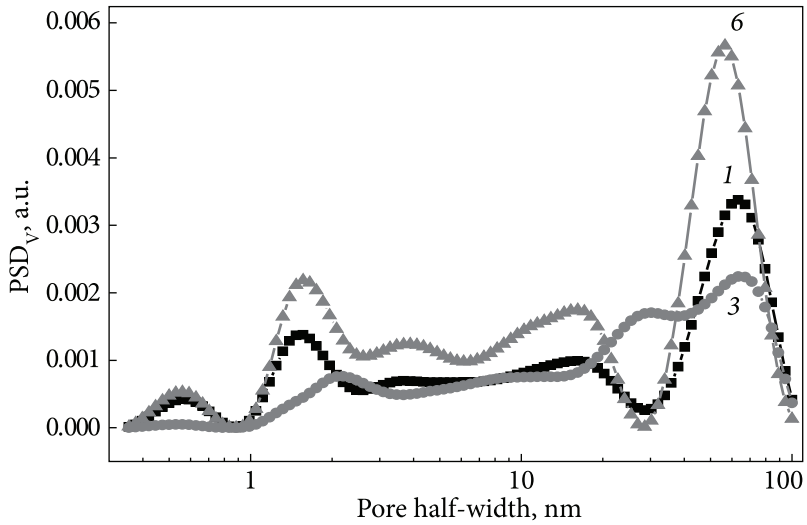

Fig. 2.10. Porosity of EG samples

Based on the data obtained, we can propose a hypothesis according to which defects are formed in EG, the structure of which is similar to linear dislocations and disclinations, or is caused by the bending of graphene layers of the type shown in Fig. 2.8.

In the first case, the length of an oriented nanopore, which is equal to 4 nm (Table 2.14), may correspond to the length of a linear defect similar to the dislocation and, in the second case, is equal to the width of graphene ribbon layer, which is shown in Fig. 2.9 [68].

In [68, 77], the authors examined the mechanism of carbon nanotubes formation based on minimizing the system energy. According to their calculations, the minimum energy is achieved in the structure shown in Fig. 2.9. If the folded structure in Fig. 2.9 is related to the thermodynamic equilibrium, it is sufficient to reliably assume the existence of such structures in the process of thermal exfoliation of the intercalated (oxidized) graphite. Broken by a "steam explosion" of the intercalant, the graphene layers relax and form an equilibrium folded structure, which can lead to the formation of nanoscale voids and anomalous behavior of some properties of the EG. Such structures (the graphene plane bend) were observed in [78], where the structure of multiwall carbon nanotubes was studied using high-resolution transmission electron microscopy.

Thus, from the analysis of the experimental data on positron annihilation, transmission electron microscopy, and Raman scattering, it follows that there are nanoscale defects in the EG structure, such as cavities of extended structure.

2.2.4. Surface studies of the intercalated and exfoliated graphite

The chemical and electrochemical intercalation of graphite with sulfuric acid has been well studied [18, 19, 28, 29, 32, 36—42, 79, 80]. But there are a number of issues that are important both for understanding the nature of the processes and for the practical application of the compounds synthesized and the exfoliated graphite. In particular, the mechanism of processes occurring during an oxidative graphite intercalation with peroxide compounds such as hydrogen peroxide, ammonium peroxodisulfate, or peroxosulfuric acids is not clear so far.

Usually, the classical scheme of intercalation, in which peroxides are electron acceptors and the anions and molecules of sulfuric acid are intercalants, is applied. However, in fact, the properties of compounds formed are absolutely different from the classical graphite bisulfates. Very little attention has been paid to the mechanism of the processes occurring during the hydrolysis of intercalation compounds or, generalizing, under the influence of the nucleophilic reagents. At the same time, the known patent graphite data [81, 82] certifies that the treatment of graphite intercalated by the organic compounds (presumably serve as nucleophiles for the graphite intercalated) can markedly increase its expansibility under the thermal shock and decrease the temperature of expansion. It is important to improve the quality of products from the exfoliated graphite and to use the intercalated graphite in fire-retardant bloat compositions. The process of the electrochemical graphite intercalation in aqueous solutions of the sulfuric acid (30—60%), where intercalation and hydrolysis occur simultaneously, still remains under investigation. At that, the quality of the final products (EG and its products) depends essentially on the modes of intercalation and hydrolysis. Therefore, these studies were carried out in order to determine the chemical reactions occurring during the oxidative intercalation of graphite with sulfuric acid and hydrolysis of GICs, as well as to consider the effect of these processes on the formation of surface chemistry of the GICs and EG.

It is known that the crystalline graphite forms intercalation compounds containing the intercalary anions and the acid molecules during chemical or electrochemical oxidation in an acid medium. For example, the dark blue graphite bisulfate of stage I ($C^{+}_{24} \cdot HSO^{-}_{4} \cdot 2{,}5H_2SO_4$) is formed in the strong sulfuric acid at a sufficient amount of the oxidant [18].

It is also known that GICs are unstable and gradually decompose in a wet medium. At that, a large part of the intercalant leaves the interlayer space of the graphite forming the graphite oxide, which is revealed on the XRD patterns as a low-intensity broad band. Analysis of the diffraction patterns of the hydrolyzed graphite revealed the presence of an intense broadened peak corresponding to the main (002) reflection from the crystalline graphite. The weak peaks, which

can be attributed to the residual GICs, were observed as well in [83]. On the basis of these data, it can be concluded that the hydrolysis of graphite bisulfate leads to phase separation of the graphite and graphite oxide. It can be assumed that this process is as follows. A water molecule, due to its relatively high nucleophilicity, cannot diffuse deep into the interlayer space of graphite, but it is attached to the positively charged π-polycation of the graphene layer near the periphery of graphene layers. This creates a sigma-bond in carbon hydroxyl, and the released proton goes into the solution. One electron goes to an aromatic graphene layer reducing its charge, while the intercalated acid anion leaves the depth of interlayer space and diffuses into the solution. Schematically, the process can be written as follows:

$$\begin{array}{ll}
\cdots\cdots\cdots\cdots\cdots\cdots\cdots\cdots\cdots\cdots\cdots & \\
\mathrm{C{-}C{=}C{-}C{=}}\mathbf{C{-}C^{+}{-}C}\mathrm{{=}C{-}C{=}C} & \\
[\mathrm{H_2SO_4}\ \mathbf{HSO_4}^{-}\ \mathrm{H_2SO_4}] & + \mathbf{H_2O} \rightarrow \\
\mathrm{C{-}C{=}C{-}C{=}}\mathbf{C{-}C^{+}{-}C}\mathrm{{=}C{-}C{=}C} & \\
[\mathrm{H_2SO_4}\ \mathbf{HSO_4}^{-}\ \mathrm{H_2SO_4}] & \\
\cdots\cdots\cdots\cdots\cdots\cdots\cdots\cdots\cdots\cdots\cdots\cdots & \\
\mathrm{C{-}C{=}C{-}C{=}}\mathbf{C{-}C{=}C}\mathrm{{-}C{=}C{-}C{-}OH} & \\
\rightarrow \mathrm{C{-}C{=}C{-}C{=}}\mathbf{C{-}C^{+}{-}C}\mathrm{{=}C{-}C{=}C} + 3\mathrm{H_2SO_4} & \\
[\mathrm{H_2SO_4}\ \mathbf{HSO_4}^{-}\ \mathrm{H_2SO_4}] & \text{(solution)} \\
\cdots\cdots\cdots\cdots\cdots\cdots\cdots\cdots &
\end{array} \tag{2.14}$$

Thus, the phase of covalent graphite compound, like graphite oxide, is formed at the periphery of graphite crystal, which is splitted into layers yet at the hydrolysis stage. These layers can be opened then under the thermal shock to form a vermi-type structure of exfoliated graphite. Obviously, accumulation of the oxide-graphite phase at the periphery of graphite crystal causes arising the tensile mechanical stress, which, in excess of a certain thickness of the carbon layer packet, can result in the crystal cleavage.

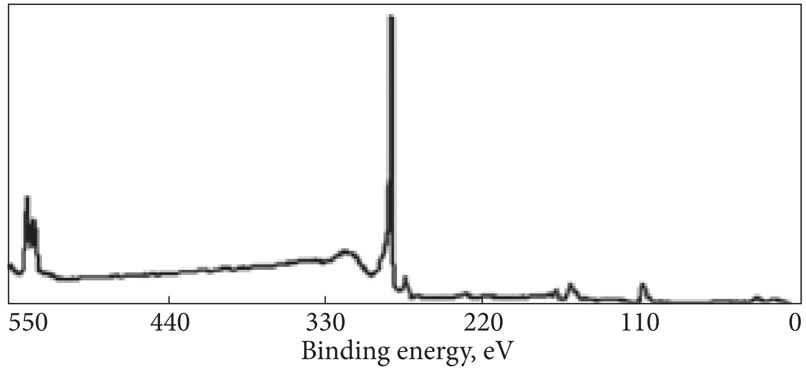

Fig. 2.11. XPS spectrum of electrochemically oxidized graphite

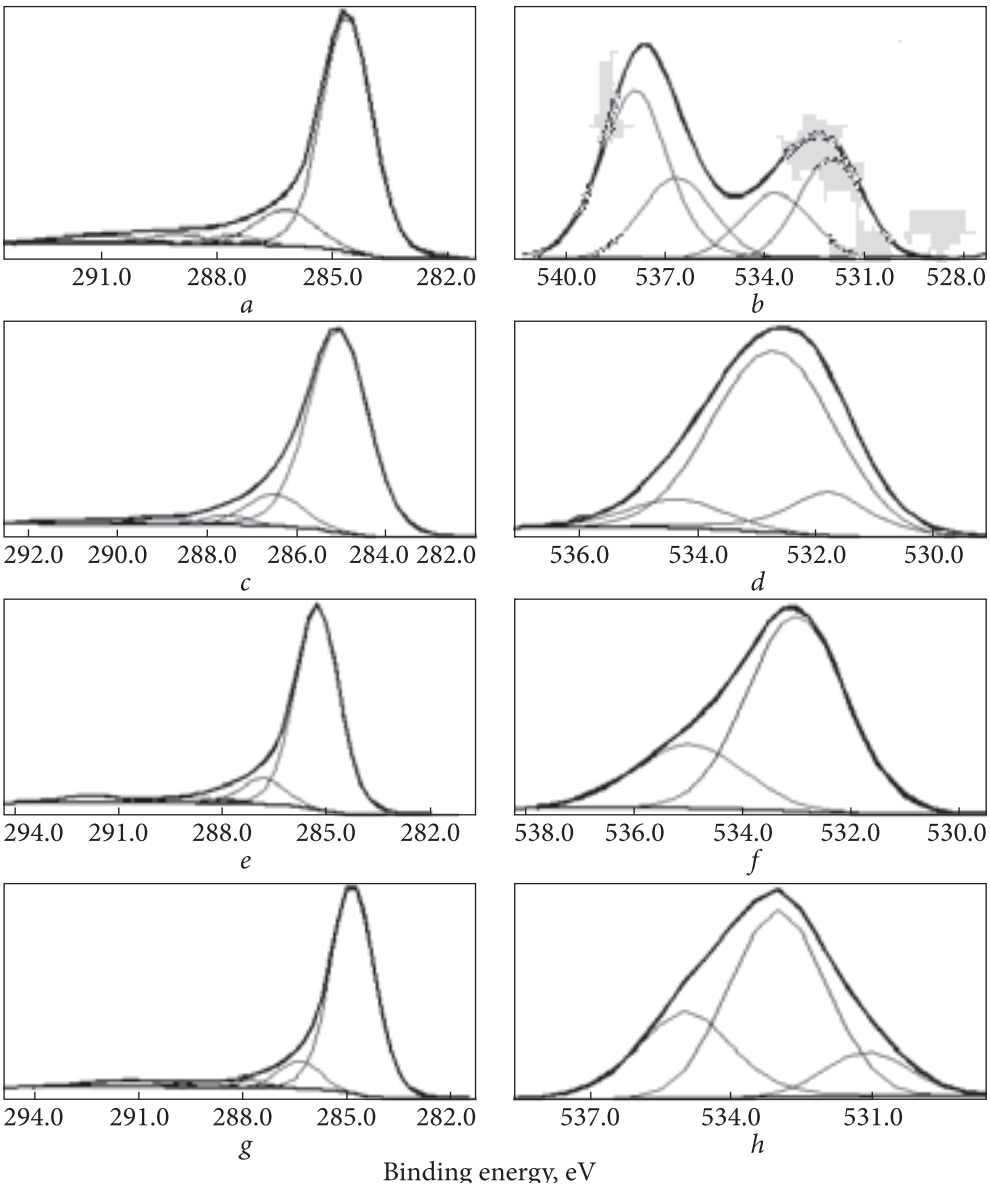

Fig. 2.12. XPS spectra of graphite: (a, b) electrochemically oxidized; (c, d) chemically oxidized (with ammonium persulfate); graphite oxidized and its exfoliated forms (*e*, *f*, *g*, h); (*a*, *c*, *e*, *g*) C 1s ; (*b*, *d*, *f*, *h*) O 1s

Fig. 2.11 shows a typical XPS spectrum of intercalated graphite. The main peak with an energy of about 284.6 eV corresponds to the carbon in the graphite lattice.

Fig. 2.12 shows typical XPS spectra obtained with a high resolution for samples of oxidized and exfoliated graphite. Results of XPS analysis of the C 1s and O 1s

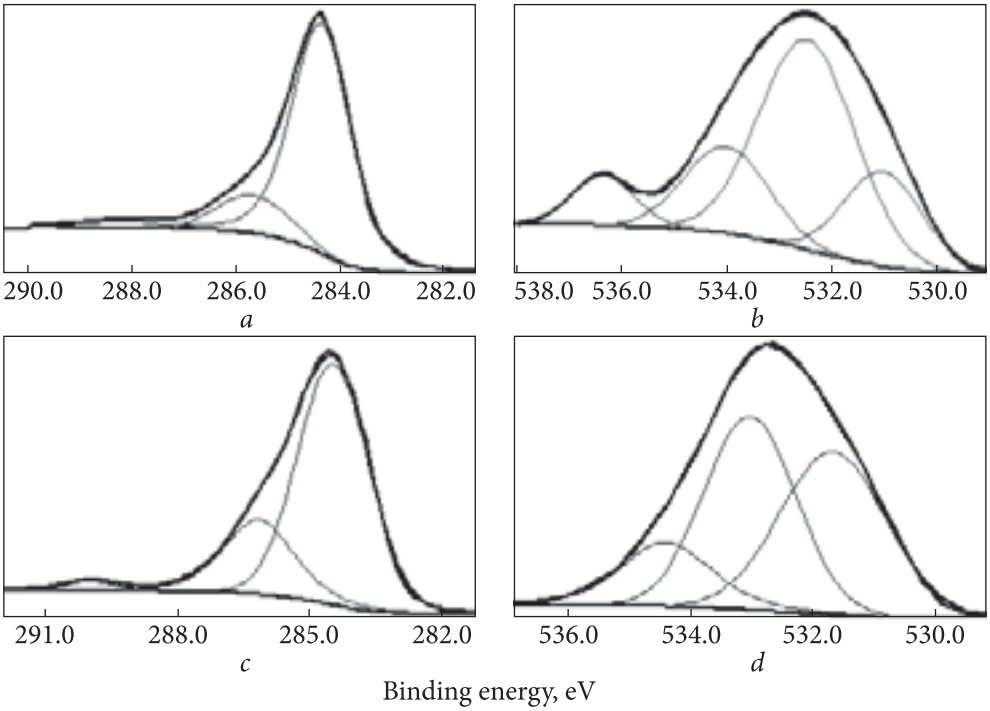

Fig. 2.13. XPS spectra of carbon sorbents: SCN (*a*, *b*); KAU (*c*, *d*); C 1s (*a*, *c*); O 1s (*b*, *d*)

peaks as the concentration distribution for different types of functional groups, the total content of oxygen and carbon by the XPS data are listed in Table 2.15.

XPS spectra and the results of their analysis for samples of SCN and KAU carbon sorbent are presented in Fig. 2.13 and Table 2.15.

Comparing the data given in Table 2.15 and Figs. 2.12 and 2.13, one can see that the electrochemically oxidized graphite samples are close by their characteristics to the samples obtained by the persulfate method. This refers above all to the value of the total oxygen content and the content distribution of the oxygen-containing groups. An increasing amount of electricity under the electrochemical oxidation leads to redistribution of the content of oxygen-containing groups in the direction of the C = O groups growth (samples 201.40 and 201.67). Electrochemical oxidation in the concentrated sulfuric acid reduces the relative contents of C=O groups and increases the content of the C—OH and C—O—C groups. Generally, the oxygen content on the surface of the exfoliated graphite obtained from electrochemically oxidized graphite is twice that on the surface of chemically oxidized graphite. The predominance of the relative content of the C—OH and C—O—C groups over the C=O groups is typical for EG obtained by chemical oxidation of graphite.

Table 2.15. **The total content of oxygen and carbon and relative content of oxygen-containing functional groups according to XPS data**

Sample	Total carbon content,%	Relative carbon content for C 1*s*,% Binding energy, eV					Total oxygen content,%	Relative oxygen content for O 1s,%, Binding energy, eV		
		Carbon of graphite	Phenolic, ethanolic (C—OH)	Carbonyl, quinone (C=O)	Carboxyl, ethers (C-OOH)	Carbonate, adsorption. CO, CO_2		Carbonyl, ketone, lactone (C=O)	C—OH, C—O—C	O_2, H_2O
GO, ECHO, 201.40	63.0	75.3	13.9	3.0	4.0	3.9	20.5	22.3	15.7	42.6—537.9 20.0—536.7
GO, CHO, $(NH_4)_2S_2O_8$	78.0	80.9	11.6	3.0	2.4	2.1	17.1	16.5	73.9	9.5
EG, ECHO, 201.40	86.5	81.0	10.0	2.1	3.4	3.6	8.2	±	73.3	26.7
EG, ECHO, 201.67	97.7	83.6	10.5	2.9	0.9	2.1	2.3	17.4	53.8	28.8
EG, CHO, $(NH_4)_2S_2O_8$	99.4	81.3	9.6	2.6	2.4	4.0	0.6	12.4	57.8	29.8
EG, ECHO, 95% H_2SO_4	97.6	83.9	16.1	±0	±0	±0	2.4	9.3	68.9	21.8
EG, 1000°C, H_2	97.5	87.8	12.2	±0	±0	±0	2.5	±0	83.0	17.0
EG, CHO, peroxide	98.8	82.1	9.2	3.4	2.3	3.0	1.2	6.1	84.8	9.1
EG, CHO, potassium dichromate	99.0	74.0	13.8	3.6	2.4	6.2	1.0	14.4	58.9	26.7
SCN	85.1	82.3	14.5	±0	3.2	±0	14.9	19.6	53.0	19.1—534.0 8.3—536.3
KAU	85.3	71.3	25.7	±0	±0	3.0	12.7	41.1	42.3	16.6 ± 0

SCN and KAU carbon sorbents differ significantly in the higher total content of oxygen.

It should also be noted that the SCN sorbent has occluded water or oxygen with the energy of 534.0 eV, close to the standard interval of (534.6—535.4) eV, and adsorbates associated with the energy of interaction of 536.3 eV. It is also observed for the electrochemically oxidized graphite (sample 201.40): adsorbates with the interaction energy of 537.9 eV and 536.7 eV with the relative oxygen contents of 42.6 and 20.0%, respectively.

As noted above, the formation of the HSO_4^- active free radical type particles, which can form a sigma-bond with the carbon atoms of graphite is possible during the electrochemical oxidation of graphite, especially by the "semi-dry" method. On the other hand, the presence of strongly bound oxygen can confirm the formation of the graphite oxide phase with higher binding energy during electrolysis.

2.2.5. Formation of solid materials from exfoliated graphite and their characteristics

The effect of internal and external factors. The main method of the formation of products from EG is pressing. Direct compression in a mold or rolling mills (single- and double-sided) is the most common technique. As a molding material, the EG powder differs essentially from other powdered materials. Its particles have a complex structure, developed surface, a specific "worm-like" shape, great volatility, and propensity to self-sealing. The pressing of graphite without binders is accompanied by the formation of the two types of bonds, namely the Van der Waals bonds between the graphite planes and the chemical ones between the active sites available on the graphite planes and the crystallite faces [84]. The process of pressing the exfoliated graphite without a binder is related to the presence of thermal degradation products of GICs formed during heating [85]. These products act as a plasticizer, which provides sliding of the EG layers and their crosslinking under compacting. At the same time, during the formation of the EG products, the content of paramagnetic centers in the briquette is reduced by about five orders of magnitude. [84]. This can be explained by the fact that as a result of the thermal cracking of GICs, a large number of carbon radicals with free bonds affects the strength of the final product.

The formation of a dense material from EG takes place in several stages; the morphology and structure defects of EG particles affect the kinetics of the process of pressing: they change the dependence of density ρ on pressure P [86]. It is possible to obtain materials with a density of from 0.02 to 2.0 g/cm^3 by the direct compression method.

Thermal compression of EG in a closed gas-permeable form is another promising technique [87]. In this case, first, GIC is obtained by any of the known meth-

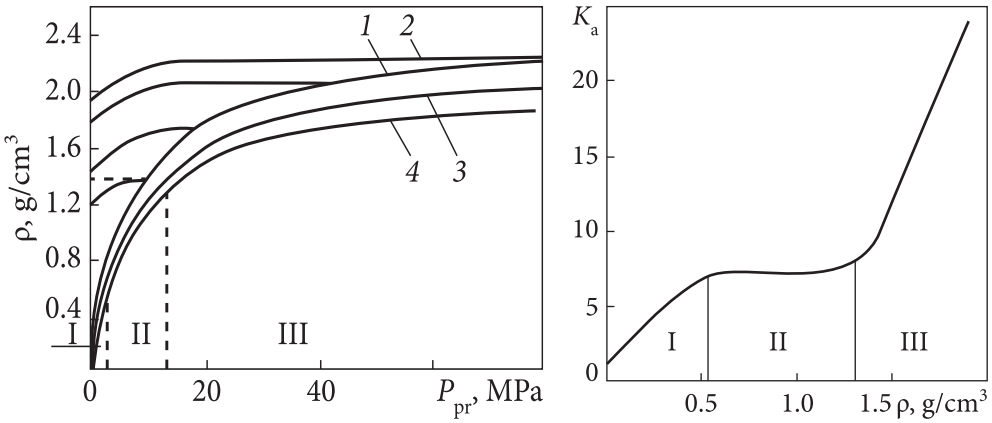

Fig. 2.14. Dependence of the apparent density of EG samples on the pressure during their compacting (*1*), unloading (*2*), and after the removal of pressure before (*3*) and after (*4*) sample compaction

Fig. 2.15. Coefficient of compacting anisotropy vs the apparent density of the material

ods, and then it is placed in a closed and gas-permeable form and heated. When heated, the powder of GIC swells, becoming the EG; this increases the pressure, and self-compacting of EG occurs in a closed form. The processes of compression and expansion occur almost simultaneously. This method can produce a highly porous graphite material with an apparent density from 0.05 to 0.40 g/cm^3. Besides, to obtain a material density of more than 0.2 g/cm^3, GIC powder must first be compacted in a mold. Achieving a density greater than 0.4 g/cm^3 is complicated by the need for a heat- and corrosion-resistant mold due to the graphite tendency to swell and penetrate through gas-exhausting holes.

Sample formation by the single-action compacting method was carried out on the 2167P-50 apparatus [88]. To eliminate the effect of dynamic factors on the process of structure formation, pressing was performed with smooth loading and unloading at a low rate (10 mm/min). According to the diagrams of the exfoliated graphite formation (Fig. 2.14), the process is complex; wherein a springback in the material after removal of the pressure plays a significant role in the formation of the pressing structure (curve *2*). Based on the flowability and the final density measurements, the dependence of the pressing density on the pressure in the compacting process (curve *1*) is significantly different from that obtained after the removal of the load (curve *4*). This is related to the change in the elastic compact dimensions after depressurization. The springback is a result of the elastic deformation of the mold and release of the elastic forces in the powder with a very strong influence on the elastic expansion factor of the crystallographic anisotropy of particles [84]. Stresses arising in the mold and punches when forming EG are small enough, so their elastic deformation may

be disregarded. At the same time, when forming EG materials with a high density, it approaches the graphite XRD density 2.24 g/cm^3 [89] (Fig. 2.14, curve *1*) solely under pressure and does not exceed 2.0 g/cm^3 with relieving pressure. The forces of elastic interaction between the graphite planes caused by the presence of nanoscale defects make a significant impact on the springback, and thermal degradation products of graphite bisulfate, which are placed on planes of EG particles play the role of a plasticizer in the process of compacting, becoming a kind of a damper between the graphite layers. All this leads to the fact that after pressure removal the material density can be decreased by 40—50%.

Anisotropy coefficient K_a of pressed EG samples was determined as the ratio of the reflection intensities of the (002) plane measured parallel and perpendicular to the pressure direction. The nature of changes in this ratio, depending on the material density (Fig. 2.15) corresponds to the character of the $\rho = f(P)$ dependence shown in Fig. 2.14.

The process of compacting takes place in three stages: I — seal and partial destruction of particles (to a density of 0.5 g/cm^3); II — mutual movement, crushing, and disintegration of particles and fragments (to a density of 1.3 g/cm^3); III — plastic deformation of particles throughout the fragmented volume [84, 86, 90]. In the first stage, characterized by a linear change in density depending on the pressure, K_a is growing, which is obviously due to the deformation of the contact surfaces of EG particles and partial orientation of their basic planes perpendicular to the pressing axis. In the second stage, the $\rho = f(P)$ dependence is curvilinear, and the anisotropy coefficient is almost unchanged, which can be explained by the crushing and mutual movement of already oriented particles. As a result of this process, the anisotropy growth stops, porosity is reduced, and the initial contacts of particle boundaries are blurred. By the end of this stage, the surface layer structure acquires a uniform finely fragmented shape; besides, the visible boundaries between particles disappear.

The rapid growth of the anisotropy coefficient in the third stage (Fig. 2.15) is due to the formation of a layered structure with a preferred orientation of the graphene planes perpendicular to the external load direction. In this stage, the convergence of macrolayers of compression takes place along with their closing and mutual penetration, which may lead to the formation of microlens-like bundles due to the springback after pressure removal.

2.2.6. Mechanical properties of EG solid materials

As follows from the previous sections, EG is a complex heterogeneous system, the structural state of which is determined by the GIC synthesis conditions. Its hydrolysis, heat treatment, and so on, to a large extent, determine the physical and mechanical properties of solid materials obtained from the EG. Here are some aspects of the analysis of the strength characteristics of

low-density EG materials at the key stages of their preparation: preliminary, intercalation stages, thermal treatment, and the molding step.

Tests were carried out on samples of 20 mm in diameter and in height, made of EG prepared from the natural graphite from the Zavale field (Ukraine), brand GAK-2. Graphite powder was treated with concentrated sulfuric acid with the participation of ammonium persulfate. After washing and drying, the resulting residual compounds of graphite bisulfate were heat-treated at 800 °C. Thus, the exfoliated graphite with a bulk density of 8 g/dm^3 was obtained. Samples were prepared by a one-way compression in a cylindrical mold as well as by the thermochemical compacting of the GIC powder in a closed cylindrical permeable steel mold at the same temperature.

Compression testing was performed by a continuous deformation of the sample as well as by the method of repeated deformation after unloading with the further increased load to full destruction (materials of high density), or up to 20% of the sample deformation. The rate of deformation was 2 mm/min. Load direction coincided with the direction of compression. The value of compression stress at 10% deformation of the contact (σ_{10}) was used for comparison with the compression resistance characteristics.

The mesh-size distribution of the source graphite powder and GICs obtained in the standard oxidation conditions are shown in Table 2.16. More than half particles have sizes in the range of 100—200 μm. Intercalation results in an increase

Table 2.16. **Mesh size distribution, fraction parameters of GAK-2 source graphite and GIC powders obtained**

Fraction, μm	Weight content, %		Bulk density, g/dm^3			Weight loss of GIC after heat treatment, %
	GAK-2	GIC	GAK-2	GIC	EG	
<100	27	9	446	189	22.5	15
100—200	57	51	469	214	7.0	20
>200	16	40	530	193	4.0	26
Total	100	100	476	200	6.0	22

Note: $m_{ox}/m_{graph} = 0.7$; H_2SO_4 concentration 93%; treatment temperature 800 °C.

Table 2.17. **Weight loss of GIC, bulk density of EG powder, density, and strength of EG samples of different source graphite fractions**

Source graphite, μm	Weight loss of GIC,%	Bulk density of EG, g/dm^3	Sample density, g/cm^3	σ_{10}, MPa
>100	13	26	0.6	1.10
100—200	19	6.5	0.6	1.35
>200	28	3.0	0.6	1.55

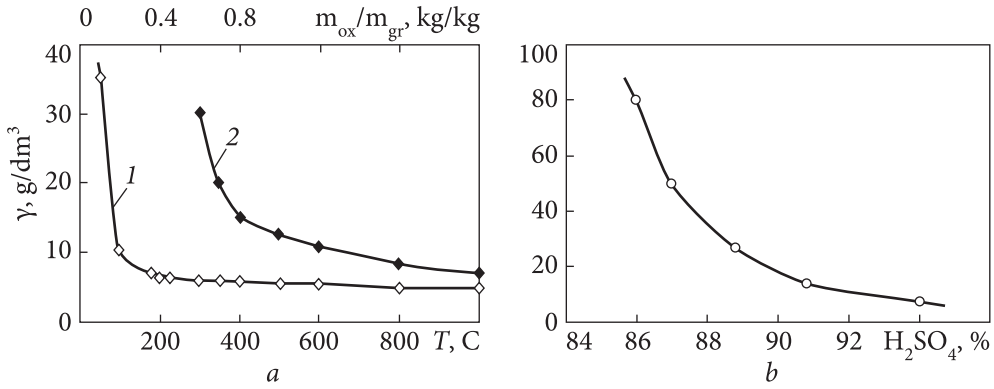

Fig. 2.16. Dependence of EG bulk density on: *a — 1* — the oxidant-graphite ratio (content of H_2SO_4 = 93%, T_{tr} = 850 °C); *2* — the treatment temperature of GIC (content of H_2SO_4 = 93%, m_{ox}/m_{gr} = 0.7); *b* — the content of H_2SO_4 (m_{ox}/m_{gr} = 0.7, T_{tr} = 1000 °C)

of the average particle size. Bulk density of the graphite is reduced by more than twice. Subsequent heat treatment of each GIC fraction showed a decrease in the EG bulk density with increasing particle size. In addition, a greater weight loss was observed for larger particles or a higher content of the intercalant lost during the exfoliation. Intercalation of individual fractions of the source graphite particles under the same conditions and subsequent thermal treatment indicated according to [36], similar to the above trend of growth and reduction of the EG bulk density with the particle size increasing (Table 2.17). The strength of the compacted EG samples obtained from different factions increases as well with the size of the source graphite particles in the area investigated.

As shown by the research results, the bulk density and thus the characteristics of the pressed samples are dependent on the method of their chemical and thermal treatments.

Fig. 2.16 presents the results of the study of the dependence of the EG bulk density on the mentioned conditions of treatment of source graphite. With changing one of the process parameters during the experiment (the amount of oxidant (m_{ox}) or the concentration of sulfuric acid during intercalation, the heat treatment temperature (T_{tr}), and other parameters remained unchanged and corresponded to the standard conditions in accordance with [91].

As follows from Fig. 2.16, the EG bulk density (γ) monotonically decreases with the increasing amount of the oxidant or acid concentrations and the treatment temperature of GIC. The EG bulk density is most sensitive to the sulfuric acid concentration: concentration decreases with the 10% increasing the bulk density by more than 10 times.

Increasing the amount of oxidizer during intercalation or heat treatment leads to a practically identical decrease in the bulk density. Furthermore, the

bulk density changes rapidly with the increasing amount of the oxidizer to about 0.7 kg per 1 kg of graphite. The further increase in the ratio m_{ox}/m_{gr} does not affect significantly the bulk density. Tables 2.18 and 2.19 summarize the results of tests on compression of the samples made of EG obtained at different concentrations of sulfuric acid (Table 2.18) and the heat treatment temperatures (Table 2.19). With increasing the sulfuric acid content, the strength of samples increases monotonically. A maximum on the dependence of strength on the heat treatment temperature was observed at about 600 °C.

Typically, the GIC processing temperature also significantly affects the strength of samples (Table 2.19).

This effect is apparently due to features of the thermal decomposition of intercalation compounds of graphite with sulfuric acid. The temperature dependence of the mass-loss rate of GIC-H_2SO_4 has two peaks: the first at about 250 °C, the second in the range of 600—850 °C [92]. Therefore, a significant amount of degradation products of graphite bisulfate (sulfate sulfur and sulfur) are chemically bonded with the graphite carbon) remains on the surface of EG particles obtained at 300 and 400 °C [93]. The amount of residual sulfur compounds (the second peak on the thermogravimetric curve [92]) is significantly reduced at temperatures above 800 °C, which obviously impairs the EG compressibility, respectively, the strength of the samples. In addition, the EG obtained at 600 °C is characterized by a high degree of heterogeneity of the structure of particles [86] and the deformation requires a considerable amount of energy in its restructuring. Therefore, EG samples of low density (up to 1.3 g/cm^3) obtained at 600 °C have a higher deformation resistance [94].

Fig. 2.17 summarizes the dependences of the compressive strength on the bulk density of EG obtained under different intercalation conditions and heat

Table 2.18. **Dependence of the compressive stress of samples up to 10% deformation (σ_{10}) on the sulfuric acid concentration (m_{ox}/m_g = 0.7; T = 1000 °C) ***

H_2SO_4,%	85.3	86.4	88.7	93.64
σ_{10}, MPa	1.15	1.7	2.1	2.9

* Sample density 1.0 g/cm^3.

Table 2.19. **Dependence of the compressive stress of samples up to 10% deformation (σ_{10}) on the GIC treatment temperature (m_{ox}/m_g = 0.7; H_2SO_4 concentration 93%)***

T,°C	300	400	600	800	1000
σ_{10}, MPa	1.8	2.76	3.14	3.04	2.9

* Sample density 1.0 g/cm^3.

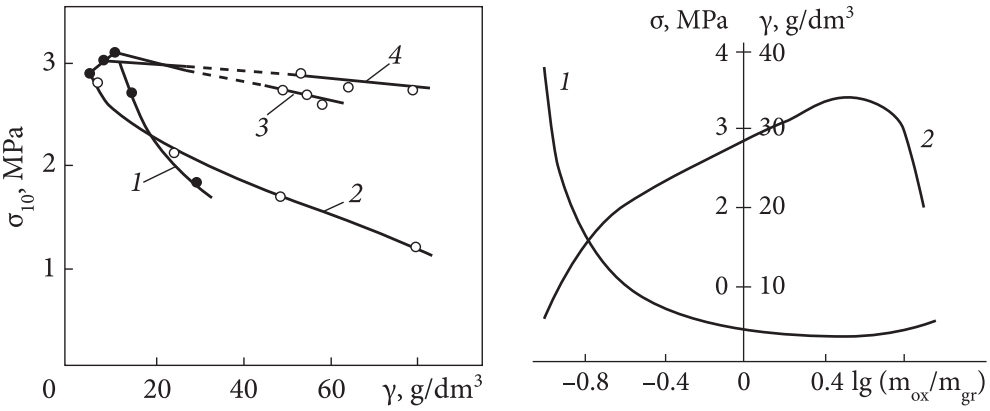

Fig. 2.17. Dependence of the compression stress of samples up to 10% strain (σ_{10}) on the bulk density at: *1* — change in the treatment temperature (thermal shock) (concentration of H_2SO_4 = 93%, m_{ox}/m_{gr} = 0.7); *2* — change in H_2SO_4 during intercalation (m_{ox}/m_{gr} = 0.7; T_{tr} = 1000 °C); *3* — GIC sequential incremental heating from 200 to 600 °C; *4* — rarely phase grinding of EG (m_{ox}/m_{gr} = 0.7; H_2SO_4 concentration = 93%, T_{tr} = 800 °C). Apparent density of the pressed samples ρ = 1 g/cm^3

Fig. 2.18. Dependence of the bulk density (γ) (*1*) and tensile strength (*σ*) (*2*) on the mass ratio of oxidant to graphite for m_{acid}/m_{gr} = 2, ρ = 0.9 g/cm^3

treatment. Samples used for analysis were obtained: at the standard oxidation conditions and heat treatment under varying temperatures; at variable concentrations of sulfuric acid with constant oxidizer content and temperature; standard oxidized samples are heated at increasing stepwise temperatures from 200 to 600°C with exposure for 30 min every 100 °C, and samples obtained by milling particles of standard EG in distilled water. As seen in Fig. 2.17, the most significant decrease in strength of the samples was observed with an increase in the bulk density by reducing the processing temperature (thermal shock) of GIC (curve *1*) and reducing the sulfuric acid concentration in the process of graphite intercalation (curve *2*). Despite the substantial EG bulk density increase (by 5—8 times) due to gradually heating the GIC (curve *3*) obtained under standard conditions, or by liquid-phase crushing of EG (curve *4*), no significant reduction of the compressive strength was observed. Consequently, the strength of the compressed EG depends not only on the degree of opening patterns (the specific surface area or bulk density) but also on the physical-chemical state of the surface of particles, which is determined by the properties of source graphite and the conditions of its chemical and subsequent heat treatments.

Certain influence on the mechanical properties of the EG samples belongs to peroxidation. In particular, intercalation with sulfuric acid in the presence of strong oxidants ($KMnO_4$, $K_2Cr_2O_7$, $(NH_4)_2S_2O_8$, SO_3 et al.) affects the properties

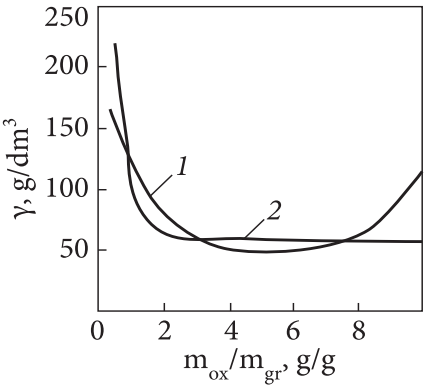

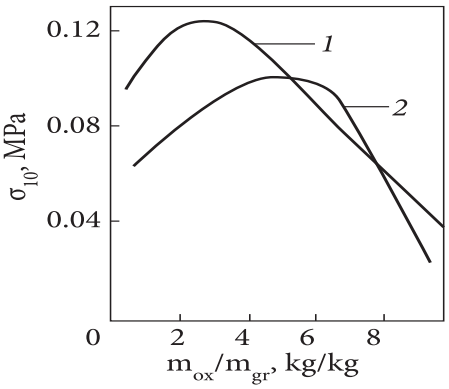

Fig. 2.19. Dependence of the bulk density on the mass ratio of graphite to oxidant at a constant mass ratio of acid to graphite: 1 — $m_{acid}/m_{gr} = 2$; 2 — $m_{acid}/m_{gr} = 4$

Fig. 2.20. Dependence of the tensile strength on the mass ratio of graphite to oxidant at a constant mass ratio of acid to graphite: *1* — $m_{acid}/m_{gr} = 2$; *2* — $m_{acid}/m_{gr} = 4$

of materials produced. The authors of [95, 96] have shown that the phase composition of GIC depends on the redox potential of the oxidation mixture, which in turn depends on the concentration and amount of sulfuric acid in the oxidizer mixture. It is alleged that the bulk density of EG obtained is a function of the GIC phase composition and is virtually independent of the oxidant nature. In [96], it was shown that the chemical oxidation of graphite in the presence of strong oxidants in the intercalated GIC layer includes peroxydisulfuric anions $HS_2O_8^-$. Hydrolytic deintercalation of such GIC can lead to the formation of the surface layer of graphite oxide in an amount of 6—10% by weight [97] and to an increase in the strength of final materials.

Therefore, we have studied the effect of the content of the oxidizing agent in the graphite–$(NH_4)_2S_2O_8$—H_2SO_4 system and the content of sulfuric acid on the strength of the EG pressed (ceteris paribus*)*. For tensile tests, samples were used in the form of a fillet from a tape with a working part of 100 mm long, at least 5 mm wide, and 0.3 mm thick. They were formed by pressing a unilateral EG powder obtained at 800 °C to the density of 0.9 g/cm^3. For compression testing, samples of 20 mm in diameter and high were prepared by thermal pressing at 500 °C in a closed permeable mold to a density of 0.07 g/cm^3. Fig. 2.18 shows the change in the bulk density of EG and the tensile strength (σ_B) depending on the amount of the oxidizing agent per mass of graphite with an unchanged content of sulfuric acid in the reaction mixture. The sharp decrease in the bulk density with the increasing amount of the oxidant is accompanied by a significant increase in the σ_B value, which is clearly associated with an increase in the EG specific surface area and consequently with the number of its active sites. Further

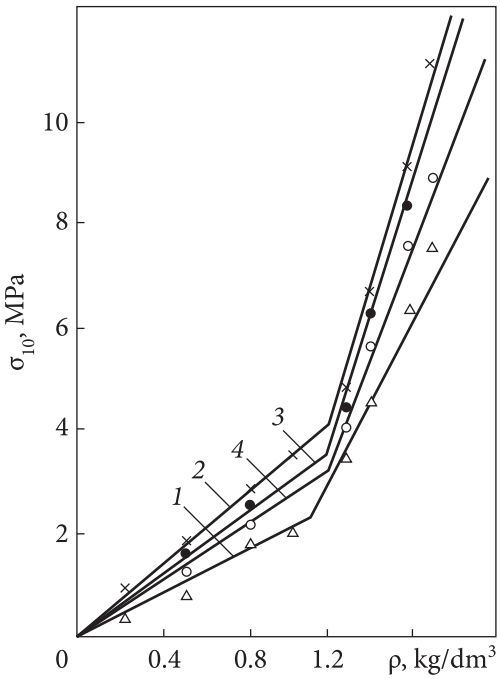

Fig. 2.21. Dependences of the compression strength on the apparent density of EG samples obtained at temperatures: *1* — 400; *2* — 600; *3* — 800, and *4* — 1000 °C

increase in the strength at the stable bulk density is caused apparently by the increase in the free radicals on the EG surface. They arise from the graphite inclusion followed by decomposition of the peroxydisulfuric acid anions [97]. Further increase in the oxidant amount leads to a sharp drop in strength due to sticking of both GIC (drying process) and EG (heat treatment process) particles. The active centers thus recombine, resulting in deterioration of compression and, consequently, the strength of the material.

A similar picture was observed when changing the compressive strength of the GIC compacted thermally with an increasing amount of oxidant in the reaction mixture (Figs. 2.19, 2.20). During the intercalation process, the graphite crystals swell considerably more than in the case of intercalation under stoichiometric conditions. This process is accompanied by a significant decrease in the bulk density of the dried GIC (Fig. 2.19). Exfoliation of the graphite crystals is caused, obviously, not only by the interlayer switching intercalant but also by an intense release of oxygen between graphene layers as a result of the partial decomposition of the intercalated peroxysulfate $HS_2O_8^-$ ions. When the graphite-acid mass ratio is 2 (Fig. 2.19, curve *1*), the GIC bulk density starts increasing due to the agglomeration of particles during drying. Particles' sticking is caused apparently by the formation of a significant amount of graphite oxide particles on their surface in the course of GIC hydrolysis [97]. The character of changing in the compressive strength (Fig. 2.20) and the reasons for this change are the same as described above for the tensile strength. Thus, the strength becomes slightly higher with more acid in the reaction mixture (Fig. 2.20, curve *2*) than in similar situations with less amount of the acid (Fig. 2.20, curve *1*).

The material density influences both the EG structure features and strength characteristics. Experimental studies showed that the loading mode (continuous or repeated-with increasing static load) does not affect the stress at a given deformation. Fig. 2.21 presents data on the strength of uniaxial compression of

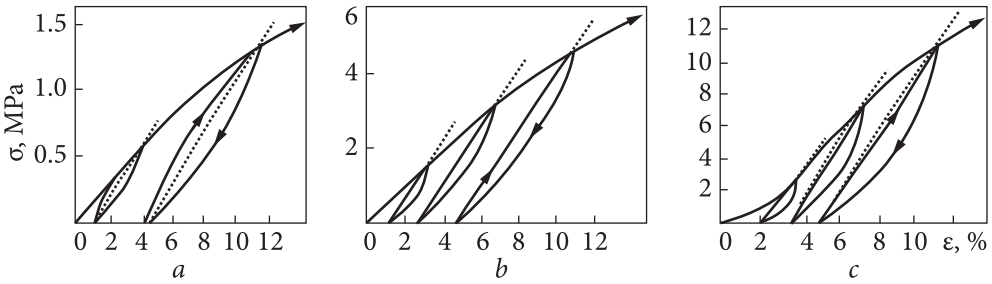

Fig. 2.22. Deformation diagrams for the static reloading of EG samples with a density: *a* — 0.5; *b* — 1.3; *c* — 1.7 g/cm^3

samples of different EG powder densities obtained at different treatment temperatures of GIC.

As seen, the test results are approximated by a piecewise-linear dependence, which has at least two specific regions. The heat treatment temperature changes the compression resistance of the samples. The analysis of the strain diagram allows for establishing the reasons for changing the compression resistance of the samples (Fig. 2.22).

Thus, with the sample low density, regardless of the EG powder temperature, the deformation diagram of the samples is similar to that of cellular polymeric materials with a small initial linear region due to sealing "weak" elements of the structure, an elastic deformation region of the "framework" structures and a plastic deformation region (Fig. 2.22, *a*).

This is because, as shown by the optical microscopy experiments [86], a highly porous structure is formed during pressing EG samples of low density, having graphite layers with different orientations. The axis of the hysteresis loop in the diagram of static reloading is placed inside the hysteresis loop, which indicates scattering in energy materials associated with a significant restructuring during deformation. In the density range from about 0.8 to 1.3 g/cm^3, the material structure has a dispersed character when the EG particles are already destroyed [90]. During a static loading of such a structure, the re-loading line starts getting positive curvature, repeating the form of the discharge curve, and the hysteresis loop axis starts running beyond it (Fig. 2.22, *b*). This indicates that most of the energy dissipated in the material due to deformation is formed during pressing, and to a lesser extent due to rearrangement of the structure itself.

In EG samples with a density over 1.3 g/cm^3, as shown by the optical microscopy, a layered structure with interlayer defect density is mainly formed. For a continuous or repeated-static uniaxial compression of such a structure, the deformation curve becomes S-shaped. Under static reloading, the hysteresis loop axis goes markedly beyond the hysteresis loop and the re-deformation curve repeats the form of the initial part of the curve (Fig. 2.22, *c*). This char-

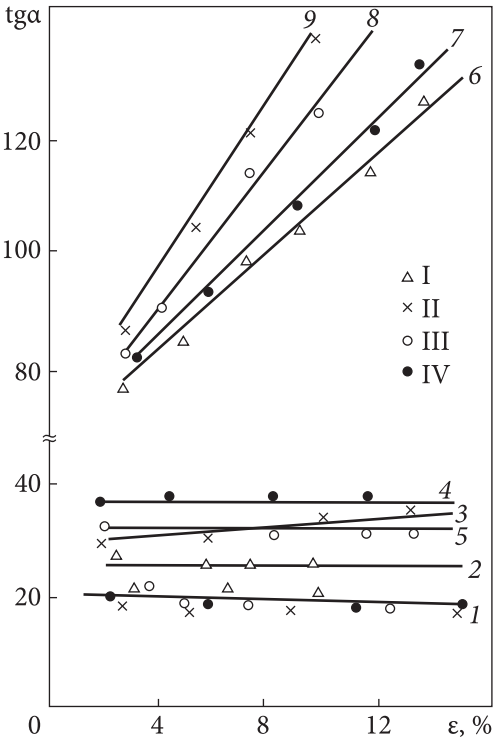

Fig. 2.23. Dependences of the hysteresis loop slope on the total deformation of samples with density 0.5 (*1*), 0.9 (*2—4*), and 1.7 g/cm^3 (*5—9*) of EG obtained at temperatures of 400 (I) 600 (II), 800 (III) and 1000 (IV) °C

acter of EG sample deformation is caused obviously by the effect associated with the presence of the layered structure of the lens-like pores and microlayers. In the deformation of these structures, their elastic resistance is implemented similar to the effect of lenticular spring with a consequent loss of elastic stability, while the initial section of the deformation curve has a positive curvature. The collapse of microlayers and pores leads to the fact that the next stage of the stress and compression rise is linear up to the start of plastic deformation in the material layers. Closing of microlayers does not mean their disappearance, so the initial compression section of the diagram after removing and reloading is non-linear up to the sample destruction.

Analysis of the deformation diagrams has shown that regardless of the temperature of obtaining EG, the angle α of the hysteresis loop is different from the angle of the tangent of the initial section α_0, which reflects the initial stiffness of the structure "frame" (Fig. 2.22). Further, the rigidity of the "frame" can be evaluated by a slope (tgα) of the hysteresis loop, the nature of which changes during deformation and reflects the ability of a material to cyclic hardening or softening. It was found that in the process of static compression, the value of tgα in samples uniquely depends on the temperature of obtaining EG (Fig. 2.23). Thus, for low-density samples, tgα tends to decrease with increasing deformation (line 1), and its value does not depend on the temperature of obtaining EG. The material is cyclically softening to the density approximately equal to 0.8 g/cm^3. The slope angle changes slightly with the strain increasing (lines 2—5) for the samples of 0.8—1.3 g/cm^3 density. In this case, the materials are cyclically-stable, but have different "frame" stiffness structures depending on the temperature of EG obtaining. At a density of 1.3 g/cm^3, the value of tgα increases with the deformation (lines 6—9), cyclic softening of material takes place, and the EG samples obtained at 600 °C acquire a greater ability to cyclic hardening.

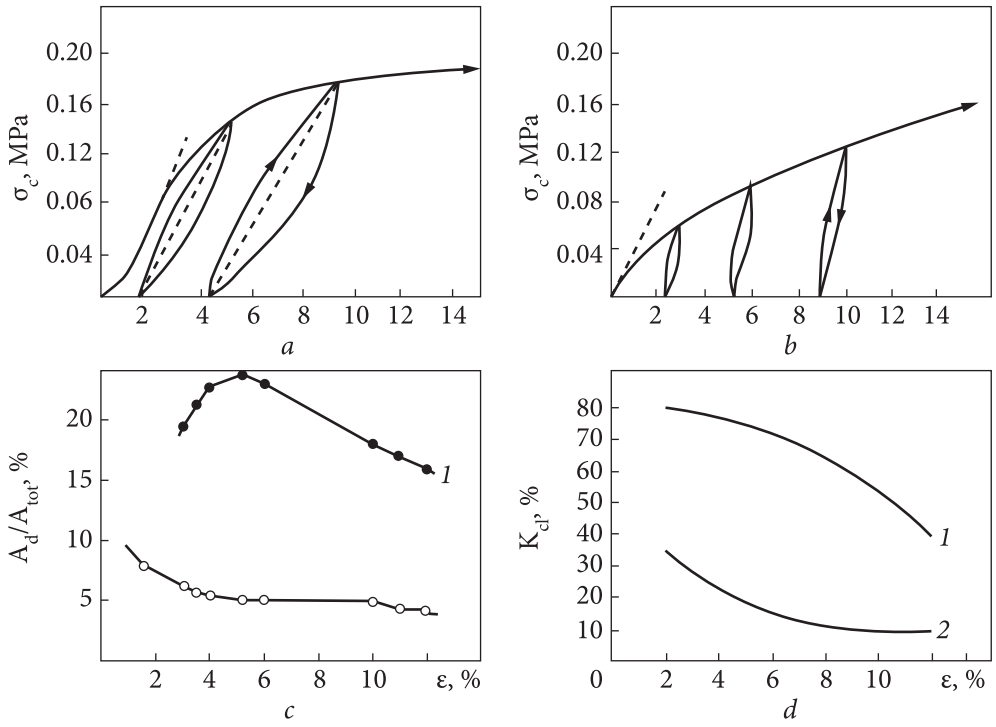

Fig. 2.24. Dependences of the compression stress (*a*, *b*), the part of scattered strain energy (*c*), and the elastic coefficient (*d*) on the compression strain of samples obtained by a unilateral compression of the EG powder (*1*) and by the expansion of the GIC-H_2SO_4 residual compounds in a limited volume (*2*)

Let us consider the effect of a structure forming method on the EG strength characteristics. The comparative XRD analysis of the natural graphite and EG samples obtained by free expansion and expansion of the residual compounds in a limited volume showed that the general view is similar to diffraction patterns. However, a significant difference was observed in the (002) profiles for these samples: the half-width was 18.5, 28.0, and 21.0 min, respectively. Physical broadening of XRD reflection determines, as known, coherent scattering domain size and the microstrain value characterized by the structural state of the crystal (degree of disorder). Thus, the above values of half-width peaks indicate that a limited expansion causes EG structure disordering significantly less in comparison with the material prepared by free expansion.

Of course, these mold-related methods also affect mechanical characteristics. The test samples were prepared in two ways: one-way compression of the EG powder into a cylindrical mold, and expansion in a limited volume (thermochemical compression) of residual compounds of the graphite bisulfate. The diameter and height of the tested samples of compression were 20 mm. Tests have been con-

ducted on the 2167 P-50 device in a cyclic mode with a static load increasing value during the deformation at a rate of 2 mm/min and recording the stress-strain diagram. Thus, the load vector was parallel to the extrusion axis.

The effect of these structure differences on the mechanical properties of the materials was studied by the method of static reloading. To eliminate the effect of sample macrostructure features, in particular, their anisotropy, the samples had the same low density (~0.1 g/cm^3) and were almost isotropic. Analysis of σ_c on ε dependences (Fig. 2.24) shows that the nature of deformation of the material obtained by free extension of residual compounds is predominantly elastic.

This is because of the formation of specific defects in crystal lattices of the graphite and honeycomb structure during expansion in the free volume due to the high structure disordering caused by bending deformation and flat carbon layers [56], the particles acquire features of the elastic elements with high residual stresses. This specificity is determined by the deformation process of the samples consisting of such particles (Fig. 2.24, *a*). In the initial stage after the compression deformation of the weak elements of the "frame" formed as a result of the springback under compacting, the process enters the stage of elastic deformation of the frame. Thereafter, the compression switches to elastic-plastic deformation of the structural elements. The dependence of the discharge re-load forms a wide hysteresis loop. In this case, the scattered energy of deformation A_s (the hysteresis loop area) is a significant part of the total energy A_{tot} spent on the deformation of the material (the area under the stress-strain curve). In the beginning, the part of the scattered energy increases with increasing deformation (Fig. 2.24, *c*, curve *1),* thus picking up internal stresses and structural defects. Upon reaching the critical level of internal stress, the structure elements stop working as elastic elements, and the processes of the local and total destruction of particles begin. As a result, the part of dissipated energy is significantly reduced, and the deformation becomes predominantly plastic (Fig. 2.24, *d*, curve *1*). Upon expansion of the residual compounds into the limited volume, the process of formation of residual stresses associated with the disordered structure, obviously, is accompanied by their simultaneous relaxation due to the interaction of particles at stacking in shape. As a result, the ductility of the sample structure elements increases and the strain-stress diagram changes substantially (Fig. 2.24, *b*). Elastic-plastic deformation begins almost immediately with the increase in the compressive stress, the part of the scattered energy of deformation is small (Fig. 2.24, *c*, curve *2*). With increasing strain, it is decreased continuously, the deformation is mostly plastic (Fig. 2.24, *d*, curve *2*).

Thus, differences in the structural condition of particles of the graphite obtained via expansion of residual compounds in both a free and limited volumes cause a change in the nature of compression resistance of materials made from these particles.

2.2.7. Application of the exfoliated graphite

The residual intercalation compounds of the natural crystalline (flake) graphite of high purity from different deposits, which exhibit the greatest effect of unidirectional thermal expansion, are successfully used for industrial application [2].

The most important property, which the natural graphite acquires turning on EG is the ability to form a solid material with no binder, by conventional pressing or rolling. At the same time, it keeps all the inherent properties of natural graphite: the highest thermal stability in a non-oxidizing environment, chemical and radiation stability, biological inertness, high heat capacity, thermal and electrical conductivity, low coefficient of thermal expansion, and high anti-friction properties. Thanks to such a complex of high characteristics of solid materials made of EG (foil, sheet, packing), they are used as a sealing element (packing rings, gaskets), and for pipelines, valves, pumps, pressure vessels, and so on to work in conditions of high temperatures and pressures, [4, 98]. Using EG seals instead of traditional asbestos and asbestos-containing materials (paronite et al.) allows increasing the average turnaround cycle operation of pipeline valves by 2.5—8 times and centrifugal pumps by 5—13 times. Of course, in this case, the energy loss and heat transfer fluids are reduced significantly and drinking water withdraws from the use of carcinogenic asbestos-containing materials. Thus, EG sealing is an integral part of energy-saving environmentally friendly technologies. The world output of seals on the basis of EG in 2000 was from 20 to 25,000 tons per year and has been steadily expanded.

Fig. 2.25 shows a simplified scheme of manufacturing EG and its products for various purposes. The most widely used materials of EG are seals, as mentioned above. However, the oxidized graphite is used as a flame retardant filler material. Disperse EG is a heterophile sorbent that can be used as a highly effective sorbent of crude oil and petroleum products with a capacity of up to 80 g of oil per 1 g of EG, which is the highest value for oleophilic sorption materials, for example, [99—101]. It is also possible to apply both as a hemosorbent [102] and as the cathode of an electrochemical reactor for water purification from non-ferrous metal ions [103, 104].

The equipment for thermal expansion of the residual GIC and the line for rental EG powder obtained, of course, are tied in a common line. EG foil of thickness from 0.1 to 1.0 mm and sheets of 2 mm thickness with a density of 1.0 g/cm^3 are usually rolled. The packing rings, smooth and corrugated tape for sealing gland "in place" are made of such foil by cold pressing. The tape is used, above all, as a part of spiral-wound gaskets. In particular, reinforced cotton tape or fiberglass, and steel wire are used for spinning and weaving graphite packings. The flange gaskets are made from EG sheets, unreinforced and reinforced perforated steel by the notch or cutting-out treatment.

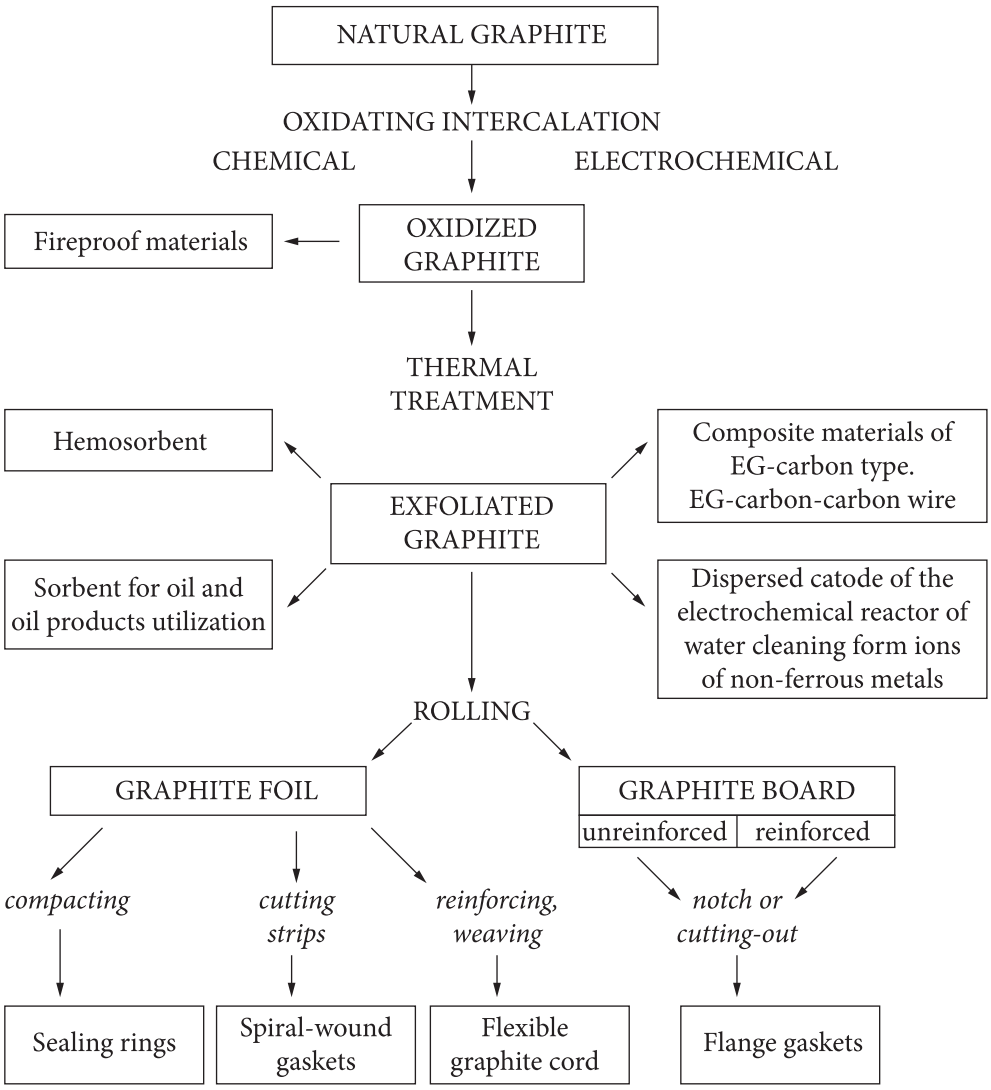

Fig. 2.25. A simplified scheme of obtaining exfoliated graphite and its products for various applications

Sealing EG materials, as noted earlier, reproduce the whole complex of unique properties of graphite. The list of corrosive media for which an EG sealing may be used is given in List of media where it is possible to use EG seals. It should be noted that the EG products have unique characteristics of compressibility and recoverability, which are shown in Fig. 2.26. The physical and chemical characteristics of EG foil from different manufacturers are shown in Table 2.20.

List of media where it is possible to use EG seals

Gases and vapors	Aromatic hydrocarbons
Water vapor (up to 550 °C)	Chlorocarbons
Air, nitrogen (up to 400 °C)	Aqueous salt solutions (brines)
Oxygen (up to 350 °C)	Sulfates, Alums
Freons	Chlorides
Fluorine (up to 150 °C except for fiberglass)	Fluorides
Chlorine dry	Nitrates
Chlorine wet (20 °C)	Phosphates
Chlorine dioxide (up to 70 °C)	Carbonates
Propane, natural gas	Sulfites, thiosulfates
Acetylene	Alkalis, aqueous ammonia
Ammonia	Chromates (up to 20%)
Carbon dioxide (up to 600 °C)	Inorganic acids
Ethylene, propylene	chlorine hydride
Formaldehyde	Hydrofluoric acid (up to 60% except fiberglass)
Hydrogen chloride	Hydrobromic acid
Hydrogen fluoride (except fiberglass)	Anodizing solutions
Hydrogen sulfide	Chromizing solutions
Sulfur dioxide, dry	Nickelizing solutions
Sulfur dioxide, dry	Phosphorous (up to 85%)
Oil products	Fluorosilicate (up to 5%)
Crude oil	Sulfuric (up to 70%)
Asphalt, bitumen, tar	Sour 70–93% (up to 100 °C)
Creosote oil	Sulfuric 93–96% (room)
Paraffin	Nitric (up to 20%)
Gasoline, kerosene, diesel fuel	Nitric higher 20% (room)
Gas oil, petroleum ether	Chrome up to 10% (95 °C)
Mineral and vegetable oils	Oxidants
Solvents, Organic Compounds	Bromine, bromine water (room
Alcohols, glycols	Iodine (room)
Ethers, aldehydes, ketones	Bleaching (room)
Amines, amino acids	Hydrogen peroxide (up to 30%)
Acids	Chlorates, hypochlorites (room)
Hydrocarbons	

N o t e s: 1. Restrictions for the use of media for packings are listed just for the graphite component. At high temperatures and in corrosive environments as packings binder loss, the seal assembly must be periodically tightened. 2. Not recommended for use in an environment of strong oxidizers such as concentrated nitric acid, oleum, chrome, and perchloric acids as well as molten salt oxidants.

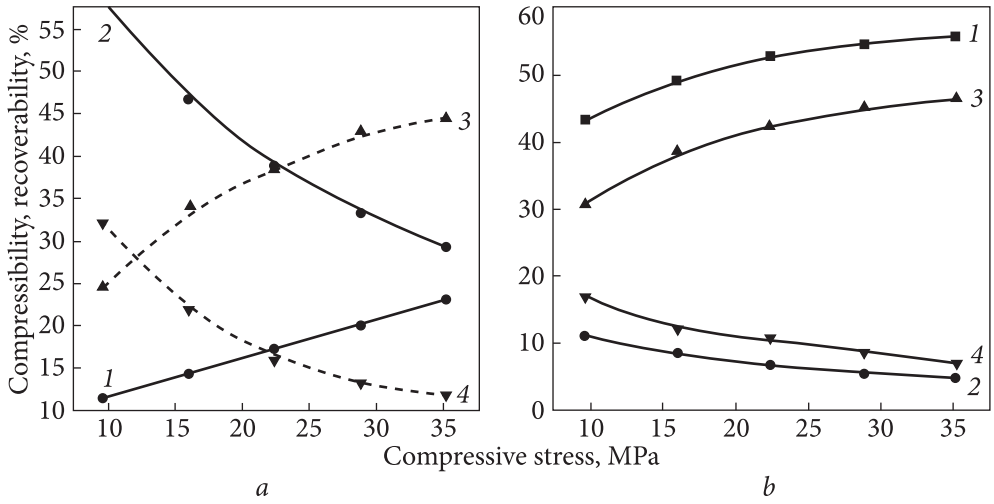

Fig. 2.26. Dependence of compressibility (*1*, *3*) and recoverability (*2*, *4*) on the compressive stress (*a*): *1*, *2* — EG paperboard by "TMSpetsmash" (Ukraine), junction without glue, thickness of 3.4 mm, density of 0.87 g/cm^3; *3*, *4* — EG paperboard by "Unikhimtek" (Russia), glue junction, thickness of 3.05 mm, density of 1.0 g/cm^3. Dependence of compressibility (*1*, *3*) and recoverability (*2*, *4*) on the compressive stress (*b*): *1*, *2* — EG foil, thickness of 0.45 mm, density of 1.5 g/cm^3; *3*, *4* — EG foil, thickness of 0.6 mm, density of 1.2 g/cm^3, the production of "TMSpetsmash" (Ukraine)

Table 2.20. **The characteristics of the EG foil from different manufacturers**

Characteristics	«Graphlex», Russia				"Grafoil", USA		«Thermographenit», Ukraine	
Density, g/cm^3	0.6—1.1				1.1		0.6—1.2	
Application field	General		Atomic		General ind.	Atom.	General	Atomic
Carbon content,%	99.5	99.6	99.8	99.9	95.0	99.5	99.0; 99.5	99.85
Sulfur content,%	<0.12	<0.01	<0.10	<0.01	0.1	0.07	≤0.15; ≤0.10	≤0.05
Chlorine ions, ppm	<50	<30	<30	<20	100	700	<40	<20
Compressibility P = 35 MPa,%	35—40				40		45—20 ρ = 1.2—1.5 g/cm^3	
Thermal conductivity of sheet, W/m · K:								
along	130—200				140		130—200	
across	3—5				5		—	
Tensile strength, MPa	3.5—7.0				4.4	6.9	5.0; ρ = 1.0 g/cm^3	6.0; ρ = 1.0 g/cm^3

2.3. The technological line for the production of rolled materials

The most important property that the natural graphite acquires upon becoming an EG is the ability to form a solid material without any binder, by conventional pressing or rolling. But as a forming material, the EG powder, due to the complex "worm-like" structure of particles, which have a honeycomb surface with a specific surface area of 35—75 m^2/g, is markedly different from other materials of very low bulk density. The fresh product from it can be manufactured with a density of 1.5—2.0 g/dm^3, high volatility, and the possibility of self-sealing [34].

It is easy to verify that to obtain a rolled material, such as a sheet of 1 mm thickness and a density of 1 g/cm^3, it is necessary to seal an EG layer having a density of 2.0 $g/dm^3$and a height of 50 cm. That is, during rolling it is necessary to reduce the layer thickness by about 500 times. This problem is rather complicated in the technical performance, the more that you must first create an even thickness of the layer of 50—100 cm, fairly uniform in density. It appears that this problem can be simplified by reducing the layer thickness via using EG with greater bulk density. However, as shown by our studies (Fig. 2.27 [105, 106]), the bulk density increase, regardless of the method of EG obtaining, significantly reduces the tensile strength of the rolled material, which is undesirable.

Therefore, from the first known patent [107] until the latest one [108], the problem of EG rolling into a solid material of a sheet form was solved with some variations as follows. The apparatus consists of the EG storage hopper and conveyor belt comprising two belt shafts and made of suitable material (rubber, metal, etc.). The conveyor is also equipped with walls. The vibrating device is placed under the storage hopper, which provides the movement of the exfoliated graphite on the conveyor belt (in this case, the bulk density of EG increases). The rolls with adjustable gaps between them are arranged in pairs after the conveyor to compress the EG layer. The gap between the rolls provides the desired thickness and density of the compressed particles of EG. Then we have two or more pairs of pressing rolls, which enable a gradually compressed layer to acquire a graphite tape shape of uniform density and thickness. Between the pairs of pressing rolls, the apparatus for high-temperature treatment (annealing) of the graphite tape, for example, at 1000 °C is placed. It is proposed to use many pairs of pressing rolls to obtain a smooth tape. Often in the rolling line design, there is an additional tool for modifying the graphite tape with suitable materials, such as paper having an adhesive rear surface to be pasted on the graphite foil. Then the unit for winding the tape obtained on the reel is set.

Horizontal placement of the conveyor belts does not allow obtaining an EG sheet of substantial thickness and reasonable size. This is due to the phenomenon of the so-called "critical capture angle for powder rolling", which is the

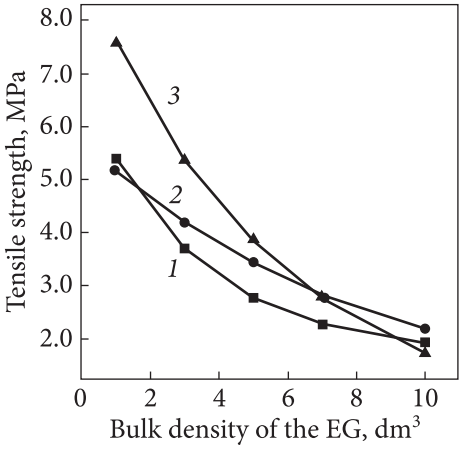

Fig. 2.27. Dependence of the tensile strength on the bulk density of rolled EG samples obtained by different methods: *1* — raw GT-1-graphite, 96% of carbon, chemical oxidation; *2* — raw GSM-2 graphite, 99.5% of carbon, chemical oxidation; *3* — raw GSM-2 graphite, 99.5% of carbon, electrochemical oxidation

maximum angle between the horizontal axis and the plane of the conveyor or tangential to the cylindrical surface of the roll at the point where the powder is still "captured" and compacted. It depends on the properties of the powder such as bulk density, actual density, particle shape, coefficient of friction, etc. If the corresponding angle in the mechanism is higher than this critical value, then there is a periodic ejection of powder and the material obtained has a density around the critical value corresponding to the critical capture angle. That is, an increase in the angle of inclination of the conveyor causes uneven capture of the EG powder, which disrupts the layer uniformity and worsens the quality of the product. A device for manufacturing products of great thickness is characterized by considerable dimensions and consumption. It is for this reason that the world's largest manufacturers of EG products, e.g. enterprise in China, in its nomenclature have rolled materials without an adhesive junction, with a thickness of only 1 mm, preferably 0.6 mm. They get thicker materials by gluing. In this case, the material properties are largely determined by the quality of glued junction.

Obviously, there are no analogs of our developments of EG rolled, and the problem of a heat-treating device have not been even considered yet. Its structure and role in the entire process of the EG formation are not considered either. All one need is rapid heating. Hence, the most popular way of the EG production is via a thermal shock in the flame of a gas burner [5]. The gas-graphite mixture is placed in a device with burning gas jets, where the process of exfoliation of the oxidized graphite takes place in a high-temperature gas flame; EG is removed from the top of the reactor [109]. That is, the burner is arranged vertically, like in a conventional gas fluidized bed or upstream. EG surface adsorbs the GIC degradation products which perform as plasticizers that provide sliding of EG layers and their crosslinking during pressing or rolling. Sulfur oxides, hydrogen sulfide, and water are the raw materials to obtain EG from the residual graphite bisulfate compounds [18]. However, it should be appreciated that the seal of EG used in the equipment of nuclear power plants should have a purity level of 99.85% wt. of carbon. Given that chemically purified natural graphite source has 99.9% wt. of carbon, impurities, i.e., sulfur compounds, should not

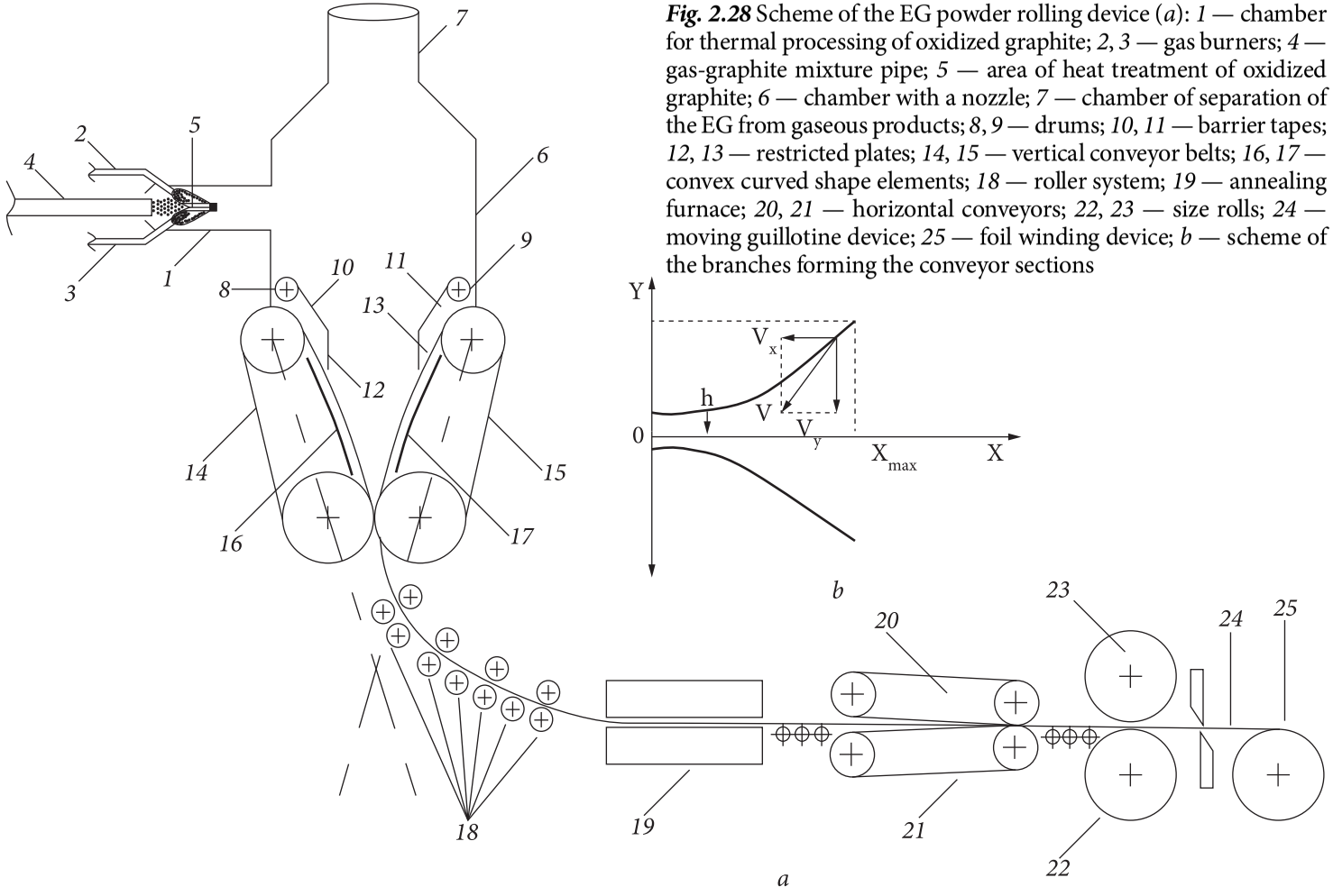

Fig. 2.28 Scheme of the EG powder rolling device (*a*): *1* — chamber for thermal processing of oxidized graphite; *2*, *3* — gas burners; *4* — gas-graphite mixture pipe; *5* — area of heat treatment of oxidized graphite; *6* — chamber with a nozzle; *7* — chamber of separation of the EG from gaseous products; *8*, *9* — drums; *10*, *11* — barrier tapes; *12*, *13* — restricted plates; *14*, *15* — vertical conveyor belts; *16*, *17* — convex curved shape elements; *18* — roller system; *19* — annealing furnace; *20*, *21* — horizontal conveyors; *22*, *23* — size rolls; *24* — moving guillotine device; *25* — foil winding device; *b* — scheme of the branches forming the conveyor sections

exceed 0.05% wt. Thus, there is a need to minimize the sorption process of GIC products.

Considering the comments above mentioned, the authors have developed a technological scheme of a continuous rolling line for the highest possible purity and thickness of EG (Fig. 2.28) to obtain solid materials from EG by rolling [110], which was implemented in the company TMSpetsmash Ltd in Kyiv, Ukraine. The use of a gas burner in a horizontal position was suggested. As a result of thermal shock, the oxidized graphite swells and turns into EG. In this case, it is removed from the volatile residues, e.g., SO_3, steam, etc. As a result, there is a layering of the flow: the volatile components rise up with the OG and EG powder falls down. Thus, separation of the reaction products is provided even at the initial stage of EG production.

Next, a mixture of EG and gaseous products enters chamber 6 (Fig. 2.28, *a*), dimensions of which are much greater than the diameter of tool 1. At this speed of EG particles decreases sharply, hot product gases move upward through pipe 7 and enter the recycling system (not shown). EG particles settle freely on the bottom of chamber 6. With reels 8 and 9 and wound restrictive tapes 10 and 11, the desired width between the limiting plates 12 and 13 is exhibited, which relates to conveyor belts 14 and 15. With these elements, we can regulate and maintain consistency of desired thickness for a layer of the EG, subjected to rolling. Thus, the fresh EG manufactured without any influence, or keeping the surface state of the structure, enters the rolling mill, and then transporters 14 and 15. Plates 12 and limited vertical pillar 13 of exfoliated graphite move downwards gradually compressing to the desired thickness by the conveyor belts 14 and 15, which have the desired curvature of the working surface due to the convex strip elements 16 and 17 of a curved shape [110]. By using roller conveyor 18, the compacted material (prepreg) is sent to the annealing furnace 19, where heat treatment and removal of residual volatiles take place. After annealing, the prepreg of 0.2—0.3 g/cm^3 density and of 1 to 25 mm thickness is compacted further by conveyor belts 20 and 21 to a density of 0.8—0.9 g/cm^3 and finally calibrated between rolls 22 and 23. Depending on customer requirements and the desired product thickness, the rolled material obtained by a movable guillotine device 24 may be cut into sheets of desired size (material thickness of more than 1 mm) or folded into a roll with drum 25.

The current production line at the company TMSpetsmash is about 18 m in length, and the products manufactured (foil in rolls, sheets) have a width of 1000 mm (finishing dimension) and virtually infinite length. Thus, on an industrial scale, you can make the following products with thickness: foil 0.3—1.0 mm; sheets 1.0—2.0 mm.

The forming surface of the conveyor branches 14 and15 are curved so that their cross-section forms a curve that corresponds to the equation (Fig. 2.28, *b*) [110, 111]:

$$Y = a \cdot X^b - h, \tag{2.15}$$

where X and Y are the coordinates of surface points in the rectangular coordinate systems; the OX axis bisects the angle between the tangents to the symmetrical shape of the surface of pipelines, directed opposite to their movement and measured from the center of the rolls; the axis Y is collinear with respect to the diameters of rolls, measured from the middle of the gap between the rolls (Fig. 2.28, *b*); h is the half gap between the rolls; a is a numerical coefficient that depends on the type of powder and is not significantly different from 1.

Limit values of the exponent degree b and its dependence on the transporter parameters are selected from the values of the critical capture angle. The capture angle of the conveyor surface with a curved profile is taken equal to 25°. On this basis (tg 25° ≈ 0.46) and in the approximation of $h << Y_{max}$, we obtain a criterion for the conveyor options:

$$Y_{max}/X_{max}\, b < 0.46, \tag{2.16}$$

where Y_{max} is the maximum Y coordinate, which corresponds to half the maximum distance between the forming surfaces, that is, half the maximum thickness of the layer of powder compact; X_{max} is the maximum X coordinate, which corresponds to the maximum height of the EG column determined by the position of restrictor plates 12, 13 (Fig. 2.28) at the maximum distance between the forming surfaces; $b > 1$ for curvilinear relation. Thus, $1 < b < 0.46\, X_{max}/Y_{max}$.

Restrictions on rolling speed and rolling thickness are also due to the presence of gases adsorbed by the EG surface and the need to remove them during the rolling process. It is experimentally established [55] that the EG compaction process has several stages. The first step is stacking EG particles and their deformation. That is, at this stage, the material is not continuous, has an open porosity, the sorbed gases are easily removed, and therefore it is possible to achieve high rates of compression. We can assume that this state is maintained to a density of 0.10—0.15 g/cm^3. The circuit for horizontal rolling described in [108] and the restriction of 500 mm/min rate for the material with a density of 0.5 g/cm^3 and thickness of 0.5 mm were used. Thus, the rate of material contraction during the entire rolling process remains unchanged. At an angle of inclination of the upper conveyor of 10°, the speed is about 87 mm/min. When the material density is 0.07—0.10 g/cm^3, the material compression rate may be much higher and gradually decreases to 87 mm/min. At that, the material density is approaching 0.5 g/cm^3. This provides the possibility of increasing the rolling speed and productivity of the process.

Suppose that during the conveyor operation, the belt is moving with a speed V. The surface of the forming conveyor branch is described by the relation $Y = a \cdot X^b - h$. Then the module of the compression rate (movement speed) be-

tween the forming surfaces of the Y-axis direction by one branch as the derivative of the dependence on time corresponds to the expression:

$$V_y = V/(1+1/(ab)^2 X^{2(b-1)})^{0,5}, \quad (2.17)$$

where V is the belt speed, $b > 1$, and taking into account the action of the two conveyors, the compression rate is doubled:

$$V_y^{ob.} = 2V/(1+1/(ab)^2 X^{2(b-1)})^{0,5}. \quad (2.18)$$

It follows from this relation that if $X \to 0$, regardless of the conveyor belt speed, $V_y \to 0$. That is, this design provides a seal of the powder during the operation with high speeds at the beginning of the compression process, at low densities rolled, reducing the compression rate and increasing density of the material in the final stage.

Tables 2.22 and 2.23 show the data for devices and comparative performance characteristics of the product that was obtained by the scheme in Fig. 2.28 and with a horizontal conveyor as in [108].

Table 2.22 shows the sulfur content in the product of EG, which confirms its reduction in EG samples obtained by using the circuit device of Fig. 2.28. Thus, the use of vertically arranged conveyors with a predetermined curvature surface increases the production capacity of the line, compared with a horizontal conveyor circuit arrangement with decreasing the size and design of metal. Due to the curvature of the surface conveyors, the possibility of reducing the rate of

Table 2.22. **Comparative characteristics of rolled materials from EG**

Thickness of material rolled, mm	Tensile strength (σ) of the material rolled (MPa) obtained		Productivity, kg/h	
	Horizontal scheme	Scheme in Fig. 2.28	Horizontal scheme	Scheme in Fig. 2.28
0.6	3.8	5.8	9	18
1.0	3.4	4.9	12	22
1.5	—	4.4	—	18
2.0	—	4.0	—	18

Table 2.23. **The sulfur content in the EG product**

Material rolled by	Mass fraction of total sulfur, %		
	Before annealing	After annealing at 600 °C	After annealing at 800 °C
Horizontal scheme	0.22	0.16	0.12
Scheme in Fig. 2.28	0.15	0.09	0.05

loading at the rental with an increase in its density has been realized, that is, an increase in time for the diffusion of the sorbed gas near the output EG surface, which makes it possible to obtain the rolled sheets over 2 mm of thickness. The horizontal arrangement of the oven gas for EG production provides separation of the products of decomposition of the oxidized graphite and EG still at the initial stage of its production and results in a decrease in their sorption, which gives a high purity of the rolled material from the EG. The described device for rolling the powder of exfoliated graphite is relatively simple in structure, reliable in operation, and can be produced on standard equipment.

2.4. Physicochemical characteristics of materials from expanded graphite obtained in different ways

The properties of materials and products made of compacted EG are determined by its characteristics, in particular, the chemical composition containing certain mineral inclusions (i.e. ash content) along with sulfur and its compounds introduced by oxidative intercalation with sulfuric acid and subsequent heat treatment. Typically, the strength characteristics of rolled materials from EG are also an important criterion for use in various industries.

2.4.1. Determination of total sulfur and sulfates in carbon materials

Methods of chemical analysis to determine the content of total sulfur and sulfates are described in [18, 112], the authors of which investigated the effect of heat treatment on the behavior of sulfur in EG. Residual sulfur in graphite was shown to exist as sorbed sulfuric acid and sulfur chemically bound to graphite. The existence of two types of sulfur in EG, which are characterized by different binding energies, confirmed the results of thermoprogrammed desorption with mass spectroscopic analysis of products in the gas phase. As seen in Fig. 2.29 [18], the thermodesorption spectrum of particles with the atomic mass 64, identified as sulfur dioxide, has two maxima at 300 and 555 °C.

The activations calculated by the method of reduced energy contents are equal to (117 ± 8) kJ/mol (maximum 1 in Fig. 2.29) and (273 ± 12) kJ/mol (maximum 2), respectively.

Fig. 2.30 [18] shows the dependences of pH of the aqueous extract of EG (curve *1*) and the sulfur content of chemically bound (2) and sulfate (3) on the treatment temperature. As seen, chemically bound sulfur is removed only at temperatures (550 ± 10) °C and above, i.e., at the temperature of the beginning of graphite oxidation, and almost completed (Fig. 2.31, curve II [18]). The bulk of sulfate sulfur is removed from the material at 400 °C and it can be stated with

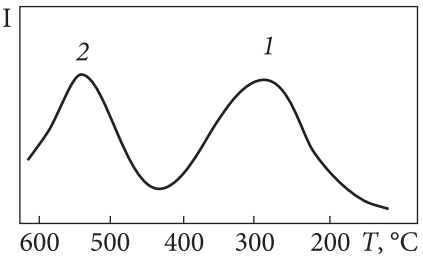

Fig. 2.29. Thermodesorption spectrum of EG [18]

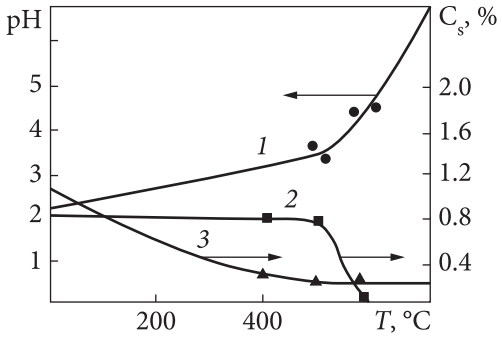

Fig. 2.30. Dependence of pH of aqueous extract of EG (*1*) and sulfur content of chemically bound (*2*) and sulfate (*3*) [18]

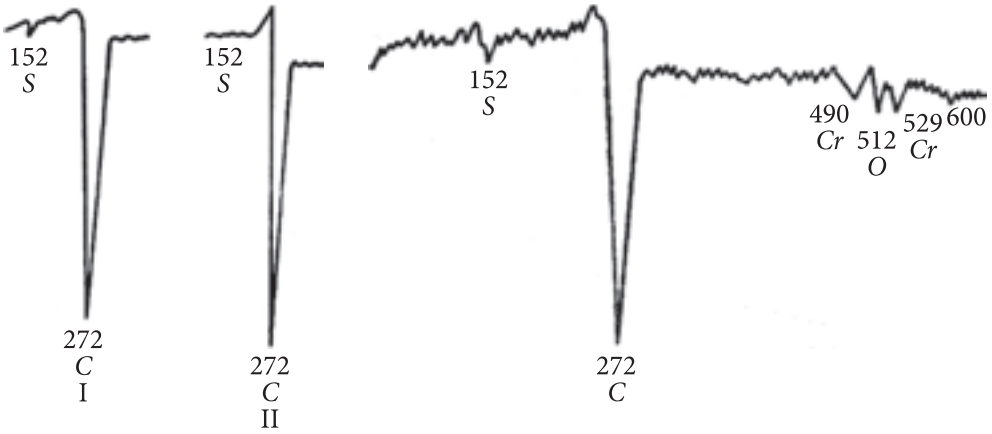

Fig. 2.31. Auger spectra of EG: I — before heat treatment, II — after heat treatment [18]

Fig. 2.32. Auger spectra of EG after heat treatment [18]

certainty that it is physically sorbed sulfuric acid.

The residual proportion of sulfate sulfur is obviously related to the metal sulfates that are mineral impurities in the form of oxides in the original natural graphite and reduced during oxidative intercalation with oxidants $K_2Cr_2O_7$, $KMnO_4$, CrO_3, et al. (for example, chromium, Fig. 2.32) and do not decompose at given processing temperatures.

Usually, natural graphite contains impurities of slightly different concentrations for different deposits (Tables 2.1, 2.2).

Aluminosilicates react only with hydrofluoric acid, while oxides of iron, calcium, and magnesium in reactions with sulfuric acid form sulfates of these metals. If the initial content of metal oxides is 1000 ppm, then due to the increase in the molecular weight of sulfates of iron, calcium, and magnesium, their content is approximately 300—600 ppm. In order to reduce the content

of sulfates (i.e. sulfur), it is necessary to take a purer source of natural graphite, rather 99.99% than 99.9% wt. of carbon

You can eliminate sulfur almost completely if you take another intercalant, for example, nitric acid instead of sulfuric acid. There will be no sulfur, but metal nitrates will be formed, which can cause corrosion by the same mechanism as sulfates. In this case, it is necessary to control the nitrogen content and also to reduce the content of metal nitrates by choosing a cleaner source of natural graphite.

2.4.2. Method for determination of sulfur in graphite materials

To determine the proportion of sulfur in graphite or graphite materials, an Eschke mixture (2 parts of MgO and 1part Na_2CO_3). 1 g of the graphite material is mixed with 3 g of the Eschke mixture, then 2 g of the mixture is mixed on top and burned together at 850 °C, upon gradually raising the temperature from room temperature [112].

$$S^0 \rightarrow SO_4^{-2}. \quad (2.19)$$

As a result, magnesium and sodium sulfates are formed, which are washed away by hot water. To the resulting solution, a 10% barium chloride solution is added to the precipitate barium sulfate:

$$BaCl_2 + SO_4^{-2} \rightarrow BaSO_4 + 2Cl^-. \quad (2.20)$$

After filtering the precipitate, the filter is burned in a crucible. The calculation of the sulfur content by weight is carried out according to the formula:

$$Ms = (m_1 - m_2) \times 0.1374 \times 100/m, \quad (2.21)$$

where m_1 is the mass of barium sulfate obtained from the analysis of graphite (weight of the burned filter); m_2 is the mass of barium sulfate obtained from the control experiment (weight of the filter during the analysis without graphite); 0.1374 is the conversion factor for barium sulfate to sulfur; m is the weight of the sample (graphite).

The method for the determination of sulfate sulfur in a sample of graphite material. To determine the sulfur content in graphite or graphite materials, a weighted sample of the material is boiled in dilute hydrochloric acid [112].

The sulfates are converted into a solution, then they are precipitated with a solution of barium chloride according to the above formula, and the precipitate obtained is filtered off. The filter is burned to constant weight at 850 °C. The sulfate content in the graphite material is calculated by the formula (2.21).

The obtained data are given in Table 2.24 [113].

Analysis of Table 2.24 data shows the following: laboratory gas horizontal furnaces and electric vertical open furnaces equally efficiently separate the volatile products and the formed EG. The values of total sulfur have insignificant deviations in one direction or another (samples 1—3, 7—8), both for anode-oxidized graphite and chemically oxidized. In general, the content of total sulfur in the EG obtained from anode-oxidized graphite in dilute sulfuric acid is 0.10—0.17% wt., which is lower compared to the EG obtained from chemically oxidized graphite 0.25—0.28% wt. without additional heat treatment (samples 1—6, 7—8).

Short-term heat treatment within (600—800) °C significantly reduces the content of both total and sulfate sulfur (samples 7—8, 12, 10). The effect of ash content on the total sulfur content cannot be detected from the data obtained.

Summarizing the above, we can draw the following conclusions.

1.A basic scheme of anodic oxidation of graphite has been developed. It solves the problems of filtering the formed gases, ensuring effective electrical contact of dispersed graphite particles, optimizing the amount of intercalant (H_2SO_4), and compensating for the increase in the volume of graphite particles in the formation of inclusion compounds.

2. A reactor of continuous action for electrochemical oxidation of production capacity of 10—50 kg/h has been created. Operating modes that provide stable quality of oxidized graphite needed to obtain functional products have been defined.

It has been shown that the mechanism of obtaining EG under heating conditions in the mode of thermo-shock of hydrolyzed intercalated graphite compounds [GIC-H_2SO_4] to high temperatures (1000 °C) is structured converting by type of exfoliation. Residual fragments [GIC-H_2SO_4] at all stages of thermolysis are heterogeneous structures comprising graphite crystals and region due *to* the distribution of intercalant residues of different disperse. The structure of the initial [GIC-H_2SO_4], conditions of hydrolysis, and the processing temperature determine the qualitative composition and the ratio of phase formations, as well as the nature of the EG surface, typical for dispersed oxidized carbon materials.

3. From the analysis of Raman spectra, electron-positron annihilation data, nitrogen adsorption isotherms, transmission electron microscopy images, and certain elastic-plastic characteristics for compression deformation of dense materials with EG**,** defects were found that prove that natural graphite in an expanded state is a nanosized cluster-assembled system characterized by long cylindrical, conical, and slit-like defects with average cross-section diameters (0.7—20) nm, caused by folding and bending of several layers of graphene.

5. The strength of extruded samples from EG increases with increasing particle size and amount of oxidant relative to the mass of graphite within certain limits. EG under pressure is formed into a solid material with a nonlinear change in density through three stages: I, a linear change in density (limit condition for density up to 0.5 g/cm^3); II, a nonlinear density dependence (with

Table 2.24. **Sulfur content in EG samples**

Sample	Type of graphite sample	Intercalation parameters	Heat treatment conditions	Sulfur content, % wt.	
				total	sulfate
1	China, 94% C, 50 mesh	EChO[1], ρ_a = 1.47 g/cm^3, V_a/m_g = 2.25 cm^3/g, Q = 110 A · h/kg, W = 19%	Mine electric furnace, 900 °C	0.1 ± 0.04	
2	China, 94% C, 50 mesh	EChO[1], ρ_a = 1.47 g/cm^3, V_a/m_g = 2.25 cm^3/g, Q = 120 A · h/kg, W = 12.5%	Mine electric furnace, 900 °C	0.16 ± 0.04	
3	China, 94% C, 50 mesh	EChO[1], ρ_a = 1.47 g/cm^3, V_a/m_g = 2.25 cm^3/g, Q = 120 A · h/kg, W = 12.5%	Gas, horizontal furnace	0.2	
4	Ukraine, GSM-2, 99.8% C, 50 mesh	EChO[1], ρ_a = 1.42 g/cm^3, V_a/m_g = 3 cm^3/g, Q = 80 A · h/kg, W = 20%	Mine electric furnace, 900 °C	0.19	
5	China, Xiang Yang, 99% C, 50 mesh	EChO[2], (2 cartridges of 600 g) ρ_a = = 1.435 g/cm^3, Q = 150 A · h/kg, W= 15%	Gas, horizontal furnace	0.17	
6	China, Xiang Yang, 99% C, 50 mesh	EChO[2], (1 cartridges of 600 g), ρ_a = = 1.434 g/cm^3, Q = 120 A · h/kg, W = 16.5%	Gas, horizontal furnace	0.163	
7	China, Xiang Yang, 99% C, 50 mesh	Graphite, expandable	Mine electric furnace, 900 °C Gas, horizontal furnace, rolling. Gas, horizontal furnace, annealing 600 °C Gas, horizontal furnace, rolling, annealing 600 °C	0.263 0.285 0.16 0.132	
8	China, Xiang Yang, 99% C, 50 mesh	Graphite, expandable	Gas, horizontal furnace, rolling Gas, horizontal furnace, rolling, annealing 850 °C: 1 min 2 min 5 min	0.25 0.14 0.13 0.12	
9	China, Xiang Yang, 99% C, 50 mesh	Graphite, expandable	Gas, horizontal furnace, rolling up to 0.2 g/cm^3, annealing in a through furnace, T = 800 °C	0.088	
10	China, Xiang Yang, 99% C, 50 mesh	Graphite, expandable	*Low-quality propane-butane:* Gas, horizontal furnace, rolling		0.216

			Gas, horizontal furnace, rolling, annealing 800 °C — 1 min. Gas, horizontal furnace, annealing T = = 800 °C, annealing *Quality propane-butane:* Gas, horizontal furnace, rolling		0.037 0.038 0.064
11	China, Xiang Yang, 99% C, 50 mesh	EChO[3], ρ_a = 1.454 g/cm^3, V_a/m_g = 0.75 cm^3/g, Q = 24 A · h/kg, W = 12.5%	Mine electric furnace, 900 °C	0.08	
12	China, Xiang Yang, 99% C, 50 mesh	EChO in a horizontal reactor for 5 kg[4], ρ_a = 1.425 g/cm^3, V_a/m_g = 0.85 cm^3/g, Q = 32 A ·h/kg, W = 12.5%	Mine electric furnace, 900 °C Mine electric furnace, 900 °C, pressing, annealing, T= 850 °C, 2 min Gas, horizontal furnace, rolling up to 0.2 g/cm^3, annealing in a through furnace, T= 800 °C	0.089 0.059 **0.045**	
13	China, Xiang Yang, 99% C, 50 mesh	EChO[4], ρ_a = 1.438 g/cm^3, V_a/m_g = 0.9 cm^{3}g, Q = 36 A · h/kg, W = 12.5%	Mine electric furnace, 900 °C	0.09	
14	China, Xiang Yang, 99% C, 50 mesh	EChO[3], purification from ash with ammonium difluoride, ρ_a = 1.468 g/cm^3, V_a/m_g = 0.75 cm^3/g, Q = 32 A · h/kg, W = 14%	Mine electric furnace, 900 °C Drying on glass Drying on stainless steel	0.092 0.092	
15	China, Xiang Yang, 99,9% C, 50 mesh	EChO[4], ρ_a = 1.453 g/cm^3, V_a/m_g = 0.75 cm^3/g, Q = 35 A · h/kg, W = 12.5%	Mine electric furnace, 900 °C Mine electric furnace, 900 °C, annealing, T= 850 °C	0.1 0.074	
16	China, Xiang Yang, 99% C, 50 mesh	EChO[3], purification from ash with ammonium difluoride, ρ_a = 1.468 g/cm^3, V_a/m_g = 0.75 cm^3/g, Q = 40 A · h/kg	Mine electric furnace, 900 °C	0.165	
17	China, Xiang Yang, 99.9% C, 50 mesh	EChO[4], ρ_a = 1.445 g/cm^3, V_a/m_g = = 0.85 cm^3/g, Q = 38 A·h/kg, W = 12.5%	Gas, horizontal furnace	0.26	
18	China, Xiang Yang, 99% C, 50 mesh	EChO[4], ρ_a = (1.44—1.47) g/cm^3, V_a/m_g = (0.75—1.0) cm^3/g, Q = (30—40) A · h/kg, W = 12.5%, averaged	Gas industrial horizontal furnace		

[1] Anodic oxidation in a vertical cylindrical cell; [2] Anodic oxidation in a vertical cassette cell; [3] Anodic oxidation in a horizontal cell; [4] Anodic oxidation in a horizontal cassette; P_a, acid density; V_a/m_g, ratio of the volume of acid to the mass of graphite; Q, amount of electricity; W, weight loss or volatile impurities.

almost constant texture up to 1.3 g/cm^3); III, plastic deformation of the samples with the formation of a layered structure, which is dominated by graphene planes, oriented perpendicular to the action of external load. This allows solving the problem of compaction of thick up to 100 cm and wide with an area of ~100×100 cm^2 layers of EG with bulk density from 1.5 g/dm^3 to 2.5 g/dm^3 using vertical conveyors with a given curvature of the surface.

At the same time, with the increasing density of EG, the rate of loading decreases, and the diffusion exit of the gases sorbed by the EG surface simplifies. It is possible to obtain rolled sheets with a thickness of ≥ 2 mm and to increase the production capacity of the line; herein the dimensions and metal consumption of the design decrease. To separate volatile emissions and EG, even at the initial stage of production, a horizontal gas furnace was created for its production, which guarantees the high purity of manufactured rolled materials obtained on the basis of EG.

REFERENCES

1. Yu.I. Sementsov, S.L. Revo, K.O. Ivanenko and S. Hamamda, *Expanded graphite and its composites*, edited by M.T. Kartel (Akademperiodika, Kyiv, 2019).
2. Yu.I.Sementsov and M.L. Pyatkovskii, in: *Neorganicheskoe materialovedenie. Materialy i tekhnologii*, edited by G.G. Gnesin and V.V. Skorokhod (Naukova dumka, Kyiv, 2008), vol. 2, book. 2, pp. 410—425 [in Russian].
3. N.E. Sorokina, A.V. Redchitz, S.G. Ionov and V.V. Avdeev, Journal of Physics and Chemistry of Solids. 67 (5–6), 1202 (2006).
4. V.V. Yanchenko and Yu.I. Sementsov, Armaturostroenie. 4(36), 41 (2005).
5. A. Celzard, J.F. Mareche and G. Furdin, Progress in Materials Science. 50 (1), 93 (2005).
6. Yu-Ying Huang, Da Han, Yan-Bing He, Qinbai Yun, Ming Liu, Xianying Qin, Baohua Li and Feiyu Kang, Electrochimica Acta. 184, 364 (2015).
7. R.Ya. Shvets, I.I. Grygorchak, A.S. Kurepa, N.T. Pokladok, Yu.I. Sementsov, G.I. Dovbeshko, Ye. Sheregii and B. Seredyuk, Acta Physica Polonica A. 128 (2), 208 (2015).
8. A.S. Tikhomirov, N.E. Sorokina, O.N. Shornikova, V.A. Morozov, G. van Tendeloo and V.V. Avdeev, Carbon. 49 (1), 147 (2011).
9. I.M. Afanasov, G. Van Tendeloo and A.T. Matveev, New Carbon Materials. 25 (4), 255 (2010).
10. P. Yu, S. E. Lowe, Ge. P. Simon and Y. L. Zhong, Current Opinion in Colloid & Interface Science. 20 (5–6), 329 (2015).
11. M. Belekoukia, M.S. Ramasamy, S. Yang, X. Feng, G. Paterakis, V. Dracopoulos, C. Galiotis and P. Lianos, Electrochimica Acta. 194, 110 (2016).
12. Y. Sementsov, S. Makhno, M. Kartel, W. Bo, G. Dovbeshko, V. Styopkin and S. Nedilko, IJISET. 4 (8), 71 (2017).
13. M. Kartel, Y. Sementsov, G. Dovbeshko, L. Karachevtseva, S. Makhno, T. Aleksyeyeva, Y. Grebel'na, V. Styopkin, W. Bo and Y. Stubrov, Advanced materials letters. 8 (3), 212 (2017).
14. S.G. Nedilko, S. Revo, V. Chornii, V. Scherbatskyi, K. Ivanenko, M. Nedielko, Y. Sementsov, M. Skoryk, A. Nikolenko and V. Strelchuk, Nanoscale Res Lett. 12, 28. (2017). https://doi:10.1186/s11671-016-1770-5.

15. I.M. Inuwa, A. Hassan, De-Yi Wang, S.A. Samsudin, M.K.M. Haafiz, S.L. Wong and M. Jawaide, Polymer Degradation and Stability. 110, 137 (2014).
16. R. Sengupta, M. Bhattacharya, S. Bandyopadhyay and A.K. Bhowmick, Progress in Polymer Science. 36 (5), 638 (2011).
17. S.M. Makhno, O.M. Lisova, G.M. Hunia, Yu.I. Sementsov, Yu.V. Hrebelna and M.T. Kartel, Physics and chemistry of solid state. 17 (3), 421 (2016).
18. I.G. Chernysh, I.I. Karpov, G.P. Prikhod'ko, V.M. Shay, *Fiziko-khimicheskie svoystva grafita i ego soedineniy* (Nauk. dumka, Kyiv, 1990).
19. D.D.L. Chung, J. Matter. Sci. 22 (12), 4190 (1987).
20. Yu. I. Sementsov, M. L. Pyatkovskii and I. G. Chernysh, Powder Metallurgy and Metal Ceramics. 37 (9–10), 545 (1998).
21. I.D. Buraya, L.L. Vovchenko, L.L. Voznaya, Yu.I. Sementsov, I.G. Chernysh and O.P. Yatsyuk, Khimiya tverdogo topliva. (6), 106 (1990). [in Russian].
22. M.L. Piatkovskyi, Yu.I. Sementsov and I.G. Chernysh, Khim. prom. Ukrainy. (3), 42 (1996) [in Ukrainian].
23. Yu.I. Sementsov, L.G. Koval, V.P. Didukh and V.I. Lysov, Khim. prom. Ukrainy. (4), 34 (1994) [in Ukrainian].
24. Yu.I. Sementsov, L.G. Koval and A.A. Chuyko, Ekotehnologii i resursozberezhenie. (2), 27 (1997) [in Russian].
25. I.G. Chernysh, Him. prom. Ukraine. (4), 3 (1994). [in Ukrainian]
26. M.M. Zaiats, Him. prom. Ukraine. (4), 9 (1994) [in Ukrainian].
27. M.L. Piatkovskyi, Yu.I. Sementsov, G.P. Prykhodko and M.T. Kartel, Khim. prom. Ukrainy. (6), 17 (2011). [in Ukrainian]
28. N.E. Sorokina, I.V. Nikolskaya, S.G. Ionov and V.V. Avdeev, IzvestiyaAN RF, Ser. Khim. 54 (8), 162 (2005) [in Russian].
29. Sorokina, Doctor of Science dissertation, Moscow State University, 2007. [in Russian]
30. A. Metrot and H. Fuzellier, Carbon. 22 (2) 131 (1984).
31. F. Beck and H. Krohn, Synthetic metals. 14 (1-2), 137 (1986).
32. A.V. Yakovlev, A.I. Finaenov, S.L. Zabud'kov and E. V. Yakovleva, Russ J Appl Chem. 79 (11), 1741 (2006).
33. O.V. Melezhik, M.L. Piatkovskyi, V.V. Yanchenko, G.P. Prihodko and Yu.I. Sementsov, Khim. Prom. Ukrainy. (6), 7 (2005). [in Ukrainian].
34. Yu.I. Sementsov, G.P. Prykhodko, N.A. Havryliuk, A.Io. Senkevych, M.L. Piatkovskyi and V.V. Yanchenko, Khim. prom. Ukrainy. (2), 19 (2007). [in Ukrainian].
35. G.P. Homchenko and I.K. Tsitovich, Neorganicheskaya khimiya, (Vysshaya shkola, Moscow, 1978). [in Russian]
36. A.I. Finaenov, S.P. Apostolov, V.V. Krasnov and V.A. Nastasin, Russ J Appl Chem. 72 (5), 800 (1999).
37. S.P. Apostolov, V.V. Krasnov and A.I. Finaenov, Russ J Appl Chem. 70 (4), 577 (1997).
38. A.V. Yakovlev and A.I. Finaenov, Zhurnal prikladnoy khimii. 72 (1), 88 (1999) [in Russian].
39. N. Watanabe, T. Kondo and J. Ishiguro, USA Patent No. 4350576 (21 September, 1982).
40. A. Jnioni, A. Metrot and A. Storck, Electrochim. acta. 27 (9), 1247 (1982).
41. F. Kang, Y.-P. Zheng, H.-N. Wang, Y. Nishi and M. Inagaki, Carbon. 40 (9), 1575 (2002).
42. A.S. Fialkov and L.S. Maley, in: *Elektrougolnye i metallokeramicheskie izdeliya dlya elektrotekhniki* (Energoatomizdat, Moskva, 1985), pp. 65—72 [in Russian].
43. M.L. Pyatkovskiy, Yu.I. Sementsov, G.P. Prirhodko and V.V. Yanchenko, Khim. prom. Ukrainy. (3), 8 (2010) [in Russian].
44. V.V. Yanchenko, M.L. Piatkovskyi and Yu.I. Sementsov, Ukraine Patent № 77533 (15 December, 2006).

45. M.L. Pyatkovskiy, Yu.I. Sementsov, G.P. Prikhod'ko and N.T. Kartel, Khim. prom. Ukrainy. (1), 16 (2011) [in Russian].
46. N.E. Sorokina, A.I. Finaenov, V.V. Avdeev, V.S. Leshin, V.A. Sezemin, V.V. Krasnov, A.V. Krasnov, D.A. Kramskoy, S.G. Ionov and V.A. Nastasin, RF Patent № 2264983 (27 November, 2005).
47. A.I. Finaenov, V.V. Avdeev, V.V. Krasnov, S.P. Apostolov, L.A. Monyakina and I.V. Nikolskaya, RF Patent No. 2083723 (10 July, 1997) [in Russian].
48. V.V. Avdeev, A.I. Finaenov, S.P. Apostolov, V.V. Krasnov, A.V. Yakovlev, V.A. Sezemin, N.E. Sorokina, O.A.Tverezovskaya, I.V. Nikolskaya and L.A. Monyakina, RF Patent No. 2142409 (10 December, 1999) [in Russian].
49. A.I. Finaenov, V.V. Avdeev, V.V. Krasnov, A.V. Krasnov, A.I. Trifonov, D.A. Kramskoy, N.E. Sorokina, A.V. Sezemin, S.G. Ionov and I.V. Nikolskaya, RF Patent No. 2263070 (27 October, 2005) [in Russian].
50. W. Zhang, X. Zhang, H. Liu, G. Zhou, Z. Li, L.W. Ren; Y. Zhang; X.-B. Wang; S. Zhang, J. Wei, Y. Wang, Yu.I. Sementsov, M.L. Pyatkovskiy, N.T. Kartel, O.Yo. Kozik, and S.M. Gozhdzinskiy, CN Patent No ZL 2015 1 0372161.8 (26 April, 2017) [in Chinese].
51. . Zhang, X. Zhang, G. Zhou, H. Liu, Z. Li, L.W. Ren, Y. Zhang, X.-B. Wang, S. Zhang, J. Wei, Yu.I. Sementsov, M.L. Pyatkovskiy, N.T. Kartel, O.Yo. Kozik, and S.M. Gozhdzinskiy, CN Patent No ZL 2015 1 0372162.2 (03 May, 2017) [in Chinese].
52. A.R. Ubbelohde and F.A. *Lewis, Graphite and its crystal compounds* (Clarendon Press, Oxford, 1960).
53. K.E. Makhorin, A.P. Kozhan and V.V. Veselov, Khim. tehnologiya. (2), 3 (1985) [in Russian].
54. A. M. Glauert, editor, *Practical methods in electron microscopy*. (North-Holland Pub. Co., Amsterdam, 1972).
55. Yu.I. Sementsov, M.L Pyatkovsky, G.P. Prikhod'ko, V.M. Ogenko, I.G. Sidorenko and V.V. Yanchenko, in: *Chemistry, physics and technology of surfaces. Interdepartamental Digest of Scientific Papers*, edited by A.A. Chuiko (NAS of Ukraine. Institute of Surface Chemistry, Kyiv, 2002), iss. 8, pp. 190—214.
56. I.M. Yurkovskiy, T.Yu. Smirnova and L.S. Moley, Khimiya tverdogo topliva. (1), 127 (1986) [in Russian].
57. L.M. Utevskiy, *Difraktsionnaya elektronnaya mikroskopiya v metallovedenii (Metallurgiya*, Moscow, 1973). [in Russian].
58. N.F. Gadzyra, Yu.I. Sementsov and I.G. Chernysh, Doklady AN USSR. (12), 57 (1990) [in Russian].
59. V.Ya. Prokhorenko, B.I. Sokolovskiy and Ya.I. Dytchak, AS USSR № 935764 (15 June, 1982).
60. D.S. Tsiklis, *Tekhnika fiziko-khimicheskikh issledovaniy pri vyisokikh i sverkhvysokikh davleniyakh.* (Khimiya, Moscow, 1976). [in Russian].
61. V.M. Glazov, M. Vobet and V.M. Timoshenko, *Metody issledovaniya svoystv zhidkih metallov i poluprovodnikov* (Metallurgiya, Moskva, 1989). [in Russian].
62. C. Mazieres, G. Colin, J. Jegoudez and R. Setton, Carbon. 13 (4), 289 (1975).
63. I.M. Yurkovskiy. Khimiya tverdogo topliva. (5), 136 (1989) [in Russian].
64. G.I. Dovbeshko, V.S. Kopan, S.L. Revo, M.M. Nishchenko, G.P. Prikhod
65. ko, M.L Pyatkovsky, Yu.I. Sementsov and M. Westermayer, Metallofizika i noveyshie tekhnologii. 27 (3), 1001 (2005) [in Russian].
66. S.P. Likhtorovich, M.M. Nishchenko, G.P. Prikhod'ko, Yu.I. Sementsov, E.V.Polshin, V.Yu. Koda and I.Ye. Fomenko, in: *VIII International Hydrogen Materials Science and Chemistry of Carbon Nanomaterials Conference Proceedings* (Sudak, Crimea, 2003), pp. 608—609.

67. D.M. Schrader and Y.C. Jean, *Positronium and Positronium Chemistry*, (Elsevier, Amsterdam, 1988).
68. Y. C. Jean, Y. Rhee, Y. Lou, H. L. Yen, H. Cao, K. Cheong, and Y. Gu, Phys. Rev. B 54 (3), 1785 (1996).
69. O.V. Mikhailenko, M.Yu. Kornilov, T.V. Ljubchik and S.D. Isaev, in: *VIII International Hydrogen Materials Science and Chemistry of Carbon Nanomaterials Conference Proceedings* (Sudak, Crimea, 2003), pp. 490—491.
70. Yu.I. Sementsov, G.P. Prikhod'ko, S.L. Revo, A.V. Melezhyk, M.L. Pyatkovskiy and V.V. poYanchenko., in: *VIII International Hydrogen Materials Science and Chemistry of Carbon Nanomaterials Conference Proceedings* (Sudak, Crimea, 2003), pp. 488—489.
71. G.I. Dovbeshko, O.P. Repnystka and Y.V. Shtogun, Chem. Phys. Lett. 372, 432 (2003).
72. S.Ya. Brichka, G.P. Prikhod'ko, A.V. Brichka, M.I. Terets, V.A. Pokrovskiy, G.I. Dovbeshko and O.P. Repnystka, Zhurn. fiz. khim. 78 (1), 157 (2004) [in Russian].
73. Yu.I. Sementsov, G.I. Dovbeshko, S.Ya. Brychka, A.V. Brychka and G.P. Prikhod'ko, in: *Proc. 12th Intern. Symp. on Intercalation Compounds* (Poznan, Poland, 2003), p. 107.
74. J. Robertson, Mater. Sci. Eng. R. 37, 129 (2002).
75. M.S. Dresselhaus and G. Dresselhaus, Adv. Phys. 51, (1), 1 (2002).
76. B.N. Kuznetsov, N.V. Chesnokov, N.M. Mikova, T.G. Shendrik, S.B. Lyubchik and M.V. Savos'kin, in: *VIII International Hydrogen Materials Science and Chemistry of Carbon Nanomaterials Conference Proceedings* (Sudak, Crimea, 2003), pp. 512—515.
77. Yu.I. Tarasevich, S.V. Bondarenko, V.V. Brutko, A.I. Zhukova, G.N. Malysh and I.G. Polyakova, Russian Journal of Applied Chemistry. 76 (10), 1577 (2003).
78. S. Iijima, Nature. 354 (6348), 56 (1991).
79. S.V. Rotkin and Yu. Gogotsi, Matter. Res. Innovat. 5, 191 (2002).
80. I.V. Nikolskaya, N.E. Fadeeva, K.N. Semenenko, V.V. Avdeev and L.A. Monyakina, Zhurn. obshchei khimii. 59 (12), 2653 (1989) [in Russian].
81. V.V. Avdeev, L.A. Monyakina and I.V. Nikolskaya, Neorganicheskie materialy. 31 (3), 393 (1995) [in Russian].
82. Patent US Applications 0020182387, 0030044614.
83. Patents US 6416815, 6406612, 6149972.
84. I.G. Chernysh, N.F. Gadzyra, Yu.I. *Sementsov and O.P. Yatsyuk, Strukturno-fizicheskie prevrashcheniya kristallicheskikh form grafita*, Preprint. (ISC AN USSR, Kyiv, 1990). [in Russian].
85. A.S. Fialkov, *Uglegrafitovye materialy.* (Energiya, Moscow, 1979). [in Russian].
86. A.I. Antonov, V.A. Timonin, S.D. Fedoseev and L.F. Makevnina, Khimiya tverdogo topliva. (1), 114 (1984) [in Russian].
87. I.G. Chernysh, Yu.A. Nikitin and N.V. Levental', Powder Metallurgy and Metal Ceramics. 30 (6), 459 (1991).
88. L.S. Maley, A.S. Fialkov and M.M. Maley, A. S. USSR No. 1054332. (15 November, 1983). [in Russian].
89. Yu.A. Nikitin and M.L. Pyatkovskii, Powder Metallurgy and Metal Ceramics. 36 (1/2), 41 (1997).
90. M.E. Dritsa, editor, *Svoystva elementov* (Metallurgiya, Moscow, 1985). [in Russian].
91. Yu.A. Nikitin, I.G. Chernysh and M.L. Pyatkovskiy, Tsvet. metally. (3), 38 (1992) [in Russian].
92. I.G. Chernysh, I.D. Buraya, V.P. Goncharik et al., in: *Organizatsiya proizvodstva nerudnykh i nemetallorudnykh materialov v usloviyakh samofinansirovaniya i samookupaemosti* (Soyuznerud, Tolyatti, 1989), pp. 50—54 [in Russian].

93. T.M. Komarova, E.V. Puzyireva and S.V. Puchkov, Trudy Moskovskogo khimiko-tekhnologicheskogo in-ta. (141), 75 (1986) [in Russian].
94. I.D. Buraya, Yu.I. Sementsov, I.G. Chernysh, T.D. Akulova and N.G. Khudyakov, in: *Organizatsiya proizvodstva nerudnykh i nemetallorudnykh materialov v usloviyakh samofinansirovaniya i samookupaemosti* (Soyuznerud, Tolyatti, 1989) pp. 43—45 [in Russian].
95. Yu.A. Nikitin, M.L. Pyatkovskii and I.G. Chernysh, Powder Metallurgy and Metal Ceramics. 37 (5/6), 253 (1998).
96. V.V. Avdeev, N.E. Sorokina, I.Yu. Martynov, L.A. Monyakina and I.V. Nikol'skaya, Inorganic materials. 33 (6), 580 (1997).
97. A.K. Tsvetnikov, T.Yu. Nazarenko, L.A. Matveenko and N.M. Mishchenko, Russian journal of inorganic chemistry. 42 (5), 625 (1997).
98. A.V. Melezhik and A.A. Chuyko, Khimicheskaya tekhnologiya. (2), 3 (1992) [in Russian].
99. V.V. Yanchenko, M.L. Piatkovskyi, O.P. Yatsiuk, S.L. Revo and Yu.I. Sementsov, Naukovyi visnyk UkrNDIPB. 1 (7) (2003) [in Ukrainian]. http://firesafety.at.ua/visnyk/2003_No_1-07/jacjuk.pdf
100. V.V. Yanchenko, S.L. Revo, Yu.I. Sementsov, M.L. Piatkovskyi and O.P. Yatsyuk, Naukovyi visnyk UkrNDIPB. 2 (6), 223 (2002) [in Ukrainian].
101. S.G. Kotov and A.Yu. Lupey, Nauchnoe obespechenie pozharnoy bezopasnosti. (10), 92 (2001) [in Russian].
102. S.V. Pakhovchyshyn, Yu.I. Sementsov, V.F. Grytsenko, L.G. Koval', O.O. Chuiko, I.G. Chernysh and A.P. Shymanskyi, Ukraine Patent No. 27395 (15 September, 2000).
103. Yu.I. Sementsov, T.A. Alekseyeyva, M.L. Pyatkovskii, A.I. Kostuchenko and V.V. Yanchenko, in: *Proceedings 12th International Symposium on Intercalation Compounds* (Poznan, Poland, 2003), Poster 49.
104. V.M. Ogenko, G.M. Zagorovskiy, I.G. Sidorenko and Yu.I. Sementsov, in: *Problemy sbora, pererabotki i utilizatsii otkhodov* (OTsNTI. Odessa, 2001), pp. 258—261 [in Russian].
105. V.M. Ogenko, G.M. Zagorovskiy, I.G. Sidorenko et al., in: Problemy sbora, pererabotki i utilizatsii otkhodov (OTsNTI. Odessa, 2001), pp. 165—168 [in Russian]
106. Yu.I. Sementsov, M.L. Piatkovskii, V.V. Yanchenko and G.P. Prikhod'ko, Khim. prom. Ukrainy. (3), 31 (2011) [in Ukrainian].
107. Yu.I. Sementsov, M.L. Pyatkovskii, V.V. Yanchenko, G.P. Prukhodko and S.Ya. Brychka, in: *Proc. II Mezhdunarodnoy konferentsii «Uglerod: fundamentalnye problemy — nauka, materialovedenie, tekhnologiya* (Moscow, 2003), p. 178 [in Russian].
108. High temperature material, Patent FR1395964 (16 April, 1965). (Shane James Harry, Russel Robert John, Bochman Raymond A, Patent US3494382 (10 February, 1970).
109. V.V. Avdeev, S.G. Ionov, A.V. Kozlov, I.V. Nikolskaya, H.I. Serebryanikov, B.A. Sakov, G.V. Presnov, B.V. Lomakin, V.A. Shkirov, RU Patetnt No. 2111190 (20 May, 1998) [in Russian].
110. O.Yu. Isaev, D.V. Smirnov, V.P. Lepikhin and I.V. Zakharov, RU Patetnt No. 2118942 (20 September, 1998) [in Russian].
111. Yu.I. Sementsov, M.L. Piatkovskii and V.V. Yanchenko, Ukr. Patent No. 81198 (10 December, 2007) [in Ukrainian]..
112. V.V. Yanchenko, Declarative patent of Ukraine for invention No. 48463 (15 August, 2002). [in Ukrainian].
113. I.D. Buraya, Ph.D. dissertation, Institute of Surface Chemistry NAS of Ukraine, 1990 [in Russian].
114. Yu.I. Sementsov, *Formation of structure and properties of sp^2-carbon nanomaterials and functional composites with their participation* (Interservis, Kyiv, 2019).

CHAPTER 3

INFLUENCE OF TECHNOLOGICAL PARAMETERS OF THE SYNTHESIS PROCESS ON THE CHARACTERISTICS OF CARBON NANOTUBES

The synthesis of carbon nanotubes is usually carried out using catalysts. The catalyst initiates the chemical conversion of the substance used as a carbon source for the growth of CNT and directs this conversion to obtain an ordered carbon structure. Often it is the catalyst that determines which carbon structure can be obtained: nanotubes, nanofibers, amorphous carbon, or other forms of it. The processes of conversion of carbon compounds with the release of carbon have long been known. However, only in recent years, such effective catalysts have been found that allow one to obtain via these processes new nanostructured forms of carbon such as nanotubes and nanofibers [1—19].

An effective catalyst for the synthesis of CNTs should provide:

- high mass yield of CNT (not less than 10 mass of CNT per 1 mass of catalyst);
- high activity for a long time without deteriorating the quality of CNTs obtained;
- high growth rate of CNTs and selectivity of structure formation in a given range of technological modes;
- low sensitivity to changes in technological modes of CNT synthesis, such as temperature, the composition of the reaction gas mixture, gas supply rate, to-bags in the applied gases, the amount of catalyst in the reactor, the mode of mixing the reaction mixture components;
- required structural indicators of CNTs: number of graphene layers, internal and external diameters, length, uniformity of diameter along the length, structure defects, the content of inorganic impurities, inclusions and other structural forms of carbon, aggregation of CNTs;
- obtaining a product in a form suitable for unloading from the reactor and subsequent processing (in the form of a light powder);
- manufacturability of purification of the product from catalyst residues;

- the absence of components harmful to human health or the environment;
- manufacturability of the synthesis process, availability of starting materials, absence of hazardous waste, low cost;
- easy preparation for loading into the reactor for the synthesis of carbon nanotubes;
- the possibility of its loading into the reactor by technologically convenient methods;
- suitability for long-term storage without loss of activity.

3.1. Synthesis of three-component systems-catalysts for the growth of carbon nanotubes

From the data published and obtained in our experiments, it follows that the optimal composition of Fe_2O_3/NiO—MoO_3—Al_2O_3 catalysts has the following atomic ratio Al : Fe/Ni : Mo = (1—3) : 1 : (0.04—0.21) [20, 21]. For co-coated catalysts, the change in molybdenum content within the specified limits has little effect on the properties of the target product, i.e. CNT, provided that the catalytic activity and selectivity of the catalyst for CNT are high enough. In another case, an excess of molybdenum changes the direction of the process towards the formation of polynuclear aromatic hydrocarbons from ethylene or propylene.

The function of molybdenum is, first, to create surface acid centers that activate molecules of saturated or unsaturated hydrocarbons by protonation with the Brønsted acid centers or the donor-acceptor interaction of the double carbon-carbon bond with the Lewis acid centers.

Secondly, the participation of lower valence molybdenum oxides (which can be formed in the reducing atmosphere of the CNT synthesis reactor) in the elementary stages of dehydrogenation of hydrocarbon molecules is not excluded, as is known for lower tungsten oxides [22]. Thus, molybdenum-containing centers, from this point of view [20, 23, 24], are involved in the chemisorption and dehydrogenation of hydrocarbons, and possibly lead to the formation of polynuclear compounds. When a cluster of metallic iron (or nonstoichiometric iron oxide with a low degree of oxidation) is arranged in a row, the formed intermediate carbon compounds are then finally dehydrated; the formed carbon dissolves in iron and then crystallizes, giving rise to the nanotube. As the iron content decreases, as expected, the diameter of the obtained CNTs decreases, and their specific surface area increases. However, at the ratio Al : Fe > 3, the yield of CNT decreases sharply, and the process in most cases is directed towards the formation of aromatic hydrocarbons. This is consistent with the known data that under certain conditions, the catalytic system MoO_3—Al_2O_3 causes the aromatization of non-aromatic hy-

drocarbons. However, as experiments with the same composition have shown, the properties of these catalysts depend on the method of their synthesis.

The authors [1, 2] have determined optimal methods for the synthesis of Fe_2O_3—MoO_3—Al_2O_3 catalysts. They include aerosol (formate) catalyst production technology, which allows the synthesis of CNTs with a high specific surface area (340 m^2/g) and a small number of defects in the graphene surface as well as co-precipitation using ferrous compounds [1], which makes it possible to obtain CNTs, that are sensitive to the mode of catalyst synthesis and have a high specific surface area. Modification of the co-precipitation method via the formation of magnetite nanoparticles allows for obtaining inhomogeneous in diameter CNTs, the specific surface area of which is about 240 m^2/g [1, 2]. The method of co-precipitation with slow hydrolysis using urea has been proved to be the most convenient for the synthesis of high-quality nanotubes, while the aerosol method allows obtaining thin CNTs [21, 25].

3.1.1. Synthesis of three-component systems-catalysts for the growth of carbon nanotubes by co-precipitation method

Synthesis of catalysts by co-precipitation is characterized by long-term preparation, which proceeds in several stages, deposition of metal hydroxides from solution, and the absence of hazardous waste.

Synthesis of iron-containing catalysts of composition $Al_2FeMo_{0.21}$. There is a method of obtaining catalysts for gas-phase precipitation of CNT, which consists in the co-precipitation of ferric iron hydroxide with aluminum and/or magnesium hydroxides in the presence of ammonium molybdate and salts of carboxylic acids (formic, acetic, propionic, butyric) [11]. The precipitation of hydroxides was performed by adding to the solution of salts of these metals a precipitating reagent having the ability to increase the pH (solutions of ammonia and ammonium bicarbonate). The precipitate was washed with water, dried, ground, and added to the CNT synthesis reactor heated to 680 °C. Ethylene mixed with hydrogen was used as a carbon source.

According to the method of obtaining catalysts for gas-phase precipitation of CNTs described in [18], a solution containing magnesium acetate, acetates or nitrates of catalytically active metals (iron, cobalt, nickel), and citric acid is prepared. When boiled, this solution turns into a homogeneous gel. The gel is dried at 200 °C and calcined for 5 h at 700 °C. The compounds of metals with carboxylic acids decompose to form mixed metal oxides.

To obtain a catalyst for the growth of CNTs by co-precipitation via slow hydrolysis, the atomic ratio of metals Al: Fe: Mo = 2 : 1 : 0.21 was used (hereinafter the ratio of components in the synthesis of this and other catalysts is denoted

by a conventional formula reflecting the atomic ratio of metals without taking into account oxygen and hydroxyl groups, in this case by $Al_2FeMo_{0.21}$). For this purpose, aluminum was introduced in the form of basic aluminum nitrate, and iron in the form of ferric chloride. The pH was carried out due to ammonia released during the hydrolysis of urea.

The method for preparation of stock solutions for the production of iron- and nickel-containing catalysts by co-precipitation in examples

Example 1. A catalyst was obtained at a ratio of components Al : Fe : Mo = = 2 : 1 : 0.21 ($Al_2FeMo_{0.21}$). The following solutions were prepared for this purpose:

$Al(NO_3)_3 \cdot 9H_2O$. 225 g (0.6 mol.) of aluminum nitrate was dissolved in 214 ml of water in a 1—1.5 l conical flask. To obtain the basic aluminum nitrate (via constant stirring with a mechanical or magnetic stirrer) with a molar ratio of OH^-: (Al^{3+}) = 1:5, ammonia was injected. To do this, 500 ml of aqueous ammonia solution (concentration 4 mol/l) was added in portions of 50 ml, and each subsequent portion of ammonia was introduced after complete dissolution of the intermediate precipitate formed from the previous portion. After the addition of the entire ammonia solution, the stirring of the basic aluminum salt lasted 30 min, and then defended for 1 h.

$FeCl_3 \cdot 6H_2O$. 81.15 g (0.3 mol) of ferric chloride was dissolved in 470 ml of water in a 1—1.5 l beaker or flask.

$(NH_4)_6Mo_7O_{24} \cdot 4H_2O$. 78 g (0.063 mol) of ammonium molybdate was dissolved in 1356 ml of water at room temperature in a 2 l beaker or flask with constant stirring with a magnetic or mechanical stirrer.

$(NH_2)_2CO$. 180 g (3 mol) urea was added to a 1L beaker and dissolved in 669 ml of water.

Then the solution of ferric chloride was poured into a six-liter three-necked glass round bottom reactor equipped with a mechanical stirrer, and the solution of basic aluminum nitrate and then ammonium molybdate was introduced with constant stirring. Adding ammonium molybdate led to the formation of a suspension of dark orange colour. After that, the solution of urea was added. Residues of reagents on the dish were washed off with distilled water. Then the reactor was placed on an electric stove. As a support, a circle of thick plate made of low density expanded graphite, pressed along the reactor bottom radius for better heat transfer, was used. The reactor was thermally insulated with basalt felt and brought to (98—100) °C with continuous stirring for 2 h, during which; carbon dioxide was released. Stirring was not stopped for another 3.5 h, and water was added instead of evaporated to maintain a constant volume. At the end of this period, a faint odor of ammonia appears (moistened indicator paper is blue). A red-brown suspension was formed with pH = 7. The reactor was switched off at 15 min before stopping the stirrer and removing the insulation to avoid overheating the bottom layer

and boiling the suspension. The flask was kept cold. On the following day, the precipitate was filtered off and washed with 1% ammonium bicarbonate solution until almost complete disappearance of chloride ions (test with silver nitrate).

Example 2. The ratio of the obtained catalyst components was to be Al : Ni : Mo = = 2 : 1 : 0.21 ($Al_2NiMo_{0.21}$). To reach that, the following solutions were prepared:

$Al(NO_3)_3 \cdot 9H_2O$. 75 g (0.2 mol) of aluminum nitrate was put into a conical flask with a capacity of 1 l and dissolved in 150 ml of water. Ammonia was taken to obtain basic aluminum nitrate with a molar ratio of OH^- : (Al^{3+}) = 1 : 5. Under constant stirring with a magnetic or mechanical stirrer, 75 ml of aqueous ammonia solution (concentration 4 mol/l) was injected in portions of 10 ml. Then the process went on as in example 1.

$NiCl_2 \cdot 6H_2O$. 23.8 g (0.1 mol) of nickel chloride is dissolved in 50 ml of water in a flask of 150—250 ml.

$(NH_4)_6Mo_7O_{24} \cdot 4H_2O$. In a liter beaker or flask, with constant stirring for 1 h with a magnetic or mechanical stirrer, 24.72 g (0.02 mol) of ammonium molybdate was dissolved in 400 ml of water.

$(NH_2)_2CO$. 36 g (0.6 mol) of urea was added to a 250 ml beaker and dissolved in 100 ml of water.

As in example 1, a six-liter three-necked glass round bottom reactor equipped with a mechanical stirrer was used, a solution of nickel chloride was poured into it, and a solution of basic aluminum nitrate and ammonium molybdate was introduced with constant stirring. After that, a solution of urea was added. The total volume of the solution was adjusted to two liters with water, then heated to reflux on an electric stove and boiled until complete precipitation of hydroxides, which took 3.5 h. The resulting lime-colored suspension was kept at room temperature. In order to purify the suspension from chloride ions, 2 l of 1% ammonium bicarbonate solution was added. Check of the absence of such ions in the washing liquid was performed by breakdown with silver nitrate. The washed suspension was again allowed to settle to precipitate the precipitate. The liquid was decanted and the precipitate was subjected to heat treatment and grinding.

3.1.2. Synthesis of three-component systems-catalysts for the growth of carbon nanotubes by aerosol method

In order to improve the process of obtaining catalysts for CNT growth, increase productivity, as well as eliminate environmentally harmful waste, an aerosol method was proposed, which does not use co-precipitation of metal hydroxides from solution [21]. Instead, mixed metal oxides are obtained by thermal decomposition of a mixture of their salts of organic ac-

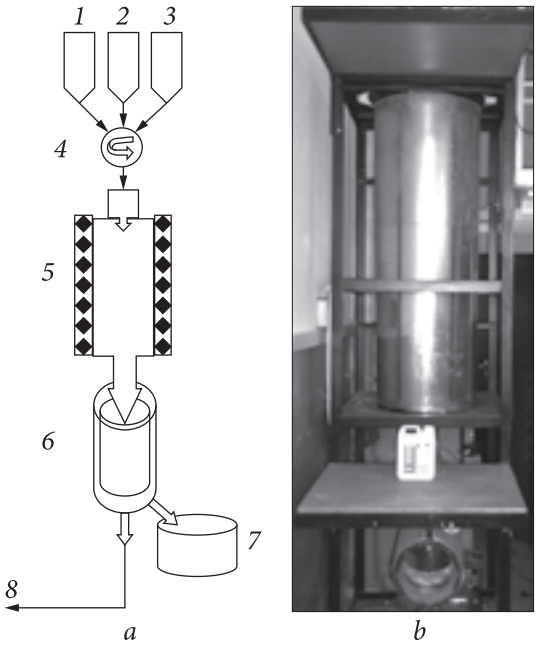

Fig. 3.1. Installation for aerosol synthesis of catalysts: *a* — scheme: *1—3* — containers with saline solutions; *4* — mixer; *5* — electrical furnace; *6* — electrostatic precipitator; *7* — capacity; *8* — water vapor; *b* — current layout

ids (preferably formic). This method of catalyst synthesis can be implemented in continuous technology.

To obtain a catalyst for the growth of CNT by the aerosol method with an atomic ratio of metals Al : Fe : Mo = 2 : 1 : 0.21, ($Al_2FeMo_{0.21}$), a source aqueous solution containing aluminum formates($(HCOO)_3Al{\cdot}3H_2O$),ammonium molybdate ($(NH_4)_6Mo_7O_{24} \times \times 4H_2O$), and iron citrate ($C_6H_{11}FeO_1$) was sprayed into a through vertical furnace (Fig. 3.1).At the furnace temperature 600—800 °C, the processes of water evaporation and thermal decomposition of metal salts of organic acids to metal oxides occur quickly and such a procedure gives an opportunity to obtain 1—3 μm catalyst particles. Stages of washing, filtering, drying, heat treatment and grinding of the finished product in the ball mill lose their value and therefore the catalysts are ready for participation in the synthesis of CNT. The resulting catalyst is $Al_2FeMo_{0.21}$.

3.1.3. Pyrogenic method for obtaining three-component oxide systems-catalysts for the synthesis of carbon nanotubes

Fast heating technology (in the thermoshock mode) *aqueous solution of metal salts* is based on the use of hydrocarbon liquid or gas-like fuels. The resulting high-temperature coolant creates a shock load on an aqueous solution of metal salts. The nature of combustion of carbohydrate fuels allows for broad limits to regulate the temperature of combustion products and provides an opportunity to organize the process of thermal cleavage and evaporation in an optimal way.

A functional scheme of the developed installation is shown in Fig. 3.2. It has the following basic functional blocks:

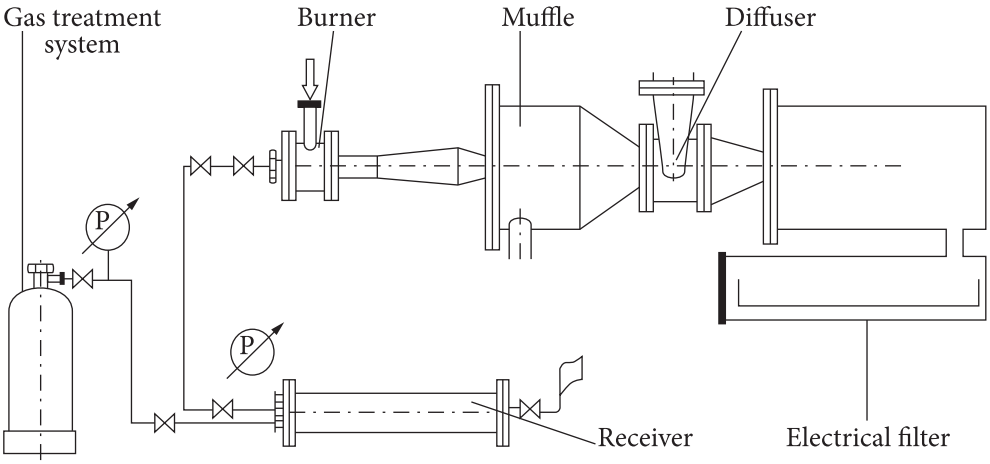

Fig. 3.2. Block scheme of installation for high-temperature hydrolysis with a propane-butane burner

- water supply unit for metal salts;
- fuel gas supply system (mixture of propane-butane);
- supply of compressed air;
- filtration block and accumulation of dispersed oxide.

The pilot installation of high-temperature hydrolysis was developed, in which a gas fuel was used as a mixture of propane (50% wt.) + butane (50% wt.). The mixture has a comparatively low saturation pressure and high-calorie (about 105 MJ/m^3) heat of the gas combustion.

3.2. Phase composition and structural characteristics of the catalyst

3.2.1. Iron-containing catalysts

Fig. 3.3 shows the results of XRD analysis of catalysts obtained by various methods and under different conditions. As seen, the XRD patterns are weak enough and extended.

Sample 1, obtained by pyrolysis of metal formates by aerosol method, is XRD-amorphic, while sample 4, obtained via co-precipitation, shows very expanded weakly pronounced XRD reflexes, that is, the system state is tense, and crystallites are small. For samples 2 and 3, obtained via co-precipitation with oxidation of bivalent iron with air oxygen in the conditions of formation of magnetite, XRD spectrum is sufficiently expressed, which allows determining its phase composition. In Table 3.1, the experimental and estimated values of interplanar distances are given. It can be argued that the crystalline Fe_3O_4 phase of is formed, whereas aluminium and molybdenum oxides are removed in the XRD-amorphous state.

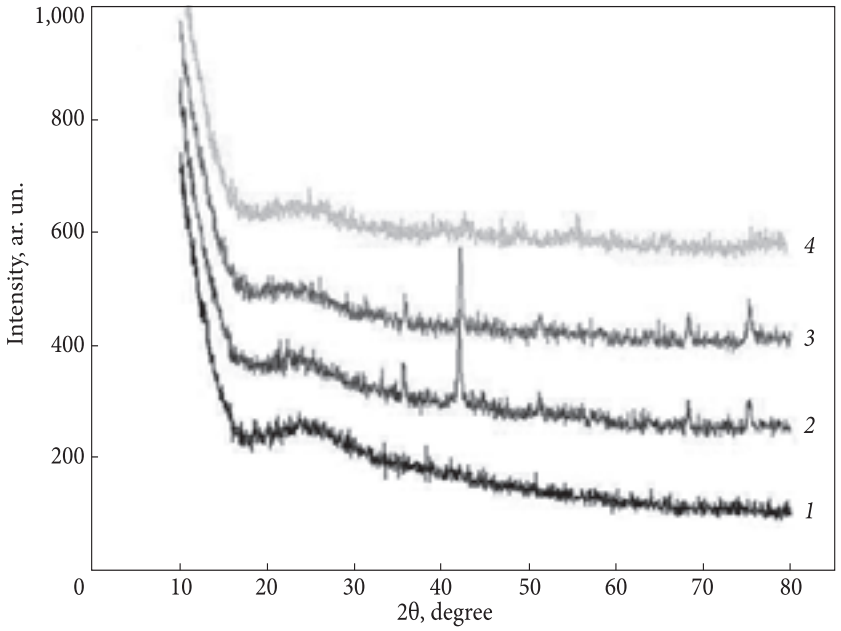

Fig. 3.3. XRD patterns of catalyst samples obtained under different conditions: *1* — pyrolysis of metal formates by aerosol method; *2*, *4* — co-precipitation; *3* — co-precipitation with oxidation of bivalent iron hydroxide with air oxygen in the condition of magnetite formation

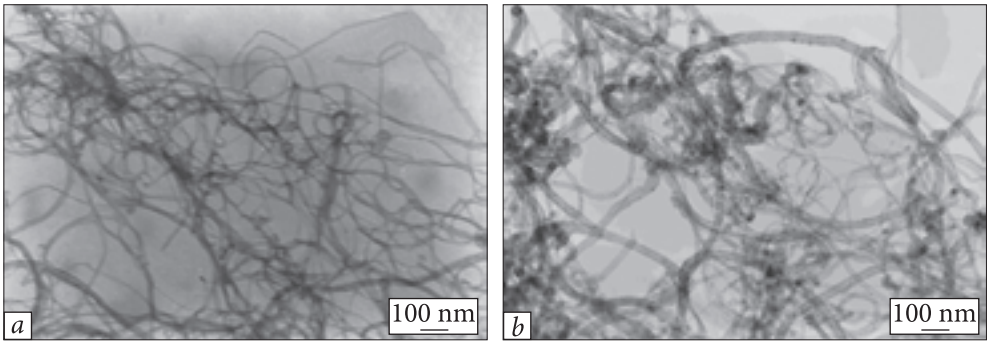

Fig. 3.4. TEM images of CNT samples obtained on catalysts of the composition: *a* — $Al_3FeMo_{0.21}$, *b* — $AlFeMo_{0.07}$

The catalyst composition, amount of ethylene, the content of the mineral residue of non-purified and purified CNTs, as well as the specific surface area (S_s) of the samples of purified CNTs, determined by low-temperature desorption of argon, are given in Table 3.2.

It should be noted that the S_s of CNTs varies significantly depending on the selected catalyst and gas consumption per gram of catalyst. Thus, for the

Table 3.1. **XRD data for the Al-Mo-Fe-O system**

Intensity exp., a.u.	2θ exp., degree	d exp., nm	Phase composition				
			Fe_3O_4				
			Intensity, a.u.	d, calc., nm	h	k	l
30.0	35.581	0.29411	29.7	0.29399	0	2	2
100.0	41.966	0.25076	100.0	0.25071	1	1	3
16.4	51.148	0.20785	20.8	0.20788	0	0	4
7.3	63.711	0.16988	8.9	0.16973	2	2	4
18.3	68.166	0.15996	26.7	0.16003	3	3	3
41.2	75.110	0.14703	35.6	0.14699	0	4	4

Table 3.2. **CNTs characteristics depending on the catalyst composition and the hydrocarbon volume**

Sample	Catalyst Me_xO_y,	Volume of ethylene per catalyst mass, l/g	Specific surface area, m^2/h	Ash content in CNT, % wt.	
				not purified	purified
1	$Al_3FeMo_{0.21}$	1.36	313	42.0	1.4
2	$Al_3FeMo_{0.21}$	2.27	303	28.5	1.0
3	$Al_3FeMo_{0.21}$	3.46	229	23.7	1.1
4	$Al_2FeMo_{0.14}$	1.08	152	47.0	6.7
5	$Al_2FeMo_{0.14}$	4.08	142	17.8	2.7
6	$Al_2FeMo_{0.14}$	9.20	148	11.5	2.3
7	$AlFeMo_{0.07}$	1.76	132	36.2	4.3
8	$AlFeMo_{0.07}$	3.01	146	23.1	2.9
9	$AlFeMo_{0.07}$	4.34	151	17.0	2.9

catalyst $Al_3FeMo_{0.21}$ with increasing gas consumption, S_s of CNT decreases monotonically. For the catalyst $Al_2FeMo_{0.14,}$ S_s decreases non-monotonically, while for $AlFeMo_{0.07}$ it increases with increasing consumption of ethylene. Obviously, being depended on the synthesis conditions and primarily on the selected composition of the catalyst, defects in the structure of the CNTs will be different.

For example, Fig. 3.4 shows transmission electron microscopy (TEM) images of samples of multiwall CNTs obtained with different catalysts.The TEM images of CNTs (Fig. 3.4) indicate a sufficient level of homogeneity of the synthesis products. There are no visible inclusions of a form other than

Table 3.3. **Characteristics of CNTs depending on the synthesis conditions**

Parameter	Carbon source											
	Ethylene			Ethylene from ethanol	Propylene from isopropanol							Propan-butane
Al : Fe in the catalyst	Al_3Fe	Al_3Fe	Al_3Fe	Al_3Fe	Al_3Fe	Al_3Fe	Al_2Fe	Al_2Fe	Al_3Fe	Al_3Fe	Al_3Fe	Al_3Fe
T of synthesis, °C	700	700	700	700	700	650	650	700	700	700	700	700
Bulk density, g/dm^3	33	31	28	31	34	35	35	27	28	39	29	38
Ash content,%	20	25	21.0	21.0	17.9	20.7	19.7	19.2	18.1	20.1	20.3	20.0
$S_{\text{not purified}}$ of CNT, m^2/g	365	467	224	189	221	242	232	217	221	280	343	255
S_{purified} of CNT, m^2/g	394	500	214	194	218	252	242	221	—	—	343	278
$\rho_{\text{not purified}}$, Ω · cm, ±10%	0.15	—	0.11	0.12	0.094	0.090	0.11	—			0.070	
Content of ash in purified CNT after TG 1000 °C,%	—	1.1	—	—	—	—	0.5	2.4	—	0.8	—	0.65
Temperature of TG (purified CNT):												
5% mass loss*	552	507	598	598	605	590	594	591	—	—	588	582
10% mass loss*	609	556	637	638	642	630	631	636	—	—	637	
15% mass loss*	655	596	669	669	675	664	662	675	—	—	676	
At. Mo: Fe cat. ±20%	—	—	0.11	—	0.017	0.017	0.052					

* Heating rate 10 °C/min.

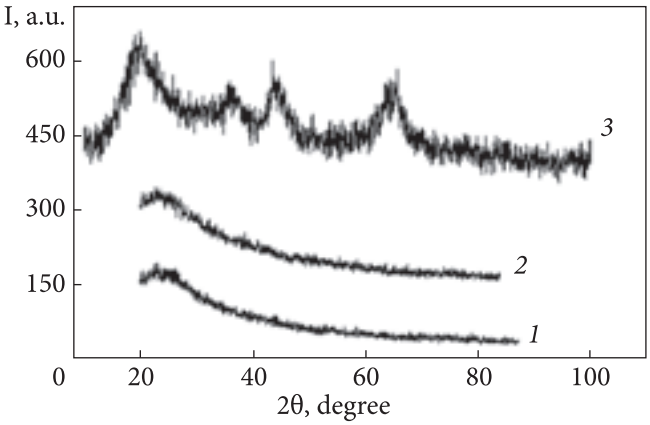

Fig. 3.5. XRD spectra of catalysts $Al_2FeMo_{0.21}$ (*1*, *2*) and $Al_2NiMo_{0.21}$ (3) synthesized by co-precipitation (*1*, *3*) and aerosol method (*2*)

Table 3.4. **XRD data for the Al-Mo-Ni-O system**

Intensity exp., a.u.	2θ exp., degree	d exp., nm	Phase composition NiO				
			Intensity, a.u..	d calcul., nm	h	k	l
100.0	37.332	2.4071	54.4	2.4079	0	0	3
90.1	43.346	2.0860	90.1	2.0855	0	1	2
41.6	62.986	1.4746	63.3	1.4746	1	0	4

CNT, i.e. we can assume that the content of the amorphous phase of carbon is negligible.

Some characteristics of CNTs obtained with iron-containing catalysts depending on the synthesis parameters are given in Table 3.3.

3.2.2. Nickel-containing catalysts

Three-component nickel-containing catalysts were prepared by co-precipitation with slow hydrolysis using carbamide for the synthesis of CNT with an atomic ratio of metals Al : Ni : Mo = 2 : 1 : 0.21 ($Al_2NiMo_{0.21}$) and 1.65 : 0.8 : 0.025 ($Al_{1.65}Ni_{0.8}Mo_{0.025}$) [26, 27]. There were taken aluminum nitrate prepared by partial neutralization of ammonia aluminum nitrate solution, nickel chloride, and ammonium molybdate prepared by the technique described in the previous subsection.

Catalysts (gray-green powders) were obtained similar to the synthesis of the iron-containing $Al_2FeMo_{0.21}$.

XRD spectra (DRON-3M, λ_{Co} = 0.17902 nm) of catalysts $Al_2FeMo_{0.21}$ and $Al_2NiMo_{0.21}$ are shown in Fig. 3.5 [21]. It is evident that samples 1 (iron-containing catalyst produced via co-precipitation) and 2 (iron-containing catalyst produced via pyrolysis of organometallic compounds by aerosol method) are XRD-amorphic, since halo and weakly pronounced X-rays are observed, that is, the state of the system is tense, and the crystallite sizes are small. However, the phase composition of sample 3 (nickel-containing catalyst obtained via co-precipitation) is

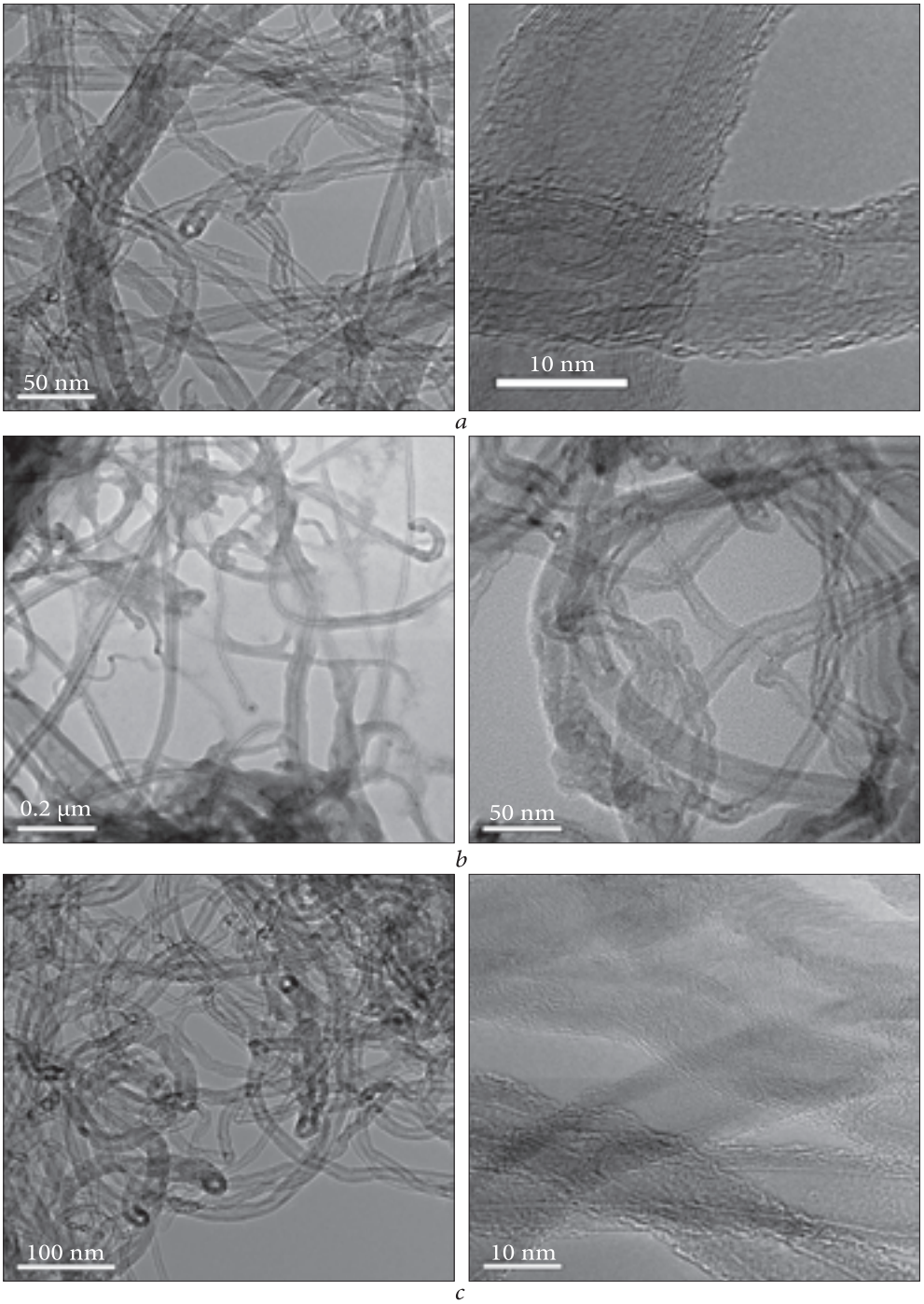

Fig. 3.6. TEM images of CNTs synthesized with catalysts $Al_2FeMo_{0.21}$ (*a*) and $Al_2NiMo_{0.21}$ (*c*), obtained by co-precipitation, and catalyst $Al_2FeMo_{0.21}$ (*b*), obtained by an aerosol method

Table 3.5. **Characteristics of CNTs obtained using iron and nickel-containing catalysts**

Sample	Catalyst composition, production method	Properties of non-purified CNTs		S_s purified, m^2/g	Outer diameter, nm
		Bulk density, g/dm^3	S_s, m^2/g		
1	$Al_2FeMo_{0.21}$, co-precipitation	34	195	214	10—50
2	$Al_2FeMo_{0.21}$, aerosol	33	248	293	10—25
3	$Al_2NiMo_{0.21}$, co-precipitation	40	254	303	10—40

an XRD-amorphous matrix and a crystalline NiO. On analyzing the data in Table 3.4, in which the experimental and estimated values of interplanar distances are given, one can state that a highly dispersed crystalline NiO phase was formed.

The TEM images of CNTs synthesized with the participation of catalysts (obtained by co-precipitation) is shown in Fig. 3.6.

The studied CNTs have similar morphological characteristics, close values of the specific surface area and content of impurities. CNT synthesized with the participation of an aerosol catalyst is significantly different in morphology (Fig. 3.6). This manifests a decrease in external diameters, their homogeneity, lack of acute fractures, and the formation of other carbon nanostructures such as fibers.

As follows from Table 3.5, the specific surface of the CNT synthesized with the participation of a co-precipitated nickel-containing catalyst, in comparison with the CNT obtained with an iron-containing catalyst (co-precipitate), increases by 1.5 times.

The obtained CNTs have close diameters ranging from (10—40) nm to (10—50) nm. The outer diameters of the CNTs synthesized with the participation of the aerosol iron-containing catalyst are reduced relative to the previous CNTs samples by about half due to the small cluster sizes of metal oxide phases in the aerosol type catalyst. It is important that CNTs based on nickel-containing catalysts can be studied by *NMR,* because such catalysts, in contrast to iron-containing ones, show poorer magnetic properties, and therefore it is possible to conduct such studies.

3.2.3. Catalysts obtained by pyrogenic synthesis using propane-butane and hydrogen-air burners

Comparative XRD patterns of complex oxide (AlFeMo) obtained by the pyrogenic synthesis in propane-butane burner and molybdenum oxide are shown in Fig. 3.7. They indicate that the complex oxide catalyst obtained by high-temperature pyrolysis has an amorphous-crystal structure, and, like in the previous cases, there is a weakly distorted crystalline structure of iron oxide and XRD-amorphous oxides of aluminum and molybdenum.

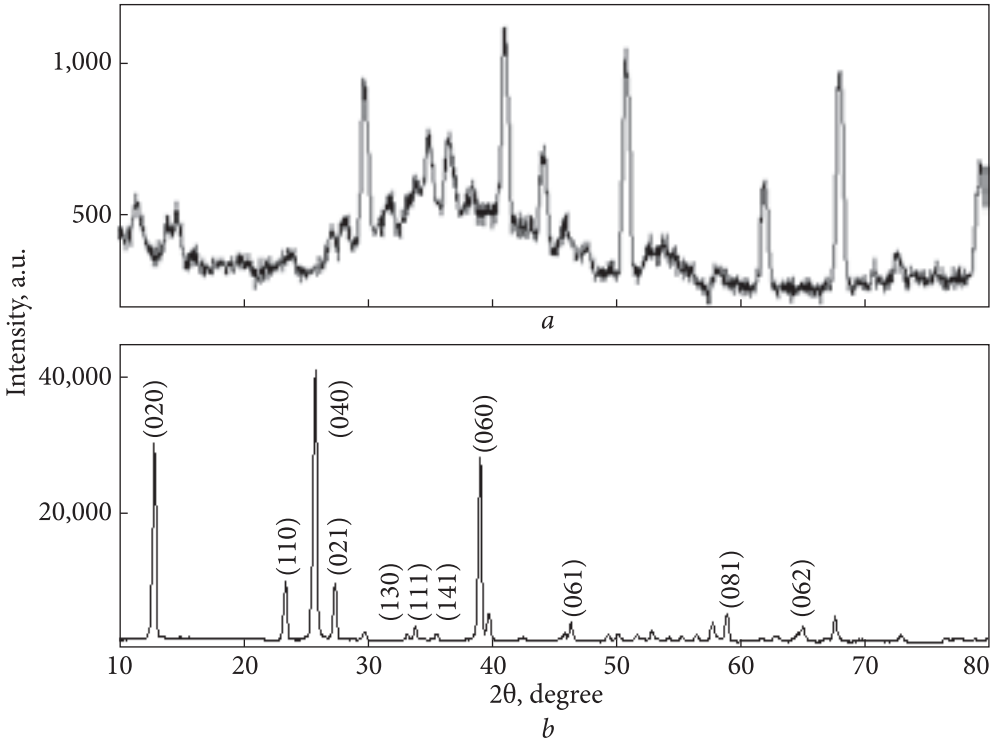

Fig. 3.7. XRD pattern of: *a* — complex (AlFeMo) oxide, *b* — molybdenum oxide [28]

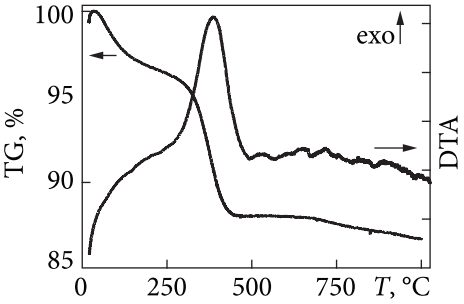

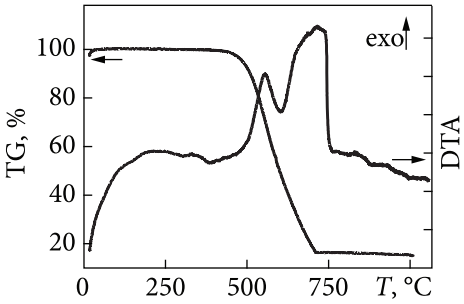

Fig. 3.8. Derivatogram of a complex oxide catalyst quenched in installation with a propane-butane burner

Fig. 3.9. Derivatogram of multiwall CNTs obtained on a pyrogenic catalyst

Catalyst derivatograms (Fig. 3.8) show the weight loss of the test samples at the level of 12%. This effect can be divided into two components: water loss and burnout of the carbon component, which have an almost equal contribution.

Fig. 3.9 shows a derivatogram of multiwall CNTs, which shows that the dependence of CNTs mass loss on temperature is monotonic without fractures, which

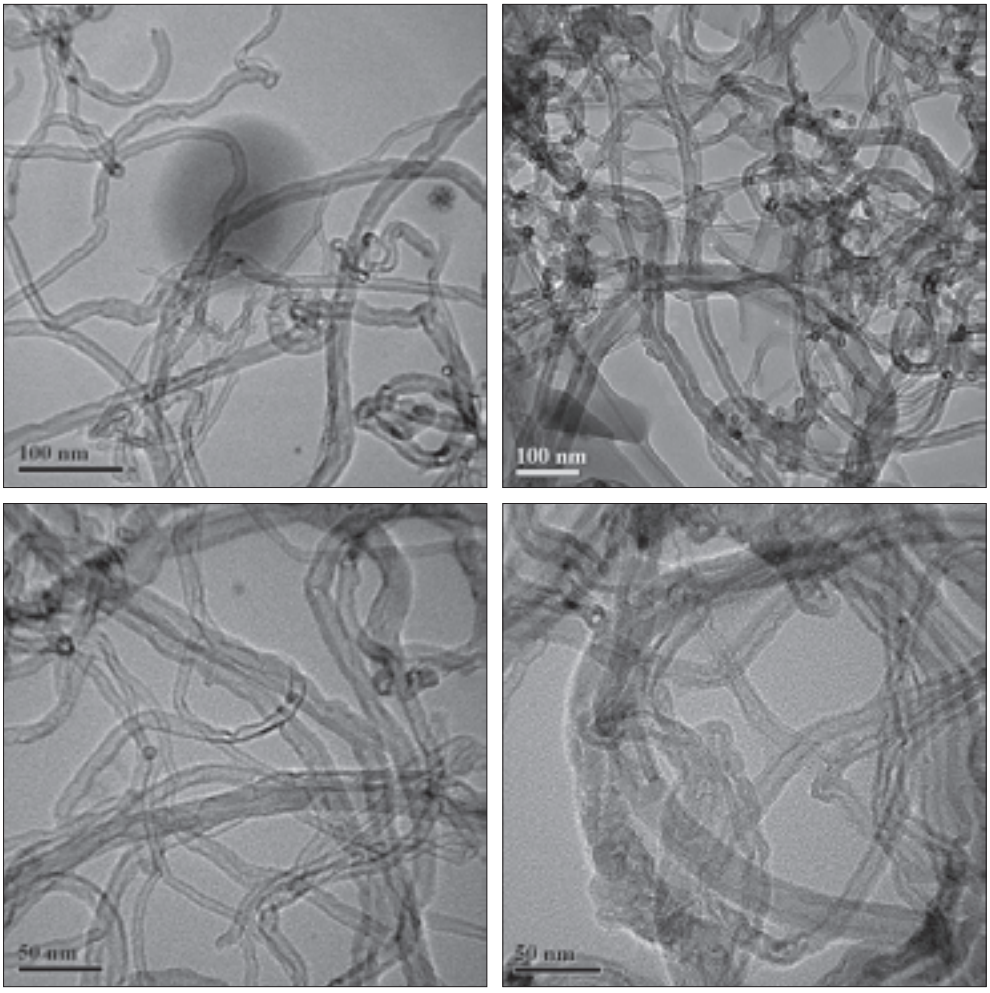

a *b*

Fig. 3.10. TEM images of multiwall CNTs obtained on the catalysts: *a* — pyrogenic, *b* — aerosol

Table 3.6. **Specific surface area determined by the method of thermal desorption of argon**

Sample	Catalyst AlFeMo	CNTs non-purified	CNTs purified
Specific surface area, m^2/g	**42** (aerosol)	320	295
	67 (pyrogenic, propane-butane burner)	360	358

a

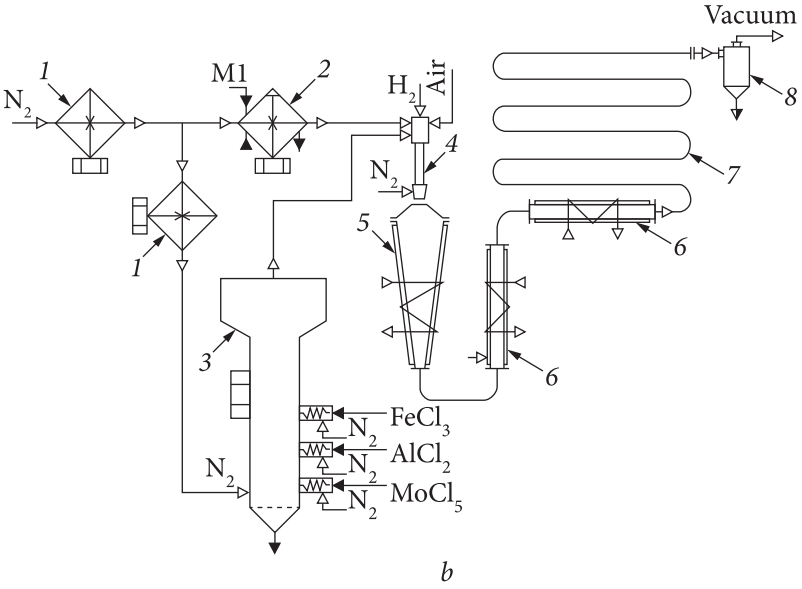

b

Fig. 3.11. The current installation for pyrogenic synthesis of a complex oxide catalyst in a hydrogen burner (*a*) and its scheme (*b*)

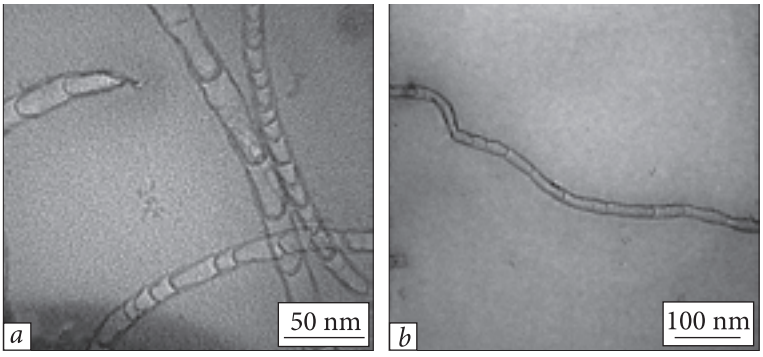

Fig. 3.12. TEM images of multiwall CNTs obtained on a pyrogenic catalyst (hydrogen-air burner)

indicates the homogeneous nature of the carbon material, i.e. CNTs, and the absence of amorphous carbon phase.

Table 3.7. **The total silicon content and the Al : Fe : Mo ratio**

Si, %	Al : Fe : Mo ratio
Si — 98.8	6.7 Al : Fe : Mo 0.14
Si — 98.4	3.8 A l : Fe : Mo 0.07
Si — 97.4	0.95 Al : Fe : Mo0.02

Table 3.6 contains the values of the specific surface area of the catalysts obtained by aerosol and pyrogenic methods, the comparison of which shows that the specific surface area of the catalyst obtained by the pyrogenic method is approximately 50% larger than the surface area of the catalyst obtained by the aerosol method.

As seen in Fig. 3.10, the morphological differences of CNTs obtained on catalysts synthesized by pyrogenic and aerosol methods are not significant, i.e. CNTs are not fundamentally different.

A system with a 20 mm diameter hydrogen-air burner was implemented at the Kalush Research-Experimental Plant ICS NAS of Ukraine.

Such a system provides a high production capacity (up to 1500 kg per month) under the conditions of meeting all the necessary environmental requirements for production (Fig. 3.11). With its help, experimental batches of pyrogenic complex oxide systems have been developed. Aluminum, iron, and molybdenum chlorides, as well as methyl trichlorosilane (CH_3SiCl_3) were used as precursors. Determination of the specific surface of the samples by the method of thermal desorption of argon (GOST 23401-90) showed that its value for all samples is close to 200 m^2/g. The study of the elemental composition of oxides was performed on an ElvaX spectrometer from "Elvatech". High-temperature hydrolysis under different technological modes allowed us to obtain complex oxide systems with the ratio of metals given in Table 3.7.

Fig. 3.12 shows TEM images of multiwall CNTs obtained with a pyrogenic (hydrogen-air burner) catalyst. From them, we can estimate the CNT diameter value as (10—15) nm. The bamboo-like structure is related to the fact that the synthesis was carried out in the presence of ethylenediamine impurities (see subsection 3.5.3).

3.3. Technological process of experimental and industrial production of carbon nanomaterials

From the analysis of data described in the literature [1, 2, 8, 10, 29—68], it can be concluded that today for experimental and industrial production of multiwall carbon nanotubes, the most acceptable option is the technology of catalytic CVD in the form of a fluidized bed using hydrocarbons as a carbon source and metal oxides as catalysts. Although aerosol technology is promising, bringing it to the scale of research and industrial production requires solving many technical and scientific problems.

In view of the above, the research and industrial technology of CNTs production were based on the CCVD technology in the version of a fluidized bed. In this case, as shown by previous studies [1, 20, 35, 69], as carbon sources, it is most appropriate to take ethylene or propylene, and as a metal oxide catalyst — a complex oxide of iron, molybdenum, and aluminium with the addition of pyrogenic silica in the form of a mechanical mixture. Regarding the method of maintaining the fluidized state of the catalyst and nanotubes, the traditional scheme was changed so that this state could be maintained by the gas flow from the bottom up through the layer of solid particles. In previous experiments on a laboratory scale, it was found that for particles having a low bulk density (20—40 g/dm^3), a state close to fluidized is achieved by rotating a horizontal or inclined reactor. The reactor is made in the form of a polyhedron (quadrilateral or pentagon) to prevent the powder mass from sliding along its walls. This technical solution makes it possible to optimize the feed rates of gaseous reagents in the reactor regardless of the maintenance of the fluidized state of solid particles. The reactor rotation speed is chosen so that the centrifugal acceleration could be lower than the acceleration of gravity.

General characteristics of the process of experimental and industrial production of carbon nanomaterials. Installation for the synthesis of carbon nanotubes. The central element of the CNTs synthesis plant is a reactor made of stainless steel in the form of a pentagonal prism with conical flanges (Fig. 3.13).

The reactor has two "necks" (pipe sections), through one of which the loading of catalyst and the addition of a gas mixture (propylene with hydrogen) take place, and through the other — the unloading of the product. The exhaust gas mixture is carried out through the inlet throat. The reactor is placed in an electric oven with heating and thermal insulation of several layers of basalt cardboard, inside which the optimum temperature (700 °C) is maintained with a thermal controller. In the synthesis of CNTs, the reactor is rotated with an electric motor. The rotation axis is inclined at a small angle to the horizon. At the end of the set time of CNTs cultivation (about one and a half hours), the reactor is purged with argon, a container for unloading is attached to the outlet throat and the axis of rotation of the reactor is inclined at an angle of 45—50 ° to the horizon. The powdered product (CNTs) is poured from the reactor into a container. The reactor together with the furnace and the units for the reactor rotation is fixed on the horizontal axes on the frame. For unloading, a change in the angle of inclination of the reactor is made by means of the electric drive fixed on the bed. The installation also has other units designed to ensure the tightness of the sliding seals of the gas inlet and outlet, pneumatic transport of the catalyst, to avoid spillage of the product through the outlet throat until the end of the technological cycle, and so on. Control and regulation of gas flow rate (argon, hydrogen, propylene) is carried out with rotameters. For the synthesis of CNTs in the rotating reactor and heating to the optimum synthesis

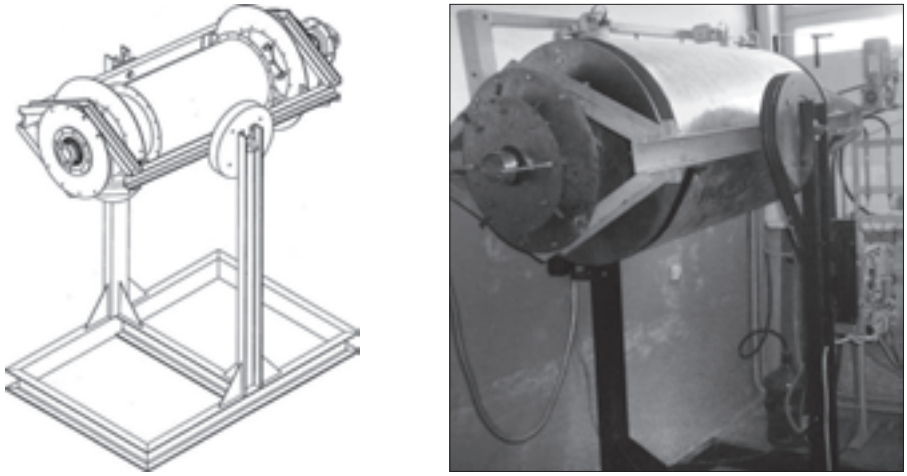

a *b*

Fig. 3.13. General view of the reactor with electric furnace: *a* — drawing of the general view; *b* — photo of the current layout

temperature (700 °C), a highly dispersed catalyst is fed by the pneumotransport method. First, the reactor is purged with argon to remove air for some time, and then a working gas mixture (ethylene or propylene with hydrogen) is added. The duration of CNTs synthesis is about an hour and a half. The gases leaving the reactor consist mainly of hydrogen with a small amount of impurities in the form of unreacted hydrocarbons. Exhaust gases are burned in the torch with safety precautions. After a certain time, the supply of hydrogen and hydrocarbons is stopped, the reactor is purged with argon and the resulting nanotubes, which have the form of a dark gray powder, are poured into a container, and after cooling, packaged.

The first pilot plant for CNTs synthesis was created on the basis of the enterprise for EG production TMSpetsmash Ltd Kyiv. The working volume of the reactor is 24 dm^3. The fluidized state of particles is maintained by the reactor rotation. At a certain configuration and rotation speed, the catalyst and the growing nanotubes are in the fluidized bed state. At operation temperature, one can visually observe a glow of the wave of the nanotube fluidized bed. This technological option is convenient in that the layer state does not depend on the gas flow rate, provided that it is not very high, so the product is not removed from the reactor. In this case, due to efficient mixing, there is no need for a complex gas distribution device for passing gas through a layer of fluidized particles: it is sufficient to introduce a gas mixture (hydrogen and ethylene or propylene) above the layer. Thus, the gas flow rate is selected solely on the basis of the rate of its conversion into nanotubes, which makes it possible to reach almost 90—100% conversion of ethylene or propylene and thus to obtain in the exhaust gases almost pure

hydrogen. One technological cycle (90 min) produces about 0.5 kg of carbon nanotubes containing 20% of impurities of the mineral residue of the catalyst. At the end of the cycle, 1/2—2/3 of the reactor volume is filled with a fluidized product. Removal of particles from the reactor is almost absent.

A catalyst for this process has the form of a mechanical mixture of subcrushed oxides of aluminum, iron, and molybdenum with the addition of pyrogenic silica. It is a light powder with a density of about (25—30) g/dm^3. To obtain such a mixture by the aerosol method, a spray aerosol solution of aluminum formates and iron and ammonium molybdate was prepared in a vertical continuous furnace, which was developed. If necessary, the grinding of this mixed oxide was carried out in a ball mill or in the installation of mechanochemical activation of the catalyst. The catalyst can also be obtained by co-precipitation from an aqueous solution [70].

3.4. Structural and physicochemical characteristics of carbon nanotubes

Carbon nanotubes consist of a single graphene layer (single-walled CNT) or of multiple coaxial graphene layers or convolutions of graphene layers (multiwall CNTs), and have almost ideal structures with extremely high characteristics. However, in the process of real growth of CNTs, a large number of defects is formed. Such defects are pentagonal, heptagonal, paired or even linear defects. They break the symmetry of the graphene layer and, thus, reduce the mechanical strength and degrade other characteristics of nanotubes, i.e. significantly affect the possibility of their application [71—73]. Depending on the angle of chirality and the diameter of CNTs, their properties also change, in particular, the conductivity can be both metallic and semiconductor, or dielectric [74]. Similarly, mechanical, emission, sorption, optical, and other properties acquire significant changes [75, 76]. The structure of nanotubes is related to the synthesis methods [77, 78]. The tubes themselves, forming bundles, can be placed regularly, creating periodic structures [79]. In contrast to single-walled nanotubes, the properties of which mainly depend on the method of bending the graphene surface and covalent interaction of carbon atoms, in studying multiwalled CNTs it is necessary to take into account the presence of van der Waals' forces between layers. As in graphite, the existence of a weak interlayer interaction determines the correlation of the packing of planes along the direction perpendicular to the tube axis [80], and the change in this interaction causes differences in the dispersion of coherent scattering domain and microstresses.

Despite the fact that the study of CNT growth defects has received enough attention in the literature, for example [29], as well as given that the number

of species and types of CNTs synthesized by different methods reaches tens, and possibly hundreds, it seems appropriate for this method of implementing the CVD process to investigate the influence of its parameters on the CNTs structure defects, and on the other hand, to obtain the most complete description of the synthesized products. Therefore, a comprehensive study of the structure of CNTs by various methods depending on the parameters of the synthesis process, including such factors as the catalyst composition, structural state (amorphous, crystalline), and the type of hydrocarbons (propylene, ethylene, propane-butane) is necessary.

An iron-containing catalyst of variable composition was used for the synthesis of multilayer CNTs. To purify from mineral impurities, the obtained CNTs were treated with a solution of $NH_4F \cdot HF$: H_2O: HCl with the appropriate ratio of components 150 : 1200 : 300, and then washed with distilled water to neutral pH. It should be noted that even after purification, CNTs contained a mineral residue.

Characteristics of CNTs were determined by the methods: transmission microscopy (JEM-100CXII), XRD (DRON-3M, λ_{Co} = 0.17902 nm), Raman spectroscopy (Brucker RFS 100/s spectrometer with an argon laser, λ = 514.5 nm) differential thermal and gravimetric analyzes (derivatograph Q 1500, heating rate 10 K/min). The CNT surface was characterized by the XPS method ("SERIES 800 XPS" Kratos Analytical spectrometer, X-ray source MgK_α of 1253.6 eV). Analysis of the XPS spectrum lines was performed using XPSPEAK 95 software, version 2, based on the change in the Gaussian — Lorentz distribution function [81].

3.4.1. X-ray structural analysis of CNTs

Fig. 3.14 [82] shows the XRD patterns of multiwall CNTs synthesized using ethylene (curve *1*) and propylene (curve *2*) and the catalyst $Al_3FeMo_{0.21}$, which indicate a hexagonal densely packed structure. There are diffraction reflexes 100, 101, 110, 112, and 004 of low intensity, but with good resolution. The general picture of diffraction peaks does not significantly depend on the type of catalyst used (Figs. 3.14, 3.15) and hydrocarbons (ethylene, propylene) in these synthesis conditions, although there is observed a change in relative intensities, splitting of individual peaks, their asymmetry from small angles.

The interplanar distance d_{002}, which indicates the packing density of the curved nanotube surfaces along the **c** direction, is in the range (0.3436… 0.3453) nm, which is higher than the similar lattice parameter for graphite equal to 0.3354 nm. The parameter c is not very sensitive to the type of catalyst and depends on the gas consumption per gram of catalyst varying for the same catalyst. Thus, for the catalyst $Al_2FeMo_{0.14}$ of a certain dispersion, with increasing time of synthesis of nanotubes, the interplanar distance increases

from 0.3436 to 0.3439 nm. In other cases, the change in the parameter c is nonmonotonic (Table 3.8).

Using the decomposition of diffraction reflexes (002) and (004) into Gaussian γ_f and Lorentz γ_d components at known values of $d_{002} = d_c$, we can determine the number of layers N in the nanotube and the magnitude of microstresses $\Delta d_C/d_C$, basing on the expressions [80, 83, 84]:

$$N = \frac{2(\pi \ln 2)^{1/2}}{\gamma_f \cdot d_c} \quad \text{and} \quad \frac{\Delta d_c}{d_c} = \frac{\gamma_d \cdot d_c}{\pi \cdot l},$$

where l is the reflex index (00l).

As follows from Table 3.8, even for the reflex (002), which is in the region of small diffraction angles, it is impossible to neglect the Lorentz expansion component associated with microstresses. Its value is larger even compared to the Gaussian component, which is attributed to the size of the coherent scattering blocks. For $Al_3FeMo_{0.21}$ catalysts, which promote the growth of CNTs with a

Table 3.8. **Specific surface area and structural characteristics of multiwall CNTs depending on the synthesis conditions**

Sample	Catalyst Me_xO_y	Volume of ethylene per mass of catalyst, l/g	Specific surface area, m^2/g	d_{002}, nm	Components of diffraction reflex expansion (002)		Calculated number of CNT layers	Outer diameter of CNT, nm	Micro stress, $\Delta d/d$
					Gaussian, γ_f	Lorentz, γ_d			
1	$Al_3FeMo_{0.21}$	1.36	313	0.3451	0.0427	0.0559	20	20	0.0307
2	$Al_3FeMo_{0.21}$	2.27	303	0.3431	0.0204	0.0422	42	43	0.0230
3	$Al_3FeMo_{0.21}$	3.46	229	0.3452	0.0528	0.0491	16	16	0.0269
4	$Al_2FeMo_{0.14}$	1.08	152	0.3436	0.0275	0.0362	31	32	0.0197
5	$Al_2FeMo_{0.14}$	4.08	142	0.3439	0.0308	0.0386	28	28	0.0211
6	$Al_2FeMo_{0.14}$	9.20	148	0.3438	0.0296	0.0409	29	29	0.0223
7	$AlFeMo_{0.07}$	1.76	132	0.3438	0.0271	0.0355	32	32	0.0194
8	$AlFeMo_{0.07}$	3.01	146	0.3442	0.0275	0.0352	31	32	0.0193
9	$AlFeMo_{0.07}$	4.34	151	0.3444	0.0259	0.0371	33	34	0.0203

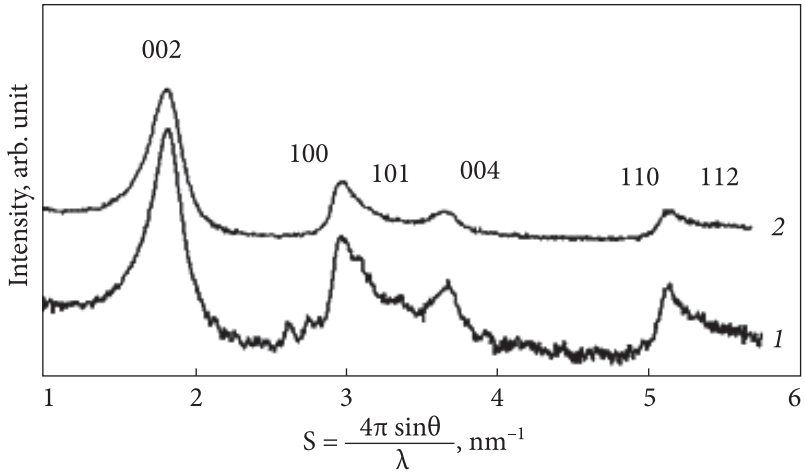

Fig. 3.14. XRD patterns of multiwall CNTs synthesized using ethylene (*1*) and propylene (*2*) and the catalyst $Al_3FeMo_{0.21}$ (CoK_α-radiation) [20]

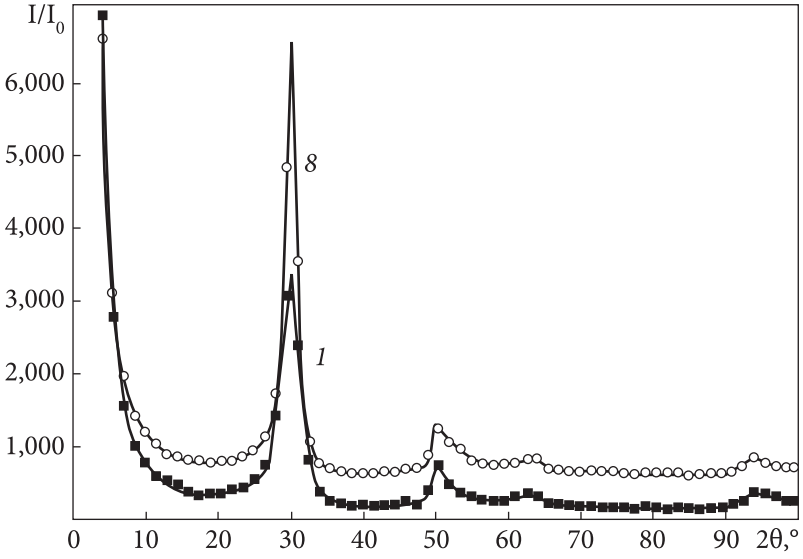

Fig. 3.15. XRD patterns of CNTs synthesized using ethylene and the catalysts $AlFeMo_{0.21}$ (*1*) and $AlFeMo_{0.07}$ (*8*) (Table 3.8) [20]

larger specific surface area due to their smaller diameters, the Gaussian component is the largest at a higher consumption of hydrocarbons.

The synthesis at an ethylene consumption of 2.27 l/g of this catalyst leads to a smaller size of the coherent scattering domain, fairly large micro-stresses, and the highest number of CNT layers (Table 3.8). Synthesis at an ethyl-

ene consumption per gram of catalyst of 3.46 l/g also gives noticeable microstresses with fewer N layers. The use of catalyst compositions $AlFeMo_{0.07}$ and $Al_2FeMo_{0.14}$ in all cases gives similar values for the number of layers and microstresses in nanotubes. The outer diameter of the CNT, which was calculated under the assumption that the inner diameter is equal to the wall thickness, $D = 3Nd_c$, correlates with the values determined from the TEM images and reflects its dependence on synthesis methods. The largest difference in the diameters of nanotubes is observed when using the powder catalyst $Al_3FeMo_{0.21}$. It should also be noted that the reflex (112) is of low intensity and extended, but its presence indicates an interlayer correlation, although rather weak, under these synthesis conditions [80].

3.4.2. Raman spectroscopy of CNTs

The defect in the structure of multiwall CNTs, associated with the presence of microstresses and the lack of proper layering, causes the transformation of the Raman spectrum, the D-band of which is responsible for small areas of coherent scattering and disorder of CNTs structure [85, 86].

Figs. 3.16 and 3.17 show the Raman spectra of multiwall CNTs in the frequency range of bands D and G. It is seen that for the catalyst $Al_3FeMo_{0.21}$, with the largest diameter of tubes and the smallest microstresses (Table 3.8), the intensity of the D-band is lower than that of the G-band, which corresponds to the oscillatory mode of symmetry E_{2g} [71—73]. Usually, this ratio of intensities indicates a slight disorder of the structure caused by defects. At low defect contents, including the presence of perfect packing of the layers in highly oriented graphite, the D-band is not observed. If the half-width of line D remains almost unchanged, then with decreasing microstresses and increasing the tube diameter, the G-band components become narrower and there is a shift towards lower frequencies, i.e. the oscillating mode of symmetry E_{2g} "softens". This behavior of oscillations, the frequency of which tends to the E_{2g} mode frequency in crystalline graphite (1585 cm^{-1}), indicates that with increasing CNT diameter, the CNT structure becomes closer to the hexagonal structure of graphite due to reducing the shear through bending small surface radius [80]. In the transition to another catalyst, the ratio of intensities at different durations of synthesis (i.e. amounts of hydrocarbon) of CNTs is preserved, as in the previous case. This correlates with the magnitude of microstresses. A shift of the symmetry fashion components E_{2g} is almost absent because the tube diameters at the specified hydrocarbon flow rate change little.

The conditions of CNTs synthesis, in particular the amount of hydrocarbon per unit mass, significantly affect the structural defects (coherent scattering domain size (CSD), microstresses) and the number of layers of multiwall CNTs, which varies depending on the tube diameter. This disorganization of the CNT

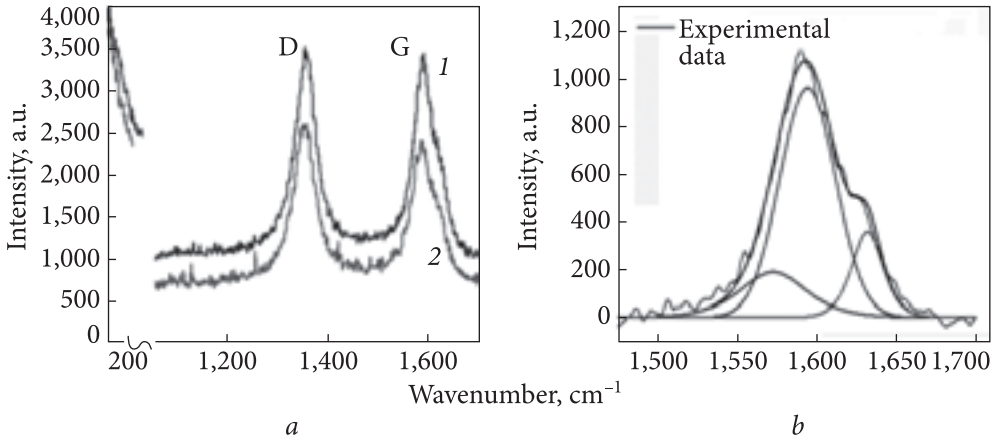

Fig. 3.16. Raman spectrum of multiwall CNTs synthesized using ethylene and the catalysts: $AlFeMo_{0.21}$ (1), $AlFeMo_{0.07}$ (2) [20] (*a*); the G peak splitting into components (*b*)

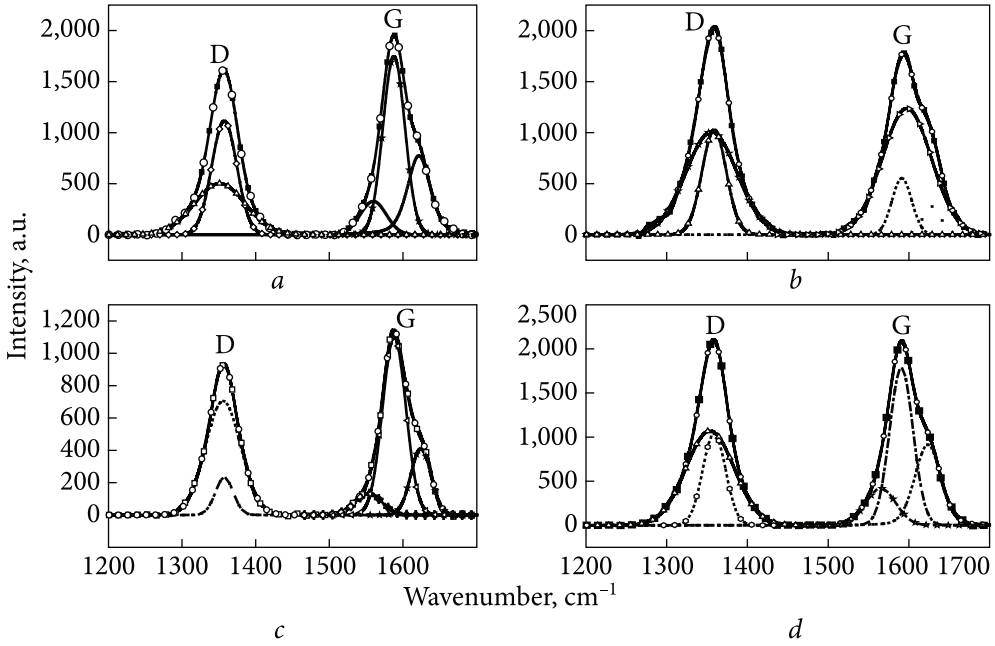

Fig. 3.17. Raman spectra in the frequency range of the D and G bands of multiwall CNTs synthesized using catalysts $Al_3FeMo_{0.21}$ and $AlFeMo_{0.07}$, respectively. Table 3.2: *a* — 2, *b* — 3, *c* — 6, *d* — 9 [20]

structure is manifested in the transformation of not only the D-band but also the G-band component, which includes scattering from the oscillatory mode of symmetry E_{2g}. The "softening" of this mode and the decrease in the intensity of the D-band indicate a decrease in the defect of the CNT structure.

3.4.3. X-ray photoelectron spectroscopy of CNTs

The properties of carbon materials, including CNTs, in particular their ad- and absorption characteristics, are undoubtedly influenced by chemisorbed oxygen. X-ray photoelectron spectroscopy (XPS) is an effective physical method for determining the surface chemical state [87—89]. A typical XPS spectrum of initial not purified CNTs is presented in Fig. 3.18. The main peak with an energy of 284.6 eV corresponds to carbon with the graphite lattice type.

Fig. 3.19, *a*, *b* shows the high-resolution spectra of C 1s and O 1s of multiwall CNTs. The decomposition of the C 1s spectrum [88] gives five peaks: carbon in the graphite hexagonal lattice (I, 284.6 eV), carbon — in the phenolic, alcohol, and/or C=N groups (II, 286.1—286.3 eV), carbonyl or quinone groups (III, 287.3—287.6 eV), carboxyl or ether groups (IV, 288.4—288.9 eV) and carbon represented in carbonate groups and/or adsorbed molecules of CO and CO_2 (V, 290.4—290.8 eV) (Fig. 3.19, *a*).

Decomposition of the spectrum of O 1s, relative to [88], provides three peaks: peak I (531.2—531.6 eV), which corresponds to the double bond C=O (ketones, lactones, carbonyl groups); peak II (532.2—533.4 eV), according to the single bond C—OH and/or C—O—C groups; peak III (534.6—535.4 eV)

Table 3.9. **Concentrations of impurities on the surface of CNTs, determined via XPS analysis**

Electronic band	Binding energy, eV	Concentration,% at.	Electronic band	Binding energy, eV	Concentration,% at.
C 1*s*	284.3; 285.0; 286.1; 288.9	94.9	Cr 2*p*	577.0	0.1
O 1*s*	531.9; 533.0; 534.2	4.7	S 2*p*	168.2	0.1
F 1*s*	687.8	0.2			

Table 3.10. **Relative concentrations of oxygen-containing CNT centers and corresponding binding energies**

CNT sample	Relative concentration of oxygen-containing groups,%			
	E_b = 286.1—286.3 eV Phenolic, alcohol (C—OH)	E_b = 287.3—287.6 eV Carbonyl, quinone (C=O)	E_b = 288.4—288.9 eV Carboxyl, ether (C—OOH)	E_b = 290.4—290.8 eV Carbonate and/or adsorbed CO, CO_2
Initial	49.1	17.2	17.2	16.5
Anodic oxidation	53.8	19.8	13.6	12.8
Heat treated	51.1	23.4	15.3	10.2

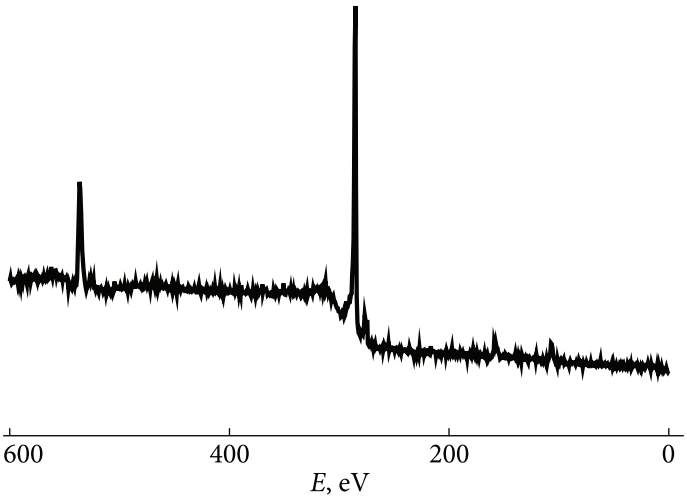

Fig. 3.18. General view of the XPS spectrum of CNTs [20]

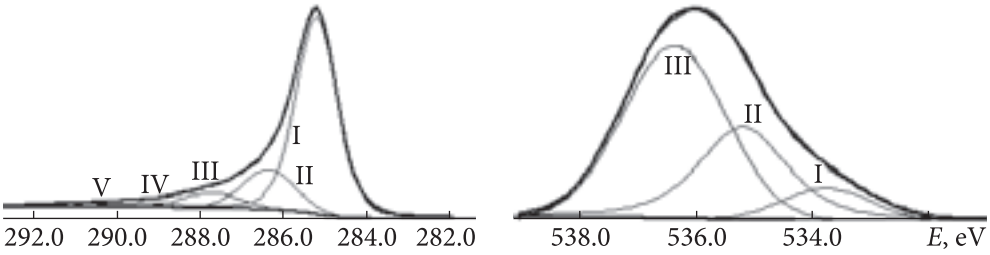

Fig. 3.19. Typical high-resolution XPS spectra of multiwall CNTs: C 1s (*a*); O 1s (*b*) [20]

of low intensity may correspond to the chemisorbed oxygen or adsorbed water (Fig. 3.19, *b*).

After purification from mineral impurities, the composition of CNTs, according to the XPS, had the following review (Table 3.9)

The relative distribution among different types of oxygen-containing centers, calculated from the decomposition of the C 1s spectrum, is as follows: phenolic, alcohol 49.1%; carbonyl, quinone 17.2%; carboxyl, ether 17.2%; carbonate and/or adsorbed molecules of CO, CO_2 16.5% (Table 3.10) [20].

3.4.4. Differential thermal and gravimetric analyses of CNTs

Fig. 3.20 shows typical types of diagrams of DTA, TG, and DTG for samples of purified CNTs, the results of which are shown in Fig. 3.21.

Oxidation of such materials in air begins with a noticeable rate in the region (560—600) °C. As expected, materials with a larger specific surface area

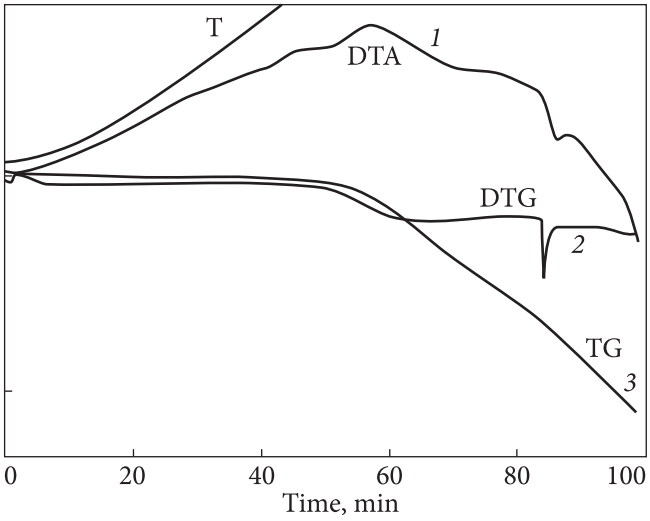

Fig. 3.20. Typical view of the DTA (1), DTG (2), and TG (3) diagrams for CNT samples [20]

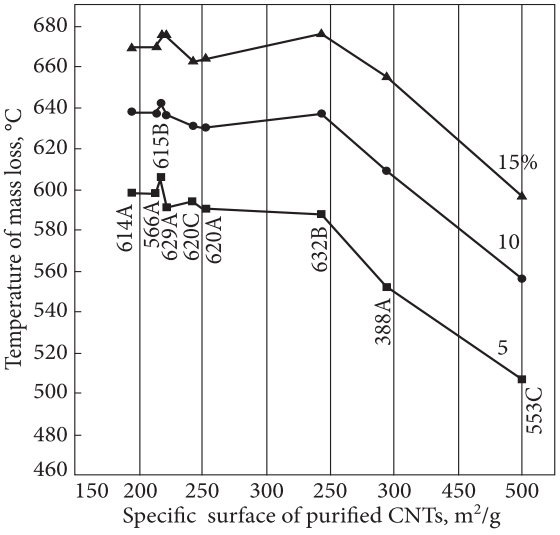

Fig. 3.21. Dependence of the temperature of mass loss of 5, 10, and 15% wt. of samples of purified CNTs on their specific surface when heating in a derivatograph under the wind [20]

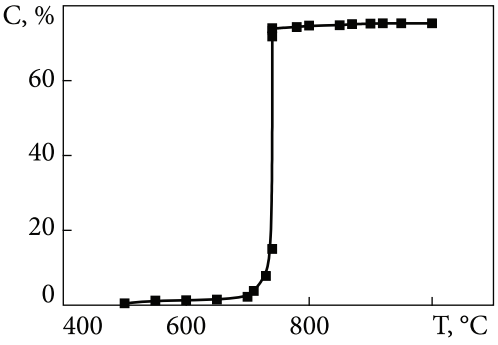

Fig. 3.22. Dependence of CNT mass loss on the oxidation temperature

oxidize more rapidly. However, it is known that amorphous carbon is oxidized fairly quickly in air at (350—400) °C. These data confirm that the impurities of amorphous carbon in the obtained CNTs are insignificant. At the same time, inflections on the thermogravigraphs indicate the possible presence of carbon materials of different structures in the samples.

The authors [90], according to the developed ideas about the formation and oxidation of nanoscale carbon structures [91] investigated CNTs, the characteristics of which are given above, and showed (Fig. 3.22) that they have a strong monostructure because the temperature dependence of mass loss for the precleaned samples has one jump without fracture.

3.4.5. Transmission electron microscopy of CNTs

Images obtained using high-resolution TEM provide clear information about the structure of CNTs. As seen in Fig. 3.23 images-fragments of multiwall CNTs, graphene planes are well separated (Fig. 3.23, *a*, *b*), which allows one to visually observe and count the number of CNT layers. The cross-sections of the CNT layers are collinear at a sufficiently long length, which may indicate the stability of the growth process. The number of layers and the outer diameters of the CNTs determined by high-resolution TEM correlate well, at least within the order of magnitude (10—40 layers, 10—40 nm*)* with the cal-

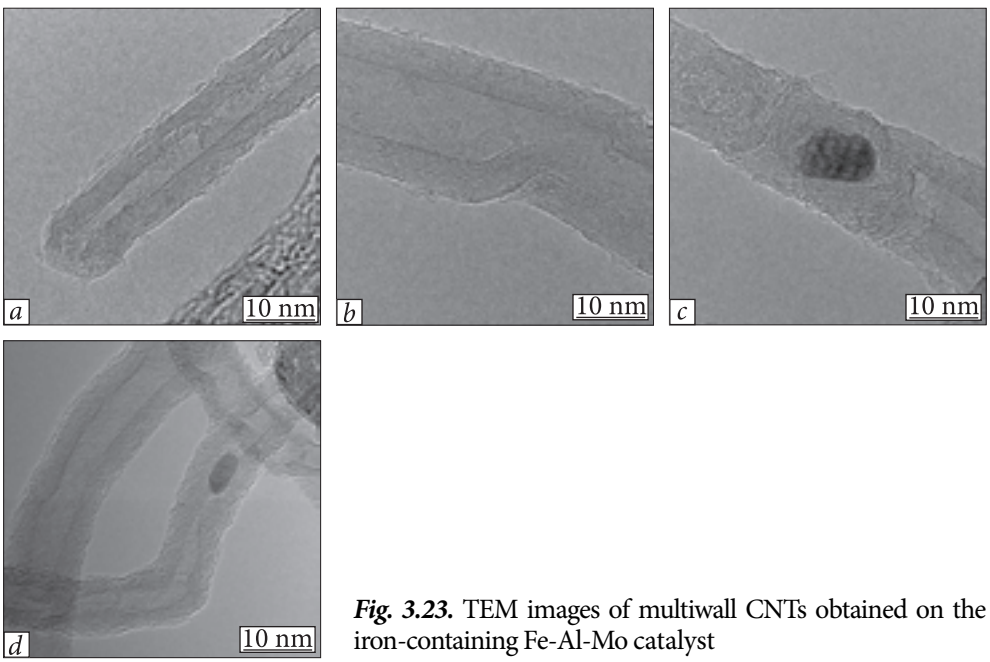

Fig. 3.23. TEM images of multiwall CNTs obtained on the iron-containing Fe-Al-Mo catalyst

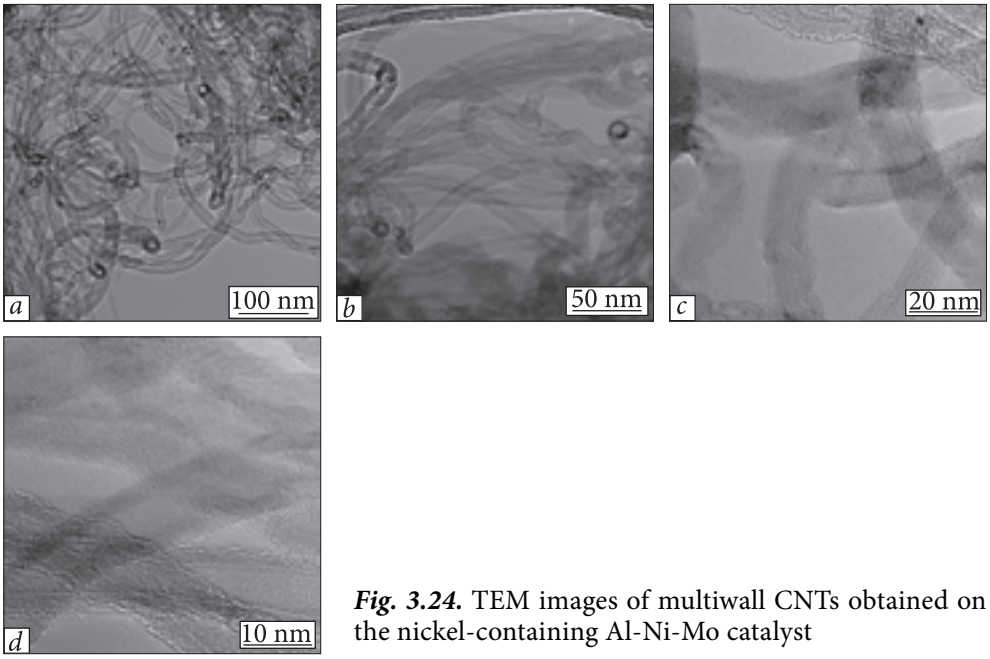

Fig. 3.24. TEM images of multiwall CNTs obtained on the nickel-containing Al-Ni-Mo catalyst

culations according to XRD data (Table 3.8). It can also be seen from the figure that the catalyst remains in the form of inclusions in the nanotube channels (Fig. 3.23, *c*, *d*) and determines the residual ash content of CNTs even after their purification from mineral impurities. It should be noted that the residual catalyst particles have an oval shape with dimensions of ~10 nm along and ~5 nm across. Such dimensions cannot be achieved even with the use of mechanochemical activation. That is, in the process of synthesis, there is a spontaneous grinding of the triple oxide catalysts of the Fe-Al-Mo composition.

It is clear from Fig. 3.23 that if CNTs are not formed, the carbon material still settles in the crystalline form, as evidenced by a number of cross-sections of ordered layers of graphene.

TEM images of CNTs obtained for a nickel-containing Al-Ni-Mo catalyst are shown in Fig. 3.24. They also confirm the above observations. Figs. 3.24, *a* and *b* show *a* "vertex" model of CNT growth, revealing catalyst particles at the CNT ends.

Thus, comprehensive studies of structural, thermodynamic, and spectral characteristics of CNTs have shown the reproducibility of these characteristics in the developed technological process of CNT production, which allowed us to create Technical conditions (Carbon nanotubes: TU U 24.1-03291669-009: 2009. No. 0251718182 from September 1, 2009. Authors: Yu.I. Sementsov, O.V. Melezhik).

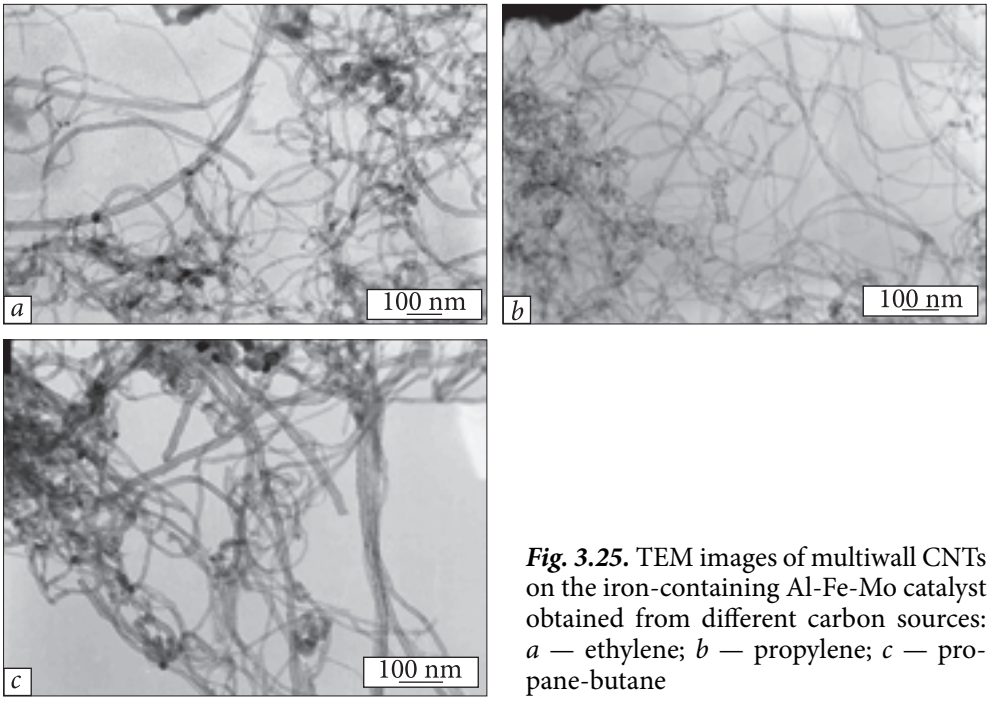

Fig. 3.25. TEM images of multiwall CNTs on the iron-containing Al-Fe-Mo catalyst obtained from different carbon sources: *a* — ethylene; *b* — propylene; *c* — propane-butane

From the comparison of TEM images of CNTs obtained using different carbon sources (Fig. 3.25), it turns out that ethylene and propylene yield almost the same structure of CNTs provided with the identity of all other conditions, and that from propane-butane CNTs of larger diameter are obtained. It seems that there are two "varieties" of CNTs: thinner and thicker.

3.5. Modification of carbon nanotubes

3.5.1. Activation of CNTs with a solution of potassium dichromate in sulphuric acid

To activate multiwall CNTs with a solution of potassium dichromate in sulfuric acid, the well-known technology for oxidation of natural graphite was used to obtain expandable graphite intercalation compounds, based on the following scheme, which involves the use of sulphuric acid and potassium oxide as an intercalant [92]:

$$C_n + 25H_2SO_4 + K_2Cr_2O_7 \rightarrow$$

$$\rightarrow 6C_{24}^{+}HSO_4^{-} \cdot 2{,}5H_2SO_4 + Cr_2(SO_4)_3 + K_2SO_4 + 7H_2O + C_{n-144}.$$

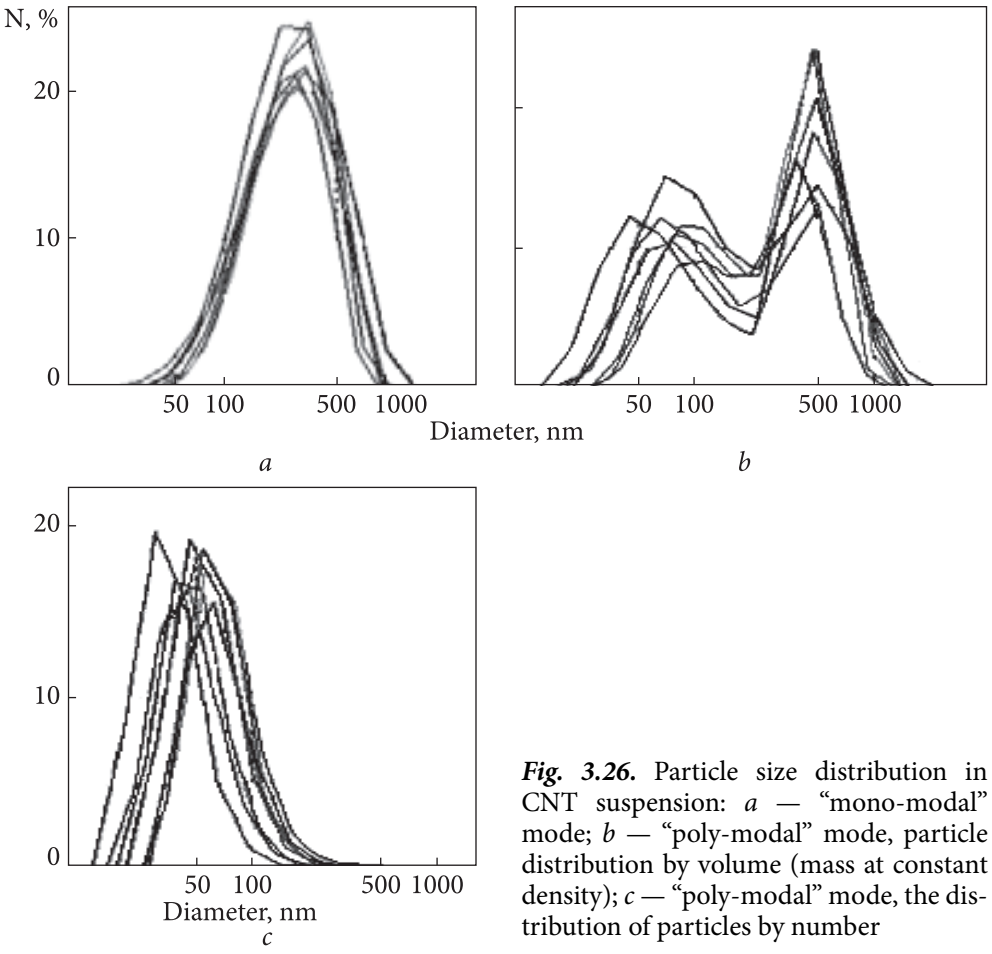

Fig. 3.26. Particle size distribution in CNT suspension: *a* — "mono-modal" mode; *b* — "poly-modal" mode, particle distribution by volume (mass at constant density); *c* — "poly-modal" mode, the distribution of particles by number

This scheme provides the production of intercalation compounds of stage 1 graphite (so-called blue graphite). However, the specific surface area of natural graphite can be in the range of 2—5 m^2/g, when CNTs have a surface area of at least 200 m^2/g, that is, increased by almost 40 times. The exothermic reaction was very active and was stopped by diluting with water to about 15% H_2SO_4, after which ammonium difluoride was added. This allowed at the same time to clean the pyrogenic silica brand A 300.

Aqueous dispersions of CNTs oxidized in a solution of potassium dichromate in concentrated sulfuric acid were investigated by laser (photon) correlation spectroscopy (Fig. 3.26).

The dependences were registered in the so-called mono-modal and poly-modal modes. The particle distribution for the sample obtained by oxidation of CNTs is shown in Fig. 3.26. The aqueous dispersion of the sample is stable over

time: the average particle size ~50 nm; two fractions: the particle size from 20 to 100 nm, amount 99.9%, mass ~10%, and the particle size from 250 to 500 nm, amount 0.1%, mass ~90%; high polydispersity ranges from 0.35 to 0.4. It should be noted that the suspension when diluted 10 times did not require additional shaking throughout the study and on the following day the data on polydispersity did not differ from the previous ones.

Thus, the results of LCS indicate that the chemical treatment of CNTs with powerful oxidants such as potassium dichromate in the presence of concentrated sulfuric acid grinds CNTs to form a stable suspension of particles of almost the same size.

3.5.2. Modification of CNTs by anodic oxidation

Anodic oxidation is one of the most controlled methods of oxidative modification of the CNT surface. CNTs according to TU U 24.1-03291669-009: 2009 were anodically oxidized under different conditions: in 55% aqueous solution of sulfuric acid according to the scheme presented in Fig. 3.27 [92]. The reactor consists of a rectangular housing *1*, in which cathode *2* made of lead sheet is vertically mounted. In the reactor vessel, there is a vertically placed cassette *3*, which consists of housing *4* in the form of an open on one side rectangular parallelepiped, in which anode *5* made of lead sheet is embedded. The open side of the housing is closed with a separator cover 6. Between the anode and the separator cover there is a layer of graphite 7. The width of the gap is 15 mm. Electrolyte 8 is filled in such a way that its level is 1—2 cm above the upper edge of the graphite when the cassette is installed in the reactor. The current density was 25…30 mA/cm^2.

After passing 200 A · h/kg electricity (Q), the samples were washed to pH = 6—7, dried, and ground. Part of the CNTs after drying was subjected to heat treatment at 800 °C for 20 s. The specific surface area for the original, oxidized, and heat-treated tubes was determined by argon desorption to equal 240 m^2/g, 220 m^2/g, and 280 m^2/*g,* respectively. The CNTs surface was characterized using the XPS method. According to XPS, the oxygen content in CNTs corresponding to TU U 24.1-03291669-009: 2009 was significantly lower than that of carbon fibers [88] and CNTs obtained by the template method, and of CNTs (NanothinX, Greece) in the original state, after anodic oxidation and short-term heat treatment in air, and was, respectively, 0.6% at.; 1.1% at.; 2.3% at. Table 3.9 [20] presents the relative contents of oxygen-containing centers, which were determined by the magnitude of the binding energy [87—89]. According to XPS, the oxygen content on the surface of multiwall CNTs is about 0.6% at.

Anodic oxidation of CNTs in 94% sulfuric acid was carried out in the reactor according to the scheme [92] shown in Fig. 3.28.

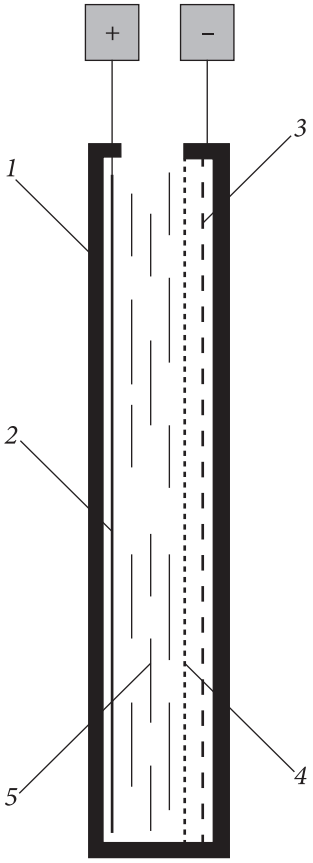

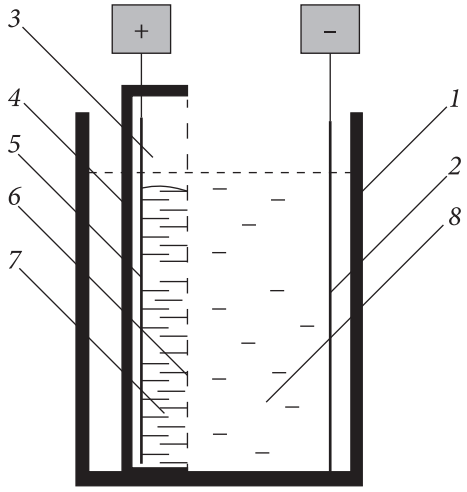

Fig. 3.27. Scheme of a cassette electrochemical reactor with a vertical arrangement of electrodes: *1* — housing, *2* — cathode, *3* — cassette, *4* — cassette housing, *5* — anode, *6* — separator cover, *7* — CNTs, *8* — electrolyte

◄

Fig. 3.28. Scheme of a vertical electrochemical reactor: *1* — housing, *2* — anode, *3* — cathode, *4* — separator (membrane), *5* — CNTs [92]

It consists of a rectangular polypropylene housing *1*, in which cathode *2*, made of a stainless steel sheet and inverted by a fabric of the membrane-separator (polypropylene fabric for filters) stands vertically. Anode *5*, made of stainless steel sheet (99.4% pure iron), is also placed vertically in the reactor vessel. The open side of the cassette body is not covered. The space between anode and cathode is filled with a mixture of CNTs with sulfuric acid in a mass ratio of about 1 : 2. The width of the gap between the electrodes is ~20 mm.

The surface condition of washed and dried CNTs was studied by chemical microtiter and X-ray photoelectron spectroscopy. The specific surface area was determined by nitrogen adsorption-desorption after drying at 120 °C for 30 min. Dependences of the oxygen content, obtained from XPS O1s spectra, and specific surface area, determined by the nitrogen adsorption-desorption method, on the amount of transmitted electricity are shown in Fig. 3.29.

As seen, they are opposite: the increase in the amount of oxygen corresponds to the decrease in the specific surface area in the studied range of transmitted electricity.

The relative distribution between different types of oxygen-containing centers, calculated according to the schedule of the C 1s spectrum, for the original CNTs and after oxidation via passing 120 A · h/kg of electricity is given in Table 3.11. Obviously, the oxidation of CNT leads to an increase in the bonds C—OH and C=O.

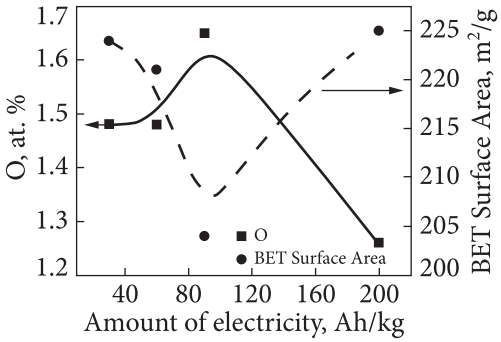

Fig. 3.29. Dependence of oxygen content from O1s XPS spectra and specific surface area from nitrogen adsorption-desorption on the amount of electricity passed

Changes in the structural state of CNTs under oxidation were studied by the method of Raman scattering. The Raman spectra of CNTs were recorded using a T-64000 Horiba Jobin-Yvon spectrometer in combination with the backscattering geometry at room temperature under excitation with an argon laser (λ = 488 nm, 1 mV). As a reference for calibration of the wavelength, the Raman band of silicon at

Table 3.11. **Relative content of oxygen-containing groups,%**

CNT Sample	E_b = 286.1–286.3 eV (C—OH)	E_b = 287.3–287.6 eV (C=O)	E_b = 288.4–288.9 eV (C—OOH)	E_b = 290.4–290.8 eV (CO, CO_2)
Initial	49.1	17.2	17.2	16.5
120 A · h/kg	53.8	19.8	13.6	12.8

Table 3.12. **The main parameters of characteristic bands manifested in the micro-Raman spectra of CNTs of different oxidation states**

Sample	1	2	3	4	5
Synthesis conditions	120 A · h/kg	90 A · h/kg	60 A · h/kg	30 A · h/kg	Initial CNTs
D, cm^{-1}	1352	1350	1350	1352	1348
G, cm^{-1}	1583	1576	1574	1576	1573
2D, cm^{-1}	2711	2700	2703	2700	2706
D_{FWHM}, cm^{-1}	55	48	52	25	51
G_{FWHM}, cm^{-1}	59	58	58	57	53
I_D, a.u.	11.78	12.18	11.24	12.3899	9.0
I_G, a.u.	11.34	14.37	11.85	13.63036	10.4
I_D/I_G	1.04	0.84	0.95	0.96	0.86

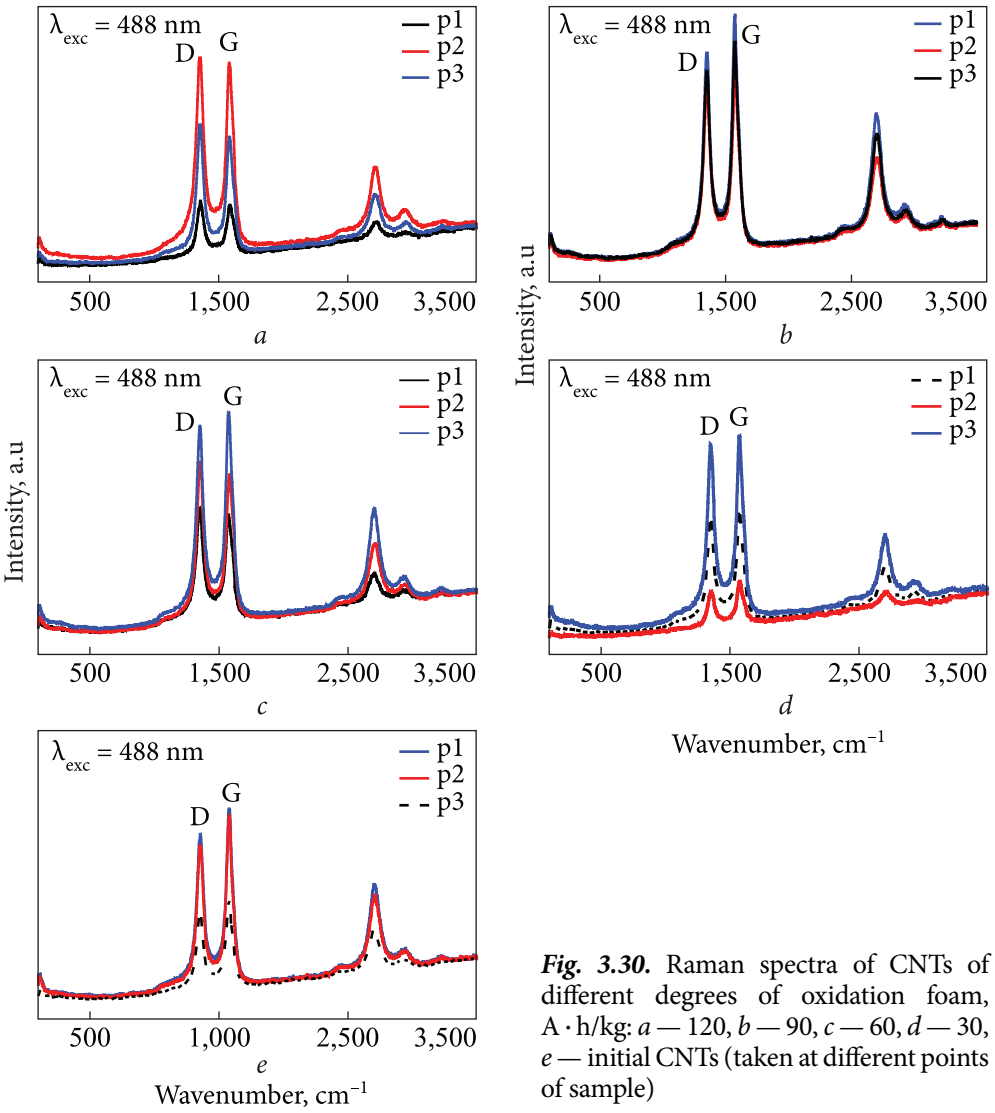

Fig. 3.30. Raman spectra of CNTs of different degrees of oxidation foam, A · h/kg: *a* — 120, *b* — 90, *c* — 60, *d* — 30, *e* — initial CNTs (taken at different points of sample)

520 cm^{-1} was used. The experimental error in determining the wavelength of the reflected radiation due to sample heterogeneity was ±2 cm^{-1}.

Fig. 3.30 shows the Raman spectra of CNTs with different degrees of oxidation. They are characteristic for multiwall CNTs.

Table 3.12 and Fig. 3.30 show the main parameters of characteristic bands manifested in the micro-Raman spectra of CNTs with different degrees of oxidation.

The G-band (the so-called "graphite" mode of symmetry E_{1g} at the G-point of the Brillouin zone) was recorded at 1573 cm^{-1} for the original CNTs, which corresponds to the tangential oscillations of carbon atoms in graphene layer

rings [93]. The D-band at 1348 cm^{-1} was also recorded for the original CNTs, which characterizes the disorder in graphene multilayer structures and is absent for an ideal hexagonal graphite lattice [94]. This mode corresponds to the "breathing" oscillations of graphene layer rings at the point K of the Brillouin zone. The relative intensities and full width at half maximum (FWHM) of the D and G bands reflect the degree of ordering of graphite-like structure (expansion of the bands corresponds to a greater degree of disorder).

As follows from Fig. 3.30 and Table 3.12, the intense G-mode for the original CNTs is slightly higher than the intense D-band and this relationship persists until oxidation at 90 A · h/g, indicating a slight disorder of the structure requiring defects. At a low content of defects, which include the ideal packing of layers in highly oriented-new graphics, the D-band is not observed. Only 120 A · h/kg of electricity changes the intensity ratio: the D-bands become higher. Naturally, I_D/I_G is smaller up to 90 A · h/kg and becomes larger under conditions of transmission of 120 A · h/kg of electricity.

If the FWHM of line D remains almost unchanged, then as the degree of oxidation of the G-band nitrogen becomes larger and there is a shift towards higher frequencies, the defectiveness of the CNTs increases.

The second-order vibration mode D (2D band) is recorded for CNTs in the range of 2700…2711 cm^{-1} with a higher intensity than usual [95] and is observed for the second-order vibration. This may indicate the similarity of carbon nanostructures, which show a strong electron-phonon interaction and a strong dispersion dependence of the D-mode. More conductive materials have a stronger electron-phonon interaction than semiconductors.

Single-wall carbon nanotubes have a low-frequency high-intensity mode, which, according to [96], is associated with oscillations of the tube as a whole a noticeable intensity of the low-frequency mode, which has a maximum at ~100 cm^{-1}, which obviously indicates the presence of single- and double-wall CNTs in the samples, is also characteristic for the multiwall CNTs studied.

3.5.3. Modification of CNTs with nitrogen

Carbonaceous materials have been popular for the oxygen reduction reaction, in particular in developing catalytic systems. Carbon nanotubes attract more and more attention due to their outstanding mechanical, physical and chemical properties. As known, CNTs are found to show catalytic properties. Additional treatment, namely functionalization and doping with heteroatoms, modifies the CNTs electronic system, facilitates the electron transfer, and in this way increases the oxygen electro-reduction reaction [97—99]. Oxidation is the most common method of chemical modification of CNTs. As a result of such treatment, different oxygen content groups are formed on the surface of

Fig.3.31. Scheme of growth of nitrogen-containing CNTs: *a* — a "top" model of CNT growth; *b* — a "root" model of CNT growth

CNTs. Most often carboxyl, hydroxyl, carbonyl, and lactone groups are observed on the surface of oxidized CNTs. In order to accelerate the activity and stability against degradation, the introduction of nitrogen, sulfur, boron, or phosphorus atoms to the nanotube structure has been proposed [100, 101]. As a rule, nitrogen doping is carried out by using two methods. The first one is the CNTs doping during their synthesis by arc or chemical vapor deposition. The second one is the doping of pre-synthesized CNTs through their treatment by nitrogen-enriched precursors (urea, melamine, pyridine, ammonia, *etc.*) [102—104].

Nitrogen atoms are similar to carbon ones by size, consequently, such atoms successfully replace the carbon ones in crystal lattice [102, 105]. The π-electrons of carbon atoms conjugate with unshared electron pairs of nitrogen atoms [104, 105], built into the carbon lattice. In this case, nitrogen exhibits the properties of an electron donor in relation to carbonaceous material [106]. Nitrogen on the surface of carbon material is represented by a variety of forms (pyridine, pyrrole, *etc.*) [102—108].

Based on the model representations of CVD synthesis of CNTs by analogy, a model scheme of growth of nitrogen-containing CNTs was constructed.

First, the metal particles of the catalyst are distributed and retained on the substrate, taking a spherical or pear-shaped shape. Deposition of carbon atoms occurs only on half the surface of the particles (this is the lower curved side of the pear-shaped particles of the catalyst). Carbon atoms diffuse in the direction of the content gradient and are deposited on the half area located around and below the diameter that halves the particle. However, they do not settle in the hemisphere, which leads to the formation of an empty core of the tube. In summary, it can be argued that nanotube filaments are formed on metal particles either by "extrusion, also known as base or root growth", in which CNTs grow starting from the metal particle that remains in contact with the substrate (Fig. 3.31, *b*), or by the growth mechanism that looks so that the metal particle detaches from the substrate and is held on top of the growing nanotube (Fig. 3.31, *a*).

Carbon and nitrogen atoms involved in the growth of nitrogen-containing CNTs are formed by thermal decomposition of nitrogen-containing volatile organic compounds such as acetonitrile and ethylenediamine:

$$2CH_3{-}C{\equiv}N \rightarrow 4C + 2N + 3H_2;$$

$$NH_2{-}CH_2{-}CH_2{-}NH_2 \rightarrow 2C + 2N + 4H_2.$$

The carbon and nitrogen formed are dissolved in the molten metal particle of the catalyst, after which they participate in the nanotube formation as shown in Fig. 3.31. Nitrogen atoms are embedded in the graphene plane of the CNT wall, replacing carbon atoms, and can be in different states: pyridine, quaternary or pyrrole. The hydrogen formed leaves the reactor together with the remains of

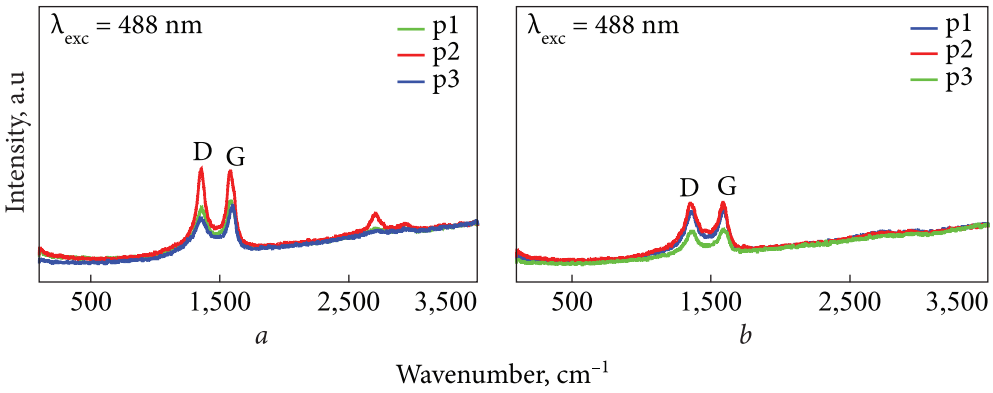

Fig. 3.32. Raman spectra of samples of CNTs modified with nitrogen in the amount of: *a* — 10% wt.; *b* — 20% wt., taken at three different points

undecomposed raw materials and decomposition by-products (various hydrocarbons, ammonia, molecular nitrogen, dicyan).

Modification of CNTs obtained from propylene was performed by injecting acetonitrile in the liquid state into a stream of argon carrier gas saturated with propylene and hydrogen, which was fed to the CNTs synthesis reactor.

It is usually difficult to predict how the reaction will proceed in such a system, however, the inclusion of nitrogen in the hexagonal lattice of CNTs should lead to certain changes in the physicochemical properties of CNTs. Table 3.13 shows a protocol for determining the value of the specific surface area of the samples obtained as described above.

As seen, the specific surface area of CNTs modified with acetonitrile decreases from 310 ± 3 m^2/g, the typical value of the specific structure of CNT kept under standard conditions, to 174 and 144 m^2/g during the change of increasing nitrogen content from 10% wt. to 20% wt.

The curves of the Raman spectra change significantly (Fig. 3.32), and their intensity decreases sharply.

Table 3.14 shows the main parameters of the characteristic bands that appear in the micro-Raman spectra of CNTs obtained with the participation of acetonitrile. As compared with the parameters of Raman spectra for the original CNTs and their oxidized forms (Table 3.12), the frequency of the D-band (1353 cm^{-1} for both samples) is significantly higher relative to the original CNTs (1348 cm^{-1}) and close to the values of the D-band for CNTs with the highest degree of oxidation.

Similarly, the frequency of the G-band for both samples increases compared to the original CNTs, and it is higher for the sample with a calculated content of 20% wt. nitrogen. This indicates a strong tension of the CNT lattice, which can be related to the nitrogen embedded in the CNT "body".

undecomposed raw materials and decomposition by-products (various hydrocarbons, ammonia, molecular nitrogen, dicyan).

Modification of CNTs obtained from propylene was performed by injecting acetonitrile in the liquid state into a stream of argon carrier gas saturated with propylene and hydrogen, which was fed to the CNTs synthesis reactor.

It is usually difficult to predict how the reaction will proceed in such a system, however, the inclusion of nitrogen in the hexagonal lattice of CNTs should lead to certain changes in the physicochemical properties of CNTs. Table 3.13 shows a protocol for determining the value of the specific surface area of the samples obtained as described above.

As seen, the specific surface area of CNTs modified with acetonitrile decreases from 310 ± 3 m^2/g, the typical value of the specific structure of CNT kept under standard conditions, to 174 and 144 m^2/g during the change of increasing nitrogen content from 10% wt. to 20% wt.

The curves of the Raman spectra change significantly (Fig. 3.32), and their intensity decreases sharply.

Table 3.14 shows the main parameters of the characteristic bands that appear in the micro-Raman spectra of CNTs obtained with the participation of acetonitrile. As compared with the parameters of Raman spectra for the original CNTs and their oxidized forms (Table 3.12), the frequency of the D-band (1353 cm^{-1} for both samples) is significantly higher relative to the original CNTs (1348 cm^{-1}) and close to the values of the D-band for CNTs with the highest degree of oxidation.

Table 3.13. **Protocol for determining the specific surface area of CNTs and CNTs modified with nitrogen**

Sample	Weight, mg	Specific surface area, m^2/g	
		Value	Average value
Initial CNTs	22.0 23.2	307 312	310
Initial CNTs purified	21.8 23.4	308 317	313
Initial CNTs «short»	20.7 22.2	274 272	273
CNTs + 10% wt. nitrogen *	24.4 23.4 23.4	177 170 317	174
CNTs + 20% wt. nitrogen *	22.0 22.1 22.2	143 144 272	144

* Calculated data.

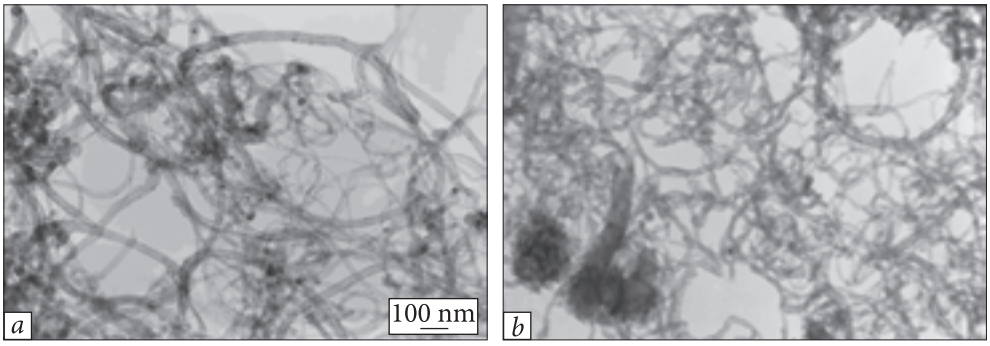

Fig. 3.33. TEM images of CNTs: *a* — initial; *b* — synthesized with acetonitrile

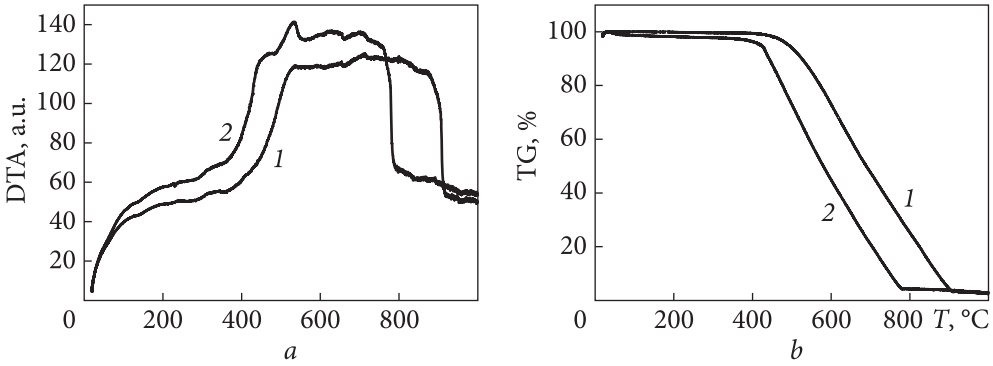

Fig. 3.34. CNT derivatograms: *a* — DTA; *b* — TG; *1* — initial CNTs, *2* — synthesized with acetonitrile (20% wt. nitrogen according to the calculated estimate)

Table 3.14. **The main parameters of the characteristic bands manifested in the micro-Raman spectra of CNTs obtained with the participation of acetonitrile**

Parameters	Number samples	
	1	2
Synthesis conditions	Catalyst Al–Fe–Mo–O, T_{synth} = 650 °C	
	10% wt. nitrogen *	20% wt. nitrogen *
D, cm^{-1}	1353	1353
G, cm^{-1}	1580	1585
2D, cm^{-1}	2705	—
D_{FWHM}, cm^{-1}	80	112
G_{FWHM}, cm^{-1}	75	108
I_D, a. u.	5.0	3.1
I_G, a. u.	4.7	3.0
I_D/I_G	1.06	1.03

* Calculated data.

Similarly, the frequency of the G-band for both samples increases compared to the original CNTs, and it is higher for the sample with a calculated content of 20% wt. nitrogen. This indicates a strong tension of the CNT lattice, which can be related to the nitrogen embedded in the CNT "body".

In the Raman spectra for nitrogen-modified CNTs, the FWHM of the G-band and D-band increases significantly compared to the original CNTs and even to the CNTs having a high degree of oxidation, which indicates a significant disorder of the structure of this product.

TEM images of the original and nitrogen-modified CNTs are shown in Fig. 3.33. It can be argued with some stretch that synthesis involving nitrogen compounds increases the fragmentation of CNTs.

A comparison of nitrogen-modified derivatograms and initial nanotubes is demonstrated in Fig. 3.34.

It should be noted that the yield of CNTs per unit mass of catalyst used in the synthesis, i.e. acetonitrile, decreased significantly. Therefore, the next step was to increase the synthesis temperature by 100 °C, i.e. up to 750 °C. The synthesis was carried out using 100% acetonitrile and 100% ethylenediamine as a hydrocarbon source at a temperature up to 750 °C on the Al-Fe-Mo-O catalyst.

TEM images of the product obtained with acetonitrile and ethylenediamine are shown in Figs. 3.35 and 3.36, respectively. As seen, the synthesized filamentous formations have a pronounced fragmentary structure.

If we turn to the classification of nanosized carbon filamentous structures, according to [109], the resulting structures can be attributed to bamboo-like nanofibers or carbon nanotubes with spherical sections.

As follows from the DTA diagrams (Fig. 3.37), intensive oxidation of nitrogen-containing structures begins 100 °C earlier than that of the original CNTs. However, the heat capacity of this process is significantly higher than for the former.

In other studies, in which nanosized carbon materials with nitrogen inclusion were obtained by CVD: decomposition of ethylene-ammonia mixtures on metal catalysts [110], pyrolysis of xylene/pyridine and ferrocene [111] according to the modified feed technology of the precursor, from acetonitrile [108], pyridine or N, N-dimethylformamide with a Fe-, Co- or Ni catalyst in the temperature range (823—1123) K, similar structures were also observed. Moreover, the authors in [110] in N-CNTs recorded a uniform distribution of nitrogen and the formation of ordered defects. According to the performed structural modeling, the ordered defects contain four carbon vacancies and pyridine-like nitrogen. On the contrary, it was found that N-CNFs (carbon fibers) have an uneven distribution of nitrogen; their structural defects are disordered and also contain pyridine-like nitrogen. In [111], it is noted that the system creates a nitrogen content gradient that modifies the CNTs from the hollow cylinder to a bamboo-like structure containing

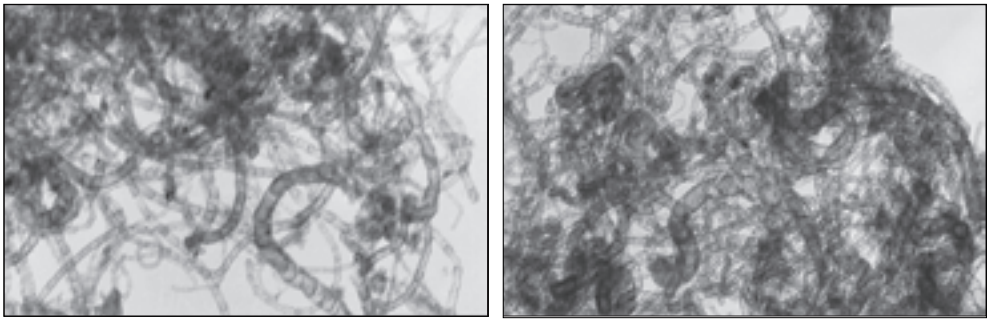

Fig. 3.35. TEM images of the product obtained using 100% acetonitrile

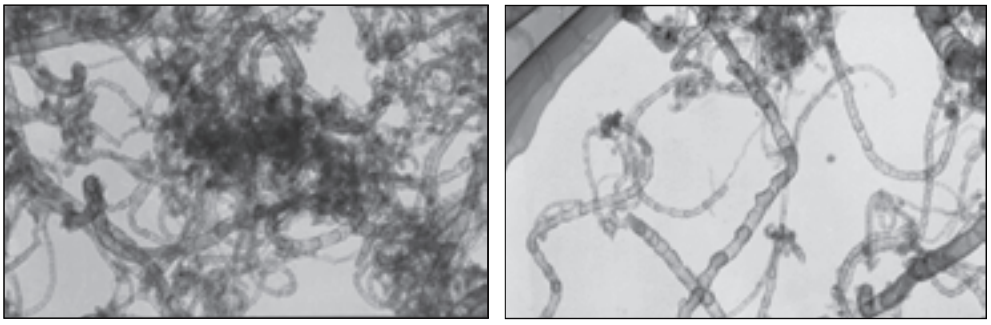

Fig. 3.36. TEM image of the product obtained using 100% ethylenediamine

a number of compartments, the lengths of which gradually decrease as the nitrogen content increases.

Physicochemical properties of the obtained N-CNTs, such as C/N ratio or type of nitrogen, are related to the synthesis parameters. The authors [110] found that the C/N ratio increases with increasing temperature, which may be due to the thermodynamic stability of metal carbides and metal nitrides. Also, the type of nitrogen present in the graphene layer changed with increasing temperature from mainly pyridine to Quaternary nitrogen. N-CNTs prepared with Fe-catalyst showed bamboo morphology regardless of C/N source or growth temperature, whereas straight tubes were obtained with Co or Ni catalyst. The authors [110] suggest that this difference in morphology can be explained by the thermodynamic stability of different metal carbides, which leads to a "pulsating" growth for the case of Fe in contrast to the more continuous growth in the case of Co or Ni catalysts.

The aim of our work [112] was to synthesize nitrogen-containing CNTs by various methods, investigate their structure characteristics, and study the catalytic properties of N—CNTs. For comparison with the N—CNTs samples described above, one sample of nitrogen-containing CNTs was synthesized from

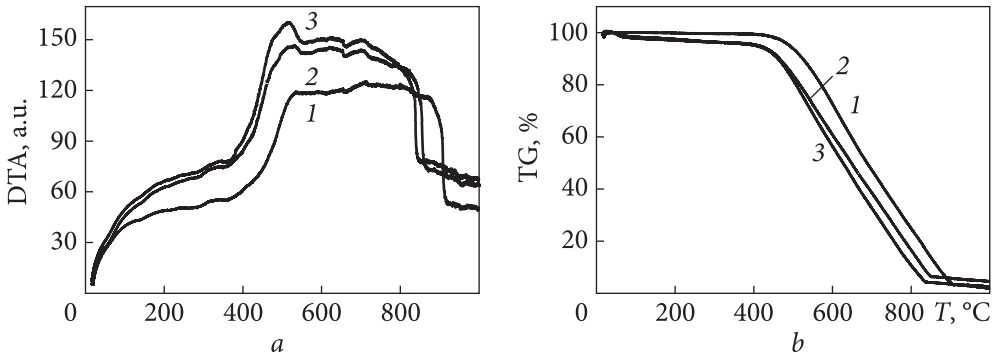

Fig. 3.37. CNTs derivatograms: *a* — DTA; *b* — TG; *1* — initial CNTs, *2* — synthesized using 100% acetonitrile, *3* — synthesized using 100% ethylenediamine.

the original CNTs by oxidation with nitric acid followed by impregnation with urea (10% wt.) and heat treatment at 700 °C according to the method previously developed for activated carbon [102].

The synthesized N—CNTs contain a certain amount of amorphous carbon and catalyst components. Purification of the original samples was performed by treating them with HCl solutions and NH_4HF_2 followed by washing the reagents with distilled water.

In kinetic experiments, aqueous solutions of hydrogen peroxide with a content of 0.1÷0.5% were used to study the catalytic properties of N—CNTs synthesized from ethylenediamine and 0.2÷1.5% to determine the properties of N-CNTs synthesized from acetonitrile. The experiments were performed at pH 5.0, 6.0, 7.0, and 8.0, which were stabilized with phosphate buffer and at room temperature. Stable suspensions of N-CNTs were used for the reaction.

To perform this, samples were dissolved in phosphate buffer (the volume of the solution varied as dependent on the content of H_2O_2 in the reaction mixture). Hydrogen peroxide was then added to the suspension so that the total volume of the reaction mixture was 50 ml. In the case of N—CNTs, the process of H_2O_2 decomposition was investigated using the microvolumometric method [113]. The experiments were performed in a sealed thermostated cell with stirring connected to a microburette (measurement error 0.01 ml), which was used to measure the microvolumes of oxygen released during the reaction. In the study of catalase activity a standard method for determining the content of H_2O_2, namely titrimetry, was [99, 113], and evaluation of catalytic activity was performed by determining the kinetic characteristics (rate constants, Michaelis constant) of this reaction. To compare the values of the reaction rate constants for all objects, the optimal sample and the optimal range of H_2O_2 contents were chosen, at which the reaction rate linearly depends on the substrate content. To determine the reaction rate constant, the rate of decomposition of hydrogen peroxide at different pH was measured.

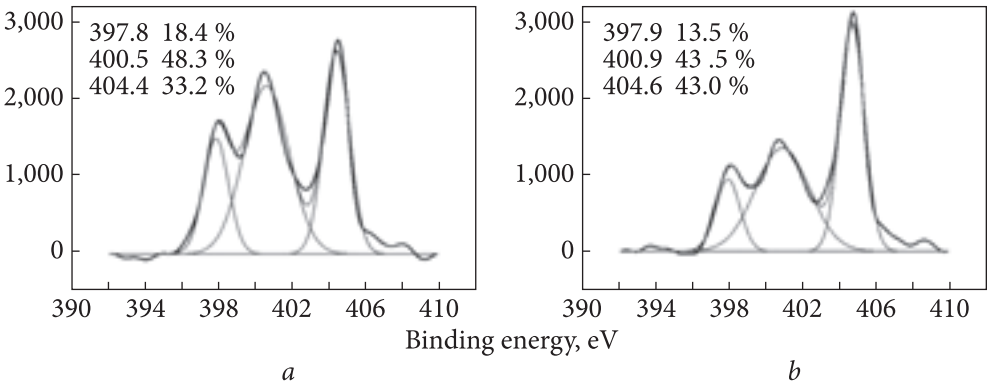

Fig. 3.38. XPS N1*s* spectra of nitrogen-containing CNTs: *a* — synthesized with the participation of ethylenediamine; *b* — synthesized with the participation of acetonitrile [112]

Table 3.15. **Chemical composition of the surface of synthesized nanotubes (% at.) [112]**

Sample	C, % at.	O, % at.	N, % at.
CNTs	98.78	1.22	0.00
N-CNTs (urea)	98.27	1.11	0.62
N-CNTs (acetonitrile)	95.13	1.86	3.22
N-CNTs (ethylenediamine)	93.68	1.65	4.46

Table 3.16. **The content and chemical state of nitrogen and oxygen atoms in CNT depending on the nitrogen-containing compound used for CNT synthesis [112]**

Sample	Pyridinic, % at.	Pyrrolic and quaternary, % at.	N-oxide, % at.	N, % at.
N-CNTs (urea)	51.6	33.9	14.5	0.62
N-CNTs (acetonitrile)	13.5	43.5	43	3.22
N-CNTs (ethylenediamine)	18.4	48.3	33.2	4.46

High-resolution XPS was used to determine the chemical composition of the CNTs surface. The state of the surface of the washed from mineral impurities and dried CNTs was investigated on an XPS spectrometer "SERIES-800" Kratos Analytical using monochromatic MgK_{α}-radiation with an energy of 1253.6 eV.

According to the obtained results (Table 3.15, Fig. 3.38), treatment of oxidized CNTs samples with urea leads to the appearance of 0.6% at. nitrogen in their structure. Despite the fact that the vast majority of nitrogen atoms are on the side surfaces of CNTs, as well as located along the surface.

When modifying CNTs by directly introducing ethylenediamine and acetonitrile in the liquid state into a stream of argon and hydrogen carrier gas, we

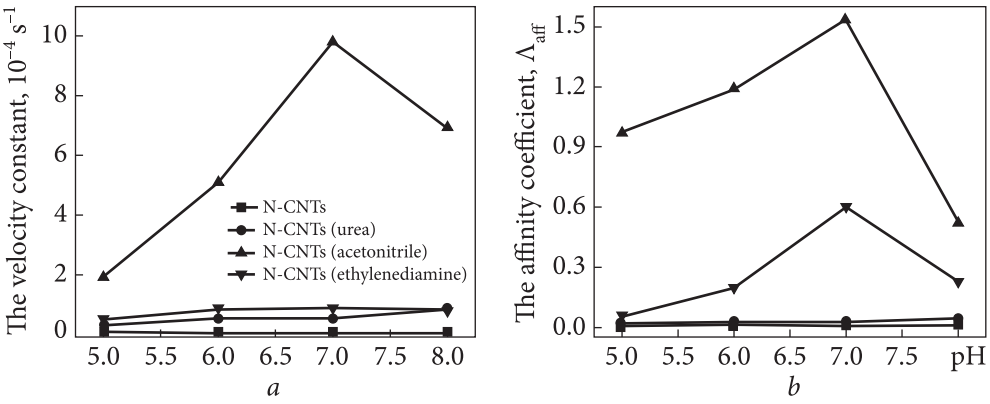

Fig. 3.39. The velocity constant (*a*) and the affinity coefficient A_{aff} (*b*) vs pH for different N—CNTs [112]

observe an increase in the number of nitrogen atoms embedded in the structure of nanotubes. When nitrogen atoms are included in a carbon nanotube (precursor acetonitrile), we observe a 5-fold increase in the heteroatoms and a 7-fold increase in case of precursor ethylenediamine.

From the N1*s* spectra (Fig. 3.38) of the obtained nitrogen-containing CNTs, one can see how the state of nitrogen atoms changes depending on the conditions of their synthesis (Table 3.16)

From the above data, it can be seen that in the direct synthesis of nitrogen-containing CNTs, not only the total content of nitrogen atoms but also the proportion of pyrrolic and quaternary nitrogen increases significantly against the background of a significant decrease in the amount of the pyridinic form. This can be explained by the fact that, in the direct synthesis, nitrogen is uniformly distributed throughout the entire volume of the carbon matrix of CNTs, whereas after CNTs nitriding with urea-predominantly in the surface layers and near defects. Since the pyridinic form is characteristic of the edge arrangement of nitrogen atoms in the graphene plane, it is obvious that for samples with a uniform distribution of nitrogen in the volume, the ratio between pyridinic and pyrrolic/quaternary forms will be shifted towards the latter.

Catalytic properties of N—CNTs. From the data obtained for the catalytic decomposition of hydrogen peroxide on initial and nitrogen-modified CNTs, the reaction rate constants and affinity coefficients were calculated for different pH solutions. Based on these data, the corresponding dependences were built (Fig. 3.39).

The presented dependences show that for all pH values, nitrogen-containing CNTs show greater activity in catalysis of hydrogen peroxide decomposition than unmodified tubes.

The catalytic activity rapidly increases with an increase in the content of nitrogen heteroatoms, which fully corresponds to the theoretical models of the

effect of heteroatoms on the electron-donating properties of the carbon matrix. It should also be noted that nitrogen-containing CNTs reach their maximum catalytic activity at pH values close to 7, which is important for the use of such materials for catalysis in biological media.

From the data obtained, it can be concluded that the method of direct synthesis of nitrogen-containing CNTs makes it possible to obtain more catalytically active carbon nanotubes containing a larger amount of nitrogen, predominantly of the pyrrole and quaternary type. It was found that, regardless of the synthesis method, the maximum catalytic activity in the decomposition of hydrogen peroxide is observed at pH 7.

Conclusions

From the above, we can conclude that the methods of TEM, SEM, XRD, Raman scattering, thermal desorption of argon or nitrogen, X-ray photoelectron spectroscopy, thermogravimetric, and differential thermal analyses have shown that the problem of CNTs synthesis with high structural selectivity (practically with the absence of amorphous carbon) is solved.

This is achieved by using a complex oxide system of gross formula $Al_2O_3(Me_xO_y)MoO_3$, where Me is Fe or Ni with the ratio of the metals (1…3) Al : (1) Fe (Ni) : (0.04…0.2) Mo act as catalysts in the synthesis of CNTs. They can be obtained by co-precipitation from an aqueous solution of a mixture of salts of Al, Fe, and Mo in the presence of carboxylic acid or by an aerosol method where a source is an aqueous solution containing aluminum formates ($(HCOO)_3Al \cdot 3H_2O$), ammonium molybdate ($(NH_4)6Mo_7O_{24} \cdot 4H_2O$), and iron citrate ($C_6H_{11}FeO_{10}$), which are sprayed into a vertical through furnace. CNTs were produced by catalytic precipitation from the gas phase onto a fluidized bed created by the rotating reactor with carbon sources ethylene, propylene, or propane-butane in the temperature range (600…700) °C.

The formation of structural parameters of CNTs (diameter, specific surface area, length, yield, etc.) is set by the adjusting ratio of the active cluster (Fe, Ni) ratio (1…3) Al : Me, hydrolysis and thermal decomposition of Al, Fe, Mo salts of carboxylic acids at different temperatures. These processes are carried out using an electric furnace (aerosol method, temperature ~600 °C), propane-butane burner (T ~(1000…1200) °C), synthesis of complex oxide $SiO_2Al_2O_3(Fe_xO_y)MoO_3$ in a hydrogen burner within ~(1400—1600) °C) and chlorides of the corresponding metals as precursors. As a result, the CNT specific surface area increased from 200 to 400 m^2/g, the average diameter of CNTs decreased from 20…40 nm to 10…15 nm, and 0.4—0.5 kg of stable-quality CNTs was synthesized in a 24 dm^3 reactor for 30—60 min.

The chapter has considered methods of modification of carbon nanotubes with the formation of "carbon-oxygen" bonds such as activation of CNT by a solution

of potassium dichromate in sulfuric acid, anodic oxidation in sulphuric acid; modification with nitrogen in the CVD process with a carbon source of acetonitrile, ethylenediamine or their mixtures with propylene on a complex iron-containing catalyst. A qualitative model of the growth of nitrogen-containing CNTs and the possibility of using them to catalyze enzymatic reactions is proposed.

REFERENCES

1. A.V. Melezhik, Yu. I. Sementsov and V. V. Yanchenko, Russian Journal of Applied Chemistry. **78** (6), 917 (2005).
2. V.V. Yanchenko, O.O. Kovalenko, Yu.I. Sementsov and O.V. Melezhik, Ukraine Patent No. 17386 (15 September, 2006).
3. V.V. Yanchenko, O.O. Kovalenko, Yu.I. Sementsov and O.V. Melezhik, Ukraine Patent No. 17387 (15 September, 2006).
4. V.V. Yanchenko, O.O. Kovalenko, Yu.I. Sementsov and O.V. Melezhik, Ukraine Patent No. 83532 (25 July, .2008).
5. V.V. Yanchenko, Yu.I. Sementsov and O.V. Melezhik, Ukraine Patent No. 69291 (12 November, 2007).
6. A.A. Volodin, P.V. Fursikov, A.V. Ivanov et al., in: *VIII International Conference Hydrogen materials science and chemistry of carbon nanomaterials,* edited by D.V. Schur, S.Yu. Zaginaichenko and T.N. Veziroglu (IAHE, Kiev, 2003), pp. 476—477.
7. L.B. Avdeeva and V.A. Likholobov, RF Patent No. 2146648 (20 March, 2000).
8. D. Moy and A. Chishti, US Patent Application No. 20060239897 (26 October, 2006).
9. Z. Zhou, L. Ci, X. Chen, D. Tang, D. Liu, Y. Liang, H. Yuan, W. Zhou, G. Wang and S. Xie, Carbon. **41** (2), 337 (2003).
10. Z. Zhou, L. Ci, L. Song, X. Yan, D. Liu, H. Yuan, Y. Gao, J. Wang, L. Liu, W. Zhou, G. Wang and S. Xie, Carbon. **41** (13), 2607 (2003).
11. D. Moy and A. Chishti, US Patent Application No. 20010014307 (16 August, 2001).
12. A. Tarafdar, A.B. Panda and P. Pramanik, Microporous and Mesoporous Materials. **84**, 223 (2005).
13. F. Fajula, A. Galarneau and F. Di Renzo, Microporous and Mesoporous Materials. **82**, 227 (2005).
14. B.F. Chmelka, J. Nolla, C.A. Steinbeck, G.L. Athens and D. Wildemuth, US Patent Application No. 20070248760 (25 October, 2007).
15. A. Harutyunyan, E. Mora and T. Tokune, US Patent Application No. 20060228289 (12 October, 2006).
16. Z. Ren, J.G. Wen, J.Y. Lao, W. Li and S. Chen, US Patent Application No. 20060057050 (16 March, 2006).
17. E. Flahaut, Ch. Laurent, and A. Peigney, Carbon. **43** (2), 375 (2005).
18. Y. Soneda, L. Duclaux, and F. Beguin, Carbon. **40** (6), 965 (2002).
19. A. Harutyunyan, L. Grigorian and T. Tokune, US Patent No. 6974492 (13 December, 2005).
20. Yu.I. Sementsov, A.V. Melezhyk, G.P. Prykhodko, N.A. Havryliuk, M.L. Piatkovskyi and V.V. Yanchenko, in: *Physico-chemistry of nanomaterials and supramolecular structures*, edited by A.P. Shpak, P.P. Gorbik (Naukova dumka, Kyiv, 2007), vol. 2, pp. 116—158.

21. E. O. Koval'ska, Yu. I. Sementsov, M. T. Kartel and G. P. Prikhod'ko, Himia, Fizika ta Tehnologia Poverhni. **3** (3), 335 (2012).
22. V.V. Brei, Theoretical and Experimental Chemistry. **41** (3), 165 (2005).
23. A.V. Melezhyk, V.V. Yanchenko and Yu.I. Sementsov, in: *Hydrogen materials science and chemistry of carbon nanomaterials*, edited by T.N. Veziroglu, S.Yu. Zaginaichenko, D.V. Schur, B. Baranowski, A.P. Shpak, V.V. Skorokhod and A. Kale (Springer, Dordrecht, 2007), pp. 529—537.
24. A. Corma, Chem. Rev. **95** (3), 559 (1995).
25. E.O. Koval'ska, S.V. Zhuravskyi, Yu. I. Sementsov and G. P. Prikhod'ko, in: *Ukrainian conference with international participation of young scientists "Chemistry, physics surface technology": Book of Abstract* (Kyiv, 2012), pp. 13—14.
26. V.O. Khavrus, N.V. Lemesh, S.V. Gordijchuk, A.I. Tripolsky, T.S. Ivashchenko and P.E. Strizhak, Physics and chemistry of solid state. **10** (2), 417 (2009).
27. E.O. Koval'ska, Yu. I. Sementsov and G. P. Prikhod'ko, Ukraine Patent No. 70847 (25 June, 2012).
28. S. Rajagopal, D. Nataraj, O. Yu. Khyzhun, Yahia Djaoued, Jacques Robichaud, K. Senthild and D. Mangalaraj, Cryst.Eng.Comm. **13** (7), 2358 (2011).
29. W.Z. Qian, T. Liu, Fei Wei, ZW Wang, G. Luo, Hao Yu and Z.F. Li, Carbon. **41** (13), 2613 (2003).
30. S.-G. Yu, W.-K. Yi, J.-H. Lee, Y.-W. Jin and T.-W. Jeong, United States Patent Application No. 20030141179 A1 (July 31, 2003).
31. F.R. García-García, M. Pérez-Cabero, D.M. Nevskaia, I. Rodríguez-Ramos and A. Guerrero-Ruiz, Catalysis Today. **133-135** (4-6), 815 (2008).
32. M.Corriasa, B.Caussat, A.Ayral, J.Durand, Y.Kihn, Ph.Kalck and Ph.Serp, Chem. Eng. Sci. **58** (19), 4475 (2003).
33. Y.-L. Li, I.A. Kinloch, M.S.P. Shaffer, J. Geng, B. Johnson and A.H. Windle, Chem. Phys. Lett. **384** (1-3), 98 (2004).
34. F. Wei, Q. Zhang, W.-Z. Qian, H. Yu, Y. Wang, G.-H. Luo, G.-H. Xu and D.-Z. Wang, Powd. Techn. **183** (1), 10 (2008).
35. A.V. Melezhik, Yu. I. Sementsov and V.V. Yanchenko, Russian Journal of Applied Chemistry. **78** (6), 924 (2005).
36. Y. Yang, M.P. Grosboll and K.A. Smith, United States Patent Application No. 20050074392 A1 (April 7, 2005).
37. A. Harutyunyan, United States Patent Application No. 20050123467 A1 (June 9, 2005).
38. D. Moy and A. Chishti, US Patent No. 6,221,330 (April 24, 2001).
39. R.E. Smalley, R.H. Hauge, P.A. Willis and W.C. Kittrell, US Patent Application No. 2002/0102203 A1 (August 1, 2002).
40. I.M. Glikina, V.S. Novitskiy, N.F Tyupalo and M.A. Glikin, Khim. prom. Ukrainy. (3), 24 (2003) [in Russian].
41. V.V. Yanchenko, Yu.I. Sementsov and O.V. Melezhik, Ukraine Patent No. 15733 (17 July, 2006) (utility model) [in Ukrainian].
42. A. Harutyunyan and S. Isobe, US Patent Application No. 20050121545 A1 (June 9, 2005).
43. D. Moy and A. Chishti, US Patent Application No. 20030190277 A1 (October 9, 2003).
44. P.M. Ajayan, B. Wei, H. Zhu, C. Xu and D. Wu, US Patent Application No. 20030161950 A1 (August 28, 2003).

45. S. Maruyama and S. Chiashi, US Patent Application No. 20060073275 A1. (April 6, 2006).
46. R. Smalley and R.H. Hauge, US Patent Application No. 20030147802 A1 (August 7, 2003).
47. D. Moy and A. Chishti, US Patent No. 7097821 (August 29, 2006).
48. D. Moy and A. Chishti, US Patent No. 7144564. (December 5, 2006).
49. D. Moy and A. Chishti, US Patent No. 7074379 (July 11, 2006).
50. O.T. Heyning, P. Bernier and M. Glerup, Chem. Phys. Lett. **409** (1-3), 43 (2005).
51. A.G. Nasibulin, A. Moisala, D.P. Brown, H. Jiang and E.I. Kauppinen, Chem. Phys. Lett. **402** (1-3), 227 (2005).
52. A.G. Nasibulin, P.V. Pikhitsa, H. Jiang and E.I. Kauppinen, Carbon. **43** (13), 2251 (2005).
53. A. Moisala, A.G. Nasibulin, S.D. Shandakov, H. Jiang and E.I. Kauppinen, Carbon. **43** (10), 2066 (2005).
54. A.G. Nasibulin, D.P. Brown, P. Queipo, David Gonzalez, H. Jiang and E.I. Kauppinen, Chem. Phys. Lett. **417** (1-3), 179 (2006).
55. K. Edgar and J.L. Spencer, Curr. Appl. Phys. **4** (2-4), 121 (2004).
56. M. Pinault, M. Mayne-L'Hermite, C. Reynaud, O. Beyssac, J.N.Rouzaud and C.Clinard, Diamond Relat. Mater. **13** (4-8), 1266 (2004).
57. R.L. Vander Wal and T.M. Ticich, Chem. Phys. Lett. **336** (1-2), 24 (2001).
58. A. Barreiro, C. Kramberger, M.H. Rummeli, A. Grüneis, D. Grimma, S. Hampel, T. Gemming, B. Büchner, A. Bachtold and T.Pichler, Carbon. **45** (1), 55 (2007).
59. F. Iskandar, S.-G. Kim, A.B.D. Nandiyanto, Y. Kaihatsu, T. Ogi and K. Okuyama, Journal of Alloys and Compounds. **471** (1-2), 166 (2008).
60. S.H. Kim and M.R. Zachariah, Mater. Lett. **61** (10), 2079 (2007).
61. M. Gulas, M. Caplovicova, M. Michalka, F.Le Normand, M. Rayar, P. Macko and P. Veis, Vacuum, **82** (8), 805 (2008).
62. M. Pinault, M.Mayne-L'Hermite, C. Reynaud, V.Pichot, P.Launois and D.Ballutaud, Carbon. **43** (14), 2968 (2005).
63. A.A. Koos, M. Dowling, K. Jurkschat, A. Crossley and N. Grobert, Carbon, **47** (1), 30 (2009).
64. Y. Yao, L.K.L. Falk, R.E. Morjan, O.A.Nerushev and E.E.B.Campbell, Carbon. **45** (10), 2065 (2007).
65. M. Mayne, N. Grobert, M. Terrones R.Kamalakaran, M.Rühle, H.W.Kroto and D.R.M.Walton, Chem. Phys. Lett. **338** (2-3), 101 (2001).
66. V.O. Khavrus, A. Leonhardt, S. Hampel, C. Täschner, C. Müller, W. Gruner, S. Oswald, P.E.Strizhak and B.Büchner, Carbon. **45** (15), 2889 (2007).
67. A. Moisala, A.G. Nasibulin, D.P. Brown, H. Jiang, L. Khriachtchev and E. I.Kauppinen, Chem. Eng. Sci. **61** (13), 4393 (2006).
68. M. Glerup, H. Kanzow, R. Almairac, M. Castignolles and P. Bernier, Chem. Phys. Lett. **377** (3-4), 293 (2003).
69. V.V. Yanchenko, Yu.I. Sementsov and O.V. Melezhik, Ukraine Patent No. 69292 A (16 August, 2004) [in Ukrainian].
70. A.P. Shpak, Yu.A. Kunitskii and V.L. Karbovskii, *Cluster and nanostructured materials* (Akademperiodika, Kyiv, 2001), vol.1. [in Rassian]
71. M. Damnjanovic, I. Milosevic, T. Vukovc and R. Sredanovic, Phys. Rev B. **60** (4), 2728 (1999).
72. O.E Alon, Phys Rev B. **63**, 201403(R) (2001).

73. E. Dobardžić, I. Milošević, B. Nikolić, T. Vuković, and M. Damnjanović, Phys.Rev.B. **68**, 045408 (2003).
74. A.V. Eletskii, Phys. Usp. **40** (9), 899 (1997).
75. A.V. Eletskii, Phys. Usp. **47** (11), 1119 (2004).
76. A.V. Eletskii, Phys. Usp. **45** (4), 369 (2002).
77. Yu.E. Lozovik and A.M. Popov, Phys. Usp. **40** (7), 717 (1997).
78. V.I. Trefilov, D.V. Schur, B.P. Tarasov, Yu.M. Shul'ga, A.V. Chernogorenko, V.K. Pishuk and S.Yu. Zaginaichenko, editors, *Fullereny — osnova materialov budushchego* (ADEF—Ukraine, Kyiv, 2001) [in Russian].
79. A. Thess, R. Lee, P. Nikolaev, H. Dai, P. Petit, J. Robert, C. Xu, Y. H. Lee, S. G. Kim, A.G. Rinzler, D.T. Colbert, G.E. Scuseria, D. Tománek, J.E. Fischer and R.E. Smalley, Science. **273** (5274), 483 (1996).
80. D. Reznik, C.H. Olk, D.A. Neumann and I.R.D. Copley, Phys. Rev.B. **52** (1), 116 (1995).
81. Yu.I. Sementsov, A.V. Melezhyk, M.L. Pyatkovsky, V.V. Yanchenko, N.A. Gavrilyuk, G.P. Prikhod'ko, A.I. Senkevich, S.L. Revo and E.A. Ivanenko, in: *Hydrogen materials science and chemistry of carbon nanomaterials*, edited by T.N. Veziroglu, S.Yu. Zaginaichenko, D.V. Schur, B. Baranowski, A.P. Shpak, V.V. Skorokhod and A. Kale (Springer, Dordrecht, 2007), pp. 713.
82. V. Dyyakon, O.P. Dmytrenko, M.P. Kulish, Yu.I. Sementsov, N.A. Gavrylyuk, M.M. Byelyi, Yu.E. Grabovskyi, V.B. Molodkin and G.P. Prykhod'ko, Nanosistemi, Nanomateriali, Nanotehnologii. **5** (1), 233 (2007) [in Ukrainian].
83. O. Zhou, R.M. Fleming, D.W. Murphy, C.H. Chen, R.C. Haddon, A.P. Ramirez and S.H. Glarum, Science. **263** (5154), 1744 (1994).
84. F. Sánchez-Bajo, A.L. Ortiz and F.L. Cumbrera, Acta Materialia. **54** (1), 1 (2006).
85. M. Profeta and F. Mauri, Phys Rev.B. **63**, 245415 (2001).
86. M. Souza, A. Yorio, C. Fantini, B.R.A. Neves, M.A. Pimenta, R. Saito, A. Ismach, E. Joselevich, V.W. Brar, Ge. G. Samsonidze, G. Dresselhaus, and M. S. Dresselhaus, Phys. Rev.B. **69**, 241403(R) (2004).
87. V.I. Nefedov, *Rentgenofotoelektronnaya spektroskopiya khimicheskikh soyedineniu. Directory* (Khimiya, Moscow, 1984) [in Russian].
88. Z.R. Yue, W. Jiang, L. Wang, S.D. Gardner and C.U. Pittman, Carbon. **37** (11), 1785 (1999).
89. H.P. Boehm, Carbon. **40** (2), 145 (2002).
90. V.V. Garbuz and V.V. Zakharov, Nanostrukturnoye materialovyedyeniye. (1), 74 (2007) [in Russian].
91. V.V. Garbuz, V.V. Zakharov, L.N. Kuz'menko and S.V. Nuzhd, in: *IX International Conference Hydrogen materials science and chemistry of carbon nanomaterials. Abstract books*, edited by D.V. Schur, S.Yu. Zaginaichenko and T.N. Veziroglu (IAHE, Kyiv, 2005), pp. 704—705.
92. Yu.I. Sementsov, S.L. Revo, K.O. Ivanenko and S. Hamamda, *Expanded graphite and its composites,* edited by M.T. Kartel (Akademperiodika, Kyiv, 2019).
93. R. J. Nemanich and S. A. Solin, Phys. Rev. B. **20** (2), 392 (1979).
94. G.I. Dovbeshko, O.P. Gnatyuk, A.A. Nazarova, Yu.I. Sementsov and E.D. Obraztsova, Fullerenes, nanotubes, and carbon nanostructures. **13** (1), 393 (2005).
95. C.S.S.R Kumar, editor, *Raman Spectroscopy for Nanomaterials Characterization*, (Springer-Verlag, Berlin-Heidelberg, 2012). DOI: 10.1007/978-3-642-20620-7.
96. M.S. Dresselhaus and G. Dresselhaus, Adv. Phys. **51** (1), 1 (2002).

97. M.M. Brzhezinskaya, E.M. Baitinger, E.A. Belenkov and L.M. Svirskaya, Phys. Solid State. **55** (4), 850 (2013).
98. D.S. Su, S. Perathoner and G. Centi, *Chem. Rev.* **113** (8), 5782 (2013).
99. K. Voitko, A. Tóth, E. Demianenko, G. Dobos, B. Berke, O. Bakalinska, A. Grebenyuk, E. Tombácz, V. Kuts, Yu. Tarasenko, M. Kartel and K. László, J. Colloid Interface Sci. **437**, 283 (2015).
100. Z. Huang, Z. Liao, W. Yang, H. Zhou, C. Fu, Y. Gong, L. Chen and Y. Kuang, Electrochim. Acta. **245**, 957 (2017).
101. T. Maiyalagan, and V.S. Saji, editors, *Electrocatalysis for Low Temperature Fuel Cells: Fundamentals and Recent Trends.* (Wiley-VCH Verlag GmbH & Co, 2017).
102. S.V. Zhuravsky, M.T. Kartel, Yu.O. Tarasenko, S. Villar-Rodil, G. Dobos, A. Toth, J. Tuscon and K. Laszlo, Appl. Surf. Sci. **258** (7), 2410 (2012).
103. S. Ratso, I. Kruusenberg, U. Joost and R. Saar, Int. J. Hydrogen Energy. **41** (47), 22510 (2016).
104. Q. Wei, X. Tong, G. Zhang, J. Qiao, Q. Gong and Sh. Sun, Catalysts. **5** (3), 1574 (2015).
105. R. Arrigo, M. Hävecker, S. Wrabetz, R. Blume, M. Lerch, J. McGregor, E.P.J. Parrott, J.A. Zeitler, L.F. Gladden, A. Knop-Gericke, R. Schlögl and D.Sh. Su, J. Amer. Chem. Soc. **132** (28), 9616 (2010).
106. K.A. Wepasnick, B.A. Smith, J.L. Bitter and D.H. Fairbrother, Anal. Bioanal. Chem. **396** (3), 1003 (2010).
107. L. He, F. Weniger, H. Neumann and M. Beller, Angew. Chem. **55** (41), 12582 (2016).
108. S. van Dommele, A. Romero-Izquirdo, R. Brydson, K.P. de Jong and J.H. Bitter, Carbon. **46** (1), 138 (2008).
109. E.G. Rakov, *Nanotrubki i fullereny*: Uchebn. posobiye (Universityetskaya kniga, Logos, Moscow, 2006) [in Russian].
110. O.Yu. Podyacheva, S.V. Cherepanova, A.I. Romanenko, L.S. Kibis, D.A. Svintsitskiy and A.I. Boronin, Carbon. **122**, 475 (2017).
111. E. Xu, J. Wei, K. Wang, Z. Li, X. Gui, Yi Jia, H. Zhu and D. Wu, Carbon. **48** (11), 3097 (2010).
112. Yu.I. Sementsov, O.A. Cherniuk, S.V. Zhuravskyi, Wang Bo, K.V. Voitko, O.M. Bakalinska and M.T. Kartel, Himia, Fizika ta Tehnologia Poverhni. **12** (2), 135 (2021).
113. K.V. Voitko, D.M. Haliarnyk, O.M. Bakalinska and M.T. Kartel, Catal. Lett. **147** (8), 1966 (2017).

CHAPTER 4

NANOPARTICLES AND NANOCOMPOSITES BASED ON EXPANDED GRAPHITE

4.1. Synthesis, phase composition, structural features, and properties of modified forms of expanded graphite

One of the ways of the development of EG-based composites is a modification by organic and inorganic compounds for improving and expanding the range of carbon material properties. Several studies [1—5] have been devoted to the determination of the correlations of the phase composition, structure, and properties of modified EG with the physical and chemical conditions. It is known that the nature of the initial transformations of modifying compounds is largely determined by the composition of the reaction gas environment, in which the modification process is carried out. The thermodynamic analysis of the gas was carried out in a gas fluidized bed furnace or an electric furnace using iron and zinc chlorides as starting compounds for modification [2]. The analysis was performed to estimate the probability of the presence of different iron and zinc compounds in the reaction mixture in the range of 773—1373 K at normal temperature and pressure conditions. The process of modifying graphite in a gas fluidized bed furnace takes place in a medium of natural gas combustion. By adjusting the ratio of natural gas and the oxygen in the air, it is possible to change the gaseous medium composition and vary the EG surface phase composition (Table 4.1) [2—4].

Table 4.1 shows that for the ratio of 1: 5 of initial CH_4 and O_2 and an increasing amount of oxygen in the system with respect to methane, the character of gas environment is oxidizing (Example 2), at $CH_4 : O_2 = 1 : 4$ it is close to neutral (Table 4.1, Example 1), while at the ratio $CH_4 : O_2 = 1 : 3$ and oxygen decrease reduction relative to methane it is reducing (Examples 3 and 4). So, obviously, the greatest difference in phase transformations of the modified and the original compounds

is expected in these areas. The choice of the optimal ratio of the initial components for the oxidizing environment by controlling the excess of oxygen is determined by the decrease in temperature in the reaction zone for a specific furnace design and the total heat release. As for the reaction medium with an excess of CH_4 relative to O_2, it is limited by the possibility of soot formation and the loss of the energy carriers.

Table 4.1. **The phase composition of the coating depending on the modifying conditions in a gas furnace with a fluidized bed**

No.	Phase composition of gaseous medium for the system of air oxygen			Thermodynamically probable composition of condensed phase		Experimentally determined phase composition of modifying coating	
	Initial components,% wt.		Main components of methane combustion gas medium	Initial modifying compound			
	CH_4	O_2		$FeCl_3$	$ZnCl_2$	$FeCl_3$	$ZnCl_2$
1	10	40	CO_2, H_2O	Fe_3O_4	ZnO	Fe_3O_4	Traces of ZnO
2	10	50	O_2, CO_2, H_2O	Fe_2O_3	ZnO	—	—
3	10	30	CO, H_2, CO_2, H_2O	FeO	—	Fe_3O_4, FeO, traces of Fe	Traces of ZnO, Zn
4	10	20	CO, H_2, CO_2, H_2O	Fe	—	—	—

Table 4.2. **The phase composition of the coating depending on the modification conditions in the electric furnace reactor**

No.	Phase composition of the gaseous medium to the system of air oxygen			Thermodynamically probable composition of condensed phase		Experimentally determined phase composition of modifying coating	
	Initial components, % wt.		Main components of the graphite oxidation medium	Initial modifying compound			
	C	O_2		$FeCl_3$	$ZnCl_2$	$FeCl_3$	$ZnCl_2$
1	10	26.7	CO_2, H_2O	Fe_2O_3, Fe_3O_4	$ZnCl_2$, ZnO	Fe_3O_4, traces Fe_2O_3	ZnO
2	10	40	O_2, CO_2, H_2O	Fe_2O_3	ZnO, $ZnCl_2$	Fe_2O_3, traces Fe_3O_4	ZnO
3	10	15	CO, H_2, CO_2, H_2O	Fe, $FeCl_2$	$ZnCl_2$	Traces Fe_2O_3, Fe_3O_4, α-Fe	Traces ZnO, $ZnCl_2$
4	10	10	C, CO >> CO_2, H_2	Fe	$ZnCl_2$	α-Fe, traces γ-Fe	Traces ZnO, $ZnCl_2$

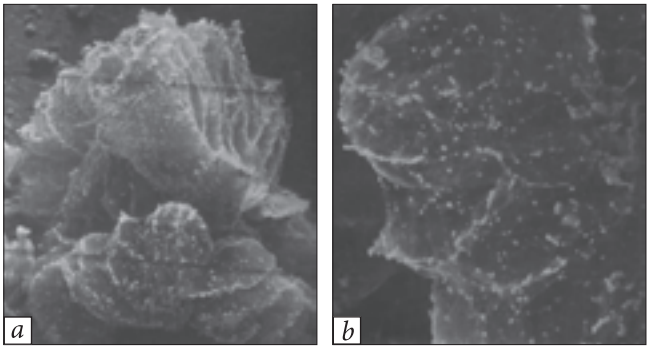

Fig. 4.1. The EG surface modified with zinc oxide with an excess of the modifier. Magnification: *a* — ×100; *b* — ×300

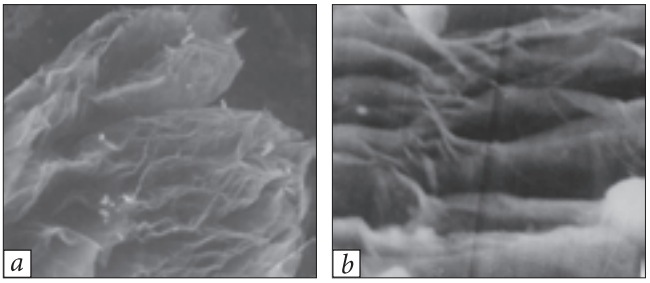

Fig. 4.2. The EG surface modified with zinc oxide. Nearly uniform distribution of modifier. Magnification: *a* — ×300; *b* — ×1000

It was revealed from the thermodynamic analysis that for the $FeCl_3$ system-the reaction medium, in this temperature range (773—1373 K), the formation of the following phases is the most likely: Fe_3O_4 in optimal conditions of the gas furnace (complete combustion), Fe_2O_3 in an oxidizing medium, and FeO and Fe in a reducing one. This is confirmed experimentally (Table 4.1).

For the zinc chloride system, the thermodynamic analysis enables the formation of only the solid zinc oxide phase in an oxidizing medium, but in a reducing medium, the formation of the solid phase in the temperature range 773—1373 K is thermodynamically impossible.

The results of thermodynamic analysis and experimentally determined phase composition of coatings for modifying the electric reactor conditions are shown in Table 4.2. Under experimental conditions, the amount of oxygen may vary. When the ratio of the original graphite and oxygen is 1 : 2.67, the medium nature is weakly oxidizing close to neutral. With an increase in oxygen, the medium becomes strongly exhibiting oxidation properties (Table 4.2, Example 2). Reducing the amount of oxygen in the system to $C : O_2 = 1 : 1.5$ results in changing the ratio of components in the gaseous medium and providing reducing properties. Further reduction of the oxygen leads to increased recovery properties (Table 4.2). The most thermodynamically stable solid phase in an oxidizing environment to $FeCl_3$ system-the reaction medium is iron oxide Fe_2O_3, in the near-neutral environment — Fe_3O_4, and in reducing one — Fe and $FeCl_2$.

Analyzing the system $ZnCl_2$–the reaction medium of variable composition, it is seen that over the entire temperature range, the formation of the ZnO and $ZnCl_2$ is possible.

So, from the above thermodynamic calculation, it is seen that the main condition for obtaining a condensed phase of the defined composition is the ratio of the gas components of the reaction medium, which is qualitatively confirmed by experimental data as well.

The investigations carried out in [4, 5] have shown that the distribution of modifying coating, which indirectly refers to the mechanism of its interaction with the surface, is determined by the structural state of the graphite surface. For the system of natural graphite—$ZnCl_2$, the modifier phase forms spherical particles sizing from a few to hundreds of microns, which is typical for condensation on a non-wettable surface. The most uniform coating corresponds to the system of bisulfate graphite residual compounds—$ZnCl_2$ where the processes of the thermal exfoliation of the graphite, that is the formation of its surface and modification, occur simultaneously. As mentioned in the previous sections, steam explosion and thermal exfoliation of graphite particles are usually accompanied by many tear bonds and the formation of an active surface, which easily absorbs the modifier molecules. The coating in the form of an island film (Figs. 4.1, 4.2) was formed as a result of this process.

By this technique, EG modified with titanium oxide, zirconium, silicon, magnesium, cadmium, iron, calcium, tungsten, and a group of rare-earth metals has been obtained [6].

4.2. Structural transformation of crystalline forms of graphite during thermochemical interaction with iron and zinc chlorides

The analysis of trends of using graphite intercalation compounds (GIC) [7, 8] has shown that they are promising for heterogeneous catalysis. In [7, 9], the catalytic activity of GIC in ammonia synthesis reactions, artificial diamond, and decomposition of formic acid, alcohols, etc. is described. However, the industrial application of GIC as catalysts is still not popular because of the complexity of their synthesis process, especially with transition metals, i.e. of their high cost and lack of thermal stability with metal chlorides [10, 11]. Therefore, expanded graphite (EG) can be used as an active metal carrier [8].

The high-temperature chemical modification may be provided in order to obtain non-conventional properties of EG-based composite materials, such as ferromagnetic and catalytic at the stage of EG [3—5]. The essence of this process consists in the fact that the rapid heating of the disordered intercalation compound graphite-sulfuric acid (GIC-H_2SO_4), which is *a* precursor for EG, is held

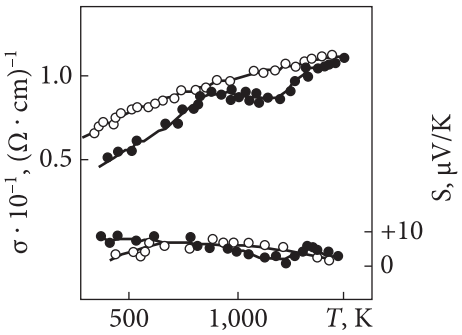

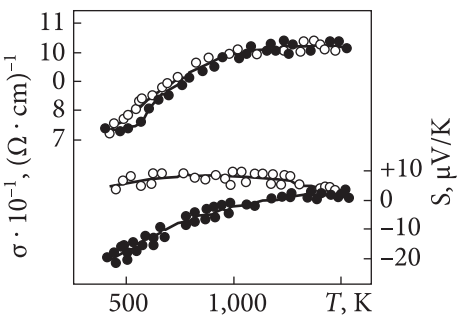

Fig. 4.3. Temperature dependence of the electrical conductivity and thermopower of GIC—H_2SO_4 disordered samples with ferric chloride: ○ heating, ● cooling

Fig. 4.4. Temperature dependence of the electrical conductivity and thermopower of the GIC—H_2SO_4 disordered samples with zinc chloride: ○ heating, ● cooling

in a liquid or a gaseous modifier. Electron microscopic studies of the EG particles after modification by the iron and zinc chlorides have shown the presence of these compounds not only on the particle surface but also in their volume [12, 13]. To interpret the volume distribution of modifying compounds, we consider the two ways of the process. Firstly, within the framework developed in [8], the process of thermal exfoliation of graphite can be considered as a "capture" of liquid or gaseous modifier at "disclosure" or "collapse" of internally-crystalline voids of the graphite matrix during heating and expansion of the disordered GIC-H_2SO_4 at the EG formation. Secondly, the secondary intercalation nonequilibrium process with a subsequent partial deintercalation of the modifier for a short time of the EG formation was proposed in [1]. Such a possibility seems at the first glance to be almost unbelievable in view of the experimental experience of obtaining GIC with metal chlorides only. For example, according to [7], in the current methods for producing GIC-$FeCl_3$, the anhydrous iron chloride is used exclusively and the intercalation process requires several hours involving the reaction of liquid or gaseous chlorine pressurized. Thus, according to [14], the presence of water vapor and the addition of oxygen inhibit the reaction.

In order to clarify the nature of the volume distribution of modifying compounds in the graphite matrix, the studies of the iron and zinc chlorides with disordered GIC-H_2SO_4 and natural graphite GAK-2 have been carried out [15, 16]. We studied the temperature dependence of the electrical conductivity (σ) and thermoelectric power (S) in the temperature range of 500—1500 K under a pressure of 10 MPa on disordered GIC-H_2SO_4 samples interacting with iron and zinc chlorides, and extension at a constant volume, as described in [17]. As can be seen from Fig. 4.3, the main feature of $\sigma(T)$ and $S(T)$ dependences for samples with iron III chloride is a periodic, stepwise increase in the conductivity and, respectively, a periodic change in the thermopower. For samples with

zinc chloride (Fig. 4.4), such a statement is less clear, but, in our view, the rapid growth of conductivity within 600—800 K can be considered a "jump". This type of conductivity dependence or changes in sample mass is typical for the intercalation process and reflects its stages. There is a transition from the higher to the lower stage of intercalation, which is abrupt and corresponds to an increase in the total concentration of the intercalant [18].

Note that the reverse temperature dependence of σ, for a system with ferric chloride and zinc chloride does not reproduce a stepwise nature of σ (T), but, in contrast to the pure GIC-H_2SO_4 [17], the conductivity of modified samples under cooling acquires larger values than when heated. If we compare the two systems, assuming secondary intercalation, the structural transformations involving zinc chloride are less important than the interaction of GIC-H_2SO_4 with iron III chloride. Such an activity ratio of iron and zinc chlorides is observed in the interaction with natural graphite. XRD analysis of natural graphite samples after heating in a mixture with zinc chloride found no significant changes in the diffraction pattern, but there was a slight change in the half-width of the (002) line. Diffraction patterns of the natural graphite samples after rapid heating to 900 and 1300 K in a mixture with a crystalline hydrate of the iron III chloride in the air at atmospheric pressure are shown in Fig. 4.5.

As seen from Fig. 4.5, *a*, due to the thermochemical interaction of natural graphite with ferric chloride III, the formation of disordered graphite-$FeCl_x$ compounds occurs. Without determining quantitative ratios of carbon, iron, and chlorine, the stoichiometry of these compounds cannot be specified, but the fact of their formation is beyond doubt. Further rapid heating of the disordered GIC-$FeCl_x$ leads to thermal expansion with the formation of EG. XRD pattern of this sample is shown in Fig. 4.5, *b*. Along with the graphite reflections, the peaks corresponding to the α-Fe and α-Fe_2O_3 are observed, which are distributed, perhaps, on the surface of graphite particles. Reflections, which correspond to d/n 5.82 and 2.94 Å, indicate the formation of a new inclusion compound of graphite due to the bulk distribution of the intercalant residues in the graphite matrix.

Thus, the disordered GIC are formed and then decomposed as a result of thermochemical interaction between the crystalline forms under the thermal shock of graphite with iron and zinc chlorides resulting in nonequilibrium intercalation or reintercalation. As a result, thermochemical modification of the exfoliated graphite during its formation and distribution of the modifying compounds on the surface of EG and in its volume take place.

It should be emphasized that in contrast to the known reactions of direct thermo-oxidative conversion of the natural graphite into exfoliated [19, 20], where the oxidizer uses aggressive explosive substances (nitrates, perchlorates), the oxidizing agent used by us, $FeCl_3 \cdot 6H_2O$, is a relatively inert material. Thus,

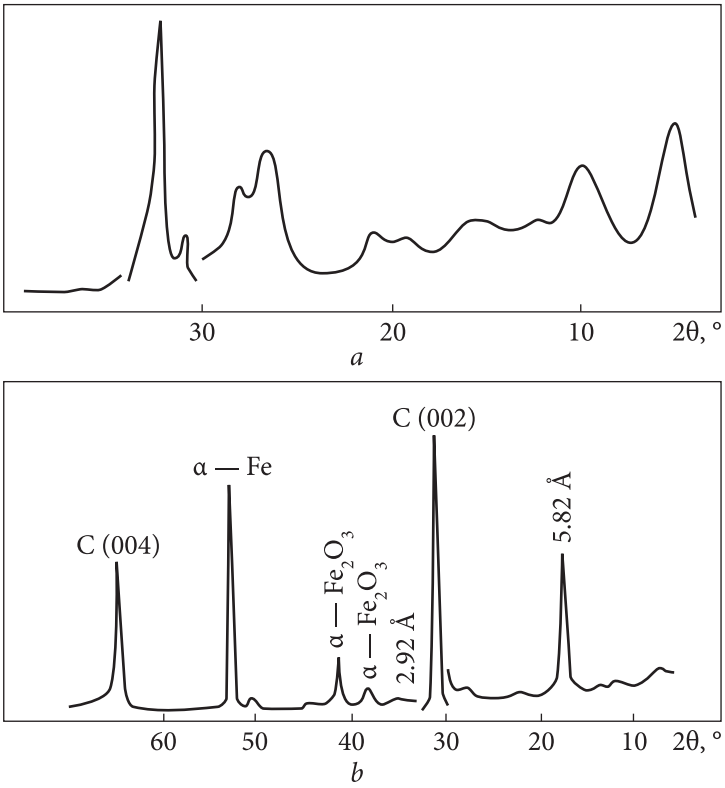

Fig. 4.5. XRD patterns of the natural graphite after the thermochemical reaction with iron III chloride: *a* — heating up to 627 °C; *b* — thermal shock at 1027 °C

the proposed method for obtaining GIC with iron and iron chloride is express (the reaction runs within a few minutes [15, 16]), safe, and technologically simple. Therefore, the next step of this work was to study the crystal structure and thermal stability of GIC with iron and iron chloride, obtained by the direct thermo-oxidative conversion, and to determine the effect of the production parameters on the product characteristics [21].

Synthesis of the samples was performed as follows. The mixture of the particulate natural graphite and the crystalline hydrate of iron chloride ($FeCl_3 \cdot 6H_2O$) was put in the quartz ampoules and heated to a predetermined temperature with the linear rate in the air. After soaking for 5—10 min at the final temperature, the ampoule was cooled rapidly to room temperature, making it possible to fix the structural state of the compound reached. Excess of iron III chloride and its decomposition products were washed in a boiling aqueous HCl solution and distilled water. We determined the increase in the sample mass through the XRD studies (DRON-3M, Co Kα radiation). The thermal stability

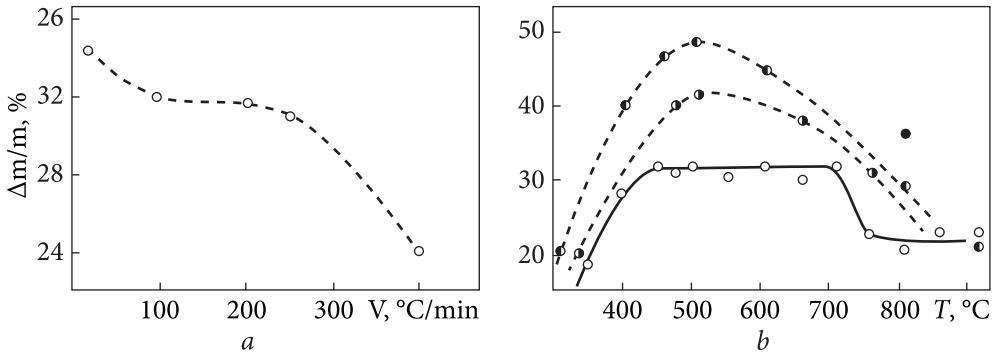

Fig. 4.6. Dependence of the sample weight gain: *a* — on the heating rate of the reaction mixture for weight ratio of graphite and $FeCl_3 \cdot 6H_2O$ as 1 : 4; *b* — on the heating temperature of the final mixture for weight ratio of graphite and $FeCl_3 \cdot 6H_2O$ as: ○ — 1 : 4; ◑ — 1 : 8; ◐ — 1 :12; ● — 1 : 4 — two cycles of the intercalation

of the samples was investigated using a thermal analysis derivatograph Paulic Erden *(Q-1500)* in the air in the temperature range of 20—1000 °C and at a heating rate of 5—10 °C/min. Calibration of the device was carried out on the alumina samples. For comparison, the thermal stability of the investigated and initial graphite samples of GIC-H_2SO_4 which was prepared by the sulfate method [22] has been provided.

As seen in Fig. 4.6, *a*, the weight gain patterns, i.e. the amounts of intercalated ferric chloride, depend on the heating rate of the reaction mixture and varies from 34 to 24% at the heating rate changes from 20 to 400 °C/min and a final heating temperature of 550—600 °C. In particular, in the heating rate range of 100—250 °C/min the weight increase is practically unchangeable and equals 30—32%. The intercalant content in the samples depends on the temperature of synthesis and the initial amount of intercalant (Fig. 4.6, *b*).

The maximum content of intercalant up to 50% is achieved at a temperature of about 500 °C and a mass ratio of 1 : 12 or after three cycles of intercalation, with a mass ratio of intercalant and graphite 4 : 1. As follows from the XRD patterns (Figs. 4.7, 4.8), during the heating of the graphite mixture $FeCl_3 \cdot 6H_2O$, the implantation of iron compounds into the graphite matrix takes place with the formation of the graphite intercalation compounds. GIC formed are disordered (diffraction reflections are strongly broadened), and probably represent a mixture of different intercalation stages. According to [23], the synthesis of GIC-$FeCl_3$ in a classical way, when the temperature does not exceed 300 °C, leads to the implantation into the graphite matrix of both the iron (III) chloride and the iron (II) chloride wherein the amount of $FeCl_2$ in the GIC may be up to 10% wt. Pyrolysis of the GIC-$FeCl_3$ provided at a temperature up to 400 °C causes the loss of the intercalant in the form of $FeCl_3$ gas and the decomposition of $FeCl_3$ to $FeCl_2$.

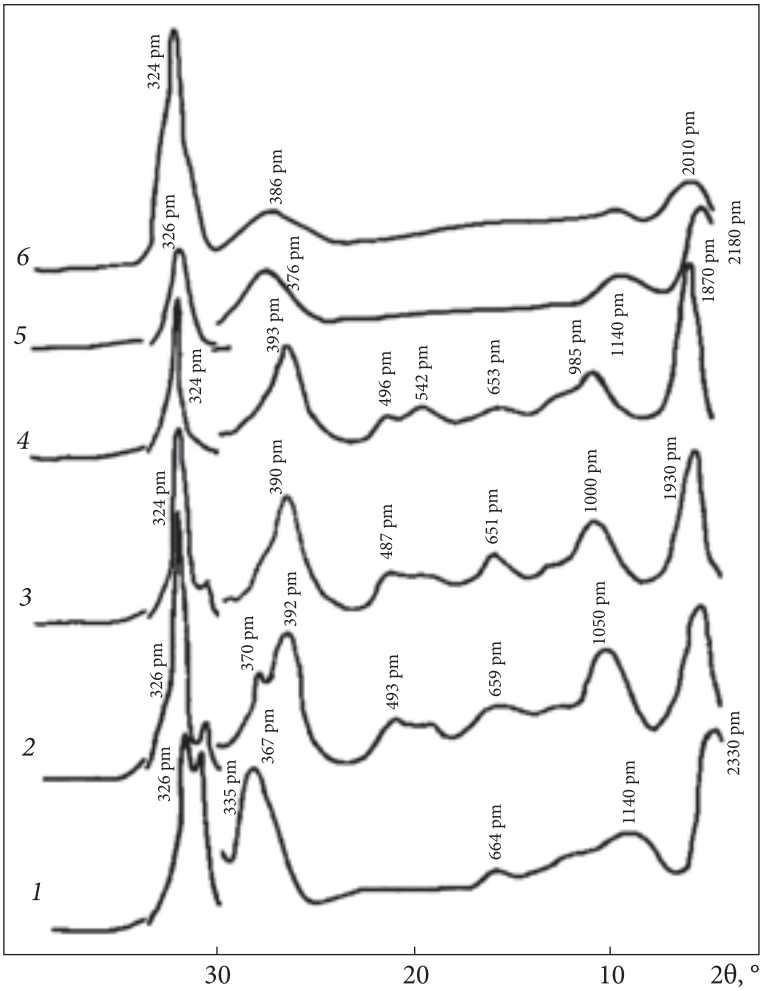

Fig. 4.7. XRD patterns of the natural graphite sample after reaction with $FeCl_3 \cdot 6H_2O$ at 480°C and weight ratio of graphite and $FeCl_3 \cdot 6H_2O$: *1* — 1 : 4; *2* — 1 : 8; *3* — 1 : 10; *4* — 1 : 12; *5* and *6* — 1 : 4, two or three cycles of intercalation

Besides, GIC-$FeCl_2$ stability is high enough ($FeCl_2$ remains in the graphite matrix even when heated up to 1000 °C) [23]. Therefore, it can be assumed that as a result of synthesis in the temperature range of 400—600 °C, the final intercalation compounds will be composed predominantly of $FeCl_2$. Based on this assumption, the structural state of the samples synthesized at 480 °C can be interpreted as a mixture of 4—6 stages of GIC-$FeCl_2$ intercalation (Fig. 4.7, curve *1*).

Changing the structural state of samples depending on the initial intercalant concentration is shown in Fig. 4.7 (curves *1—4*). Crystalline graphite volume

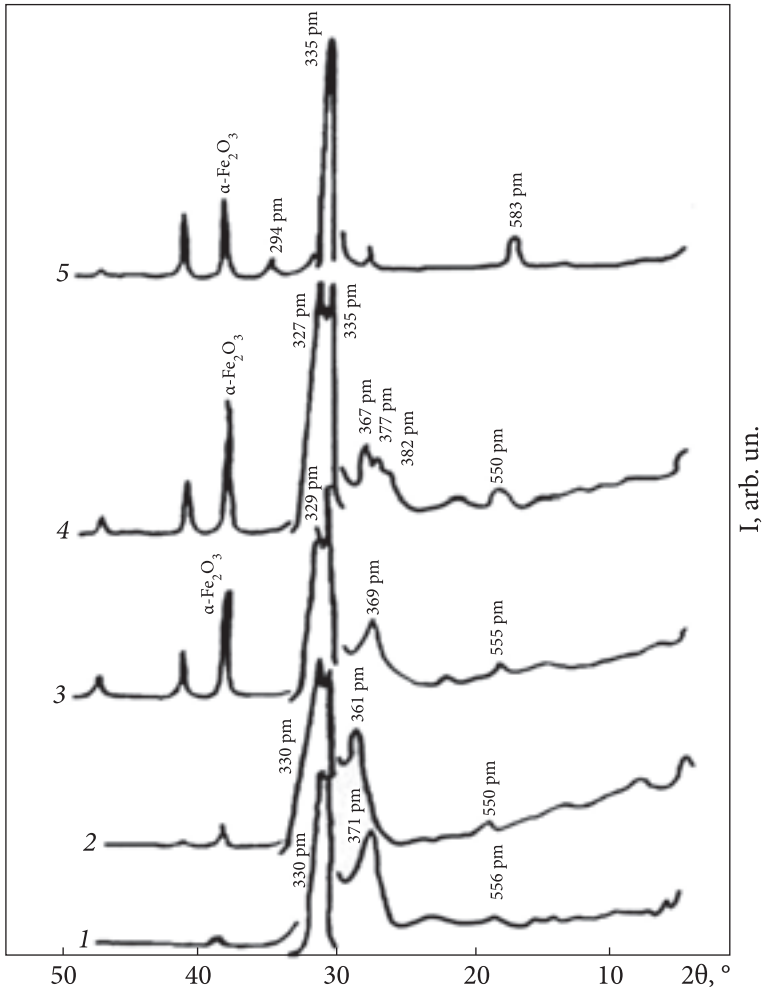

Fig. 4.8. XRD patterns of natural graphite sample after reaction with $FeCl_3 \cdot 6H_2O$ for weight ratio of graphite and $FeCl_3 \cdot 6H_2O$ as 1 : 4 and temperatures: *1* — 300 °C; *2* — 400 °C; *3* — 500 °C; *4* — 600 °C; *5* — 1000 °C

decreases with increasing mass ratio of $FeCl_3 \cdot 6H_2O$ and graphite from 1:4 to 1:12, provided that the maximum concentration of the graphite intercalant phase disappears (Fig. 4.7, curve *4*). At the same time, a decrease in the staging of *GIC*-$FeCl_2$ from 4—6 to 2—4 stages is observed. The appropriate d/n value of the most intense line decreases from 327 pm to 324 pm. The maximum (001) reflection is also shifted to higher angles and the 2θ value varies from 4.4 to 5.2°.

A similar process of structural change is observed with repeated intercalation (Fig. 4.7, curves *5*, *6*). The second cycle of intercalation leads to the

Table 4.3. **Parameters of the thermal stability of samples studied**

Sample	Temperature, °C; Weight loss,%							
	t_1-t_2	t_2-t_3	t_3-t_4	t_4-t_5	t^{I}_{max}	t^{II}_{max}	t^{III}_{max}	t^{IV}_{max}
Graphite	90—200 0—0.5	200—580 0.5—0.8	580—1000 0.8—7	— —	140 0.28	— —	660 0.9	— —
GIC-H_2SO_4	90—240 0—6.5	240—400 6.5—17	400—640 17—20	640—1000 20—84	— —	280 10	390 16.5	840 55
GIC-$FeCl_2$ 320 °C, 20%*	120—280 0—0.8	280—540 0.8—5	540—920 5—27	920—1000 27—36.6	— —	330 1.5	560 6	920 28
GIC-$FeCl_2$ 400 °C, 39%*	110—300 0—2	300—500 2—12	500—860 12—39	860—1000 39—54	— —	330 3.5	540 14	690—880 24—42
GIC-$FeCl_2$ 450 °C, 47%*	110—280 0—4.6	280—500 4.6—8.8	500—700 8.8—18.5	700—1000 18.5—35	150 1.5	335 5	540 11	700 18
GIC-$FeCl_2$ 600 °C, 45%*	120—300 0—6	300—540 6—8.6	540—870 8.6—39	870—1000 39—52	180 2.5	— —	520 560 8—10	780—880 26—43
GIC-Fe 800 °C, 26%*	100—300 0—3.4	300—540 3.4—4.8	540—940 4.8—38	940—1000 38—49	180 1.7	— —	— —	800—960 22—40
GIC-Fe 500 + 800 °C, 36%*	150—300 0—2	300—540 2—4	540—940 4—36	940—1000 36—45	200 0.6	— —	— —	800—960 22.5—38

* Synthesis temperature; intercalant content.

disappearance of the graphite phase and a decrease in the staging of the GIC-$FeCl_2$. However, carrying out several cycles of intercalation, unlike a single process, with the same total number of intercalants leads to the formation of a homogeneous, but a more disordered structure of these samples (very few broadened reflections are observed at the diffraction pattern resembling the diffraction pattern of XRD-amorphous materials). The synthesis temperature increasing from 300 to 600°C, provided the same intercalant amount, results in a decrease in the staging of GIC-$FeCl_2$ as seen in Fig. 4.8 (d/n values of the most intense line decrease from 330 pm to 327 pm). This changes the ratio between amounts of graphite and GIC phases. A similar process is observed after annealing at the final temperature. The disorder and GIC staging are reduced, i.e. the structural changes take place by the layered type.

Thus, at thermochemical interaction of natural graphite with the crystalline hydrate of iron (III) chloride ($FeCl_3 \cdot 6H_2O$) within 300—600 °C, a disordered GIC-$FeCl_2$, which is the mixture of 4—6 GIC stages, is formed. Increasing the initial intercalant content from 1 : 4 to 1 : 12 and the synthesis temperature reduces GIC stages to a mixture of steps 2—4 Heat treatment of the samples at 800—1000 °C results in the formation of intercalation compounds of graphite-iron (Fig. 4.8, curve *5*). Stage 1 GIC-Fe is formed corresponding to the reflection (001), its d is 582—585 pm. There is also a graphite phase (d_{002} = 335 pm) and reflections related to the iron oxide α-Fe_2O_3. The iron oxide phase is distributed on the surface of graphite particles in the form of a film [16]. If the heat treatment process is performed in two stages: heating to 300—500 °C, washing of the residual product, and then thermal shock at 800—1000 °C, the phase composition of the resultant compound varies. The volume of the graphite phase is reduced, and the α-Fe phase prevails on the sample surface [16]. That is, we have obtained the so-called graphimet materials, which have commercial use as catalysts [24]. Maximum sample weight gain is 36—37%, which corresponds to the C_8Fe composition. This experimental fact, unlike representations of [11] indicates that GIC-Fe may be prepared via reduction of GIC by heat treatment with iron chlorides.

Table 4.3 and Figs. 4.9—4.10 present the experimental results for the thermal stability of the synthesized samples. To quantify the thermal stability, the temperatures at which there is an inflection in the TG curves t_1, t_2, t_3, t_4, t_5 were used. Extreme points on the differential TG curves (t^{I}_{max}, t^{II}_{max}, t^{III}_{max}, t^{IV}_{max}) are the temperature of the maximum destruction rate in the given temperature interval.

As seen in Fig. 4.10 and Table 4.3, the temperature of the beginning of the intensive weight loss of the compounds of graphite intercalated with iron chloride is about 500 °C, which is 100—150 °C above this value for the compounds produced in a classical way [23]. Moreover, as in [25], a large weight loss is observed in the compounds that have a greater intercalant concentration in the

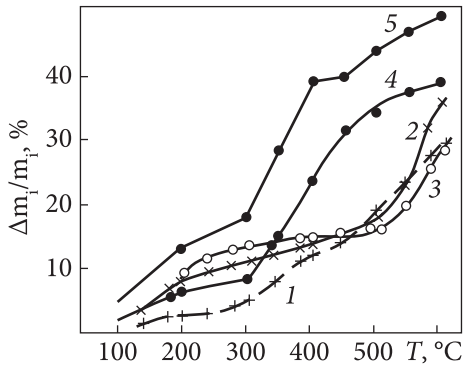

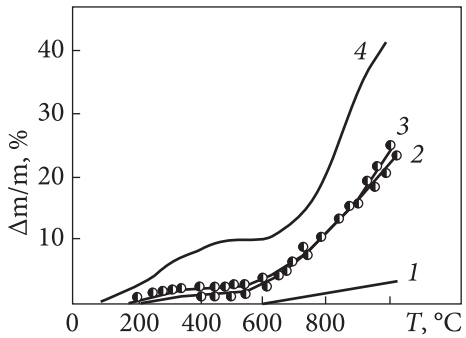

Fig. 4.9. Temperature dependences of the weight loss of the GIC intercalant iron chloride. The synthesis temperature: *1* — 320 °C; *2* — 450 °C; *3* — 600 °C; *4*, *5* — data of [26]

Fig. 4.10. Temperature dependences of weight loss of *1* — natural graphite; *2*, *3* — GIC-Fe; *4* — GIC-H_2SO_4

initial state. According to the analysis of the temperature dependence of the weight loss of the synthesized GIC-$FeCl_2$ in terms of the linear pyrolysis [26], by DTA and XRD methods, the thermal degradation process can be divided into three temperature ranges: 100—300 °C corresponds to the loss (up to 5% by weight) of adsorbed excess of the intercalant and its degradation products; 300—500 °C — to the weight loss associated with the structural and phase transformations of the disordered GIC (total weight loss is up to 12%); above 500 °C — to intensive air oxidation (combustion). Structural transformations in GIC-Fe during heat treatment to 600 °C are not observed, according to the XRD and DTA.

Weight loss (up to 5%) in this temperature range can be attributed to the degradation products adsorbed by the intercalated compound. At high temperatures, intensive air oxidation is observed, i.e., combustion of GIC-$FeCl_2$. It should be noted that the thermal stability of GIC-Fe, which can be attributed, by its particle structure, to the exfoliated graphite [22], is higher than that of the EG produced by the sulfate method (Fig. 4.10). This is probably due to the lower (3—5 times) specific surface of GIC-Fe.

Thus, by the method of direct thermal-oxidative conversion of natural graphite due to its interaction with $FeCl_3 \cdot 6H_2O$ the following compounds can be obtained: the disordered GIC-$FeCl_2$ intercalant with a maximum of up to 50% wt. in the temperature range of 300—600 °C and GIC-Fe of the first stage with a maximum 36—37% of intercalant (C_8Fe) in the temperature range of 800—1000 °C, which can be used in an oxidizing environment where the temperature is 500—600 °C.

4.3. Composite materials expanded graphite-carbon

EG modification by the thermosetting organic compounds allows us to create an ultra-thin layer of polymeric material on the developed surface of EG. Thus, sequential carbonation of EG modified in a compact form lets the creation of a composite material comprising two interpenetrating structures of crystalline graphite and amorphous carbon material. So, through the combination of EG plasticity and hardness of amorphous carbon and considering their high adhesion interactions, it becomes possible to regulate the mechanical characteristics of the composite material and to create EG-carbon-carbon fiber systems.

The manufacture of exfoliated graphite was performed as described in [27, 28]. To obtain EG filled with carbon fiber (CF) [29], the finely chopped CF (segments 3—5 mm length) and natural graphite were added to the ammonium persulfate solution. The mixture was stirred vigorously. CF concentration was 1 wt.% in relation to the weight of the graphite. After heat treatment at 800 °C for 10 min, the bulk density of EG-CF was 20 g/dm^3. To obtain compositions of EG-carbon, EG-carbon-CF, the bakelite lacquer (BL) with a density of 1.05 g/cm^3 was used as an organic filler. It was added to the EG powder or EG-CF and mixed in a mechanical mixer until smooth. Concentrations of BL were 50, 70, and 80% by weight. The mixture was dried at 120 °C for 1 h. The resulting powders were compacted into cylindrical samples of 20 mm in diameter and height with the same initial density of 1.2 g/cm^3. Samples were stepwise heat-treated in the electric furnace under the conditions of 200 °C for 5 h, 300 °C for 3 h, 400 °C for 2 h, and 500 °C for 1 h. During heat treatment, due to carbonization occurring in BL, the samples' weight loss and changes in their volume take place, therefore the density of samples and the concentration of carbon material change as well. The initial and final average data for the samples are given in Table 4.4. During the calculations, considering the relatively low processing temperatures, the graphite mass is considered constant.

Table 4.4. **Initial and final parameters of the EG-carbon-CF composites**

Composite	Polymer content in initial mixture, % wt.	Initial density, g/cm^3	Final density, g/cm^3	Carbon content, % wt.
EG-carbon	30	1.2	1,1	22
EG-carbon	50	1.2	1,07	35
EG-carbon	70	1.2	1.0	47
EG-carbon-CF	30	1.2	1.06	21
EG-carbon-CF	50	1.2	0.97	47
EG-carbon-CF	70	1.2	0.99	61

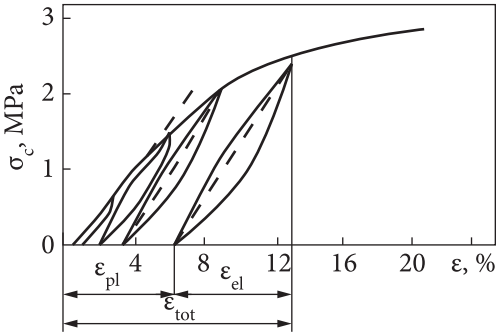

Fig. 4.11. EG compression diagram under re-static loading

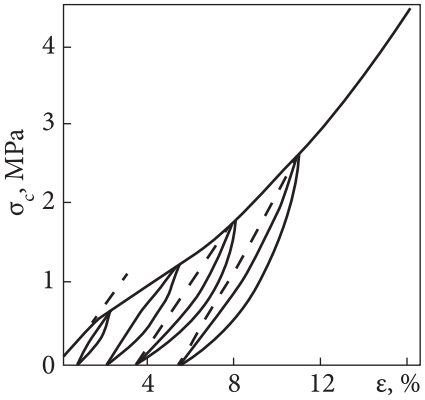

Fig. 4.12. Diagram of compression of the EG-carbon composite material under re-static loading

For comparative analysis, we studied the mechanical characteristics of EG samples of the same shape and size with a density equal to the density of the final composite materials, using the method of uniaxial compression. The tests were performed on a 2167 P-50 universal apparatus in the mode of re-static loading with a given strain rate. In this case, the load vector was parallel to the pressing axis of samples. The deformation diagrams were recorded in an automatic mode.

A comparative analysis of the compression diagrams of samples of "pure" EG and EG-carbon composites (Fig. 4.11, 4.12) showed that the carbon component makes a significant change in the behavior of the material during compression.

Thus, for EG samples (Fig. 4.11), with a density of about 1 g/cm^3 the compression is like compression diagrams of other low-density materials and, at least, is similar to the compression diagram for isotropic porous materials. The compression diagram of such materials is characterized by three sections corresponding to different stages of the deformation process: 1 — the strain of "weak" elements of the "frame" structures (small initial non-linear plot with positive curvature); 2 — elastic deformation of the "frame"; 3 — the elastic-plastic deformation of the structure with a predominance of the plastic component and the negative curvature of the corresponding portion of the chart [17]. During re-static compression of the sample, that is, during loading and re-loading, there is a lentil shape of the hysteresis loop with a large area, indicating the considerable deformation energy dissipation in the material, which is associated with the structure restructuring during deformation. In this case, the proportion of the elastic deformation component (K_{el}), which can be defined as the ratio of the elastic component of deformation after unloading (ε_{el}) to generally achieved at the time of unloading deformation (ε_{tot}), continuously decreases

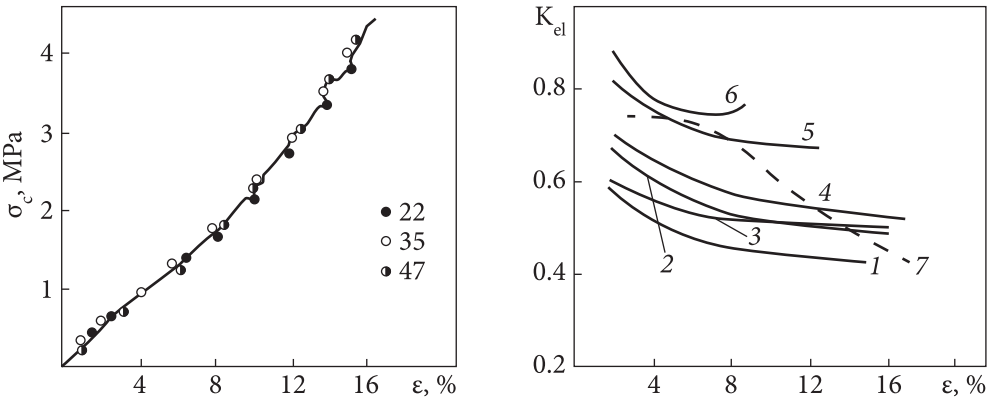

Fig. 4.13. Compression diagram for EG-carbon composites with a carbon content of 22, 35 and 47% wt.

Fig. 4.14. Dependence of the elastic deformation component on the magnitude of deformation for the samples: *1—3* — EG-carbon, *4—6* — EG-carbon-CF, *7* — EG

with increasing deformation at high strains (more than 10%), and the plastic component dominates in the deformation process.

The addition of the carbon component in the range of concentrations studied changes the behavior of the material during compression (Fig. 4.12). The strain diagrams are similar to those for compression of plastic material capable of deformation without fracture [30]. The positive curvature in the area of elastic-plastic deformation is typical for such materials. As seen in Fig. 4.12, for the investigated compositions, the hysteresis, which also has a lentil shape for small deformation, is observed. However, with the strain growth, the loop starts to curve and the hysteresis loop axis goes beyond its limits. This apparently indicates the formation of closed cavities, that is, defects of lens-like shape in the studied materials at large deformations. Such defects during re-load are deformed as a lenticular spring and give this form to the hysteresis loop. At small deformations, the strain in the EG-carbon compositions does not differ from that in the initial EG samples. However, at large deformations, the EG-carbon composites have much greater strength.

As can be seen from Fig. 4.13, a change in the carbon component concentration in the range studied has a slight effect on the compression strength, and the studied compositions have approximately equal strength. The proportion of the elastic component of deformation of the composites, as well as of "pure" EG continuously decreases with increasing deformation; even for large deformations, some stabilization of the material elastic properties is observed (Fig. 4.14, curves *1—3*).

As seen from the compression diagram of the EG-carbon-CF composites, the addition of small amounts of carbon fiber significantly affects the behavior and strength of the composite during compression (Fig. 4.15).

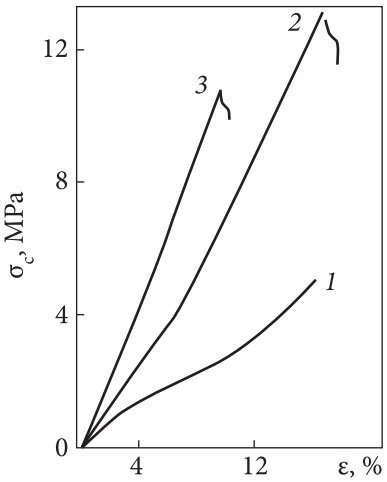

Fig. 4.15. Compression diagrams for EG-carbon-CF composites with the carbon content: *1* — 21, *2* — 47, *3* — 61%

If at low carbon concentrations, the compression diagrams differ little from the charts for the EG-carbon composites in the nature and level of stress diagrams, then with increasing carbon concentration the compression diagrams become almost linear up to the sample destruction; besides the destruction becomes fragile. Thus, the strength of samples increases by 3—5 times, and the proportion of the elastic deformation component predominates in the process (Fig. 4.14, curves *5* and *6*). For the EG-carbon-CF composites with a carbon concentration of 61% wt., K_{el} coefficient increases even before the destruction.

Thus, adding carbon components into EG changes the behavior of the materials during compression and increases their strength at large strains. The carbon content in the range investigated (20—60%) has a little effect on compressive strength, so the samples have almost the same strength. Deformation of the EG-carbon-CF composites with a high carbon content is predominantly elastic; their strength is greater than the strength of the EG-carbon materials by 3—5 times, and the destruction is fragile.

4.4. Expanded graphite-carbon nanotubes composite materials

As shown earlier in Chapter 2, EG preserves all the properties of natural graphite and acquires the ability to be pressed and rolled without binders. Rolled and extruded EG materials with a density of 1.0—1.8 g/cm^3, in addition, have a set of unique elastic-plastic properties and therefore they are widely used as sealing materials in current engineering. Increasing wear resistance and elastic component of deformation is a proper way to increase the reliability and service life of such consolidations.

The known methods for obtaining carbon-carbon composite materials (CCCM) without binders are reduced to two options: either pyrolytic deposition of carbon from the gas phase due to the decomposition of hydrocarbons, or sequential processes of impregnation of carbon material with liquid hydrocarbons followed by their decomposition under the heating conditions with increasing temperature in the selected range from 700 to 3000 °C [31]. In

the latter case, the quality of the carbon material directly depends on the final processing temperature and the amount of impregnation. Both methods are energy- and labor-intensive, so they are used to solve uniquely important, in particular, defence problems.

4.4.1. Expanded graphite-carbon nanotubes composite materials obtained using a binder

Another way to create carbon composite materials is to use binders [32—34]. In the technology of production of sealing materials and products from EG, the so-called glue of constant stickiness is used, which is an aqueous solution of an acrylic copolymer in which isodecyl alcohol ethoxylate is used as a surfactant. It is used to create EG-CNT compositions.

The results of treatment of suspensions of the system "water-soluble polymer-surfactant-multiwall CNTs" in a rotary homogenizer after preparation (a) and a year later (b) (*VP* is acrylic copolymer; surfactant is isodecyl alcohol ethoxylate) are given in Chapter 5, Fig. 5.6, which show that the obtained dispersion is stable.

Layered carbon material. A method for manufacturing a layered carbon material, which includes preparing a dispersion of CNTs and applying it to the surface of an expanded graphite sheet, according to [32]. To prepare the dispersion of CNTs, water and acrylic dispersion were mixed in a volumetric ratio of 2 : 0.75—1.5 for (0.5—5) min. Then carbon nanotubes, (8—15) g of carbon nanotubes per 1 liter of the aqueous acrylic mixture, were added and homogenized for (0.5—5) min. The manufactured dispersion of CNTs was applied to the EG sheet surface of density (0.3—1.0) g/cm^3 by a solid layer of the thickness (0.05—0.5) mm and heated to (150—155) °C. Then a (2—12) mm layer of EG powder was additionally sprinkled. Further, the primary rolled resulting layered carbon material was heated to (165—170) °C. After that, the finishing rolling of the resulting layered carbon material to thickness (0.17—0.45) mm was performed.

The material was prepared on the line of manufacturing layered carbon materials, which included a universal rotary homogenizer, a device for application of CNTs dispersion, a unit for giving and leveling EG powder, two furnaces for heating layered carbon materials, two rollers, and a unit for winding the layered carbon material. The specific implementation of this method confirms the following examples. Numerical parameters of some examples, as well as the properties of the layered carbon material, are given in Table 4.5. For comparison, a sample of layered carbon material was obtained by the method described in [35]. Its compressibility was 50.7%, and recoverability only 8.3%

These examples confirm the achievement of the desired result by the above method. While for the sample of layered carbon material obtained as in [35], the

compressibility was 50.7% and the recoverability was only 8.3%, the layered carbon material obtained by the method [32] provided an increased elasticity: the resultant samples exhibited compressibility (52.3—56.6)% and recoverability (10.7—13.6)%.

Table 4.5. **Properties of layered carbon material depending on the technological process parameters**

Example	Correlation water : acrylic dispersion	Stirring time, min	Mass of CNTs per *l*, g	Dispersion time, min	Thickness of CNTs dispersion layer, mm	Temperature of the first furnace, ° C	Thickness of EG powder layer, mm	Temperature of the second furnace, °C	Thickness of layered carbon material, mm	Compressibility,%	Recoverability,%
1	2 : 1	2	10	2	0.25	150	12	170	0.25	53.4	11.5
2	2 : 0.75	0.5	8	0.5	0.05	155	2	165	0.17	52.3	10.7
3	2 : 1.5	5	15	5	0.5	155	10	170	0.20	54.5	12.3
4	2 : 1	2	10	5	0.25	150	12	165	0.35	55.6	12.9
5	2 : 1	2	10	5	0.05	155	2	170	0.25	54.7	12.1
6	2 : 1	2	10	5	0.5	155	10	170	0.45	56.6	13.6

Table 4.6. **Properties of braided carbon material depending on the parameters of the technological process of its production**

Example	Thickness of layer of adhesive dispersion of CNTs, mm	Temperature of the first heating furnace, °C	Thickness of EG powder layer, mm	Temperature of the second heating furnace, °C	Final thickness of reinforcing foil, mm	Width of tape of reinforced foil, mm	Diameter of received thread, mm	Section or diameter of braided cord, mm	Compressibility,%	Recoverability,%
1	0.25	150	8	165	0.2	10	3	12 × 12	46.8	12.4
2	0.05	155	2	170	0.17	8	2	12 × 12	48.8	11.7
3	0.5	155	12	170	0.25	15	4	50 × 50	44.8	13.6
4	0.25	150	8	165	0.2	8	2	4 × 50	47.0	12.6
5	0.25	150	8	165	0.2	8	2	4 × 25	47.1	12.7
6	0.25	150	8	165	0.2	15	4	25 × 50	46.6	12.2
7	0.5	155	12	170	0.25	6	2	ø10	44.9	13.8
8	0.5	155	12	170	0.25	12	3	ø30	44.7	13.7

Sealing materials. The next step was the creation of packing and sealing elements for sealing various connections of control, shut-off, and safety valves of pipelines, pumps, and compressors of nuclear power plants and other equipment in the energy, chemical, and petrochemical industries. This problem was solved by creating a sealing material in the form of a cord woven from reinforced threads. Each reinforced filament consisted of EG and a reinforcing fiber placed in the middle of the filament. It additionally contained an adhesive dispersion of carbon nanotubes [33, 34].

The process of manufacturing a sealing material included laying reinforcing threads on foil with EG and cutting the foil into strips so that each strip could have one reinforcing thread. The reinforced foil was cut into strips 5—20 mm wide, each strip was twisted into a thread and passed through a series of forming dies to a thread diameter of (2—4) mm. Sealing material in the form of a cord was woven from the obtained reinforced threads. EG foil with CNTs adhesive dispersion was prepared as described above.

According to [34], in the method for manufacturing sealing materials, the plaited rope sealing material in the form of a cord was further rolled with rollers in two perpendicular planes to obtain a square cross-section of the cord with cross-sectional dimensions from 4 × 4 mm to 50 × 50 mm.

The sealing material was made as described above, changing the parameters of the method within the limits given in the method of obtaining a layered material [32]. Specific numerical values of the method parameters along with the characteristics of the elasticity of the manufactured sealing material are given in Table 4.6.

Properties of layered carbon material depending on the parameters of the technological process are listed in Table 4.6.

These data confirm the achievement of the technical result. As compared with the sample of braided carbon cord of square section 12 × 12 mm obtained according to [36], whose compressibility was 53.8% and recoverability was only 8.9%, the sealing material obtained by method [34] exhibits the best parameters of elasticity: compressibility 44.8—48.8% and recoverability 11.7—13.6%.

4.4.2. Expanded graphite–carbon nanotubes composite materials without binders

Effective deagglomeration agents for CNTs are strong acids and oxidizing agents, as reported e.g. in [37]. Therefore, our idea was to use a simultaneous process of deagglomeration CNTs and intercalation of natural graphite.

This procedure was performed in two ways: the first way consisted in chemical oxidation in solutions of strong oxidants as described in Chapter 2; the second way was electrochemical (anodic) oxidation as in Chapter 2 as well. The

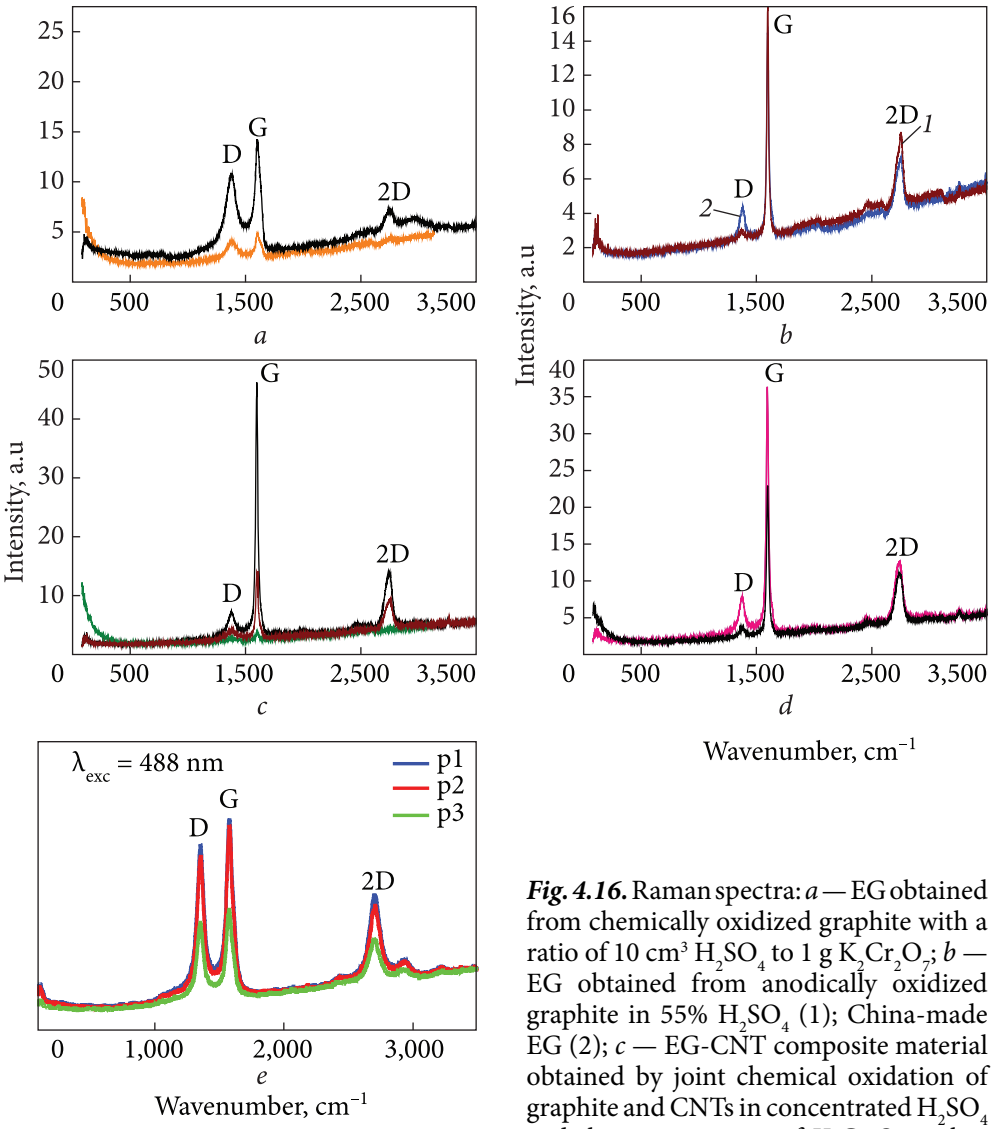

Fig. 4.16. Raman spectra: *a* — EG obtained from chemically oxidized graphite with a ratio of 10 cm^3 H_2SO_4 to 1 g $K_2Cr_2O_7$; *b* — EG obtained from anodically oxidized graphite in 55% H_2SO_4 (1); China-made EG (2); *c* — EG-CNT composite material obtained by joint chemical oxidation of graphite and CNTs in concentrated H_2SO_4 and the participation of $K_2Cr_2O_7$ with a ratio of 10 cm^3 H_2SO_4 to 1 g of $K_2Cr_2O_7$; *d* — composite material EG-CNT obtained by joint anodic oxidation of graphite and CNTs in concentrated H_2SO_4; *e* — initial CNTs

first option was carried out as follows. Sulphuric acid was mixed with an oxidizer and CNTs in proportion per 1 dm^3 of sulphuric acid, 0.5—10 g of CNTs, and 55—80 g of potassium permanganate or 85—125 g of potassium dichromate. Then, to the mixture of sulfuric acid with CNTs and oxides, graphite was added by stirring in the ratio of 1.6—2.2 dm^3 of sulfuric acid-CNTs-oxide mixture per 1 kg of graphite. Stirring lasted 5—20 min. The resulting product was washed

using a water filter to pH = 6—7 and dried. The dried product was heated in the heat-stroke mode to 850—1250 °C. After cooling, it was rolled into a foil. Then the recoverability, compressibility, and tensile strength were determined. The mechanical tensile and compression tests of the prepared composites were carried out on a 2167 P-50 breaking machine with continuous automatic recording of the load-strain diagram on the PC.

The essence of the second option is as follows. The concentrated sulfuric acid is mixed with CNTs and graphite in proportion: per 1 dm^3 of sulfuric acid, 1—30 g of CNTs, and 0.8—1.1 kg of graphite. This mixture was subjected to anodic oxidation at a current density of 5—35 mA/cm^2 and electric power consumption of 80—120 A · h/kg. The obtained product was washed with water to pH ≈ 6—7 and dried. The dried product is heated to 850—1250 °C in the thermal shock mode. A composite carbon material was obtained with composition: CNTs 0.1—3.0% wt.; expanded graphite the rest. After cooling, it was rolled into a foil and characterized for compressibility, recoverability, and tensile properties. The chemicals used for this synthesis procedure were as follows: carbon nanotubes at TU 24.1032911669–009, graphite brand GSM-2, GOST 17022-81; sulphuric acid according to GOST 4204. Changes in the structural state of CNTs under the influence of their oxidation, as well as the composite materials EG-CNTs structure were investigated using Raman spectroscopy. Raman spectra of CNTs were recorded using the T-64000 Horiba Jobin-Yvon spectrometer in the backscattering geometry at room temperature when excited by an argon laser (λ = 514.5 nm, 1 mV).

The Raman spectra of the EG-CNT composite materials are shown in Fig. 4.16. The main parameters of the characteristic bands observed in the micro-Raman spectra of EG of different origins and EG-CNT composites are shown in Table 4.7.

From the comparison of Raman spectra of the EG samples obtained under different conditions, it can be concluded that the most defective structure is that of the EG synthesized by chemical oxidation in a solution of potassium bichromate in sulfuric acid with their ratio (1 g $K_2Cr_2O_7$ to 10 cm^3 H_2SO_4, 2 dm^3 of the solution to 1 kg graphite) significantly exceeding the stoichiometric value. The result is the so-called peroxidation graphite, as well as a significant defectiveness of the EG prepared after the hydrolysis, drying, and heat treatment [38, 39]. The G-band is shifted towards higher frequencies, its half-width increases, and the I_D/I_G ratio acquires the maximum value in comparison with EG samples of other origins.

As follows from Table 4.7, the EG samples obtained from anodically oxidized graphite in 55% H_2SO_4 have the least quantity of defects. CNTs not significantly change the Raman spectra of the composite material EG-CNTs, which can be explained by low CNTs content of ~1% wt.

Table 4.7. **The main parameters of characteristic bands manifested in micro-RS spectra of EG of different origins and of EG-CNT composites**

Sample according to Fig. 4.16						
Parameters	a	b (1)	b (2)	c	d	e
Sample, synthesis conditions	EG chemically oxidized with 1 g $K_2Cr_2O_7$ to 10 cm^3 H_2SO_4	Anodic oxidation with 55% H_2SO_4	Chemically oxidized product from China	EG-CNTs, chemically oxidized with 1 g $K_2Cr_2O_7$ to 10 cm^3 H_2SO_4	EG-CNTs, anodic oxidation	Initial CNTs
D, cm^{-1}	1378	1374	1378	1377	1375	1348
G, cm^{-1}	1602	1598	1598	1598	1597	1573
2D, cm^{-1}	2794	2752	2752	2748	2737	2706
D_{FWHM}, cm^{-1}	89	—	—	—	51	51
G_{FWHM}, cm^{-1}	53	18	27	22	23	53
I_D, a. u.	8.1	3	8	14	5.0	9.0
I_G, a. u.	11.1	117	53	126	33.6	10.4
I_D/I_G	0.73	0.03	0.15	0.11	0.15	0.86

Table 4.8. **Tensile strength of EG samples obtained by different methods and EG-CNT composite material**

Sample	Density, g/cm^3	Specific surface area for argon desorption *, m^2/g	Tensile strength, MPa	Ratio of strength to density
EG + CNTs anodic	0.35	92	1.2 ± 0.2	3.4 ± 0.6
EG + CNTs anodic	0.60	92	1.9 ± 0.4	3.2 ± 0.4
EG anodic	0.62	33	1.0 ± 0.2	2.7 ± 0.6
EG chem.	0.54	62	1.3 ± 0.5	2.3 ± 0.9
EG + CNTs chem.	1.1	—	4.9 ±1.2	4.45 ± 1.1

* Method of determination is thermal desorption of argon (GOST 23401-90).

Table 4.9. **Compressibility and recoverability of EG samples and EG-CNT composites**

Content of CNTs,% wt.	Compressibility, %	Compressibility change, %	Recoverability, %	Change in recoverability, %
0	84 ± 6		44.7 ± 1	
1.0	63 ± 5	25	51.4 ± 2	18
3.0	63 ± 3	25	52.9 ± 1	18

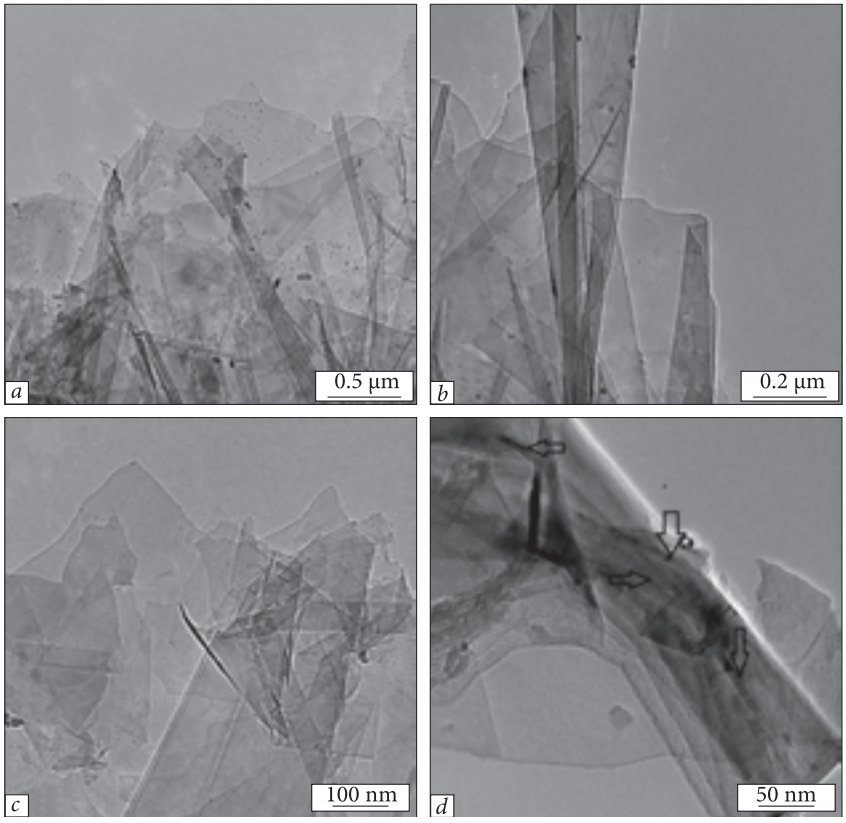

Fig. 4.17. TEM images of EG-CNTs composite material

TEM images of the EG samples and EG-CNT compositions are shown in Fig. 4.17. They show that EG-CNT samples have a folded structure, with clearly visible CNTs embedded in the EG body (shown by arrows).

Table 4.8 presents the tensile strength data for EG samples obtained by different methods and EG-CNTs composites. As seen, an addition of 1% wt. CNTs to natural graphite, under the conditions of their joint, and CNTs anodic oxidation leads to an increase in tensile strength of rolled samples from thus obtained EG by ~22%.

The values of compressibility and recoverability of EG samples and EG-CNTs composites obtained by co-oxidation in a solution of potassium dichromate in sulphuric acid are given in Table 4.9. With the addition of CNTs into the EG matrix, the compressibility decreases by 25%, and the recoverability increases by 18%.

It should be noted that the recoverability is the same for the composites with a CNTs content of 1% wt. and 3% wt., which, in our opinion, indicates the formation of a continuous bulk grid by a CNTs concentration of 1% wt. in such a system.

4.5. Graphene nanoparticles and composites with carbon nanotubes

Graphene is a single graphite plane in which sp^2-hybridized carbon atoms form a hexagonal lattice. Graphene can be represented as a "building block" of graphite, nanotubes, intercalated graphite compounds, and other carbon materials. Graphene nanoparticles (GNPs) consisting of two or more layers (up to ten) as well as a monolayer of graphene have unique physicochemical properties [40—43]. Therefore, they are widely studied as individual particles, continuous films, and fillers of polymeric materials [44—49]. They are more stable compared to single-layer graphene and are suitable for mass production according to the "top-down" scheme, i.e. splitting of various precursors with a graphite-like structure, using various methods (Fig. 4.18) [44].

The addition of GNP into polymeric materials significantly increases the dielectric constant, changes the thermodynamic characteristics of the composite, increases the degree of crystallinity and resistance to thermal destruction, and causes a synergistic increase in the absorption of electromagnetic radiation when interacting with carbon nanotubes in a porous system up to 21% of biothermoplasts at insignificant concentration [44, 45, 47—49]. Modifications of synthetic polymer fibers of GNP lead to a number of improved and new properties, such as adsorption capacity, antibacteriality, hydrophobicity, and conductivity, which are useful for wide applications.

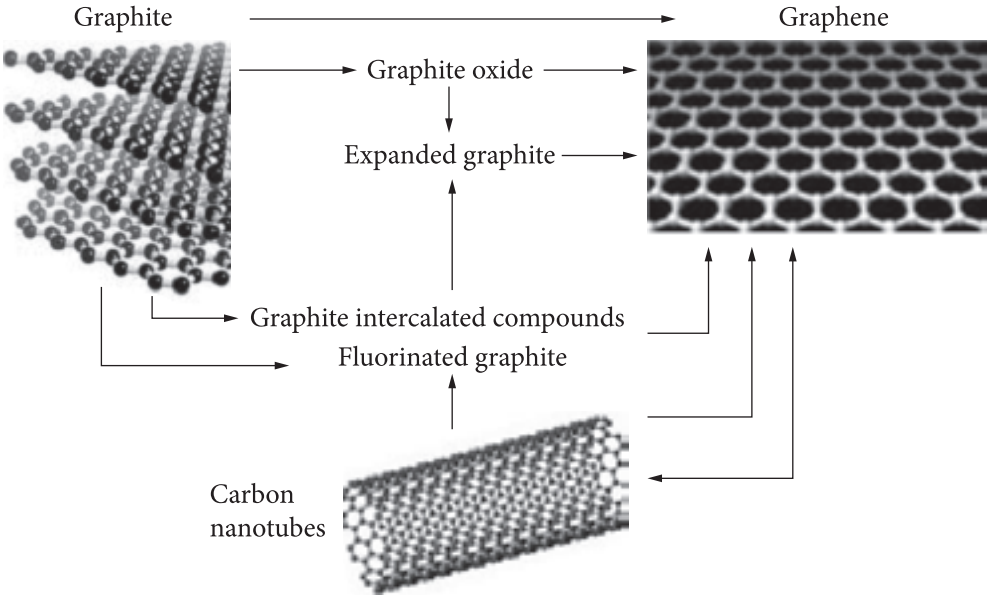

Fig. 4.18. Methods of obtaining graphene nanoparticles by splitting different precursors [44]

The problem of obtaining GNPs does not consist in the difficulties of their production, but rather in developing a method that allows one to obtain GNPs of specified sizes and properties, i.e., allows control of the nanoparticle characteristics [44].

Methods using dispersions based on compounds containing graphene layers and obtained from natural, artificial highly oriented pyrolytic, expanded, intercalation compounds, graphite oxide, fluoride, and carbon are promising for large-scale production and relatively simple modification of GNPs properties. [44]. Among these methods, electrochemical or anodic oxidation of graphite-like structures stands out as a method that allows for regulating the process conditions and properties of the product obtained [46, 50, 51].

In Chapter 2, it has been shown that EG is a nanoscale cluster-assembled system that contains cylindrical, conical, slit-like defects with an average cross- section of 0.7—20 nm (Figs. 2.7, 2.8). The CSD sizes measured by XRD analysis in the basal and perpendicular planes are about 20 nm. Therefore, EG is the most attractive precursor of GNPs for industrial production. Electrochemical intercalation (or anodic oxidation) is the most environmentally friendly, resource- and energy-saving method for obtaining graphite intercalation compounds in controlled modes [52, 53] and allows achieving specified characteristics of EG, including regulating the structural and chemical state of both volume and surface. It is known that reintercalation of EG in the classical sense does not occur. Diffusion of the electrolyte (intercalant) proceeds on the existing defects. Repeated pseudo intercalation of dense material from EG makes it possible to "reveal" nanoscale defects in the structure of EG and to obtain a dispersion of GNPs in an aqueous solution of electrolyte.

GNPs was obtained by secondary "intercalation" of electrodes from graphite foil (according to TU U 26.8-30969031-002-2002) in an alkaline electrolyte (KOH) of low concentration with a current transmission of 6.0 to 60.0 mA/cm^2. The separation of nanoparticles was provided by a membrane made of polypropylene fabric (Fig. 4.19) [47—49, 54].

The method of electrochemical production of graphene (Fig. 4.19) includes the movement of the controlled mechanical device (3) of the graphite strip (4), which is the anode, through the bath (1) with electrolyte solution (7) and electrolytic stratification of the graphite strip. As a graphite tape, fiberglass-reinforced EG foil of various bulk densities is used. The fiber-reinforced glass foil is continuously passed at a rate of 0.5—2.0 cm/h through a solution of potassium hydroxide electrolyte, which moves at a controlled speed through an electrolytic bath with an electric field strength of 2—30 V/cm. The electrolytic bath is separated with a membrane into anode and cathode space, and the anode space is separated with a porous filter partition, which passes the suspension of graphene nanoparticles and retains the coarse-dispersed suspension of graphite.

The nanoscale of GNPs was confirmed by studies of Raman spectra (Brucker RFS 100/s spectrometer, the source of radiation was an argon laser,

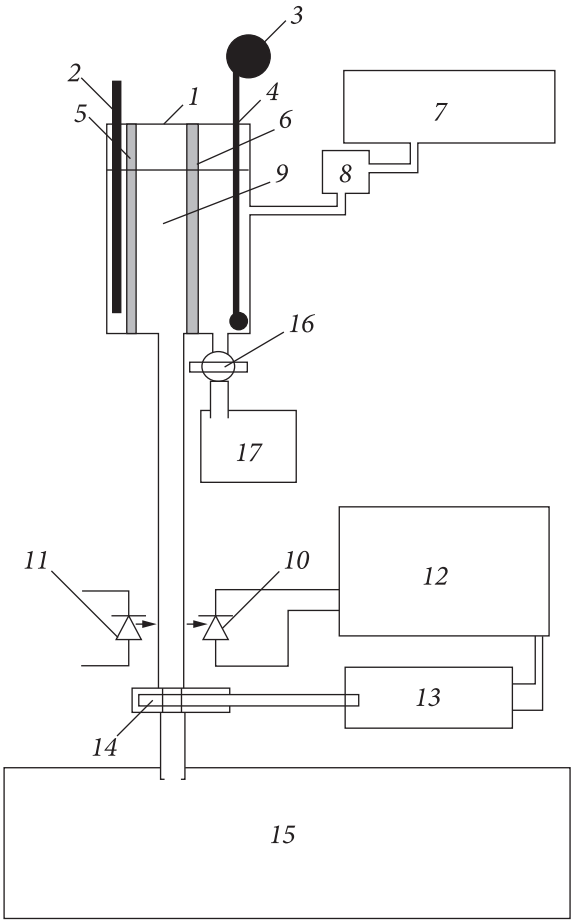

Fig. 4.19. Block diagram of the installation for obtaining a suspension of graphene nanoparticles: *1* — electrolytic bath, *2* — cathode, *3* — cassette device with a strip of fiberglass-reinforced graphite foil, *4* — anode, *5* — polypropylene membrane, *6* — filter, *7* — tank with an electrolyte solution of potassium hydroxide, *8* — float valve, *9* — part of the electrolytic bath for suspension of graphene nanoparticles, *10* — photodiode, *11* — LED, *12* — control unit, *13* — control valve drive, *14* — control valve, *15* — tank for suspension of graphene nanoparticles, *16* — tap for removing coarse suspension of EG, *17* — container for coarse suspension of expanded graphite

λ = 514.5 nm), XRD patterns (powder diffractometer DRON-4 07 with CuKα radiation in nickel from JEOL Bragg-Brentano surveys) (see Chapter 6), thermogravimetric measurements (Derivatograph Q-1500 D (Hungary) in a static atmosphere, and SEM images (JSM-35, JEOL)).

Aqueous dispersions of the obtained materials were analyzed using laser correlation spectroscopy (LCS) (spectrometer "ZetaSizer 3" Malvern Instrument (UK) with a correlator 7032 and helium-neon laser LG-111 with a power of 25 mW for wavelength λ = 633 nm). The software [55] for LCS in the corresponding mode CONTIN ("polymodal" approximation) also allows one to determine the distribution of particles by volume (in the case of constant density — by mass) and by the number of particles of certain sizes, in the approximation of spherical particle shapes. The test suspension electrolyte-surfactant-GNPs in the amount of 1 ml in a cylindrical glass cuvette with a diameter of 10 mm was placed in a thermostat cell of a laser correlation spectrometer. Registration and

statistical processing of laser radiation were performed for 300—400 s. The autocorrelation function was processed using the program PCS-Size mode v 1.61. As a result, we obtained particle size distribution functions [56].

The dependence of the size and shape (the degree of deviation from the sphere, reflecting the coefficients of polydispersity) on the parameters of the process of obtaining nanoparticles of graphene material are given in Table 4.10.

Analysis of the particle size obtained by the LCS method shows that there are two groups of particles in the solution that differ in size. Large particles (13 μm) were found in the suspensions, which eventually sedimented. The second group of particles sizing up to 450 nm was more stable (Fig. 4.20).

Since the variance is unstable over time, the results should be considered qualitative. The average particle size is ~1350 nm. Two fractions: fraction I — size from 10 to 200 nm, quantity — 99,9%, weight ~26%, the most probable size ~40 nm; fraction II — size from 200 to 3200 nm, quantity 0,1%, weight ~74%, the most probable size ~640 nm; the average polydispersity is ~0.6, i.e., the particles have a shape not very far from spherical. The dependence of size and shape on the parameters of the process of obtaining nanoparticles of graphene material is given in Table 4.10.

From the given in Table 4.10 data, the following conclusions can be made:

• within the framework of this method it is possible to adjust the size of graphene particles formed during the anodic oxidation of EG;

• particles are mostly far from spherical (polydispersity coefficient is 1), which is quite natural because they are flat.

A 20-fold diluted GNPs suspension was examined by the SEM method. It was applied to the surface of the substrates (films of gold or carbon on the glass) and dried. Two types of particles were detected (Figs. 4.21 and 4.22). The first

Table 4.10. **Particle sizes of graphene material obtained under different conditions of electrochemical oxidation of EG, determined by the LCS method**

N* sample	Average size, nm	Fraction I size, nm			Fraction II size, nm			Polydispersity
		Minimum	Maximum	Probable	Minimum	Maximum	Probable	
1	2162	8	130	40	130	31 000	7 954	1
2	623	12	300	54	300	25 000	4 133	1
3	1529	11	200	35	200	68 000	16 500	1
4	3251	11	280	35	280	70 000	16 500	1
5	1264	12	300	55	300	43 000	10 048	1
6	1349	12	200	40	200	3 200	642	0.6
7	7049	33	800	42	800	8 000	1 664	1

* Process conditions.

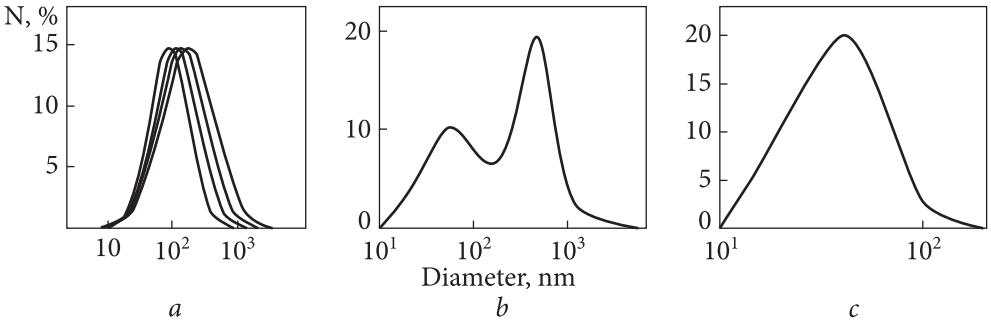

Fig. 4.20. Particle size distribution in suspension (sample 6): *a* — "monomodal" mode; *b*, *c* — "polymodal" mode: *b* — mode of particle distribution by volume (mass at constant density); *c* — particle distribution

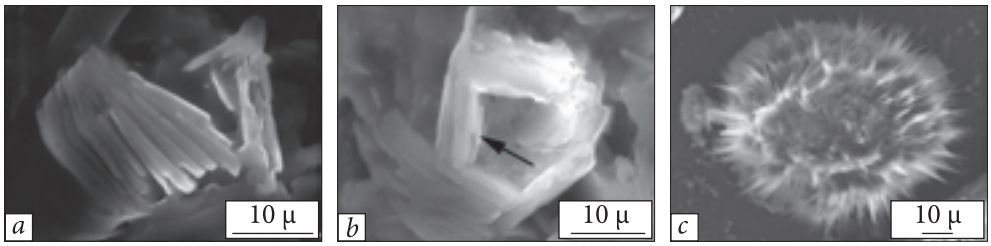

Fig. 4.21. SEM image of the graphite structure on the carbon surface: *a*, *b*, — lamellar agglomerates with an ordered structure, in the form of stacks, prisms, etc., *c* — agglomerates of very thin plates ("flower")

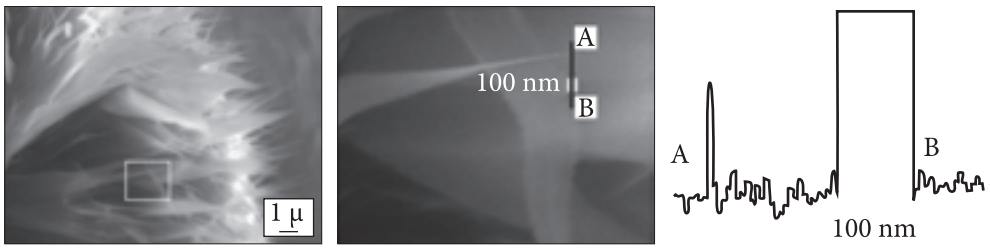

Fig. 4.22. SEM image of graphene structures on the surface of gold (the substrate is inclined at an angle of 60° to the electronic probe): *a* — graphene-like particle; *b* — enlarged images of sections of a graphene-like particle (*a*), respectively (selected square-volume); *c* — the curve of change in the image brightness along the line AB

type is a lamellar agglomerate with an ordered structure. Such particles were encountered in the form of stacks (Fig. 4.21, *a*) or a pentagonal hollow prism (Fig. 4.21, *b*) of plates. The second type of particles is formed into a laminar structure similar to a "flower" and consists of very thin plates (Fig. 4.21, *c*). The

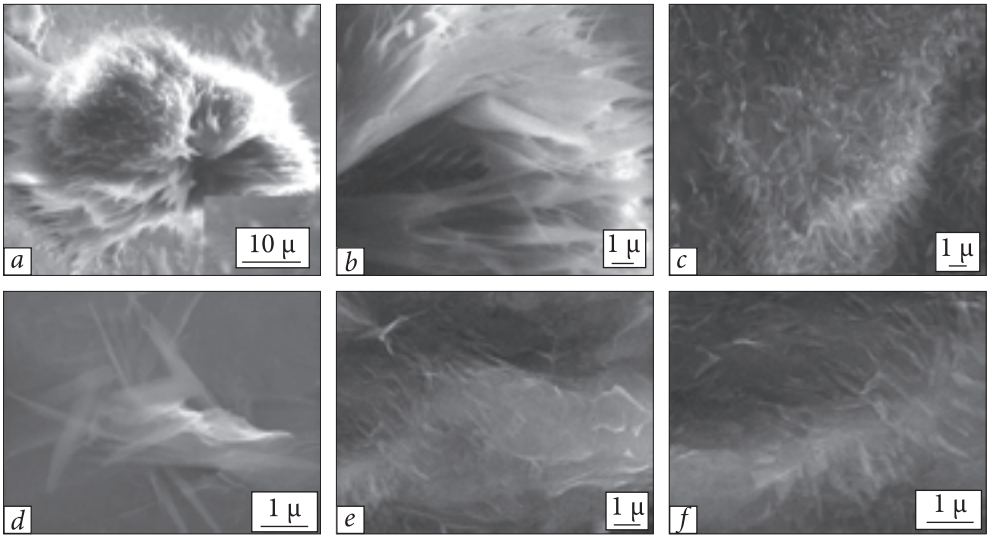

Fig. 4.23. SEM images of GNP samples: *a*, *b* — on a gold base; *c*—*f* — continuous films; *c*, *d* — "free" drying; *e*, *f* — under vacuum ~1 atm in a limited volume

difference between these particles was manifested not only in the shape but also in the conditions of their formation and the thickness of the plates that made up these formations.

The first type of particles was mostly observed in slow drying. The shape of such particles was stable and did not change when irradiated with an electron probe. The minimum thickness of individual plates for this type was 25—30 nm and was recorded for the particle in Fig. 4.21. *b* in the place marked by the arrow. The structures of the second type were formed mainly during the rapid drying of the suspension, which was stimulated by heating the substrate. Such particles were more often observed on gold substrates (Figs. 4.21, *c*, 4.22, *a*, *b*). The thickness of the plates was determined for the particle shown in Fig. 4.22, *a*. It is 5—7 nm. This is illustrated in Fig. 4.22, *c*, where the curve shows the change in brightness of the image along the line AB. The width of the protrusion in the left part corresponds to the plate size in Fig. 4.22, *b*, and on the right — a marker of 100 nm. Since the values of 5—7 nm for this type of SEM are the maximum resolution, it can be assumed that the

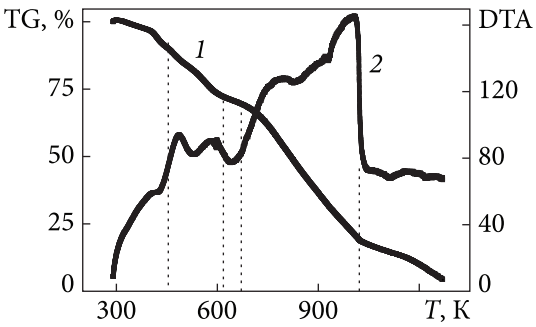

Fig. 4.24. Dependences of TG (*1*) and DTA (*2*) of GNPs films on temperature

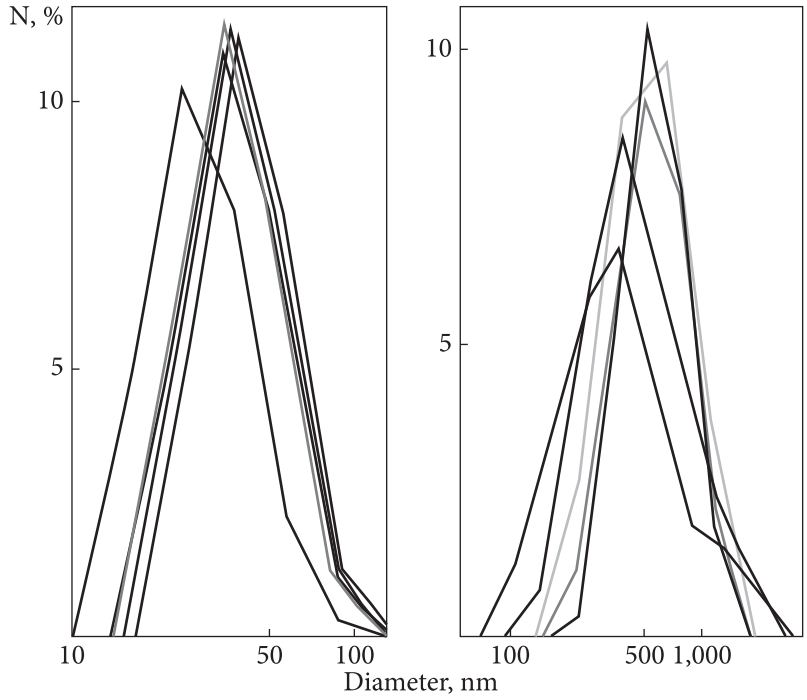

Fig. 4.25. Particle size distribution: left GNPs, right GNPs + CNTs

thickness of the plates is at least twice smaller and is 3—4 nm, i.e. about ten layers.

Dispersions of high concentration form solid films of complex structure (Fig. 4.23 *c—f).* Moreover, depending on the drying conditions, the surface may be more embossed, with the manifestation of the appearance of individual GNP and a smoother film. Figs. 4.23 (*c*, *d*) depict "free" drying; it is possible to distinguish individual GNP, or rather their agglomerates. Fig. 4.23 (*e*, *f*) — infusion "pressing", i.e. drying under vacuum, in a limited volume, the relief is weak.

Fig. 4.24 presents the dependences of TG (1) and DTA (2) of GNP films. Temperatures 450, 620, 660, 690, and 1020 K correspond to temperature anomalies, at which there is a decrease in the sample mass during the thermal destruction of certain components.

Temperature fractures (Fig. 4.24) are associated: 450 K with the desorption of chemically bound water, 620 K with the destruction of amorphous carbon, 660 K with the melting of KOH, and 1020 K with the oxidation of polycrystalline graphite (large particles). In the temperature range of 450—620 K, a mass loss of about 18% occurs, which indicates the decomposition of oxygen-containing functional groups and is accompanied by the release of water and carbon dioxide. In the range of 670—1020 K, about 50% of the initial mass is lost, which is obviously the result of the oxidation of graphene nanoparticles. After 1020 K

there is only polycrystalline graphite (weight loss up to 17% wt.). Thus, by the gravimetric analysis of annealed films (without volatile) (Fig. 4.24), GNPs is about 75% wt., the rest are graphite particles.

Recently, composite nanosystems of graphene-carbon nanotubes, nanoparticles, GNPs, and other nanosized carbon materials have been intensively studied, for example in [57—59]. Moreover, their producing both for the purpose of obtaining composite dispersions in liquid, as composite films with high characteristics of electrical and thermal conductivity [26, 27], and as a composite filler of polymeric materials [60, 61]. The section above has described the process of obtaining EG-CNTs composite and its characteristics. It is quite natural that GNPs-CNTs composites were obtained by the method of secondary anodic oxidation of graphite foil from EG-CNTs composite (in an alkaline electrolyte (KOH) of low concentration; current from 6.0 to 60.0 mA/cm^2). The method of laser correlation spectroscopy showed that the obtained dispersions are stable with particle sizes of 20...70 nm and 200...1000 nm (Fig. 4.25).

The graphene nanoparticle films formed during drying of dispersion on the substrate are quite heterogeneous but show the thermal conductivity at the level of the EG-CNTs composites. Both dispersions and solid films exhibit photoluminescent properties (see Chapter 6).

Based on the above, we can draw some ***conclusions***.

1. The possibility of creating modifying coatings on expanded graphite with metals and their oxides in the form of an island film with the addition of precursors in the process of thermal expansion of graphite is shown.

2. By the method of direct thermal-oxidative conversion of natural graphite due to its interaction with $FeCl_3 \cdot 6H_2O$ in the temperature range (300—600) °C, it is possible to obtain disordered GIC-$FeCl_2$ with the maximum content of intercalant up to 50% wt., and in the range (800—1000) °C — GIC-Fe of the first stage with the maximum content of intercalant 36—37% (C_8Fe). The latter can be used in an oxidizing environment at a temperature of (500—600) °C.

3. When chemically modifying the surface of EG particles, namely, thermosetting organic compounds, an increase in interparticle interaction and creation of a continuous distributed carbon structure in the graphite matrix take place, which changes the physical (especially mechanical) characteristics of the composite materials obtained. The addition of a high-modulus component such as carbon fiber into the EG-carbon or EG-polymer systems changes the behavior of materials during deformation and allows one to create an EG-CNT system without binders.

4. A method for the synthesis of graphene nanoparticles and composite nanoparticles GNPs-CNTs by anodic oxidation of rolled materials from EG and EG-CNT composites, which allows adjusting the size and structural characteristics of the obtained dispersions of nanoparticles and solid films from them, has been developed.

REFERENCES

1. I.G. Chernysh, Yu.I. Sementsov and O.P. Yatsyuk, in: *Proceeding 2nd All-Union School of Physics and Chemistry of Loose and Layered Crystal Structures* (Harkov, 1988), p.112. [in Russian]
2. I.G. Chernysh, L.A. Mironova, O.P. Yatsyuk and Yu.I. Sementsov, *Thermodynamic analysis of heterogeneous systems in the process of obtaining modified graphite* (VINITI № 6105, Kiev, 1989) [in Russian]
3. I.G. Chernysh, O.P. Yatsyuk, A.A. Chuyko, Yu.I. Sementsov and L.L. Voznaya, A.S. USSR No. 1686792 (22 June, 1991) [in Russian]
4. I.G. Chernysh, Yu.I. Sementsov, O.P. Yatsyuk, L.L. Voznaya and L.A Mironova, *High-temperature surface modification of dispersed graphite with zinc oxide* (VINITI № 3404, Kyiv, 1990) [in Russian].
5. I.G. Chernyish, Yu.I. Sementsov, O.P. Yatsyuk, L.L. Voznaya and L.L. Vovchenko, *Physico-chemical properties of thermally expanded graphite modified with iron compounds* (VINITI № 3403, Kiev, 1990) [in Russian].
6. O.P. Yatsyuk, Ph.D. dissertation, Institute of Surface Chemistry National Academy of Sciences of Ukraine, Kyiv, 1992. [in Russian]
7. I.G. Chernysh, I.I. Karpov, G.P. Prihodko and V.M. Shay, *Physico-chemical properties of graphite and its compounds* (Nauk. dumka, Kyiv, 1990). [in Russian].
8. D.D.L. Chung, J. Matter. Sci. **22** (12), 4190 (1987).
9. Yu.N. Novikov and M.E. Volpin, Zhurn. Vsesoyuznogo himicheskogo obschestva im. D.I. Mendeleeva. **32**, (1), 69 (1987) [in Russian].
10. G.S. Petrov, A.C. Skoropanov and A.A. Vecher, Russian chemical reviews. **56** (8), 701 (1987).
11. A.W. Morawski and K. Kallucki, Carbon. **27** (6), 951 (1989).
12. I.G. Chernysh, N.F. Gadzyra, Yu.I. Sementsov and O.P. Yatsyuk, in: *Abstract Book 1st All-Union. conf. "Chemistry and physics of interstitial compounds"* (Rostov–na–Donu, 1990), p. 40. [in Russian].
13. I.G. Chernysh, N.F. Gadzyra, Yu.I. Sementsov and O.P. Yatsyuk, *The effect of iron chloride modification of the residual graphite bisulfate compound on the structural features of expanded graphite* (VINITI №3405, Kyiv, 1990) [in Russian].
14. P.C. Eklund, in: *Intercalation in Layered Materials: Proceedings of the 10th Course of the Erice Summer School*, edited by M. S. Dresselhaus (Springer, Boston, MA, 1986), NATO ASI Series (Series B: Physics), vol.148, pp. 167—172.
15. Yu. I. Sementsov, L.G. Koval, V.P. Didukh and V.I. Lysov, Him. prom. Ukraine. (4), 34 (1994). [in Ukrainian]
16. Yu.I. Sementsov, L.G. Koval and A.A. Chuyko, Ekotehnologii i resursozberezhenie. (2), 27 (1997). [in Russian]
17. Yu.I. Sementsov, M.L. Pyatkovsky, G.P. Prikhod'ko, V.M. Ogenko, I.G. Sidorenko and V.V. Yanchenko, in: *Chemistry, physics and technology of surfaces*, Interdepartamental Digest of Scientific Papers, edited by O.O. Chuiko (NAS of Ukraine. Institute of Surface Chemistry, Kyiv, 2002), iss. 8, pp. 190—214.
18. S.A. Solin, Adv. Chem. Phys. **49**, 455 (1982).
19. S.V. Lyubchik and V.V. Shapranov, Functional Materials. **2**, 124 (1995).
20. M.V. Savos'kin, T.V. Khabarova, A.P. Yaroshenko, V.V. Shapranov, V.A. Kucherenko and S.B. Lyubchik, RF Patent No. 2057064 (27 March, 1996). [in Russian]

21. Yu.I. Sementsov, L.G. Koval, L.L. Mihaylova and M.L. Pyatkovskiy, Himichna promislovist Ukraine. (3), 16 (2000) [in Ukrainian].
22. K.E. Mahorin, A.P. Kozhan and V.V. Veselov, Him. tehnologiya. (2), 3 (1985). [in Russian].
23. R. Schlögl, P. Bowen, G.R. Miiward, Jones IV. and H.P. Boehm, J. Chem. Soc, Faraday Trans, I. **79**, 1793 (1983).
24. G. Sirokman, A. Mastalir, A. Molnar, M.Bartók, Z.Schay and L.Guczi, Carbon. **28** (1), 35 (1990).
25. T.A. Kizina, A.C. Skoropanov, A.A. Vecher, G.A. Protsenko, Yu.N. Novikov and M.E. Volpin, Zhurnal obshchei khimii. **56** (9), 1936 (1986). [in Russian].
26. A.C. Skoropanov, T.A. Kizina, N.G. Rafalskiy, A.A. Vecher, Yu.N. Novikov and M.E. Volpin, Zhurnal neorgan. khimii. **29** (10), 2521 (1984). [in Russian]
27. Yu. I. Sementsov, M. L. Pyatkovskii and I. G. Chernysh, Powder Metallurgy and Metal Ceramics. **37** (9–10), 545 (1998).
28. I.D. Buraya, L.L. Voznaya L.L. Vovchenko, Yu. I. Sementsov, I. G. Chernysh and O.P. Yatsyuk, Himiya tverdogo topliva. (6), 106 (1990) [in Russian].
29. M.L. Pyatkovskiy, Yu.I. Sementsov and I.G. Chernysh, Khimichna promyslovist Ukrainy. (3), 42 (1996).
30. Yu.A. Nikitin, M.L. Pyatkovskii and I.G. Chernysh, Powder Metallurgy and Metal Ceramics. **37** (5/6), 253 (1998).
31. S.V. Shulyepov, *Fizika uglyerodnykh materialov* («Myetallurgiya» Chyelyabinskoye otdyelyeniye, Chyelyabinsk, 1990) [in Russian].
32. Yu.I. Sementsov, M.T. Kartel, N.A. Mykhailenko and V.V. Yanchenko, Ukraine Patent No. 92773 (10 September, 2014) [in Ukrainian].
33. Yu.I. Sementsov, M.T. Kartel, N.A. Mykhailenko and V.V. Yanchenko, Ukraine Patent No. 91436 (10 July, 2014) [in Ukrainian].
34. Yu.I. Sementsov, M.T. Kartel, N.A. Mykhailenko and V.V. Yanchenko, Ukraine Patent No. 118743 (11 March, 2019) [in Ukrainian].
35. Jong-sam Yu, US Patent Application No. 20120219719 (30 August, 2012).
36. T. Ueda and T. Shiomi, US Patent No. 5240769 (31 August, 1993).
37. Z. Wang, M.D. Shirley, St.T. Meikle, R.L.D. Whitby and S.V. Mikhalovsky, Carbon. **47** (1), 73 (2009).
38. A.V. Melezhik and A.A. Chuyko, Khimicheskaya tekhnologiya. (2), 3 (1992).
39. Yu.I. Sementsov, S.L. Revo, K.O. Ivanenko and S. Hamamda, *Expanded graphite and its composites,* edited by M.T. Kartel (Akademperiodika, Kyiv, 2019).
40. A.K.Geim and K.S.Novoselov, Nat. Mater., **6**, 183 (2007).
41. C.N.R.Rao, A.K.Sood, K.S.Subrahmanyam and A.Govindaraj, Angew Chem Int. Ed Engl, **48** (42), 7752 (2009).
42. C.N.R. Rao, A.K. Sood, R .Voggu and K.S. Subrahmanyam, J. Phys. Chem. Lett., **1** (2), 572 (2010).
43. B. Jang and A. Zhamu, J.Mater. Sci., **43** (15), 5092 (2008).
44. E.D. Graifer, V.G. Makotchenko, A.S. Nazarov, S.J. Kim and V.E. Fedorov. Russ. Chem. Rev. **80** (8), 751 (2011).
45. V. Dhand, K.Y. Rhee, H.J. Kim and D.H. Jung, Journal of Nanomaterials. **2013**, 763953, (2013). https://doi.org/10.1155/2013/763953.
46. S. Yang, S. Brüller, Z.-S. Wu, Z. Liu, K. Parvez, R. Dong, F. Richard, P. Samorì, X. Feng and K. Müllen, J. Am. Chem. Soc. **137** (43), 13927 (2015).

47. M. Kartel, Yu. Sementsov, G. Dovbeshko, L. Karachevtseva, S. Makhno, T. Aleksyeyeva, Yu. Grebel'na, V. Styopkin, W. Bo and Yu. Stubrov, Advanced Materials Letters. **8** (3), 212 (2017).
48. Y. Sementsov, S. Makhno, M. Kartel, W. Bo G. Dovbeshko, V. Styopkin and S. Nedilko, International Journal of Innovative Ṡcience, Engineering & Technology. **4** (7), 71 (2017)**.**
49. S.G. Nedilko, S. Revo, V. Chornii, V. Scherbatskyi, K. Ivanenko, M. Nedielko, Y. Sementsov, M. Skoryk, A. Nikolenko and V. Strelchuk, Nanoscale Res Lett. **12**, 28 (2017).
50. P. Tripathi, Ch.R.P. Patel, M.A. Shaz and O. N. Srivastava, Materials Science (cond-mat.mtrl-sci) (2013), https://doi.org/10.48550/arXiv.1310.7371
51. K.S. Rao, J. Senthilnathan, Y.-F. Liu & M. Yoshimura, Scientific reports. **4**, 4237 (2014). https://doi.org/10.1038/srep04237
52. Yu.I. Sementsov and M.T. Kartel, Chemical industry Ukraine. (3), 56 (2015).
53. M. Kartel, Yu. Sementsov, S. Makhno, W. Zhang, X. Zhang, L.V. Gen and Bo Wang, IJISET. **4** (7), 203 (2017).
54. Yu.I. Sementsov, S.M. Makhno, M.T. Kartel, S.M. Gozhdzins'kii, K.O. Ivanenko, Yu.V. Grebel'na, A. Ding, B. Wang, D. Wang and T. Li, Ukraine Patent Application No. a202102264 (28 April, 2021).
55. S.E. McNeil, editor, *Characterization of Nanoparticles Intended for Drug Delivery* (Humana Press, New York, 2011). DOI 10.1007/978-1-60327-198-1
56. E.O. Kovalska and Yu.I. Sementsov, in: *Nanomaterials Imaging Techniques, Surface Studies, and Applications*, edited by O. Fesenko, L. Yatsenko and M. Brodin (Springer, New York, 2013), pp. 61—72.
57. C.P. Bosnyak and K.W. Swogger, USA Patent No. 20170037252 (9 February, 2017).
58. D. Wang, Di Lijie, D. Xianbo and V. Zhongqiang, China Patent No. 107317034 (A) (03 November, 2017).
59. Yu.I. Sementsov and N.T. Kartel, in: *Surface physics and chemistry*, edited by N.T. Kartel and V.V. Lobanov (Interservis, Kyiv, 2018). vol. 2, pp.1035—1047 [in Russian].
60. J. Kim, J. Oh, K. Y. Lee, I. Jung and M. Park, Composites Part B. **114**, 445 (2017).
61. S. Lin, M.A.S. Anwer, Y. Zhou, A. Sinha, L. Carson and H.E. Naguib, Composites Part B. **132**, 61 (2018).

CHAPTER 5

COMPOSITIONS FILLED WITH CARBON NANOMATERIALS

Currently, the need for the development and implementation of innovative technologies for the creation of composite materials (CM) based on polymer, elastomeric, ceramic, metal, carbon, and other matrices [1—5] is inspired by the understanding that their use in aircraft designs [6—8], cars, ships of other vehicles, elements of equipment in mechanical engineering, etc. [9—20] can provide the following improved features: reduced weight of fuselage, car, ship, etc.; increased the fuel efficiency of their systems; prolonged resource; reduced operating costs and maintenance costs due to increased corrosion resistance. The elements of aircraft structures of large size and low rigidity require the use of rubber heat-protective coatings that do not break during the structure deformation. The use of rubber for supersonic aircraft and spacecraft is limited due to high requirements for heat and frost resistance of materials, as well as their resistance to radiation and vacuum. Therefore, the development of new rubbers with improved characteristics as well as other polymer CMs is an urgent technological task.

Thus, the use of composite materials reduces costs by up to 10%, and the expected savings in costs of maintenance, such as for aircrafts, can be up to 30% due to reducing the number of parts in the structure, and, consequently, reducing the complexity and cost of their assembly.

The use of nanosized particles as fillers in polymer binders in order to improve the physical and mechanical properties of polymer composites has been actively studied recently [12—19]. For example, pyrogenic silica was used in [12], particles of nanographite in [13], nanoplates of graphite and oxidized graphene in [14], — particles of SiO_2 and Al_2O_3 of nanometer and micron size in [15]. Epoxy resin was reinforced with fresh rubber scrap powder in [16], and the mechanical properties and durability of fiberglass composite, phenolic resin filled with nanoclay and mul-

tilayer composite with an expanded polystyrene core, have been investigated in [17, 18]. The authors of work [19] showed that the addition of 2 mass% of one of the oxides ZrO_2, ZnO, SiO_2, and Fe_2O_3 increases the hardness and modulus of elasticity of the epoxy-polyamide system by 71 and 26%, respectively. However, the most common is the use of carbon nanotubes as the most effective reinforcing element [1—5, 20]. The mechanical and thermal properties of ideal single-wall CNTs are unique and are determined by several factors [21]: high strength of sp^2 C—C bonds; superdense packing of atoms in the graphene plane; absence or low-density structural defects. As calculations show, the average modulus of elasticity of multiwall CNTs is more than 1.8 TPa, and the measured value is 1.3 TPa [22]. With that and, taking into account the aspect ratio (η) (length to diameter ratio, which is ~10^3), the flow threshold Fp ~ 1/η (i.e. the content at which a continuous CNTs grid is formed) may be ~0.1% wt. if CNTs distribution is uniform in the polymer matrix [23, 24]. CNTs are widely used to obtain new high-strength composite materials for both structural and functional purposes, which are predicted to be widely used in engineering [6—13].

5.1. Preparation of multiwall CNTs to obtain composite materials: deagglomeration of carbon nanotubes

The addition of CNTs to the polymer matrix affects the structure of composite material (degree of crystallinity of the matrix), biocompatibility, as well as increases its strength, electrical and thermal conductivity, and thermo-oxidation stability [1—5, 23—40]. With an industrial production by precipitation from a gas phase (CVD) [25, 31, 32, 36, 41—43], carbon nanotubes are obtained in the form of agglomerates of confused tubes with dimensions of 20—500 μm (Fig. 5.1).

Homogeneous distribution of carbon nanoparticles (CNP) in matrices of different nature is a fundamentally important task in implementing the high effects of filler and achieving composite materials of unique characteristics [23, 24, 44, 45]. The tendency of nanotubes to aggregation is transcribed by achieving high levels of dispersion. Therefore, mixing, addition of surfactants, and modification of CNTs permit homogenization of the filler and, as a consequence, improvement of the composition properties [46—53]. The result of the CNT-surfactant interaction depends on the nature of the latter (Fig. 5.2) and the environment.

It is believed that the presence of ionic surfactants [48] stabilizes aqueous dispersions of CNTs. For example, 0.3% wt. of surfactant and 0.02% wt. of CNTs is a stable dispersion, and the absence of surfactants leads to rapid sedimentation of nanotubes [49].

The authors of [50] showed that the structure of surfactants affects the diameter of dispersed CNTs aggregates. Obtaining stable suspensions of CNTs is

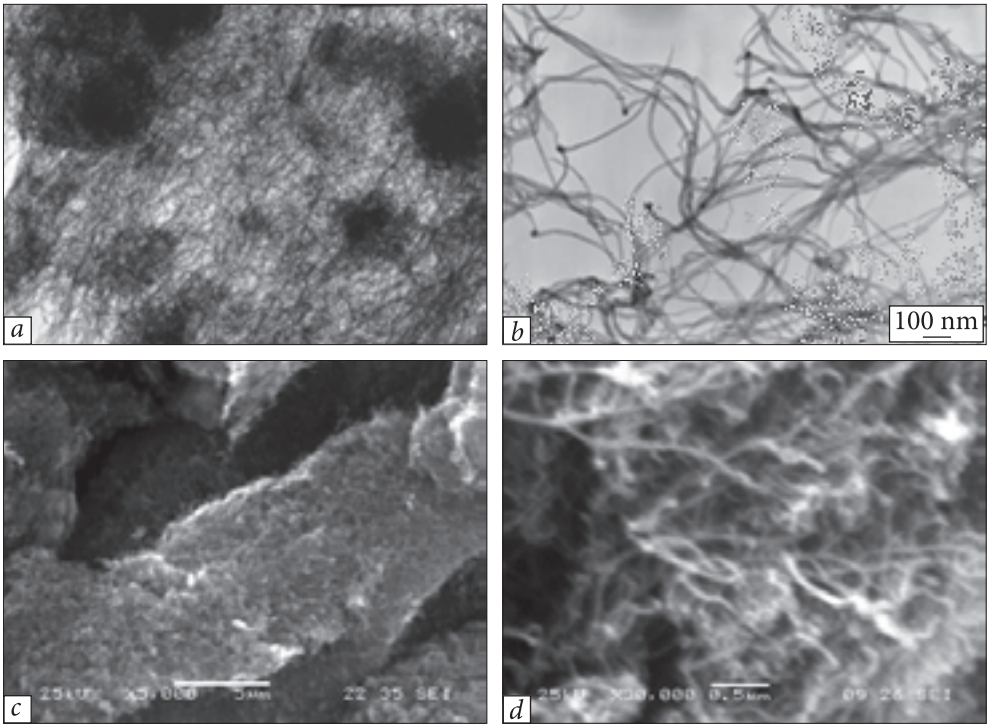

Fig. 5.1. TEM (*a*, *b*) and SEM (*c*, *d*) images of carbon nanotubes obtained by the catalytic CVD method

Table 5.1. **Electrostatic superplasticizers**

Name, composition	Structural formula
Lignosulfonate (LST), lignosulfonates purified	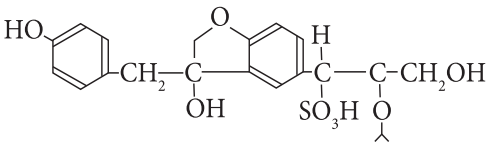
Naphthalene formaldehyde NF), sulfonated naphthalene-formaldehyde polycondensates	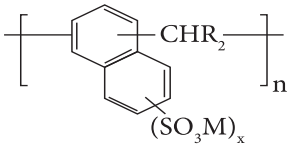
Melaminoformaldehyde (MF), sulfonated melamine-formaldehyde polycondensates	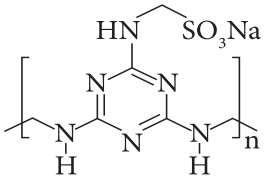

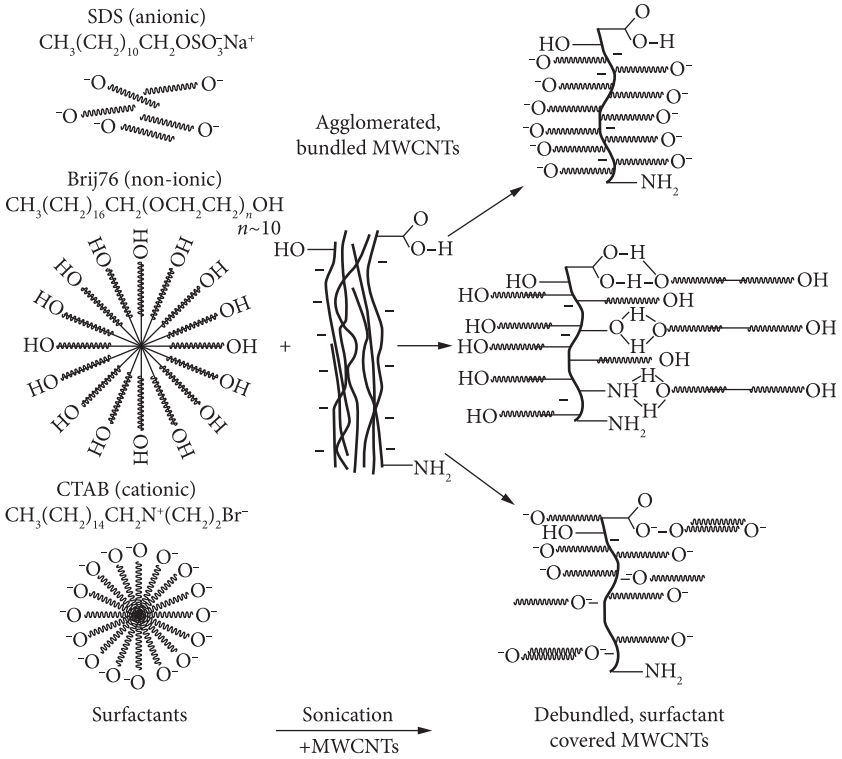

Fig. 5.2. Schematic representation of possible interactions of multiwall CNTs with surfactants of different nature during sonication [47]

due to the affinity of the structures of nanotubes and copolymers, for example, 1 wt.% of CNTs in ethanol solution with the addition of 20 wt.% of non-ionic surfactants [51]. A necessary condition for the effective action of surfactants is a mechanical impact (e.g. ultrasonic action), which provides the first act of detachment of CNTs from each other [52].

An example of ionic surfactants is plasticizing additives (plasticizers), which are used in the technology of concrete and reinforced concrete structures [53]. Based on the results [54—57], some superplasticizers are listed in Table 5.1: lignosulfonate (LS, Sika-Plast 520), naphthalene-formaldehyde (NF, Polyplast SP-1), and melaminoformaldehyde (MF), Muraplast FK 98).

This choice is due to the well-studied and effective use of them in cementitious materials: mortars and concretes.

The mechanism of action of plasticizers [58] is schematically presented in Fig. 5.3. Plasticizer molecules are adsorbed on the surface of cement particles and new nanoforms are formed. This creates a thin mono or bimolecular layer, which reduces the interfacial interaction energy and facilitates the disaggrega-

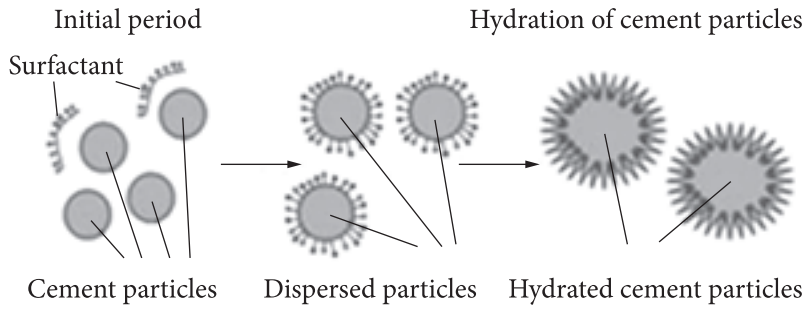

Fig. 5.3. Scheme for the mechanism of action of traditional plasticizers [58]

tion of particles. At the same time, immobilized water is released, which acts as a plasticizing oil. In addition, the adsorbed layer smoothes the microroughness of the particles, thereby reducing the friction coefficient between them. The creation of the same electric charge on the particle surface eliminates the possibility of their adhesion due to electrostatic forces and thus reduces the suspension viscosity. In the process of hydration, the repulsive action of the electric charges of the same sign gradually ceases, and the mortar loses its mobility.

Multiwall CNTs [59] synthesized by the method of catalytic CVD-synthesis using three-component iron-containing catalysts were used to prepare "plasticizer-CNTs" suspensions [59]. Fig. 5.1 presents images of CNTs obtained using TEM (transmission electron microscope JEM-100CXII, accelerating voltage 100 kV, resolution 2.04 Å). The size of CNTs agglomerates lies in the interval of 20—500 μm, while the outer diameter of CNTs is 10—40 nm; the purity of purified from mineral impurities CNTs is about 99%; the specific surface area is 200—400 m^2/g, and the bulk density is 20—40 g/dm^3.

The systems were prepared as source aqueous dispersions of plasticizers with a content of 4% wt. filled with CNT in the amount of 0; 0.5; 1.0 and 1.5% wt. [60]:

- "NF-CNT" is a solution of naphthalene-formaldehyde plasticizer, the dispersions codes are: "NF-0", "NF-0.5", "NF-1", "NF-1.5";
- "MF-CNT" is a solution of melamine-formaldehyde plasticizer, the dispersion codes are: "MF-0", "MF-0.5", "MF-1", "MF-1.5";
- "LS-CNT" is a solution of lignosulfonate plasticizer, the dispersions codes are: "LS-0", "LS-0.5", "LS-1", "LS-1.5".

Processing of the prepared CNT suspensions was carried out in a rotary homogenizer, namely a hydrodynamic unit-homogenizer [61] (Fig. 5.4), which provided the simultaneous action of shear deformation and cavitation mixing.

The device developed by the Department of Applied Hydro-aeromechanics of Sumy National University is characterized by a low level of energy consumption, high product quality, minimum dimensions, and a high level of reliability.

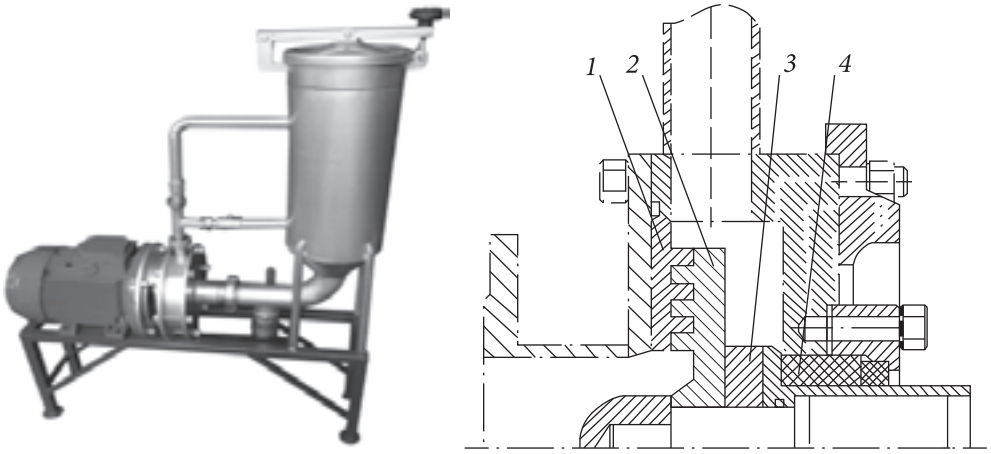

Fig. 5.4. Rotary hydrodynamic unit-homogenizer: *a* — photo; *b* — drawing of the flowing part [61]: *1* — stator; *2* — rotor; *3* — washer adjusting gap between the stator and rotor disks; *4* — end seal

Studies of the processes of homogenization and stabilization of dispersions were performed on samples of the composition "plasticizer-CNT", in particular, the size of CNT agglomerates was determined using photon or laser correlation spectroscopy (PCS or LCS). The particle size distribution function was determined on a Zeta Sizer-3 spectrometer (Malvern Instrument, UK) with a correlator 7032 using a helium-neon laser LG-111 with a power of 25 mW and wavelength $\lambda = 633$ nm. The investigated suspension of multiwall CNTs in the amount of 1 ml in a cylindrical glass cuvette with a diameter of 10 mm was placed in a thermostatic cell of a laser correlation spectrometer. Registration and statistical processing of laser radiation were performed for 300—400 s. The autocorrelation function (ACF) was processed using PCS-Size mode v1.61 [62].

As a result of the LCS research, the particle size distribution functions were obtained. Dependences were registered in the so-called "monomodal" mode several times after periodic shaking of the cuvette. Within the framework of this technique, it is considered that the dispersion is stable, provided the maximum distribution is not shifted due to "shaking", and "conditionally stable" when the maximum fluctuates near a certain middle position. When the maximum distribution is shifted after "shaking" to one side, the variance is considered unstable. The obtained polydispersity coefficient reflects the average statistical deviation of the particle sizes from the ideal sphere of the corresponding size because the particle is modeled as a sphere. For unstable systems, the results are considered only qualitatively because of large errors, which can be several tens of percent. The software [62] in the corresponding counting mode ("polymodal" approxi-

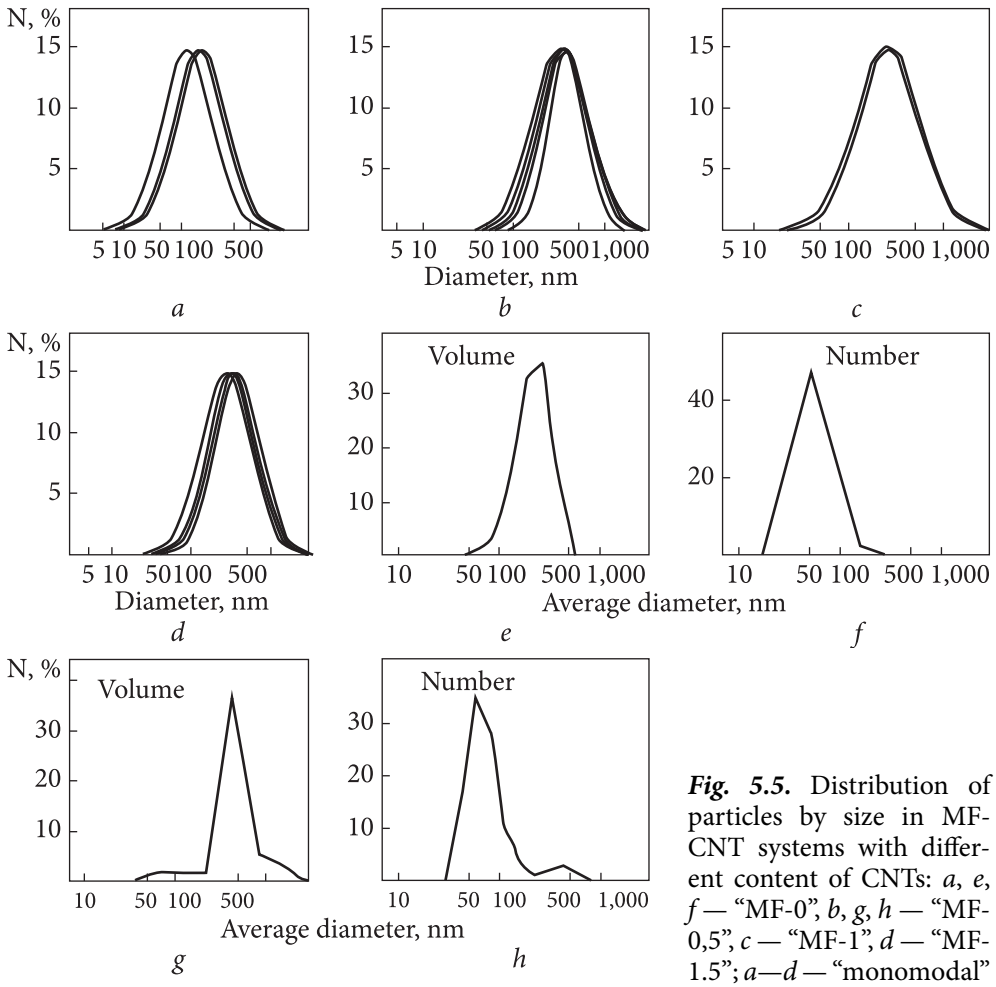

Fig. 5.5. Distribution of particles by size in MF-CNT systems with different content of CNTs: *a*, *e*, *f* — "MF-0", *b*, *g*, *h* — "MF-0,5", *c* — "MF-1", *d* — "MF-1.5"; *a*—*d* — "monomodal" mode in the dependence of particle size distribution; *e*—*h* — "Polymodal" mode in the development of an effective volume (*e*, *g*) and the number of particles (*f*, *h*) from their average diameter [60]

mation) also allows one to determine the distribution of particles by volume (or by mass for constant density) and the number of particles of certain sizes, again in the approximation of the spherical shape of particles.

The colloid-chemical properties of dispersed systems significantly depend on the particle size, but for many technological processes associated with the formation of a homogeneous spatial structure of primary particles, the polydispersity of powders also plays an important role. Disperse systems, including carbon, are not always monodisperse, because they often contain particles of different shapes and sizes. An urgent problem, in addition to the stabilization of CNTs dispersions, is the search for conditions for obtaining dispersed systems

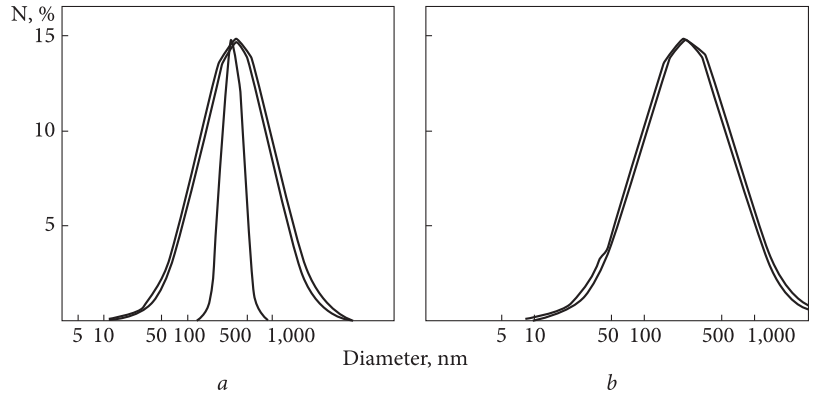

Fig. 5.6. Laser correlation spectroscopy. Particle size distribution: after obtaining an aqueous dispersion (*a*) and after holding it for one year (*b*)

with a high degree of homogeneity of particles in their shape and size (with low polydispersity).

Fig. 5.5 shows, as an example, the size distribution of particles in the MF-CNTs systems with different content of CNTs.

For the other two systems, particle distribution dependences are similar.

Thus (Fig. 5.5), within the framework of the accepted approximations, the systems have to be considered as "MF-0" — unstable, "MF-0.5" and "MF-1.5" — conditionally stable, and"MF-1" — stable.

The system "MF-0" which has an average particle size of about 870 nm, contains two fractions. One is from 20 to 200 nm, the number of particles is 99.9%, the mass is 0.1%, and the smallest size is 64 nm. The other is from 300 to 50,000 nm, the number of particles is 0.1%, and the mass is 99.9%. The most probable particle size is 18,100 nm. The system has a high polydispersity: PI = 1.

The system "MF-0.5" has an average particle size of about 360 nm and contains two fractions. One is from 30 to 250 nm, the number of particles is 92.5%, their mass content is 6.9%, and the most probable size is 99 nm. The other is from 250 to 3000 nm, the number of particles 7.5%, mass content 93.1%. The most probable particle size is 553 nm. The system has an average polydispersity PI = 0.37.

The results of treatment of suspensions of the system "water-soluble polymer-surfactant-multiwall CNTs" in a rotary homogenizer as-prepared (*a*) and after holding for a year (*b*) (WSP is an acrylic copolymer, surfactant is an ethoxylate of isodecyl alcohol) are shown in Fig. 5.6.

From the data of Fig. 5.6, it can be seen that the resulting dispersion is stable.

In most cases, the synthesis results in closed CNTs with a fairly perfect structure, which leads to their high hydrophobicity and low reactivity. Gasification and destruction reactions are used to open CNTs and increase their reactivity. Oxygen and its mixtures, ozone, CO_2, wet Cl_2, radicals, and ions formed

in oxygen or aqueous plasma are used as oxidants. No less common is the use of aqueous solutions of acids (nitric, sulfuric, hydrochloric, pyroxyacetic, trifluoroacetic, a mixture of nitric and sulfuric, hydrochloric acids and hydrogen peroxide, some peracids, etc.), solutions of H_2O_2, O_3, Br_2, $K_2Cr_2O_7$, $KMnO_4$, CrO_3, MnO_2, and other reagents. Some methods of modifying multiwall CNTs have been described in Section 3.

5.2. Inorganic compounds with carbon nanotubes

5.2.1. Building materials modified by CNTs

Today and with a view to the near future, concrete remains the main construction material. It is an artificial system of a mixture of binder (cement), aggregates (sand, slag, ash, zeolites, etc.), water and, if necessary, special additives and is characterized by the complexity of the structure, relatively low cost, low energy consumption, available raw material base and thus can be used in a variety of operating conditions. The study of concrete is reflected in many works on cement chemistry, informing about the formation of clinker and chemical aspects of hydration, as well as concrete technology, which considers in detail the practical features of its production and physicochemical properties [63—65]. To implement the targeted structure formation of building composites, it is proposed to introduce nanosized fillers [66], in particular CNTs [67—70]. They play the role of not only the centers of crystallization but also objects that change direction and regulate the rate of physicochemical processes in hardening materials. The presence of nanosized fillers promotes the formation of waterproof, frost-resistant, and refractory characteristics of concrete. The use of CNTs also provides radio-absorbing ability [71]. The need to solve the problem of ever-increasing "electromagnetic smog", which when interacting with the human electromagnetic field partially suppresses it and, as a consequence, leads to dysfunction of the body and the emergence of serious diseases [72—74], requires the development of highly effective, technological, easy-to-operate shielding and radio-absorbing materials [75]. For example, ordinary concrete, the conductivity of which depends on the moisture content (for dry sample, the value of conductivity ~10^{-8} S/m, and for wet ~10^{-3} S/m), is used not only as a structural material but also as a dielectric and conductive. The addition of CNTs to the concrete mixture leads to the reinforcement of cement stone, turning it into a high-strength composite material [76]. In a number of works [77—78], the modification of cement compositions by nanoparticles was considered, in particular, an increase in the compressive strength of fibroconcrete by 50%, as filler content of 0.002% wt. [79]. A necessary condition for the effective action of CNTs is to achieve their uniform distribution in the matrix

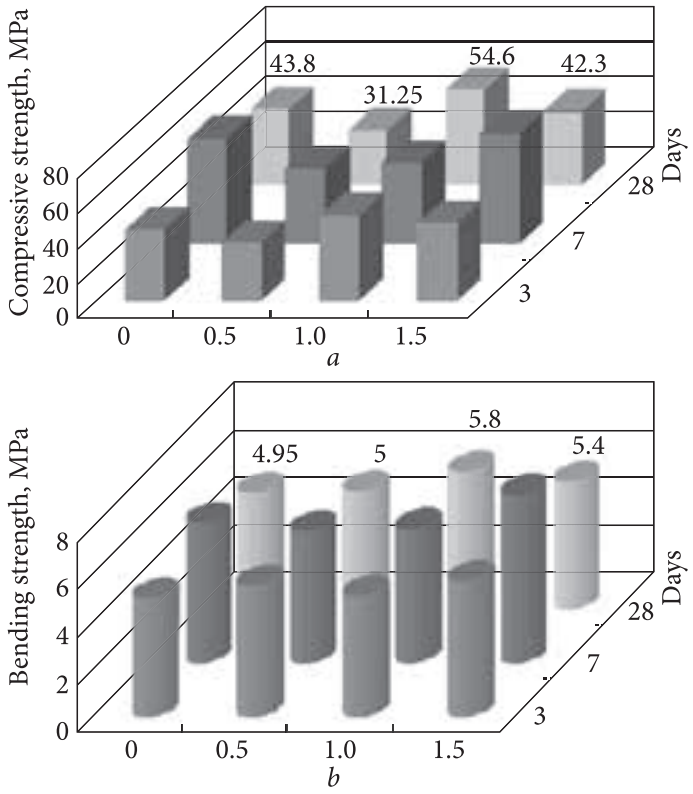

The content of CNT in the aqueros dispersion, % wt.

[40, 44]. Therefore, mixing, adding surfactants as well as modifying nanotubes make it possible to homogenize the filler and, as a consequence, improve the properties of the cement structure.

The use of surfactants can significantly facilitate the formation of products or, with constant mobility of the mixture, reduce the water content and thus reduce the porosity, increase the density, strength, and some other characteristics of concrete. This, in turn, increases the service life of products and significantly reduces unit costs. The choice of additives for concrete or their solutions is carried out according to the purpose. There are three groups of such substances [54] aimed to:

• regulate the properties of ready-to-use concrete and dissolved mixtures (plasticizing water-reducing, stabilizing, regulating mobility, pore-forming);

• control the kinetics of hardening, shrinkage, and expansion processes that increase the strength, protective properties against steel reinforcement, frost, and corrosion;

• improve frost-resistant, hydrophobic and biocidal properties of concrete and mortars, as well as increase resistance to salinity.

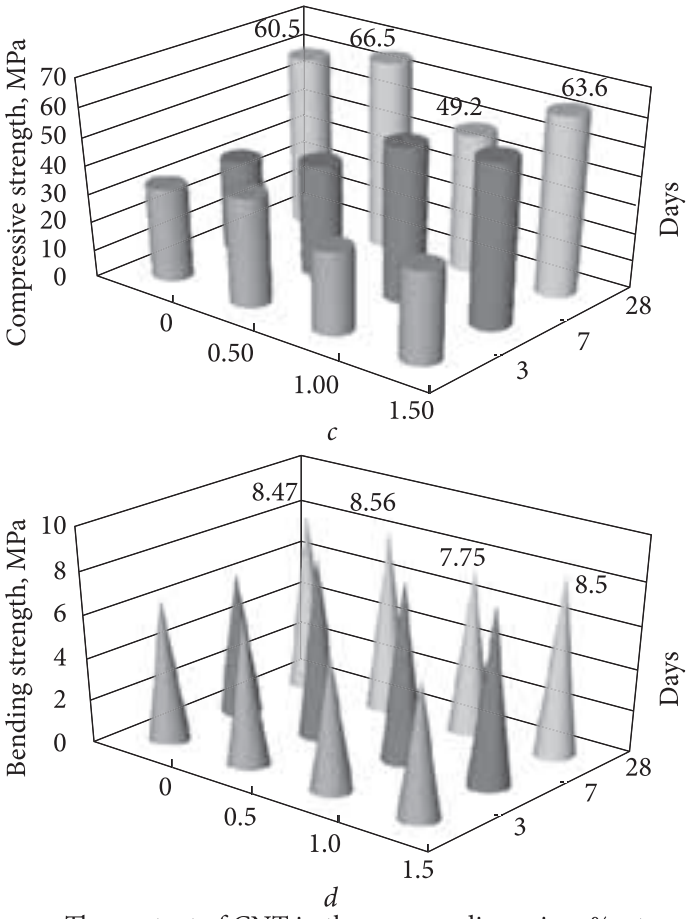

Fig. 5.7. Kinetics of change in compressive strength (*a*) and bending (*b*) of Portland cement dough samples modified with a dispersion of naphthalene-formaldehyde plasticizer SP-1 with different content of carbon nanotubes; strength (*c*) and bending strength (*d*) of cement-sand samples modified with dispersions of naphthalene-formaldehyde plasticizer SP-1 with different content of carbon nanotubes

In [80], the study of physicochemical processes of structural formation of building mixtures reinforced with nanocarbon materials with mechano- and chemically activated components is described in detail. Prototypes were obtained that showed an increase in the performance of building mixtures. The effect of the composition of the aqueous dispersion of CNTs surfactant, i.e. the effect of plasticizer type and CNTs content on the strength characteristics of cement paste and sand-cement mixture, was investigated according to existing standards for 3, 7, and 28 days of curing. For clarity, Figs. 5.7 show the results of the study of the effect of CNTs content in a solution of naphthalene

Table 5.2. **Characteristics of aqueous dispersions of multiwall CNTs in plasticizer solutions and mechanical properties of composite materials filled with CNTs [32]**

Dispersion	d_{verage}, nm	Number of fractions, units	Dimensions of fractions, nm	The most probable size, nm	Number of particles,%	Mass (volume) of particles,%	The most probable particle ensemble size, nm	Suspension stability	Compressive strength, MPa, 28 days		Bending strength, MPa, 28 days	
									Cement dough	Cement-sand mixture	Cement dough	Cement-sand mixture
1	2	3	4	5	6	7	8	9	10	11	12	12
Melamine-formaldehyde plasticizer (Muraplast FK 98)												
MF-0	870	2	20—200 300—$5 \cdot 10^4$	64 $18 \cdot 10^3$	99.9 0.1	0.1 99.9	$18 \cdot 10^3$	Unstable	66.25	65.0	8.5	9.50
MF-0.5	360	2	30—250 250—$3 \cdot 10^3$	99 553	92.5 7.5	6.9 93.1	521.6	Conditionally stable	44.5	77.3	5.7	9.64
MF-1	257	2	20—300 300—$2.5 \cdot 10^3$	93 683	99.9 0.1	26.6 73.4	538.5	Stable	45.9	72.5	6.5	9.56
MF-1.5	325	2	14—200 200—$3 \cdot 10^3$	65 911	99.9 0.1	33.7 66.3	625.9	Conditionally stable	47.25	70.4	8.7	9.09
Naphthalene formaldehyde plasticizer (SP-1 polyplastic)												
NF-0	870	2	4—150 150—$5 \cdot 10^3$	19 1038	99.9 0.1	91.8 8.2	102.5	Unstable	43.8	60.5	4.95	8.47
NF-0.5	291	2	10—150 150—$4 \cdot 10^3$	43 805	99.9 0.1	63.6 36.4	320.3	Conditionally stable	31.25	66.5	5.0	8.56
NF-1	296	2	14—200 200—$3 \cdot 10^3$	59 799	99.9 0.1	31.5 68.5	565.8	The same	54.6	49.2	5.8	7.75

NF-1.5	270	2	16—200	86	99.9	37.3	467.2	" "	42.3	63.6	5.4	8.5	
			200—2.3 · 10^3	694	0.1	62.7							
Lignosulfonate plasticizer (Sika-Plast 520)													
LS-0	538	1	140—2 · 10^3	470	100		470	" "	68.75	52.8	5.4	8.13	
LS-0.5	69	2	10—150	55	99.9	37.5	410	" "	89.75	49.6	5.8	8.38	
			150—4 · 10^3	624	0.1	62.5							
LS-1	330	2	27—200	88	98.8	18.8	515	" "	107.5	60.6	6.6	9.2	
			200—2.5 · 10^3	614	1.2	81.2							
LS-1.5	297	2	40—200	129	99.9	0.1	496	" "	93.8	61.6	6.1	8.87	
			200—2.3 · 10^3	497	0.1	99.9							

formaldehyde plasticizer SP-1 on the change in strength, compression, and bending of samples of Portland cement and cement-sand mixtures. They indicate a non-monotonic change in the strength of samples of both Portland cement paste and cement-sand mixtures with the CNTs content.

For greater clarity, Fig. 5.8 shows the dependences of the compressive strength for Portland cement dough and cement-sand mixture modified with dispersions of naphthalene formaldehyde plasticizer (polyplast SP-1) on the 28th day of curing on the CNTs content.

It should be noted that in low-filled polymers [35—37, 81], there is also a non-monotonic change in structural and physicochemical characteristics with the content of CNTs. Therefore, un urgent task, along with the development of new composite materials filled with high-performance carbon nanoparticles, is to find a mechanism that would at least qualitatively explain the unusual content dependences of low-filled CNTs matrices. Typically, the addition of any nanosized filler, including CNTs, to the binder of a composite system increases its physical and mechanical properties. Theoretical analysis conducted in different models, for example in [82, 83], shows that this change in properties is related to the characteristics of different phases formed at the interface between the nanofiller and the bulk polymer. Molecular dynamics modeling [82] demonstrates the formation of an ordered layer of polymer matrix around CNTs. This layer, known to be interfacial, plays a central role in the overall mechanical response of the composite. Due to poor load transfer from the matrix to CNTs, the gain effect attributed to the CNTs is negligible; therefore, the interface is considered to be the only reason for strengthening the composite. If this approach is correct, it is possible to ex-

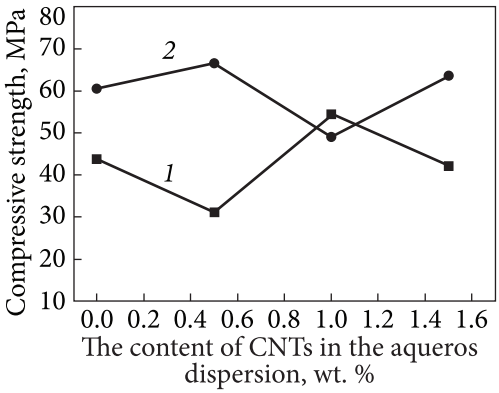

Fig. 5.8. Dependences of compressive strength for Portland cement dough (*1*) and cement-sand mixture (*2*), modified with aqueous dispersions of naphthalene-formaldehyde plasticizer (polyplast SP-1), on the 28th day of hardening on the content of CNTs

perimentally determine some structural parameters of the system, which would characterize the interfacial and show a monotonic change in the strength characteristics of the composite with changing this parameter.

Table 5.2 shows the characteristics of aqueous dispersions of CNTs in solutions of all three plasticizers discussed in subsection 5.1 and mechanical properties (compressive and bending strength) of composite materials (Portland cement paste and cement-sand mixture) filled with CNTs.

The influence of the composition of the aqueous dispersion of CNT-surfactant, i.e. the type of plasticizer (ionic surfactant), and the content of CNT on the strength characteristics of the cement paste can be analyzed as follows. If we imagine that the cement paste is an aqueous "solution" of high viscosity, then the addition of nanoscale fillers, e.g. agglomerates of CNTs, creates a boundary between the solid (CNTs) and "liquid" (cement paste) phases. Moreover, nanosized cells of the porous structure of the CNTs agglomerate become the nucleus of nanosized areas of cement paste. Despite the fact that a continuous CNTs grid has not yet been formed, this effect should lead to significant changes in the structural state and mechanical properties of composites. In this case, the larger the surface of the interaction of solid and liquid phases, the more effectively the properties must change. Table. 5.2 shows that all three surfactant-CNT systems have two types of particles (column 3), with a certain range of sizes (column 4), the most probable size (column 5), and the ratio of masses or volumes (at constant density) (column 7). You can find the most probable size of the ensemble of particles, which will be proportional to the area of interphase interaction as the sum of the most probable particle sizes, taking into account their weight (volume) coefficients (column 8 of Table 5.2). A Comparison of data in columns 8, 10, and 12 (compressive and flexural strength for cement paste filled with CNTs) indicates their obvious correlation (Fig. 5.8). That is, an increase or decrease in the most probable particle size (in the approximation of the spherical shape of the CNTs agglomerate particles) corresponds to the change in the same

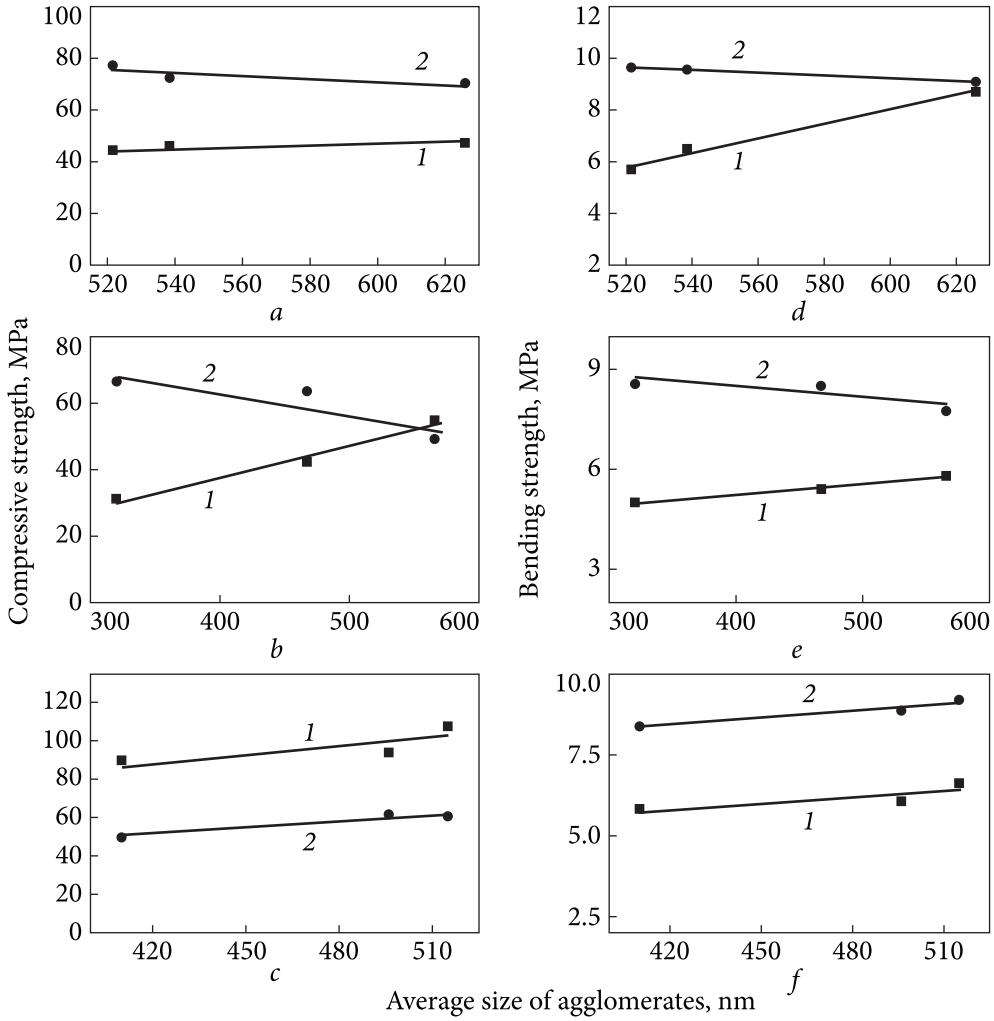

Fig. 5.9. Dependence of compressive strength (*a*—*c*) and bending strength (*d*—*f*) on the average size of agglomerates: *1* — cement paste; *2* — cement-sand mixture; for plasticizers: *a*, *d* — formaldehyde melamine; *b*, *e* — formaldehyde naphthalene; *c*, *f* — lignosulfonate [44]

sign of the compressive and flexural strength. This coincides with the ideas of the polystructural theory of building composite materials, according to which the strength of the composite with optimal filling can significantly exceed the strength of the unfilled hardened binder.

This process occurs as a result of the self-organization of the filled system, which seeks to reduce the potential of surface energy by consolidating the formation of new clusters and their integration into a rigid lattice framework. This strengthening of the system with low entropy provides a sharp strengthening of

the composite material. Of course, this effect is enhanced by the nano-dimensionality of the filler, i.e. by a greater contribution of surface energy. Note that this is observed for all three studied systems, i.e., all surfactants (plasticizers) and therefore can be considered reliable.

Another situation is observed in cement-sand mixtures. They already have a two-phase system "liquid-solid" with the optimal ratio of these components, which should ensure the structural organization of the system and increase the composition strength. Theoretically, the size distribution of sand particles is in the range of 0—100 μm. Although the percentage of nanosized sand particles is clearly small, they still occupy a certain fraction in the nanosized region of a complex polystructure and almost optimally structure the microsized region. Therefore, agglomerates of CNT surfactants of smaller sizes compared to the filled cement paste should be more effective structure formation in this case, which was observed for the cement-sand mixture with melamine-formaldehyde and naphthalene-formaldehyde plasticizers (Fig. 5.9, *a*, *b*).

Thus, for building mixtures filled with CNTs at their low contents (up to the flow threshold), the idea of forming a nanosized interphase with increased strength characteristics [40] is fully confirmed, which is obviously due to the increase in surface energy.

5.2.2. Characteristics of hydroxyapatite reinforced with CNTs

The addition of CNTs as a filler in the matrix of hydroxyapatite (HA) [36] led to a change in the structure porosity, specific surface area (Fig. 5.10, Table 5.3), mechanical strength, which non-monotonically depend on their content.

The lowest compressive strength of HA–CNTs was observed at 0.42% wt. CNTs, and the largest — at 0.08% wt. CNTs.

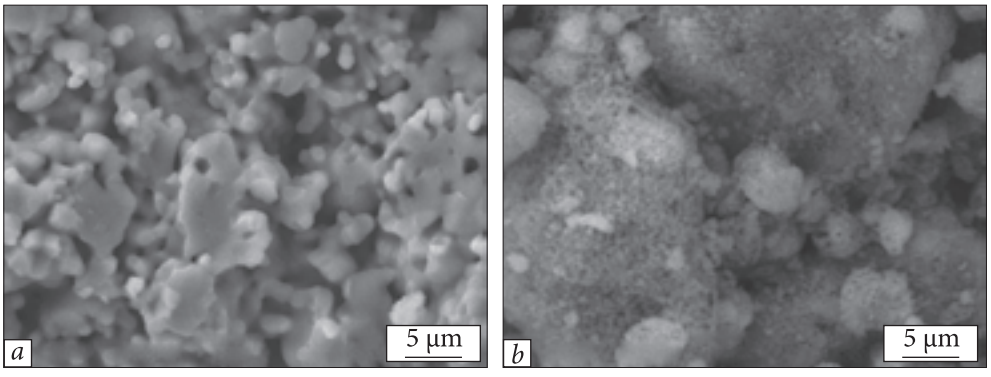

Fig. 5.10. SEM images: *a* — HA system-CNTs; *b* — HA

Table 5.3. **The specific surface area of HA samples and HA + CNTs compositions**

Sample	CNT, % wt.	Specific surface area, m^2/g	Sample	CNTs, % wt.	Specific surface area, m^2/g
Initial HA	—	7.5	HA + CNTs	0.42	19.6
HA + CNTs + + SiO_2	0.33 + + 0.08% SiO_2	14.3	HA + CNTs HA + CNTs	0.12 0.08	15.3 22.3

It should be emphasized that the specified content of CNTs in HA corresponds to their content in the initial mixture. In the process of sintering at 600 °C for 30—60 min, the porous structure of HA (Fig. 5.10) is formed with a specific surface according to Table 5.3. CNTs burn out, but the structure formed in their presence is preserved, which leads to a noticeable change in the characteristics of the ceramic material.

5.3. Polymers filled with carbon nanomaterials

5.3.1. Linear polymers with expanded graphite. Fluoroplast composition

To create composite materials (CM) using a polymer matrix and various fillers (depending on the area of application), first of all, researchers are guided by the functional properties the material must satisfy. Thus, while creating conductive polymer composite materials (CPCM), their goal is not only to obtain desired conductivity but also to improve other important properties. They can be strength, hardness, wear resistance, magnetic susceptibility, etc. To ensure the electrical conductivity of the composition, a conductive filler, for example, graphite can be added to a polymer matrix. However, the percolation threshold of spectrally pure graphite is about 34% vol. Such an amount of graphite as a rule significantly impairs the physical and mechanical properties of the polymer matrix composition. The percolation threshold for nanoscale carbon forms does not exceed 5% vol. Thus it does not affect CM strength properties but also provides good conductivity. That is why we consider the incorporation of EG as a nanoscale form of graphite for creating CPCM.

Description of the main methods for obtaining CM, comprising a polymer matrix and filler particles, is usually qualitative and defined by the distribution of component particles in CM and their sizes. In our case, we examine two methods of obtaining compositions: so-called "wet" and "dry". In the "wet" method, one or all components of CM are used as a solution or dispersion of the solvent. The solubility of the components in the solvent may be poor. Besides,

components can be chemically unstable regarding the solvent. Some difficulties may arise in the process of the solvent removing from the composition at the finishing stages of CM production. For this reason, most researchers prefer a "dry" process. In fact, polymer-immobilized particles can be produced at the initial stages of obtaining nanocomposite materials (NCM), and then they can be compacted into a composition. This method may include hetero-coagulation in polymer powders, films, fibers.

Depending on the required properties for CM containing dispersed carbon in polymer matrices, there are certain methods for obtaining compositions. The most common of them include the incorporation of surfactants or polymerization with surfactant monomers. Besides, there are known methods for encapsulation with phase separation, which implement various mechanisms of film formation from solution. In this case, surface phenomena play a special role in the core-shell contact.

Nano-heterogeneous CM are obtained from heterogeneous polymer systems. These materials have specific optical and electrical properties, caused by special processes associated with the interaction of small charged particles or their ensembles where redistribution of charges takes place under external effects of the relevant fields.

Among the analyzed methods of formation of chemisorbed macromolecules with colloidal carbon particles, the most applicable of them are electrochemical and electroflotational. Reactions of electrochemical polymerization (initiation) occur mainly on the electrode surface, while the growth, restriction or breaking of chains occur usually in the liquid phase surrounding the electrodes.

Despite the fact that CM with special properties can be obtained by the electrochemical method, the thermal method has several advantages. First of all, the *o*btained carbon-polymer particles are less decomposed and degraded during formation. The other way to obtain carbon-polymer materials (particles and CM) is (except for microencapsulation) their retrieving at the polymerization stage. So, in this case, synthesis of the material occurs not in the presence of prepared polymers, but in the simultaneous formation of the matrix and particles. The generation of cluster dispersions occurs here in matrices, which polymerize and limit the growth of the formed particles.

In our case, the method of electrical resistance was used for the analysis of the PCM formation conditions. It allowed optimization of the mixing modes for composite components powder mixtures and temperature-time intervals for their compaction into bulk compositions [84]. The electrical resistance of powder mixtures was measured on devices, the functional diagrams of which are given in [84]. It is measured in two ways: 1) in the process of mixing powder mixtures; 2) in the process of pressing specified powder mixtures.

The structure of compounds (distribution of powder components) was studied with an optical microscope "Neophot-2". Aside from fluoroplastic (FP)

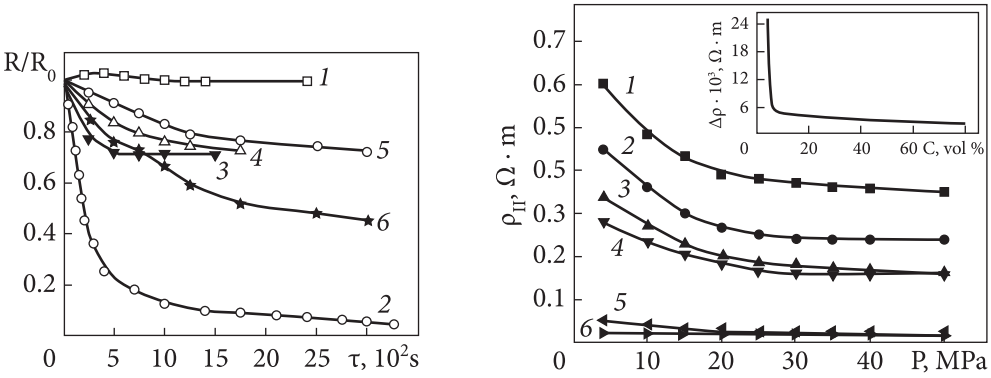

Fig. 5.11. Changes in the normalized electrical resistance (R/R_0) of FP powder (*1*), EG powder (*2*) and FP-EG powder mixtures with the EG content C (% vol.) of 30 (*3*), 40 (*4*), 70 (*5*), 90 (*6*) regarding the mixing time τ [84]

Fig. 5.12. Resistivity of the container with FP-EG powder mixtures vs compacting pressure. EG contents (% vol.) of 3.9 (*1*), 4.0 (*2*), 4.5 (*3*), 5.0 (*4*), 10.0 (*5*), 20.0 (*6*) [1]. *Insert.* Resistivity of the container with FP-EG powder mixtures vs EG content at compression to 50 MPa

powder B3, EG with a bulk density of about 15 kg/m^3 and a specific surface area of $5 \cdot 10^4$ m^2/kg was used for the production of composite mixtures.

The research results for changes in the standardized electrical resistance (R/R_0) of FP and EG powder mixtures and their individual powders regarding the mixing time are displayed in Fig. 5.11.

The dependence displayed in the figure evidences that possible changes in the morphology of FP particles during mixing have a slight effect on the electrical resistance of the filled cell (Fig. 5.11, curve *1*), whereas the mixing of EG powders (Fig. 5.11, curve *2*) and composition mixtures of FP-EG with different contents of graphite instantly cause a significant decrease in the electrical resistance R. Since at the very start of such mixing, EG particles change their morphology, and their bulk density increases considerably from 15 to 50 kg/m^3, this, undoubtedly, causes a decrease in R. Moreover, after comparing curves *3*—*6*, we can state that the increased content of the conductive component in the mixtures is followed by the increase in the electrical resistance stabilization time. These facts should be taken into consideration while elaborating the NCM production technologies similar to the described above.

The results of the study of the powder mixtures compression effect on the mixture resistivity measured in the pressing direction ($\rho_{||}$) are shown in Fig. 5.12. It can be seen that $\rho_{||}$ decreases with increasing the compression degree (*P*). The dynamics of such a reduction depends on the content of EG and manifests itself significantly in EG contents (*C*), which are close to the percolation threshold

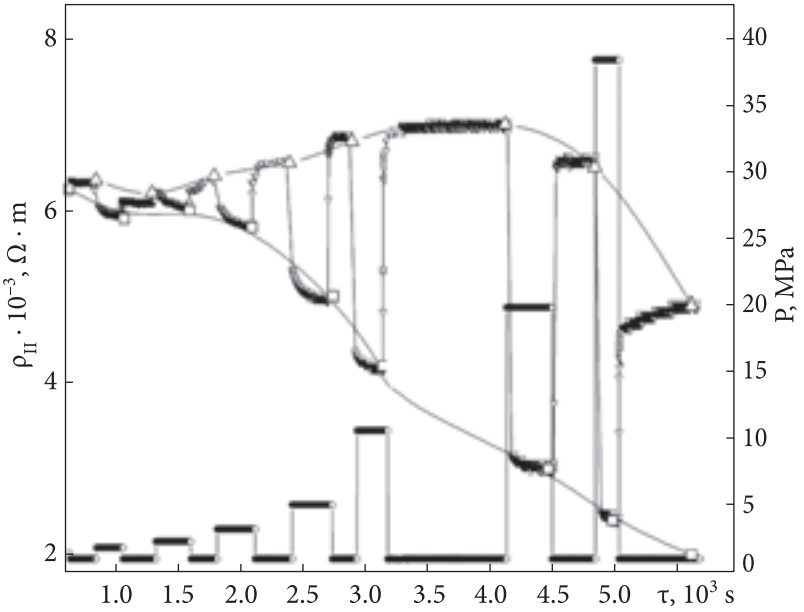

Fig. 5.13. Resistivity changes in the compression direction of the composite powder mixture of FP EG under their cyclic stepped loading. EG content is C = 5.5% vol. [84]

(insert in Fig. 5.12). Furthermore, the higher EG content naturally results in the lower electrical resistance of compressed composite mixtures.

Nevertheless, it was interesting to analyze processes of structural relaxation and the corresponding resistance changes in the cell with compressed EG after removing the load. The results are represented in Fig. 5.13. The specific feature of the displayed relations is that in the process of uniform compression of powders, their cyclic compression (Fig. 5.12) first causes reducing the electrical resistance of compressed samples and then its increasing after the structural relaxation, which corresponds to the degree of compression. In the direction perpendicular to the compression direction, the dependence between the resistance ($\rho_{\perp}$) and the density of EG samples at a pressure of P = 0.8 MPa tends to a maximum (Fig. 5.14). For EG + FP mixtures, such a maximum is also found. Though these features are not observed along the compression direction in similar relations $\rho = f(P, d)$.

These findings undoubtedly characterize the structural changes occurring in the conductive CM cluster, and morphological and structural defect changes of cluster particles and their graphene layers, when samples are compressed. The resistance is low along with the layers (up to 10^{-6} Ω·m) and high perpendicular to them. The ratio of these resistances is about ~10^4 for natural graphite and ~10^3 for artificial pyrolytic graphite. When the density of the EG is (0.2…0.3) × × 10^3 kg/m^3, that is when its compression equals $P \leq 1$ MPa, the resistivity anisot-

ropy is practically not observed. Thus, the electrical resistance of such material in both perpendicular and parallel pressing directions has the same value ~(4…6) · 10^{-3} Ω · m. When the density of samples increases, i.e. the compaction pressure grows, the resistivities $\rho_{||}$ and $\rho_{\perp}$ begin to differ.

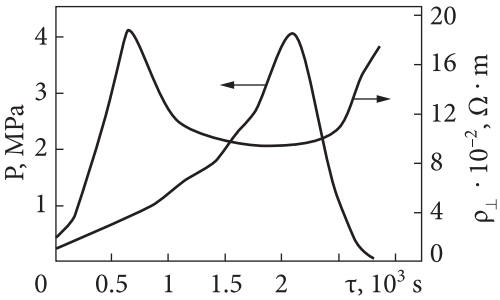

Fig. 5.14. Resistivity changes of the composite powder mixtures of FP and EG under their loading and unloading perpendicular to the compression direction. EG content is C = 5.5% vol. [84]

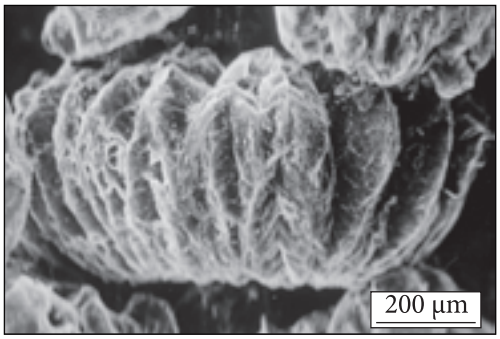

Fig. 5. 15. Microstructure of the initial EG particle [87]

Generally, the electrical resistance of EG powder samples consists of the material (graphite) resistance, considering the chaotic or ordered arrangement of its vermicular particles and their components, and the resistance of different section borders. These are mainly the surface borders of the vermicular particles and pores at small pressures (P < 0.5 MPa) and borders between planes of layered particles (lenticular flakes) (P > 0.5 MPa) and at pressures leading to the flake destruction (P > 40...50 MPa), which are the micro-structure borders. From dependences in Figs. 5.12—5.14, one can conclude that the electric resistance method enables monitoring the pressing process kinetics of composite mixtures, the nature and the size of the carbon component elastic aftereffect in the NCM considered.

We note that EG samples with different densities (compressed at different P) show different compression resistance and relax differently after compression. The structure framework compaction and the porosity reduction occur at the initial stages of compression (up to P = 0.5 MPa), herewith, most EG particles are still intact. Thus, the electrical resistance formation involves both particle interfaces and the crystallographic graphite planes unsusceptible-oriented in the measuring direction. The increase of the compressive stress of EG up to P > 0.5 MPa leads to the vermicular particles' delamination.

The flakes line up perpendicularly to the compression direction, which results in the material densification and, correspondingly, in the decrease of its resistivity. When the material density reaches $d = 1.7 \cdot 10^3$ kg/m^3, the samples compression is accompanied by the elastic-plastic deformation of structural elements. At the

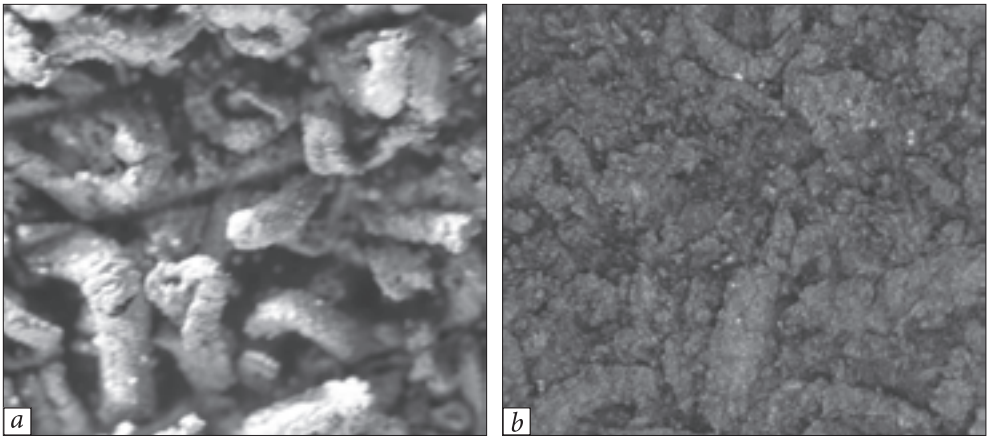

Fig. 5.16. Microstructure of powder mixture of FP-EG (*a*) and FP-EG (*b*) NCM with EG content C = 5% vol. (magnification ×40)

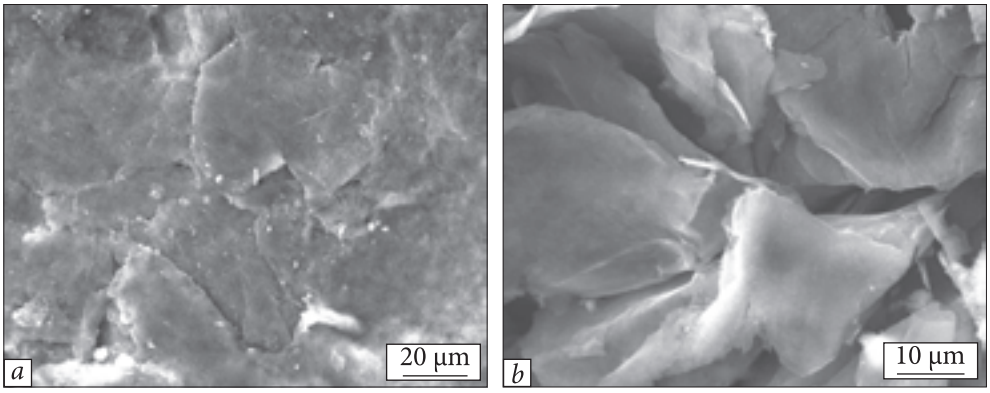

Fig. 5.17. Microstructure of EG samples with the mean particle size of 40 μm, compacted at a pressure of 450 kg/cm^2: *a* — along the pressure direction, *b* — perpendicular to the pressure direction

same time, the dissipated deformation energy constitutes a significant part of the energy that is spent on the material deformation, thereby, the internal pressure and the density of structural defects increase. When the internal pressure reaches its critical value, the structure elements lose their elastic-plastic properties due to processes of local and general particle destruction. The deformation mainly acquires a plastic nature. Therefore, when manufacturing products from the EG + + FP mixtures, their revealed structural changes occurring during mixing and compaction must be taken into account, and the optimal modes must be chosen.

Microstructure. The results of EG microstructure study have shown (Fig. 5.15) that each vermicular particle consists of micro-crystallites, which have

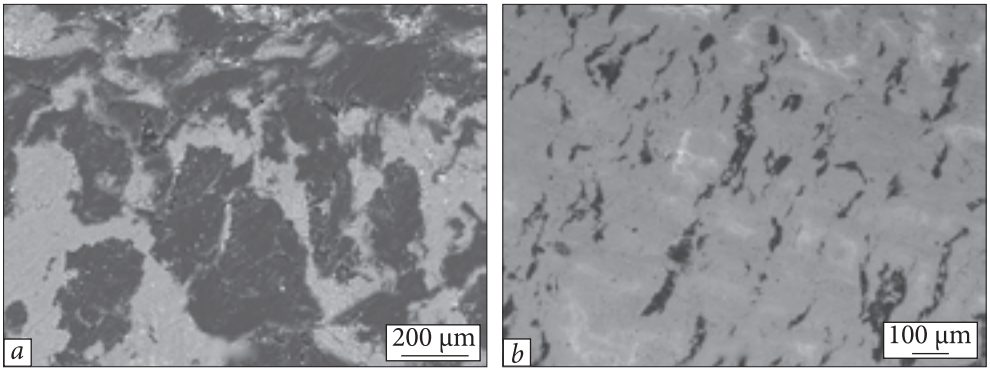

Fig. 5.18. Microstructure of the samples from FP-EG powder mixtures with the mean particle size of 260 μm and EG content of 20% vol. compacted at a pressure of 450 kg/cm^2: *a* — along the pressure direction, *b* — perpendicular to the pressure direction [88]

a structure similar to the structure of natural graphite. The distance between parallel-oriented planes in particle varies from 10 nm to 10 μm [85], while the size of separate fragments ranges from units to hundreds of nanometers [86], i.e., each microcrystal consists of a series of graphene layers.

Analysis of the microstructure of PCCM mixture components shows that there are small white FP blotches on the surface of EG particles (Fig. 5.16, *a*). Their shape is spherical with a diameter not exceeding few microns. After pressing and sintering, EG particles delaminate and more or less evenly spread in the FP matrix (Fig. 5.16, *b*). At the same time, due to the structural features of EG, NCM acquires some macro-layering with layers arranged perpendicular to the sample compression direction (Figs. 5.17, 5.18). Overall, the research has shown that the structure of graphite clusters in NCM FP-EG depends on both the content of EG and the conditions of preparing compositions.

The analysis of the structural changes in PCCM during its sintering suggests that EG filler is capable of structuring the polymeric matrix, changing its mechanical stress and the crystallinity degree of the polymer matrix. Let us consider the FP-EG composition as an example.

Typically, these features depend on the degree of EG dispersion. Thus, the nature of contact at the interface is essential in the interaction mechanism of filler particles surface with the polymer macromolecules. In most cases, it is necessary to ensure close and full contact of components, therefore, the choice of dispersed fillers is, first of all, determined by the size of particles and their morphology. The smaller size of the filler particles and their more flaked shape result in more intense interaction between the polymer and the filler particles. Thereby, the powder dispersion is the most important characteristic as long as it forms properties of all dispersed system.

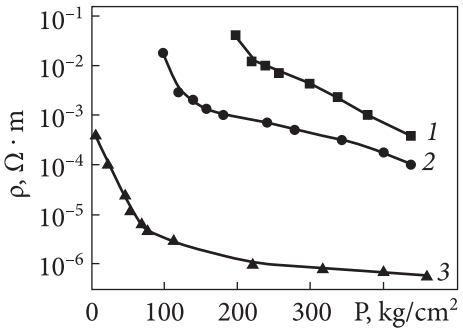

Fig. 5.19. Dependence of the resistivity of the cell with FP-EG powder mixture with a mean EG particle size *s* = 80 μm and its content *C* (% vol.) of 15 (*1*), 20 (*2*), 100 (*3*) on the compaction load

Depending on the degree of dispersion influence on the properties of heterogeneous systems, dispersed systems can be divided into the following types [89, 90]:

- clustered (nanosized) with a cross-section of particle sizes s = 0.5...10 nm;
- ultramicroheterogeneous (ultradispersed) with *s* = 10...100 nm;
- microheterogeneous with *s* = (0.1...1) μm;
- coarse-dispersed with particles size more than 10 μm.

One of the most important characteristics of the dispersity is a surface area or a specific surface S_s of the dispersed particles, related to the particle size as follows:

$$S_{sp} = \frac{k}{\rho_F \cdot s},$$

where *k* is a coefficient of particle shape (for spherical particles k = 6, for prismatic k = 12) [91, 92], ρ_F is the real density of material, *s* is the mean particle size of the dispersed phase.

The filler specific surface increase leads to the growth of phase boundaries in the polymer-filler system. So, starting with S_s = 2.3 m^2/g, corresponding to a particle diameter of 10 μm, the proportion of the phase separation surface, i.e., the interfacial layer in the polymer-filler system, increases sharply, while the polymer content in the boundary layers may exceed 10% at layer thickness 0,1 μm [92]. This determines relations between the composite material characteristics and the properties of the boundary layer.

Another important evaluation parameter of disperse systems is a packing factor (*F*), which determines the maximum volume fraction of the dispersed phase in a fixed volume. In case of the disperse filler particles with a size of *s* > 40 μm, the packing factor does not significantly depend on the equivalent particles diameter and corresponds to the average density of a cubic packing of particles (0.55). The decrease in the particles size results in the packing density reduction, especially when s < 10 μm. It is connected with the change of the particles shape and with formation of large particle aggregates with an increased number of pores. At the same time, the total porosity of the material increases, leading to decrease in the bulk density and *F* parameter.

According to the research results displayed above, the method of electrical resistance is more efficient for analyses of the structural changes occurring in the process of nanocomposite manufacturing.

The effects of uniform compression of the FP-EG powders composite mixtures with a mean EG particle size of s = 80 μm and their different contents on the electrical resistance along the pressing direction are shown on Fig. 5. 19.

Fig. 5.19 displays that the electrical resistance decreases with increasing compression degree for the FP-EG mixtures, as well as for mixtures with non-dispersed graphite (Fig. 5.11). It is also clear that when the electrical resistivity is higher, the volume content of EG particles in the composition is lower.

The pressure at which samples become conductive indicates that a continuous conductive cluster has been formed in the mixture. That means the electrical conductance occurs in mixtures with a mean EG particle size 80 μm at a pressure of about 200 kg/cm^2 for EG content of 15% vol. and at a pressure of 100 kg/cm^2 for EG content C = 20% vol. Similar dependences were obtained for FP-EG samples with different mean particle sizes.

The effect of the manufacturing conditions on the structure. The XRD methods allow investigation of microstresses in a sample containing several phases [93]. Technology for polymer composite materials manufacturing includes heating, cooling, and compressing under temperature. To produce the NCM under consideration, a raw material was used in the form of powder mixtures of the relevant components.

The samples were mainly sintered under pressure at the polymer melting temperature. It has been found that EG has a different density and resistance, depending on the compaction pressure P [84]. It is obvious that an amount of pressure applied to samples during NCM manufacturing will affect the degree of the EG lattice microdistortions and microstresses occuring therein. The greater pressure applied to the material, the greater these stresses. As we have pointed out, in case of compaction of vermicular EG particles, consisting of scales arranged perpendicular to the applied pressure [84], that is confirmed by the increase in the resistivity anisotropy. After reaching a certain load, graphene layers begin to slide over each other and break. At the beginning of planes sliding, microstresses of the graphite crystal lattice are maximal.

The XRD method helps to study stresses in small areas and analyze their heterogeneity inside the sample. Analysis of macroscopic residual stresses was performed according to the results of precise determination of the lattice parameter corresponding to phase components. Thus, via using the approximation method and mathematical treatment of physical vapor broadening present in the pattern profiles {002}, {004}, the coherent scattering domain size (CSD) for EG was determined (Fig. 5.20 and Table 5.4). Though, this method was not successful for determining the microdistortions ($\Delta d/d$) of EG crystal lattice. Apparently, they are too small, within the error.

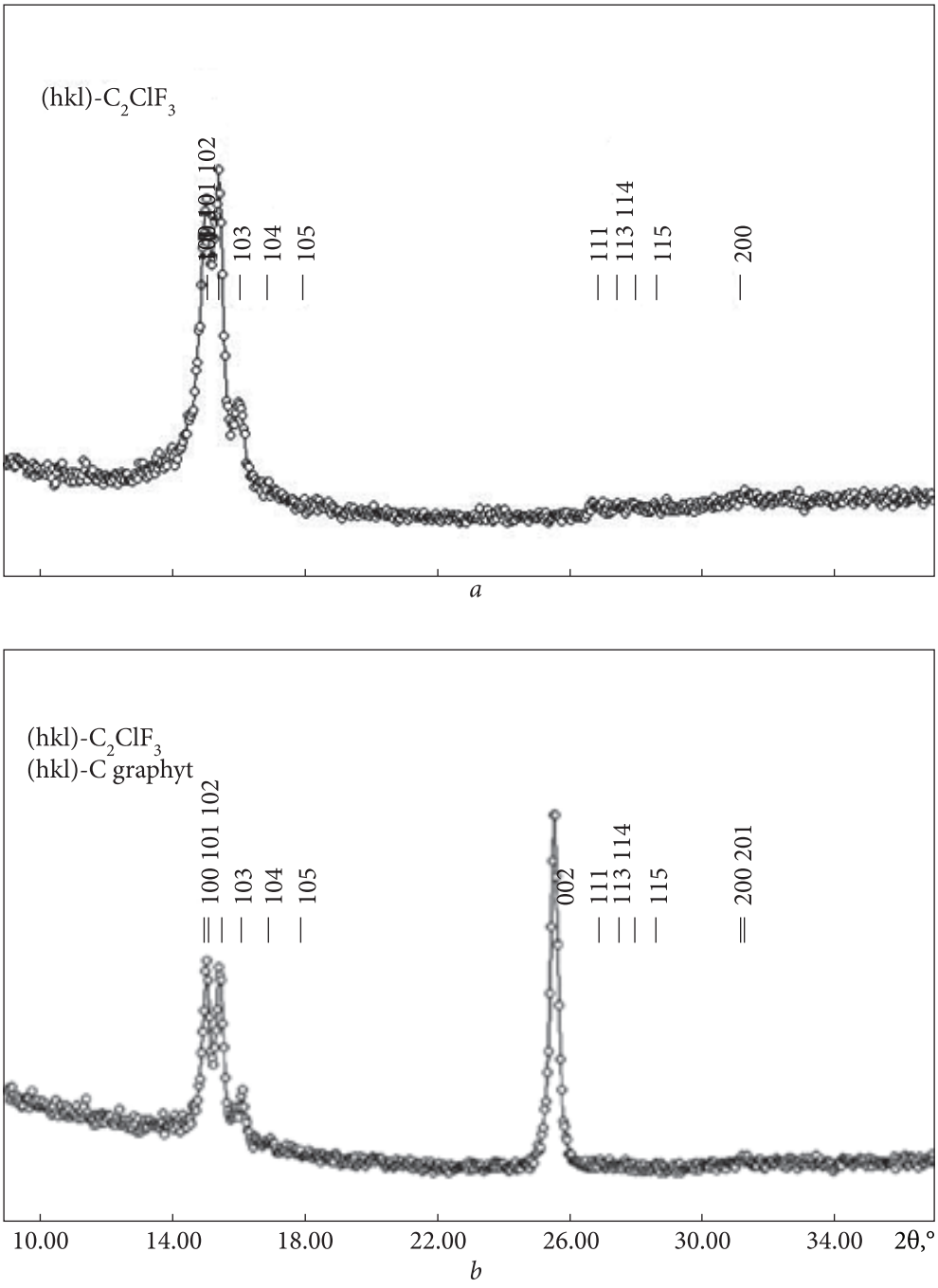

Fig. 5.20. Fragments of XRD patterns of FP (*a*) and FP-EG NCM with EG content of 4.2% vol. (*b*). Samples were made under a load of 32 MPa

Table 5.4. **CSD size for EG samples produced at different temperatures**

Pressure, MPa	CSD size A, nm		Dislocation density $N_d \cdot 10^{-12}$	Pressure, MPa	CSD size A, nm		Dislocation density $N_d \cdot 10^{-12}$
	20 °C	215 °C			20 °C	215 °C	
0.2	18 (2)	18 (2)	—	24.0	12 (1)	15 (1)	0.968 (6)
1.6	22 (2)	—	0.508 (6)	32.0	13 (1)	14 (1)	1.100 (6)
8.0	17 (2)	16 (2)	0.620 (8)	40.0	12 (1)	18 (1)	1.130 (5)
16.0	14 (1)	15 (1)	0.750 (7)				

Table 5.5. **FP lattice parameters in FP-EG NCM samples with EG content of 4.2% vol.**

P_{prod}, MPa	Lattice parameters, nm; lattice volume, nm^3					
	After manufacturing			After annealing at T = 200 °C		
	a	c	V	a	c	V
4.0	0.642 (1)	4.569 (2)	1.6308 (3)	0.642 (1)	4.453 (2)	1.5895 (3)
8.0	0.642 (1)	4.493 (2)	1.6047 (3)	0.642 (1)	4.458 (3)	1.5913 (5)
16.0	0.642 (1)	4.420 (2)	1.5776 (5)	0.642 (1)	4.456 (2)	1.5905 (4)
26.0	0.642 (1)	4.351 (2)	1.5530 (2)	0.642 (1)	4.462 (2)	1.5927 (3)
32.0	0.642 (1)	4.330 (2)	1.5455 (2)	0.642 (1)	4.454 (2)	1.5898 (3)
33.4	0.642 (1)	4.325 (2)	1.5437 (4)	0.642 (1)	4.455 (1)	1.5902 (3)
40.0	0.642 (1)	4.320 (2)	1.5419 (5)	—	—	—

Table 5.6. **FP lattice parameters in FP-EG NCM samples with EG content of 5.5% vol.**

P_{prod}, MPa	Lattice parameters, nm; lattice volume, nm^3					
	After manufacturing			After annealing at T = 200 °C		
	a	c	V	a	c	V
1.6	0.642 (1)	4.569 (2)	1.6309 (2)	—	—	—
4.0	0.642 (1)	4.505 (2)	1.6080 (3)	0.642 (1)	4.455 (3)	1.5902 (2)
8.0	0.642 (1)	4.499 (3)	1.6059 (2)	0.642 (1)	4.458 (2)	1.5912 (6)
16.0	0.642 (1)	4.435 (2)	1.5830 (3)	0.642 (1)	4.456 (2)	1.5905 (4)
26.0	0.642 (1)	4.359 (2)	1.5559 (2)	0.642 (1)	4.455 (2)	1.5902 (2)
32.0	0.642 (1)	4.350 (3)	1.5527 (1)	0.642 (1)	4.454 (2)	1.5898 (3)
33.4	0.642 (1)	4.329 (1)	1.5452 (1)	0.642 (1)	4.455 (2)	1.5902 (3)
40.0	0.642 (1)	4.318 (3)	1.5413 (2)	—	—	—

Table 5.4 shows that when the load increases during sample compression, the CSD size of EG (*A*) monotonically decreases compared to the typical values for this phase in the initial state (~20 to ~12 nm at a load of P_{ben} = 40 MPa). Moreover, it hardly changes at pressures of (16...40) MPa.

It should be noted that the powder samples compacted at 215 °C have slightly higher limits for CSDs , which can be explained by the fact that the EG powder is better compacted at 215 °C than at RT.

The XRD method was also used for determination of the crystal lattice parameters of the second component of FP-EG NCM that is a fluoroplastic. Via using [94], the diffraction pattern of the initial FP was indexed for pure FP with the lattice parameters *a* = 0.64 nm and c = 4.25 nm (Fig. 5.20) as well as the crystal lattice periods were specified. The obtained values (*a* = 0.642 nm, *c* = 4.569 nm) were slightly higher than reported in the literature. The latter were used to determine the crystal lattice parameters of this phase in the FP-EG compositions. Two series of NCM samples with the EG content *C* (% vol.) = 4.2 and 5.5 were studied by XRD. According to the phase analysis, all investigated samples are diphasic and contain FP and EG phases (Fig. 5.20). The crystal lattice parameters of fluoroplastic 3 in the FP-EG NCM are given in Tables 5.5 and 5.6.The deformation of the FP crystal lattice in the FP-EG NCM is illustrated by the dependency of its volume on the load. It can be seen that the increasing load in the compressed samples, regardless of the EG content, causes a gradual decrease in the FP unit cell volume. After an hour of isothermal annealing of samples at 200 °C and their slow cooling, the volume of the FP unit cell becomes independent of the load during sintering (Tables 5.5 and 5.6).

The fall in the dependency of the unit cell volume on the pressure $V(P_{prod})$ indicates that the EG density increases with increasing pressure. During solidification of the fluoroplastic matrix, EG phase remains under stress. Annealing leads to "defreezing" of stresses in the graphite component characterized by the corresponding changes in the unit cell volume .

Parameters of the EG real structure in FP-EG NCM samples were determined by using an etalon (Ceylon graphite). The results are shown in Tables 5.7 and 5.8.

As seen, the CSD size of graphite in NCM samples increases with the pressure increase to P_{prod} ~ 20 MPa, though its further increase leads to the size decrease. It has been experimentally established that the composite EG material compaction proceeds through two stages. The first stage is characterized by compaction of EG particles and perpendicular orientation of the crystallographic planes (001) along the pressing direction. At the second stage, when the overwhelming majority of grains are placed in the latter planes perpendicular to the pressing direction, the planes' sliding against each other occurs, resulting in the change in structure parameters. Particularly, in the first compaction phase, the CSD size increases, but with the beginning of the second phase growing, the CSD size reduces.

The maximum increase is observed in the dependence curves of the CSD size and sintering pressure when EG content increases. Annealing of samples FP-EG NCM leads to a slight reduction in the CSD size. If we compare these relationships with those for pure EG presented in Table 5.4, we can conclude about the influence of the FP matrix on the structuring process of EG.

In the NCM manufacturing process, the samples are compressed and rolled, which results not only in structural defects in the composition layers but also in arising stresses, which eventually affect NCM physical-mechanical properties. Tables 5.7 and 5.8 show that the stress remains unchanged up to the pressure of P_{prod} = 25 MPa, whereas when P_{prod} = 32 MPa, a maximum appears associated with the processes occurring in the composition when the graphite planes slide over each other.

Since the EG structures the polymer matrix, the effect of EG content on these processes is of interest. The pure FP diffractogram [94] displays Bragg peaks on the diffuse halo background, their maxima range within $2\theta = 15^{\circ}$. Besides, there is a wide diffuse halo around 40° [95].

Such Bragg diffraction indincates that FP has an amorphous-crystalline structure. The ratio of Bragg peaks integral intensity in the crystalline phase to the area under the peaks and the halo was taken as a crystallinity characteristic χ. It does not indicate the actual content of the crystalline phase, but it is indirectly related to the content of the crystalline phase in the material. The degree of the matrix crystallinity for this case is determined by the formula:

$$\chi = \frac{I_c}{I_c + I_a} \ , \tag{5.1}$$

where I_c is the area under the curve that characterizes the crystalline phase and I_a is the area under the amorphous halo.

To determine the crystallinity degree of the NCM matrix, the multiple maxima at 2θ = 16° (curve *1* Fig. 5.21) was examined. The background set was taken from the initial data by the method of baseline. Considering that the multiplet is composed of three Bragg peaks and the diffuse amorphous halo with a maximum at 2θ = 15°, it was divided into individual peaks according to Lorenz. Three main peaks correspond to reflections from {100}, {101} and {102} planes. The diffuse halo forms due to the presence of an amorphous phase in the polymer matrix. Fig. 5.21 shows the initial data and peaks corresponding to the amorphous and crystalline phases and the sum of these maxima.

Sintering of polymer composite materials in a mold includes application of pressure to the samples during moving up to the matrix melting point and their following cooling under pressure. The crystallinity degree vs the manufacturing pressure of FP-EG NCM samples with EG contents of C = 4.2 and 5.5% vol. before and after annealing at 200 °C is shown in Fig. 5.22. It is obvious that the

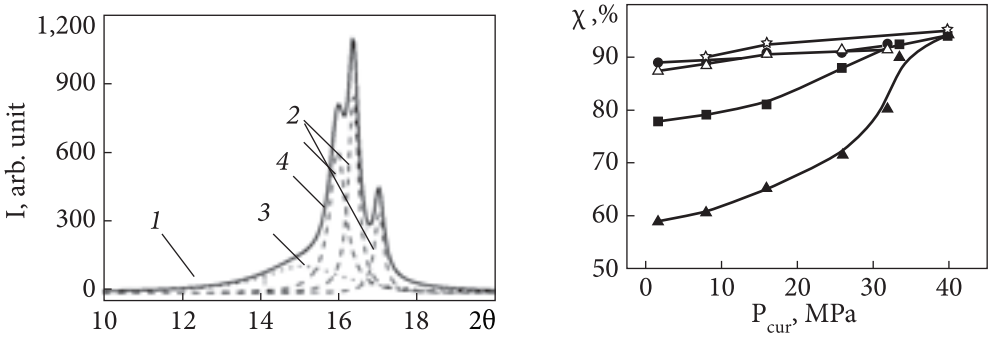

Fig. 5.21. Fragment of XRD pattern of FP-EG NCM with EG content of 4.2% vol. The sample was produced at 215°C under the load of 32 MPa: *1* — initial data, *2* — crystalline peaks, *3* — amorphous halo, *4* — the sum of amorphous and crystalline peaks

Fig. 5.22. Crystallinity degree of pure fluoroplastic samples (1) and NCM FP-EG with EG content of *C* (% vol.) of 4.2 (2, 3) and 5.5 (4, 5)% vol., sintered at *T* = 215 °C and cooled to the room temperature in compressed states (different P). Curves 3 and 5 show changes in the matrix crystallinity of samples pressed under these conditions after annealing at *T* = 200 °C for 30 min

crystallinity degree of the NCM matrix monotonically increases with increasing P_{prod}, which increases for all the samples up to 90% after isothermal annealing at 200 °C. This suggests their structural changes. At the same time, a decrease in the crystallinity degree was observed with increasing carbon content in the composition (Fig. 5.23). It becomes smaller at a sintering pressure of 33.4 MPa. For the pressure of 40 MPa, the crystallinity degree vs the carbon content remains constant.

Such a behavior of the matrix crystallinity degree can be caused by the effect of EG on the crystalline structure. The carbon filler prevents from formation of an ordered globular-lamellar structure during the sintering of the composite. This results in decreasing crystallinity degree. As shown in Tables 5.7 and 5.8, the EG phase has the largest CSD and the highest stresses of the second type at the pressure 33.4 MPa. This indicates the beginning of sliding of EG planes against each other and, as a result, EG lamination with the further increase in pressure. There is no dependence of the FP matrix crystallinity degree on the EG content in the composition at the pressure of 40 MPa. To sum up, the crystallinity degree of a composite material is influenced by the conditions of annealing, sintering pressure and the carbon filler content. The FP crystallinity degree is more dependent on the content of the carbon filler under low pressures ($P < 30$ MPa) than under high pressures. The effect of pressure on the crystallinity degree is stronger when EG content is >4% vol. and weaker when it is lower. Under a specific pressure (33 MPa), the crystallinity degree of the polymer matrix depends neither on the pressure nor on EG content.

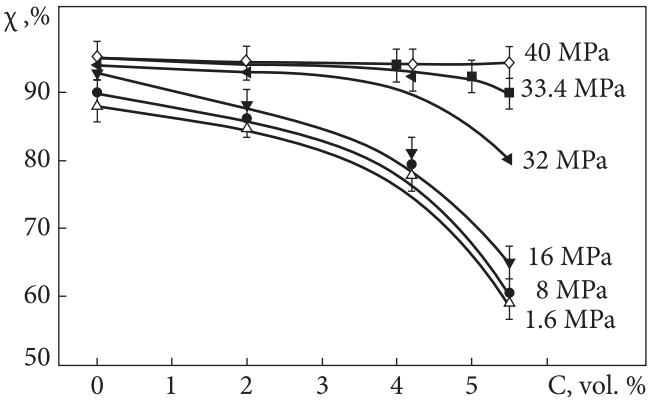

Fig. 5.23. Matrix crystallinity of FP-EG NCM samples produced at various pressures and EG contents.

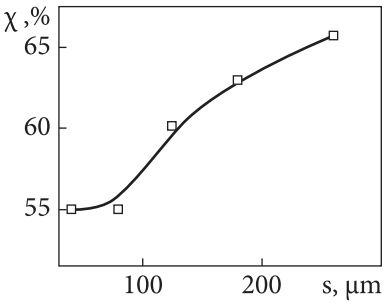

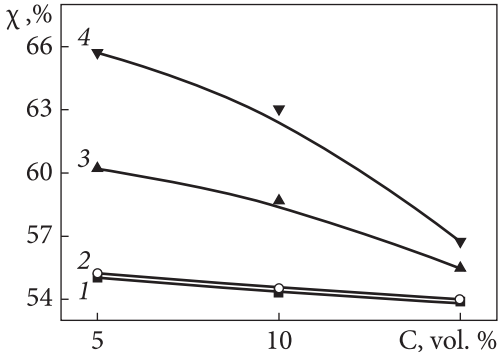

Fig. 5.24. Relationship between the fluoroplastic crystallinity degree in FP-EG NCM with EG content C = 5% vol. and EG dispersity of samples manufactured in the same conditions

Fig. 5.25. Relationship between the degree of FP crystallinity in the FP-EG NCM with a mean EG particle size of 40 (*1*), 80 (*2*), 180 (*3*), 260 (*4*) μm and the EG content

Table 5.7. **Parameters of the real EG structure in FP-EG NCM samples with EG content C = 4.2% vol.**

P_{prod}, MPa	Before annealing			After annealing at T = 200°C		
	A, nm	$\Delta d/d$	ε_{II}, GPa	A, nm	$\Delta d/d$	ε_{II}, GPa
0.0	18 (1)	—	—	18 (1)	—	—
4.0	20 (2)	0.00163 (4)	0.163 (4)	21 (3)	—	—
8.0	24 (1)	0.00147 (4)	0.147 (4)	32 (2)	0.00102 (3)	0.102 (3)
16.0	38 (3)	0.00158 (4)	0.158 (4)	22 (2)	0.00208 (5)	0.208 (5)
26.0	36 (3)	0.00170 (2)	0.170 (2)	80 (9)	0.00540 (6)	0.540 (6)
32.0	76 (6)	0.00435 (4)	0.435 (4)	17 (1)	0.00210 (2)	0.210 (2)
40.0	25 (3)	0.00125 (3)	0.125 (3)	—	—	—

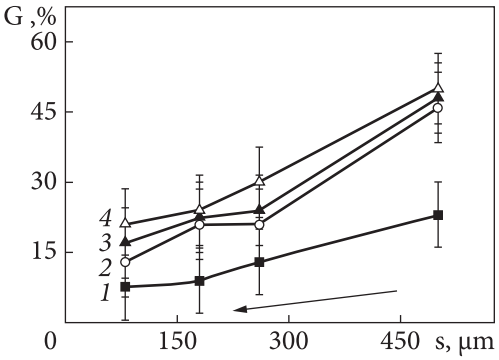

Fig. 5.26. Dependences of structural anisotropy parameter of FP-EG NCM with EG content *C* (% vol.) of 5(*1*); 10(*2*); 15(*3*); 20(*4*) on the dispersity level of EG

Moreover, the degree of the FP matrix crystallinity depends on the dispersion of the used filler. The character of changes in the crystallinity degree χ depending on the EG dispersion is displayed in Fig. 5.24. This dependence points out certain peculiarities of the dispersion influence (and so the carbon component morphology) on the FP crystallization processes.

Fig. 5.24 shows that the degree of the FP matrix crystallinity increases with decreasing the EG dispersion, which can be related to the change in the filler particles' morphology and the peculiarities of their distribution in the polymer volume. As known, the decrease in macromolecule mobility near the filler surfaces creates favorable conditions for the appearance of crystallization nuclei [96]. By the analogy with nanoclays [97, 98], we can assume that large EG particles, due to their morphology, better delaminate in the FP matrix. As a result, the total active surface of the filler particles rises, and the number of nucleation centers increases. Therefore, the FP crystallinity increases with an increase in the mean particle size of EG. So, for FP-EG NCM with the EG content C = 5% vol. and mean particle size s = 40 μm, χ is ≈ 55%, whereas for s = 260 μm, χ is 65.7%.

When the carbon filler content increases, the aggregation of particles occurs and the heterogeneity of the system decreases. The crystallinity degree also decreases. Fig. 5.25 shows the content dependence of χ for NCM FP-EG.

Table 5.8. **Parameters of the real EG structure in FP-EG NCM samples with EG content C = 5.5% vol.**

P_{prod}, MPa	Before annealing			After annealing at T = 200 °C		
	A, nm	*Δd/d*	ε_{II}, GPa	*A, nm*	*Δd/d*	ε_{II}, GPa
0.0	18 (1)	—	—	18 (1)	—	—
4.0	27 (5)	0.00141 (3)	0.141 (3)	22 (5)	—	—
8.0	32 (7)	0.00131 (4)	0.131 (4)	27 (3)	0.00200 (4)	0.200 (4)
16.0	34 (4)	0.00143 (2)	0.143 (2)	36 (5)	0.00215 (3)	0.215 (3)
26.0	41 (5)	0.00188 (5)	0.188 (5)	22 (1)1	0.00219 (5)	0.219 (5)
32.0	79 (8)	0.00441 (3)	0.441 (3)	91 (9)	0.00422 (7)	0.422 (7)
33.4	—	—	—	35 (4)	0.00261 (3)	0.261 (3)
40.0	23 (3)	0.00170 (2)	0.170 (2)	—	0.00177 (3)	0.177 (3)

The marked decrease in the crystallinity degree, accompanied by the increased amount of the filler, is associated with the size of crystallites, formed during the NCM creation. At the same time, the supramolecular structure, characterized by the formation of small spherulites distributed in the matrix volume, exerts its influence as well [99]. It is determined by the increase in structurally active part of the EG surface, where FP crystallization processes occur. Furthermore, the volume fraction increase regarding the friable boundary layer at the filler-matrix interface contributes to the amorphous part of the composition.

Microstructure analysis of the FP-EG NCM with a different EG content and dispersion showed that the NCM structure is layered.

In the process of sample sintering, EG flakes are oriented perpendicular to the pressure direction. Besides, the average thickness of the carbon layers increases with decreasing dispersion. For example, if FP-EG NCM has the content of EG C = 10% vol. and particle size of s = 80 μm, the average layer thickness is ≈ 8μm, and for EG dispersion s = 180 μm, it is ≈12 μm. The increase in EG content leads to the conglomeration of aggregates. The thickness of carbon layers increases and ranges from 8 to 20 μm. The examination of shear microstructure shows the main conductive EG channels and individual graphite flakes' aggregation.

Analytical assessment of structural anisotropy of FP-EG NCM samples was performed on the basis of their microstructure. The ratio of the carbon component area to the total area of the composition was defined, and the structural anisotropy parameter (G_a) was calculated according to the following formula:

$$G_a = \frac{S_{EG}}{S_{EG} + S_{FP}} \cdot 100\%, \tag{5.2}$$

where S_{EG} is the area occupied by EG particles and S_{FP} is the area occupied by FP.

The dependence of parameters of FP-EG NCM structural anisotropy on the mean filler particle size is shown in Fig. 5.26. G_a parameter provides the possibility to estimate the filler content distribution on the cut surface of the NCM.

The value of G_a decreases with increasing the filler dispersion and increases with increasing the carbon component content in the polymer matrix. So, for FP-EG NCM with the filler content C (EG) = 5% vol., G_a decreases from 20% to 9% with the increasing EG dispersion, while for EG with C (EG) = 20% vol. the structure anisotropy parameter decreases by almost 2.5 times.

Effect of thermally expanded graphite dispersity on the percolation characteristics. Fig. 5.27 shows the dependences of the specific resistivity for samples of FP spectrally pure graphite (SPG) and FP-dispersed EG (dEG) on the filler content [100]. The experimental dependences (Fig. 5.27) have a threshold character and can be described by the percolation theory. Ideally, according to the theory of lattice models of junctions [101], the conductivity must

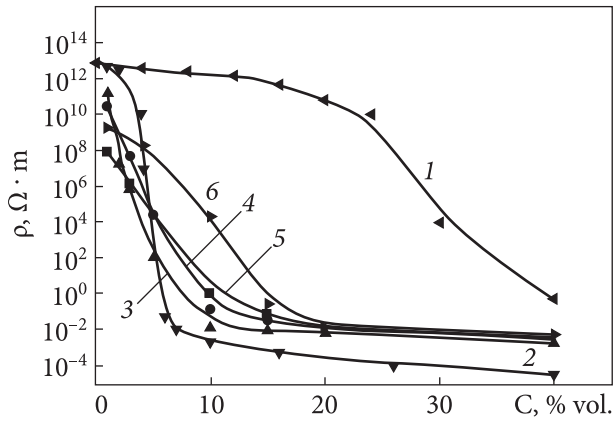

Fig. 5.27. Content dependences of the resistivity of FP-spectrally pure graphite CM (*1*); FP-initial EG CM (*2*), and FP-dEG with mean sizes of EG particles of 260 (*3*), 180 (*4*), 80 (*5*), and 40 (*6*) μm [100]

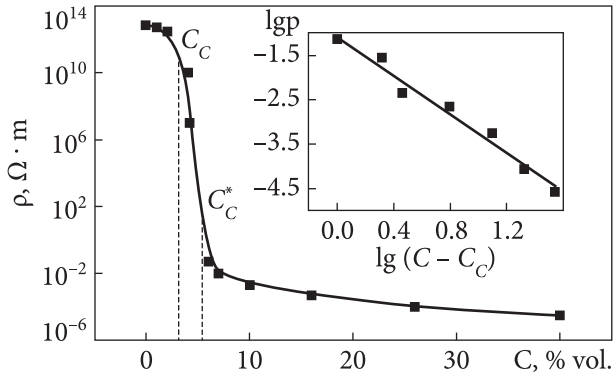

Fig. 5.28. Content dependence of the resistivity of FP-EG CM. *Insert*: logarithmic dependence of lg ρ on lg $(C - C_C)$ [100]

vary jumpwise (changing by several orders). In reality, as seen from the curves obtained, a drop in resistivity occurs in a certain narrow region of contents, which is referred to as a smeared region [102] or the width of percolation transition. For such systems, two percolation transitions, C_C and C_C^*, can be seen (Fig. 5.28). In his model, S.M. Aharoni [103] showed that the appearance of C_C and C_C^* can be associated with the number of contacts per single filler particle (of the conducting phase). According to this model, at $C = C_C$, one contact falls within one particle, and the composition is insulating. An increase in the number of particles leads to an increase in the number of contacts, and at $C = C_C^*$, at least two contacts fall within one particle, the particles can form conducting chains, and the system becomes conducting. That is, in the region of the percolation transition, an increase in continuous clusters occurs, which is considered to be formed at $C = C_C^*$. A further decrease in resistivity is attributed to the increase in the conducting branches of the continuous cluster with an increase in the conducting phase content in the material.

The ρ (C) dependences for CM of FP-dEG and FP-SPG can be divided into three sections, namely, the high ohmic one, where the resistivity of the sys-

tem varies weakly; the section of maximum change in ρ (*C*); and the range of minimal resistivity, which precisely corresponds to percolation theory and allows us to analyze the formation of the percolation cluster in the systems under study. In turn, on the experimental ρ (*C*) dependences for FP-dEG CM, the high ohmic section is absent, and a drop of the resistivity is observed to be followed by its minimal change in the low ohmic section of the curve. This and the different widths of the percolation transition of the considered systems are related to different areas of contacts between carbon component particles [104] and, as a consequence, to a different capacity of filler particles to form conducting chains in a composite system.

The threshold dependences of the specific resistivity (Fig. 5.27) can be described using the percolation theory by the scaling dependence [105]

$$\rho\,(C\,) \sim \rho_0\,(C - C_C)^t, \tag{5.3}$$

where ρ_0 is the specific resistivity of the electrically conducting component, C and C_C are the arbitrary and critical contents of the electrically conducting phase, respectively, and t is the critical index.

Using the $\rho(C)$ dependences for the FP-SPG and FP-EG compositions, the C_C value of the percolation transition was determined as the intersection of straight lines that approximate the decreasing section of the ρ (C) characteristics and the low ohmic branch of the experimental curve [104]. Then, using the approximated value of the percolation threshold, we constructed the dependences of the logarithm of the resistivity on the logarithm of the difference $(C - C_C)$ (Fig. 5.29). The ρ value was taken in the content region of $C > C_C$.

Using the least squares method and applying the linear approximation of the dependences $lg\rho = f\,(lg\,(C - C_C))$ (Fig. 5.29) [100], we determined the critical index t. Table 5.9 lists the results of the calculation of the percolation parameters for the composite FP–SPG and FP-dEG systems.

The value of the critical index for the FP-initial EG CM is 1.76, which corresponds to the model of a 3D lattice with electrically conductive joints con-

Table 5.9. **Percolation threshold and critical index for FP-graphite and FP-disperse EG CM [100]**

NCM	Percolation threshold, C_0,% vol.	Critical index, t	NCM	Percolation threshold, C_0,% vol.	Critical index, t
FP-graphite	32	2.06	FP-EG (180 μm)	7.5	1.96
FP-EG (initial)	5.2	1.7	FP-EG (80 μm)	9	1.81
FP-EG (260 μm)	6.5	1.78	FP-EG (40 μm)	12.5	2.3

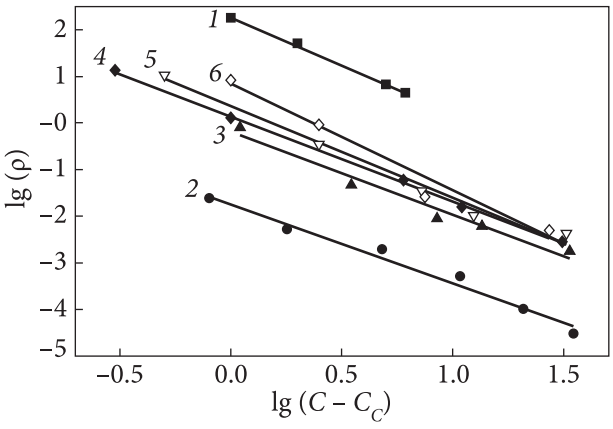

Fig. 5.29. Logarithm dependences of the specific resistivity ($lg\rho$) on the content ($lg(C - C_C)$) for samples of FP spectroscopically pure graphite (*1*), FP-initial EG (*2*), and FP-dEG NCM with a mean size of EG particles s = 260 (*3*), 180 (*4*), 80 (*5*), and 40 (*6*) (μm) [100]

sisting of EG particles and blocked joints from fluoroplastic particles. With an increase in the EG disperse level, the increase in the values of both the percolation threshold and the critical index of the compositions was observed. This can be explained by the deterioration of immediate electric contacts between the electrically conducting particles of the filler and, hence, distortion of the conductive 3D lattice of the filler. Since dispersion causes a change in the morphology of EG particles and their form approaches equiaxial (as shown above), the uniformity of distribution of the conducting component in the CM matrix is perturbed, which is related to the agglomeration of fine filler particles and the formation of an insulation region from fluoroplastic. The shift of the percolation threshold toward higher contents for the FP–EG CM with decreasing average size of filler particles results from the impairment of the capacity of particles of a higher dispersion level to form continuous electroconducting clusters.

For lattice models where the charge transfer in a continuous cluster can be considered a problem of percolation of the flow through lattice joints, H. Scher and R. Zallen [106] suggested that it is possible to relate the volume fraction filled with spheres (when conductivity arises) to the lattice parameters:

$$C_C = X_c \cdot F, \tag{5.4}$$

where X_C is the critical parameter that characterizes the type of distribution of the conducting phase. Fig. 5.30 shows the experimental relation between F and C_C.

As seen, in logarithmic coordinates, C_C increases with increasing F. The proportionality coefficient in this case, with a decrease in the dispersion level of EG from 40 to 500 μm, increases from ≈1.4 to 6. These values far exceed the value of X_C = 0.25, which is typical for volume lattice models and corresponds to the statistical distribution of spheres [106]. The failure of Eq. (5.4) can be explained by the fact that the F value for EG substantially depends on particle shape, and

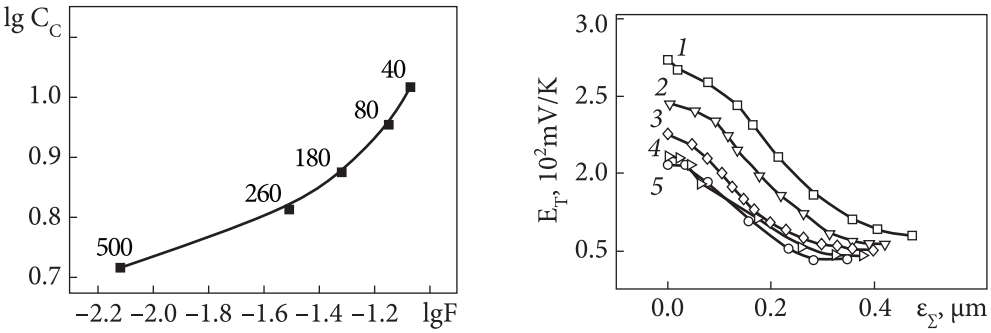

Fig. 5.30. Dependence of the percolation threshold on the compaction factor of carbon component particles. The numbers next to points designate the EG dispersion level (μm) [100]

Fig. 5.31. Dependence of the thermopower of FP-EG NCM with EG content C = 10% vol. and particle dispersity of 40 (*1*), 80 (*2*), 120 (*3*), 180 (*4*), 260 (*5*) μm on the relative deformation (ε_Σ)

thus, owing to the developed morphology of EG, *F* takes lower values. In the manufacturing process of NCM samples, the filler particles undergo deformation and fragmentation, and their packing factor increases significantly. That is why, taking into account the *F* value to describe the percolation processes in the NCM with the initial EG, it is incorrect to use models that relate conductivity to the lattice parameters.

The research results for the differential thermopower. Deformation of FP-EG NCM by rolling leads to filler structure changes, which is shown up in the change in the thermopower.

As follows from Fig. 5.31, the thermopower decreases with increasing degree of relative rolling deformation of NCM. This drop behaviour of the thermopower indicates that with the increase in the degree of rolling, the number of carriers in the samples decreases, which can be related to the change in the surface area of the carbon component in NCM during rolling. In the non-deformed state, the total EG cluster surface will be the largest; more carriers will be on it and the thermopower will be maximum. The compaction of the structure of an infinite EG cluster occurs with the strain growth, and contacts between the separated cluster parts are improving. The total area of its skeleton is reduced, and the thermopower is also reduced. However, changes in E_T increase with increasing EG dispersity.

As it was noted, with a decrease in the mean size of EG particles, their shape is close to spherical and with increasing EG dispersity, the percolation threshold of NCM is shifted to higher contents. This suggests that dispersed EG particles are separated in the matrix, and, in comparison with initial EG the percolation threshold of which is 5.2% vol. (due to its large surface), the effective filler surface, which affects the thermoelectric power behavior, is greater in EG particles of greater dis-

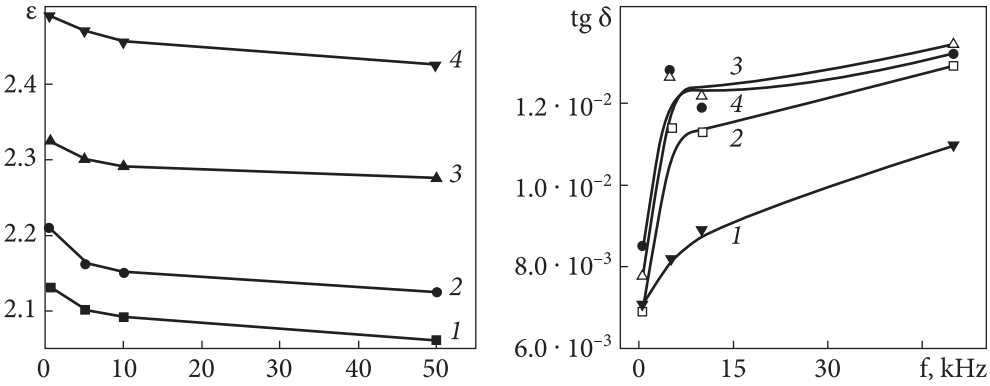

Fig. 5.32. Frequency dependence of the dielectric permittivity (*a*) and tangent of angle of dielectric losses (*b*) for NCM FP-dEG with an EG content of 3% vol. and dispersion of its particles *s* = 40 (*1*), 80 (*2*), 120 (*3*), and 260 (*4*) μm [100]

persity. Furthermore, the developed morphological structure of EG particles of smaller dispersity favors the formation of larger clusters, in which defective structures can accumulate and affect the carrier diffusion.

Dielectric characteristics. The FP-EG NCM is a two-phase system, which consists of a good dielectric in the form of an FP matrix and a carbon phase as a good conductor. The morphology of EG particles and their distribution are related to the electrical properties of NCM and affect the percolation parameters of the conductivity system. We can assume that the spatial distribution and morphology of EG particles will also affect the dielectric properties of compositions.

Electrically conductive PCMs are characterized by a frequency-dependent complex dielectric permittivity $\varepsilon(f)$, which consists of a real part $\varepsilon'(f)$, representing the relative dielectric permittivity of the material, and an imaginary part $\varepsilon''(f)$, which falls on losses [107]:

$$\varepsilon(f) = \varepsilon'(f) + i\varepsilon''(f). \tag{5.5}$$

The relation is the tangent of the angle of dielectric losses, or the loss coefficient, which characterizes the degree of energy absorption of an alternating electric field in a dielectric, which results from the difference in phases δ between the oscillations of the electric shift and the external field E.

In the case of filled polymers, the dielectric properties of compositions are determined not only by the polarization mechanisms in the dielectric but also by the interaction of local electric fields that exist around each filler particle with the induced charge on the conducting phase surface.

Figure 5.32 shows the frequency dependences of the dielectric permittivity and the tangent of the angle of dielectric losses for NCM FP-dEG measured at

room temperature. The dielectric permittivity decreases with increasing frequency. Thus, for the NCM FP-dEG with $C = 3\%$ vol. and s (EG) = 40 μm (curve *1*), the dielectric permittivity ε at $f = 0.5$ kHz is 2.13, and at $f = 50$ kHz, $\varepsilon = 2.06$.

In NCM FP-EG, the particles of the conducting phase that result from the action of the external electric field become macrodipoles, the reduced (induced) dipole moment of which varies depending on the alternating current frequency. Here, due to the appearance of microcurrents in the particles, migration polarization occurs [108], the physical cause of which is the presence of bulk phases with different electric conductivity in nonuniform materials. This leads to compression of free carriers at the boundaries of a more conducting phase and the formation of the corresponding macrodipoles. As the nonuniform materials are introduced into the electric field, the free electrons begin to migrate within the limits of each insertion, forming polarized regions. In the NCM FP-dEG, with an increase in the mean EG particle size (40—260 μm), the number of contacts between the EG particles increases, resulting from the change in the morphology of particles and their exfoliation in the polymer bulk. The length of macrodipoles increases as well. However, since the dielectric permittivity and the tangent of the angle of dielectric losses depend on the alternating current frequency, we can confirm that the particle polarization process is slower than the variation in the external field frequency, and in this situation, high energy consumption is expended on the polarization of large EG particles.

For NCM FP-EG samples with a filler content of 3% vol. (the experimental frequency is $f = 0.5$ kHz), with an increase in the EG particle mean size from 40 to 260 μm, ε increases from 2.1 to 2.5, and the tangent of the angle of dielectric losses varies from 5.5×10^{-3} to 8.5×10^{-3}. That is, both ε and $tg\delta$ increase in proportion to the decrease in the dispersion level of the filler. This again can be attributed to the increase in the interface surface area between the matrix and filler, which enhances surface polarization and, hence, leads to higher dielectric losses that characterize high energy consumption for polarization of EG particles with a lower dispersion level.

Physical-mechanical and percolation characteristics. In producing polymer compositions with non-conductive matrices and conductive fillers, the material becomes electrically conductive when the filler content exceeds the percolation threshold. Such CPCMs are prospective for use in various fields of technology. They have a wide range of useful properties. Particularly, they can be used for the production of sensitive electrodes [109], sensors for fixing low chemical vapor contents [110], elements of electrical heaters [111], items for protection from radiation and electronic smog, as well as controllers, load cells, etc.

In our case, the expanded graphite is a filler in CPCM. Since the electrical and physical-mechanical characteristics depend on the particle size and morphology, the ways for optimizing these parameters for EG particles are described below. The initial powder of EG was dispersed in a mechanical mixer and separated with

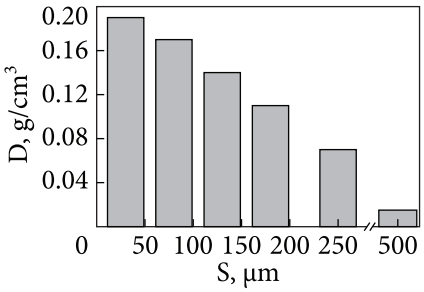

Fig. 5.33. Relationship between the EG powder bulk density and its dispersity [88]

sieves into fractions with the cross-sectional size of particles (*s*) in the range of (40...60), (60...100), (160...200) and (200...315) μm [88]. The value of the bulk density (*D*) of the obtained powders of different dispersion is displayed in Fig. 5.33.

To obtain composite mixtures, FP and EG powders were mixed in a rotary mixer. The EG content varied from 5 to 20% vol. in the obtained mixtures. A device for measuring the electrical resistivity of a cell with the mixture during compression is presented in [84].

To get a compacted material, the corresponding mixtures were sintered in a mold under a pressure of 20 MPa at a temperature of (217 ± 0,5) ˚C. The sample thickness was 1.5...3 mm, and the diameter was 20 mm. The resistivity ρ of the compacted NCM samples was measured by the four-point method. The horizontal tensile testing machine with a computer was used for measuring the dependence between the voltage and the sample relative deformation (σ_M). The relative error of these measurements did not exceed 3%.

The dependence of the resistivity (ρ_k) of the container with the FP-EG powder mixtures, measured in the pressing along the applied load, is shown in Fig. 5.34.

It is clear that with an increase in the compression, ρ_k decreases, and the decrease degree depends on the EG content in mixtures. Thus, larger values of ρ_K are fixed at a lower volume content of EG. For example, in FP and EG mixtures with an EG particle dispersity of 260 μm, the resistivity decreases by almost 5 orders of magnitude at P = 45 MPa, meanwhile, in the EG mixtures with *C* = 20% vol., this decrease is not more than two orders of magnitude, and when *C* = 5% vol. it is about 0.158 Ω·m [88]. With the further increase in *C* and *P*, the material compacts, the mean size of conductive clusters grows, and the isolated clusters merge into the so-called "infinite" cluster, which permeates the entire system. Thus, a conduction channel or a number of such channels appear. The further increase in both *C* and *P* causes the further growth of the infinite cluster, whereas the resistivity of the container with the mixture decreases. The decrease in EG particle size reduces their ability to form cluster structures.

Thus, the FP-EG powder mixtures with EG dispersity of 80 μm and EG content *C* = 10% vol. behave as insulators. At the same time, the conductivity of mixtures with EG dispersity *s* = 260 μm arises for *C* = 5% vol. when the pressure is higher than 10 MPa. When the EG particle cross-section decreases to 80 μm, the resistivity of the cell with the initial EG at P = 5 MPa increases to $\Delta\rho_K$ =

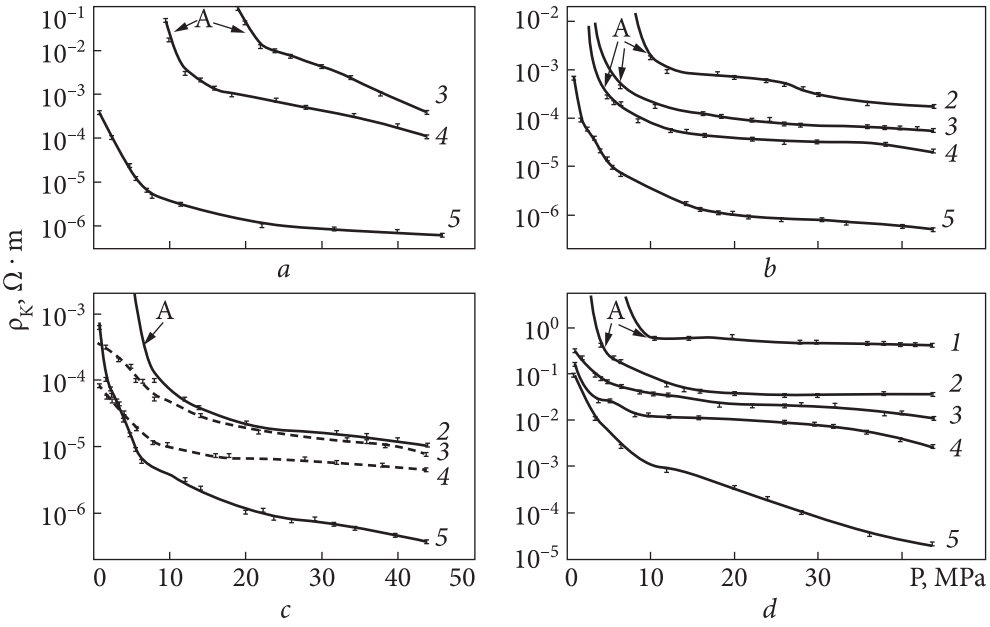

Fig. 5.34. Dependence of the resistivity of the cell with FP-EG powder mixtures, EG content (% vol.) of 5 (*1*); 10 (*2*); 15 (*3*); 20 (*4*); 100 (*5*), and a mean particle size (μm) of 80 (*a*), 130 (*b*), 180 (*c*), 260 (*d*) on the applied load. **A** indicates points corresponding to the pressure under which the resistivity is noticeable [88]

$= 1.67 \times 10^{-2}$ Ω·m, whereas, the change of ρ_K is to $6.94 \cdot 10^{-4}$ Ω·m at $P = 30$ MPa. Despite the fact that the electrical resistance of the initial EG consists of the electrical resistance of the individual particles and the contact resistance between them, it can be stated that the increase in EG dispersity during grinding, followed by a change in its morphology, causes the growth of the integrated area of interparticle contacts, which results in reducing electrical resistance. The lamination of the initial EG powder into flakes and their orientation perpendicular to the pressing direction cause an increase in ρ anisotropy. After dispersing and approaching the particle shape to the equiaxed type, the resistivity of the powder decreases, and when the pressure ranges 5...45 MPa, it hardly depends on the degree of compression (Fig. 5.34).

Analysis of the received results allows us to introduce the concept of a dynamic coefficient of the electrical resistance reduction for graphite, which depends on its dispersity. This makes it possible to follow the rate of the electrical resistance change in FP-EG powder mixtures during their compression. The dynamic coefficient is easy to find after approximation of the curves (Fig. 5.34) in the pressure range when the mixtures are conductive, by the following equation:

$$\ln(\rho_K) = \ln(\rho_0) + QP,$$

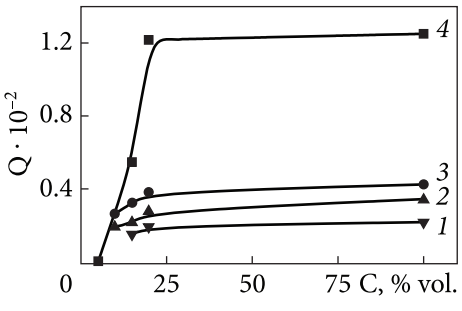

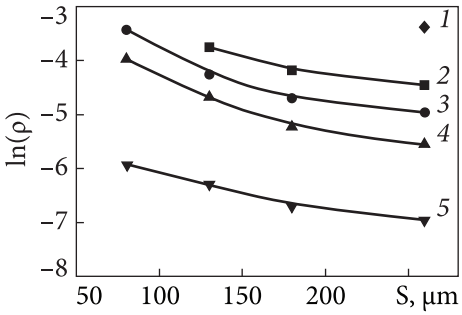

Fig. 5.35. Dependence of the dynamic coefficient of the electrical resistance reduction for FP-EG powder mixture with a dispersity (μm) of 80 (*1*); 130 (*2*); 180 (*3*); 260 (*4*) on the EG volume content [88]

Fig. 5.36. Logarithm dependence of the resistivity of the cell with powder mixtures FP–EG, compacted at $P = 45$ MPa, with an EG content (% vol.) of 5 (*1*); 10 (*2*); 15 (*3*); 20 (*4*); 100 (*5*) on the dispersity of filler particles

where $\rho_K(P)$ is the electrical resistivity depending on the degree of compression, ρ_0 is the mixture resistivity before compression, P is the pressure applied to the sample, Q is a constant (dynamic coefficient of reducing electrical resistance as pressure increases).

Consequently, the dynamic coefficient (Q) is a numerical parameter determined by the ratio of changes in the logarithms of the resistivity to the pressure at which the change occurs. It characterizes the dynamics of electrical resistance reduction in the material during its compaction.

The dependence of the dynamic coefficient of resistivity reduction of the FP-EG powder mixtures on the EG volume content is given in Fig. 5.35, which shows that when the EG volume content in the mixtures with EG content up to 20% vol. increases, Q increases as well, though its further growth hardly depends on the content. Furthermore, with changing EG particle dispersity from 80 to 260 μm, the dynamic coefficient of the mixture resistivity reduction (with C (EG) > 20% vol.) increases by almost 5 times.

Fig. 5.36 shows the dependences of the resistivity of the container with compacted FP-EG powder mixtures on the EG particle dispersity.

It is seen that the higher proportion and the larger size of EG particles in the material results in the higher composite mixture resistivity. At the same time, a decrease in the content of the graphite component causes an increase in the influence of EG particle size on the system conductivity. Thus, with the decrease in the EG particle size, the electrical resistance doubles for the mixture with EG content $C = 20\%$ vol., whereas for the initial EG powder it increases only by one order of magnitude.

The dependence shown in Fig. 5.37 gives a more detailed estimation of the effect of the EG dispersity on the electrical properties of FP-EG powder mixtures.

As seen in the figure, when the EG particle size decreases from 260 μm to 80 μm and the EG mixture content increases from 5 to 20% vol., the curves shift toward higher pressures. For the FP-EG mixture with an EG particle dispersity of ≈260 μm and its content C = 5% vol. at P = 30 MPa, the ρ_K value equals 0.46 Ω · m, but for the FP-EG mixture, in which EG particles are three times smaller, similar values of ρ_K are fixed only when C = 20% vol. Such a behavior of the composite mixture is determined by the decrease in the EG ability to form continuous net structures in the material when the particle dispersity decreases. Consequently, the size of EG particles, or rather their morphology and the content are the main factors affecting the quality and quantity of the contacts between structural elements of the graphite component and the conductivity of the system as a whole.

We can conclude that the ability of EG particles to form infinite electrically conductive clusters in FP-EG powder mixtures decreases when the EG particles' dispersity increases, and it increases during compression of the corresponding mixtures. The electrical resistance method allows one to control percolation processes for the systems under examination and, accordingly, to correct their dispersity and morphological features in order to obtain electrically conductive polymer compositions. Particularly, the conductivity of the FP-EG nanocomposite powder mixtures decreases with the decrease in the cross-section and content of graphite particles in the mixtures and increases with the increase in the degree of compression [88].

The electroconductivity anisotropy of the mixtures is defined by EG particles morphology, therefore when the particle dispersity increases from 260 to 40 μm, it decreases by ~30%. The morphology of the dispersed EG particles (up to 40 μm) approaches an equiaxed one. This causes a weak dependence of the conductivity of mixtures with such particles on the compression degree (when P = 5...45 MPa) [88].

The conductivity of NCM with another content and dispersity of the filler, measured in the direction perpendicular to the sample plane, is shown in Table 5.10.

The table displays that with a decrease in the filler dispersity, the NCM conductivity increases. The content has a similar effect on the conductivity.

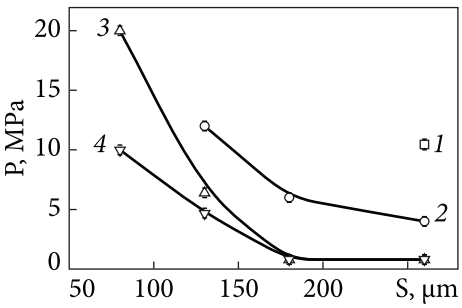

Fig. 5.37. Dependence of the pressure, at which FP-EG powder mixture with an EG content (% vol.) of 5 (*1*); 10 (*2*); 15 (*3*); 20 (*4*); 100 (*5*) becomes conductive, on the particle dispersity

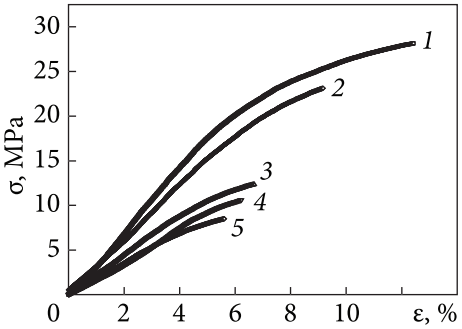

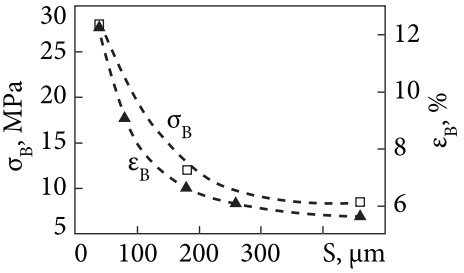

Fig. 5.38. Stress-strain dependence $\sigma(\varepsilon)$ for FP-EG CM samples (C = 10% vol. EG) with different EG dispersity (μm): 40…60 (*1*), 60…100 (*2*), 160…200 (*3*), 200…315 (*4*), and initial EG (*5*)

Fig. 5.39. Dependence of the tensile strength limit and the critical relative deformation of FP-EG samples with C(EG) of 10% vol. on the mean particle size

Table 5.10. **Dependences of conductivity of FP-EG NCM on the content and cross-section of EG particles [112]**

C (EG), % vol.	σ, $\Omega^{-1}m^{-1}$			
	s = (40…60) μm	s = (60…100) μm	s = (160…200) μm	s = (200…315) μm
5	$3.5 \cdot 10^{-13}$	$4.1 \cdot 10^{-7}$	$6.2 \cdot 10^{-5}$	$8.3 \cdot 10^{-3}$
10	$5.2 \cdot 10^{-5}$	$4.5 \cdot 10^{-1}$	10.1	91
15	3.5	18.7	36.1	$1.1 \cdot 10^{2}$
20	40.3	67.6	$1.2 \cdot 10^{2}$	$1.9 \cdot 10^{2}$

Thus, for FP-EG samples (C = 5% vol.) with a change in the mean size of the filler particles from 40 to 260 μm, the value of σ increases from 3.5×10^{13} to 8.3×10^{-3} Ω^{-1} m^{-1}, meanwhile, the conductivity increases from 40.3 to $1{,}9 \times 10^{2}$ $\Omega^{-1}m^{-1}$ in the same conditions at the EG content C = 20% vol. This fact indicates a change in the nature of conductivity, mainly connected to the spatial distribution of the filler particles and their ability to form a continuous cluster in the polymer matrix.

Since the research purpose is to obtain conductive NCM with the optimal physical and mechanical properties and to establish an effect of the dispersity of the carbon filler on them, the results of the NCM strength properties are presented below (Fig. 5.38).

When the EG particle dispersity increases, the tensile strength limit of the samples increases as well as its relative elongation recorded at the break.

This is supported by the dependence of the strength (σ_B) on the critical relative deformation of samples with the mean particle size of EG, shown in Fig. 5.39.

The NCM sample with an EG dispersity of (40...60) μm fails at a stress of σ_B = (28 ± 0.5) MPa, whereas its elongation is about ε_B = 12%. The tensile strength is three times lower for NCM with the initial EG powder. Thus, at the critical strain ε_B = 5.57%, its σ_B = (8.4 ± 0.5) MPa. This can be explained by the fact that smaller particles, by changing their morphology, effectively block the spread of defects under the increased load and delay the reorientation of macromolecules in the matrix [112].

The increase in the EG content leads to deterioration of the strength properties of the composition. The results of the strength investigation of these samples with different EG contents prove that the increase in the EG content results in decreasing σ_B in NCM. For example, the samples with *C* (EG) = 20% vol. and mean particle size *s* = = (200...315) μm are the most fragile. Their σ_B = (9 ± 0.5) MPa, which is almost three times less than the strength limit for NCM with *C* = 5% vol. and *s* = (40...60) μm, whereas, the critical deformation of the examined samples is 5.1 and 17%, respectively. For compositions with *C* = 15% vol. and the EG dispersity ranging from 40 to 260 μm, the stress at break decreases from about 15 to 10 MPa and the elongation does from about 11 to 6%, correspondingly. Such a behavior of the NCM parameters is caused by the structural changes that occur when the content and dispersion of the filler change. When the former increases, its clusters become structurally dominant in CM volume. As long as FP is characterized by a weak adhesive interaction with EG particles [113], the material failure occurs between the EG cluster areas and the contact zones of FP and EG structural elements. Thus, crack propagation in the CM occurs in the filler, as well as in the poor adhesive contact areas of filler and matrix. Furthermore, due to the morphology, large EG particles with the increased content exhibit a better ability to form a continuous cluster in the polymer matrix. Small particles have another morphology, their shape tends to equiaxial, and their ability to form continuous chains decreases. Thus, the increase in the EG content and the decrease in its dispersity results in the polymer layers evolution between the filler particles. Their geometric parameters change, and the number of direct contacts between EG particles increases. The nature of σ_B change can be related to the transition from the adhesive strength of filler-matrix bonds to the dominant role of the cohesive strength of filler-filler bonds.

It is especially important that with increased EG dispersity, CM becomes more rigid. For example, when the EG content (*C* = 5% vol.) remains the same but its dispersity varies, the elastic properties of NCM are not constant. With the increasing mean size of the filler particles, the effective elastic modulus (E) decreases (Fig. 5.40). As for a pure FP, with a modulus of elasticity of about 1.2 GPa [113], the addition of 5% vol. EG with the dispersity of 40 μm results in decreasing the composite material rigidity, thus, *E* = (262 ± 0.5) MPa. The addition of EG powder with a mean particle size of 200...315 μm causes reducing the effective modulus of more than down to ~46 MPa [112].

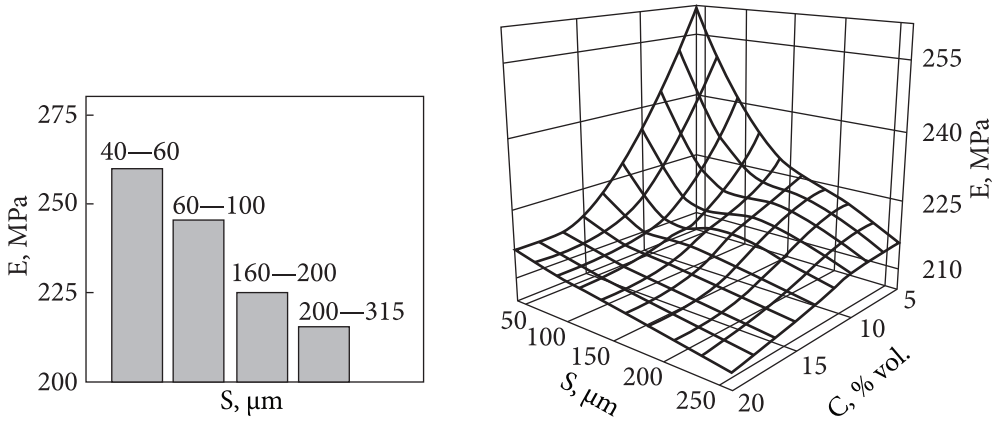

Fig. 5.40. Dependences of the effective modulus of FP-EG NCM samples with EG content C = 5% vol. on the mean EG particle size

Fig. 5.41. Dependence of the effective elastic modulus of FP-EG NCM samples on the content and dispersity of EG [112]

The general effect of both the dispersity and the volume content of EG on the FP-EG NCM stiffness is shown by the respective dependences of the effective modulus (Fig. 5.41).

The increase in the filler content reduces the effective modulus. For example, for compositions with the filler particle size of below 60 μm, the increase in the filler content from 5 to 15% vol. is accompanied by a decrease in the modulus from 260 to 220 MPa. Moreover, the dynamics of changes in E (C) increases with increasing EG particle dispersity. For example, for the NCM, a mean size of EG particles (200...315) μm, the increase in the EG content from 5 to 20% vol. leads to a decrease in the E value by only 7 MPa. At the same time, for the FP-EG samples with s (EG) = 40 μm the corresponding change constitutes almost 50 MPa [112]. The obtained results enable us to assert, that with the decrease in the EG particle size, the energy of their interaction with the internal FP matrix increases, as a result, the NCM becomes more rigid.

The analysis of the data presented in this section allows us to conclude that the decrease in the EG particles cross-section from 260 to 40 μm improve the physical and mechanical properties of the FP-EG nanocomposite materials. That is because the small particles effectively inhibit the mobility of the structural defects and prevent the reorientation of the polymer macromolecules during deformation. The dispersity and the morphology of the conductive filler particles are the main factors, which influence the formation of the percolation clusters in the polymer matrices. The optimization of these factors allows us to obtain a conductive composition without significant loss of its strength properties.

5.3.2. Linear polymers with carbon nanotubes

Due to the combination of mechanical, thermal, and electrophysical properties that are inherent in CNTs, there is a constant expansion of the spectrum not only of their application but also of the possibilities of using for fundamental research.

The complex physical properties of nanotubes make them ideal fillers for polymer composite materials [23—25, 45, 82, 83, 114—117]. Today, it is possible to significantly increase the thermal conductivity of matrices and obtain leading polymers with a low content of MWCNTs. Such materials are used to create conductive elements, battery electrodes, sensors, protective screens, antistatic and anticorrosive coatings, and the like. At the same time, mechanical properties, such as the average modulus of elasticity of MWCNTs, which is above 1.8 TPa (measured value 1.3 TPa) [22], and tensile strength of 63 GPa [118] put them among the most promising reinforcing fillers in the creation of composite materials with increased mechanical characteristics.

However, the tendency of CNTs to form agglomerates due to van der Waals forces (0.5 eV/nm) is a limiting factor in realizing the potential of these materials [22, 24, 45, 82, 83, 114—118,]. For effective use of CNTs, it is important to ensure high homogeneity of their distribution in the polymer matrix, which is relevant to the efforts of many researchers [23—25, 114—117]. The promise for CNT-filled polymers is much higher because they have higher mechanical characteristics than unfilled materials.

In [119], have been considered the regularities of the influence of carbon nanotubes and another nanoscale system of pyrogenic silica A-300 on the electrical and mechanical characteristics of a composite material based on polymers such as polyethylene (PE), polypropylene (PP), and polytetrafluoroethylene (PTFE). These systems are selected for comparison.

Low-density PE and FP as matrixes as well as MWCNTs and ground EG as fillers were chosen for the preparation of NCM samples for testing. The multiwalled carbon nanotubes (Fig. 3.23) (TU U 24.1-03291669-009:2009 (ISC NAS of Ukraine)) were synthesized using the CVD procedure in a rotating reactor. Characteristics of the produced MWCNTs were: average diameter between 10 and 20 nm; specific surface area (determined through Ar-adsorption) between 200 and 400 m^2/g; bulk density between 20 and 40 g/dm^3 [120, 121].

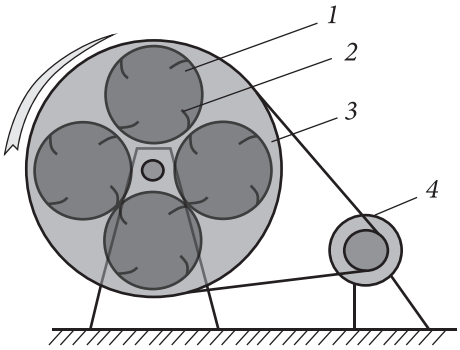

Fig. 5.42. Rotary stirrer of the revolver type for 4 mixtures: *1* — drum, *2* — membrane, *3* — cassette for drums, *4* — engine

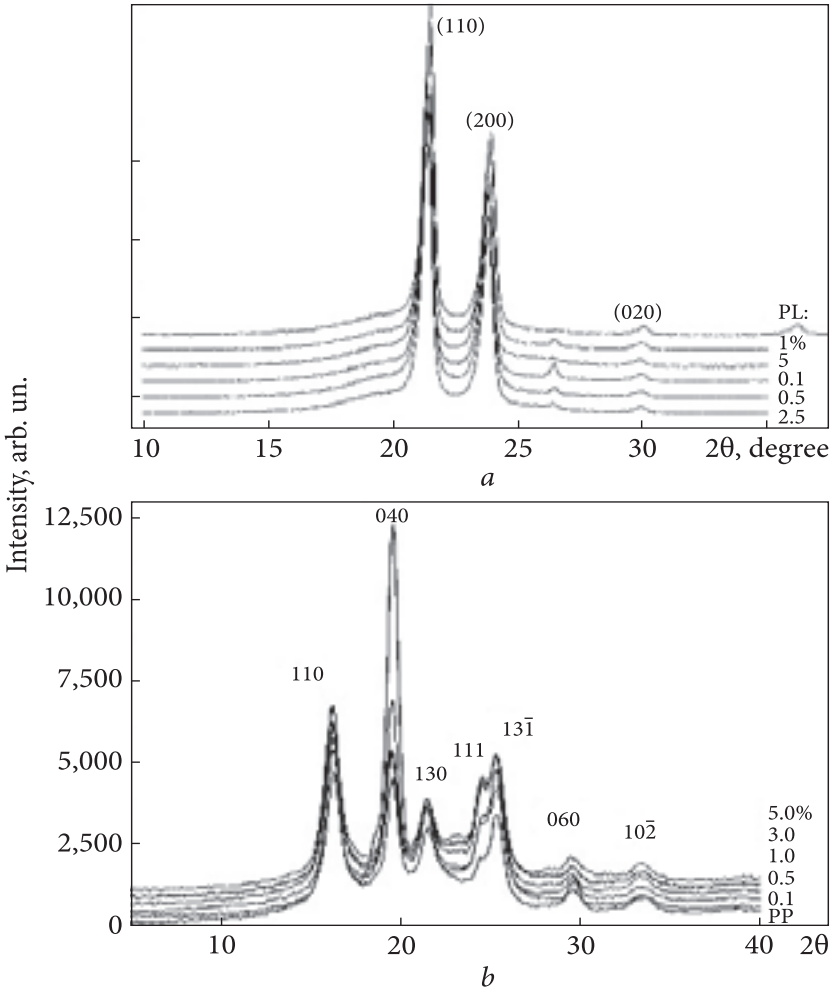

The MWCNTs synthesized by the CVD method are obtained in the form of agglomerates. Powders of the initial components (PE-MWCNT) of the composite material were mechanically mixed in a drum (*1*, Fig. 5.42) with a speed of 120 min^{-1}. The drum has membranes with holes (*2*), forcing the mixture to move along a complex trajectory. The drum is placed in a revolver-type cassette (*3*), in which 4 mixtures can be mixed simultaneously in the same mode. The cassette is driven by a motor (*4*). Mixing lasts 4 h. At this time, the mixture is completely isotropic.

After mixing, the mixtures were put into a vacuum mold, where they were heated to (377 ± 5) K and kept at a pressure of ~30 MPa for 20 min, after which they were cooled without removing the pressure. The heating time was 60 min, and the total time was 140 min.

Polypropylene composites with MWCNT were obtained in the form of granules by mixing in a twin-screw extruder, then samples were also made in

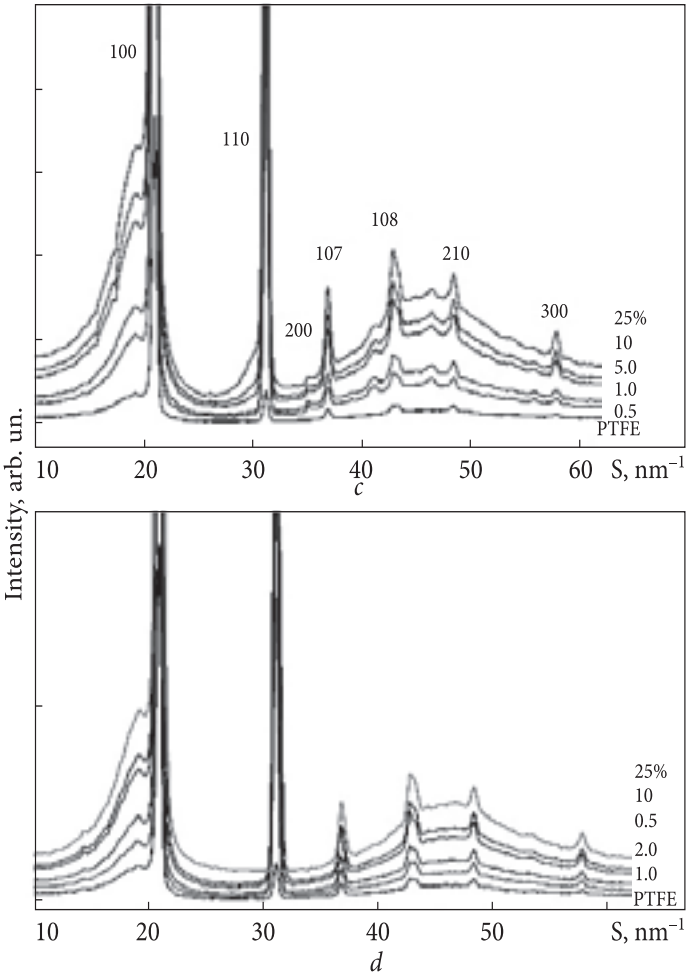

Fig. 5.43. XRD patterns of PE-MWCNTs (*a*), PP-MWCNTs (*b*) PTFE-MWCNTs (*c*), and PTFE-A300 (*d*) composites with different nanofiller contents

the form of films and volumetric cylinders. The content of nanotubes was 0.1, 0.5, 1.0, 3.0 and 5.0% wt. [122].

In the case of PTFE, which is insoluble and non-fusible, coagulation of the aqueous dispersion of PTFE was carried out using a mixture with the addition of CNTs ethanol and mechanical stirring.

Deagglomeration of CNTs was performed in a device operating on a cavitation effect, with a capacity of 4—7 kW in an aqueous medium. Into the system, working by the cavitation principle, 10 l of water was poured and 124 g of initial MWCNTs, that is about 100 g of purified CNTs, was added. The

treatment lasted 4 min. After that, the CNTs were cleaned in the traditional way, that is, with a solution of hydrofluoric acid. After cleaning, CNTs were washed to pH = 6—7.

The PTFE-MWCNTs system was prepared by mixing an aqueous emulsion of PTFE with an aqueous dispersion of MWCNTs, which was obtained by homogenization in a cavitation device and without it. The PTFE-A300 system was prepared by introducing the A300 powder into the PTFE suspension and mechanical stirring [123, 124].

XRD studies were carried out on an automated diffractometer DRON-3M with radiation λ_{Co} = 0.17902 nm.

Compression or tension tests of the polymeric materials and their composites were performed using a tensile machine 2167 P-50 with automatic recording of the deformation diagram. Measurements were carried out at a load speed of 5 mm/min.

Conductivity measurements were carried out by a two-contact method at low frequencies using an E7-14 immitance meter at room temperature.

Structural features of polymer nanocomposites. Fig. 5.43 shows the XRD data, and Table 5.11 presents the crystallinity degree of PE-MWCNTs, PP-MWCNTs, PTFE-MWCNTs, and PTFE-A300 composites and the crystallite size depend-

Table 5.11. T**he crystallinity degree (χ), X-ray coherent scattering domain size (D) of PE-MWCNTs, PP-MWCNTs, PTFE-MWCNTs and PTFE-A300 systems against the nanofiller content**

System	Content of CNTs, % wt.	Degree of crystallinity (χ),%	D, nm	System	Content of CNTs, or A300, % wt.	Degree of crystallinity (χ),%	D, nm
PE-MWCNTs	0	85.6	21.92	PTFE-MWCNTs	0	28.1	25.04
	0.1	85.1	19.28		0.5	40.0	23.05
	0.25	79.5	20.50		1	31.8	21.58
	0.5	82.8	21.04		5	28.9	21.00
	1.0	83.8	21.46		10	34.3	20.11
	2.5	81.4	20.12		25	30.5	19.28
	5.0	82.3	21.35				
PP-MWCNTs	0	70.9	11.97	PTFE-A300	0	28.1	25.04
	0.05	71.8	13.01		0.5	47.6	24.78
	0.1	60.9	11.24		1	37.6	24.77
	0.5	63.5	10.85		2	32.7	24.86
	1.0	63.8	10.40		10	34.8	24.29
	3.0	64.0	10.32		25	26.7	18.18
	5.0	68.2	10.27				

ing on the CNTs content were calculated from the X-ray reflex profile. The addition of CNTs into the polymer matrix demonstrates the structure-forming properties of CNTs. This is confirmed by a non-monotonic change in the crystallinity degree depending on the content of CNTs (Table 5.11). The result is in good agreement with the data [114, 122—126], where it was shown that crystallization of the polymer under shear deformation in the presence of single, five, and multi-wall CNTs leads to a change in the matrix structure. For the PE-CNTs system, the distances between the crystal planes (110) and (200) are smaller than the interplane distances in the PE control sample, and the polymer chains are oriented along the CNT axis.

It can be concluded that the nanofiller creates effective crystallization centers. For example, for PTFE, small contents of MWCNTs or pyrogenic silica A-300 lead to an increase in the crystallinity degree. When the content of the filler increases, the crystallization centers become too many, they "interfere" with the growing crystal phase, which leads to an increase in the number of globules, their "tails", that is, in the content of the disordered phase PTFE.

The same result (increase in the crystallinity degree) is observed for the PP-MWCNTs system, but in a very narrow range of MWCNTs content up to 0.05% wt., from 70.0 to 71.8% wt. Adding 0.1% wt. MWCNTs reduces the crystallinity degree to 61%, followed by an increase in the content of MWCNTs to 5% wt.

Electrical conductivity of filled polymers. One of the most common areas of research of polymer-MWCNTs composite materials is the creation of conductive compositions [114, 125, 127, 128]. The value of the percolation threshold in the PE-MWCNTs systems in different sources differs by several orders of magnitude. Thus, in [127] it is noted that in the composition of PE with multiwall CNTs obtained by mixing the melt in a twin-screw extruder, the percolation threshold is observed at a content of 7.5% wt., and the conductivity jump is 16 orders of magnitude from 10^{-20} to 10^{-4} S/cm.

The percolation theory is most often used for the analytical description of conductivity dependences on filler content [101, 129], in the framework of which the probability of formation of clusters from contacting particles is considered. Description of the critical electric current in composite materials is given by means of the percolation problem formulated for a continuous medium. According to this problem, a point of space with probability $p = \theta_F$ corresponds to conductivity $\sigma = \sigma_F$ and that with probability $(1 - p)$ — to conductivity $\sigma = \sigma_m$. The threshold in the percolation terms means the filler content at which the phase transition of the second type, dielectric-conductor, occurs. In this case, the regions with high conductivity occupy a minimum fraction of the space, θ_F. At small p, all conductive elements are contained in isolated clusters of finite size. With increasing p, the average size of clusters increases, and at $p = \theta_F$, a through conduction channel, which is a continuous grid of conducting clusters,

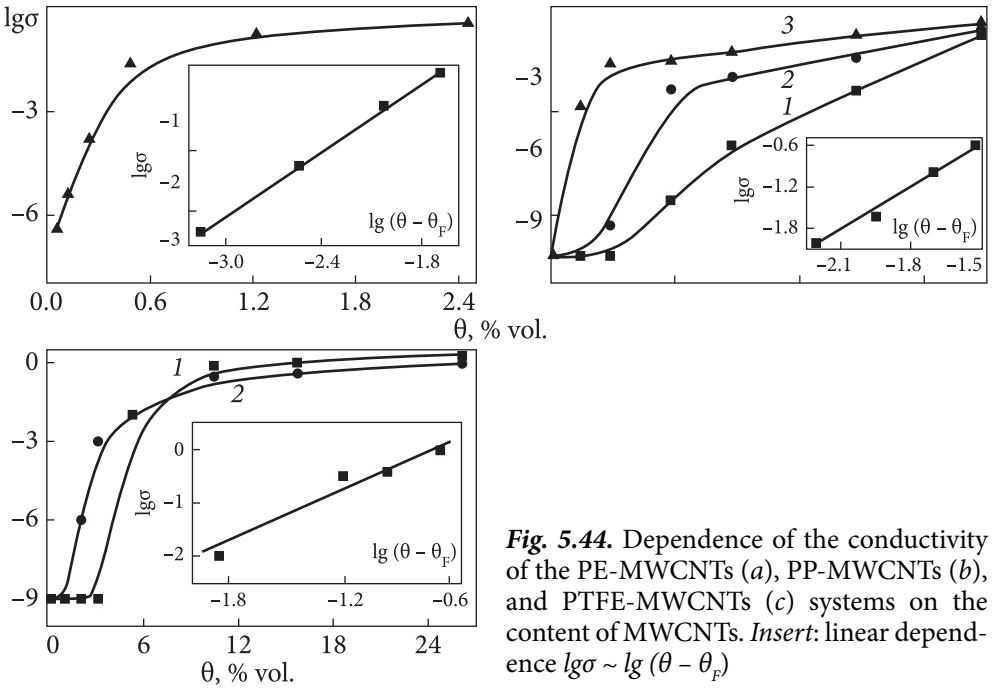

Fig. 5.44. Dependence of the conductivity of the PE-MWCNTs (*a*), PP-MWCNTs (*b*), and PTFE-MWCNTs (*c*) systems on the content of MWCNTs. *Insert*: linear dependence $lg\sigma \sim lg\,(\theta - \theta_F)$

appears in the system for the first time. At high p values, non-conducting regions may already be isolated from each other.

Based on the percolation theory, the following expressions are obtained to describe the dependence of electrical conductivity on the filler content [101, 129]:

$$\sigma \sim \sigma_F (\theta - \theta_F)^t,\ \theta > \theta_F\,,$$
$$\sigma \sim \sigma_m (\theta - \theta_F)^q,\ \theta > \theta_F\,, \qquad (5.6)$$

where *t, q* are critical indices of percolation theory.

For the 3D model of composite materials with spherical filler particles, the following values of the threshold and critical indices are obtained: θ_F = 17% vol., t = 1.6...1.9, q = 1. In practice, significant deviations from the theoretically calculated values are possible. For example, for the graphite-polystyrene system [130] θ_F = 2% vol., t = 0.35; for the carbon black-polyvinyl chloride system, the authors [131] obtained θ_F = 11% wt., the authors [132] 9...9.5% wt. at t = 1.9 ± 0.2, and for the PE-CNTs system the authors [128] obtained θ_F = 0.07% wt. at t = 2.1.

The dependence of the conductivity on the MWCNT content for the studied systems is shown in Fig. 5.44. The conductivity jump in the transition to a composition with a content of 5% wt. is almost seven orders of magnitude for PE-MWCNTs (Fig. 5.44, *a*) and nine orders for PP-MWCNTs (*b*),

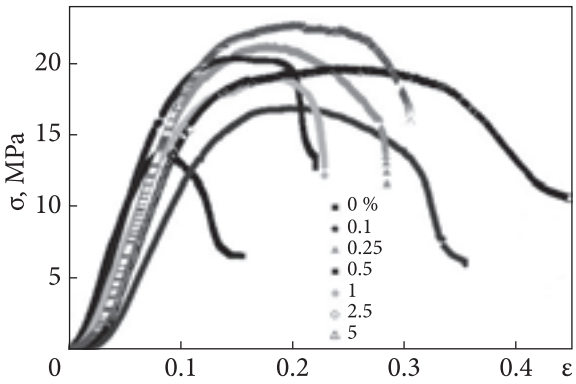

Fig. 5.45. Relationship between the relative elongation and tensile stress for samples of PE and PE-MWCNTs system

PTFE–MWCNTs (c). Therefore, to create a continuous conductive grid in the polymer matrix, the filler size (length of MWCNT agglomerates) and its distribution in the matrix are of great importance.

Analysis of the results for the electrical conductivity of the obtained systems indicates a significant role of the polymer particle size in the formation of conductive clusters, which is related to the MWCNTs distribution in the polymer matrix provided that the polymer particles have a much larger size than MWCNTs agglomerates [114]. Due to mechanical mixing, the filler covers the surface of polymer particles, and during hot pressing, this structure changes little and the filler remains at the boundary of polymer particles. Therefore, a cluster conductive structure with the content of MWCNTs above the average and a system of cells with a lower content of MWCNTs or their absence can be formed. In this case, the PE-MWCNTs system has a sufficiently low percolation threshold and a relatively low influence of the MWCNTs agglomerate size on the percolation properties of the systems [114].

The mechanical characteristics of the nanocomposites. The tests of tensile (Fig. 5.45) and compression (Fig. 5.46) showed that the addition of MWCNTs changes the mechanical characteristics of the considered composite systems. The dependence of elongation on the tension stress (Fig. 5.45) for the PE-MWCNTs system can be divided into four regions: the region with positive curvature in the range up to 5% of deformation for composites, which may be due to the presence of nanosized pores, working as elastic deformation elements [133], the elastic region, the plastic regions, and the fracture of the samples. Thus, adding nanotubes into the polymer matrix leads to an increase in the limit of the tensile strength modulus of elasticity (120—213 MPa), and in the conditional yield strength (by ~50—60%) as well as to a significant expansion of the area of plastic deformation of the material, which increases the destruction deformation from 8% to almost 40%, and means a rise of the work of fracture, or fracture energy (the area under the curve of deformation).

The stress-strain relationships of the relative strain with respect to compression for the PP-MWCNTs, PTFE-MWCNTs, and PTFE-A300 systems are shown in Fig. 5.46. As can be seen from the above compression diagrams, the

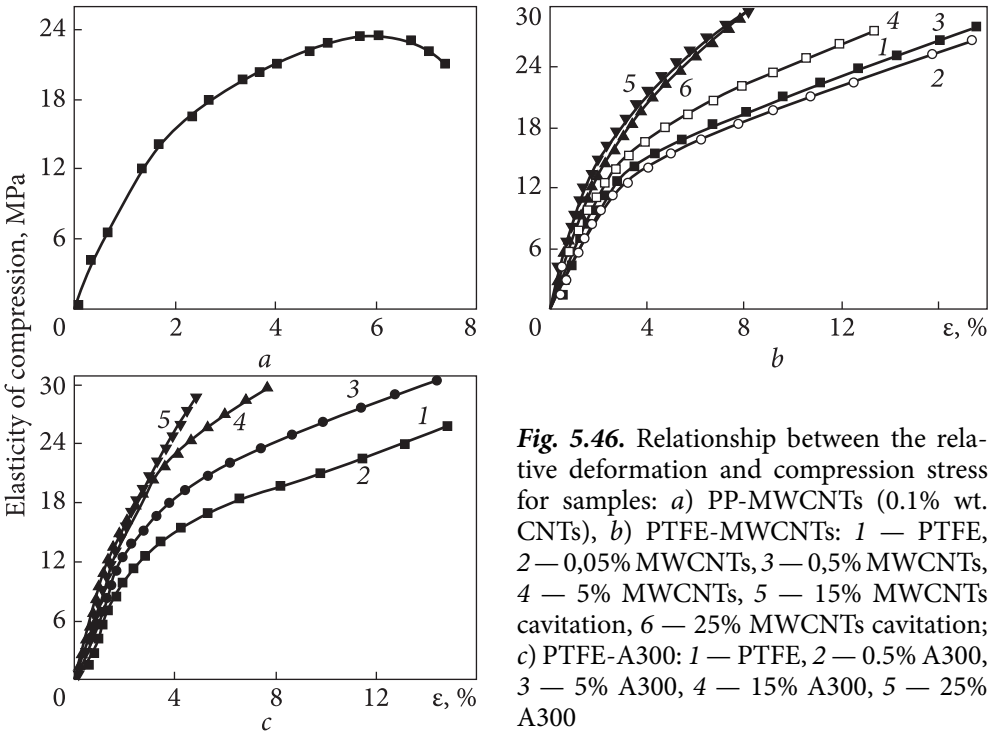

Fig. 5.46. Relationship between the relative deformation and compression stress for samples: *a*) PP-MWCNTs (0.1% wt. CNTs), *b*) PTFE-MWCNTs: *1* — PTFE, *2* — 0,05% MWCNTs, *3* — 0,5% MWCNTs, *4* — 5% MWCNTs, *5* — 15% MWCNTs cavitation, *6* — 25% MWCNTs cavitation; *c*) PTFE-A300: *1* — PTFE, *2* — 0.5% A300, *3* — 5% A300, *4* — 15% A300, *5* — 25% A300

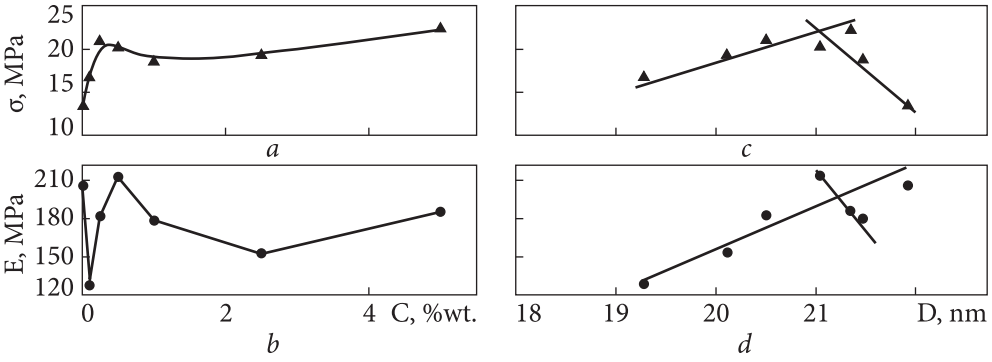

Fig. 5.47. Dependences of the conditional yield strength of composites PE-MWCNTs (*a*, *c*) and the modulus of elasticity (*b*, *d*) on the CNTs content (*a*, *b*) and the CSD size (*c*, *d*)

addition of MWCNTs into composites does not change the nature of the deformation-compression stress curve, only the values of the characteristics change. The curves are typical for solid polymers [134]. However, with the addition of MWCNTs, the fracture stress increases and the fracture strain decreases. The reduction of fracture deformation under compression indicates an increase in the polymer brittleness in the presence of MWCNTs.

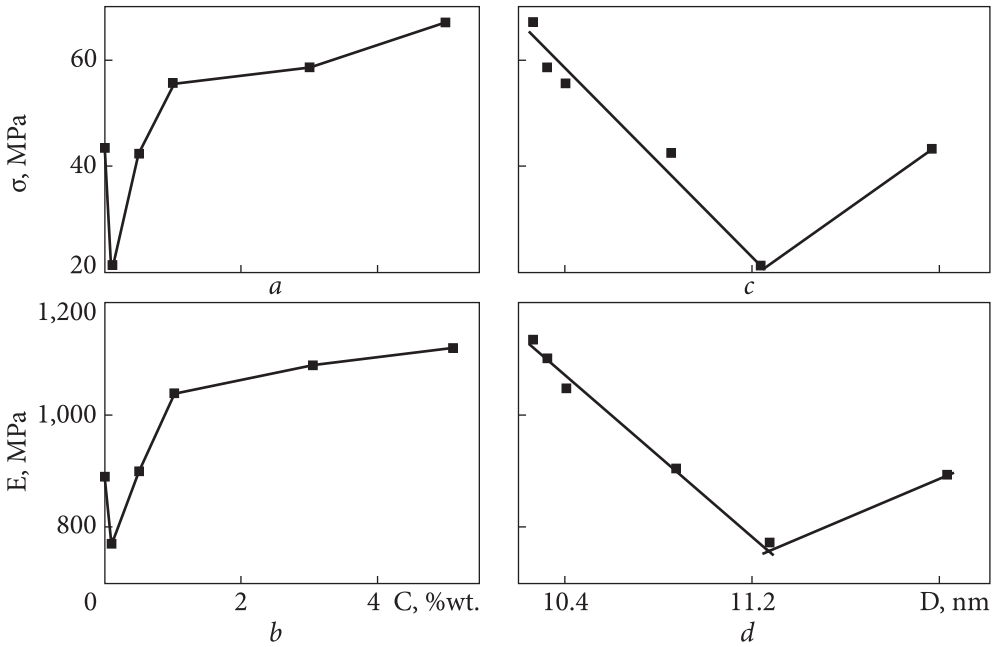

Fig. 5.48. Dependences of fracture stress under compression of PP-MWCNTs composites (a, c) and modulus of elasticity (*b*, *d*) on the CNTs content (*a*, *b*) and X-ray coherent scattering domain size (*c*, *d*)

Note, the dependences of strength characteristics on the nanotube content are not monotonous (Figs. 5.47—5.50, *a*, *b*). Theoretical analysis of various models, for example [81—83, 135, 136], shows that such a change in properties is due to the peculiarities of different phases formed at the nanofiller-polymer interface. The molecular dynamics modeling [82] demonstrates the formation of an ordered polymer matrix layer around CNTs, which, known as the interfacial, plays a central role in the overall mechanical response of the composite. In case of a bad load transfer from the matrix to CNTs, the effect of amplification related to CNTs is insignificant. Therefore, the presence of an interfacial surface is considered to be the only reason for the enhancement of composite characteristics. If this approach is correct, it is possible to determine experimentally a structural parameter of the system that would characterize the interfacial surface and show a monotonic change in the strength characteristics of the composite due to such a parameter.

For polymeric materials, a parameter that reflects the influence of CNTs on the structural hierarchy of the matrix can be, for example, the X-ray CSD size or the crystallinity degree [81—83]. The average crystallite size was calculated by Scherer's formula [137].

Figs. 5.47, *c*, *d* show the dependences of the conditional yield strength and elasticity modulus on the CSD size for the PE-MWCNTs systems. Figs. 5.48, *c*, *d*

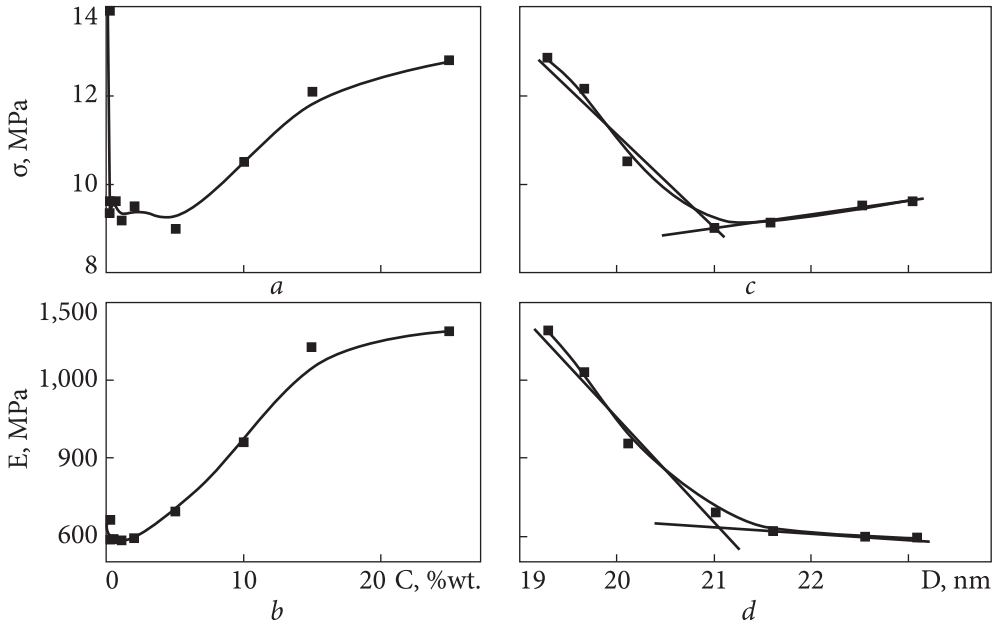

Fig. 5.49. Dependences of the conditional yield strength of PTFE-MWCNTs composites (*a*, *c*) and the modulus of elasticity (*b*, *d*) on the CNTs content (*a*, *b*) and the CSD size (*c*, *d*)

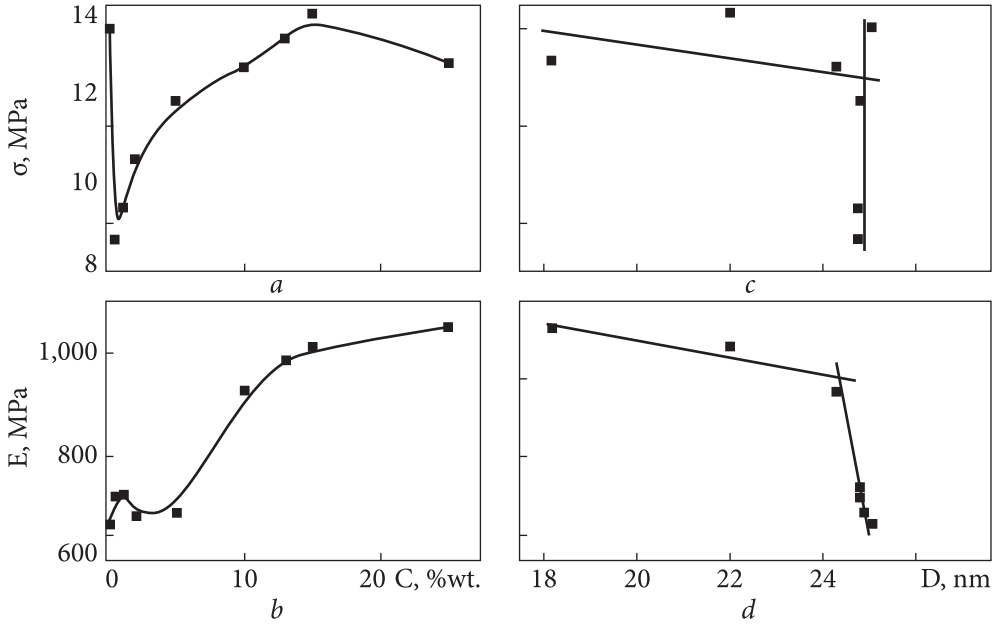

Fig. 5.50. Dependences of the conditional yield strength of PTFE-A300 composites (*a*, *c*) and the modulus of elasticity (*b*, *d*) on the CNTs content (*a*, *b*) and the CSD size (*c*, *d*)

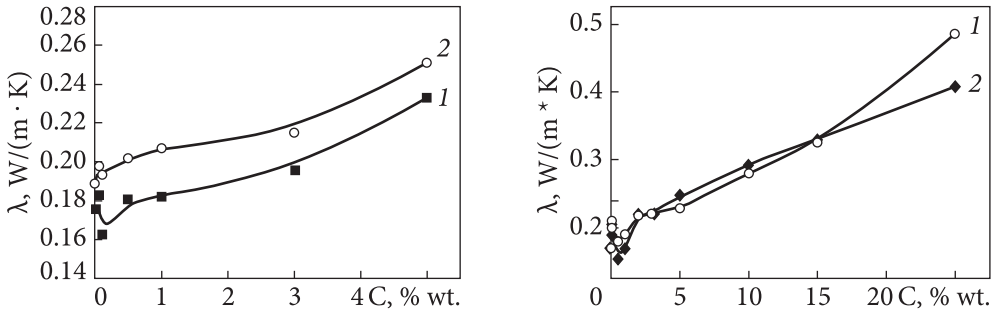

Fig. 5.51. Dependences of thermal conductivity of the PP-CNTs system on the CNTs content at: *1* — 60 °C, *2* — 120 °C

Fig. 5.52. Dependences of thermal conductivity of the F4-CNTs system on the CNTs content at 70 °C: *1* — not dispersed; *2* — dispersed CNTs

represent dependences of fracture stress under compression and modulus of elasticity on the X-ray CSD size for PP-MWCNTs systems. Figs. 5.49 and 5.50, *c*, *d* show the dependences of conditional yield strength and modulus of elasticity on the CSD size for the PTFE-MWCNTs and PTFE-A300 systems.

All of the above strength characteristics depending on the CSD size are linear and divided into two regions, the boundary between which is obviously the percolation threshold. For example, for the PE-MWCNTs system, the CSD size is D ~ 21 nm, which corresponds to a CNTs content of ~0.5% vol. and is in good agreement with the percolation threshold determined from the dependence of conductivity on the MWCNTs content. Similar results are observed for PP-MWCNTs, PTFE-MWCNTs, and PTFE-A300 systems, for which the CSD size is approximately 11.2, ~21, and ~24 nm, respectively.

The proposed approach is valid for small MWCNTs content. In the PTFE-MWCNTs system, a continuous grid is created at the content of MWCNTs ~ 3% wt. This area of small MWCNTs contents and large CSD sizes is characterized by a monotonic (almost linear) dependence of the strength characteristic on the size of the zones of structural inhomogeneity created by the filler.

The CSD size of the PP-MWCNTs system is almost half that of the PE-MWCNTs and PTFE-MWCNTs systems. In [138], the authors conducted a quantum-chemical study of the interaction energy of carbon nanotube fragments with polyethylene and polypropylene oligomers and optimized the most probable structures of their intermolecular complexes. The interaction energy of a carbon nanotube fragment with a polypropylene oligomer was found to be greater than that with polyethylene, which may explain the smaller CSD size for the PP-CNTs system. Since the polymer forms with the outer surface of carbon nanotube a micromolecular complex, which is not covalently bound and is held by intermolecular dispersion forces [138], that is, the polymer oligomers

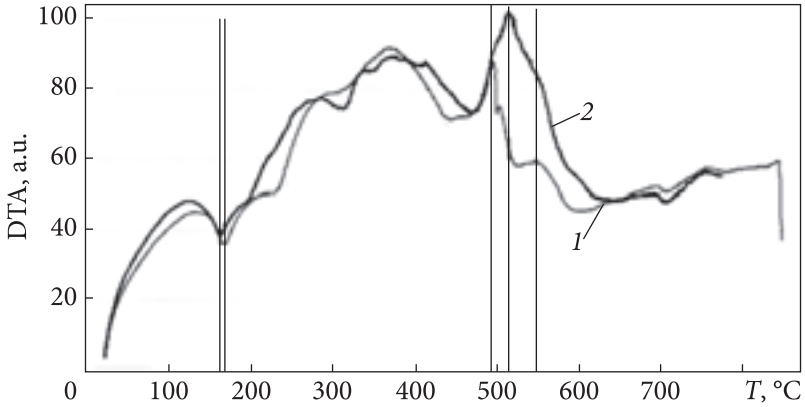

Fig. 5.53. DTA curves: *1* — initial PP, *2* — PP sample after processing in a planetary mill

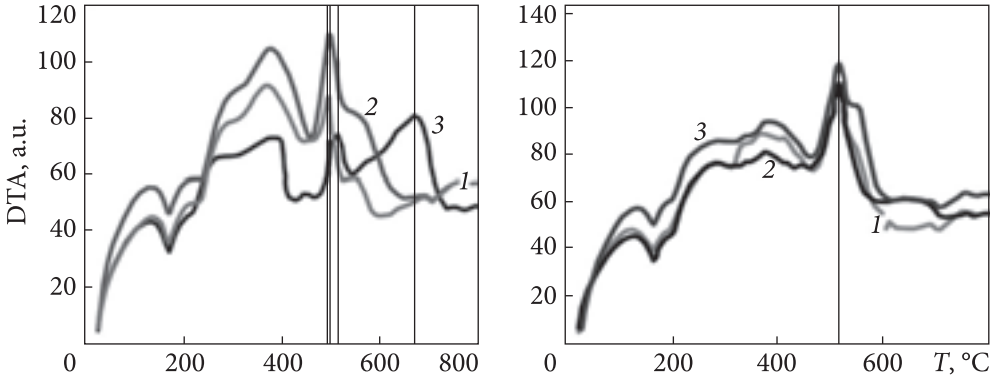

Fig. 5.54. DTA curves for the PP-CNTs system with CNTs content: *a* — *1* — 0%, *2* — 0.5%, *3* — 5.0%; *b* — processed in a ball mill, *1* — 0%, *2* — 0.2%, *3* — 1.0%

and nanotube surfaces in the formed nanocomposites are placed closer to each other than separated ones.

Figs. 5.51 and 5.52 demonstrate the thermophysical characteristics of PP-CNTs and F4-CNTs systems depending on the CNTs content [20, 25, 30, 37, 38], which also reflect the structural features of nanocomposite systems related to the structure-forming properties of CNTs. The thermal conductivity curves practically coincide in appearance with the content dependence curves of the crystallinity degree and mechanical characteristics.

Studies of the effect of machining of polymer powder on the thermodynamic properties of the PP matrix obtained by hot pressing have been performed as well. Fig. 5.53 shows the DTA diagrams of PP samples obtained by hot pressing of granules and after grinding of granules in a planetary mill.

It is known that the high-energy effect that occurs in a planetary mill causes significant changes in the structure during grinding, up to the formation of new phases, for example, in metal alloys.

As seen in Fig. 5.53, pre-dispersion in a planetary mill reduces the melting point of hot-pressed PP samples from 164 to 159 °C (the first endothermic peak). Oxidation of low-structured regions of the polymer (the first exothermic peak) becomes more energy-intensive, and its maximum is shifted to lower temperatures from 287 to 276 °C.

On the other hand, the exothermic peak of oxidation of the main crystalline phase (the second exothermic peak) is shifted towards higher temperatures and splits. The "burning" temperature of carbonized polymer residues (maximum at 511 ^{0}C) is also shifted towards higher values.

Figs. 5.54, *a*, *b* show the DTA curves for the above described PP systems after adding CNTs.

The dependences shown in Fig. 5.54, *a* demonstrate a qualitative agreement of the experimental data with the previously considered hypothesis. A low content of CNTs (0.5% wt.) leads to an increase in the content of the crystalline phase, and a high one (5% wt.) — to an increase in the disordered component in the composition. The melting point for all compositions remains virtually unchanged, and the oxidation temperature of low- and high-molecular fragments for the composite PP-0.5% wt. CNTs increases with increasing process energy (area under the DTA curve). In the PP-5% wt. CNTs system, the opposite process takes place. The higher the content of CNTs, the higher the temperature of the final thermal-oxidative destruction of carbonized polymer and CNTs residues as well as the energy of the process.

The presence of a significant component of low molecular weight fragments in samples processed in a planetary mill neutralizes the effect of CNTs. However, the tendency of the temperature of the final thermal-oxidative degradation to increase with increasing CNTs content persists.

Of particular interest are the results of DT analysis of PE-CNTs systems (Fig. 5.55). They show that the temperature of the endothermic melting peak of polymer nonlinearly depends on the CNTs content and may indicate a change in the PE crystallinity and thermal conductivity of the composite as a whole.

The second exothermic peak, which characterizes the removal of low molecular mass fractions from the polymer, shifts to the low-temperature region by almost 20 °C with increasing the CNTs content to 4%. That is, the addition of a significant amount of CNTs into the polymer can provoke an increase in low molecular mass fragments in the polymer after processing in a ball planetary mill.

The temperature of the next peak of thermo-oxidative destruction of the polymer increases with the content of CNTs 1% wt., but the total contribution of this process to the energy decreases. When the CNTs content increases to

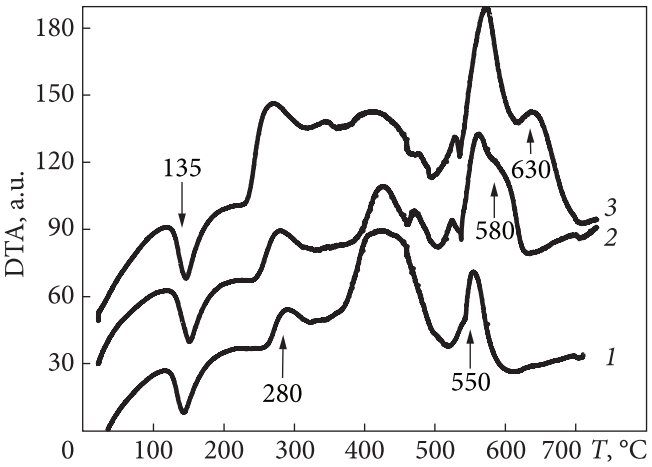

Fig. 5.55. DTA curves for the PE-CNTs system obtained after mixing PE powder with CNTs in a planetary ball mill and forming samples by hot pressing at a pressure of 5 MPa, with different content of CNTs: *1* — 0%, *2* — 1%, *3* — 4% [31]

4% wt., the conversion temperature decreases, and the energy contribution increases. With a further increase in temperature, endothermic peaks are observed at approximately the same temperature for all compositions. The DTA curves are completed by an exothermic peak, which increases and bifurcates into a high-temperature region with increasing CNTs content, which characterizes the temperature increase for the destruction of polymer residues and CNTs.

Systems polyamide-CNTs. In obtaining the polyamide-CNTs system, the following sequence of technological operations was used: dispersion of CNTs under the action of ultrasound in a liquid containing surfactants, resulting in a stable dispersion of CNTs; "soft" dispersion of granules or polymer powder and drying at 110—120 °C in a vacuum chamber; heating of the polymer-CNTs mixture to a viscous-fluid state and stirring the melt in a twin-screw mixer for 10—20 min at a given temperature. The resulting melt was unloaded and cooled in air.

The study used polyamides of the following brands PA6, PA 6.6, and PA 12.12 (manufactured in China).

Polyamide belongs to a new class of heat-resistant polymers, whose aromatic nature determines their high strength up to the decomposition temperature, chemical resistance, and refractoriness. Polyamide includes both synthetic and natural polymers containing the amide group —$CONH_2$ or —CO—NH— It is obvious that the polymer remelting, especially under conditions of stirring in an oxidizing medium (air), can lead to its destruction, gas saturation, etc. The effect of the polymer remelting on some of its characteristics is evident in Table 5.12.

As follows from Table 5.12, re-melting of polymers under study in an oxidizing medium (air) at the appropriate temperature in a twin-screw mixer for 10—20 min leads to a decrease in the density of hot-pressed samples and the limit of their tensile strength. For PA6 (Table 5.12, line 1), the density decreases

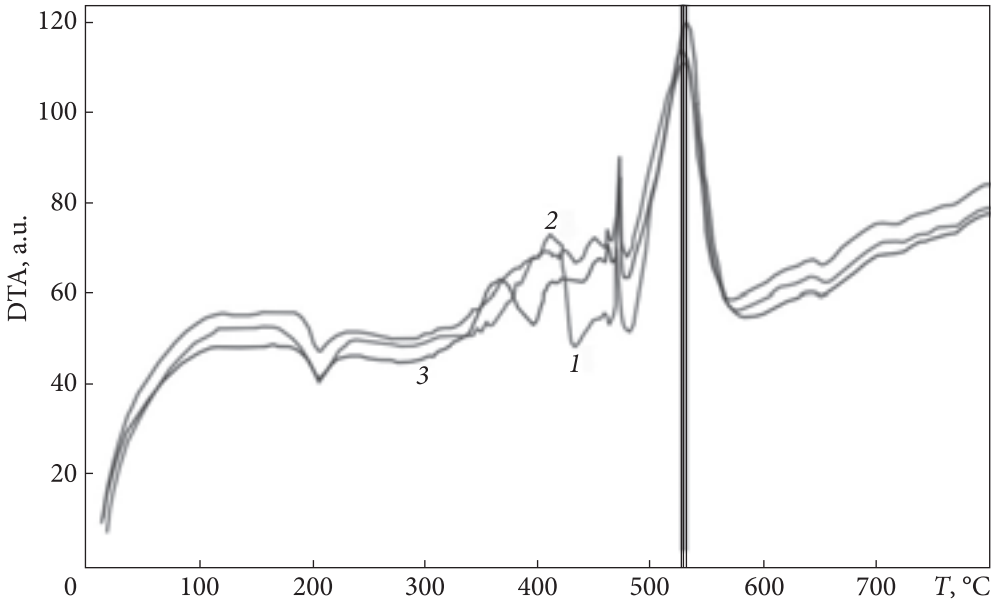

Fig. 5.56. DTA curves of samples of polyamide brand PA6: *1* — initial; *2* — re-melting at 250 °C for 10 min; *3* — mixing of the melt with CNTs (0.5% wt.) at 250 °C for 10 min

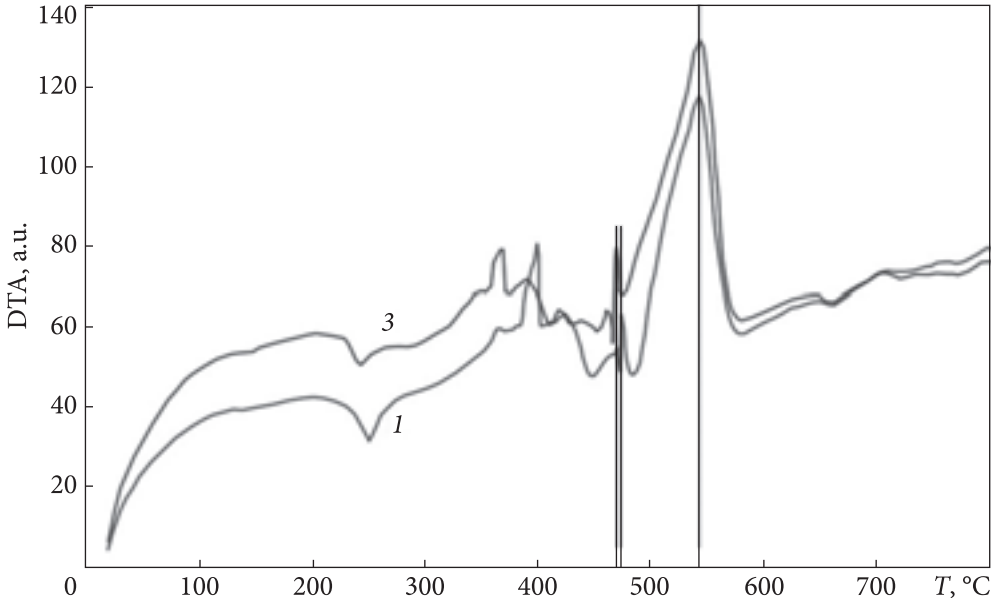

Fig. 5.57. DTA curves of samples of polyamide brand PA6.6: *1* — initial; *3* — mixing of the melt with CNTs (0.25% wt.) at 270 °C for 10 min

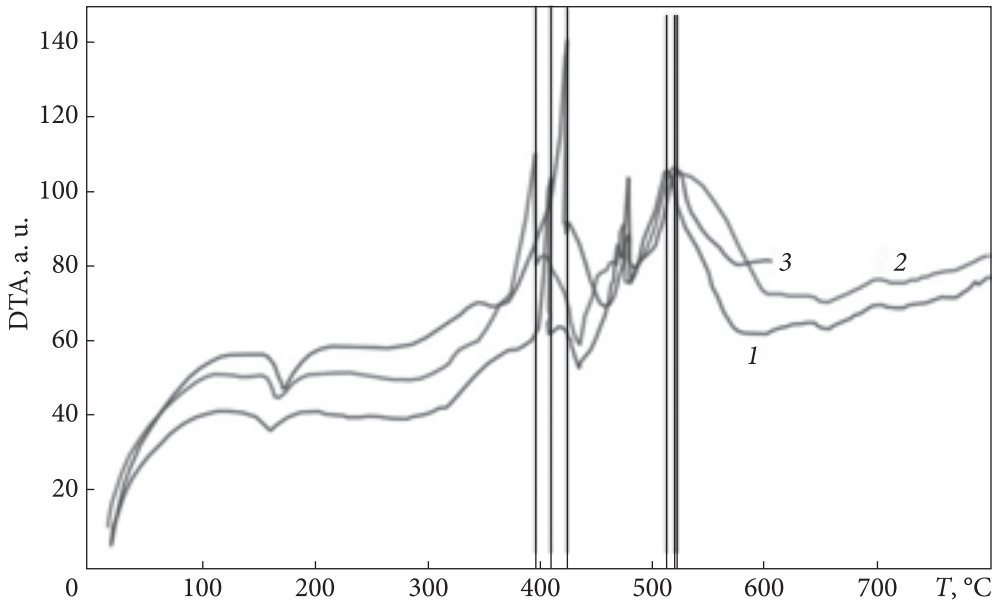

Fig. 5.58. DTA curves of samples of polyamide brand PA12.12: *1* — initial; *2* — re-melting at 250 °C for 10 min; *3* — mixing of melt with CNTs (0.25% wt.) at 250 °C for 10 min

Table 5.12. **Characteristics of samples of polymers hot-pressed from the original polymer and after remelting in two-screw mixers**

Sample	Melting point, °C	Density, g/cm^3		Tensile strength, MPa	
		Initial	Melted	Initial	Melted
PA6	250	1.187	1.107	75.1 ± 7.1	25.0 ± 1.2
PA2.12	220	1.319	0.950	41.3 ± 0.4	28.4 ± 1.8

by 6—7% and the strength limit by three times. The density of PA12.12 polyamide decreases by almost 28%, and the tensile strength by more than 31%. DTA diagrams for polymers, their remelting, and composites with CNTs are presented in Figs. 5.56—5.58 [81].

As seen, for all systems, remelting in an oxidizing environment leads to an increase in the content of low-molecular-mass regions of the polymer, which is manifested in the decrease in the temperature of maximal oxidation and increase in the energy of this process. At the same time, the maximum oxidation temperature of the high-molecular-mass (crystalline) regions of the polymeric material decreases and the adding CNTs systems does not fully compensate for these effects, although this brings the composite characteristics closer to the initial polymer state.

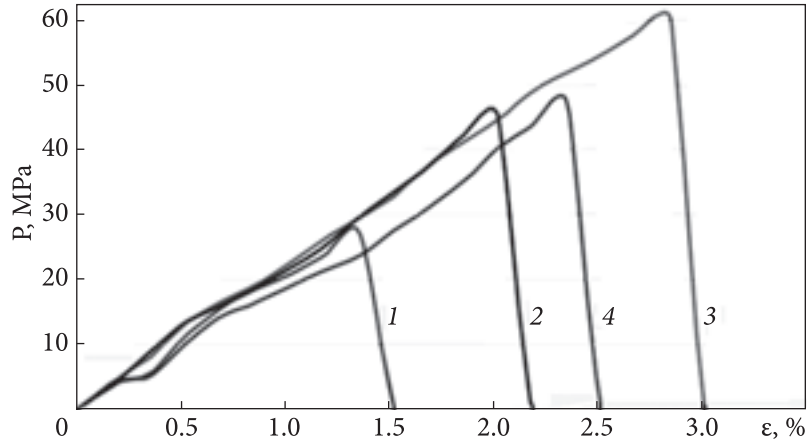

Fig. 5.59. Load diagrams in the coordinates "stress–strain" for PA6 samples with different mass content of CNTs: *1* — 0%; *2* — 0.125%; *3* — 0.25%; *4* — 0.5% [81]

Table 5.13. **Tensile strength characteristics of the PA6-CNTs system depending on the CNTs content (all samples were subjected to the same thermo-mechanical treatment)**

Properties	Content of CNTs,% wt.			
	0	0.125	0.25	0.50
Tensile strength (σ_b), MPa	25.0 ± 1.2	31.2 ± 11.2	41.2 ± 1.0	37.5 ± 0.4
Tensile fracture,%	1.5	2.0	3.0	2.5
Modulus of elasticity, MPa	1700	2200	1900	1700

It is obvious that such a strong effect of thermo-mechanical treatment on the characteristics of the polymer composite is due primarily to the oxidizing medium where the mixing process takes place. Even above 100—120 °C, a noticeable oxidation occurs with formation of double carbon bonds, i.e. the destruction of the polymer. Therefore, comparative tests of polymer samples and compositions filled with CNTs were performed after the same thermo-mechanical treatment.

Table. 5.13 presents the mechanical characteristics of the PA6-CNTs system for the PA6 sample treated in a twin-screw mixer at 250 °C for 20 min, as well as of samples of PA6-CNTs compositions with contents of 0.125, 0.25 and 0.50% wt. CNTs. As seen, the strength characteristics of the PA6-CNTs system change non-monotonically with the addition of CNTs into the polymer matrix. The maximum tensile strength and maximum fracture deformation are revealed for a composite with a CNTs content of 0.25% wt., which also exhibits the highest energy of fracture deformation (area under the deformation curve in Fig. 5.59, curve *3*).

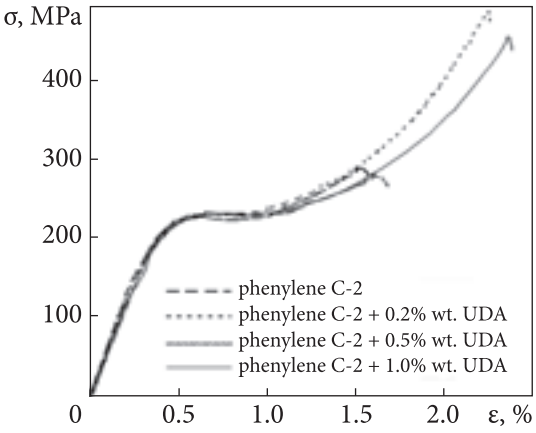

Fig. 5.60. Compression curves for phenylene C-2 and nanocomposites based on it and filled with nanodiamonds

As a rule, for elastic-plastic systems, the increase in the tensile strength is accompanied by a decrease in the fracture deformation, that is, the destruction energy changes little. As for the PA6-0.25% wt. CNTs, the destruction energy (Fig. 5.59) increases by near 3 times as compared with the original polymer. The modulus of elasticity, at the same time, is maximal for the system PA6-0.125% wt. CNT [81].

For comparison, Fig. 5.60 shows the deformation curves during compression of samples of aromatic polyamide phenylene C-2 (TU U 6-05-226-72), which is a linear heterochain copolymer containing in the main chain of the macromolecule amide group —HNCO—, connected on both sides by phenyl fragments filled with ultrafine diamonds (UDA). The stress-strain curves (Fig. 5.60) for samples of phenylene C-2 and composites based on it are characteristic of polymeric materials and belong to the V-type curves. Such curves are characterized by a rectilinear section to the voltage, which corresponds to the limit of proportionality; the area where there is some deviation from Hooke's law is associated with the manifestation of segmental mobility of macromolecules and the yield strength, after which plastic deformation develops followed by stages of deformation hardening and destruction [20].

The stress-strain curves for our PA6-CNTs system look similar. However, the areas of plastic deformation of the polymer, which corresponds to the restructuring of the structure ("pulling balls"), are followed by strengthening (Fig. 5.59).

Table 5.14. **Characteristics of tensile strength of the system, consisting of three layers of fiberglass and two layers of polymer: fiberglass-PA6 and fiberglass-PA6-0.25% wt. CNTs**

Sample	Tensile strength characteristics		
	Strength limit (σ_b), MPa	Fracture deformation, %	Elasticity modulus, MPa
Fiberglass-PA6	209 ± 6	17 ± 3	1230
Fiberglass-PA6-0.25% wt. CNTs	391 ± 2	12 ± 1	3255

Thus, the most significant result of the research is determination of the degree of influence of small additives of CNTs to the polymer on the complex of its mechanical characteristics. The addition of up to 0.5% wt. CNTs into the PA6 matrix nonlinearly increases the composite strength characteristics compared to the original ones for the same thermomechanical treatment conditions. The maximum tensile strength is exhibited by the PA6-0.25% wt. CNTs composite.

The obtained results and materials were used to create a fiberglass composite consisting of three layers of oriented fiberglass and two layers of PA6 and PA6-0.25% wt. CNTs (Table 5.14).

Thus, adding 0.25% wt. CNTs to PA6, which is used as a binder in fiberglass, increases the tensile strength by almost twice.

Conclusions. It is experimentally shown that adding a small content of nanofillers (MWCNTs and pyrogenic silica) into the polymer matrix (PE, PP, PTFE) significantly changes the structural characteristics of composites, namely the crystallinity degree and the CSD size.

The dependence of the electrical conductivity of CNT-filled polymers on their content is percolation. At a critical content, the phase transition of the second kind, namely the dielectric-conductor transition, occurs. Critical indices showing the three-dimensionality of these systems are calculated for the systems studied. The critical content, at which a continuous volumetric current grid is formed, depends on the degree of homogeneity of MWCNTs distribution in the matrix and can thus be a parameter that characterizes it.

The strength characteristics of the studied composites are non-monotonically dependent on the filler content but linearly dependent on the CSD size. These dependences have two sections, the inflection point for which corresponds to the critical content for the percolation transition. This confirms the theoretical calculations of various approximations that quantitatively the response of the matrix is proportional to the surface area of the interface.

5.3.3. Linear polymers with graphene

Two systems filled with graphene nanoparticles (GNPs) have been investigated: amorphous polymer polychlorotrifluoroethylene (PCTFE) F-3M brand A and Polyamide 12/12 (PA12/12). Samples of PCTFE-GNPs and PA12/12-GNPs were prepared as follows. Polymer powder was moistened with ethyl alcohol and added with a stable aqueous solution of graphene, then mixed by hand with the addition of distilled water to reach a homogeneous consistency. The mixture was dispersed with an ultrasonic dispersant (USDN-A) for 2 min. The resulting homogeneous mixture was dried to constant mass, ground, and pressed: the system PCTFE-GNPs at a temperature of 513 K and a pressure of 2 MPa, and the system PA12/12-GNPs dried at 350 K and pressed at 450 K and 5MPa.

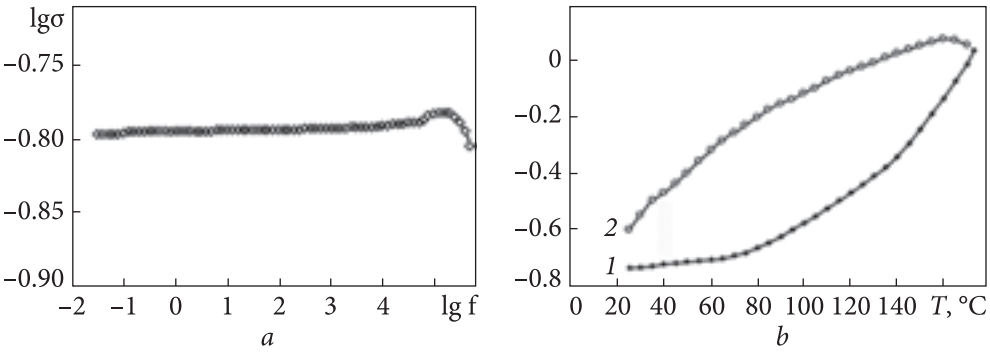

Fig. 5.61. Dependence of the real component of conductivity of the film agglomerate GNPs: *a* — on the frequency; *b* — on the temperature: *1* — heating, *2* — cooling

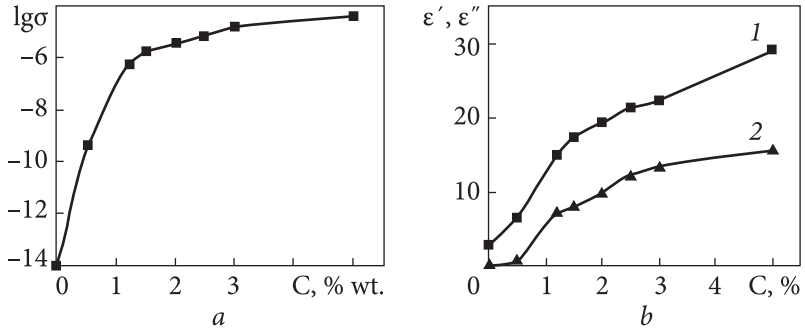

Fig. 5.62. Dependences of the conductivity of PCTFE-GNPs samples at a frequency of 0.1 kHz (*a*) and the real ε′ (*1*) and the imaginary ε″ (*2*) components of the complex dielectric constant (*b*) at a frequency of 9 GHz on the GNPs content

Thermogravimetric measurements, namely the weight loss (TG) and differential thermal (DTA), were carried out using a "Derivatograph Q-1500 D (Hungary) in a static air atmosphere. A 100 mg sample was heated from room temperature to 1273 K at the 10 K/min heating rate in a ceramic crucible.

The dependence of complex electric conductivity of the composites on the frequency was determined by means of calculations of the impedance spectra within the frequency range of 10^{-2}—10^{6} Hz provided by a Solartron SI 1260 impedance spectrometer. Conductivity at low frequencies (0.1, 1, and 10 kHz) was recorded by a double-contact method using an immittance measurer E7-14. To measure the real (ε') and imaginary (ε") parts of complex dielectric permittivity of the composites in the ultrahigh frequency (UHF) range of 8—12 GHz, an interferometer with a phase difference RFK2-18 measurer and an R2-60 measurer of standing wave ratio and deamplification with the electrodeless technique were used [139].

The graphene nanoparticle films formed during drying of the dispersion on the substrate are quite inhomogeneous but show the thermal conductivity

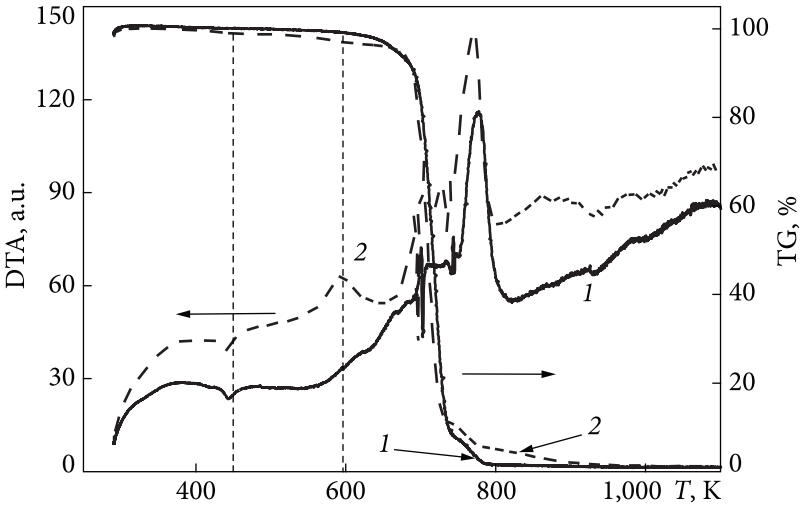

Fig. 5.63. Dependences of TG and DTA samples of PA 12.12 (*1*) and PA 12.12-GNPs systems, with GNPs content of 0.03 volume fraction (*2*), on temperature

at the level of EG-CNTs composites. Both dispersions and solid films exhibit photoluminescent properties (see Chapter 6).

The study of the electrical conductivity of the dispersed GNPs system showed (Fig. 5.61) that it increases linearly with frequency (Fig. 5.61, *a*) in the range of 10^2—10^5 Hz. This indicates the invariance of the level of electronic conductivity with frequency, as well as the absence of manifestation of the ionic component of conductivity [140].

The electrical conductivity also increases with increasing temperature, which may indicate its activation nature (Fig. 5.61, *b*), and its increase after heating may be associated with a decrease in contact resistance between particles, i.e. with a change in the surface chemical state.

Fig. 5.62 shows the content dependences of electrical conductivity at low frequencies and ε' and ε'' at 9 GHz for the PCTFE-GNPs system.

Even with small amounts of GNPs, ε' and ε'' increase rapidly. The analysis of the results shown in Fig. 5.62, *a* from the standpoint of the percolation theory according to the equation:

$$\sigma = \sigma_i(\phi - \phi_c)^t, \tag{5.7}$$

where σ_i is the electrical conductivity of the filler, ϕ is its volume content, ϕ_c is the filler content corresponding to the percolation threshold, t is the critical index allowed for the determination of the threshold and critical indices of the system: $\varphi_c = 0.0045$, $t = 2.48$, $\sigma_i = 0.17\ \Omega^{-1} \cdot cm^{-1}$.

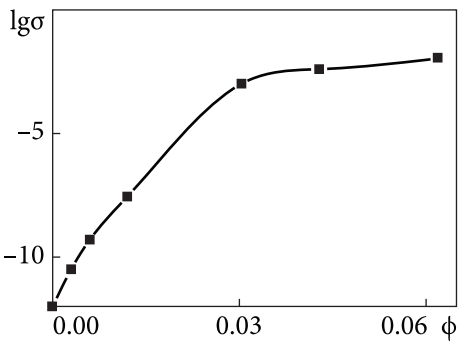

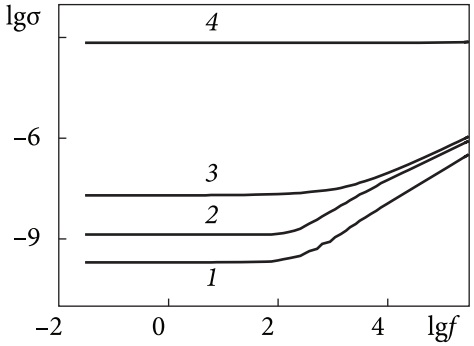

Fig. 5.64. Dependence of the conductivity logarithm for the PA 12.12-GNPs system on the GNPs volume content (φ) at a frequency of 1 kHz

Fig. 5.65. Dependence of the conductivity logarithm of composites for the PA-12.12–GNPs system on the frequency logarithm: *1* — 0.003, *2* — 0.006, *3* — 0.012, *4* — 0.03

The increase in the electrical conductivity of PCTFE samples (Fig. 5.62, *a*) occurs not monotonically: a sharper change in the σ values was observed in a narrow range of contents (C) of graphene (0 < C < 1%), which indicates the implementation of the percolation transition. When the graphene content is <0.5%, the leading particles are combined into local clusters; with increasing content, the average size of the clusters increases; within 0.5 < C < 1%, a significant part of the isolated clusters passes into an infinite (branched) cluster, which penetrates the polymer composite in all directions; there is formed the so-called conduction channel, which leads to an increase in σ by several orders of magnitude. A further increase in the GNPs content (φ > 1%), leads to an increase in the infinite cluster volume, which is reflected in the monotonic nature of the increase in conductivity in this range of contents. This is due to the fact that the contribution of additional channels into nanoparticle clusters to the conductivity is significantly less than the total conductivity of the channels formed during the formation of the percolation cluster at the flow threshold. The increase in the number of dipoles formed from GNP's clusters and their further growth in size and number leads to the formation of a bulk grid, which causes more effective interaction with electromagnetic radiation of this frequency (Fig. 5.62, *b*) and a gradual increase of dielectric constant.

Thermodynamic characteristics for composites on the basis of polyamide 12.12 with a GNPs content up to 0.06 volume fraction were observed. DTA curves in a specific polymer and a composite with a volume of 0.03 vol. parts of GNPs, may be similar in shape (Fig. 5.63).

The peak corresponding to the polymer melting at 450 K is shifted by 5 degrees to lower temperatures for the sample containing a 0.03 volume fraction of

GNPs. The peak at 598 K is more intense for the sample PA 12.12-(0.03 volume fraction) GNPs, which can be associated with the polymer destruction with increasing content of GNPs.

The dependence of the electrical conductivity of the system on the volume content (ϕ) of GNPs is nonlinear (Fig. 5.64).

The electrical conductivity at low frequencies increases sharply by 9 orders of magnitude in the region of change in the GNPs volume content within $0 < \phi < 0{,}03$, which indicates the realization of the flow threshold. The electrical conductivity increases yet at a volume content of 0.006. And in the interval of $0.006 < \varphi < 0.03$ a continuous grid with GNPs is formed, i.e. there is formed a conduction channel. The analysis of the experimental results has made it possible to determine the parameters of percolation equation (5.7) for the PA 12.12-GNPs system, namely the percolation threshold $\varphi_c = 0.011$, the critical index $t = 2.38$, and the effective electrical conductivity of the GNPs array $\sigma_i = 1.36 \cdot 10^1\ \Omega^{-1}\ cm^{-1}$.

The values of ε' and ε'' at a frequency of 9 GHz increase with increasing GNPs content in the studied content range and reach the values of $\varepsilon' = 29.8$ and $\varepsilon'' = 26$ at $\phi = 0.06$. An increase in the number of dipoles formed from GNPs clusters and their further growth in size and number leads to the formation of a bulk grid, which leads to more efficient interaction with electromagnetic radiation at a given frequency and to a gradual increase in dielectric constant.

Fig. 5.65 presents the logarithmic dependence of the real component of the electrical conductivity of the PA 12.12-GNPs system composites on the frequency.

The dependence for pure GNPs is linear and is absent in the frequency range (10^{-2}—10^2) Hz, which indicates a high level of electronic conductivity and thus a relatively low level of ionic conductivity. Areas of smooth growth of conductivity with frequency increasing from 100 Hz are observed for samples with an GNPs content up to 0.012, which occurs due to the jumping mechanism of electrical conductivity and is satisfactorily described by the equation:

$$\sigma = \sigma_0 \cdot \left(1 + \left(\frac{f}{f_0}\right)^{0.8}\right), \tag{5.8}$$

where σ_0 is the initial electrical conductivity; f_0 is the frequency at which the angle of inclination of the electrical conductivity changes with the frequency.

The percolation threshold for the PA 12.12-GNPs system is twice lower compared to the similar system of PCTFE – GNPs. The conductivity of the PA 12.12-GNPs system after the percolation threshold is also five orders of magnitude higher than that for the PCTFE system [141], which may be related to the dielectric and adhesive properties of polymers.

5.4. Modification of rubber filled with carbon black and carbon nanotubes

One of the most common materials used in everyday life and industry is rubber, which has a history of more than 180 years. Rubber compositions are multicomponent systems based on rubbers (the product can contain up to 12—18 components). They include targeted additives for various purposes such as stabilizers, activators, antioxidants, modifiers, etc. and fillers such as white soot, clay, carbon black, bamboo fibers, and more. Recently, the possibility of using nanosized fillers, such as nanoclay, pyrogenic silica, carbon nanotubes, graphene nanoplates, their combinations, and combinations with macro fillers (hybrid fillers) has been considered in many works [142—157]. References [142—145) indicate that the effect of CNTs on the mechanical properties of natural rubber (NR)-based compounds will be more pronounced if functionalized CNTs are used. However, the obtained level of enhancement properties is different and depends on the type and number of CNTs used, as well as on the method used for the manufacture of nanocomposites. In Ref. [146], the effect of carbon fillers of various structures, such as carbon black (spherical), carbon nanofibers (CNF) (fibrous), CNTs (tubular), and hydroxylated CNTs on the efficiency of acrylonitrile-butadiene rubber composites (NBR) was studied. Studies prove a significant influence of the filler structure, surface characteristics, and the interaction of filler particles with each other on the characteristics of the reinforced composition. This study determined the curing behavior, crosslinking density, thermal stability, electrical conductivity, and mechanical properties of the filled NBR compounds. It turned out that the greatest strengthening effect was created by CNTs. However, all tested carbon fillers significantly affected the characteristics of the compositions with NBR, which makes them attractive additives for elastomeric composites. Studies of the effect of hybrid fillers on the properties of compositions based on both natural and synthetic rubbers have been performed in [147—157]. Review [147] focused on recent studies on elastomers containing carbon nanomaterials such as CNTs, CNFs, graphene nanoparticles, expanded graphite, and graphene oxide, as well as hybrid fillers containing multiwall carbon nanotubes (MWCNT) (or CNF)-montmorillonite clay MWCNT-hectorite, MWCNT (or CNFs)-layered double hydroxide (LDH), and MWCNT-graphene in various rubber matrices. Methods for mixing in liquid and melt are most widely used for the preparation of polymer nanocomposites, although [148] proposed sonication in latex to obtain a hybrid soot-CNT filler. It was concluded that the addition of such fillers in the matrix from NR, styrene-butadiene rubber (SBR), NBR, and silicone rubber (SR) leads to a significant improvement in tensile strength, impact strength, elongation at break, Young's modulus, stability modulus, a storage

module and the like. Hybrid carbon black or CNTs fillers with inorganic compounds in various rubbers and their compositions were investigated in [149, 150]. Thomas S. et al. [149] investigated the influence of MWCNT and nanoclay on the mechanical, electrical, and transport properties of mixtures of NBR, NR, and their composite NBR/NR. The authors note a kind of synergism, which provides a finer dispersion of CNTs and clay in the rubber matrix and a certain orientation of CNTs. The improved interaction of the matrix and the hybrid filler caused an increase in the crosslinking density and mechanical properties such as tensile strength, modulus of elasticity, and also improved electrical and thermal properties. The main purpose of [150] was to investigate the synergistic effect of the simultaneous use of two reinforcing fillers in rubber compounds based on NBR containing pyrogenic silica of 25 phr and a multiwall CNTs of 3 and 5 phr. The study of the effect of hybrid CNTs/SiO_2 filler on the mechanical and vulcanization characteristics of rubber compounds showed that its addition reduced the optimal curing time, firing time, and increased mechanical characteristics. Chuayjuljit S. et al. [151] investigated the influence of particle size and amount of two fillers, carbon black and calcium carbonate, for the curing characteristics and dynamic mechanical properties. The study of the synergistic effect of hybrid fillers on the characteristics of rubber compositions was carried out in [152—157]. In [152, 153], carbon black was partially replaced by a hybrid filler of graphene oxide (GO) and CNTs. NR composites filled with GO CNTs/CB exhibited excellent resistance to crack growth, low heat accumulation, and high mechanical properties compared to CB/NR composites. Mechanical tests showed significant synergistic enhancement between GO/CNTs and CB in NR composites. The improved dispersion of hybrid fillers GO/CNTs and CB in the NR matrix was characterized by transmission electron microscopy (TEM).

This brief review does not claim to be generalized. Its purpose is to emphasize an intensive search for optimal methods of reinforcing rubber compositions with nanoscale fillers and their hybrid compositions with traditional ones. The use of nanofillers leads to a significant improvement of the properties of the polymer matrix with their ultra-low content compared to conventional fillers. The maximum realization of the properties inherent in nanosized fillers is possible when used together with carbon black in a combined filler.

As a rule, improvement of rubber compositions, developed and optimized over many years, is carried out by the method of search for options, which requires much effort and time. Therefore, it is obviously interesting to consider the possibility of predicting the composition and content of hybrid fillers depending on their, above all, structural characteristics for known, optimized rubber compositions. Thus, the purpose of this work was to determine the possibility of predicting an optimal content of the hybrid filler carbon black (soot) — CNTs in rubber compositions with optimized formulation by soot content.

From this point of view, it is reasonable to compare the results of [155, 156], which considered the improvement of mechanical properties for systems based on natural rubber, almost the same composition, except that in [155] used carbon black N220, and in [156] — brand N320. In both cases, carbon black was partially replaced with the same amount of CNTs with approximately the same structural characteristics, so that the filler proportion remained constant. For the system with filler N220, the maximum increase in tensile strength by ~14% was obtained for the composition: mass ratio, including rubber to carbon black and CNTs, was 100 : 29 : 1. And for the system with N320, the maximum increase in strength was ~7% at the appropriate ratio of rubber and fillers of 100 : 29.5 : 0.5. This result suggests that the characteristics of fillers, in this case carbon black, affect the efficiency of reinforcement.

A systems approach based on a holistic view of a complex object, phenomenon, or process, known as "Systems Theory", when applied to composite materials has acquired the name of the polystructural theory, for example, in [158, 159]. It is a set of methods and tools to study the properties, structure, and functions of objects in general, presenting them as a system with all complex interelement relations, the action of elements on the system and the environment, and the impact of the system on its structural elements. That is, the essence of this approach is to distinguish in a single structure many interdependent structures from the atomic level (nanosized) to coarse constituent structures (macrosized), which "germinate" into each other ("structure in structure" or "composite in composite").

In the rubber industry, classification of fillers by particle size is often introduced, which in the simplest case can be determined as follows [160]. “Diluent” fillers have particle sizes in the range of 10÷1 μm, semi-reinforcing ones — in the range of 1000÷100 nm, reinforcing ones — in the range of 100÷35 nm, and finally, super-reinforcing ones — in the range of 35÷10 nm. “Diluent” and semi-reinforcing fillers are formed by the particle-cluster mechanism (by attaching carbon or silicon atoms to the growing particle while reinforcing and super-reinforcing fillers are formed by the cluster-cluster mechanism (combining small particles into larger ones).

Thus, we have proceeded from the fact that we have a well-developed rubber composition optimized for all components, including the content of filler — carbon black. The task is to determine the amount of nanosized filler, namely CNTs, which are to be introduced to improve the mechanical properties of rubber, and the method of their addition: to carbon black, its replacement, or partial replacement.

Consider the interacting system: rubber, carbon black, and carbon nanotubes. To create a dense material, the rubber must wet the entire system, creating a layer of a certain thickness on the filler surface. That is:

$$\frac{V_{rub}}{S_{cb} \times m_{cb} + S_{CNT} \times m_{CNT}} \geq h_{min}. \tag{5.9}$$

where V_{rub} is the volume of rubber; S_{cb} is the specific surface area of carbon black; m_{cb} is the carbon black content in parts per hundred rubber; S_{CNT} is the specific surface of CNT; m_{CNT} is the CNT content in parts per hundred rubber; h_{min} is the minimum thickness of the rubber layer, which provides complete wetting of the fillers.

Assume that h_{min} is twice the diameter of the CNTs (d_{CNT}), i.e.

$$\frac{V_{rub}}{S_{cb} \times m_{cb} + S_{CNT} \times m_{CNT}} = 2d_{CNT}. \tag{5.10}$$

On the other hand, subject to before the addition of CNTs, it becomes necessary to adjust the proportion of carbon black depending on the ratio of their specific surface areas, and the following is acceptable:

$$m_{cb} = m_{cb}^0 - \frac{S_{cb}}{S_{CNT}} \times m_{CNT}, \tag{5.11}$$

where m_{cb}^0 is the carbon black content in parts per hundred parts of rubber in the optimized original composition of the rubber.

Then the total amount of filler will be:

$$m_{cb+CNT} = m_{cb}^0 - \frac{S_{cb}}{S_{CNT}} \times m_{CNT} + m_{CNT}. \tag{5.12}$$

Hence, when the specific surface area of carbon black is much smaller than that of CNTs, the tubes are simply added to the composition. When their SSA values are close, CNTs replace carbon black. In this case, we hope that due to the large shape factor (ratio of length to diameter) ~10^3, CNTs are more effective reinforcing fillers.

After simple transformations we obtain the definition content of CNTs and the total content of the fillers:

$$m_{CNT} = \frac{\frac{m_{rub}}{2\rho_{rub} \cdot d_{CNT} \cdot S_{CNT}} - m_{cb}^0 \cdot \frac{S_{cb}}{S_{CNT}}}{1 - \left(\frac{S_{cb}}{S_{CNT}}\right)^2}, \tag{5.13}$$

where m_{rub} and ρ_{rub} are the mass and density of rubber.

Having calculated the mass fraction of CNTs by equation (5.13), we can determine the mass fraction of carbon black by equation (5.11). Next, we will try to test our hypotheses on known experimentally tested systems.

Two systems based on the natural rubber (NR) type SMR 20 CV/BP1 and a copolymer of acrylonitrile with butadiene NBR 3365 were experimentally investigated. We used multiwall carbon nanotubes according to TU U 24.1-03291669-009:2009 (ISC NAS of Ukraine).

In the composition based on NR, which had been previously studied [155], the carbon black type N220 was used as a filler, which was gradually replaced by CNTs. In the 100 phr of rubber, we injected: 30 phr of carbon black — 0.0 phr of CNTs, 29.5 phr of carbon black — 0.5 phr of CNTs, then 29.0—1.0, 27.0—3.0, 25.0—5.0 phr. Sulfur was used as a hardener, while zinc oxide (ZnO) and stearic acid were used as activators. CBS (N-cyclohexyl 2-benzothiazole-sulfenamide) was used as a curing accelerator. The complete composition of the compounds is listed in Table 5.15.

Table 5.15. **Recipe of a rubber composition based on natural rubber [155]**

Composition	NR	CNT	Carbon clack	CBS	Sulphur	ZnO	Stearic acid
	Content in phr [a]						
NR (CNT_x + CB_{30-x})	100	x [b]	30-x	2.5	1.7	3	1

[a] phr, the compound ingredients are given in mass parts 1: 100 of the rubber polymer;
[b] x = 0.0, 0.5, 1.0, 3.0, 5.0

Table 5.16. **Recipe of rubber composition based on NBR 3365 [161]**

Tradename	Phr	Chemical name	Note
NANTEX NBR 3365	100.0	NBR: acrylonitrile butadiene copolymer	Ingredient 1#
ZnO	5.0	Zinc oxide	Weighing together, Ingredient 2#
Stearic acid 1801	1.5	Stearic acid	
Antioxidant IPPD	2.0	N-Isopropyl-N'-phenyl-phenylene diamine	
Releasing agent 935P	1.0	Blend of metal soap-based compounds and surface active substance	
FEF N550	80.0	Carbon black N550	Weighing together, Ingredient 3#
DOP	10.0	Dibutyl phthalate	
Sulphur powder	0.5	Sulphur 98.5% mini	Ingredient 4#
CBS	1.5	N-cyclohesyl-2-benzothiazyl sulphonamide	Weighing together, Ingredient 5#
TMTD	2.0	Tetramethyl thiuram disulphide	

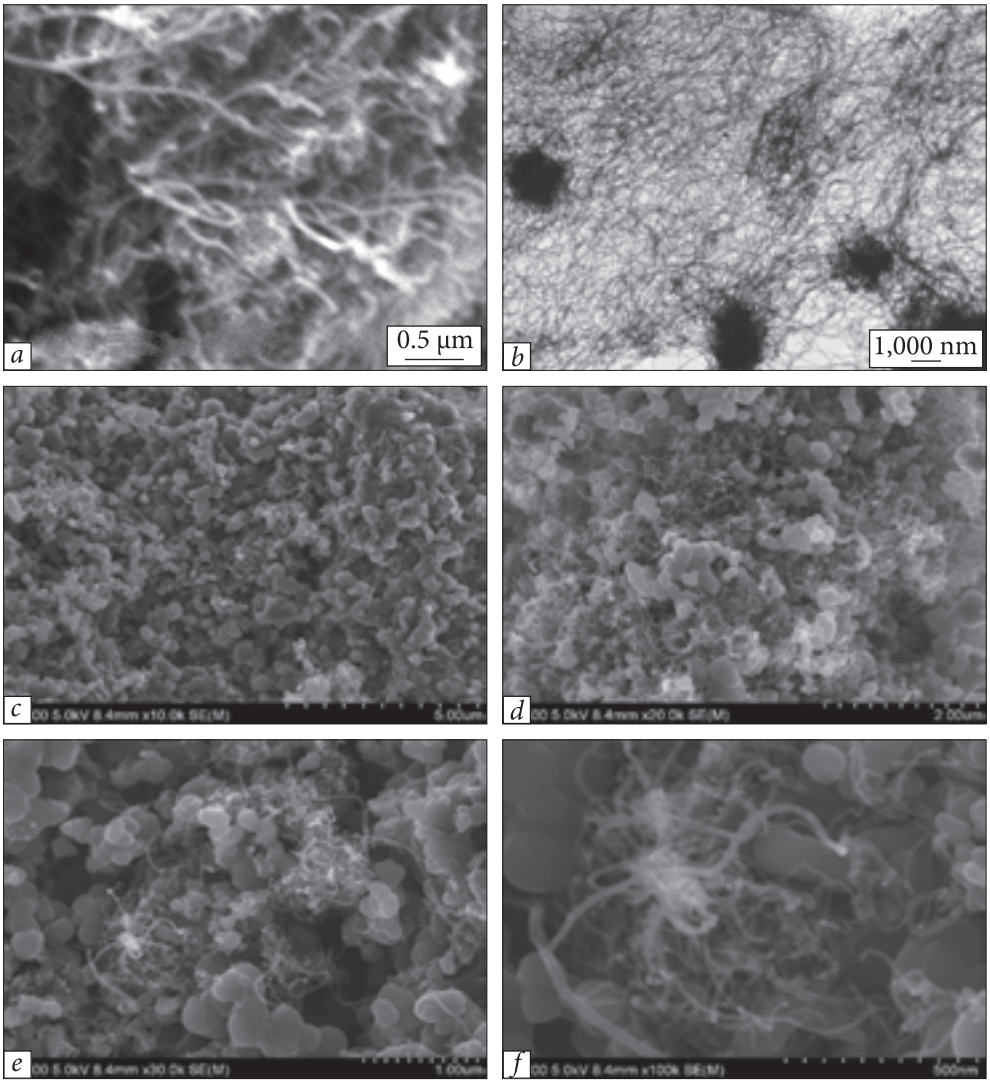

Fig. 5.66. Agglomerates of multi-walled carbon nanotubes (TU U 24.1-03291669-009:2009 (ISC NAS of Ukraine) — (*a*, *b*); CEM images of the composition carbon black — carbon nanotubes after joint deagglomeration in a rotary hydrodynamic disperser in ethanol (*c*—*f*)

NR-based rubber compounds containing CB and hybrid CB + MWCNT were mixed in a Brabender plastograph at 60 °C, 60 rpm, and 80% fill factor. Chemicals in the proportions shown in Table 5.15 were sequentially added as follows: the elastomer was stirred for 3 min, followed by stirring the hybrid fillers for 2 min. After 24 h conditioning at an ambient temperature of 20 °C and relative humidity of 40%, the mixture was formed into sheets of 125 × 125 ×

×2 mm and vulcanized in an electric "hot" hydraulic press at 160 °C and a force of 200 kN. Uniaxial tensile tests were performed on a test machine Testometric MT350 [155].

For such a system, CNT and carbon black were first suspended in ethanol. The prepared suspensions were mixed in the ratio calculated by equations (5.11)—(5.13) [162], additionally sonicated in an ultrasonic mixer-M900T and dried to constant mass and loosened in a mixer (Fig. 5.66). Then, all the ingredients were introduced according to the scheme of Table 5.17 and mixed first in a Z-shaped Banbury mixer, then in an open two-roll mixer.

The samples were used to determine the tensile strength, fracture strain and stress for 10% strain, using bursting machines 2167 P-50 and Testometric MT350.

The calculations were performed according to equations (5.11) and (5.13). The parameters used and the results for the three rubber compositions are given in Table 5.18.

Table 5.17. **The modes of mixing rubber composition based on NBR 3365**

Mixing step	Feed Ingredient 1#	Feed Ingredient 2# and Ingredient 4#	Feed 50% of Ingredient 3#	Feed 50% of Ingredient 3#	Cleaning	Mixing	Discharging	Feed Ingredient 5# open mill
Mixing time, min Temperature, °C	2	2	3	3		2—5	≥110	2

Table 5.18. **Parameters of rubber and fillers**

Type of rubber	Rubber density, g/cm^3	Specific surface of CNTs, m^2/g	Diameter of CNTs, nm	Specific surface of CB N550, m^2/g	Specific surface of CB N220, m^2/g	Specific surface of CB N330, m^2/g	Calculated optimal content, phr	
							CNTs	Carbon black
NBR 3365	0.915	230	15	40.0	—	—	2.2	80.0
				42.0	—	—	1.2	80.0
				44.0	—	—	0.6	80.0
NR SMR 20 [155]	0.86	230	15	—	118	—	1.97	29.0
				—	120	—	1.64	29.1
				—	122	—	1.31	29.3
NR SMR L [156]	0.86	230	15	—	—	80.0	2.51	29.13
				—	—	82.0	2.23	29.20
				—	—	84.0	1.93	29.30

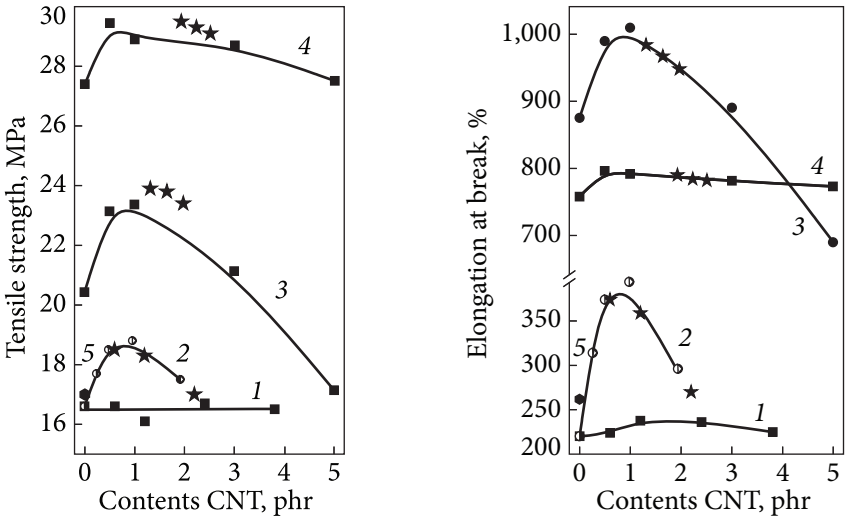

Fig. 5.67. Dependences of tensile strength for systems: NBR 3365 (curves *1*, *2*), NR SMR 20 (curve *3*), and NR SMR L (curve *4*). The asterisks show the calculated content of CNTs [163]

Fig. 5.68. Dependences of tensile fracture for systems: NBR 3365 (curves *1*, *2*), NR SMR 20 (curve *3*), and NR SMR L (curve *4*). The asterisks show the calculated content of CNTs [163]

Figures 5.67 and 5.68 [163] show the dependences of the tensile strength and elongation at the break for systems: NBR 3365 (curves *1*, *2*), NR SMR 20 (curves *3*), and NR SMR L (curves *4*). The dots with the number 5 indicate the experimental results obtained for the NBR 3365 system with standard composition, without CNTs, but the carbon black was further dispersed in ethanol under the action of ultrasound. This gave a small increase in the strength and elasticity of the rubber, possibly due to the increase in the specific surface area of carbon black. The asterisks show the calculated content of CNT, which should correspond to the maximum increase in strength characteristics.

Curves *1*, *3*, *4* (Figs. 5.67 and 5.68) represent samples where CNTs replace carbon black, i.e. the total content of filler does not change. For the rubber sample based on NBR 3365 (curve 1), in which carbon black N550 has a minimum specific surface area (S_{cb} = 42 m^2/g) is used as a filler, the replacement of carbon black with CNT did not change the characteristics. And in the case CNTs were added according to the calculation (curves *2*), the characteristics of the system increased.

For systems based on NR SMR 20 (curves *3*) and NR SMR L (curves *4*), where carbon black N220 (S_{cb} = 120 m^2/g) and N320 (S_{cb} = 80 m^2/g) are used as a filler, respectively, replacement of carbon black with CNT (S_{CNT} = 230 m^2/g) gives an increase in performance. Moreover, the effect is greater for a system in which the specific surface area of carbon black is larger.

Comparing the experimental values of CNTs content, at which the maximum effect of improving the characteristics of rubber compositions is achieved, with its calculated values, we can say that this calculation allows us to estimate the range of CNTs contents where we want to find the optimal values.

In work [162], we compared the properties of the rubber composition based on natural rubber Vistalon 706 (EPM), namely in mass parts: natural rubber Vistalon 706 (EPM) — 100, coagulant ZDMA — 15, paraffin oil — 10, antioxidant — 1, retarder — 0.3, curing agent (peroxide Vul-Cup 40KE) — 5 (Table 5.19), carbon black N550 or N220 created by the authors [164], and our data for samples made according to the same recipe and calculated content of hybrid filler. The following parameters were used for the calculation: ρ_{rubber} = 0.86 g/cm^3, S_{CNT} = 1300 m^2/g, S_{cb}. (brands N550) = 42 m^2/g, S_{cb} (brands N220) = 120 m^2/g. The value of the CNT diameter was varied, for which 6, 7, and 8 nm were taken (Table 5.19).

As can be seen from the comparison of samples *1—3* synthesized by calculation and sample *4* (carbon black N550), the addition of CNTs in the amount of 3.8—5.4 phr and CB of 60.0—59.8 phr gives larger values of tensile strength, fracture strain, and stress for 10% strain. For samples *5—7* (carbon black N220), the tensile strength and the value for 10% tensile deformation increase, but the samples become less elastic: the amount of fracture deformation decreases.

Conclusions. The proposed semi-empirical calculation, taking into account the ratio between the specific surface of carbon black and CNTs and the average particle size, allows estimation of the amount and composition of a hybrid nanofiller (CB & CNT), as well as the method of its addition to CNTs: CB addition, CB substitution or partial replacement. A comparison of the predicted

Table 5.19. **Carbon black content, calculated CNTs content, CNTs diameter taken for calculation, and experimentally obtained values of tensile strength, fracture, and stress of 10% deformation for rubber compositions based on Vistalon 706**

Sample number	Carbon black N550	Carbon black N220	CNTs	d_{CNT} for calculation, nm	Tensile strength (σ), MPa	Tensile fracture (ε),%	Stress of 10% deformation ($\varepsilon_{10\%}$), MPa
	Content in phr						
1	59.8	—	5.4	6.0	23.2	425	1.8
2	60	—	4.6	7.0	24.5	528	1.9
3	60	—	3.8	8.0	24.6	550	1.9
4 [164]	50	—	3.87	—	22.3	522	1.8
5	—	60	2.0	6.0	30.6	450	2.3
6	—	60	1.0	7.0	29.5	430	2.2
7	—	60	0.2	8.0	28.0	420	2.0
8 [164]	—	50	3.87	—	22.3	496	1.6

values of CNTs and carbon black with the experimental data for rubber compositions with optimal tensile strength, fracture tensile strength, and stress for 10% deformation based on both natural and synthetic rubbers shows the high efficiency of the method applied.

5.5. Modification of fiberglass with carbon nanotubes and its modified forms

CNTs were added to epoxy resin (ER) by mixing EP with CNTs in a three-roll mixer of viscous liquids. The effect of curing conditions such as "free" curing without external impacts, pressure curing, and curing by vacuum pumping was investigated. The obtained data are shown in Table 5.20.

As follows from Table 5.20, the production of fiberglass by the method of infusion (vacuum pumping) is the most promising, as the tensile strength increases quite significantly, namely about twice compared to the hardening under low pressure and without pressure. Note that the density of samples varies within 3%. The average density is 1.52 g/cm^3 and the average deviation is 0.05 g/cm^3.

The summarized results of LCS measurements of highly diluted in ethanol dispersions of CNTs in epoxy resin and in the hardener are presented in Tables 5.21 and 5.22 [44]. Analysis of the results shows, first of all, that the

Table 5.20. **Influence of hardness conditions on tensile strength of fiberglass (without CNTs adding) [20]**

№	Conditions for obtaining	Density, g/cm^3	Tensile strength, MPa	Tensile strength normalized to density, MPA/(g/cm^3)
1	Without pressure and vacuum	1.46	112.5 ± 2.0	77.0
2	Under pressure, 1.4 kg/cm^2	1.59	138.1 ± 11.0	86.9
3	In vacuum $5 \cdot 10^{-1}$ mm Hg	1.51	244.0 ± 7.0	161.5

Table 5.21. **The size and number of particles in the resin solution depending on the CNTs content**

Particle distribution by	CNTs content, % wt.				
	0.1	0.2	0.4	0.8	1.6
Volume/number of particle types by size	864 nm	1—94 nm 2—408 nm	1— 3.3 μm	1— 13.3 μm	1—21 μm
Number/particle size distribution	761 nm — 100%	75.3 nm — 100%	2.8 μm — 100%	62 nm — 99%	532 nm — 26.5% 3 μm — 46.4% 17.7 μm — 25.1%

sizes of CNTs agglomerates depend on their content. Thus, at a content of 0.1% wt. CNTs in the resin, the particles are uniform in size in the range from 250 nm to 1200 nm with a maximum of 790—800 nm. When the content of CNTs is 0.2% wt. and 0.8% wt., nanosized particles are within (30—120) nm with maxima (70—80) nm and (90—120) nm and up to 40% or more, respectively. A sample of resin with a CNTs content of 0.4% wt. is characterized by the presence of large particles up to 3 μm. Like the sample containing 0.1% wt., these particles are of the same size and it is their number that predominates in the resin. When the content of CNTs reaches1.6% wt., the particles are divided by size into three groups: 500 nm — 26.5%, 3 μm — 48.1%, and 17 μm — 25.4%.

The bending strength of model layered samples of fiberglass increases non-monotonically with increasing content of CNTs and their modified

Table 5.22. **The size and number of particles in the solution of the polymerization catalyst depending on the CNTs content**

Particle distribution by	CNTs content,% wt.		
	0.5	1.0	2.0
Volume/number of particle types by size	1 max — 14.7 μm	1 max — 16.5 μm	1 max — 40.9 nm 2 max — 716 nm 3 max — 6.1 μm
Number/particle size distribution	75 nm — 99.6%	230 nm — 89.5%, 6.1 μm — 10.5%	29.7 nm — 100%

Table 5.23. **The tensile strength of model samples of fiberglass depending on the method of production of CNTs and the chemical state of their surface**

The method of obtaining a composite	Mixing on a three-roll mill in LR 285		Ultrasonic treatment in LH 286		Mixing in a three-roll mill in LR 285 and sonication in LH 286	
	Strength limit, MPa	Changing the strength limit	Strength limit, MPa	Changing the strength limit	Strength limit, MPa	Changing the strength limit
Composite without CNTs	26.96	—	26.96	—	—	—
Initial CNTs	30.57	1.13	41.51	1.54	—	—
Oxidized CNTs at 200 A · h/kg	42.88	1.59	27.36	1.01	—	—
Synergetic effect: CNTs in. — in LH 286, CNTs oxid. — in LR 285					49.61	1.84

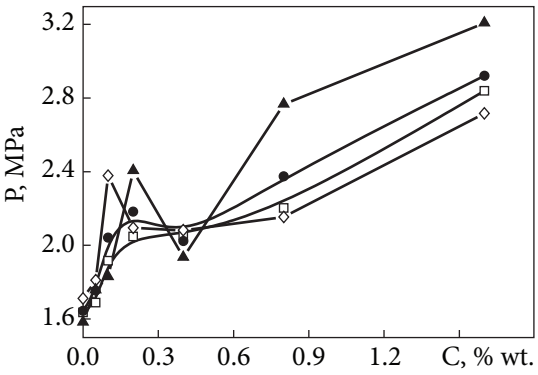

Fig. 5.69. Dependences of the bending strength of fiberglass samples filled with CNTs of different origins

forms. In the region of 0.4% wt., a minimum bending strength almost for all forms of CNTs is observed (Fig. 5.69).

Comparing the data on particle sizes and strength characteristics of fiberglass, it is seen that a decrease in the size of CNTs agglomerates leads to an increase in the strength of the composite (CNTs contents of 0.1 and 0.2% wt.). For unknown reasons, at a content of 0.4% wt. the particle size increases by almost 40 times, which causes a decrease in strength, and then again the strength increases with decreasing size of the CNT agglomerates.

Table 5.22 also shows that the size of CNT agglomerates introduced into the polymerization catalyst depends on the content as well. It is impossible to compare the size of agglomerates with the strength characteristics at this stage of the study, although the correlation of the results with the preliminary analysis of the influence of CNTs agglomerate sizes on the strength characteristics of building materials is evident.

The influence of the chemical state of CNT surface on the tensile strength characteristics of model samples of fiberglass is shown in Table 5.23. Fiberglass samples were made from two layers of fiberglass with a density of 110 g/m^2 connected with epoxy resin LR 285 with hardener LH 286, which were reinforced with CNTs of different origins. The initial CNTs or their modified forms in the amount of 0.3% wt. relative to the mass of the approved resin were homogeneously distributed in the epoxy resin or hardener using ultrasonic dispersant UZDN-2 for the latter and stirring in a three-roll mixer for the former.

As can be seen from Table 5.23, an increase in the tensile strength limit (by 59%) is observed when using oxidized CNTs for reinforcement of epoxy resin LR285. In the LH286 polymerization catalyst, on the contrary, composites with hydrophobic CNTs have the highest strength increase, by 54%.

This effect is explained by the fact that the amine hardener LH 286 in the interaction with CNTs acts as a surfactant. It orients the hydrocarbon part to the CNTs and the aminogroups to the outside, which prevents the reverse agglomeration of the CNTs after dispersion. Since the amino groups react with the resin epoxy groups, the interaction of the polymer matrix with the CNTs surface increases. For oxidized CNTs, the opposite is true. Such ideas are confirmed by the quantum chemical calculations in [165].

Table 5.24. **The tensile strength of model samples of fiberglass depending on the content of composites used**

Sample	Component of the composition	CNTs content,%		Total content of CNTs relative to solid resin,%	Tensile strength, MPa	Change in the tensile strength,%
		Non-oxidized hydrophobic	Oxidized			
1	Epoxy resin Hardener	0 0.25	0.25 0	0.25	46.0	70
2	Epoxy resin Hardener	 0.3	0.1	0.15	40.0	48
3	Epoxy resin Hardener	0 1.5	0.1 0	0.5	51	89
4	Epoxy resin Hardener	0 1.0	1.0 0	1.0	56	107
5	Epoxy resin Hardener	 0.3	2.5 0	1.9	39.0	44
6	Epoxy resin Hardener	0 1.5	2.5 0	2.2	28.5	5.6
7	Epoxy resin Hardener	0 0	0 0	0	27.0	—
8p	Epoxy composition	1.0	0	1.0	71.77	4.6
9p	Epoxy composition	0	0	0	68.62	—

In the case of dispersion of oxidized CNTs in the resin, the most oxygen-containing groups on the surface of CNTs (due to their polarity) prevent reverse agglomeration after dispersion.

The use of the original CNTs in the hardener and oxidized in epoxy resin gives a synergistic effect of increasing the strength, almost by twice.

Table 5.24 shows the compositions of composite samples and their strength characteristics.

These data confirm the achievement of such a technical result: the developed method provides fiberglass that has an increase in strength by 5.6÷107% compared to conventional composites without addition of CNTs.

The method of manufacturing fiberglass can be used in industry for the manufacture of heavy-duty parts and structures.

From the above findings, we can draw the following conclusions.

1. The method of laser correlation spectroscopy shows that the developed technique of deagglomeration of CNTs allows creating their stable dispersions in different liquids, which is the basis of methodological approach to the uniform distribution of CNTs in matrices of different nature.

2. A comprehensive study of the structural, mechanical, thermodynamic, and thermophysical characteristics of a new class of low-CNT-filled materials based on such matrices as thermoplastic and thermosetting polymers, elastomers, cement paste, cement-sand mixture, oxide ceramics, and layered glass fiber indicates that a change in properties of various matrices is determined by the structure-forming ability of CNTs, due to their uniquely large ratio length-to-diameter ~10^3, which makes it possible to form a continuous nanoscale network with a CNT content of several tenths of percent. The nanoscale grid forms layers of the matrix in the nanoscale state with significantly improved properties compared to the bulk state. The decisive role of nanosized zones of matrices, determined experimentally, is confirmed by theoretical calculations in various approximations, i.e. the matrix response is proportional to the surface area of the interfaces.

REFERENCES

1. M. Kaseem, K. Hamad and Y.G. Ko, European Polymer Journal. **79**, 36 (2016). https://doi.org/10.1016/j.eurpolymj. 2016.04.011
2. X. Yang, T. Zou, C. Shi, E. Liu, C. He and N. Zhao, Materials Science and Engineering: A. **660**, 11 (2016).
3. L. Banks-Sills, D.G. Shiber, V. Fourman, R. Eliasi and A. Shlayer, Composites Part B: Engineering. **95**, 335 (2016). https://doi.org/10.1016/j.compositesb.2016.04.015.
4. W. Feng, L. Zhang, Y. Liu, X. Li, L. Cheng, S. Zhou and H. Bai, Materials Science and Engineering: A. **637**, 123 (2015).
5. T. H. Nam, K. Goto, Y. Yamaguchi, E.V.A. Premalal, Y. Shimamura, Y. Inoue, K. Naito and S. Ogihara, Composites Part A: Applied Science and Manufacturing. **76**, 289 (2015).
6. A.V. Kalgin, Yu.Ye. Kalinin, A.M. Kudrin, A.V. Malyuchenkov, Yu.V. Panin and A.V. Sitnikov, Vestnik VGTU. (112), 147 (2011) [in Russian].
7. S.P. Savin, Izvestiya Samarskogo nauchnogo tsentra Russian Academy of Sciences. (4), 1 (2012) [in Russian].
8. T. Cowan, E. Acar and C. Francolin, Mechanical and Aerospace Engineering Department University of Florida. ST1, 1 (2006).
9. V. Zazimko, Novyi oboronnyi zakaz. Strategii. (2), 56 (2017) [in Russian].
10. S. Paunikar and S. Kumar, Computational Materials Science. **95**, 21 (2014).
11. A.V. Makunin and N.G. Chechenin, *Polimer-nanouglerodnye materialy dlya kosmicheskikh tekhnologiy. Chast' I. Sintez i svoistva nanouglerodnykh structur*: Uchebnoe posobie (Universitetskaya kniga, Moscow, 2011) [in Russian].
12. Y. Tian, H. Zhang and Z. Zhang, Composites: Part A. **98**, 1 (2017), https://doi.org/10.1016/j.compositesa.2017.03.007.

13. G. Scarselli, C. Esposito Corcione, F. Nicassio and A. Maffezzoli, International Journal of Adhesion and Adhesives. **75**, 174 (2017). https://doi.org/10.1016/j.ijadhadh.2017.03.012.
14. S. Lin, M.A.S. Anwer, Y. Zhou, A. Sinha, L. Carson and H. Naguib, Composites Part B. **132**, 69 (2018), https://doi.org/10.1016/j.compositesb.2017.08.010.
15. M. Liang and K.L. Wong, Energy Procedia. **110,** 156 (2017).
16. A. B. Irez, E. Bayraktar and I. Miskioglu, Procedia Engineering. **184**, 486 (2017).
17. M. Eesaee and A. Shojaei, Composites: Part A. **63**, 149 (2014).
18. N.R.R. Anbusagar, K. Palanikumar and P.K. Giridharan, Composite Structures. **125**, 336 (2015), doi: https://doi.org/10.1016/j.compstruct.2015.02.016.
19. M. Boumaza, R. Khan and S. Zahrani, Thin Solid Films. **620**, 160 (2016), https://doi.org/10.1016/j.tsf.2016.09.035.
20. Yu.I. Sementsov and N.T. Kartel, in: *Surface physics and chemistry*, edited by N.T. Kartel and V.V. Lobanov (Interservis, Kyiv, 2018). vol. 2, pp. 968—1008 [in Russian].
21. E.G. Rakov, *Nanotrubki i fullereny*: Uchebn. posobiye (Universityetskaya kniga, Logos, Moscow, 2006) [in Russian].
22. M.M.J. Treacy, T.W. Ebbesen and J.M. Gibson, Nature. **381**, 678 (1996).
23. W. Bauhofer and J.Z. Kovacs, Comp. Sci. Technol. **69** (10), 1486 (2009).
24. L. Bokobza, Polymer. **48**, 4907 (2007).
25. Yu.I. Sementsov, A.V. Melezhyk, M.L. Pyatkovsky, V.V. Yanchenko, N.A. Gavrilyuk, G.P. Prikhod'ko, A.I. Senkevich, S.L. Revo and E.A. Ivanenko, in: *Hydrogen materials science and chemistry of carbon nanomaterials*, edited by T.N. Veziroglu, S.Yu. Zaginaichenko, D.V. Schur, B. Baranowski, A.P. Shpak, V.V. Skorokhod and A. Kale (Springer, Dordrecht, 2007), pp. 757—763.
26. Yu.I. Sementsov, N.A. Gavrilyuk, T.A. Alekseeva, O.N. Lazarenko and V.V. Yanchenko, Nanosistemy, nanomaterialy, nanotekhnologii. **5** (2), 351 (2007) [in Russian].
27. Yu. Sementsov, N. Gavriluk, G. Prikhod'ko, T. Aleksyeyeva, O. Lasarenko, V. Yanchenko, in: *Carbon Nanomaterials in Clean Energy Hydrogen Systems.* NATO Science for Peace and Security Series C: Environmental Security. edited by B. Baranowski, S. Zaginaichenko, D. Schur, V. Skorokhod and A. Veziroglu (Springer, Dordrecht, 2008), pp.327—334.
28. Yu.I. Sementsov, T.A. Aleksyeyeva, N.A. Gavriluk, O.N. Lasarenko and G.P Prikhod'ko, Surface. (13), 224 (2007) [in Russian].
29. Yu.I. Sementsov, M.L. Piatkovskyi, G.P Prikhod'ko, V.S. Stupak, N.I. Pas'ko, N.V. Savel'eva, A.V. Melezhyk and V.V. Yanchenko, Khim. prom. Ukraine. (1), 25 (2009) [in Russian].
30. O.V. Kotenok, S.M. Makhno, G.P Prikhod'ko and Yu.I. Sementsov, Surface. 1(16), 213 (2009) [in Ukrainian].
31. Yu.I. Sementsov, S.N. Makhno, S.V. Zhuravsky and M. T. Kartel, Himia, Fizika ta Tehnologia Poverhni. **8** (2), 107 (2017).
32. Yu.I. Sementsov, A.V. Melezhyk, G.P. Prykhodko, N.A. Havryliuk, M.L. Piatkovskyi and V.V. Yanchenko, in: *Physico-chemistry of nanomaterials and supramolecular structures*, edited by A.P. Shpak and P.P. Gorbik (Naukova dumka, Kyiv, 2007), vol. 2, pp. 116—158. [in Russian].
33. A.K. Mikitaev, G.V. Kozlov and G.E. Zaikov, *Polymer nanocomposites: variety of structural forms and applications* (Nauka, Moscow, 2009) [in Russian].

34. E.A. Lysenkov, Yu.V. Yakovlev and V.V. Klepko, Physics and chemistry of solid state. **15** (2), 372 (2014).
35. O.M. Garkusha, S.M. Makhno, G.P. Prikhod'ko, Yu.I. Sementsov and M. T. Kartel, Himia, Fizika ta Tehnologia Poverhni. **1** (1), 103 (2010).
36. Yu. Sementsov, G. Prikhod'ko, N. Kartel, M. Tsebrenko, T. Aleksyeyeva and N. Ulynchych, in: *Carbon Nanomaterials in Clean Energy Hydrogen Systems*. NATO Science for Peace and Security Series C: Environmental Security, edited by S. Zaginaichenko, D. Schur, V. Skorokhod, A. Veziroglu and B. Ibrahimoğlu (Springer, Dordrecht, 2011), pp.183—195.
37. Yu. Sementsov, G. Prikhod'ko, N. Kartel, T. Aleksyeyeva and M. Tsebrenko, Himia, Fizika ta Tehnologia Poverhni. **4** (2), 191 (2013).
38. O.S. Nychyporenko, O.P. Dmytrenko, M.P. Kulish, T.M. Pinchuk-Rugal, Yu.Ye. Grabovskiy, M.A. Zabolotnyi, V.V. Strelchuk, A.S. Nikolenko and Yu.I. Sementsov, Nanosistemi, Nanomateriali, Nanotehnologii. **13** (4), 673 (2015).
39. P.K. Mallick, *Processing of Polymer Matrix Composites: Processing and Applications* (CRC Press, Boka Raton, 2017).
40. J.N. Coleman, U. Khan, W.J. Blau and Y.K. Gun'ko, Carbon. **44** (9), 1624 (2006).
41. F. Wei, Q. Zhang, W.-Z. Qian, H. Yu, Y. Wang, G.-H. Luo, G.-H. Xu and D.-Z. Wang, Powder Technol. **183** (1), 10 (2008).
42. Y. Hao, Z. Qunfeng, W. Fei, Q. Weizhong and L. Guohua, Carbon. **41** (14), 2855 (2003).
43. O.P. Krivoruchko, N.I. Maksimova, V.I. Zaikovskii and A.N. Salanov, Carbon. **38**, 1075 (2000).
44. Yu.I. Sementsov and N.T. Kartel, Himia, Fizika ta Tehnologia Poverhni. **10** (2), 174 (2019).
45. Y. Zare, Composites: Part A. **84**, 158 (2016), https://doi.org/10.1016/j.compositesa.2016.01.020
46. E.O. Koval'ska, Ph.D. dissertation, Chuiko Institute of Surface Chemistry of National Academy of Sciences of Ukraine, 2013 [in Ukrainian].
47. J. Rausch, R.C. Zhuang and E. Mader, Composites Part A. **41**, 1038 (2010).
48. L. Vaisman, H.D. Wagner and G. Marom, Adv. Colloid Interface Sci. **128–130**, 37. (2006). https://doi.org/10.1016/j.cis.2006.11.007.
49. H.-S. Kim, W.I. Park, M. Kang and H.-J. Jin, J. Phys. Chem. Solids. **69** (5–6), 1209 (2008). https://doi.org/10.1016/j.jpcs.2007.10.062.
50. M. Bystrzejewski, A. Huczko, H. Lange, T. Gemming, B. Büchner and M.H. Rümmeli, J. Colloid Interface Sci. 345 (2), 138 (2010). https://doi.org/10.1016/j.cis.2010.01.081.
51. L. Zhao and L. Gao, Colloids Surf. A. **224** (1—3), 127 (2003). https://doi.org/10.1016/S0927-7757(03)00155-9.
52. M.S. Strano, V.C. Moore, M.K. Miller, M.J. Allen, E.H. Haroz and C. Kittrell, J. Nanosci. Nanotech. **3** (1–2), 81 (2003). https://doi.org/10.1166/jnn.2003.194.
53. G. Wypych, *Hand book of Plasticizers*. (Chem. Tec. Publishing., Toronto, New York, 2004).
54. V.S. Izotov and Yu.A. Sokolova, *Khimicheskie dobavki dla modifikatsii betona* (Paleotip, Moscow, 2006) [in Russian].
55. M.N. Vauchskiy, Vestnik grazhdanskikh inzhenerov. (2), 44 (2005) [in Russian].
56. M.E. Yudovich and A.N. Ponimarev, Stroyprofile'. (6-07), 49 (2007) [in Russian].

57. Yu.D. Chistov and A.S. Tarasov, Stroitel'nye materialy, oborudovanie, tekhnologii XXI veka. (3), 69 (2007) [in Russian].
58. S.A. Dergunov and V.N. Rubtsova, Stroyprofile'. 7 (77), 13 (2009) [in Russian]. http://stroyprofile.com/files/pdf/7-09-13.pdf.
59. Yu. I. Sementsov and O. V. Melezhik, TU U 24.1-03291669-009:2009 (carbon nanotubes) № 02568182/095617 (01 September, 2009).
60. Yu.I. Sementsov, E.O. Kovalska, N.T. Kartel and O.Yu. Chunihin, Himia, Fizika ta Tehnologia Poverhni. **7** (2), 202 (2016).
61. M.S. Ovcharenko, Ph.D. dissertation, Sumy State University, 2013. Taken from <http://essuir.sumdu.edu.ua/handle/123456789/30582>.
62. S.E. McNeil, *Characterization of Nanoparticles Intended for Drug Delivery* (Humana Press, New York, 2011).
63. L.E. Copeland, D.L. Kantro and G. Verbeck, Bulletin. **153**, (1), 429 (1960).
64. L.E. Copeland and D.L. Kantro, in: *The chemistry of cements*, edited by H.F.W. Taylor (Academic Press, London, 1964), vol. 1, pp. 313—370.
65. G.C. Bye, *Portland cement: composition, production and properties* (Thomas Telford Ltd., London, 2009).
66. A.S. Ryzhov and L.N. Potselueva, Engineering and construction journal. 2 (12), 49 (2010) [in Russian].
67. A.V. Krestinin, Russian Nanotechnologies. **2** (5–6), 18 (2007).
68. E.V. Korolev, Yu.M. Bahzenov and V.A. Beregovoi, Building Materials. (8), 2 (2006).
69. A.F. Khuzin, M.G. Gabidullin, I.R. Badertdinov, R.Z. Rakhimov, F.P. Abramov, R.E. Yumakulov, A.Sh. Nizembaev and E.M. Perepelica, Izvestiya KSUAE. Stroitel'nye materialy i izdeliya. 1 (23), 221 (2013) [in Russian].
70. H.W. Zhou, L. Mishnaevsky Jr., H.Y. Yi, Y.Q. Liu, X. Hu, A. Warrier and G.M. Dai, Composites Part B: Engineering. **88**, 201 (2016).
71. G. Ferro, J.-M. Tulliani and S. Musso, Frattura ed Integrità Strutturale. **5** (18), 34 (2011).
72. N.D. Devatkov, M.V. Golant and O.V. Beletskiy, *Millimeter waves and their role in life processes* (Radio i svaz', Moscow, 1991) [in Russian].
73. Yu.B. Grigorov, M.A. Pustovoyt, Yu.P. Gnidenko, B.V. Berezhnov and S.L. Sokur, Internatıonal medıcal journal. **11** (3), 115 (2005).
74. A.B. Gapeev and N.K. Chemeris, Biomeditsinskie tekhnologii i radioelektronika. (2–4), 44 (2007).
75. A.P. Krause, Ph.D. Thesis, University of Nebraska Lincoln, 2012.
76. V.A. Krutikov, A.A. Didik, G.I. Yakovlev, V.I. Kodolov and S.G. Shuklin, RF Patent No. 2281262 (10 August, 2006).
77. A.N. Ponomarev, J. Constr. Eng. **6**, 25 (2009).
78. M.E. Yudovich, A.N. Ponomarev and S.I. Gareev, Constr. mater. **3**, 2 (2008).
79. V.A. Perfilov, U.V. Alatortseva, M.I. Dmitruk and I.L. Zhoga, News of higher education institutions, Construction. (8), 17 (2009).
80. Yu.I. Sementsov, *Formation of structure and properties of sp^2-carbon nanomaterials and functional composites with their participation* (Interservis, Kyiv, 2019) [in Ukrainian].
81. M. Kartel, Yu. Sementsov, S. Mahno, V. Trachevskiy and W. Bo. Universal Journal of Materials Science. **4** (2), 23 (2016). DOI: 10.13189/ujms.2016.040202.
82. M. Malagù, M. Goudarzi, A. Lyulin, E. Benvenuti and A. Simone, Composites Part B. **131**, 260 (2017).

83. M. Cen-Puca, A.I. Oliva-Avilés and F. Avilés, Physica E. **95**, 41 (2018).
84. S.L. Revo, F.V. Lozoviy, K.O. Ivanenko and T.G. Avramenko, Physics and chemistry of solid state. **11** (4), 1029 (2010).
85. G.H. Chen, D.I. Wu, W.G. Weng and W.-L. Yan, Polymer engineering and science. **41**, 2148 (2001).
86. G.I. Dovbeshko, V.S. Kopan, S.L. Revo, M.M. Nishchenko, G.P. Prikhod'ko, M.L. Piatkovskii, Yu.I. Sementsov and M. Westermayer, Metallofizika i noveyshie tehnologi. **27** (3), 1001 (2005).
87. Yu.I. Sementsov, G.P. Prihodko, S.L. Revo, A.V. Melezhik, M.L. Pyatkovskii and V.V. Yanchenko, Nanosistemyi, nanomaterialyi, nanotehnologii. **1** (1), 173 (2003).
88. S.L. Revo, T.G. Avramenko and E.A. Ivanenko, Agricultural Engineering, Research Papers. **45** (1), 67 (2013).
89. Yu.G. Frolov, *Kurs kolloidnoy khimii. Poverkhnostnye yavleniya i dispersnye sistemy*. (Khimiya, Moscow, 1989) [in Russian].
90. V.A. Balusov and A.N. Tikhonov, *Klasternye materialy — novyy klass plastmass s ultradispersnym napolnitelem* (LDNTP, Leningrad, 1988). [in Russian].
91. S.J. Gregg and K.S.W. Sing, *Adsorption, surface area and porosity*, 2nd ed. (Academic Press, London, 1982).
92. I.D. Simonov-Emelyanov, V.N. Kuleznev and L.Z. Trofimicheva, Plasticheskie massyi. (5), 61 (1989) [in Russian].
93. A.A. Rusakov, *X-ray analysis of metals and semiconductors* (Metalurgiya, Moscow, 1969) [in Russian].
94. Y. Miyamoto, C. Nakafuku and T. Takemura, Polym. J. **3**, 122 (1972).
95. M.A. Martyinov and K.A Vyilegzhagina, *X-ray polymers* (Himiya, Leningrad, 1972) [in Russian].
96. Y.-W. Mai and Z.-Z. Yu, editors, *Polymer nanocomposites* (Woodhead Publishing Limited and CRC Press LLC, Cambridge, Boca Raton, 2006).
97. D. Wu, C. Zhou, X. Fan, D. Mao and Z. Bian, J. Appl. Polym. Sci. **99** (6), 3257 (2006).
98. J.W. Huang, J. Polym. Sci., Part B: Polym. Phys. **46** (6), 564 (2008).
99. A.A. Ohlopkova and A.G. Parnikova, Izvestiya Samarskogo nauchnogo tsentra Rossiyskoy akademii nauk. **13** (1(2)), 394 (2011).
100. T. G. Avramenko, G. A. Maksimova, E. A. Ivanenko, V.V. Mikhailov, I.P. Shevchenko and S.L. Revo, Surface Engineering and Applied Electrochemistry. **51** (6), 509 (2015).
101. A.L. Efros, *Physics and geometry of disorder* (Nauka, Moscow, 1982) [in Russian].
102. A.L. Efros and B.I. Shklovskii, Phys. Stat. Sol. Ser. B. **76** (2), 475 (1976).
103. S.M. Aharoni, J. Appl. Phys. **43** (5), 2463 (1972).
104. V.A. Sotskov, Fizika i tehnika poluprovodnikov. **39** (2), 269 (2005) [in Russian].
105. B.I. Shklovskiy and A.L. Efros, *Electronic properties of doped semiconductors* (Nauka, Moscow, 1979) [in Russian].
106. H. Sher and R. Zallen, J. Chem. Phys. **53** (9), 3759 (1970).
107. V. Panwar and R.M. Mehra, Eur. Polym. J. **44**, 2367 (2008).
108. L.I. Melnik, D.O. Budya and V.A. Bil, Komunalne gospodarstvo mist. **103**, 125 (2012) [in Ukrainian].
109. S. Ramirez-Garcia, S. Alegret, S. Cespedes and R.J. Forster, Anal. Chem. **76**, 503 (2004).

110. E.S. Tillman and N.S. Lewis, Sens. Actuators B-Chem. **96**, 329 (2003).
111. F. El-Tantawy, K. Kamada and H. Ohnabe, Mater. Lett. **56**, 112 (2003).
112. T.G. Avramenko, K.O. Ivanenko, O.V. Mihalyuk and S.L. Revo, Visnik Kiyivskogo nats. un-tu imeni Tarasa Shevchenka. Seriya: Fiziko-matematichni nauki. (2), 271 (2013) [in Ukrainian].
113. Yu.A. Panshin, S.G. Malkevich and Ts.S. Dunaevskaya, *Fluoroplastics* (Himiya, Leningrad, 1978) [in Russian].
114. L.M. Ushakova, K.I. Ivanenko, N.V. Sigareva, M. I. Terets, M.T. Kartel, Yu.I. Sementsov, Physics and chemistry of solid state. **23** (2), 394 (2022).
115. Yu.I. Sementsov and N.T. Kartel, in: *3rd International research and practice conference: Nanotechnology and nanomaterials (NANO-2015). Abstract book* (Ivan Franko National University of Lviv, Lviv, 2015), p. 185.
116. F. Lozovyi, K. Ivanenko, S. Nedilko, S. Revo and S. Hamamda, Nanoscale Res Lett. **11,** 97 (2016). https://doi.org/10.1186/s11671-016-1315-y.
117. T.G. Avramenko, N.V. Khutoryanskaya, S.M. Naumenko, K.O. Ivanenko, S. Hamamda and S.L. Revo, Springer Proceedings in Physics. **221**, 293 (2019). https://doi.org/10.1007/978-3-030-17759-1_20.
118. A.H. Barber, S.R. Cohen and H.D. Wagner, Appl Phys Lett. **82** (23), 4140 (2003). https://doi.org/10.1063/1.1579568.
119. K.O. Ivanenko, L.M. Ushakova, T.G. Avramenko, S.L. Revo, M.T. Kartel and Yu.I. Sementsov, Springer Proceedings in Physics. **246**, 685 (2021). https://doi.org/10.1007/978-3-030-51905-6_46
120. A.V. Melezhik, V.V. Yanchenko and Y.I. Sementsov, in: *Hydrogen materials science and chemistry of carbon nanomaterials*, edited by T.N. Veziroglu, S.Yu. Zaginaichenko, D.V. Schur, B. Baranowski, A.P. Shpak, V.V. Skorokhod and A. Kale (Springer, Dordrecht, 2007), p. 529—537. https://doi.org/10.1007/978-1-4020-5514-0_67.
121. A.V. Melezhik, Yu.I. Sementsov and V.V. Yanchenko, Russian Journal of Applied Chemistry. **78** (6), 917 (2005). https://doi.org/10.1007/s11167-005-0420-y.
122. T.M. Pinchuk-Rugal, O.P. Dmytrenko, M.P. Kulish, Y.Y. Grabovskyy, O.S. Nychyporenko, Y.I. Sementsov and V.V. Shlapatskaya, Problems of Atomic Science and Technology. **96** (2), 10 (2015).
123. O.S. Nychyporenko, O.P. Dmytrenko, M.P. Kulish, T.M. Pinchuk-Rugal, Y.Y. Grabovskyy, A.M. Zabolotnyy, V.V. Strelchuk, A.S. Nikolenko and Y.I. Sementsov, Nanosystems, Nanomaterials, Nanotechnologies. **13** (4), 673 (2015).
124. Y.I. Sementsov, M.L. Piatkovsky, N.A. Gavriliuk, G.P. Prikhod'ko, M.T. Kartel and Y.E. Grabovsky, Chemical Industry of the Ukraine. (5), 59 (2009). [in Uktainian]
125. M.L. Minus, H.G. Chae and S. Kumar, ACS Appl. Mater. Interfaces. **4** (1), 32 (2012). https://doi.org/10.1021/am2013757.
126. T. McNally, P. Pötschke, P. Halley, M. Murphy, D. Martin, S.E.J. Bell, G.P. Brennan, D. Bein, P. Lemoine and J.P. Quinn, Polymer. **46** (19), 8222 (2005). https://doi.org/10.1016/j.polymer.2005.06.094.
127. D.S. Novak, N.M. Bereznenko, T.S. Shostak, V.O. Pakharenko, G.P. Bogotyrova, N.O. Oliinyk and G.A. Bazalii, Porodorazrushayushchii i metalloobrabatyvayushchii instrument — tekhnika i technologiya ego izgotovleniya i primeneniya. **14**, 394 (2011) [in Ukrainian].
128. M.O. Lisunova, Y.P. Mamunya, N.I. Lebovka and A.V. Melezhyk, European Polymer J. **43**, 949 (2007). https://doi.org/10.1016/j.eurpolymj.2006.12.015.

129. S. Kirkpatrick, Rev Modern Phys. **45**, 574 (1973). https://doi.org/10.1103/RevModPhys.45.574.
130. Y.P. Mamunya, Ukrainian Chemistry Journal. **66** (3), 55 (2000) [in Ukrainian].
131. A. Quivy, R. Deltour, A. G. M. Jansen and P. Wyder, Phys. Rev. B **39** (2), 1026 (1989). https://doi.org/10.1103/PhysRevB.39.1026.
132. I. Balberg, N. Binenbaum and S. Bozovsky, Sol St Comm. **47** (12), 989 (1983). https://doi.org/10.1016/0038-1098(83)90984-5.
133. Yu.I. Sementsov, S.L. Revo, K.O. Ivanenko and S. Hamamda, *Expanded graphite and its composites,* edited by M.T. Kartel (Akademperiodika, Kyiv, 2019), pp. 74—87.
134. V.A. Kabanova, editor, *Encyclopedia of Polymers* (Soviet Encyclopedia, Moscow, 1977), vol.3. [in Russian].
135. J.C. Halpin and J.L. Kardos, Polym. Eng. Sci. **16** (5), 344 (1976). https://onlinelibrary.wiley.com/doi/pdf/10.1002/pen.760160512
136. A. Haque and A. Ramasetty, Composite Structures **71** (1), 68 (2005). https://doi.org/10.1016/j.compstruct.2004.09.029.
137. A. Patterson, Phys. Rev. **56** (10), 978 (1939). https://doi.org/10.1103/PhysRev.56.978
138. M. I. Terets, E. M. Demianenko, S. V. Zhuravsky, O. A. Chernyuk, V. S. Kuts, A.G. Grebenyuk, Yu. I. Sementsov, L. M. Kokhtych and M. T. Kartel, Him. Fiz. Tehnol. Poverhni. **10** (1), 75 (2019).
139. L.M. Ganuk, V.D. Ignatkov, S. M. Mahno and P.M. Soroka, Ukrainian Journal of Physics. **4** (6), 627 (1995) [in Russian].
140. V.G. Shevchenko and A.T. Ponomarenko, Russian Chemical Reviews. **52** (8), 757 (1983).
141. S.M. Makhno, O.M. Lisova, G.M. Gunya, Yu.I. Sementsov, Yu.V. Grebelna and M.T. Kartel, Physics and chemistry of solid state. **17** (3), 421 (2016).
142. R.O. Medupin, O.K. Abubakre, A.S. Abdulkareem, R.A. Muriana and A.S. Abdulrahman, Sci Rep. **9**, 20146 (2019). https://doi.org/10.1038/s41598-019-56778-0
143. F. Danafar and M. Kalantari, J Rubber Res. **21**, 293 (2018). https://doi.org/10.1007/BF03449176
144. T. Jose, G. Moni, S. Salini, A.J. Raju, J.J. George and S.C. George, Industrial Crops & Products. **105**, 63 (2017). https://doi.org/10.1016/j.indcrop.2017.04.047
145. P. Kueseng, P. Sae-Oui, C. Sirisinha, K.I. Jacob and N. Rattanasom, Polymer Testing. **32**, 1229 (2013). https://doi.org/10.1016/j.polymertesting.2013.07.005
146. B. Szadkowski, A. Marzec and M. Zaborski, Composite interfaces. **26**, 729 (2019). https://doi.org/10.1080/09276440.2018.1534474
147. S.K. Srivastava and Y.K. Mishra, Nanomaterials. **8** (11), 945 (2018). https://doi.org/10.3390/nano8110945
148. Y.H. Zhan, G.Q. Liu, H.S. Xia and N. Yan, Plastics, Rubber and Composites. **40**, 32 (2011). https://doi.org/10.1179/174328911X12940139029284
149. S. Thomas, J. Abraham, S.C. George and S. Thomas, Polym Bull. **77**, 1 (2020). https://doi.org/10.1007/s00289-019-02693-3
150. M.M. Salehi, T. Khalkhali and A.A. Davoodi, Polym. Sci. Ser. A. **58**, 567 (2016). https://doi.org/10.1134/S0965545X16040131
151. S. Chuayjuljit, A. Imvittaya, N. Na-Ranong and P. Potiyaraj, J Met Mater Miner. **12**, 51 (2002).
152. L. Wei, X. Fu, M. Luo, Z. Xie, C. Huang, J. Zhou, Y. Zhu, G. Huang and J. Wu, RSC Adv. **8**, 10573 (2018). https://doi.org/10.1039/C7RA12830D

153. Y. Nakaramontri, S. Pichaiyut, S. Wisunthorn and C. Nakason, Eur Polym J. **90**, 467 (2017). https://doi.org/10.1016/j.eurpolymj.2017.03.029
154. P. Thaptong, C. Sirisinha, U. Thepsuwan and P. Sae-Oui, Polym Plast Technol Eng. **53**, 818 (2014), https://doi.org/10.1080/03602559.2014.886047
155. E. Harea, R. Stoček, L. Storozhuk, Y. Sementsov and N. Kartel, Appl Nanosci. **9**, 899 (2019). https://doi.org/10.1007/s13204-018-0797-6
156. H. Ismail, A.F. Ramlya and N. Othmana, Polym Plast Technol Eng. **50**, 660 (2011). https://doi.org/10.1080/03602559.2010.551380
157. M. Khalid, C.T. Ratnam, R. Walvekar, M.R. Ketabchi and M.E. Hoque, in: *Green Biocomposites. Green Energy and Technology*, edited by M. Jawaid, M.S. Salit and O.Y. Alothman (Springer, Cham, 2017), pp. 309—345. https://doi.org/10.1007/978-3-319-49382-4_14
158. I. Garkina and A. Danilov, IOP Conf. Ser.: Mater. Sci. Eng. **471** (3), 032005 (2019). doi:10.1088/1757-899X/471/3/032005
159. S.F. Korenkova and Y.V. Sidorenkova, Procedia Engineering. **111**, 420 (2015). https://doi.org/10.1016/j.proeng.2015.07.110
160. S.V. Reznichenko and Y.L. Morozova, editors, *Great reference book of the rubber-maker. Part 1 Rubbers and ingredients* (Ltd "Publishing Center" Techinform "of the International Academy of Informatization", Moscow, 2012), pp. 533—536.
161. Ningbo Taishun Sealing Technology Co., Ltd (2020) http://www.taisun-sealing.com
162. Y.I. Sementsov, M.T. Kartel, K.O. Ivanenko, S.M. Makhno, S.V. Zhuravsky, S.M. Gozhdzinskii, A.D. Terets, V.V. Trachevskii, Din Ang and W. Yang, UA Patent application No. a202005083 (05 August, 2020)
163. Y. Sementsov, W. Yang, K. Ivanenko, S. Makhno and M. Kartel, Appl Nanosci. **12** (3), 621 (2022). https://doi.org/10.1007/s13204-021-01730-w
164. D.J. Burlett, H. Richter, R. Sivarajan and V. Vejins, US Patent No. 20190322818 A1 (24 October, 2019).
165. O.A. Cherniuk, E.M. Demianenko, M.I. Terets, S.V. Zhuravskyi, S.M. Makhno, V.V. Lobanov, M.T. Kartel and Yu.I. Sementsov, Appl Nanosci. **10** (12), 4797 (2020). https://doi.org/10.1007/s13204-020-01448-1

CHAPTER 6

OPTICAL PROPERTIES OF CARBON MATERIALS

6.1. From graphite to intercalated graphite and then — to amorphous and disordered graphite

The optical properties of carbon materials including different coal types have been investigated both experimentally and theoretically for about 70 years. These studies and their results can be pragmatic, as they were made, e.g., to further develop an objective basis for petrographic analysis of coal (coal petrology) and to add to the knowledge of the structure and composition of coal and coal components by determining their optical constants in various ranges of the electromagnetic waves spectrum [1].

At the same time, the results of optical studies of carbon materials can be of fundamental science value. Thus, reflectivity and transmittance of light are of importance as these data allow us to understand features of electronic structure and lattice modes. Accurate determination of optical reflectivity and absorption of carbon structures is also fundamental in astrophysics [2, 3] and simultaneously it provides characteristics important for carbon materials usage in optoelectronic devices.

Optical studies of free carrier phenomena have the advantage of requiring no electrical contacts. They can be performed on samples in encapsulated ampoules with suitably chosen optical windows. To obtain reproducible optical measurements, especially on low-stage reactive compounds, samples can be prepared in the same ampoules (*in situ*) as are used for optical measurements. Reliable results have also been obtained using special optical ampoules into which the samples are transferred after cleavage in an inert atmosphere inside a dry box (see, e.g., [4—6]).

Three complementary experimental techniques are especially early used for the study of lattice mode structure: inelastic neutron, Raman and infrared spectroscopy. All three techniques have been successfully applied to graphite and its intercalation compounds [4]. We will be in touch in this work only with two

last of them. Besides, we would like to draw your attention to luminescence methods of materials study. Luminescent studies of carbon materials have become very important in the last two decades.

Infrared spectroscopy probes infrared-active modes of very small wave vectors because the wave vector of the incident photons is very small compared with the Brillouin zone dimensions. Because of the high optical absorption of graphite and other carbon materials, infrared spectra are usually taken by measurements of reflectivity. To obtain the lattice mode frequencies from the measured spectra, an analysis of the spectral lineshape is carried out, taking into account contributions to the dielectric constant from lattice mode oscillators and background terms arising because of free carrier absorption and interband transitions.

Since Raman spectroscopy is a scattering phenomenon, the change in frequency between the incident and scattered photons is measured to determine the frequency of the absorbed or emitted phonon. Because of the small wave vector of the incident and scattered photons, first-order Raman spectroscopy is limited to the observation of lattice modes close to the Brillouin zone center. Although first-order Raman spectroscopy only provides information on $q \sim 0$ phonons, information on the phonon dispersion relations for other points in the Brillouin zone can be obtained from second-order spectra, where contributions are made by pairs of phonons with wave vectors $\mathbf{q}$ and $-\mathbf{q}$. Second-order Raman lines are generally broad because many phonon pairs with different energies contribute to the line. The resulting line emphasizes those regions in the Brillouin zone that have high densities of states.

Considerable attention will be paid to the luminescent methods of research. Luminescent spectroscopy provides important data on the electronic and spatial structure of materials, and it allows you to detect the material properties to emit light, which may be of great importance for the practical use of such luminescent materials in optical and optoelectronic devices.

At the same time, it is easy to understand that the optical properties of various graphite and carbon forms have to be very similar as they are mainly determined by the electronic structure of carbon atoms and by the interaction of their outshell electrons with a neighbor. In carbon materials, the neighbor atoms are the same carbons. So, we first describe the optical properties of graphite regarding its most spread modifications. Then we will direct a reader to see the variation of the properties associated with other carbon materials and compositions, e.g. some carbon nanostructures and expanded graphite (EG). Optical properties were studied to achieve fundamental knowledge and possible usefulness. Especially the dependences of optical properties on nanostructure size, shape, and carbon quality have been the objects to be studied.

It should be noted that according to our data, in most cases, the characteristics of light interaction with carbon materials are used to study the features of

the structure of the latter. To a lesser extent, such materials are considered and studied as possible optical functional materials. It is just the intention to draw attention to the possibility of using carbon materials, in particular, thermo-expanded graphite, as optical materials led us to include the section "Optical properties of carbon materials" in this book. We also note that carbon materials, like any other solids, can be considered from two positions regarding their optical properties for practical use. First, they can act as "passive" optical materials, that is, they are used for transmission and spatial management of light streams. Second, they can also be used as active optical materials. With the help of the latter, they change the spectral composition, the duration of light flows, and their spatial and temporal coherence. Passive optical materials can be transformed into active (that is functionalization) by introducing (adsorbing) special impurities (activators) and defects, modifying their spatial homogeneity creating composites, etc.

As for what properties of solids should be considered optical, note that there is no specific list recognized in science. Therefore, we will rely on different sources and at our discretion. When white light strikes the surface of a solid, it may be scattered, reflected, refracted, transmitted, or absorbed. Light scattering and reflecting are mainly surface phenomena while refracting, transmitting, and absorbing are internal ones. Some other characteristics that are determined by mentioned above properties are color, luster, brilliance, scintillation, dispersion, etc.

The purpose of Chapter 6 is to provide the reader with an opportunity to get acquainted with the possibilities of optical methods for carbon structures and optical properties study, using one source, namely this book. That is why Chapter 6 is mainly a review of publications and analytical reviews that have already been published in these areas. The results of our research are presented here to a lesser extent. (To facilitate the perception of the material placed below, let us give here the limits of the optical range in different units of measurement, namely, wavelengths in nanometers: 100 nm — 1 mm; in reciprocal centimeters: 10^5—10 cm^{-1}; in electron volts: 12.4—$1.24 \cdot 10^{-3}$ eV; in Herz: $3 \cdot 10^{15}$—$3 \cdot 10^9$ Hz.)

6.1.1. Optical properties of graphite

Many works have been already devoted to experimental studies of the optical properties of graphite [7, 8—14]. E.g., several attempts have been made to identify the optical transitions in the band structure of graphite, which correspond to most of the characteristic features of optical spectra [15—18], and some of the measurements have been performed on natural single crystals [8, 10, 19, 20]. However, such crystals of graphite are very fragile and usually contain large concentrations of impurities. Some of these impurities may be removed by chemical treatment like prolonged boiling in concentrated hydro-

fluoric acid or heating to ~2000 °C in flowing fluorine gas, thus leaving ppm levels of metallic impurities. Since high-purity natural single crystals are hard to obtain, highly oriented pyrolitic graphite (HOPG) is often used for measurements of the physical properties of graphite. HOPG consists of a large number of crystallites with the *c* axis well aligned (within ~0.2° of the average *c* axis), so its properties are very similar to those of the natural single crystals [21]. It has been shown that, e.g., the reflectance spectrum of HOPG agrees within the experimental error with that of natural graphite single crystals [8, 10].

In general, the frequency-dependent optical properties of a solid are determined by the relative contribution to the complex dielectric tensor ε from free carriers ($\varepsilon_{\text{carriers}}$), interband electronic transitions ($\varepsilon_{\text{interband}}$), phonon excitations ($\varepsilon_{\text{lattice}}$), and other processes not treated in detail ($\varepsilon_{\text{core}}$) [4]. The transitions contributing to ε core occur at frequencies higher than the frequency range under consideration, and therefore can be treated in terms of an average quantity. The complex dielectric tensor is thus written as

$$\varepsilon = \varepsilon_1 + i\varepsilon_2 = \varepsilon_{\text{carriers}} + \varepsilon_{\text{interband}} + \varepsilon_{\text{lattice}} + \varepsilon_{\text{core}}, \tag{6.1}$$

where ε_1 and $i\varepsilon_2$ are the real and imaginary parts of the dielectric tensor. The tensor for the complex index of refraction is defined in terms of the complex value:

$$(\mathbf{n} + i\boldsymbol{k})^2 = \varepsilon_1 + i\varepsilon_2. \tag{6.2}$$

So, the next equations relate ε_1 and ε_2 with the refractive index, *n,* extinction coefficient, *k*, and absorption coefficient, α, by the following equations:

$$\varepsilon_1 = n^2 - k^2, \quad \varepsilon_2 = 2nk, \quad k = \alpha/4\pi\lambda. \tag{6.3}$$

The variables ε_1 and ε_2 are related by the Kramers — Kronig relationship:

$$\varepsilon_1(E) = 1 + \frac{1}{\pi}\int_0^\infty \frac{\varepsilon_2(E')dE'}{E - E'} \tag{6.4}$$

and

$$\varepsilon_2(E) = \frac{2\pi e^2}{N}\int_0^\infty R^2(E)N_v(E')N_c(E + E')\,dE', \tag{6.5}$$

where *N* is the atomic density, *R (E)* is the distance dipole matrix element, and *Nv* and *Nc* are the valence and conduction band density of states (DOS), respectively; *R (E)* is generally independent of energy E [4].

The dielectric tensor of graphite as a solid with hexagonal lattice symmetry has two independent components: $\varepsilon_c = \varepsilon_{1c} + i\varepsilon_{2c}$ and $\varepsilon_a = \varepsilon_{1a} + i\varepsilon_{2a}$. They correspond to two different polarization directions of the electric field *E,* where *c* is a symmetry axis perpendicular to the basal plane. Two independent tensor components, ε_a and ε_c, correspond respectively to the optical electric field parallel,

$\boldsymbol{E}||\boldsymbol{a}$, and perpendicular, $\boldsymbol{E}||\boldsymbol{c}$, to the layer planes. More specifically, $E||a$ denotes the ordinary wave and $\boldsymbol{E}||\boldsymbol{c}$ the extraordinary wave. Since the cleavage plane is perpendicular to the *c* axis, ε_c can be easily determined by the normal incidence reflectance measurements. At the same time, ε_a cannot be obtained in such a way, which is caused by difficulties involved in preparing suitable surfaces parallel to the *c* axis. Because of the very different magnitudes of ε_a and ε_c, graphite and some related compounds exhibit highly anisotropic optical properties.

The data obtained for the ordinary wave show reasonable agreement among themselves. In the case of $\varepsilon_{\|}$, however, significant disagreement exists among the available sets of experimental data. Ignoring the differences inherent in the techniques used (optical and energy-loss spectroscopy), this disagreement may be caused by the difficulty in obtaining good surfaces parallel to the *c* axis, and the fact that all-optical data are derived from reflectivity measurements [4].

Reflection and refraction of electromagnetic waves by graphite. Properties of the EMW reflection by graphite surface have been studied in a very wide range of incident photon energy (wavelength range). The obtained results provided an understanding of the role of various types of charge carriers, lattice vibrations, and features of the structure, e.g. defects. These results noted directions of reflection application (see References mentioned above).

In the case of pristine graphite, $\varepsilon_{\text{carriers}}$, $\varepsilon_{\text{interband}}$, and $\varepsilon_{\text{lattice}}$ all contribute significantly at infrared frequencies. For pure graphite, the dielectric tensor ε is dominated by the $\varepsilon_{\text{interband}}$ term in the infrared and visible regions of the spectrum, since the valence and conduction bands of graphite are essentially degenerate along the edges of the Brillouin zone, HKH and H′K′H′, where the E_3 bands are split only by very small spin-orbit interaction energy of $2.2\text{x}10^{-4}$ eV [22, 23]. Interband transitions thus occur starting at the very low spin-orbit energy for k_z where the Fermi level crosses the HKH axis [24, 25] and continuing to higher energies for different k_z values. For pristine graphite, the Fermi level is located at approximately the mid-point of the small band overlap region which is ~0.04 eV wide. The onset of interband transitions occurs at a very low frequency and therefore contributes strongly to $\varepsilon_{\text{interband}}$.

The low-frequency interband transitions effectively obscure the characteristic structure in the optical reflectivity normally identified with the plasma frequency. For pristine graphite, the plasma frequency for **E||a** is estimated to be at ~0.5 eV [26], corresponding to the room temperature carrier density for holes and electrons of $2 \cdot 10^{-4}$/atom (as determined from transport measurements [27] and an in-plane dielectric constant of $\varepsilon_a = 2.8$ [28]). At low frequencies, the structure associated with the E_{1u} IR-active lattice mode was observed by [29] at 1588 cm^{-1} (0.197 eV), and the A_{2u} mode by [30] at 868 cm^{-1} (0.108 eV). The in-plane and *c*-axis lattice modes contribute to the dielectric tensor components ε_a and ε_c respectively. At higher frequencies, the structure in the optical reflectivity of pristine

graphite is identified with specific electronic interband transitions [31, 32]. In the vicinity of 0.8 eV, K-point transitions from occupied states in the E_2 valence band to empty states in the E_3 conduction band above the Fermi level (0.706 eV) and from occupied states in the valence E_3 band to empty conduction states in the E_1 band (0.889 eV) are observed using modulated reflectivity techniques [33—35]. Because of trigonal warping effects, there is a strong admixture of the E_3 bands [36] so that both E_3 bands couple to the E_1 and E_2 bands and contribute to the lineshape of each component of the doublet structure [34].

The complex dielectric constant $\varepsilon(\omega) = \varepsilon_1 + i\varepsilon_2$ and associated functions were derived by application of the Kramers — Kronig relation to reflectance data for graphite obtained in the energy range to 26 eV. It is possible to divide the optical properties into two spectral regions. In the range of 0 to 9 eV, intra- and interband transitions involve mainly π bands. At higher energies, a broad absorption peak near 15 eV is associated with interband transitions involving 3 σ electrons per atom. Plasma resonances that produce peaks in the energy-loss function $-Im\varepsilon^{-1}$ at 7 and 25 eV are identified and described physically. At low energies, structure in the reflectance curve near 0.8 eV is attributed to the onset of transitions between the E_2 and E_3 bands at the point K. This yields a value for γ_1 of ≈0.4 eV. The dominant structure in the optical reflectivity of graphite is, however, observed at ~5 eV, and identified with interband transitions between π-bands around the M-point in the Brillouin zone [10, 15, 31, 37]. Interband transitions involving σ-bands give rise to optical structure in the around 13 eV range. A large anisotropy in the optical properties of graphite is observed primarily because $\varepsilon_{\text{carriers}}$ is much larger for the polarization **E**||**a** than for **E**||**c** due to the large anisotropy in the effective mass tensor. Furthermore, $\varepsilon_{\text{interband}}$ is significantly different for the two polarizations due to differences in selection rules and magnitudes of matrix elements [10, 15, 38, 39]. On the other hand, many of the interband transitions occur away from high symmetry points in the Brillouin zone and therefore exhibit optical structures closely associated with maxima in the joint density of states. These maxima tend to be considerably less anisotropic than the other factors dominating the optical properties. Thus, $\varepsilon_{\text{interband}}$ for pristine graphite is less anisotropic than $\varepsilon_{\text{carriers}}$.

The data obtained for the ordinary wave show reasonable agreement among themselves. In the case of $\varepsilon_{\parallel}$, however, significant disagreement exists among the available sets of experimental data. Ignoring the differences inherent in the techniques used (optical, electron-energy-loss spectroscopy), this disagreement may be caused by the difficulty in obtaining good surfaces parallel to the *c* axis, and the fact that all-optical data are derived from reflectivity measurements.

The transverse dielectric function $\varepsilon = \varepsilon_1 + i\,\varepsilon_2$ of graphite for the electromagnetic wave normally incident on the trigonal plane is calculated based on the band structure for the far-infrared region [40], where the effects of free

carriers and spin-orbit coupling are predominant. In the absorption spectrum there appears van Hove singularity arising from the transition between the two degenerate bands near point *K* of the Brillouin zone split by the effect of spin-orbit coupling, but no observable structures from the vicinity of point *H*. The strength of spin-orbit coupling λ^{z}_{33} is not determined definitely from the experiment available but is estimated as 0.004eV (at point *H*) or 0.0055eV (at point *K*) as one of the possible values [40].

The reflectivity of freshly cleaved HOPG samples between 3 and 40 eV for different angles of incidence was measured in [14]. Synchrotron radiation was polarized either parallel or perpendicular to the plane of incidence with a degree of polarization between 0.9 and 0.97. The relative reflectance measurements for nine angles between 15 and 75° were performed, and ε_c and ε_a were determined by fitting *R* with the Fresnel formula for anisotropic uniaxial crystals. Absolute *R* at 15° (near-normal incidence) was used to obtain ε_c by the Kramers — Kronig analysis. The overall agreement with other optical measurements and with the EELS data was good.

The reflectance of both natural single crystals and HOPG was measured in [10]. The HOPG samples were prepared by cutting and mechanical polishing without an etching procedure. The surface area had a high degree of flatness, and *Rs* and *Rp* (reflectances corresponding to the electric field *E* perpendicular and parallel to the incidence plane, respectively) were measured from 1.9 to 5.15 eV at incidence angles from 10° to 80° with steps of 10° and angles of 75, 85, and 87°. In addition, *R* on polished surfaces, both parallel and perpendicular to the *c* axis, was measured in the 2—9 eV range to compare $E \perp c$ and $E \| c$ under identical surface conditions. Those data were not suitable for Kramers — Kronig analysis because of the inferior quality of polished surfaces compared with the cleaved ones. The values of $n_\perp$, $k_\perp$, and $n_\|$, $k_\|$ from 0.9 to 15.5 eV were obtained by the least-squares fit of *Rs* and *Rp* at different angles of incidence using the Fresnel relations for uniaxial materials. The values of $n_\perp$ and $k_\perp$ are in good agreement (±10%) with the data from [8] and [14].

In the infrared region, the reflectivity of HOPG for $E \perp c$ on the cleaved surfaces and for $E \| c$ on the polished surfaces was measured in [29]. The surface damage induced by polishing was accounted for by scaling the $E \| c$ spectrum with the ratio of $E \perp c$ spectra obtained from the cleaved surface and the polished surface, respectively.

The reflectance of graphite at normal incidence, from about 1.8 to 300 μm, and at thirty temperatures between 10 K and ambient was measured in [41]. Ellipsometry was also used to complement these measurements down to 0.3 μm (Figs. 6.1, 6.2). The far IR data are very important for astrophysics as the average thermal spectrum of thin quiescent clouds in the local space (diffuse galactic interstellar medium (DGISM) could be fitted by a gray-body spectrum at a tem-

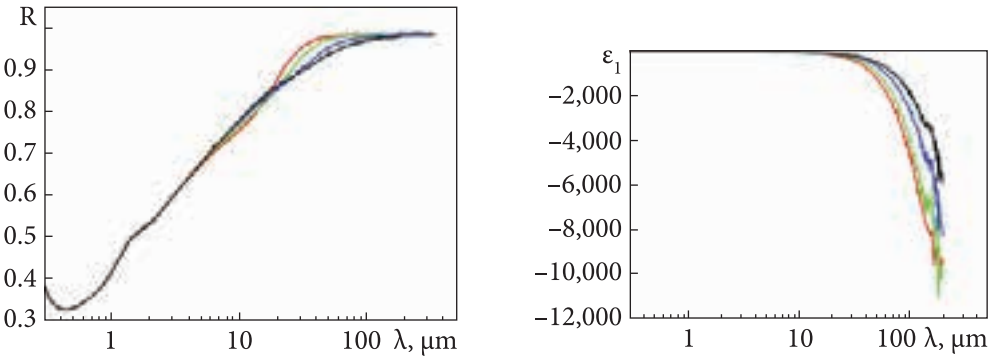

Fig. 6.1. Normal incidence reflectance on HOPG measured in [41] at 300 K (red, upper curve), 200 K (green), 100 K (blue), and 10 K (black, lower curve). The temperature effects are limited, essentially, to the range beyond 5 μm; in this range, reflectance increases with temperature by less than 10% [3]

Fig. 6.2. Real 30part of the dielectric function of HOPG measured in [41] at normal incidence, at 300 K (red, lower curve), 200 K (green), 100 K (blue), and 10 K (black, upper curve). The temperature effects are limited, essentially, to the range beyond 5 μm [3]

perature in the range 17—19 K. This spectrum, therefore, essentially covers the range from 100 to 1000 μm. The search for possible dust carriers of emission usually centers on graphite, or "astronomical graphite and amorphous silicate" [42].

The data were measured or deduced in [41, 42] for the normal incidence reflectance, R, in-plane conductivity, σ, and the real part of the dielectric function, ε_1. The imaginary part of the dielectric function, ε_2, is derived from the conductivity [43]:

$$\varepsilon_2 = 6 \cdot 10^{-3}\, \sigma\, (\omega^{-1}\mathrm{cm}^{-1})\, \lambda(\mu\mathrm{m}). \qquad (6.6)$$

From th00is, one can derive the refraction indexes n, k, the reflectance phase θ, the absorbance $\alpha = 4\pi k/\lambda$, and the absorption/extinction efficiency of small grains of radius a, *Q/a* [43].

When the temperature rises above 0 K, more and more electrons are freed from the valence band into the conduction band, leaving behind an equal number of holes. As the number of electrons per material cell is finite and constant (f-sum rule), the increased optical weight in the far-infrared (FIR) must be exactly compensated by a decrease in the adjacent part of the conductivity plateau, as evidenced by dips below the average plateau in the same figure. An adequate continuation into the FIR must account for both the increase and decrease of the conductivity (in different but adjacent parts of the IR spectrum), as the temperature varies [3].

All noted here experimental optical properties can be obtained directly from any pair among three quantities R, ε_1, and σ, for which experimental data were

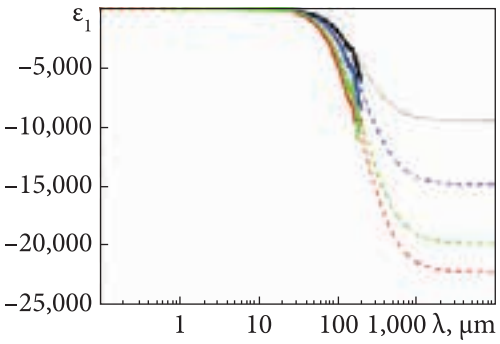

Fig. 6.3. Real part of the dielectric function of HOPG measured in [41] at normal incidence, at 300 K (red dots, lower curve)), 200 K (green dots), 100 K (blue dots), and 10 K (black dots, upper curve), superimposed upon the corresponding model spectra in dashed lines of corresponding colors [3]

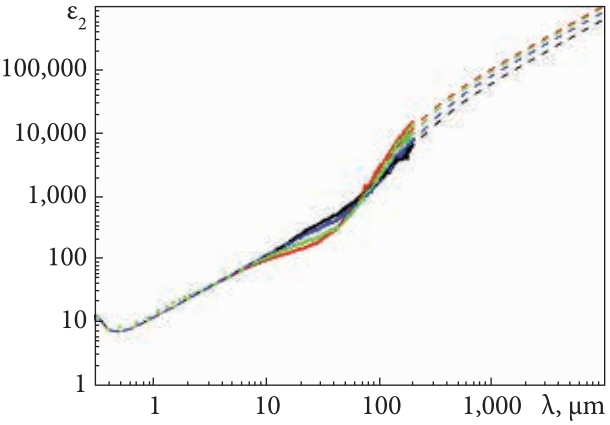

Fig. 6.4. Imaginary part of the dielectric function of HOPG as measured in [41] at normal incidence, at 300 K (red dots, upper curve), 200 K (green dots), 100 K (blue dots), and 10 K (black dots, lower curve), superimposed upon the corresponding model spectra in dashed lines of the corresponding colors [3]

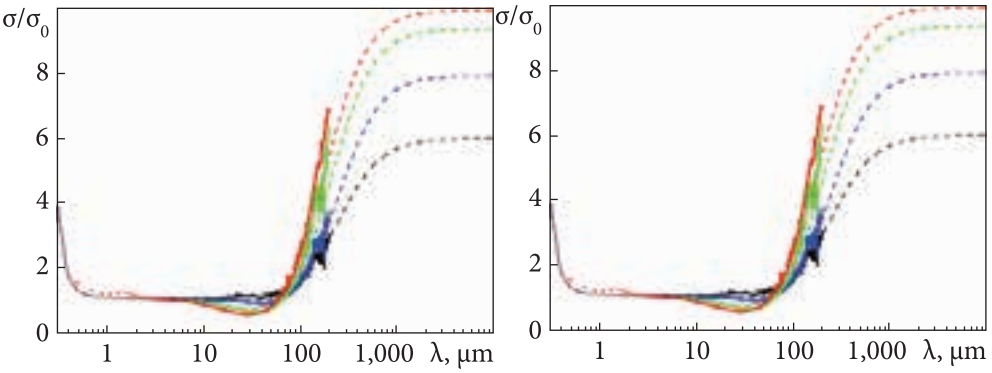

Fig. 6.5. Real part of the conductivity of HOPG as measured in [41] at normal incidence, at 300 K (red dots, upper curve), 200 K (green dots), 100 K (blue dots), and 10 K (black dots, lower curve), superimposed upon the corresponding model spectra in dashed lines of corresponding colors

Fig. 6.6. Reflectance of HOPG as measured in [41] at normal incidence at 300 K (red dots, upper curve), 200 K (green dots), 100 K (blue dots), and 10 K (black dots, lower curve), superimposed upon the corresponding model spectra in dashed lines of corresponding colors [3]

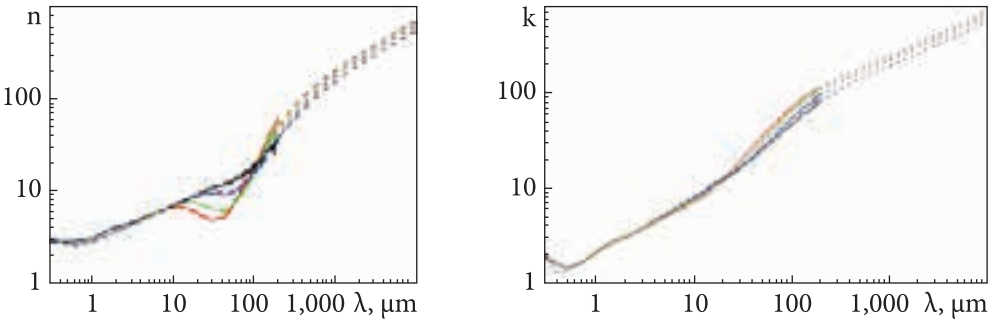

Fig. 6.7. Real part of the refraction index of HOPG as measured in [41] at normal incidence at 300 K (red dots, upper curve), 200 K (green dots), 100 K (blue dots), and 10 K (black dots, lower curve), superimposed upon the corresponding model spectra in dashed lines of corresponding colors [3]

Fig. 6.8. Imaginary part of the refraction index of HOPG as measured in [41] at normal incidence at 300 K (red dots, upper curve), 200 K (green dots), 100 K (blue dots), and 10 K (black dots, lower curve), superimposed upon the corresponding model spectra in dashed lines of corresponding colors [3]

given up to 200 μm [41]; they are therefore all labeled below as "measured". For a given temperature, a fit of this model to any of the latter two delivers all other optical quantities. In effect, the fits were optimized by simultaneous comparison of experimental and model spectra of ε_1, ε_2, σ/σ_0, R, θ, n, and k in the hope of compensating for possible measurement uncertainties. The fits were then perfected by optimizing the parameters using non-linear least-squares minimization based on the Davidon — Fletcher — Powell (DFP) method. The following figures (Figs. 6.3—6.8) illustrate the spectra delivered by the model (dashes) and superimposed upon the corresponding measured spectra (dots), using black, blue, green, and red colors for 10, 100, 200, and 300 K, respectively.

The discrepancy among the data can be partially explained by errors connected to the Kramers — Kronig analysis of reflectivity at near-normal incidence, and the difficulty of obtaining absolute values of reflectivity (particularly for large angles of incidence), and the different surface conditions which can significantly affect the reflectivity. However, these experimental difficulties do not explain why there are significant differences between ε_a obtained by reflectivity measurements and that by electron energy-loss spectroscopy (EELS) in the range 2—18 eV [7]. E.g., EELS data give a sharp peak at 11 eV in ε_{2a}, which is several times larger than the estimated experimental uncertainty [9], which is absent in the optical data. Also, the band structure calculations predict that there would be a bandgap of around 5 eV for the parallel polarization, but this does not coincide with the EELS data. Despite many attempts to correlate the experimental dielectric function features with the transitions predicted by band structure calculations [10, 12, 15, 17, 18, 44—46], the ques-

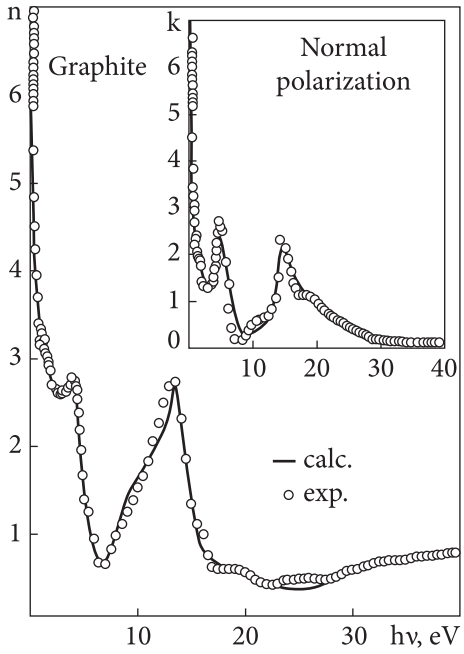

Fig. 6.9. Real part of the refraction index $n\perp$ of graphite as a function of energy for normal polarization. The inset shows its imaginary part $k\perp$ *vs* energy. The open circles represent experimental data, while the solid line represents calculated values [7]

tion as to whether EELS data or optical data would describe the optical properties for extraordinary waves in graphite more accurately is still unresolved [7].

Another model was described and discussed for the optical constants of graphite over a wide frequency range (0.12—40 eV) for ε_c and (2—40 eV) for ε_a in [7]. The modified Lorentz — Drude oscillator model was employed. In this model, damping is described with the frequency-dependent function instead of a constant, with one additional parameter per oscillator. In this way, the shape of the spectral line is an adjustable parameter of the model, thus allowing greater flexibility. Since the model is based on damped harmonic oscillators, it satisfies the causality, linearity, reality, and Kramers — Kronig requirements. The experimental data used in this work are tabulated in the Handbook of Optical Constants II [13]. For ε_c, the data obtained in [14] are used in the range 5—40 eV, the data from [10] in the range 2—5 eV, and the data of [29] in the range 0.12—0.22 eV [7].

Fig. 6.9 shows the real and imaginary parts of the refraction index corresponding to $E\perp c$ vs the energy. The open circles represent the experimental data, while the solid line represents the calculated values obtained. A good agreement between the experimental and calculated data can be observed for both the real and imaginary parts of the refraction index. It should be noted that the experimental data for ε_c obtained by the EELS and by the reflectivity measurements agree well among themselves; they also agree well with the theoretical calculations. The experimental data for ε_{2c} show a sharp peak at 4.5 eV and a broader peak at 14.5 eV, which can be accounted for by band structure calculations [7, 10, 11, 15, 16, 18, 44—46].

Plasma frequency corresponding to collective excitations of π electrons is around 7 eV [8, 11, 12, 14, 47] while the π + σ plasmon corresponding to the collective excitation of all four electrons is around 27 eV [12, 14]. This is in contrast with the earlier work [8], which predicts the π + σ plasmon to be around 25 eV. The effective number of electrons per atom calculated with the experi-

mental data for normal polarization saturates at four electrons per atom above 30 eV, as expected (for 1π and 3σ electrons) [7, 8, 12, 14].

Unlike the ε_c data, there are significant discrepancies between the EELS and the reflectance data for ε_a. The theoretical calculations also disagree in certain aspects. Major discrepancies between the EELS and the optical data occur in the range from 2 to 18 eV. Beyond 18 eV, the EELS data from [9] join smoothly the reflectance data of [9, 14] where an electron-energy-loss spectrum of HOPG samples of about 1000 Å thickness was measured. The resulting ε_a was in very good agreement with the previous EELS measurements. A sharp maximum in ε_{2a}, which is absent in the optical data, was established beyond experimental and computational errors. Band structure calculations also disagree among themselves over this point, giving no conclusive evidence in favor of or against the strong transition at ~11 eV. The existence of a peak around 11 eV is in agreement with the calculations in [45], though the calculations in [18] predict the existence of transitions at 13.5 or even at 16 eV, and calculations of [12] predict transitions to be around 11 and 16 eV [7].

A large discrepancy also exists in the range below 6 eV. The data from [10] and from [20] show no structure in this range, which is in agreement with the band structure calculations employing a two-dimensional (2D) approximation [13, 45]. However, made in [15] calculations predict a peak near 4.3 eV, which is also present in the data from [14]. A possible reason for the absence of this small peak in former cases can be the slight depolarization of light in the experiments. Transitions between π bands, which are forbidden for $E \| c$ in a single layer, are not strictly forbidden in a 3D lattice. Nevertheless, the matrix elements are much smaller than those for the perpendicular polarization, thus accounting for the small magnitude of the peak [15, 17]. However, the breakdown of the selection rules for the 3D case predicted by made in [15] calculations still does not justify the data obtained by the EELS in this region [7].

It is difficult to establish which of those two methods, the reflectance measurements or the EELS, is correct. The reflectance measurements of the optical constants for $E \| c$ cannot be performed directly because of the difficulties in preparing suitable good quality surfaces. Therefore, values of the refraction index for a parallel polarization have to be deduced from reflectance measurements under oblique incidence. For an anisotropic material, at each wavelength, a function of five variables (the real and imaginary parts of the dielectric function for perpendicular polarization, the real and imaginary parts of the dielectric function for parallel polarization, and the degree of polarization) is minimized to determine values which give minimal discrepancy between calculated and measured reflectances. It is well known that this is not a simple problem (mainly due to the existence of multiple solutions), even in a simple case of isotropic material and reflectance measurements at normal incidence, where only two variables, namely

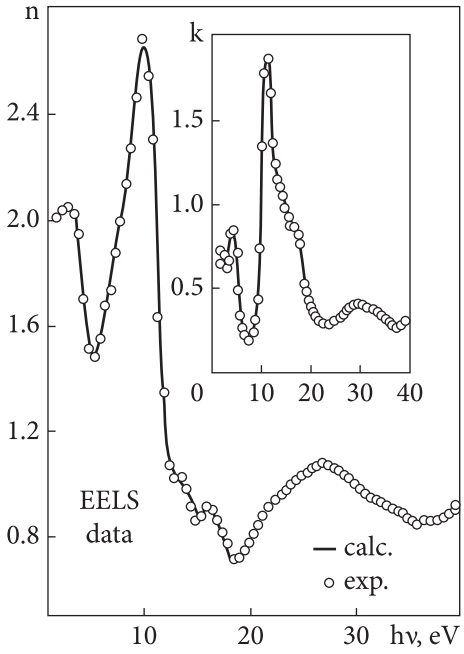

Fig. 6.10. Real part of the refraction index n_a of graphite as a function of energy for normal polarization. The inset shows its imaginary part k_a *vs* energy. The open circles represent EELS experimental data, while the solid line represents calculated values [7]

n and *k*, have to be determined. Hence, there exists a large uncertainty of the determined values (±10%). On the other hand, EELS may not be accurate in the low-energy range, because in this range, the relativistic (Cherenkov's) effects contribute significantly to the energy loss when the momentum transfer has large components along the *c* axis [12]. Another strong objection to EELS data is that they do not agree with the theoretical prediction of the bandgap of about 5 eV. In order to check the consistency of experimental data, finite-energy sum rules have been applied in the literature [12, 14]. However, the effective number of electrons per atom in case of parallel polarization, as calculated from both the EELS data [12] and reflectance data [14] is below three at 40 eV (and it is far from saturation since plots show slope of about 45°), so no conclusion can be drawn from that except that there are some higher-lying transitions involving the valence-band electrons [7].

Since all previous theoretical considerations (for recent first-principles calculations [17] have failed to resolve the issue as to whether the EELS or the optical data represent an accurate description of the optical constants of graphite for the parallel polarization; both sets of available data for $\varepsilon_{\parallel}$ were applied. One set consists of the EELS data in the 2—18 eV range [9] and in the 18—40 eV range [14]. The other set consists of the data derived from the reflectance measurements from [10] in the 2—5 eV range and from [14] in the 5—40 eV range. Plasma frequencies for ε_a are around 14 eV [12] and 19 eV [7, 12, 14].

The real and imaginary parts of the refraction index corresponding to $E \| c$ as a function of energy are shown in Fig. 6.10. The open circles represent the EELS experimental data, while the solid line represents the calculated values. A very good fitting can be noted between experimental and calculated values [7].

As mentioned earlier, the optical data show the existence of a bandgap predicted by theoretical calculations. Therefore, in modeling the optical data we do not consider the intraband contributions because they would not be consistent with the small values of k_a for low energies. However, in trying to fit the set of

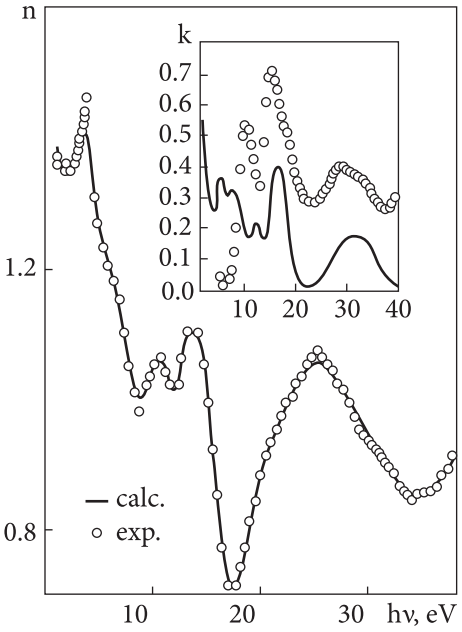

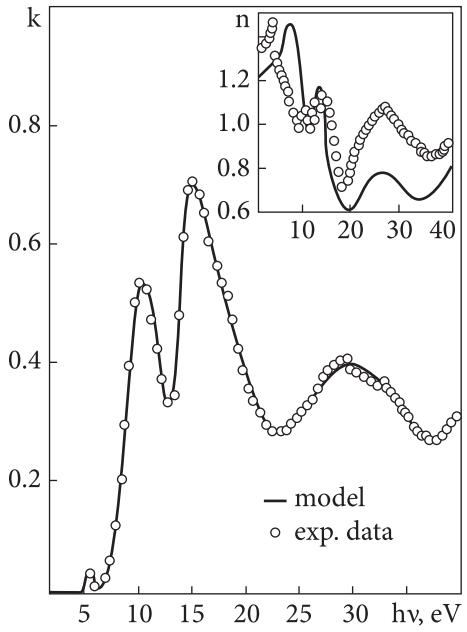

Fig. 6.11. Refraction index n_a as a function of energy. The open circles represent experimental data from optical measurements, while the solid line represents calculated values. The inset shows k_a as a function of energy [7]

Fig. 6.12. Coefficient of extinction k_a *vs* energy. The open circles represent experimental data from optical measurements, while the solid line represents calculated values. The inset shows n_a as a function of energy [7]

data derived from the reflectance measurements, we encountered unexpected difficulties. When we attempted to adopt the usual objective function which minimizes discrepancies between experimental and calculated data for both the real and imaginary parts of the dielectric function, or the refraction index, the algorithm did not converge at all. Changing the number of oscillators employed did not appear to influence that. Since we use a global optimization routine, which has been severely tested for problems with up to 100 variables and up to 15^{100} local minima [48], the only reason for divergence could be that the experimental data cannot be described with the model employed. On the other hand, there is no reason for the optical constants of any material in the studied spectral range could not be described with the Lorentz or Lorentz — Drude oscillator model. Then, an attempt to fit separately the real and imaginary parts of the refraction index was made, and the results are shown in Figs. 6.11 and 6.12, respectively [7].

In minimizing the errors for n and k separately, no numerical problems were encountered. However, it turned out that excellent agreement for the real part of

the refraction index n_a, as shown in Fig. 6.11, leads to the poor agreement for the imaginary part k_a, and *vice versa*, as shown in Fig. 6.12. Since the model automatically satisfies Kramers — Kronig relations, agreement with the experimental data should be, in principle, equally good for both the real and imaginary parts of the refraction index. Moreover, it can be observed that the refraction index experimental curve fails to show a structure corresponding to the obvious peak in the coefficient of extinction around 11 eV. Also, there is no justification for the very sharp peak in experimental n (ω) near 5 eV, which appears to be unrelated to any feature of k (ω). It should be pointed out that values for the real and imaginary parts of the dielectric function for the parallel polarization were calculated independently for each wavelength [14] so there is no guarantee that the experimental data satisfy Kramers — Kronig relations. Therefore, a check whether the experimental data are Kramers — Kronig consistent was made [7].

The Kramers — Kronig transformation for a set of data for the imaginary part of the refraction index k_a has been performed. Since the data [14] cover the 3—40 eV range, the data from 2 to 3 eV were used [10]. In the region where these two data sets overlap, the data from [14] were used because they show a weak peak in k_a, as predicted by the band-structure calculations based on 3D approximation [15]. The data for the imaginary part of the refraction index resemble the theoretically predicted structure. There is one small peak at 4.3 eV, which is due to the breakdown of selection rules for 3D lattice [15] and a two-peak structure around 11 and 14 eV [10]. Obtained results are depicted in Fig. 6.13 showing a comparison between the tabulated experimental data (solid line) and the results of the Kramers — Kronig transformation (dotted line) [7].

It can be observed that the Kramers — Kronig transformation gives a curve for n_a which significantly differs from the tabulated data, where only differences at the range end can be attributed to the errors in the Kramers — Kronig analysis. Those errors are in part due to the higher-lying transitions whose existence can be deduced from the fact that the effective number of electrons per atom for the parallel polarization is far from the saturation value at 40 eV [12, 14]. Since the real and imaginary parts of the refraction index have to satisfy the Kramers — Kronig relations, the original experimental data were modeled by k_a, while for n_a, the Kramers — Kronig transformation of experimental values of k_a in the spectral range up to around 26 eV was employed, and the original experimental values of n_a from 26 to 40 eV to avoid errors induced by the Kramers — Kronig transformation at the end of the region. Fig. 6.14 shows the real and imaginary parts of the refraction index as a function of energy.

The open circles represent the experimental data for the imaginary part, the triangles represent the real part obtained by the Kramers — Kronig transformation, and the solid line represents the calculated values. It can be observed that for this composite set of data (original experimental values for k_a and the

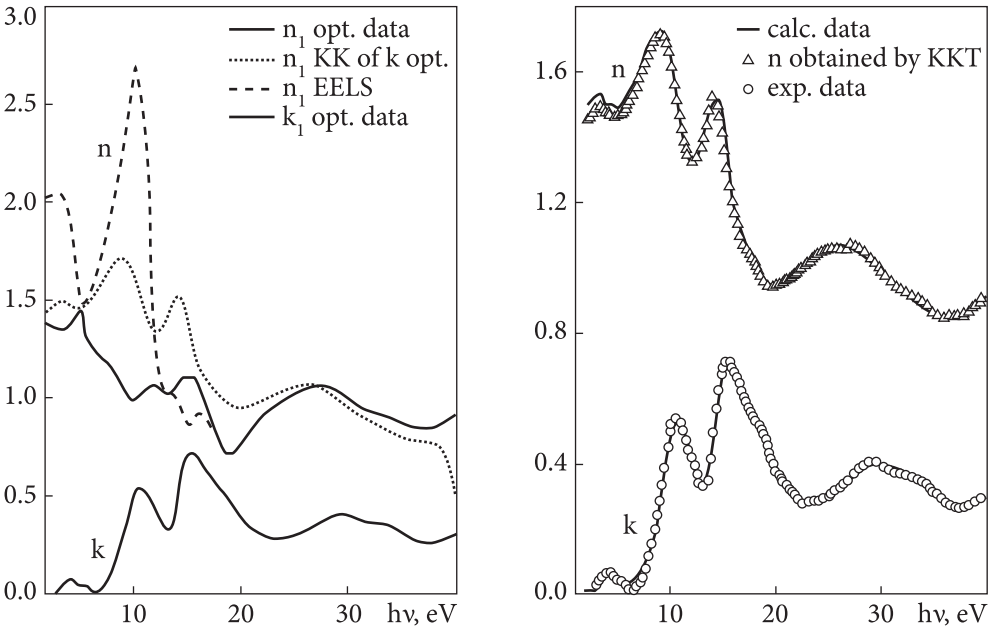

Fig. 6.13. Comparison among the available sets of data for n_a: tabulated experimental data from the optical measurements (solid line), the result of Kramers — Kronig transformation (dotted line), and data obtained by EELS (dashed line) [7]

Fig. 6.14. Real and imaginary parts of the refraction index of graphite *vs* energy for parallel polarization. Open circles represent the experimental data for the imaginary part of the refraction index, while triangles represent the real part obtained by Kramers — Kronig transformation, and the solid line represents calculated results [7]

Kramers — Kronig transformation for n_a), there exists good agreement with the experiment for both the real and imaginary parts of the refraction index [7].

Therefore, to describe the optical constants of graphite for the parallel polarization, one should use the data obtained from optical measurements for the imaginary part of the refraction index, while for the real part, the Kramers — Kronig transformation of these data should be employed. The data set obtained in such a way, which can be easily and accurately reproduced by the model described here, is internally consistent and in agreement with the theoretically predicted optical features. Taking into account the band structure calculations, there is reasonable doubt about the accuracy of EELS data for lower energies, especially when they do not confirm the existence of a gap of about 5 eV for parallel polarization [7].

The optical properties for the polarization **E||c** axis in pristine graphite are extremely difficult to measure quantitatively because of the experimental problem of preparing good optical quality "*a*-faces", containing both *a* and *c*-axes. In contrast, high-quality optical surfaces are easily prepared by cleavage on "*c*-faces", containing only *a*-axes. The most reliable *a*-face samples that have been

prepared were mechanically polished and then sputter-etched with argon ions [49]. The mechanical polish produces improved optical surfaces but degrades the crystal ordering, while the argon ion sputtering removes much of the crystal damage but introduces a pitted surface with lower reflectivity. It is shown that the values of $\varepsilon = 3.4 \pm 0.4$ have been obtained by reflectivity measurements on sputter-etched *a*-faces [49] and $\varepsilon_c = 5.8$ was obtained for mechanically polished surfaces [30]. These values are to be compared with $\varepsilon_c = 5.4$ obtained by energy loss experiments through thin *c*-face samples [50]. Optical reflectivity studies have been carried out on *a*-faces for graphite [10, 30, 38].

Theoretical considerations suggest that the free carrier contribution to the dielectric tensor $\varepsilon_{\text{carriers}}$ for **E**||**c** is smaller than for **E**||**a** by more than one order of magnitude, primarily because the effective mass component m_{zz} is about two orders of magnitude greater than m_{xx} in graphite. Thus $\omega_{p,c}$, the plasma frequency for **E**||**c**, is expected to be much smaller than $\omega_{p,a}$ for **E**||**a**:

$$\omega_{p,c}^2 = (4\pi Ne^2 / m_{zz}^*) << \omega_{p,a}^2 . \tag{6.7}$$

Anisotropy in the interband contribution to the dielectric tensor is also expected since $\varepsilon_{\text{interband}}$ depends on the momentum matrix elements $\left|\langle p_z \rangle\right|^2$ for **E**||**c** and $\left|\langle p_x \rangle\right|^2$ for **E**||**a**. On the basis of $\mathbf{k} \cdot \mathbf{p}$ perturbation theory, these matrix elements are related to the effective mass components according to the relation:

$$\frac{\left|\langle p_x \rangle\right|^2}{\left|\langle p_z \rangle\right|^2} \sim \frac{m_{zz}}{m_{xx}} . \tag{6.8}$$

The calculation of the optical anisotropy of graphite based on a three-dimensional electronic energy band structure shows that the dominant structures in ε_c and ε_a occur at approximately the same photon energies, primarily because interband transitions occur over large volumes of the Brillouin zone [15]. As for graphite, interband contributions to both ε_a and ε_c are primarily sensitive to the joint density of states. However, the structure for the **E**||**c** polarization tends to be about one order of magnitude smaller relative to that for the **E**||**a** polarization, reflecting the anisotropy in the matrix elements and polarization-dependent selection rules. These aspects are in good agreement with both optical and electron energy loss measurements on graphite (see [10] and [51], respectively). Two-dimensional models have frequently been used to discuss the optical properties of graphite, though they are not as useful for treating optical anisotropy as three-dimensional models [18, 51]. The LMTO-ASA method including the combined correction terms has also been used for the calculation of the frequency-dependent anisotropic dielectric function of graphite, and a comparison with the experimental data showed good agreement [52].

Absorption of electromagnetic waves by graphite. Even though direct measurements of graphite absorption/transmittance are very difficult as compared with measurements of reflection, they have been performed many times. The range of similar studies is very wide as well. The optical absorption of graphite was experimentally determined by reflectance [8, 14] and energy loss via Kramers — Kronig [12, 14, 51, 53]. Transmission of infrared radiation through ultrathin single-crystal flakes of graphite was measured, which shows peaks near 0.82 eV [54].

The model of absorption efficiency for grains of radius a, small relative to the wavelength λ, is defined as:

$$Q / a = \frac{24\pi}{\lambda} \frac{\varepsilon_2}{(\varepsilon_1 + 2)^2 + \varepsilon_2^2}, \tag{6.9}$$

where a and λ are in the same length units.

Fig. 6.15 shows Q/a for the same four typical temperatures as above. The same quantity directly derived from data in [41] for each of these temperatures is also shown. Again, the agreement between corresponding pairs of curves, in the range where they overlap, is excellent, confirming the consistency of the model [3].

In contrast to Q/a, absorbance α of bulk material increasing will be shown below (Fig. 6.16) in the same range, as it includes both absorption and reflectance losses. Overall, the grain efficiency scales like λ^{-2}.

Several measurements were previously performed on essentially graphitic, but disordered, materials in the form of more or less fine grains [56]. Some of them are displayed in Fig. 6.10, for comparison. The figure also includes glassy carbon data derived by [57]; this material can be imagined in the form of ribbons of graphite [58]. Also shown are our model α and Q/a for 300 K. The latter two are seen to bracket all the former.

This variety of optical data on essentially the same material is most likely due to the variety of physical structures, ranging from small, pure, isolated spheres (described by Q/a) to bulk pure material (described by α). The computations of [57] convincingly demonstrated how α varies with intermediate structures like continuous distributions of randomly oriented ellipsoids (CDE), fractal clusters of ellipsoids (FC), and homogeneous porous aggregates. These are accompanied by smaller power indexes, β, as well as absorbance enhancements relative to isolated spheres, with β ranging roughly between 0.6 and 1.25. Fig. 6.16 shows a similar variety of absorbances and power indexes, covering a significant part of the interval between the curves for α and Q/a, again for essentially the same material, graphite (at the microscopic level) [7].

This behavior can be understood by considering the large difference between Q/a and α, which is small in the UV and increases steadily with λ. It is due to the increased shielding of the isolated grain interior from the external field, by the

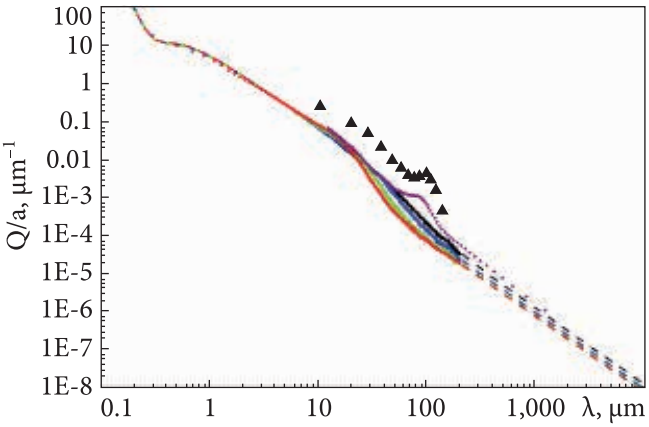

Fig. 6.15. The absorption efficiency computed from the dielectric functions of graphite in the $c \perp E$ orientation for 10, 100, 200, and 300 K (the same conventions as in previous figures). The efficiency decreases with temperature, but slightly and beyond $\lambda = 10$ μm. Also drawn is the curve deduced from the data [59] (purple dots) with its characteristic bump of around 80 μm. Triangles represent data deduced from [60] and adapted from [56]. The particles are assumed to be in the Rayleigh limit [3]

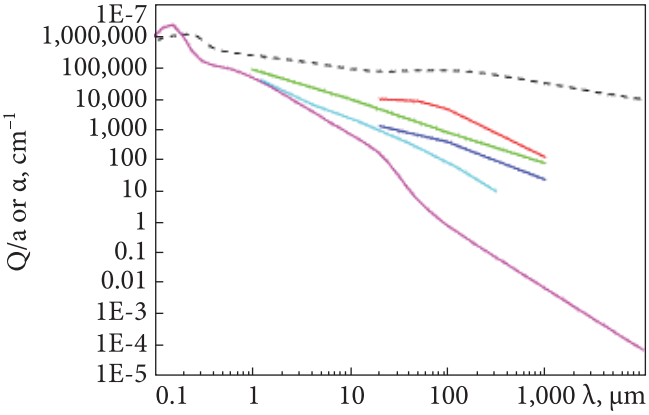

Fig. 6.16. *Q/a* for small oriented spheres of HOPG ($c \perp E$; lower, purple line). Corresponding absorbance, α (upper, black dashed line). Bottom-up: α for glassy carbon, adapted from [47] (cyan line); α for one of the lesser evolved coal [59] (blue line); α for powder graphitic material from electrical discharge in various gases, TH, BE, XY, adapted from [60] (green line); α for graphitic powder, adapted from [59] (red line). All spectra were measured at room temperature [3]

surface charges [43]. As the grains grow larger and/or closer to one another, the shielding becomes less and less effective due to the interneutralization of adjacent surface charges, resulting in increased absorption α. At the sample end of continuous solid material, there is no shielding at all. Now, the data in Fig. 6.16 were obtained not on isolated particles, but on pressed pellets of such particles. One cause of the observed behavior of the experimental data may therefore be more or less dense packing of the powder particles. The quantitative results of the present work indicate that small isolated grains of pure graphite are not suitable to model the long wavelength spectrum of IS emission for *a)* its emissivity is too low, *b)* its β

is too high in absolute value. However, these results should be of help in updating the computed properties of clusters, aggregates, and composite grains [7].

On the other hand, really (microscopically) amorphous carbons have recently shown a better potential for modeling IR emission beyond 10—20 μm. Examples are HAC or a-C : H amorphous carbons or kerogen/CHONS [3, 60—64]. When associated with amorphous silicate, the latter material ($\beta \sim 1.4$ [15]) was shown to quantitatively fit, in particular, the DGISM observed by the Planck satellite [7].

When discussing the relevance of graphite to FIR astrophysics, one must take into account all possible orientations of graphitic dust. Now, the measurement of the dielectric properties of graphite when $E||c$ is much more difficult than when $E\perp c$. Thence the dearth of results on the former orientation, except in DC (see the literature cited in the previous section). The consensus is that, roughly, the ratio of resistivities in the two orientations is about 100. If this ratio is assumed to hold all through the FIR, then the absorption efficiency for $E||c$ is expected to be 100 times higher than for $E\perp c$. This would bring it to about 100 cm^{-1} at $\lambda = 1000$ Å (Fig. 6.16), opening up the possibility to contribute to the Diffuse Galactic FIR continuum [7].

A satisfactory agreement between the level and trends of reflectances of graphites from different metamorphic environments throughout the spectrum was found in [65], with the maximum relative difference in the most difficult conditions in the blue region being approximately 4%. There was not such a good agreement between the dispersion curves of derived refraction and absorption indices for which the maximum relative difference is as high as 12% in the red region. At 546 nm, the wavelength at which optical data in organic petrology are principally reported, relative errors below 1% for all the optical parameters were well with other recent estimates and the true constants for graphite at this wavelength must lie close to these values. The use of semi-graphites as metamorphic indicators in a scale with graphite as the end-point was considered since there are implications on such a scale for the current use of natural surfaces for reflectance measurement [65].

Graphite lattice vibrations and their spectroscopy. Studies of graphite compound lattice vibrations spectra are a fruitful research area because of the wealth of microscopic information provided by them. Interpretation of these experiments is simplified by the layer structure of these compounds, exhibiting very strong intralayer binding and relatively weak interlayer bonding.

The layer structure of these materials allows the separation of the lattice modes into in-plane and *c*-axis modes. Experimental studies have largely focused on the in-plane lattice modes because the cleavage plane is a *c*-face, and good optical surfaces can be prepared by cleavage. For the case of graphite intercalation compounds, the high symmetry of the graphite lattice is an approximate symmetry for the larger real space unit cell in intercalation compounds.

This approximate symmetry gives rise to zone-folding phenomena through which certain non-zone-center q-vectors for graphite are mapped into the zone center in an intercalation compound, thereby turning on new Raman-active modes. This zone-folding phenomenon is another reason for the basic graphite mode structure to be of great importance for the understanding of intercalation compounds. Because of the high optical absorption of graphite, Raman scattering experiments on in-plane modes are conveniently performed on cleaved *c*-faces using a Brewster angle back-scattering geometry. Incident photons are typically provided by a CW argon-ion laser, though other excitation sources are preferred in certain cases, such as resonant enhancement studies. The scattered radiation is analyzed by a conventional double grating monochromator. To prevent sample instabilities and intercalant desorption, Raman measurements are conveniently made using low laser power (<50 mW) and low temperature (e.g., 77 K). Encapsulation of Raman and IR samples in ampoules fitted with suitable optical windows is usually necessary for maintaining the stage fidelity of the samples during spectroscopic measurements. To excite *c*-axis modes, light with the E-vector along the *c*-axis is introduced onto an optical *a*-face, which can be prepared by sputtering with argon ions [56, 63].

Raman and inelastic neutron scattering, as well as IR spectroscopy, being routine and non-destructive ways of various materials study, provide a good opportunity to obtain the detailed bonding structure of graphite and other carbon materials [64]. Since Raman spectroscopy is a scattering phenomenon, the change in frequency between the incident and scattered neutron or photon is measured to determine the frequency of absorbed or emitted photons. Because of the small wave vector of the incident and scattered photons, the first-order Raman spectroscopy is limited to the observation of lattice modes close to the Brillouin zone center, in contrast to the case of inelastic neutron scattering where by using a thermal neutron beam, the whole Brillouin zone can be explored. Although first-order Raman spectroscopy only provides information on phonons at $q \approx 0$, information on the phonon dispersion relations for other points in the Brillouin zone can be obtained from second-order spectra, where contributions are made by pairs of phonons with wave vectors $\boldsymbol{q}$ and $-\boldsymbol{q}$. Second-order Raman lines are generally broad because many phonon pairs with different energies contribute to the line, and the resulting line emphasizes those regions in the Brillouin zone having high densities of states. If the graphite lattice contains ordered defects, the high symmetry of the graphite lattice is an approximate symmetry for the larger real space unit cell. This approximate symmetry gives rise to zone-folding phenomena through which certain non-zone-center $\boldsymbol{q}$ vectors for graphite are mapped into the zone center for the intercalation compound, thereby turning on new Raman-active modes. That is why the basic graphite mode structure is of great importance to the understanding of any other carbon materials.

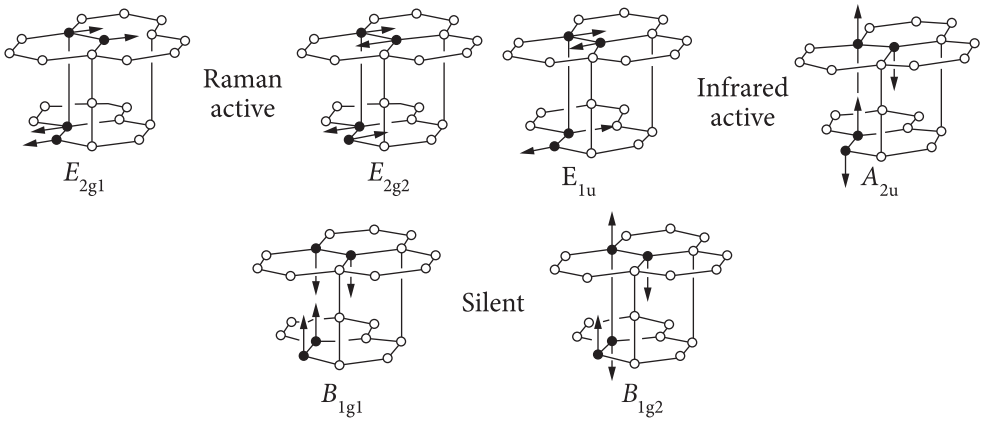

Fig. 6.17. Zone-centre optical lattice modes in pristine graphite. For the in-plane modes (E_{1u}, E_{2g1}, E_{2g2}), only one of the degenerate pairs of modes is shown. The *c*-axis modes (A_{2u}, B_{1g1}, B_{1g2}) are non-degenerate. IR and Raman activity are indicated. The zero-frequency acoustic modes (E_{1u}, A_{2u}) corresponding to pure translations are not shown [4, 29]

A brief summary of the lattice mode structure of pristine graphite and of isolated graphite layers is presented below. Pristine graphite crystallizes according to the D^4_{6h} space group and has twelve vibrational modes at $q = 0$. These modes have been classified as three acoustic modes ($E_{1u} + A_{2u}$), three infrared active modes ($E_{1u} + A_{2u}$), four Raman active modes ($2E_{2g}$), and two silent modes ($2B_{1g}$) (Fig. 6.17) [4, 29].

It should be noted that macroscopic single crystals of graphite do not occur in nature. So-called kish graphite, which is often referred to as a single crystal, consists of many small crystallites (up to 100×100 μm^2) oriented randomly. Highly oriented pyrolytic graphite (HOPG) is artificially grown graphite with an almost perfect alignment perpendicular to the carbon planes [66]. So, that is a very important circumstance that has to be taken into account when optical properties and, particularly, Raman scattering are discussed.

The frequencies of the in-plane Raman-active E_{2g} mode and the IR active E_{1u} mode are well established at $\omega(E_{2g}) = 1582 \pm 1$ cm^{-1} (usually labeled for "graphite" as "G"-line) [67, 29] and at $\omega(E_{1u}) = 1588 \pm 2$ cm^{-1} [30, 68]. Because of the strong intralayer force constants relative to the interlayer force constants, the vibrational frequencies of these modes are nearly the same and are almost entirely determined by simple optical displacements of the two inequivalent carbon atoms in a single layer plane. The small frequency difference of ~6 cm^{-1} between $\omega(E_{2g})$ and $\omega(E_{1u})$ is associated with interlayer force constants arising from differences with respect to interplanar displacements (Fig. 6.17). This small frequency difference thus provides a measure of the magnitude of these interlayer force constants.

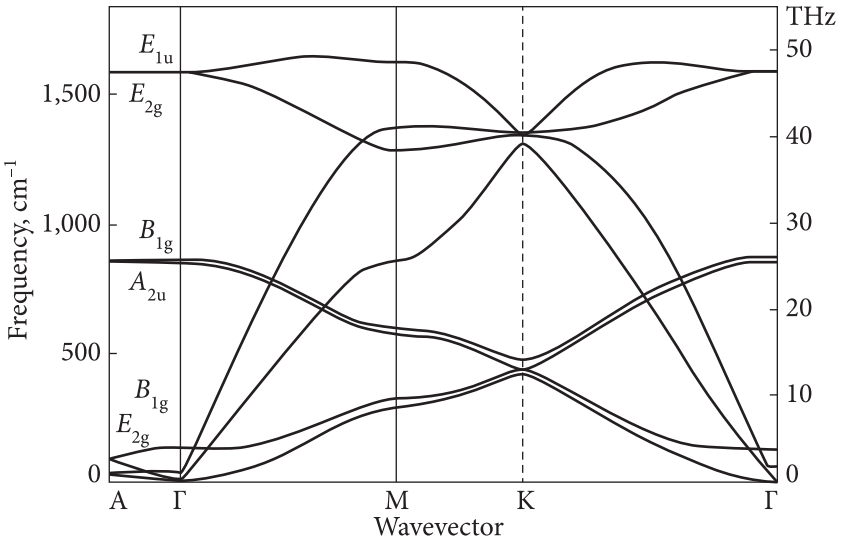

Fig. 6.18. Graphite phonon dispersion curves along several high symmetry axes. The Γ-point symmetries for the graphite structure are indicated [65]

The Raman [68] and inelastic neutron scattering data [69] have allowed identifying the caused by interplane vibrations low-frequency E_{2g1} mode at 48 and 42 cm^{-1}, respectively, while using IR spectroscopy the out-of-plane A_{2u} mode was found near 868 ± 1 cm^{-1} [30]. The silent out-of-plane B_{1g1} mode at 128 cm^{-1} (Fig. 6.17) has been identified on the basis of inelastic neutron scattering measurements on low frequency (470 cm^{-1}) phonon branches [69].

Analysis of the inelastic neutron scattering data for graphite has provided phonon dispersion curves for the two lowest frequency phonon branches along ΓM (see the Brillouin zone in Fig. 6.18) [69]. Near the M-point, the two lowest frequency modes are nearly degenerate at ~466 cm^{-1} and correspond to *z*-axis displacements. Using the two lowest frequency phonon dispersion curves obtained from these neutron diffraction measurements and the zone center A_{1u}, E_{1u} and E_{2g} mode frequencies measured by IR and Raman spectroscopy, a Born-von Karman force constant model has been used to yield the phonon dispersion relations for the higher-lying phonon modes. The results obtained on this basis are shown in Fig. 6.18 and provide a framework for discussion of the lattice mode structure for intercalated graphite [65]. Other models for the phonon dispersion relations have also been proposed [69—72] but none of these models is consistent with the identification of the A_{2u} zone center mode frequency at 868 cm^{-1}. Since the only available experimental information on a frequency above ~500 cm^{-1} is the Γ-point mode frequencies for the E_{2g2}, E_{1u}, and A_{2u} modes, the calculated dispersion relations for above ~500 cm^{-1} are more tentative than at the lower frequencies where inelastic neutron scattering information along several sym-

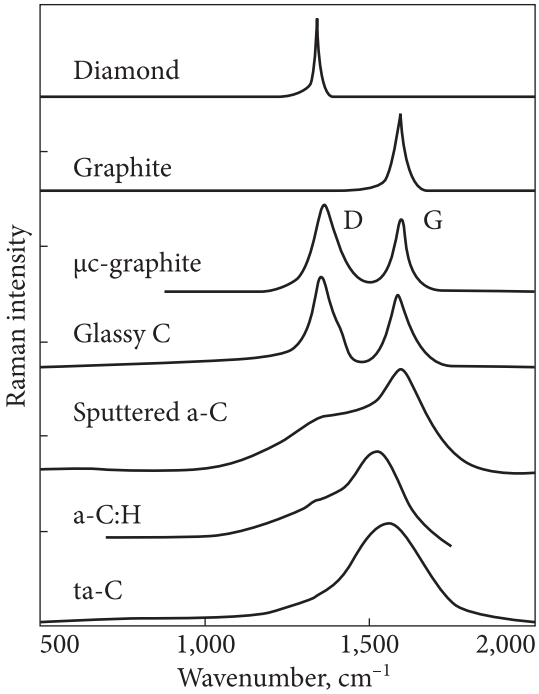

Fig. 6.19. The typical Raman spectra of some carbon materials [74]

metry directions in the Brillouin zone has been used in obtaining the dispersion relations.

Second-order Raman spectra for pure graphite have also been reported showing a strong feature near 2710 cm^{-1} and two weaker features at ~2450 and ~3250 cm^{-1} [72, 73]. Observation of the second-order frequencies higher than $2\omega(E_{1u})$ is of particular significance. This result is consistent with the phonon dispersion relations in Fig. 6.18 (and with other proposed models), which show that the maximum phonon frequency does not occur at $q = 0$. Since the second-order spectra are associated with phonons of wave vectors **q** and **–q**, these measurements are sensitive to the phonon density of states. We can note from Fig. 6.18 that the highest frequency branch along ΓM shows a large density of states near the maximum phonon frequency, thus accounting for the frequency of the 3250 cm^{-1} second-order line [72, 73].

Some patterns of the Raman scattering spectra of various types of carbon materials are shown in Fig. 6.19 [74].

IR spectroscopy can probe IR-active modes of very small wave vectors because the wave vector of incident photons is very small compared with the Brillouin zone dimensions. Being sensitive to odd-parity phonon modes, IR spectroscopy provides a complementary tool to Raman spectroscopy, which is sensitive to even-parity modes. This complementarity applies to pristine graphite because the inversion symmetry of its crystal structure designates each lattice mode by either even or odd parity. Because of the high optical absorption of graphite and of intercalated graphite, IR spectra are taken by measurements of reflectivity. To obtain the lattice mode frequencies from the measured spectra, an analysis of the spectral lineshape has to be carried out, taking into account contributions to the dielectric constant from lattice vibrations oscillators and background caused by free carrier absorption and interband transitions.

6.1.2. Optical properties of intercalation graphite

Large changes in the relative magnitudes of $\varepsilon_{carriers}$, $\varepsilon_{interband}$, and $\varepsilon_{lattice}$ contributions at IR frequencies occur upon intercalation, providing important information on both free-carrier effects and the electronic energy of graphitic and intercalant levels for each intercalation compound. Although the electronic structure of graphite intercalation compounds relates closely to the structures of the graphite host and of the intercalant, a number of important differences are found in the optical properties. These differences are described below and classified under categories of free carrier effects, other optical structures, and optical anisotropy where the behavior for the polarizations $\mathbf{E}\|\mathbf{c}$ and $\mathbf{E}\perp\mathbf{c}$ is contrasted. Optical measurements on intercalation graphite are normally carried out on samples prepared from highly oriented pyrolytic graphite (HOPG) because this host material yields samples of suitable size and good optical surfaces. Since optical measurements on HOPG and single-crystal graphite yield the same optical spectra [28], it is inferred that optical studies on HOPG and on intercalated HOPG samples provide information on the electronic and lattice mode structure of intrinsic graphite and intercalated graphite, respectively [4].

Interacalation graphite reflectivity. Intercalation with either donor or acceptor intercalants results in a large increase in $\varepsilon_{carriers}$ and a large decrease in $\varepsilon_{interband}$ at low frequencies so that the optical transmission exhibits a pronounced transmission window associated predominantly with free carrier effects. The large increase in $\varepsilon_{interband}$ arises from the large increase in carrier density (by as much as a factor of ~800 for C_6Li) and is consistent with measurements of the electrical conductivity and Hall coefficient. At the same time, $\varepsilon_{interband}$ at low frequencies is much smaller in typical graphite intercalation compounds because the Fermi level is generally upshifted above the H-point E_3 band extremum in donor compounds and down-shifted below the K-point E_3 band extremum in acceptor compounds so that the strong interband transitions across the nearly degenerate graphite E_3 bands are suppressed. Therefore, for almost all of the graphite intercalation compounds studied, the optical reflectivity exhibits the characteristic Drude edge at the plasma frequency $\omega_{p,}$ and the optical transmission is characterized by a transmission window near ω_p, typical of metallic free carrier absorption. Fig. 6.20 illustrates for alkali metal compounds with Rb that the reflectivity is high for $\omega < \omega_{p,}$ and a sharp edge and a low minimum reflectivity were found for $\omega \approx \omega_p$ [75]. In some cases, $\varepsilon_{interband}$ makes an important contribution to the dielectric constant and shifts the plasma edge toward the interband frequency.

One of the first works on the optical properties of graphite intercalation compounds was carried out by [76], where the transmission window associated with the free carrier absorption process was examined. It was noted that intercalation significantly increased $\varepsilon_{carriers}$, raised E_F for donor compounds, and

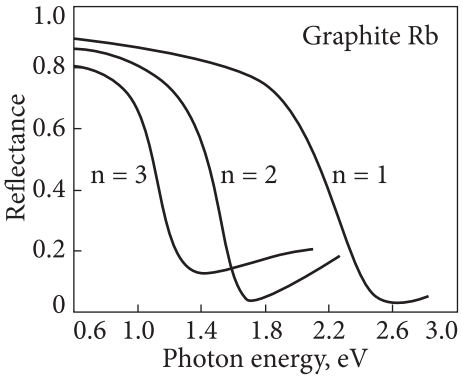

Fig. 6.20. Reflecance data for stage 1, 2 and 3 graphite-Rb donor compounds. The data exhibit a metallic-type plasma edge [75]

lowered E_F for acceptor compounds. The results obtained for the photon energy corresponding to maximum transmission are given in Table 6.1 for a number of donor and acceptor compounds. Then, the free carrier contribution to ε was studied by the reflectivity technique, and the results obtained by different researchers for the reflectivity minima for a number of donor and acceptor compounds are also given in Table 6.1. Except for the case of low stage compounds, the behavior of the reflectivity and transmission measurements can be modeled approximately by a single carrier Drude model where the plasma frequency for the polarization **E||a** is given by:

$$\omega_{p,a} = \frac{4\pi Ne^2}{m_{opt,a}\varepsilon_{core,a}} = \frac{4\pi\sigma_{opt,a}}{\tau\varepsilon_{core,a}}, \qquad (6.10)$$

where $m_{opt;a}$ and $\sigma_{opt;a}$ are the in-plane optical effective mass and the real part of the complex optical conductivity, respectively; τ is the relaxation time, N is the carrier density, and $\varepsilon_{core,a}$ is the in-plane core dielectric constant. A similar expression can be written for the plasma frequency for the polarization E||c by transcription of all subscripts $a \rightarrow c$. The quantities ω_p, $\varepsilon_{core,}$ and τ are found from a fit to the lineshape of the plasma edge structure. If interband effects can be neglected, the reflectivity minimum and the transmission maximum occur near ω_p.

The plasma frequency is upshifted with increasing intercalant concentration or decreasing stage, in accordance with (6.10), as illustrated in Fig. 6.20 for graphite-Rb for $1 < n < 3$ [75] and for graphite-$SbCl_5$ for stages $2 < n < 5$ [82] (Fig. 6.21). As was found, similar ω_p values are achieved for compounds of the same stage index for acceptor compounds with the intercalants AsF_5, SbF_5 and HNO_3 (Table 6.1). Like for the donors K, Rb and Cs, similar reflectivity curves are obtained for compounds of the same stage index. We will further note that for both donor and acceptor compounds the absolute magnitude for the reflectivity in the region $\omega << \omega_p$ increases with decreasing stage, while the reflectivity minimum decreases with decreasing stage. For some compounds (e.g., C_6Li), the low frequency reflectivity approaches 100%.

A comparison of the reflectivity data for donors and acceptors shows that ω_p for donor compounds occurs at higher frequencies than for acceptor compounds of the same stage. E.g., if ω_p for donors is twice greater than for acceptors,

this can suggest that the carrier density for donors is greater by a factor of ~4. This observation is consistent with a significantly higher carrier generation per intercalant (*f*) for donors than for acceptors. The relatively weak dependence of the reflectivity minima on the stage for certain acceptor compounds (such as graphite-$SbCl_5$ in Fig. 6.21) suggests that interband effects may contribute significantly to the dielectric constant and may result in shifts of the plasma edge.

Other acceptor compounds, however, such as graphite-AsF_5, do show significant stage dependence of the plasma edge [5]. Because of the multiple Fermi surface pieces which are present in graphite intercalation compounds, as suggested by studies of quantum oscillatory phenomena, a quantitative model for

Table 6.1. **Reflectivity minima and transmission maxima associated with free carrier effects in various donor and acceptor compounds [76]**

Intercalant	Stage	Frequency (in eV) of reflectivity minima (m) and transmission maxima (M)[a]	Authors	Intercalant	Stage	Frequency (in eV) of reflectivity minima (m) and transmission maxima (M)[a]	Authors
K	1	2.65 (m)	[62]	SbF_5	1	1.8 (m)	[81]
	2	1.8 (m)			2	1.4 (m)	
Rb	1	2.62 (m)	[75]		3	1.18 (m)	
	2	1.72 (m)			4	1.13 (m)	
	3	1.44 (m)		$SbCl_{5w}$	2	1.12 (m)	[80]
Cs	1	2.64 (M)	[76]		2	1.27 (m)	[82]
	2	1.77 (M)			3	1.16 (m)	
	4	1.27 (M)			4	1.14 (m)	
	1	2.00 (m)	[77]	HNO_3	1	1.61 (m)	[83]
	2	1.25 (m)			2	1.29 (m)	
	3	1.11 (m)			3	1.10 (m)	
Li	1	2.8 (m)	[78]	Br_2	2	1.06 (M)	[76]
	2	1.68 (m)			2	1.02 (M)	[80]
Ba	1	>3.4 (m)	[79]	ICl	2	1.10 (m)	[80]
AsF_5	1	1.77 *(m)	[5]	$FeCl_3$	1	1.09 (M)	[76]
	2	1.40 *(m)	[80]		1	1.22 (m)	[84]
	3	1.33 (m)		H_2SO_4	1	1.85 (M)	[76]
	4	1.22 (m)			2	1.29 (M)	
				$AlCl_3$	1	1.51 (M)	[76]
					2	1.10 (M)	

[a] The reflectivity minima and transmission maxima correspond approximately to the screened plasma frequency ω_p.

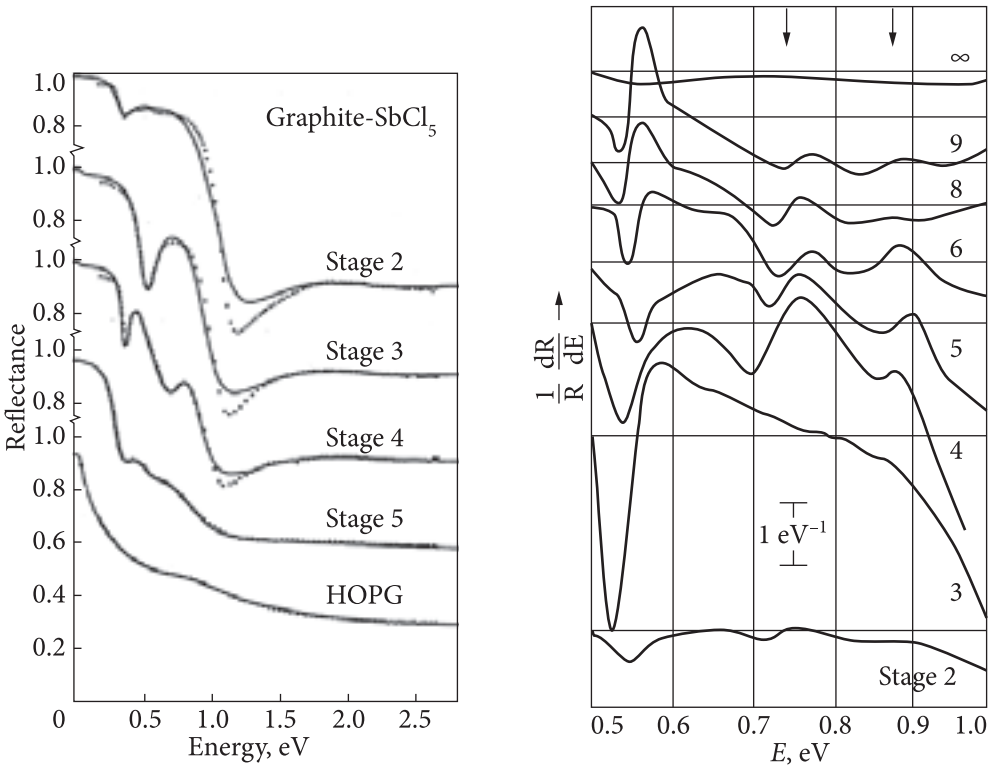

Fig. 6.21. Reflectance data for graphite-$SbCl_5$ acceptor compounds of various stages. With decreasing stage index, the plasma edge becomes more pronounced but does not shift much in frequency. An additional stage-dependent structure is found below the plasma edge and identified with intervalence band transitions. A simple model of Lorentzian oscillators (dots) is used to fit the experimental data (lines) [82]

Fig. 6.22. Progression of $1/R \cdot d\,(\ln R/dE)$ spectra during HNO_3 intercalation as the sample goes from stage 1 (i.e. graphite) to stage 2. The transitions labeled A and B are characteristic for pure graphite and sensitive to E_F [86]

the optical reflectivity should include free carrier contributions from multiple carrier pockets, as well as contributions from interband transitions. To obtain consistency between σ_{opt} and σ_{dc}, it was necessary to introduce more than one carrier type, at least for stage 1 and 2 alkali metal donor compounds [85].

As optical measurements are extended to cover a wider frequency range, it will become increasingly important to include the $\varepsilon_{interband}$ contribution when interpreting optical measurements. A simplified method for including interband contributions involves the use of an oscillator fit to reflectivity data, and the solid curves in Fig. 6.21 represent such a fit to the experimental data.

The plasma frequency $\omega_{p,c}$ for the polarization E||c is much lower than $\omega_{p,a}$, consistent with the much lower conductivity, $\sigma_{opt,c} << \sigma_{opt,a}$.

IR-modulated reflectivity studies exhibited a doublet structure in the vicinity of 0.8 eV in dilute donor and acceptor compounds (corresponding to stages $n \geq 4$) (Fig. 6.22) [86]. The similarity of this structure to the doublet structure observed in pristine graphite in the same photon energy range provides further strong evidence that the electronic structure of intercalated graphite is graphitic in nature [11, 33]. A lineshape analysis of such data on pristine graphite could yield valuable information on the weak stage dependence of the transition energies, or of the band parameter γ_1, denoting the nearest-neighbor interlayer overlap energy [35, 87]. It is also significant that the doublet structure is more pronounced for intercalation graphite than for pristine graphite, and this was attributed to a large decrease in $\varepsilon_{2,a}$, the imaginary part of the in-plane dielectric constant, with intercalation, even for as dilute a compound as stage 9 graphite-HNO_2 [86].

Such a large decrease in the interband contributions to $\varepsilon_{2,a}$ would result from the downshift of the Fermi level below the K-point extremum for acceptors and the upshift above the H-point extremum for donors. When the Fermi level is within the band overlap region, the threshold for interband transitions is the spin-orbit energy of 2.2×10^{-4} eV, so very-low-frequency transitions dominate $\varepsilon_{2,a}$ because of the $(1/\omega^3)$ dependence of ε_2. As the Fermi level passes out of the band overlap region, the threshold for interband transitions increases, and the contribution of transitions between E_3 bands to $\varepsilon_{2,a}$ decreases correspondingly. The absence of a doublet structure for $n \leq 3$ acceptors suggests that the observed phenomenon is associated with the overlap energy between atoms on two adjacent graphite interior layers. This interpretation is, however, at variance with the observation of the doublet structure in stage 3 donor compounds [86].

It should be noted that there have been performed no detailed calculations of the optical properties of graphite intercalation compounds. A model for the interband contribution to the dielectric constant for acceptor compounds has, however, been proposed on the basis of the calculation of electronic levels for a single sheet of graphite [80]. The overlap with neighboring planes was estimated from SWMcC band parameters, and the complex in-plane dielectric function $\varepsilon(\omega)$ with both interband and free carrier contributions was calculated and compared with the experiment for stage 1 and 2 acceptor compounds. This model gives an improved fit to the reflectivity data relative to a simple Drude fit and has been applied to several compounds as indicated in Table 6.1.

Some optical studies of intercalated graphite have been carried out for photon energies above the plasma edge where dominant interband transitions are observed in pristine graphite. The reflectivity and thermoreflectivity were measured with a graphite-HNO_3 sample of stage 3 [88]. They showed the dominant M-point π-band transition, which exhibits a reflectivity peak at 4.90 eV in pristine graphite, to be almost unaffected by intercalation, having a peak reflectivity

at 5.15 eV and structure in the thermoreflectivity peaking at 4.85 eV in stage 3 graphite-HNO_3. A broad semi-transparent behavior in the frequency range between 2 and 4 eV was also reported for this compound [88].

Optical reflectivity measurements in the visible and near UV ranges have also been reported [77]. They were made on stages n = 1, 2, 3 graphite-Cs compounds, and their reflectivity spectra exhibit peaks associated with the dominant M-point π-band transitions in graphite, but downshifted by ~0.2 eV in $C_{36}Cs$, and by ~0.3 eV in $C_{24}Cs$. The authors also reported the absence of such a transition in the stage 1 compound, which is surprising in comparison with the energy loss results for C_8K which show an energy loss peak at 3.8 eV, as discussed in [89]. However, it would be premature to conclude that the behavior of the dominant graphite π -band transition in C_8Cs is significantly different from that in C_8K.

The study of the optical reflectivity anisotropy has been carried out on *a*-faces for graphite and for intercalated graphite [10, 30, 38, 62]. The theoretical considerations suggest that for donor compounds a decrease in the optical anisotropy of the effective mass components should result in a decrease in the optical anisotropy and likewise a decrease in the electrical anisotropy. On the other hand, in the case of acceptor intercalation compounds where intercalation increases the electrical anisotropy and the materials become more two dimensional, the optical anisotropy should increase as well. Highly oriented pyrolytic graphite (HOPG) shows a high optical anisotropy with high transmission for **E||c**, but high reflection for **E||a**. Far-infrared polarizers based on this high anisotropy have in fact been built [90]. An increase in optical anisotropy through intercalation could perhaps result in practical device applications. Optical reflectivity experiments have been performed on *a*-face samples of C_8K and C_8Cs that were mechanically polished and sputter-etched prior to intercalation [49, 62]. Some preliminary measurements were also made on stage 2 samples of graphite-K. The results for stage 1 donor compounds exhibited Drude-like metallic reflectivity for both polarizations E||a and E||c. The reflectivity curve for the E||a polarization on the *a*-face" sample has a Drude edge similar to that for the *c*-face sample with regard to the reflectivity minimum, but a lower reflectivity than that for the *c*-face sample below 2 eV. The Drude edge for the **E||c** polarization is, however, shifted to lower energies, consistent with the lower electrical conductivity for **E||c** and the larger effective mass component m_{zz} relative to m_{xx}. The results of the analysis yield an effective mass anisotropy for 3D carriers of $m_{zz} = m_{xx}$ ~8 for C_8K [62], which is to be compared with the mass anisotropy ratio of ~10^2 for pristine graphite. It was concluded that the highly anisotropic 2D carriers located about the HKH axis make the dominant contribution to the in-plane electrical conductivity, while more spherical 3D carriers dominate the *c*-axis conductivity. This analysis also gave rough agreement

between the anisotropy ratio measured in the conductivity and inferred for the optical conductivity from the reflectivity data. Reflectivity measurements with E||c for a stage 2 graphite-K sample did not reveal a metallic plasma edge above 0.5 eV, suggesting a larger mass anisotropy and a much higher electrical anisotropy in $C_{24}K$ relative to C_8K [62]. On the basis of optical anisotropy measurements, these authors also concluded that the concentration of 3D carriers is significantly reduced in $C_{24}K$ relative to C_8K. Further work using both the optical reflectivity and the electron energy loss technique is needed to elucidate the optical anisotropy of graphite intercalation compounds and to relate such data to *c*-axis conductivity measurements on the same materials [4].

Intercalation graphite Raman scattering. Some information on transitions between graphitic and intercalant levels has been provided for the graphite-bromine system through the resonant Raman enhancement of intercalant vibrational modes for laser excitation energies close to the electronic transition energies [74].

The Raman spectra for graphite intercalation compounds with stage $n > 2$ characteristically exhibit a doublet structure at frequencies close to the singlet E_{2g2} peak found in pristine graphite [64, 91—93]. A similar doublet structure with a frequency separation of ~20 cm^{-1} is found for $n > 2$ for all intercalants studied, including the acceptors Br_2, IBr and ICl [91], $FeCl_3$ [94], $AlCl_3$ [95], $SbCl_5$ [96], and the donors K, Rb and Cs [92, 93, 97, 98].

The lower frequency component is attributed to the E_{2g2} carbon atom vibrations in interior graphite layer planes, and the lattice mode associated with these layers is denoted by E^0_{2g2}. This identification is supported by the proximity of the E^0_{2g2} mode to the E_{2g2} mode of pristine graphite, by the decrease in intensity of the E^0_{2g2} with decreasing stage (increasing intercalant concentation) and by the vanishing of the E^0_{2g2} line in stage 1 and stage 2 compounds, where there are no graphite interior layers [64, 92]. It is also significant that for $n \geq 2$ the lineshapes are Lorentzian and the linewidth of the E^0_{2g2} component is not sensitive to intercalant concentration. This result suggests that all interior graphite layers have approximately the same set of in-plane force constants. Delocalized charge density introduced by the intercalant into the interior graphitic layers is consistent with the Raman result for E^0_{2g2}.

The upper-frequency component of the doublet structure is identified with an E_{2g2}-type graphitic mode occurring in a bounding graphite layer, and this mode is denoted by $\hat{E}_{2g2}$. Support for this identification comes from the absence of the $\hat{E}_{2g2}$ line in pristine graphite, the increase of its intensity with increasing intercalant concentration, and the occurrence of a single $\hat{E}_{2g2}$ line in stage 1 and stage 2 compounds where all graphite layers are bounding layers. The upshift in the frequency of the $\hat{E}_{2g2}$ mode relative to the E^0_{2g2} mode is due to the difference in force constants arising from the different environments of the carbon atoms in graphite bounding and interior layers. The dependence of the relative intensities

of the E^0_{2g2} and $\hat{E}_{2g2}$ modes on the reciprocal stage indicates that a single bounding layer on either side of the intercalant layer effectively screens the intercalant layer from graphite interior layers. This behavior is also supported by the *z*-dependence of the charge distribution calculated on the basis of the Thomas — Fermi model, yielding a high charge density in graphite bounding layers and a rapid decrease in charge density with distance from the intercalant layer [99].

The frequencies for the E^0_{2g2} and $\hat{E}_{2g2}$ modes also exhibit a distinctive dependence on the reciprocal stage. For acceptor compounds such as with intercalants $FeCl_3$, $AlCl_3$, Br_2, AsF_5, $SbCl_5$, and HNO_3, both mode frequencies $\omega(E^0_{2g2})$ and $\omega(\hat{E}_{2g2})$ exhibit approximately the same frequency upshift as a function of the reciprocal stage $(1/n)$. A similar stage-dependent upshift of the two modes gives rise to a doublet separation of 22 ± 2 cm^{-1} for these acceptor compounds.

In contrast, donor alkali metal compounds exhibit a downshift in these mode frequencies with increasing reciprocal stages [93, 98, 100]. This mode softening is consistent with in-plane lattice expansion with increasing $(1/n)$ [101]. The stiffening of these lattice modes in acceptor compounds and their softening in donor compounds were attributed to lattice strain associated with stage-dependent changes in the lattice parameters [94]. For the case of graphite-$FeCl_3$ compounds, the constancy of the linewidth for the E_{2g2} interior layer mode as a function of intercalant concentration and the identical frequency upshift for both interior and bounding Raman modes were interpreted in terms of an identical strain within both the bounding and interior graphite layers for a given compound, a condition also necessary to prevent sample fracture upon intercalation [94]. The strain increases as the number of interior graphite layers decreases, consistent with the idea that the stress introduced by intercalation is shared by fewer layers as the stage index *n* decreases. These Raman studies indicate that the acceptor compounds should experience an inplane lattice contraction in the graphite layers as a function of $(1/n)$. Thus, the addition of electron charge density expands the lattice while its removal results in lattice contraction.

A strong dependence of the relative intensities of the E^0_{2g2} and $\hat{E}_{2g2}$ components on intercalant concentration is also observed. Increasing the intercalant concentration causes the intensity of the lower frequency component to decrease and the intensity of the upper-frequency component to increase. In this connection, it is of interest to note that for stage 4 where the numbers of graphite bounding and interior layers are equal, the two peaks have approximately equal intensity.

It is significant that there are qualitative differences observed between the Raman spectra for stage 1 alkali metal compounds and stage 1 acceptor compounds such as with the intercalants $FeCl_3$, $AlCl_3$ [95], AsF_5, HNO_3, and $SbCl_5$ [102]. This difference in behavior has been attributed to the greater coupling between intercalant and graphite layer planes in donor compounds as compared with acceptor compounds [103]. The strong coupling was further documented

by the values of the Breit-Wigner parameters for the asymmetric broad lines near 1500 cm^{-1} for C_8K, C_8Rb, and C_8Cs [97].

In addition to the high-frequency modes identified with graphite layer vibrations, lattice modes at lower frequencies are also observed and are identified with the intercalant layer, because the reported spectra are different for each intercalant, e.g., Br_2 [91, 104], IBr, ICl [91], and $FeCl_3$ [105].

A detailed study of the Raman spectra for the intercalant modes may provide a useful tool for the study of order-disorder transformations in molecular intercalation compounds. In this connection, it is of interest to note that structure in the low-frequency range was found for the intercalants AsF_5, HNO_3, and $SbCl_5$ [102], but via careful study of different spectra, the authors could show that the low-0frequency Raman lines were due to the ampoule gas in the case of HNO_3 and AsF_5, and to the surface deposit in the case of $SbCl_5$.

Raman scattering has also been applied to the study of adsorbed molecules on graphite surfaces for vapor pressures below the threshold for intercalation. For Br_2 adsorbed on graphite surfaces, surface-specific Raman modes have been reported with frequencies intermediate between 242 cm^{-1} for the intercalant Br_2 mode and 300 cm^{-1} for solid Br_2 [106].

Infrared absorption spectroscopy of intercalation graphite. Intercalation introduces a change in symmetry so that intercalation compounds have only approximate inversion symmetry. Nevertheless, it is found experimentally that the parity selection rules are preserved upon intercalation so that IR spectroscopy only excites modes that are odd in the graphite host and likewise Raman spectroscopy only excites modes derived from even-parity graphite modes. This preservation of approximate inversion symmetry indicates that the coupling between graphite and intercalant layers is weak and that inversion symmetry should be used to model the phonon modes of intercalated graphite.

Because of the high infrared absorption of graphite intercalation compounds associated with the electronic structure, infrared studies are carried out on reflection. To obtain information on the lattice modes, the lattice contribution to the dielectric constant must be determined from the measured reflectively. Therefore, interpretation of the IR lattice reflectivity spectra requires a lineshape analysis to separate the lattice mode contributions $\varepsilon_{lattice}$ to the dielectric constant from the other contributions including $\varepsilon_{carriers}$ due to free carriers and $\varepsilon_{interband}$ due to interband transitions. In carrying out the lineshape analysis, $\varepsilon_{lattice}$ is modeled by a set of oscillators. As described below, infrared structures associated with graphitic lattice modes exhibit both similarities and differences according to whether the intercalant is a donor or an acceptor. There are some traces in the spectra for a graphite-$FeCl_3$ system with stages n = 2, 4, 6, and 11 in the frequency range $1500 < \omega < 1700$ cm^{-1}. The striking difference in lineshape between the trace for graphite (labeled HOPG), for stage 11 compound, and for the lower stage compounds

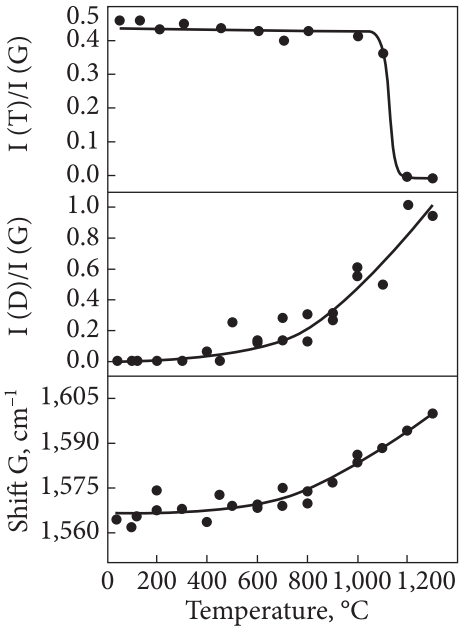

Fig. 6.23. Room temperature IR reflection spectra for stage $n = 2$, 4, 6, and 11 graphite-ferric chloride compounds and for pristine graphite (HOPG) [94]. The fit of the lineshape analysis to the experimental data is given as solid curves.

$n \leq 6$ is due to the increasing $\varepsilon_{\text{carriers}}$ with decreasing stage and the relatively smaller contribution of $\varepsilon_{\text{interband}}$ when the Fermi level falls below the K-point E_3 band extremum for acceptor compounds [25]. The results of lineshape calculation of lattice mode frequencies, linewidths, and oscillator strengths are given in Fig. 6.23 by the solid curves and yield one IR-active mode for stage 2 and two IR-active modes for stages $n \geq 3$. It should be noted that although cursory inspection of the data suggests a single IR-active mode, analysis of the observed lineshape requires the superposition of two unresolved Lorentzian infrared structures [94].

Analysis of the dependence of the mode frequencies and oscillator strengths on the reciprocal stage $(1/n)$ yields the identification of the observed structures with graphite interior layers (E^0_{1u}) and graphite bounding layers ($\hat{E}_{1u}$). The mode for which the peak frequency and oscillator strength versus $(1/n)$ extrapolate to the graphite values as $1/n \to 0$ is identified with the graphite interior layers. This mode is not found for the stage 2 compound either, which is consistent with the interpretation. The frequency for the other dominant mode versus $(1/n)$ does not extrapolate to the E_{1u} graphite mode and furthermore exhibits the oscillator strength with a weak dependence on $(1/n)$. This mode is therefore identified with the graphite bonding layers since the environment of carbon atoms on the graphite bonding layer is similar for stages $n \geq 3$.

The IR spectra observed for other acceptor compounds, such as $AlCl_3$, Br_2, IBr, and ICl, are qualitatively similar to the results obtained for the $FeCl_3$ system. For all acceptor intercalants, a general increase in oscillator strength with increasing intercalant concentration is observed and this effect can be interpreted in terms of physics on the basis of the following argument. Since the intercalation process introduces a charge density gradient in the *c*-direction [99, 107], the dipole associated with the E_1u mode is enhanced. Since the gradient in charge density is the largest near the graphite bonding layer, the $\hat{E}_{1u}$ mode is expected to have a greater oscillator strength than the interior layer E^0_{1u} mode, in agreement with observations. Furthermore, since the gradient in charge

density near the graphite bonding layer is only weakly dependent on stage for $n \geq 3$, the oscillator strength for this mode is expected to be approximately independent of stage, also in agreement with observations. The IR-active mode for $n = 2$ involves carbon atom vibrations on two neighboring bonding layers, which is a different arrangement than that which occurs in higher-stage compounds. No IR-active modes were found for either acceptor or donor stage 1 compounds, in agreement with group theoretical considerations, which predict that a single graphite layer cannot give rise to odd-parity modes. As in the case of Raman-active modes in acceptor compounds, the IR-active modes for acceptor intercalants upshift as a function of the reciprocal stage ($1/n$), and for the graphite-$FeCl_3$ system the upshifts of all Raman-active and IR-active modes exhibit similar ($1/n$) dependence [108]. Though other acceptor compounds also exhibit a general frequency upshift of the IR-active modes, the behavior does not appear to be as simple as for graphite-$FeCl_3$ [109]. This frequency upshift as a function of ($1/n$) was attributed to a strain mechanism, implying in-plane lattice contraction for acceptor compounds.

The IR oscillator strength yields the dipole moment for the E_{1u} mode and in turn the dynamic effective charge associated with that mode. Since the graphite bounding and interior layer modes occur at different frequencies, the dynamic effective charges associated with each mode can be determined independently. Analysis of IR spectra for donor and acceptor compounds indicates that a more dynamic effective charge is associated with all E_{1u} modes for donor compounds than for acceptor compounds of the same stage. Further analysis shows that a relatively more effective charge resides in the graphite interior layers for donor compounds than for acceptor compounds of the same stage, in agreement with the interpretation of magnetoreflection and electrical conductivity results in [109] and [110], respectively. The relation between the dynamic effective charge and the charge available for electrical transport, however, requires further elucidation.

6.1.3. Optical properties of amorphous carbon materials

Reflection and absorption of light by amorphous graphitic carbon materials. The optical properties of amorphous carbons similar to most other physical properties vary with the material composition and they are similar to those of glassy graphite. Strong reflectivity (dropping from ~100%) in the IR range light, weaker reflectance (less than 20%) in the visible range followed by a sharp drop for UV range (~200 nm) are the main features of amorphous carbons [111—113].

The optical properties of amorphous carbon are often related to the hydrogen concentration in the carbon film and its transparency decreases with increasing hydrogen content. The refraction index is also affected by the hydrogen content

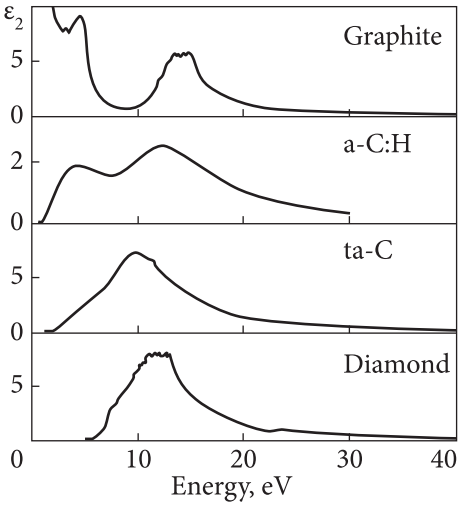

Fig. 6.24. The ε_2 part of the dielectric permittivity of some carbon forms [108, 123]

and increases with decreasing concentration of bound hydrogen [114]. Defects in amorphous carbon films are of interest because they are likely to affect the electronic and optical properties of the material [115]. When the spin density increases, e.g., the optical bandgap decreases. It depends on the configuration of the sp^2 sites, which tend to cluster. As the cluster size increases, the gap decreases. For a wide variety of films deposited near room temperature, optical bandgap varies with sp^2 content in the range of 3.0—2.5 eV. The change in the optical gap is associated with the change in sp^2 content [116]. Mentioned properties will be described in detail below. In contrast to crystal materials, amorphous carbons are a class of materials with a wide range of optical and dielectric properties due to a structure formed by atoms with different degrees of electron hybridization and affected by different kinds of disorder and due to properties tightly correlated with the film synthesis conditions. Consequently, accurate knowledge of carbonaceous matrix properties is of considerable importance for designing carbon-based nanocomposites with specific performances [117].

Generally, optical absorption evaluation of amorphous insulators and semiconductors requires parametrization of the photon energy dependence of the optical constants (refractive index, extinction coefficient, dielectric function). Several models have been developed to describe the electronic transition parameters such as the bandgap, the energy of peak transition, and the transition lifetime. These models, namely the Tauc [118], Tauc — Lorentz (TL) [119], and Forouhi — Bloomer (FB) [120] models, are of wide use. They have been applied to amorphous carbon films too and some studies were made to check their validity in the case of this particular class of materials [121, 122].

The dielectric permittivity ε_2 spectra of some carbon forms are shown in Fig. 6.24 [74, 123].

The ε_2 spectra of graphite and a-C:H show two peaks, one around 4 eV caused by π excitation and one around 13 eV caused by σ excitations. The ta-C shows evidence of its high sp^3 fraction, as it has only one main peak at 9 eV due to σ excitations [74, 123, 124]. There is also a weak shoulder at 6 eV related to π excitations. The position of the σ peak for ta-C depends sensitively on the refraction index used in the Kramers — Kronig analysis if the spectrum is derived from

energy loss. The ε_2 spectrum of graphite shows divergence at zero energy (metal property). The ε_2 spectra of other carbons are zero below their bandgaps.

The transition to the σ and π states shows two relatively separate contributions in the ε_2 spectra of carbons with sp^2 sites [125, 126]. This is related to the fact that the $\sigma \to \pi^*$ and $\pi \to \sigma^*$ transitions are weak for planar sp^2 sites, so the σ and π excitations are effectively deoccupied in the optical spectra. The separations were further shown by calculating the effective number of electrons, N_{eff}, participating in the spectrum up to a given energy E:

$$N_{eff}(E) = \frac{m}{2\pi^2 N e^2 \hbar^2} \int_0^E E' \varepsilon_2(E') dE'. \tag{6.11}$$

Thus, N_{eff} of graphite showed a plateau at 8 eV, which marks the separation of the σ and π excitations. The optical properties of materials really are much related to their electronic energy bandgap. We have seen above (Chapter 1) that the bandgap of amorphous carbons is determined by the configuration of the π states on sp^2 sites, and if the cluster model is used, the cluster bandgap is given as [127]:

$$E_g \approx \frac{2\gamma}{M^{1/2}}, \tag{6.12}$$

where γ is the nearest neighbor V(ppπ) interaction and M is the number of six-fold rings in the cluster. M can be related to the cluster diameter or in-plane correlation length L_a as $M \approx (L_a)^2$, so

$$E_g \approx \frac{2\gamma}{L_a}, \tag{6.13}$$

The cluster model overestimates the cluster sizes. Really, the bandgap is controlled by the cluster distortions. Today, it is not possible to present a simple formula for the gap, similar to (6.12), but it was found that the bandgap increases with sp^2 content decreasing (Fig. 6.25) [128, 129]. The hydrogen presence affects little as the C-H states lie well away from the bandgap region [74].

If material is amorphous, there is no true gap; an arbitrary definition must be used for the optical gap. Two most common experimental ways are: the E_{o4} gap defined as the energy at which the optical absorption coefficient α is 10^{-4} cm^{-1}, and the so-called Tauc gap defined as the intercept E_g found from plotting [74, 118]:

$$\alpha E = B(E - E_g)^2. \tag{6.14}$$

The dependences of the experimental Tauc gap values on the sp^2 fraction are shown for some carbons in Fig. 6.26. It is easy to see similarities between experimental and calculated dependences 0shown in Fig. 6.25. The bandgap increases with decreasing sp^2 fraction lowers.

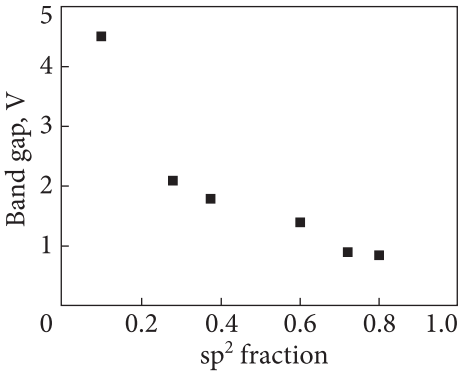

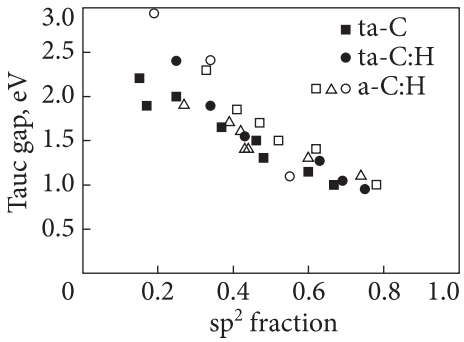

Fig. 6.25. Variation of the bandgap with sp^2 fraction [81, 140]

Fig. 6.26. Dependences of the Tauc gap experimental values versus sp^2 fraction for a-C:H [130—133], ta-C:H [134], and ta-C [135]

A simple model was proposed for the above-mentioned relation in [136—140]. A gap increasing with sp^2 fraction decreasing (Fig. 6.26) leads to a decrease in the width of the π and π* bands, with a constant π — π* separation. Of course, the gap does not depend on the configuration of sp^2 sites, which need not vary just with the sp^3 content. Thus, the gap does not vary with the sp^2 content in every situation, such as annealing, or high-temperature deposition. Besides, the range of the cluster sizes determines the shape and length of the absorption tail, not a sharp bandgap, and this statement coincides with experimental results [74].

These optical absorption spectra show a long tail for all forms of amorphous carbons. The edge can be analyzed in various ways. It was found that it fits the Gaussian model [126, 136—140].

Another way to analyze the absorption edge is to fit it with exponential slope and following extraction of the so-called Urbach energy E_0. Despite some inaccuracy of absorption edge fitting to exponential slope, E_0 is often used as a standard measure of electronic disorder in amorphous materials. Thus, it is clear that a-C:H has a large disorder if compare with a-SiC:H, as the Urbach energy E_0 of a-Si:H is about 55 meV, whereas that of a-C:H never falls below 150 meV [74].

The general layout of gap states in ta-C:H and a-C:H shows an exponential distribution of tail states and some defect states around the gap center (Fig. 6.27). Conductivity data for a-C:H suggest that E_F lies nearer the valence band [141].

Scanning tunneling microscopy data found that the slope of the valence band tail is sharper than that of the conduction band tail [142]. The slope of the valence band tail was also analyzed and compared to Urbach energy E_0 of the same sample (Fig. 6.28) [143]. The Urbach energy roughly equals the larger of the tails. The valence band slope energy E_{vo} is less than the Urbach energy E_0. This means that the conduction band tail is the wider tail. It is easy to see that

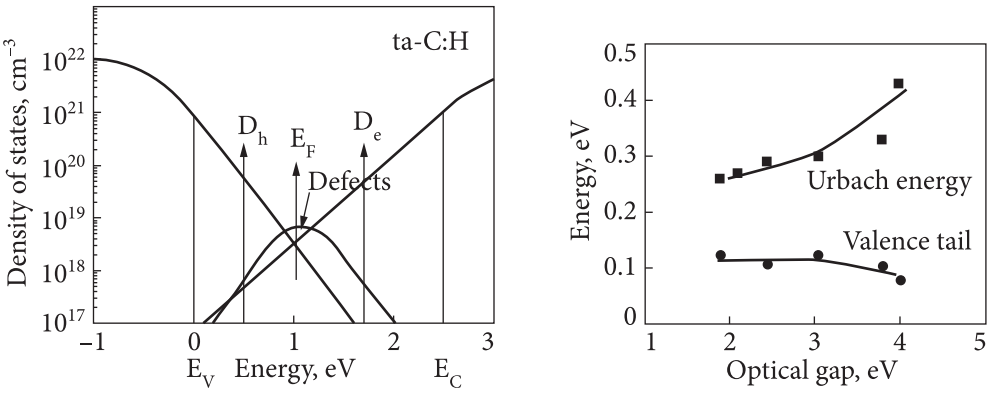

Fig. 6.27. The DOS scheme in a-C: exponential tail states, optical gap, defect states, and demarcation levels [74]

Fig. 6.28. Urbach energy evaluated from the optical edge and the valence tail energy evaluated from the photoemission data for a-C:H [74]

the valence tail is narrower than the optical edge and thus the conduction edge in a-C:H. Thus, ta-C and ta-C:H are predominantly hole conductors [170].

Another way to estimate disorder in amorphous materials is to determine bond angle distortion [74]. For a-Si, the width of the main Raman TO lines was found to be proportional to the bond angle distortion [144]. Raman G mode is equivalent to that in a-C. The Raman G line width was found to vary linearly with the compressive stress in as-deposited films, and so it is proportional to the bond angle distortion. Really, variation of the Urbach energy and the Raman G line width increases together for small optical gaps [119].

It should be noted that the Urbach energy and the Raman G line width are different measures of disorder. The G line width is a measure of homogeneous disorder and bond angle distortion within the network. The Urbach energy is a measure of an inhomogeneous disorder in the two-phase network, as it measures the range of the sp^2 cluster sizes [74].

It is known that the optical absorption and radiation transitions are vertical in real space in the Condon approximation. This rule is related to the need for the initial and final electron-vibrational states to overlap and means that electronic coordinates do not change upon optical transition. In amorphous materials, the need for overlap between initial and final states means that the following optical transitions are only allowed: extended → extended; localized → extended; and extended → localized, while localized → localized transitions are forbidden. This follows from the fact that initial and final states are usually localized in different parts of the space. On the other hand, when there are strong asymmetric fluctuations as in a-C, then localized → localized transitions are also allowed, as the initial and final states can be localized in the same π cluster [74].

Raman spectroscopy of amorphous disordered graphite. Disordered graphite has a second mode near 1350 cm^{-1} of A_{1g} symmetry labeled as "D". It is worth noting that the D mode is forbidden in ideal graphite, but disorder causes its appearance due to breathing vibrations of rings at K point of zone boundary [65, 74]. It is also important that two G and D modes of graphite dominate in the Raman spectra of most disordered carbons even when the carbons do not have particular graphitic ordering [145] (Fig. 6.19, f.e.). Let's point in detail the mentioned question.

For graphitic amorphous carbons (carbon materials where sp^2-hybridized carbon dominates) the two main Raman peaks, G and D, are always present. In similarity with glassy carbons, the observed Raman peaks for other amorphous carbons also have significantly broadened peaks compared to graphite. This peak broadening is a measure of disordering in graphitic material, especially the D-peak width. For highly disordered amorphous carbon, the peak broadening is large enough so that the two main peaks, G and D, can be superposed. In addition, shifts both of G- and D-peak positions are observed for amorphous carbons. The position of these peaks also depends on the excitation wavelength. This is in contrast to the observations for pure graphite and glassy carbon, where only the D-peak is dispersive as stated in [146, 147]. The reason is that for small graphitic clusters, the electronic and vibrational properties are influenced because the delocalized π-electron goes to a more localized character of the electron cloud [146]. The sp^2 clusters of different sizes, therefore, have different electronic and vibrational properties, and therefore they are selectively excited by different light wavelengths. Both G and D peaks shift to a lower frequency for longer wavelengths of excitation.

So, the Raman spectroscopy is also able to give a measure of the sp^2 configuration, and this allows the determination of many carbon materials characteristics in detail 74]. That is why we give below some details about the fundamental background of the disordered graphite Raman spectra.

It is known that Raman is scattering of the light incident on the material and caused by modulation of polarisability χ of the material by its lattice vibrations [148]:

$$\chi(k) = \chi_0 + \frac{d\chi}{dq} Q(k,q), \tag{6.15}$$

where χ is the polarisability for wavevector k, and Q is the phonon amplitude for wavevector q. The polarization can be performed by excitation from the ground electronic state into virtual or real states at energy E. The last case is called the resonant Raman scattering [148]. The change of χ causes an elastic transformation of the incident photon (ω, k), into the scattered photon (ω', k') (ω and ω' are the photon frequencies). The Raman scattering cross-section, C, can be expressed as

$$C = k\left(\frac{d\chi}{d\omega}\right)^2. \tag{6.16}$$

When dealing with crystals, the rule of alternative prohibition is actual. In the case of an amorphous material, there is a complete loss of lattice periodicity and breakdown of the *k* selection rule of optical and phonon transitions. The IR and Raman spectra of amorphous materials correspond to the vibrational density of states (VDOS) G(ω) weighted by the appropriate matrix elements C(ω). So, the Shuker — Gammon formula is known for the Raman spectrum [149]:

$$I(\omega) = \frac{n(\omega)+1}{\omega} C(\omega) G(\omega). \tag{6.17}$$

Nevertheless, the Raman does not simply follow the VDOS of the sp^2 sites. The main reason for the dominance of the G and D modes is that the Raman spectra are dominated by scattering by the sp^2 sites. The π states are of lower energy than the σ states and so they are much more polarizable [127]. This results in a large Raman cross-section for sp^2 sites. E.g., it is 50—230 times larger than the Raman cross-section for sp^3 sites, so sp^2 sites dominate the Raman spectra of even ta-C, which only has a residual 10—15% sp^2 content [150—152]. Another and more important reason is that the matrix element has a much stronger effect than in the σ bonded networks. The Raman spectrum becomes managed by the order of the sp^2 sites, not by the sp^2 fraction [145]. The Raman and IR spectra should be also rather smooth and resemble each other. This takes place in various materials, but it is not true for the Raman spectrum of amorphous carbon.

It has to be noted that the G mode is the stretching vibration of any pair of the sp^2 sites, either in C—C chains or in aromatic rings (Fig. 6.29) [145]. That is why G does not mean only "graphite". The D mode is the breathing mode of sp^2 sites only in rings, not in chains.

Thus, the intensity ratio I_D/I_G is also a characteristic feature of amorphous carbons [54, 72, 133]. For carbons that consist essentially of crystalline graphite, the ratio increases with the increasing number of defects since I_D is caused by Raman scattering on the breathing mode of carbon rings allowed due to the double resonance process involving scattering with lattice defects. However, at a point where the defect density becomes so high that many of the carbon rings are destroyed, the D-peak intensity decreases again. Hence, for crystalline graphite with a low number of

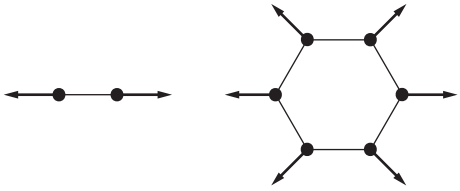

Fig. 6.29. Eigenvectors of the Raman G and D modes in graphite and amorphous carbons [74]

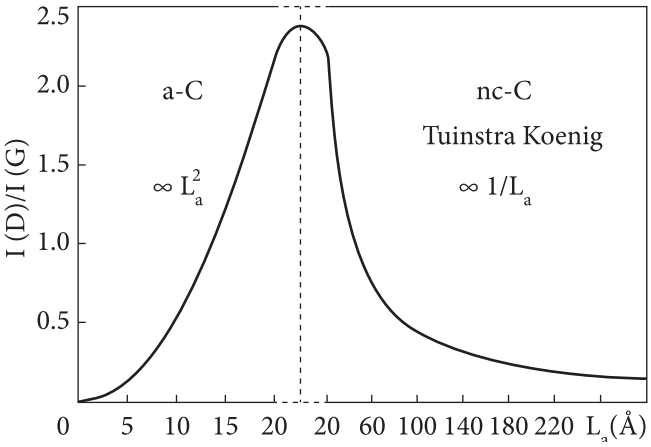

Fig. 6.30. Variation of Raman I(D)/I(G) peak intensity with in-plane correlation length L_a. (The Tuinstra — Koenig relationship only applies for L_a over 2 nm) [74]

defects, the G-peak is more intense than the D-peak. Graphitic amorphous carbon materials are composed of sp^2-hybridized atoms with some contributions of sp^3-carbon. Therefore, one would expect to get a contribution to the Raman spectra from vibrational modes corresponding to these bonds, at ~1060 cm^{-1} and ~1332 cm^{-1}. However, the excitation cross section for these modes with visible light is about 55 times lower than for the modes attributed to sp^2-hybridized carbon and therefore they are not easily distinguished unless the material has a significant amount of diamond-like carbon [72]. In addition to these sp^3-attributed peaks, the peak at ~1500 cm^{-1} is frequently observed for amorphous carbons [153, 154].

F. Tuinstra and J.L. Koening have noted that the intensity ratio of the D and G modes, *I(D)/I(G)*, undergoes inversion with the in-plane correlation length L_a or graphite grain size (Fig. 6.30) [69]:

$$\frac{I(D)}{I(G)} = \frac{c}{L_a}. \tag{6.18}$$

The fact means that I(D)/I(G) is proportional to the number of rings at the grain edge. This relationship cannot extend down to zero L_a. Recent data on the high- temperature deposition of ta-C suggest that for L_a below 2 nm, the ratio decreases according to Fig. 6.30 [145, 155].

$$\frac{I(D)}{I(G)} = cL_a^2. \tag{6.19}$$

The G peak is due to all sp^2 sites, but the D peak is only due to six-fold rings, so I(D)/I(G) falls as the number of rings per cluster falls and the fraction of chain groups rises [145]. Noted above means that the Raman spectra disordered carbons behavior is rather complicated. Thus, Fig. 6.31 shows various factors

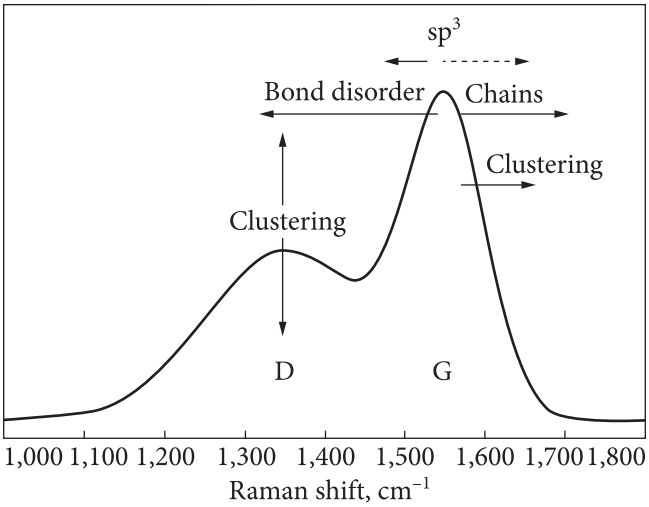

Fig. 6.31. Scheme of the factors affecting the G and D peaks' positions and intensity in Raman spectra of non-crystalline carbons [74]

that shift the G and D peaks' positions and change their intensity. (It is worth noting that visible light Raman scattering does not show C—H bonds [74].)

The shape of the carbon Raman spectra lines can be fitted with the Lorentzian-like profile known as a Breit — Wigner — Fano (BWF) contour for the G-peak and Lorentzian for the D-peak [145]. The BWF is given by

$$I(\omega) = \frac{I_0\left[1+2+(\omega-\omega_0)/Q\Gamma\right]^2}{1+\left[2(\omega-\omega_0)/\Gamma\right]^2}, \tag{6.20}$$

where I_0 is the peak intensity, ω_0 is the peak position, Γ is the FWHM, and Q^{-1} is the coupling or skewness coefficient. For $Q \neq 0$, the peak position of the Raman line is at (ω_0 has no meaning in this case).

$$\omega_m = \omega_0 + \frac{\Gamma}{2Q}. \tag{6.21}$$

A three-stage model has been proposed to classify the Raman spectra of all disordered carbons depending on disorder increase (Fig. 6.32 [74, 145]):

1. perfect graphite → nanocrystalline graphite;
2. nanocrystalline graphite → sp^2 a-C;
3. sp^2 a-C → sp^3 a-C.

Stage 1 corresponds to the reduction in grain size of ordered graphite layers, but aromatic rings remain there. When the grain size decreases, phonon confinement causes phonons away from Γ to participate with $\Delta q = 1/L_a$. The phonon bands of graphite disperse upwards from 1580 cm^{-1} at Γ [157, 158], so this causes an upshift of the G peak to 1600 cm^{-1} [74]. The D mode is forbidden in a perfect

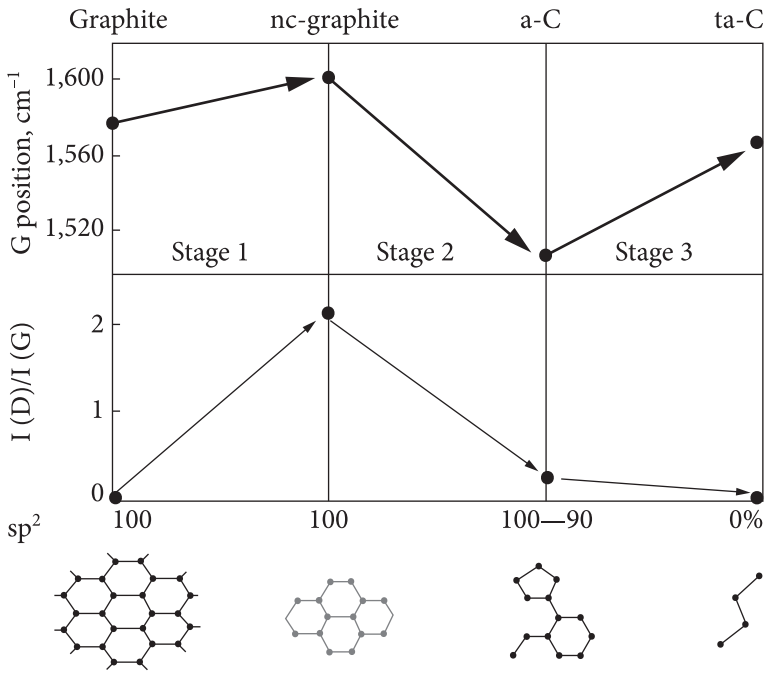

Fig. 6.32. Scheme of the Raman peak position and I (D) /I (G) ration dependence on the disorder degree [74, 156]

graphite layer, but the disorder causes its appearance, and its intensity rises with decreasing L_a in accordance with the Tuinstra — Koenig relation.

Stage 2 corresponds to the topological disorder of a graphite layer (odd membered rings) and loss of aromatic bonding, but with a purely sp^2 network. The disorder and loss of aromaticity weaken the bonds and lower the VDOS compared to that of perfect graphite [159]. This causes the G peak to shift downwards (Fig. 6.32). L_a goes below 2 nm, so the I(D)/I(G) ratio falls continuously to zero. The VDOS corresponds to sputters a-C at the stage 2 end [160].

The sp^3 content increases from 0 to 100% in stage 3, which changes the sp^3 configuration from mainly ring-like to short chains [145, 159]. The bond length of chains is shorter than that of rings, so their vibrational frequency, 1640 cm^{-1}, is higher compared to 1580—1600 cm^{-1}. Thus, the G-modes rise in stage 3, while the D peak remains at zero intensity [75, 145]. The linelike shape of the G-peak becomes more symmetric as the content reaches high values [105]. The G-peak position shifts up with sp^3 content increasing but it would apparently shift downwards when using symmetric fit or uncorrected ω_0 in equation (6.20) [74]. The most symmetric G-peak corresponds to the maximum sp^3 content [74, 161].

The described above analysis allows us to state that if the *I(D)/I(G)* ratio is near zero, we are in stage 3. The G-peak position then varies according to the

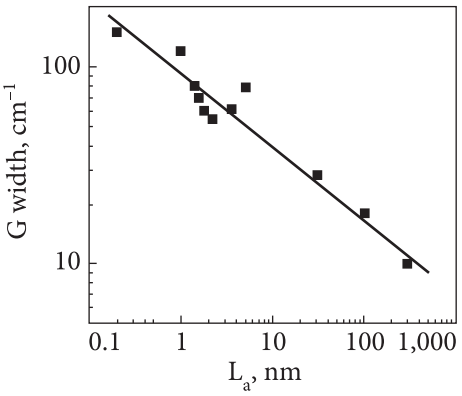

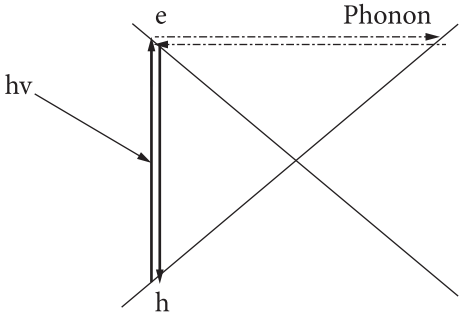

Fig. 6.33. Dependence of the FWHM G-line on in-plane correlation length L_a [74]

Fig. 6.34. Scheme of the second-order resonant Raman creation of the D-line in graphite [74, 171]

sp^3 fraction content. This relationship can be used for deriving the sp^3 fraction from the Raman spectra [74].

The FWHM of the G line scales up with the disorder. There is a way to evaluate the situation: if the FWHM of the G line is higher than 50 cm^{-1}, then L_a is below 1 nm (Fig. 6.33).

Some details about resonant Raman scattering. Carbon is really a wide-gap material; visible photons do not excite the σ states and they only excite the π states over a limited part of the Brillouin zone. So, as visible photons at 514 or 488 nm usually excite, Raman is only sensitive to the sp^2 sites [74]. Excitation of the higher-lying σ* states requires incident photons of higher energy, which allows direct excitation of the sp^2 sites [147, 162—167]. An interesting property of Raman modes in sp^2 carbons is that they are dispersive, that is, their wavenumbers vary with the photon excitation energy. This is evidence that a mode is not simply a density-of-states feature, but that the matrix element changes with excitation energy because the excitation energy resonates with a real electronic transition. It can be a virtual state in the gap, or in the broad continuum of states in the conduction band. In graphite, the lower dimensionality means that the resonance condition will select specific states.

It has been realized that resonance causes dispersion of the D peak [145, 168—170]. It was also clarified that the D mode of graphite is a double resonance condition [171]. A layer of graphite is a semi-metal, with the valence and conduction π bands touching at the K zone boundary. The π bands disperse linearly away from K, as shown schematically in Fig. 6.34 [74, 171].

A photon of energy E incident on graphite will create an electron-hole pair at wavevector k where the π gap equals E_i. The electron can then emit a photon

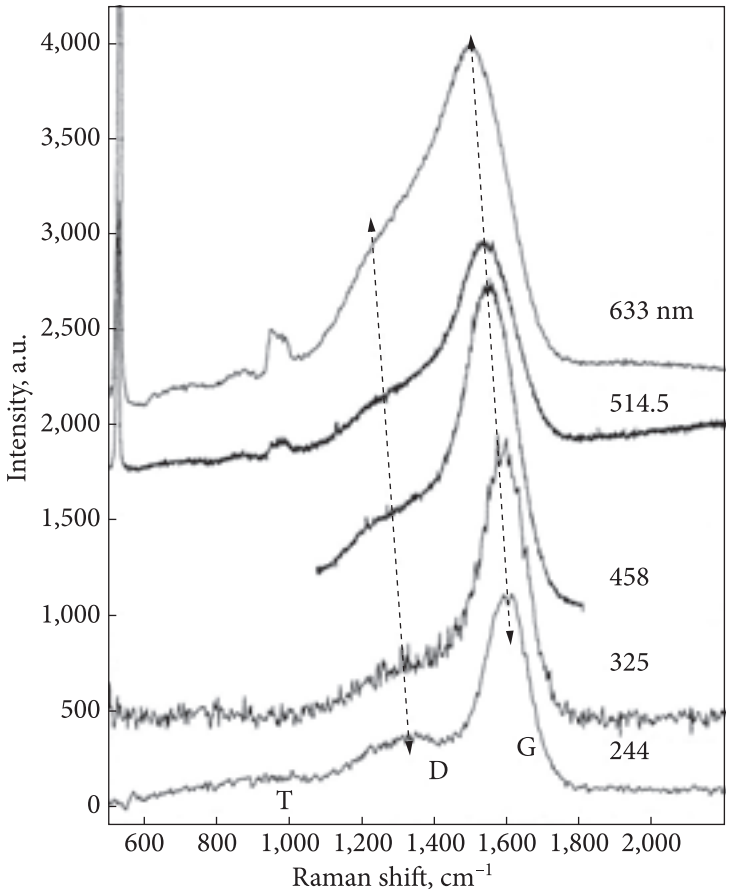

Fig. 6.35. Dependence of the ta-C Raman spectra on the excitation wavelength [74]

of wavevector q, scattering the electron from k to $k - q$. If $k - q = -k$, then the electron can be scattered back to k by the finite grain size or disorder and decay by emitting the outgoing photon. The resonant condition is therefore $2k = q$. Both the incident and outgoing photons correspond to the π gap. Raising the photon energy selects k vectors further away from K. The D mode is the singly degenerated A_{1g} mode at $E_i = 0$. As the photon excitation energy increases from 0, the D mode moves away from K, and its wavevector rises.

In general terms, incident photons will excite those clusters whose gap equals the photon energy. In fact, the D mode of graphitic clusters behaves exactly like in graphite. A graphitic cluster is a finite piece of graphite. Its electron states are folded about the K point [127]. The photon modes are found similarly. A cluster of grain size L_a maps onto a wavevector k along the ΓKM direction of the ideal graphite layer by the equation

$$1 + 2\cos(ka) = -\frac{a}{L_a}, \tag{6.22}$$

which is equivalent to $\sin(\Delta ka) = a / \sqrt{3}L_a$, where Δk is the distance away from K. This means that the dispersion behavior of an ensemble of graphitic clusters is exactly like that of a graphite layer [74, 145]. As for experimental, it is worth analyzing Fig. 6.35, where an example of dispersion of the ta-C Raman spectra with photon energy is shown [74]. The summary of the G and D modes dispersion behavior in various carbons can be given as follows [147, 172—174]:

• G mode of graphite or even glassy carbon does not disperse. It is dispersed only in stages 2 and 3 of carbons;

• G mode rises with increasing photon energy and saturates at 1600 cm^{-1} (limit of graphite VDOS) for sp^2 bonded a-C.

• G mode dispersion in ta-C is extremal. It starts at 1500 cm^{-1} for IR excitation and rises to 1690 cm^{-1} for deep UV excitation at 215 nm. This means that 633 nm radiation selectively excites clusters with weak π bonding and relatively low vibrational modes (e.g. of aromatic character). When the incident photon energy rises, those photons select clusters of increasing olefinic (chain-like) groups with higher C—C bond stretching modes. There will be C=C pairs at the highest excitation energy [74, 147].

• Dispersion of the G-line peak position is roughly linear [74].

The D mode behavior is different from the described above. The strongest dispersion characterizes the most well-ordered graphitic carbons. The D-mode dispersion increases with an order that is opposite to the G-mode behavior. The D–lines show a second harmonic at 2700 cm^{-1}, which exists even in single-crystalline graphite and disperses as well.

The I(D)/I(G) intensity ratio dispersion has been considered in [147]. It decreases faster for ordered carbons. Thus, the D line is absent for UV excitation. However, the ratio hardly disperses for very disordered a-C.

To sum up, dispersion of the Raman features occurs because the excitation resonates with the bandgap of a particular cluster, and this selects the corresponding vibrational mode. A shorter wavelength selects a smaller cluster with a wider bandgap. Smaller clusters have a higher D and G mode, and this causes the mode dispersion. A shorter wavelength also reduces the D line intensity, causing dispersion of the *I(D)/I(G)* intensity ratio [74].

Photoluminescence of amorphous and disordered carbon materials. Photoluminescence (PL) of amorphous carbons will be discussed on the pattern of the a-C:H material, which shows a Gaussian-shaped wide PL band near/or just below the optical gap energy. It is excited by photon energy at or above the gap. The corresponding absorption, PL excitation, and luminescence bands are shown in Fig. 6.36 [175].

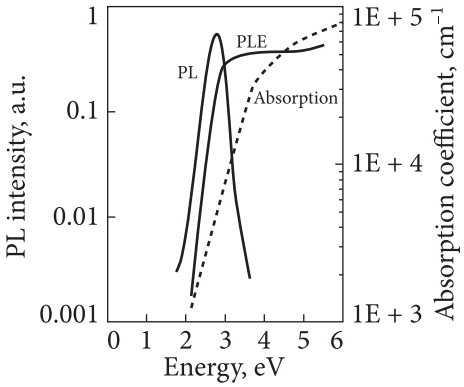

Fig. 6.36. Optical absorption, luminescence and PL excitation spectra of a-C:H [74, 175]

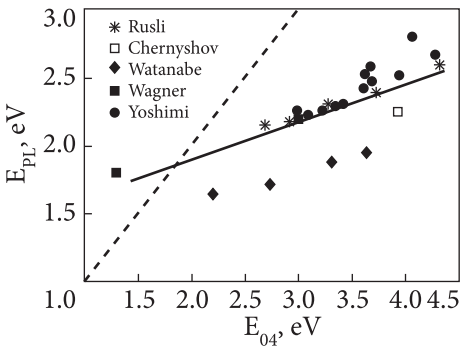

Fig. 6.37. Dependence of the PL energy on the optical bandgap [175, 177, 178]

The dependence of the average PL energy on the optical bandgap value is shown in Fig. 6.37, where data from various papers are accumulated [175—179]. The average PL energy increases with a slope of about 50 % if the gap increases. When the gap is higher than 1.7 eV, the PL energy is slightly above the gap [74]. In the case of the wide a-C:H gap, when the excitation energy is too low, the upper part of the PL spectrum is cut off.

The observed PL reveals polarization memory [180, 181], it is not dependent on the electric field [175] and is fast: the decay time is 10^{-8} s [175, 182, 183]. These features indicate that the PL centers are quite localized, as was supposed in [74]. It is worth noting that the PL of a-C:H is accompanied by a large density of defects if compare to a-Si:H. In some cases, the PL efficiency does not correlate with the density of paramagnetic defects, but, generally, there is a correlation. The PL efficiency exponentially depends on the optical bandgap.

Four types of PL mechanisms have been pointed out in [74].

• The bound electron-hole pair (Wannier excitons) can be formed in band-edge states of direct gap materials. Such pairs recombine with sharp PL lines which lie just below the bandgap. The decay time of such PL is short.

• If material is of low dielectric constant and rather high effective mass (organic solids, e.g.), the electron-hole pairs form Frenkel excitons. These excitons can be long-lived and migrate from one molecule to another by the bipolar Forster mechanism. Simultaneously, they can radiatively destroy and reveal fast PL.

• In the case of insulators or wide-gap semiconductors (a-Se, e.g.), PL related to deep defects strongly coupled with the lattice occurs. It characterizes by the large Stokes shift between maximum positions of the PL excitation and the PL emission band.

• If a material contains a large quantity of both donors and acceptors, PL can occur as radiative tunneling between them (it is known as a Donor-Acceptor Pairs (DAP) luminescence). Before the photo-excited electrons become trapped in donor levels and the holes are trapped in acceptor levels. So, the carriers can be quite separated in the lattice, and at the low temperature, they are able to recombine via radiative tunneling. The decay of this PL is slow because of the low probability of tunneling.

The exact PL mechanism in a-C:H is up to now under discussion. One of the models describes the PL as a version of that used for a-Si:H [184]: non-radiative centers are mid-gap states including defects. By another model, the PL occurs as a variant of that for organic molecules [183, 185, 186]. For comparison, let us first describe the PL processes in a-Si:H [187, 188]. In this case, the effect of disorder dominates the exciton binding. Photoexcitation creates electrons and holes in the extended states. The carriers lose energy (thermalize) and fall into localized tail states, where the electrons lose energy slowly, by hopping within the tail states. Assuming that one carrier, say a hole, has lower mobility and is effectively stationary at R = 0. At low temperatures, where there are not phonons, the electron can only hop to a state lower in energy. This is called energy loss hopping [189, 190]. The hopping rate v is then given by

$$v = v_0 \, exp\left(-\frac{2r}{a}\right), \tag{6.23}$$

where v_0 is the attempt frequency (phonon frequency, 10^{13} Hz), a is the Bohr radius of the tail state, and r is the hopping distance. As the distribution of the states decreases exponentially into the gap [74], the density of available states decreases rapidly, and the average tunneling distance increases:

$$r \sim \left(N_0 \, exp\left(-\frac{E}{E_0}\right)\right)^{1/3}. \tag{6.24}$$

Thus, the tunneling probability decreases. The electron can recombine radiatively by tunneling back to the trapped hole. The rate is

$$v_r = \tau_0^{-1} \, exp\left(-\frac{2R}{a}\right). \tag{6.25}$$

This is the same formula as (6.23) except the prefactor is dipole-allowed rate $\tau_0 \sim 10^{-9}$ s. Hopping creates the distribution of electron-hole distance R. This maps onto the distribution of the PL lifetime accordingly to (6.25). There is a broad distribution of the PL lifetimes in a-Si:H, from 10^{-9} to over 1 s with an average lifetime of $\tau_{av} \approx v_0 \tau_0^2$ s or 10^{-3} s [190]. The far-distanced electrons recombine more slowly. Electrons that have thermalized for a longer time fall

deeper into the tail and are more widely separated. Thus, the PL energy gradually falls with time [187]. This effect has been seen experimentally and thus confirmed the mechanism noted [74].

The PL in a-C:H occurs from a rather localized center because it is unaffected by strong electric fields. It shows polarization memory and it has a short lifetime of about 10^{-8} s [184]. Generally, the relative size of disorder and exciton binding can be found from the exciton energy

$$E_{ex} = -R\left(\frac{m^*}{\varepsilon^2}\right), \tag{6.26}$$

where R is the Rydberg, 13.6 eV. Using $m^* = 0.5$, $\varepsilon \sim 3.5$ for polymeric a-C:H the equation (6.26) gives $E_{ex} \approx 0.5$ eV [74]. This is larger than the disorder (Urbach) energy of ≈ 0.3 eV. However, the exciton radius

$$r = a_0\left(\frac{\varepsilon}{m^*}\right) \approx 4\text{Å}, \tag{6.27}$$

where $a_0 = 0.53$ Å, more than the localization radius of 1.9 Å for ta-C:H, which suggests that localization by disorder is at least as important.

Thus, it is assumed that recombination occurs by a mechanism similar to that for a-Si:H. The electron-hole pair is excited within a single π-bonded cluster. Assume that one carrier, say a hole, remains trapped in the cluster, then the other carrier (electron) thermalizes by energy loss hopping. The hopping causes the electron to fall progressively deeper into the tail. If the temperature is not zero, the electron can be released from the tail states by thermal excitation. The demarcation energy E_d below the top of the tail can be defined. Electrons below E_d are too deep to hop out, and must eventually recombine radiatively to give luminescence. Electrons above E_d will eventually hop out and recombine somewhere non-radiatively. E_d can be written as

$$E_d = kT\ln(\nu_0 t)\,. \tag{6.28}$$

We see that E_d increases with time. If the band tail is exponential, the PL efficiency equals the fraction of electrons below E_d,

$$\eta \sim exp\left(-\frac{E_d}{E_0}\right) = exp\left(-\frac{kT\ln(\nu_0\tau_r)}{E_0}\right). \tag{6.29}$$

The experimental PL efficiency follows the relationship:

$$\eta = \eta_0\, exp\left(-\frac{T}{T_L}\right). \tag{6.30}$$

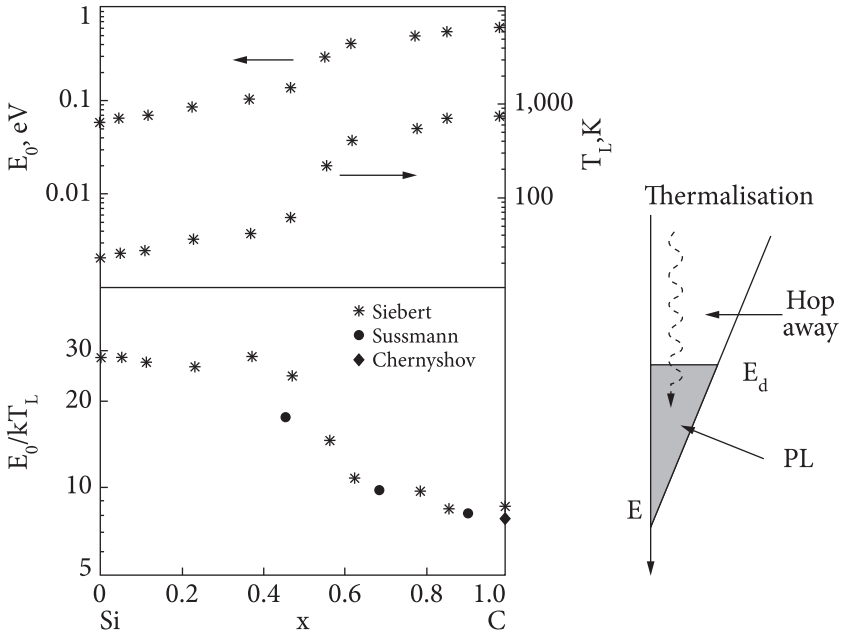

Fig. 6.38. Dependence of the Urbach energy E_0 and PL quenching temperature T_L on the composition x for a-$Si_{1-x}C_x$:H alloys [74, 184]

Mentioned above equations are equal if

$$kT_L = \frac{E_0}{ln\,(\nu_0 \tau_r)}\,. \tag{6.31}$$

Figure 6.38 shows the PL thermal quenching temperature T_L for the a-$Si_{1-x}C_x$:H alloys as depending on the x content [74, 191—194].

T_L is seen to increase sharply from about 50 K for a-Si:H to 700 K for a-C:H. Fig. 6.38 also shows that it increases from 0.05 to 0.4 eV. This figure also notes that the calculated from (6.31) T_L values follow well the experimental variation. Thus, the higher quenching temperature in a-C:H than in a-Si:H occurs because of its broader tails and faster luminescence.

The PL is also quenched if the electron-hole pair is created within a hopping distance of a non-radiative center. The capture radius around the center is usually defined as R_c [188]. Electrons created within a sphere of radius R_c are captured and recombine non-radiatively. Some of them, those created outside of the sphere R_c will be free of recombination and give rise to PL. The R_c value is defined where the rate of radiative PL tunneling equals the rate of non-radiative tunneling to the center. If (6.23) and (6.25) are taken into account, then

$$R_C = \frac{a}{2} ln(\nu_0 \tau_r). \tag{6.32}$$

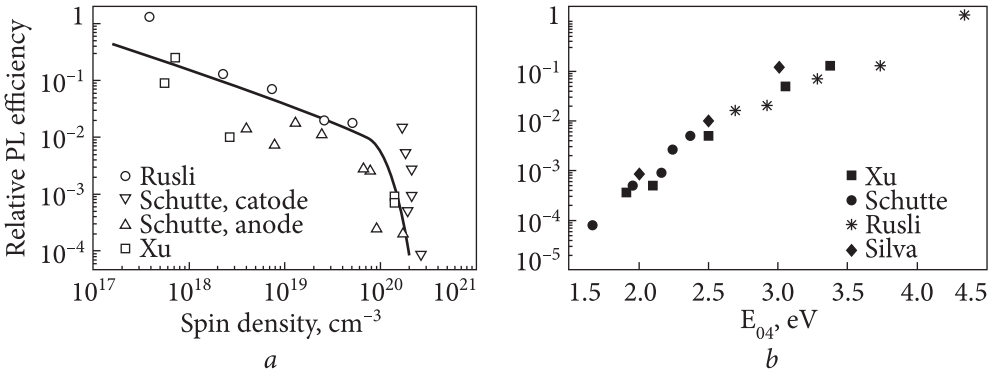

Fig. 6.39. Dependences of the a-C:H PL efficiency on spin density (a) and optical gap (b) [184]

In this case, the PL efficiency is given by the probability of excitation outside of spheres of radius R_c for centers of density N, and it is

$$\eta = exp\left(-\frac{4}{3}\pi R_c^3 N\right). \tag{6.33}$$

The PL efficiency of a-C:H versus the paramagnetic defect density for various sets of data and their comparison with expression (6.33) are shown in Fig. 6.39 [176, 177, 195, 196].

It is obvious that equation (6.33) reproduces the trend of the results if the Bohr radius is a = 2.5 eV. So, the PL efficiency correlates with high defect density as the Bohr radius is small and corresponds to the strong disorder [74].

At the same time, there are certain exceptions to the agreement shown in Fig. 6.39a. In fact, the data show that the PL efficiency changes little for a large change in the paramagnetic defect density [176]. This leads to the suggestion that the main recombination centers were not defects [192, 193]. The explanation of this question is that in a-Si:H, where the main radiative recombination centers are dangling bonds, which are half-filled and thus they are paramagnetic, the tail defect states are well separated in energy in the gap [74, 188]. As for a-C:H, there is no clear distinction. We see a continuous distribution of localized states across the a-C:H gap (Fig. 6.27). Singly occupied states near the gap center are paramagnetic. However, a different set of states could be recombination centers [197, 198], which are defined in the photoconductivity study that has been described in Chapter 1. The states near the upper gap act as electron traps or as recombination centers depending on whether the excitation probability to the conduction band edge exceeds the probability of recombination with a hole. This allows them to draw two demarcation energies as in Fig. 6.27. States between the two energies act as recombination centers, which are not necessarily paramagnetic, unlike in a-Si:H. This is the formal basis of observation [199], for

which states quench the PL. The density of recombination centers will vary in a monotonic way with the optical gap, as the Urbach energy determines.

There is another feature: the radius of localized states, a, is not constant, which is also a feature of a-Si:H. The radius has to vary with the bandgap, and also with hydrogen content. If one deals with a cluster model, a is the radius of the π states localization into the sp^3-bonded matrix [74]. The PL efficiency shows a near exponential dependence when plotted against the optical gap (Fig. 6.39). It is expected that the Bohr radius varies with the optical gap as $a = cE_g - d$. As a result, the PL efficiency varies monotonically with the optical gap because a and the density of recombination centers vary in this direction. The short decay time near 10^{-9} s is a sufficient difference between a-C:H and a-Si:H PL [175]. So, the suggestion arises that the PL center in a-C:H is an exciton and that the exciton is created as a unit by Forster tunneling [185]. The electron-hole pair forms a well-defined exciton, which is not broken by the disorder. The exciton can diffuse by dipolar (Forster) coupling from one cluster to another. Eventually, it will reveal the PL or it can disappear non-radiatively [74].

The arguments confirming the exciton model are the short luminescence decay time and the fact that the decay time does not vary across the PL band [182]. This change is the main manifestation of thermalization effects. At the same time, the decay time is unlikely to vary across the PL band, as the decay (lifetime) is already at the minimum for dipolar coupling, 10^{-9} s. Another way to clarify thermalization effects is to study the polarization memory or "the PL anisotropy" across the PL band. Really, the Pl emitted immediately after excitation or from a localized center converses the excitation polarization. But, if an electron or hole thermalizes into the tails of emitting photons, they will lose some polarization with each emitted photon [74]. The PL memory reveals an exponential range of lifetimes throughout the PL band (6.28), if thermalization takes place. The polarization memory can be defined via degree of polarization (DP),

$$DP = \frac{I_s - I_p}{I_s + I_p}, \tag{6.34}$$

where I_s and I_p are the PL intensity parallel and perpendicular to some direction determined by incident light.

It was measured that there is a continuous decrease of the DP to zero if delay time rises. This is a typical dependence not only for films with small gaps. The obtained data are evidence of thermalization in a general case, instead, a plato was found at a delay of more than 100 ps. The fact leads to a conclusion about the exciton nature of the PL [183, 185].

The exciton model seems to dominate for some polymeric a-C:H, particularly for a-C:H deposited from molecular precursors, and for high excitation energies. In the case of some polymeric a-C:H, PL shows several PL peaks, es-

pecially if excited at higher energies [186, 200]. It is obvious that this feature is evidence of internal radiation transitions.

There is a reason to believe that the band tail model is still generally correct because an exciton band is not observed in the optical absorption spectra of a-C:H, unlike in organic solids, and because the disorder still dominates electron-hole attraction [74]. On the other hand, the electron-hole interaction is more important than in a-Si:H, and in a-C:H this sets the maximum separation of geminate electron-hole pairs, which can recombine radiatively. Potential of disorder E_0 can be used to define a maximum separation in the Coulombic potential following the type of Onsager model [187],

$$R_c = a_0 \left(\frac{R}{\omega E_0} \right). \tag{6.35}$$

This sets the hopping lifetime via equation (6.23) to be $\tau = 10^{-9}$ s, which is the experimentally observed value. So, the electron-hole binding shortens the lifetime in a-C:H unlike in a-Si:H. When the thermalization effect is by times less than 10^{-9} s, it cannot be seen in the spectrum, because it is shorter than the transition rate ν_0. This means that the band tail, together with some exciton binding, is available for explanation of PL in a-C:H [74].

The concept of capture radius (6.32) was used again to describe the band states as non-radiative centers [186]. This is a question, as a non-radiative center can dissipate the energy via phonon generation, via changing configuration coordinates [74]. It is required for occurring non-radiative transition that the E point lies below point B, so the electron moves from excited state to the ground state without passing over a barrier [201, 202]. It is realized for a defect state, as it is weakly bonded and lies in the gap, but it is not likely for band states. In any case, it is an additive argument for the exciton model [74].

6.2. Optical properties of some nanosized carbon forms and expanded graphite

As noted at the beginning of this chapter, the amount of data published about the optical properties of EG is rather small. At the same time, the descriptions made in the previous chapters show that the EG by composition and structure could accumulate various carbon forms such as graphene with different numbers of layers, micro and nanosized particles of graphite, and intercalated graphite; carbon nanotubes also occur in the EG composition. As a result, this diversity of carbon forms is reflected in the optical properties of EG. However, it complicates the analysis of the results of experimental and possible theoretical studies of EG. But, on the other hand, the diversity of compositions and structures indicates the way to control the properties of EG, in particular,

its optical properties, due to the opportunity to vary the conditions of synthesis, composition, concentration of the source components, etc.

In the previous parts of this section, the main attention was paid to describing the optical properties of graphite and intercalated graphite as well as to the role of disordering their structures: amorphous and disordered graphite. In the last two decades, studies have revealed a tremendous increase in interest in optical properties and, in particular, in the luminescence of such nanosized carbon forms as graphene, carbon points, and so on. Therefore, below we will pay attention to the description of optical properties and the application of optical methods to study the structure of mentioned nanoscaled carbon forms. Since their optical properties depend on the conditions of synthesis and original composition, we also will briefly give such data.

We have noted in Chapter 2 that the structure of EG includes graphite crystals and structural heterogeneity regions due to intercalation residues of varying dispersion. The qualitative composition and the quantitative ratio of phase formations corresponding to such inhomogeneities are determined by the treatment temperature. In addition, the content of turbo-defects (due to the azimuthal disorientation of graphene layers) is noticeable in the EG structure, whose concentration is higher than in oxidized graphite. A high concentration of turbo-defects indicates the existence of a nanoporous structure, which in some way determines the properties of EGs and materials produced on their basis. We also found that there are fragments in the structure of EG-folded formations, possibly cylindrical. The sizes of nanostructured fragments lie in the range of units to hundreds of nanometers. Optical methods, in particular, Raman spectroscopy, as we have seen above, provide an opportunity to identify and explore the characteristics of various structural modifications of carbon materials: such as natural graphites of various genesis, shungites, amorphous graphite, products of thermolysis of organometallic and organic compounds, artificial and natural diamonds, etc. The application of this method is also productive in characterizing nanosized carbon forms: graphene, nanotubes, and fullerites. That is why, we will first consider the results of applying different optical methods to characterize possible individual nanosized components of thermo-expanded graphite, and then will describe the results of optical research of EG.

Some optical properties of graphene. Even though graphene is a monoatomic layer, it is not completely transparent, which makes it possible to see it. Interestingly, the absorption of graphene in the optical range does not depend on the wavelength of light and it is $\pi\alpha \approx 2.3\%$, where α is an important in the quantum physics fundamental constant of the fine structure [41]. The unusual optical properties of graphene are due precisely to the fact that its bandgap width is zero, and the conduction band and the valence band are not parabolic, as for electrons in most solid-state materials, but for graphene they are conic.

In general, the real part of the graphene dynamic conductivity is determined by the formula:

$$G_R = \frac{\pi e^2}{\omega} v(\omega)^2 D(\omega) \left[f\left(-\frac{\hbar\omega}{2}\right) - f\left(\frac{\hbar\omega}{2}\right) \right], \tag{6.36}$$

where $v(\omega)$ is a matrix element of the transition rate with the absorption of a photon, $D(\omega)$ is the density of states in graphene, $f(E) = \frac{1}{exp(E/T)+1}$ is statistical Fermi — Dirac distribution, E is the energy, T is the temperature, and ω is the photon frequency. The graphene density of states is approximately equal to:

$$D(\omega) \approx \frac{\hbar\omega}{t^2 a^2}, \tag{6.37}$$

where t is the energy of the excitation transfer from one lattice site to another (about 3 eV), and a is the interatomic distance (about 1.42 Å);

$$v(\omega) \approx v_F \approx \frac{ta}{\hbar}, \tag{6.38}$$

where v_F is the Fermi rate in graphene. The product ta can be estimated by the relationship of uncertainty: $ta \approx 0.5h$.

Thus, the limit for the universal dynamic conductivity will be determined only through the fundamental constants:

$$G_0 = \frac{e^2}{4\hbar}. \tag{6.39}$$

This value was confirmed experimentally in the range of photon energies from 0.1 to 0.2 eV [41].

Optical permeability of monatomic graphene layer can be given in the form:

$$T_{opt} = \frac{1}{\left(1 + \frac{2\pi G_0}{c}\right)^2} = \frac{1}{(1 + 0.5\pi\alpha)^2} \approx 0.977, \tag{6.40}$$

where c is the velocity of light. That is, it is completely determined by dimensionless fundamental quantities. In general, if there are several layers, $1 - T_n \approx n\pi\alpha$, where $n = 1,2,3, \ldots$ is the number of monatomic layers of graphene in the sample. For clarity, a smooth transition from a monatomic to two-atomic graphene was used and with the accuracy of several percent, the described theory then was confirmed [203].

Raman scattering and IR absorption of graphene and some other nanosized carbon forms (brief description of experimental data). Now we will consider the overall Raman spectra of nanosized carbons as they are closely

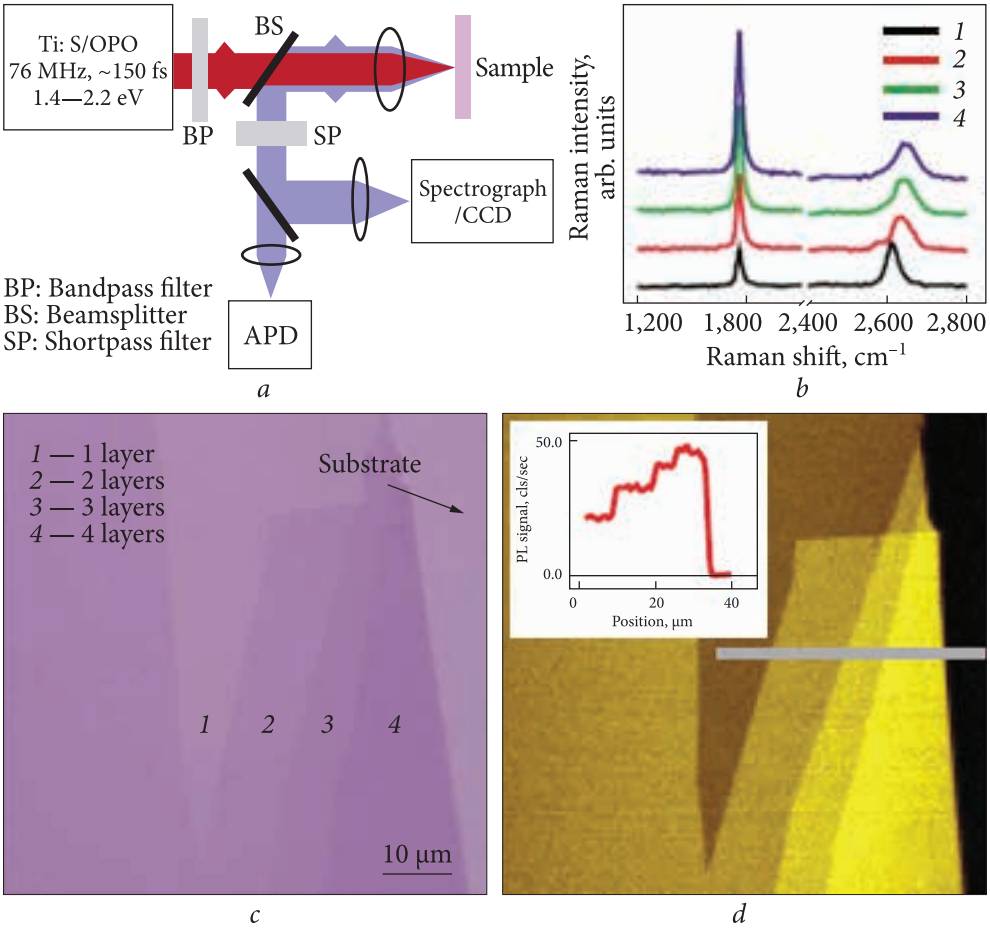

Fig. 6.40. Schematics of the experimental setup (*a*). White-light microscopy image of a thin graphene sample (*b*). CW Raman spectra taken at positions (*1*)—(*4*) (*c*). Nonlinear PL image of the same sample as excited by 1.5 eV femtosecond pulses with signal integrated from 1.66 to 3.11 eV (*d*). Inset: PL signal along the line cut [213]

related to the properties of EG, we suppose. It is not a simple task, as many various factors can affect Raman characteristics, e.g., shift of the G and D peaks and alter their relative intensity (see descriptions made above).

Quantum interference between different Raman paths, that is, scattering in graphene can be detected if some paths are blocked, the intensity of a single-phonon Raman does not decrease, as usual, but, on the contrary, increases sharply [204]. On the other hand, the signal of a two-phonon Raman decreases monotonously with decreasing quantum channels. This discovery gives a new understanding of resonant Raman scattering mechanisms in graphene. Raman scattering from few-layer graphene is readily observable and has been widely

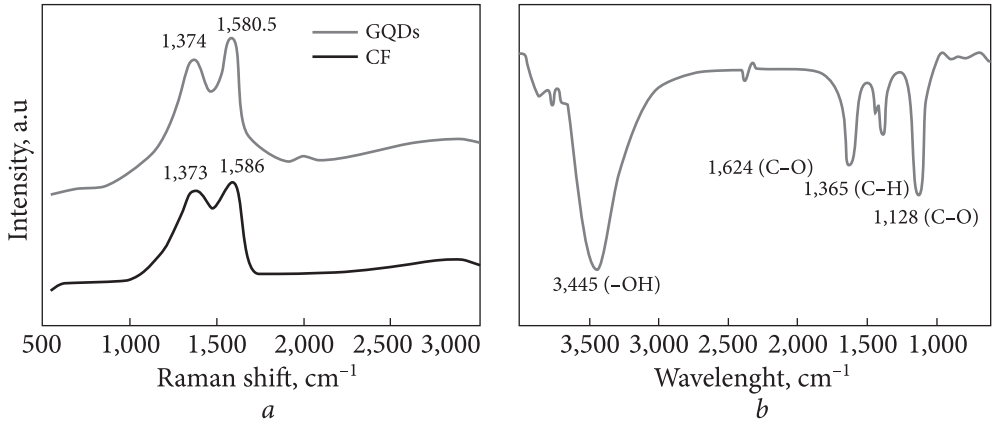

Fig. 6.41. Raman spectra of GQDs and CF (*a*) and FTIR spectrum of GQDs (*b*) [214]

used to evaluate layer thickness [205], characterize quality [206—208], and study electron-phonon interactions [209, 210].

The Raman process is very important for the study of phonons and, because of the role of electronic resonances, also for probing the electronic structure of various materials, and carbon forms are among them [206, 211, 212].

Fig. 6.40, *a* shows the scheme of equipment, and Fig. 6.40, *b* shows the bright-field optical microscopy image of a graphene sample on silicon covered by a 295-nm-thick SiO_2 layer prepared via mechanical exfoliation following the standard procedure [213]. The Raman spectra at different sample positions are displayed in Fig. 6.40, *c*. The sample was found to have one to four monolayers in different regions labeled in Fig. 6.40, *b* [213]. The continuous wave length (CW) Raman spectra were taken with a helium-neon laser at 632.8 nm. All measurements were performed in the ambient atmosphere at room temperature.

Some time ago, a new type of quantum dots, a graphene quantum dot (GQD), attracted attention due to its chemical inertness, biocompatibility, and low toxicity [214—216]. The GQDs have the excellent performance characteristics of graphene such as high carrier transport mobility, superior mechanical flexibility, and environmentally friendly nature [217, 218]. Moreover, converting the 2D graphene sheets into the 0D GQDs can enlarge the electronic and optoelectronic applications due to strong quantum confinement and edge effects [214]. Most works on GQDs have been focused on theoretical prediction, and the experimental synthesis is only a recent effort.

The carbon fiber (CF) has the small domain structure of sp^2 carbons, which makes it easy to extract GQDs since the bandgap and the PL spectrum partly depend on the fraction of sp^2 domains (Fig. 6.41) [219, 220].

Raman spectrum (red line) of GQDs is shown in Fig. 6.41, *a*, which has been usually used to confirm the quality of the prepared GQDs. One can see two ma-

jor Raman peaks at 1374 cm^{-1} (D band) and 1580.5 cm^{-1} (G band). The intensity ratio I_D/I_G is 0.89, which is similar to the high-quality few-layer graphene nanoribbons [221, 222]. The G peak shows a redshift compared with the original CF, which is opposite to the GQDs prepared by another CF [223]. The unique small ratio indicates fewer defects of the GQDs developed by chemical oxidation and exfoliation method than those synthesized by other methods [214].

The Raman spectra of the multiwall carbon nanotubes (MWCNTs) depend on the crystalline arrangement of a tube: while the I_D/I_G ratio, which is commonly taken as a measure of the graphitization index reflects the number of structural defects, the I_{2D}/I_D ratio is sensitive to the overall crystalline quality of the graphitic network and increases with long-range ordering [224]. The Raman spectrum of MWCNTs used in the study [224] will be shown below in Fig. 6.58, f. The observed Raman characteristics are very similar to those of commercial MWCNTs, i.e. high I_D/I_G ratio and low I_{2D}/I_D ratio. They were also similar to those of the GNPs previously analyzed. It was pointed out that the G band position in MWCNTs (1596 cm^{-1}) is higher than that of other carbon materials, and the fact was associated with a large compressive stress affecting the C=C bonds in highly defective tube walls. Note, however, that such an apparent blue shift of the broadened G band may be explained as well by an overlap with the unresolved D′ band at 1610 cm^{-1} (see below Fig. 6.58, *f*).

Graphene (GO) has been successfully used in practical applications and is considered one of the most promising materials for large-scale production of graphene, and surely its particles may be presented in EG. The GO is produced through chemical oxidation of graphite and subsequent exfoliation via sonication. The structural model proposed for graphite oxide composed of graphene oxide sheets involves two kinds of regions: aromatic regions with unoxidized benzene rings and regions containing aliphatic six-membered rings containing C–OH, epoxide and double bonds, the relative size of the two regions depending on the degree of oxidation [224]. The structural defects of GO that destroy the electronic structure of graphene have been already mentioned in the literature (see below). The oxidation process generates a lot of structural defects, which can be evidenced by Raman spectroscopy. Thus, the first order spectrum of GO consists of two broad bands centered at 1590 cm^{-1} (including the unresolved G and D′ bands) and at 1337 cm^{-1} for GO (including the unresolved D3, D and D4 bands). As shown by the deconvolutions (Fig. 6.58, *g*, *h*), the D3 band exhibits a large intensity that could be related to the presence of large amounts of amorphous carbon. The second order Raman spectra present two main broad bands, from which none of the different components (D + D″, 2D, D + G and 2D′) can be clearly located (Fig. 6.58, *g*, *h*) [224].

PL of graphene and some other nanosized carbon forms (experimental data). Since graphene absorbs light very strongly through band to band transi-

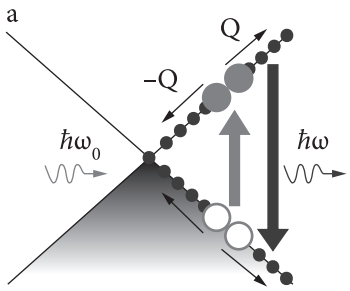

Fig. 6.42. Ultrafast PL in graphene from thermalized hot electrons (figures adapted from [214, 225]: schematic representation of ultrafast PL process from interband recombination [211])

tions, the question arises whether luminescence of graphene can be effective. The answer to this question is that effective light emission is quenched by carrier relaxation, which, because $E_g = 0$, quickly brings the energy of highly excited ***e-h*** pairs down to the ground state (Fig. 6.42) [211, 213, 225].

Below, several types of PL of carbon nanomaterials will be described. PL of un-treated graphene will be observed (at least, directed previous was not performed) and PL of functionalized graphene. Induced by ultrafast (femtoseconds) PL is observable from both thermalized [214, 225—227] and non-thermalized hot electrons [205] under appropriate conditions [211]. Up to 2010, all investigations had been devoted to light absorption in graphene. So, PL had only been reported for oxidized graphene, where the electronic structure was modified and longer-lived states could be formed [219, 228—231].

Upon excitation with a single photon, an energetic electron-hole pair is created in graphene. Then electron and hole relax independently through electron-electron and electron-phonon interactions at the ultrafast time scale. Before they reach equilibrium, the non-thermalized electron and hole have sufficient energy to emit a photon and generate hot-electron luminescence. This hot luminescence is usually very weak in solid-state materials, but can typically still be detected with modern cooled detectors. It can provide valuable information on the ultrafast dynamics of the excited state.

PL from thermalized hot electrons in pristine graphene under femtosecond laser excitation was discussed in [211, 214, 225]. The graphene nonlinear PL arises from a broad distribution of nonequilibrium electron-hole (e-h) gas created via rapid scattering among high-density photoexcited carriers. Although this mechanism is not limited to graphene, its two-dimensional 2D nature and unusual band structure strongly enhance the PL efficiency and bandwidth.

Ultrafast emission from thermalized electrons pristine graphene under continuous-wave laser excitation exhibits no measurable light emission. However, the readily measurable PL spectra from graphene when excited by 30-fs pulses from a Ti:Sapphire laser [214] (76 MHz Ti:Sapphire oscillator pumping an optical parametric oscillator with 150 fs output pulses tunable within 1.4—2.2 eV

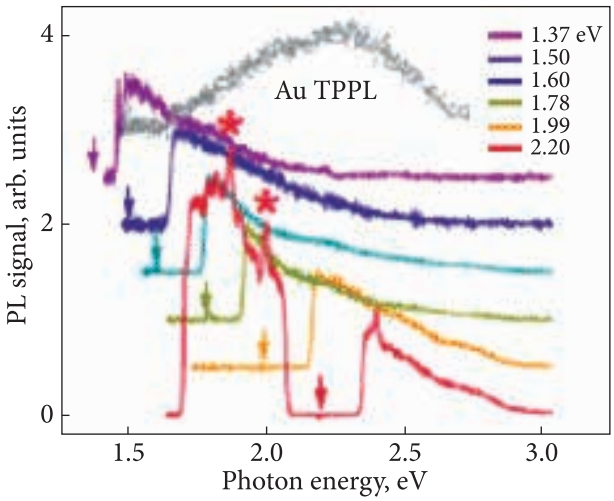

Fig. 6.43. PL under different excitation photon energies. The PL spectrum of gold is also shown for comparison [211]

was used.) were found. As shown schematically in Fig. 6.40, *a*, the beam was focused on the sample at normal incidence, and the PL was collected in the backscattered direction.

The PL quantum yield is about 10^{-9}, more than three orders of magnitude greater than that obtained from the same sample under continuous-wave excitation, which falls below the detection threshold. A distinctive feature of the emission is its wide spectral range, extending over the visible to the near-ultraviolet one. In particular, emission occurs at photon energies well above that of the incident pump photons (at 1.5 eV; $\nu_{ex} = 12100$ cm^{-1}, $\lambda_{ex} = 827$ nm). Similar blue-shifted PL spectra are observed for different pump photon energies (Fig. 6.43), all exhibiting a nonlinear dependence of the integrated intensity of blue-shifted PL on the laser photon energy.

We note that graphene is spectrally very close to an ideal blackbody over the specified spectral range because of its largely frequency-independent absorbance of $A(\omega) \approx \pi\alpha$. The measured PL spectra can be fit well by this simple model; the inferred temperature T_{em} lies in the range of 2000—3200 K and varies sub-linearly with pump fluence.

The PL intensity per atomic sheet decreased considerably in thicker layers, despite the fact that the variation in excitation intensity was small across the ultrathin sample. Representative PL spectra obtained from samples prepared on a transparent glass substrate to avoid interference effects from oxide-covered silicon substrates were presented in [232].

Dynamic response of PL to excitation was checked via autocorrelation measurements [214]. The full-width-half maximum (FWHM) of PL trace envelope in Fig. 6.44 is only 10—20 fs broader than that of the second-harmonic SH signal from quartz inset. Since broadening of the PL FWHM relative to the pulse duration roughly equals the intermediate-state lifetime, [233] it indicates that the PL must arise from an e-h distribution generated within 10—20 fs after the excitation.

The graphene nonlinear PL is particularly efficient and broadband due to several unique properties of graphene:

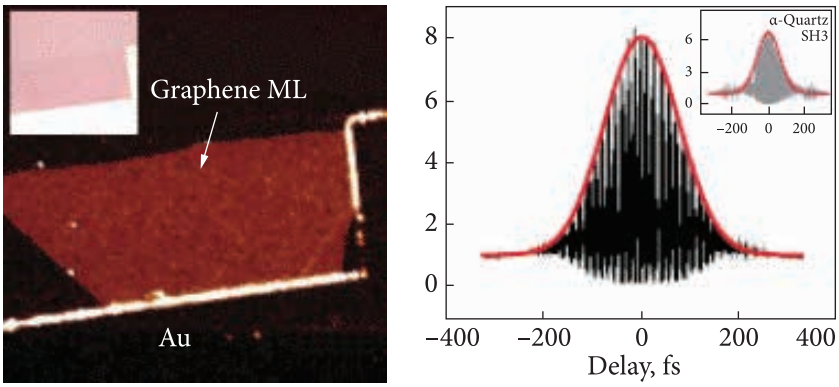

Fig. 6.44. Color online PL image of graphene monolayer along side Au film. Inset: white-light microscopy image of the same area (*a*). PL signal as a function of the delay between two excitation pulses. The red curve envelope is a Gaussian fit. Inset: the SH autocorrelation trace from quartz (*b*). The excitation frequency is 1.5 eV; PL signal is integrated from 1.66 to 3.11 eV [214]

(1) carrier-carrier scattering requires both energy and momentum conservations, which are readily satisfied in the linear bands of graphene. In contrast, the phase space for the same process is much more limited in systems with nonlinearly dispersive bands.

(2) The linear bands lead to a symmetric distribution of non-equilibrium electrons and holes, which facilitates the direct recombination of excited *e-h* pairs.

(3) The energy acquired by an *e-h* pair via intraband scattering cannot be more than its kinetic energy, which equals $h\omega - Eg$ and is the maximum in zero-gap materials such as graphene.

(4) The greatly reduced dielectric screening in 2D graphene results in a very high Coulomb scattering rate [234, 235], which is essential for establishing transient, highly nonequilibrium carrier population, and strong *e-h* recombination. In thicker graphene films, more effective screening and more attenuation of light could cause PL saturation [236].

An intensive light emission over a broad spectral range has been observed from pristine single-layer graphene under excitation by femtosecond laser pulses in the near IR [225]. This light emission process differs from conventional hot luminescence: it has a nonlinear dependence on the pump excitation and appears at photon energies well above that of the excitation laser. The single-layer graphene samples exfoliated from kish graphite (Toshiba) and deposited on freshly cleaved mica substrates were investigated under such experiment [225]. These findings can be described by a model in which the electronic excitations are largely thermalized among themselves, but are only partially equilibrated with strongly coupled optical phonons (SCOPs) and es-

sentially decoupled from the other lattice vibrations. The femtosecond pump excitation can thus produce carriers with transient temperatures above 3000 K which give rise to readily observable emissions in the visible range. In addition to manifesting new physical mechanisms in graphene, these observations provide insight into the carrier and phonon dynamics in graphene. The results indicate that electron-electron scattering under used experimental conditions is efficient on the 10-fs time scale; that coupling with the SCOPs is strong on a time scale below 100 fs, and that equilibration with other phonons occurs on a time scale near 1 ps [225].

In pristine graphene, however, hot PL has never been observed for continuous-wave (CW) excitation. The absence of any measurable hot PL reflects the fact that hot electron and hot hole will almost immediately have different momenta because of their independent relaxation processes. Momentum conservation thus prevents them from recombining and emitting a photon. In gated graphene, however, the situation can change dramatically. Fig. 6.45 shows a 2D plot of the inelastic light emission spectrum as a function of electron doping (as characterized by the value of $2\varepsilon_F$) [204]. The hot-electron luminescence in graphene was demonstrated as the Fermi energy approaches half the laser excitation energy. This hot luminescence, which is another form of inelastic light scattering, results from excited-state relaxation channels, which become available only in heavily doped graphene [204, 211]. A representative spectrum for the hot-electron luminescence at $2\varepsilon_F = 1.4$ eV, corresponding to the horizontal linecut in Fig. 6.45, *a*, is presented in Fig. 6.45, *b*. The emergence of hot-electron luminescence can be understood by noting that a new radiative recombination channel opens up in the strongly doped graphene, as illustrated in Fig. 6.45, *c*.

The hot electron, once it relaxes to energy less than ε_F, can readily undergo radiative recombination with a hole having the same momentum, which is available in heavily doped graphene. This picture implies that for a given Fermi level, hot-electron luminescence is possible only for photons at energies below $2\varepsilon_F$. Indeed, as shown in Fig. 6.45, *d*, this is what we observe experimentally: for emission at higher photon energy, a larger threshold value for $2\varepsilon_F$ is required. This hot luminescence, which is another form of inelastic light scattering, results from excited-state relaxation channels, which become available only in heavily doped graphene.

PL over a wide spectral range emerges when $2|E_F|$ is slightly below the laser excitation energy. The luminescence is distinctly different from electronic Raman scattering because zero momentum electron-hole pair excitations required for the electronic Raman scattering do not exist in strongly doped graphene [237]. The peak observed in the hot luminescence when $2|E_F|$ approaches E_{ex} also has a different physical origin compared with that in G-mode phonon Raman. Instead of being an interference phenomenon from blocked Raman quantum

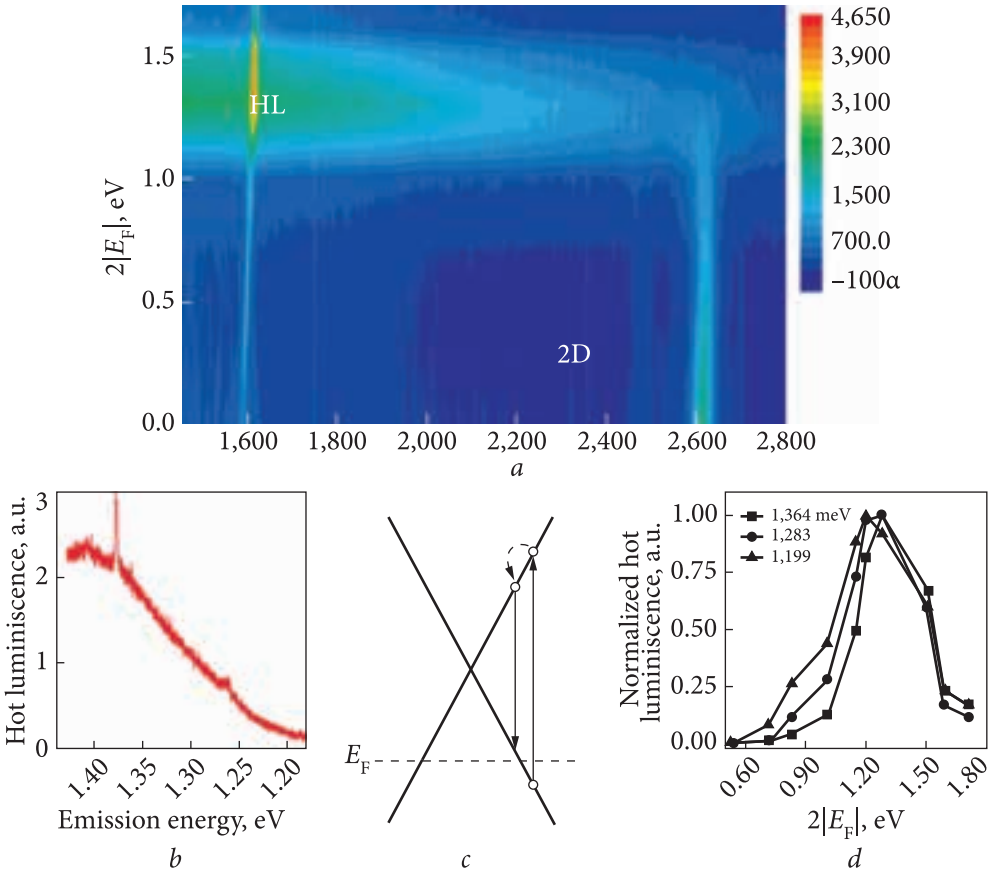

Fig. 6.45. Hot PL in graphene from non-thermalized electrons: *a* — graphene in elastic light scattering intensity as a function of Stokes Raman shift and $2\varepsilon_F$ for excitation with 1.58 eV photon energy. Besides variation in intensities of Raman G and 2D modes, abroad hot PL feature emerges as $2\varepsilon_F$ approaches to the laser excitation energy [204]; *b* — Hot PL spectrum at $2\varepsilon_F = 1.4$ eV has an integrated intensity more than 100 times stronger than from the Raman modes [204]; *c* — Schematic representation of genera-tion of hot PL. As $2\varepsilon_F$ approaches the laser exci-tation energy: the proba-bility for a hot electron (which relaxes very rapidly) to find a hole is dramatically enhanced, leading to the observed PL feature [204]; *d* — Normalized PL intensity as a function of $2\varepsilon_F$ for three different emission energies [204]

pathways, the hot luminescence maximum is a consequence of newly opened dynamic pathways for photo-excited hot carriers. An incident photon generates an electron and a hole, which then relax to the Fermi level through interactions with low-energy electrons and phonons. During the relaxation process, a hot electron has a finite probability of emitting a photon, but requires the final valence band state be empty because of Pauli blocking. This pathway is opened up only when $2|E_F|$ exceeds the light emission energy, and defines a threshold dop-

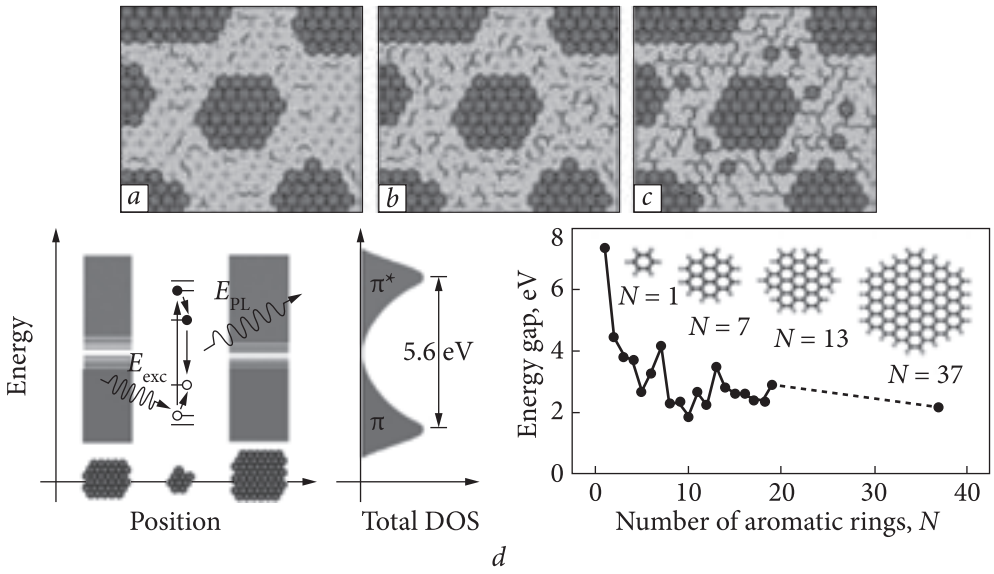

Fig. 6.46. Structural models of GO at different stages of reduction (left), and the energy gap of π-π^* transitions calculated based on DFT as a function of the number of fused aromatic rings (right) [219, 240]

ing level for hot luminescence generation. The qualitative features observed can be understood using the picture: hot luminescence emerges when the energy $2|E_F|$ is higher than the onset value which increases with the photon emission energy. When $2|E_F|$ is further increased to a value greater than the laser energy, hot luminescence at all energies suddenly disappears as the initial photo excitations are blocked. Because the hot luminescence arises from the radiative decay of excited electrons just after photoexcitation, it could become a valuable probe for ultrafast electron dynamics in graphene [204, 211].

Luminescence of functionalized (modified) graphene. Modifications of a graphene sheet by oxidation can introduce direct gap behavior [229, 230]. Although intrinsically a zero-gap semimetal may be oxidized in a manner for solid drop-cast samples and despite the high surface area of graphene oxide (GO) and the marked contrast to carbon nanotubes, it was shown that the intensity of PL from GO flakes does not differ significantly between aqueous and drop-cast samples [230].

A graphene sheet is characterized by an extended π-network, which is structurally analogous to an infinitely large planar aromatic molecule, but fundamentally different in terms of electronic transitions. The lack of bandgaps in graphene is, on the one hand, widely considered as being of unique advantage in such applications as nanoelectronics, but, on the other hand, presents challenges to the community that is more interested in the optical properties of

graphene materials [230]. Therefore, much effort has been devoted to making the π-network in graphene from infinite to finite for the creation of electronic bandgaps. In simplistic terms, this means to isolate conjugated π-domains which are structurally the same as large aromatic molecules in the graphene sheet, regardless of whether the isolation is through creating sp^2 islands in a large sheet or cutting a graphene sheet into small pieces or through other fundamentally similar means or configurations [230].

A usual approach for the creation of sp^2 islands has been the reduction of graphene oxides (GOs), which are typically obtained from exhaustively oxidizing graphite under harsh conditions (Hummers method), followed by exfoliation into predominantly single-layer sheets [238]. GOs were used as precursors for the conversion to reduced GOs (rGOs), which possess some of the basic structures found in single-layer graphene sheets. Generally, the conversion chemistry for rGOs with fluorescent π-domains is controlled to such a degree that there are no π-connections between the sp^2 islands, as that would otherwise result in quenching of the targeted fluorescence emissions [219, 239, 240]. Fig. 6.46 [219, 240] is among the representative illustrations of such an approach.

Experimentally, the observed bandgap fluorescence was not so bright in terms of quantum yields generally lower than those of defect-derived photoluminescence emissions in graphene materials (Table 6.2) [240].

Table 6.2. **PL parameters for selected graphene materials**

Sample source	Sample characteristics	Excitation wavelength (nm)	Emission quantum yield, %	Notes
GOs	Mostly single-layer sheets	325	Negligible	sp^2 islands
		450	0.5	
Aromatic hydrocarbons	132 conjugated carbons	510	2.0	sp^2 islands and edges
GOs	Small graphene pieces	420	7.5	Likely more defect-derived
		360	11.4	
		350	12.8	Butylamine functionalization
GO-like material		450	10	PEG_{600N} functionalization
GOs		360	28 %	PEG_{1500N} functionalization

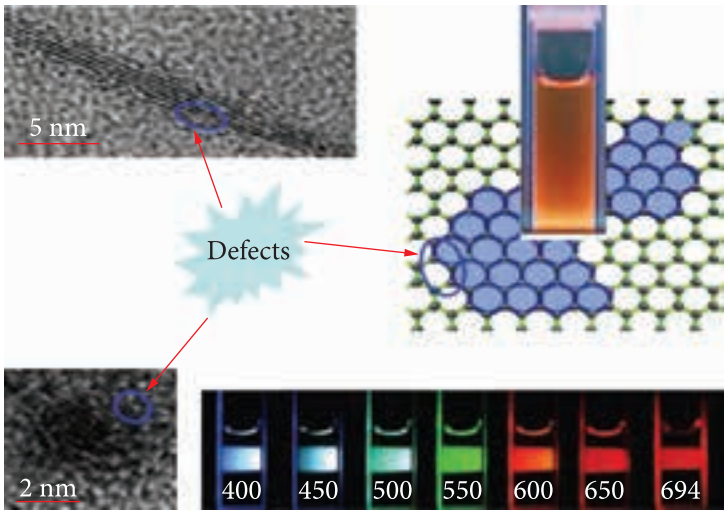

Fig. 6.47. Upper: isolated sp^2 islands in a graphene sheet and a photo showing bandgap fluorescence in solution (right, [245]), and a multiple-layer graphene piece (left). Lower: a carbon nanoparticle with surface defects (left), and emission color variations in carbon dots (right, [246]) [240]

Researchers have found defect-derived photoluminescence in carbon nanotubes and small carbon nanoparticles, dubbed carbon "quantum" dots or "carbon dots". The structural characteristics in the underlying graphene materials have been associated with those emission properties as a way of classifying them into two primary categories: emissions that originate from created or induced energy bandgaps in a single graphene sheet and emissions that are associated with defects in a single- and/or multiple-layer graphene [240]. They highlight the similarities and differences between the observed PL properties of graphene materials and those found in other carbon materials, including carbon dots and surface defect-passivated carbon nanotubes, and discuss their mechanistic implications.

It is now widely acknowledged that graphene materials could be made photoluminescent over the visible spectral region, extending into the near-IR, though various emissions observed experimentally might have different origins. A "perfect" (found in computer simulations) or nearly perfect single-layer graphene sheet is not photoluminescent for a lack of electronic bandgaps. Therefore, the creation of energy bandgaps has been a popular strategy to impart fluorescence in graphene [219, 241—245]. There are obviously many different ways to create or induce bandgaps, such as cutting graphene sheets into small pieces (or producing pieces directly) or manipulating the π-electronic network to form sp^2 "islands" in a graphene sheet (Fig. 6.47), though most of them are associated with structural defects as well. In fact, one may argue that the formation of islands is a result of specifically engineered defects in graphene sheets (Fig. 6.47) [240].

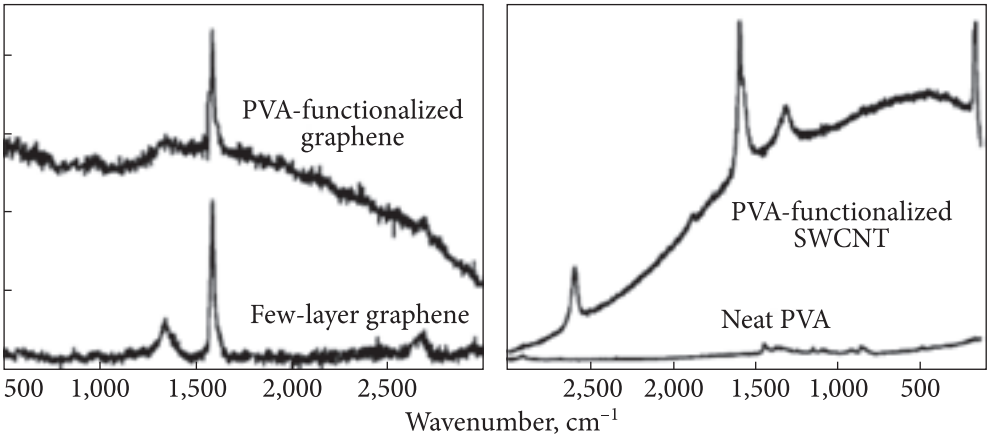

Fig. 6.48. Raman data on polyvinyl alcohol (PVA) functionalization of few-layer graphene (left [255]) and of SWCNT (right [256]) [240]

Defects and their effects on electronic transitions are apparently at the center of both opportunities (for bright PL emissions) and complications relevant to the optical properties of graphene and related materials.

There have been many literature reports on the observation of PL emissions in carbon (graphene-like) materials, which have been assigned to various origins [219, 223, 228, 229, 239, 241—254]. A closer examination of the spectroscopic features of the emissions and associated structural characteristics in the underlying materials would suggest that most of the observed PL emissions could be divided roughly into two categories. One is related to bandgap transition corresponding to conjugated π-domains, and the other with a more complex origin associated with defects in the graphene structures. The two categories may be interconnected in many cases, as the creation or induction of π-domains is often based on operation or manipulation of defects in graphene sheets.

Some remarks on PL related to defects in carbon materials. The creation of electronic energy bandgaps in graphene has been a popular approach to impart fluorescence, but many other observed PL emissions can hardly be assigned to any bandgap origin. In the bandgap-based fluorescence discussed above, the single-layer configuration and nonpercolation between sp^2 islands are necessary in order to avoid any significant interlayer and interisland fluorescence quenching effects, respectively. Therefore, the PL emissions observed in multiple-layer graphene sheets could obviously not be originated from the same kind of conjugated π-domains. An early example for such PL was related to the chemical functionalization of few-layer graphene sheets, where significant luminescence interference was observed in Raman characterization of functionalized samples similar to that encountered in the chemical modification or functionalization of carbon nanotubes (Fig. 6.48) [256]. In a number of studies on small graphene

pieces, including multiple-layer ones, similar PL emissions were observed (Table 6.2) [240, 257].

Defects in graphene sheets are loosely defined, probably due to the variety of possible structural details. Many seemingly distinctive PL emissions in graphene materials have been found, which could not be explained in terms of fluorescent sp^2 islands or the like. There are sp^2 and sp^3 carbons in the sheets that are not perfect, so defects are really any sites other than the perfect sp^2 domains. Among representative examples were emissions proposed as being originated from functionalized surface defect sites [253] ascribed to CO-related localized electronic states at the oxidation sites after oxygen plasma treatment of graphene [228, 243] and "quasi-molecular fluorescence" in oxidized graphene arising from carboxylic acid groups electronically coupled with nearby atoms in polycyclic aromatic compound-like moieties [247].

These non-bandgap emissions apparently share a common attribute for their relationships to or even dependence on defects in graphene materials, though mechanistic details are probably more complex. A characteristic feature in many of the observed PL emissions was a lack of substantial interlayer quenching, contrary to the critical requirement for being single-layer only for the bandgap fluorescence discussed above. The defect-derived PL emissions are also generally much brighter, corresponding to higher observed quantum yields (Table 6.2). For at least those emissions that are sensitive to the passivation of defects in graphene materials, with those well-passivated ones exhibiting much-enhanced emission intensities [242, 252, 253], the observed PL properties are generally similar to those found in surface-passivated carbon nanoparticles and nanotubes [240, 246, 258—262].

PL in carbon nanosized forms (nanoparticles, dubbed "quantum" dots or "carbon dots"). The blue or green luminescent GQDs were made by the hydrothermal method through cutting graphene sheets [215, 244, 263]. An electrochemical means of synthesizing green-luminescent functional GQDs has been reported in [257]. A mechanistic approach to the synthesis of atomically defined GQDs by metal-catalyzed cage-opening of C60 was presented in [264]. A simple and effective approach to easily synthesize photoluminescent GQDs using commercial carbon fibers (CFs) as the raw material was developed in [264]. This method consists of chemical oxidation and exfoliation routes, which are always used to solubilize carbon nanoparticles [265, 266]. The as-synthesized GQDs can freely disperse in water and organic solvents without further chemical modification and ultrasonic dispersion. Interestingly, the as-synthesized GQDs possess excitation-independent PL properties and can be divided into blue and green photoluminescent GQDs by different dialysis bags. 0.6 g CFs were dispersed in concentrated H_2SO_4 (120 ml) and HNO_3 (40 ml) for 5 h under continuous ultrasonic treatments (100 W), and then the mixed solu-

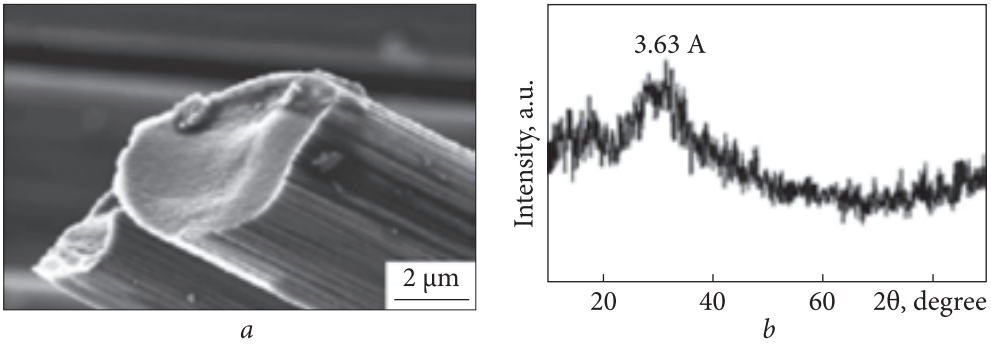

a *b*

Fig. 6.49. SEM image and (*a*) XRD pattern of the pitch-based CF (*b*) [215]

tion was refluxed for 24 h at 100^0 C with magnetic stirring. (Pitch-based CF is a kind of microcrystal graphite material, which was processed by carbonization and graphitization using organic fibers (Fig. 6.49) [215].)

As-synthesized GQDs were characterized with FTIR technology and the result reveals a predominant functionalization of the GQDs with hydroxyl–OH group ($\nu_{-OH} \approx 3448$ cm^{-1}) and carboxyl group (–COOH, $\nu_{-COOH} \approx 1624$ cm^{-1}). The presence of O-rich groups makes the GQDs soluble in an aqueous medium and provides additional advantages for the further foundation to meet various requirements. Apart from the solubility of the GQDs in an aqueous medium, as-synthesized GQDs can also be well dispersed in common organic solvents such as chlorobenzene and DMF, which facilitate the applications in non-aqueous phase and organic devices [215].

In the UV—VIS absorption spectrum (Fig. 6.50, *a*), a typical absorption band at 373 nm can be observed, which is assigned to the π-π^* transition of graphite is sp^2 domains [267]. The PL spectrum (Fig. 6.50, *b*) shows a strong peak at 507 nm when excited at 373 nm, and FWHM is about 100 nm, which approximates that of the most reported carbon nanodots [244, 257, 263—266]. When the exciting wavelengths change from 300 to 460 nm, the PL intensity decreases remarkably, but the fluorescence emission peak remained unshifted. This excitation-independent PL behavior is different from most of the reported carbon-based nanomaterials [244, 257, 263, 264], which were dependent on excitation wavelength and always shifted to longer wavelengths. This special feature may result from fewer surface defects and more uniform size of GQDs [215].

The most distinctive feature of the GQDs which sets them apart from other previously reported carbon dots is, *inter alia*, the specific process of separating green and blue luminescence GQDs. Interestingly, the dialysis process not only purifies GQDs but also makes different optical properties from inside to outside of the dialysis bag (Fig. 6.50, *d*). For comparison, most of the reported blue-

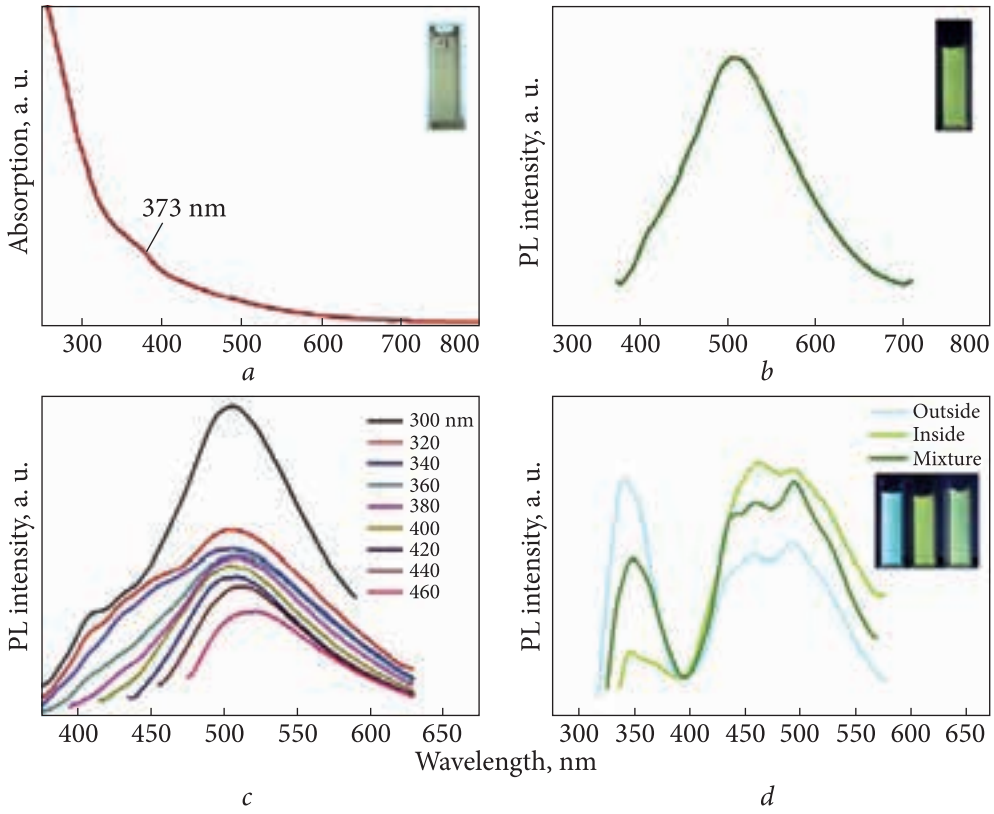

Fig. 6.50. UV—VIS absorption spectrum of GQDs; inset: photograph taken under visible light (*a*); PL (373 nm excitation) spectra of GQDs; inset: photograph taken under 365 nm UV light (*b*); PL (300—460 nm excitation) spectra of GQDs (*c*); and PL (294 nm excitation) spectra of GQDs outside, inside the dialysis bag and the mixture; inset: photograph of them taken under 365 nm UV light (*d*). (For interpretation of the references to color in this figure legend, the reader is referred to the web version of this information) [215]

luminescence GQDs had a longer wavelength at the absorption peak [220, 263]. This selective separation process confirms that the different-size GQDs show a quantum size effect, which can contribute to PL properties [215].

Generally, a small difference was seen in PL intensity for l-GO (liquid) and s-GO (solid) samples (Fig. 6.51, *a*) [230]. For isolated flakes in l-GO, diffusion of free carriers or bound excitons should be confined to the 2D GO plane. However, for s-GO, both atomic force and optical microscopy indicate films of layered GO flakes, which could give rise to additional interflake relaxation pathways. If the interlayer coupling is strong enough, the emission spectrum could redshift. s-GO indeed shows more PL spectral weight in the infrared, but the redshift in the PL peak position is not a robust feature of the experiment and was inconsistent from sample to sample perhaps due to variations in the oxidation density.

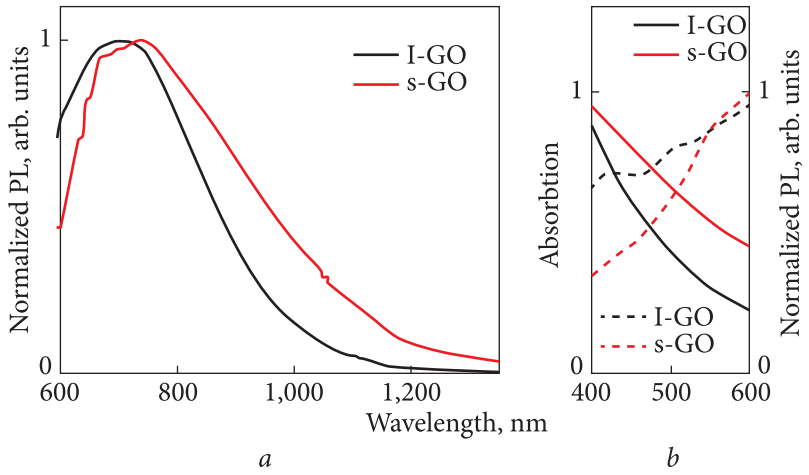

Fig. 6.51. Normalized PL spectra excited at 500 nm (s-GO taken in transmission) (*a*). Absorption (left axis, solid) and PL intensity detected at 752 nm (right axis, dashed) as a function of excitation wavelength (*b*) [230]

In addition to exciton diffusion, several plausible changes could also influence the peak position, including modifications of the dielectric environment, spectral reabsorption, and variations in oxidation density [230]. Accounting to the data, one must consider the possibility that the electronic structure within the flakes is heterogeneous, and that PL emission originates from absorbance into excited states whose total absorptive cross-section is, nevertheless, only a small contributor to the total absorptive spectrum. Nevertheless, we may qualitatively evaluate that the observed quantum yields appear to be far below unity. The process of oxidation was repeated several times to progressively reduce the sample, which resulted in a marked redshift (Fig. 6.52) [230].

A theoretical framework for interpreting these data is only just emerging. It can be expected that oxidation produces a disruption of the π-network and can open a direct electronic bandgap for single-sheet graphene in one of two ways. The first is a quantum confinement effect whereby the π-electron wave functions occupy a potential landscape with strongly repulsive hard wall barriers at oxidized sites. In the infinite potential limit, a delocalized π-electron wave function will develop nodes at each of these sites. The presence or absence of a gap for a sample with many such oxidized sites then depends on the spatial distribution of these nodes. E.g., in graphene ribbons, the edges break the sublattice symmetry; the lateral confinement of the wave function produces a bandgap at its charge neutrality level [230].

Alternatively, for the special edge that preserves sub-lattice symmetry (a "zig-zag" ribbon), one finds instead a resonant electronic state exactly at zero energy. These results generalize to a disordered potential landscape where the

nodes occur in the interior of the sample. Pereira *et al.* [268] modeled the effect of lattice vacancies in a single-valley picture and found that a hard gap opens only in the special situation where there is a complete sub-lattice asymmetry in the vacancy distribution.

Another gapping mechanism arises when one considers, in addition, the effects of intervalley scattering from the short-range potential of oxidized carbons. Within the context of bond-disorder induced energy gaps, one regards the GO plane as a landscape containing a wide range of local bandgap minima. This notion is consistent with the very broad range of observed emission energies [230].

Quantum dots (QDs) were originally referred to as semiconductor nanoparticles of sizes in the quantum-confined regime (smaller than the exciton Bohr radius, typically in a few nanometers), which exists in small particles. They are confined in the spatial dimensions with quantized energy states. Typical semiconductor QDs are nanocrystals of inorganic compounds from the group QDs elements in the periodic table. As a result of the quantum confinement, QDs often exhibit unique size- and composition-dependent optical and electrical properties. E.g., semiconductor QDs such as CdS or CdSe are well-known for their predict-

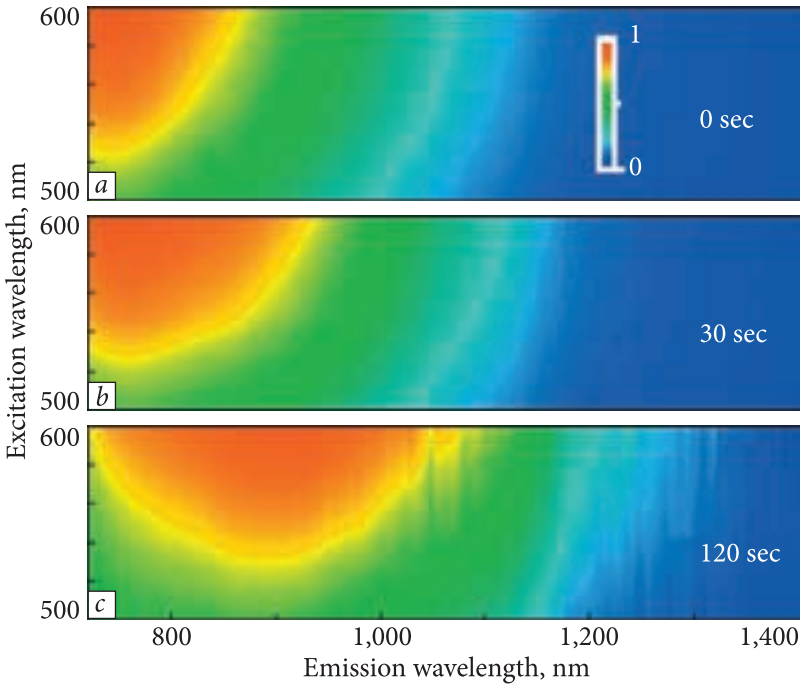

Fig. 6.52. Normalized PL excitation-emission maps for s-GO taken in transmission during hydrazine vapor exposure [230]

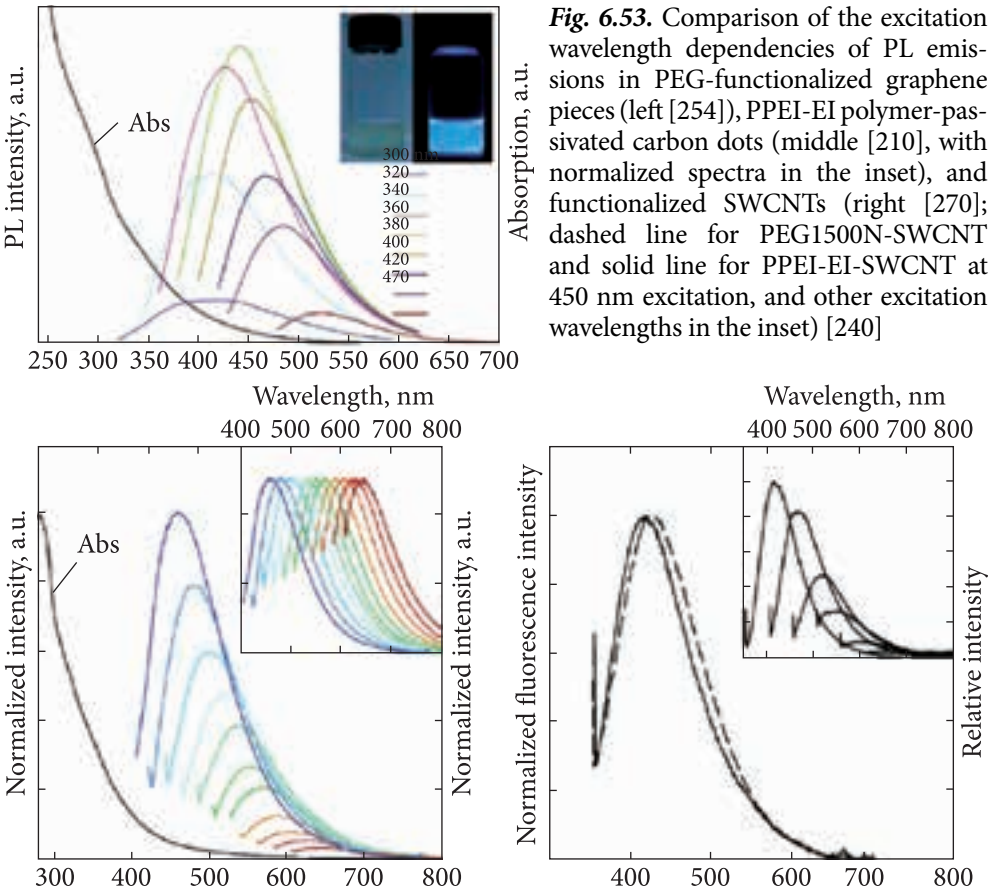

Fig. 6.53. Comparison of the excitation wavelength dependencies of PL emissions in PEG-functionalized graphene pieces (left [254]), PPEI-EI polymer-passivated carbon dots (middle [210], with normalized spectra in the inset), and functionalized SWCNTs (right [270]; dashed line for PEG1500N-SWCNT and solid line for PPEI-EI-SWCNT at 450 nm excitation, and other excitation wavelengths in the inset) [240]

able energy bandgaps at different nanocrystal sizes, corresponding to beautiful fluorescence color variations. Surface defects in conventional QDs of semiconductor nanocrystals are generally considered undesirable, causing energy "leaks" and other negative effects on the bandgap fluorescence emissions. Therefore, a number of strategies have been developed to minimize defect-related effects, such as the capping of a semiconductor nanocrystal by another wider-bandgap semiconductor (particularly famous CdSe/ZnS core-shell nanostructures, e.g.) to achieve much-enhanced fluorescence properties [240, 269].

There are obvious similarities between electrons confined in the conjugated π-domains in graphene and in nanoscale semiconductor particles, with similar size-dependent electronic energy bandgaps and corresponding variations in fluorescence colors. Therefore, the former is conceptually similar to the latter, perhaps logical to be named as graphene quantum dots (GQDs), even though isolated sp^2 islands are structurally not "dots" at all. As for small graphene pieces, they appear to be closer to dots, but issues such as effects on or possible contri-

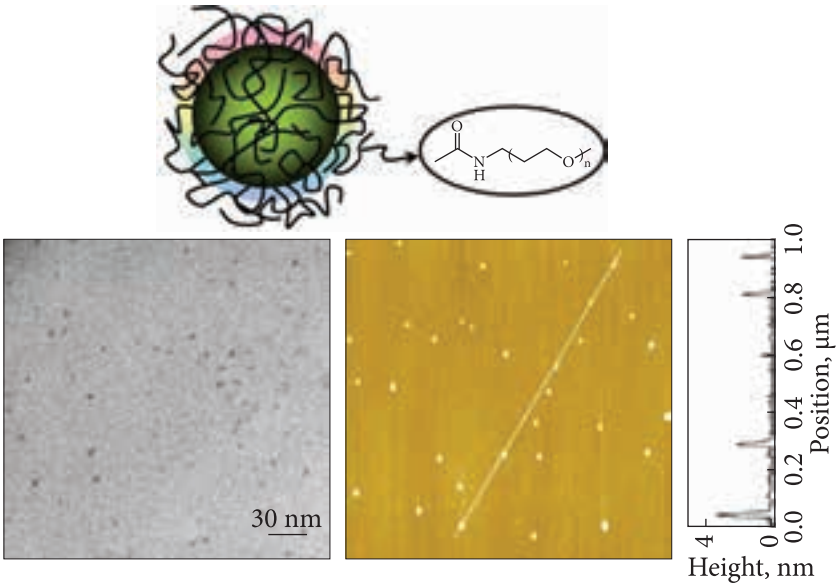

Fig. 6.54. Cartoon illustration for a typical carbon dot (upper), and representative TEM and AFM images of ultrabright PEGylated carbon dots (lower, [240, 260])

butions to the observed fluorescence emissions by the edges and/or defects still need to be addressed [240].

In fact, the fluorescence color variations with the π-domain sizes in graphene sheets are less pronounced in comparison with those found in classical semiconductor QDs due to the intrinsic properties of the created or induced energy bandgaps and also likely to the expected "contamination" by the defect-derived PL emissions [240].

The GQDs have also been used in many studies to refer to graphene materials of PL emissions that are not associated with isolated sp^2 islands and thus cannot be assigned to bandgap transitions, but with a somewhat different version of emission color variations (Fig. 6.53). Many of the observed emission properties resemble those found in surface-passivated small carbon nanoparticles (Fig. 6.53), dubbed carbon "quantum" dots or carbon dots (Fig. 6.54) where the word "quantum" is in quotation marks for the lack of the same kind of the classical quantum confinement found in semiconductor QDs [240, 246, 259]. The only quantum effect in carbon dots seems to be associated with the requirement for the carbon nanoparticles to be small enough to achieve an extremely large surface-to-volume ratio [240, 246].

Carbon dots have recently emerged as a new class of brightly photoluminescent (or fluorescent if the proposed electronic transition character is ulti-

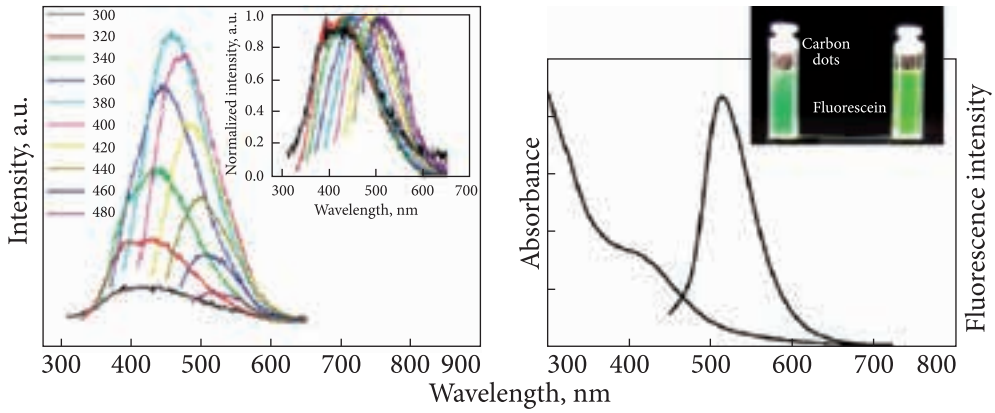

Fig. 6.55. Left ([274]): PL spectra of suspended carbon nanoparticles (excitation from 300 to 480 nm). Right ([260]): Absorption and PL (440 nm excitation) spectra of ultrabright PEGylated carbon dots, with a photo in the inset comparing to an aqueous solution of carbon dots and an ethanol solution of fluorescein with matching optical density at 440 and 490 nm, respectively, under sunlight [240]

mately proven correct) nanomaterials [246, 259—262, 271, 272] with their photophysical properties resembling in many respects those commonly found in semiconductor QDs. A typical carbon dot is a small carbon nanoparticle with the particle surface functionalized by organic molecules or coated with polymers or other species (Fig. 6.54) [240]. Spectroscopically, carbon nanoparticles are rather effective in photon harvesting, with the optical absorption covering a broad spectral region, which is primarily π-plasmon in nature [240, 273].

Upon the near-UV or visible photoexcitation of even bare carbon nanoparticles without any surface functionalization, relatively weak emissions have been observed in aqueous and other suspensions (Fig. 6.55), where the solvent molecules might have provided some relatively minor surface passivation effect) [274, 275]. With the surface passivation, carbon dots are strongly emissive in the visible, extending into the near-IR range (Fig. 6.55) [240]. So far, the ultrabright carbon dots are those with emissions in the green, marching surprisingly well the spectral coverage of green fluorescence proteins, with experimentally determined emission quantum yields up to more than 75% [261].

The observed emission decays in carbon dots are generally not single exponential, but on average not fast, with averaged lifetimes of 4—5 ns [260]. Therefore, in another way to look at the strong optical transitions in carbon dots, the radiative rate constants for the emissions, which are known to reflect on the electronic transition probability, are around 10^8 s^{-1}, much larger than those found in any organic chromophores.

As mentioned above, many of the observed PL emissions in graphene materials are similar to those in carbon dots in almost all aspects of the spec-

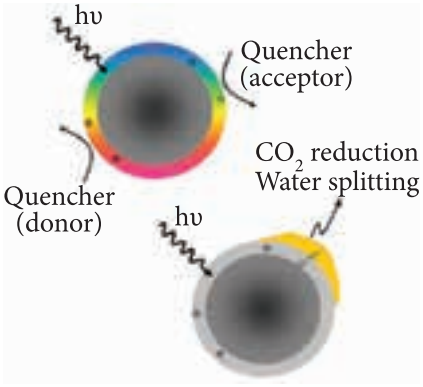

Fig. 6.56. Cartoon illustrations of structural features and related mechanistic implications in carbon dots (upper) and those with the dot surface doped with gold or platinum metal (lower) [240]

troscopic properties, including especially the passivation effect for significantly enhanced emission quantum yields (Table 6.2) and characteristic spectral changes with excitation wavelengths (Fig. 6.53). E.g., a mixture of different-sized graphene pieces for surface-passivation by polyethylene glycol (PEG) was also used. The resulting materials exhibited excitation wavelength-dependent PL emissions that are comparable with those found in carbon dots (Fig. 6.53) [240, 253].

Structurally, defects in graphene sheets involving sp^3 carbons are similar to ones on the surface of a small carbon nanoparticle with an extremely large surface-to-volume ratio (Figs. 6.42 and 6.43) [240]. It is, therefore, logical to expect them to share the same PL mechanism. As for the emission mechanism in carbon dots, it has been proposed in [246, 259] and is now increasingly adopted in the relevant research community that radiative recombinations of the carbon nanoparticle surface-confined electrons and holes (Figs. 6.42 and 6.43) are responsible for the observed bright PL (or simply called fluorescence in such a mechanistic framework) [240].

Electrons and holes are generated probably to make the surface sites more stable to facilitate more effective radiative recombinations. Experimental evidence in support of the mechanistic framework includes the PL quenching results with both electron donors and acceptors, which could apparently scavenge the surface-confined holes and electrons in carbon dots, respectively, to result in efficient and effective quenching of the emissions (diffusion-controlled with additional static contributions) [240, 276].

Recently, it was also demonstrated that the photogenerated electrons in carbon dots could be used for reduction purposes [273, 277] and, more importantly, the electrons could be concentrated onto the gold or platinum-doped carbon particle surface for the photocatalytic conversion of carbon dioxide and also the photocatalytic splitting of water for hydrogen generation (Fig. 6.56) [240, 277]. These results have reinforced the view that carbon dots essentially resemble nanoscale semiconductors in terms of photoinduced redox processes, in which the radiative recombinations in the absence of quenchers result in bright PL. For the defect-derived PL emissions in graphene materials, similar redox-driven quenching processes with both electron donors and acceptors have been

reported [248, 253]. The results are further evidence of the obvious similarities between defect-derived PL emissions in different carbon nanomaterials.

In the final analysis of GQDs and CD, the former has essentially been used loosely in the literature to refer to two rather different categories of photoluminescent graphene materials: ones fluorescent due to created or induced bandgaps and the others associated with defects. The defect-derived PL emissions in graphene materials are phenomenologically and likely also mechanistically do not differ from those in carbon dots. Since the emissions due to defects are generally much brighter, with significantly higher quantum yields (Table 6.2), there is thus the question of how much they contaminate the relatively weaker bandgap emissions in quantized sp^2 islands (probably more legitimate mechanistically for their designation as GQDs), as defects obviously play a significant role in the creation or induction of conjugated π-domains in graphene. One might even argue that some of the reported bandgap fluorescence emissions in graphene were actually combinations with defect-derived PL emissions.

For both SWCNTs and their multiple-walled counterparts (MWCNTs), the as-produced soot-like samples often contain carbon and other impurities such as residual catalysts, which thus require purification by using oxidative acids or the like. These defects become brightly emissive under some specific conditions, especially when functionalized for the purpose of dispersion at the individual nanotube level without bundling or aggregation [278, 279].

The passivated defect-based PL emissions in graphene materials, carbon dots, and carbon nanotubes likely share the same mechanistic framework, namely, that the emissions are due to radiative recombinations of trapped electrons and holes. In fact, the PL emissions in carbon nanotubes are indiscriminative between single-wall carbon nanotubes and multi-wall carbon nanotubes, similar to the same indiscrimination between single- and few-layer graphene sheets for the defect-derived emissions.

It seems that the presence and absence of quenching effects may be understood in terms of the emissive entities in these carbon nanomaterials. The bandgap fluorescence in graphene is associated with the sp^2 island (the emissive entity) on a single sheet, which is quenched by π-domains in neighboring sheets in a few-layer configuration, whereas the defect-derived emissions are associated with the defect site (the emissive entity) across several sheets in a similar few-layer configuration, and thus are little affected by the interlayer interactions.

There have been no reports in the literature on interactions between two or more graphene species that result in insignificant quenching of either bandgap fluorescence or defect-derived PL emissions. However, the quenching of this kind has been used successfully in probing the unbundling of carbon nanotubes, in particular their dispersion in polymeric and other nanocomposite materials [258,

279]. Obviously, the better the dispersion, the stronger the observed emissions due to the reduction or elimination of any intertube quenching effects. Similar applications for PL properties of graphene materials may be expected [240].

The large observed gap creates the possibility for spatially modulating the band structure within a single graphene flake by local control of the oxidation profile. Studies of progressive chemical reduction show quenching of PL for both drop-cast and aqueous samples, coordinated with changes in absorption. These studies also find signatures of bandgap manipulation, albeit with different character for solid and liquid samples [230].

6.2.1. Optical spectroscopy of expanded graphite

The procedure for making EG samples for research has been described in detail in Pt. 2.2.3. Here, we would like to emphasize that the just newly manufactured powdered EG samples, rolled powders, ribbon-like, and samples of EG powders pressed in the form of disks have been studied.

Each of the carbon forms, as shown in the review part of this section, has its own specific Raman spectrum. Therefore, Raman spectroscopy was also used to study the structure of our EG samples. The obtained data were compared with the data on Raman scattering and hence on the structure of other carbon graphite forms such as SWCNT, carbon black stock, and crystalline graphite [280—284].

Fig. 6.57 shows the Raman spectra of expanded graphite (noted as EG), SWCNT, soot (carbon black stock as a purified waste of foundry production), and crystalline graphite. (The measurements of Raman scattering were performed using a Brucker RFS 100/s spectrometer. As a source of excitation, a Neodym-YAG neodymium laser with a wavelength of radiation $\lambda = 1064$ nm was used). It should be emphasized that the main line of Raman scattering, the so-called G-mode, which characterizes the tangential fluctuations of carbon atoms and the level of perfection of the crystalline lattice of graphite structure, is about 1581 cm^{-1} and coincides with the experimental value for crystalline graphite and the theoretical calculation for a layer of carbon atoms (see above and, e.g., [74]). It should be noted that another characteristic mode of the graphite-like materials, the D mode of the A_{1g} symmetry, which characterizes the disorder of the graphene layer grid, is practically not recorded in these samples of EG and crystalline graphite. This mode is about 1300 cm^{-1} and corresponds to the respiratory vibrations of the graphene layer rings at point B of the Brillouin zone [74, 4]. There is a very wide maximum at 1318 cm^{-1} for soot and a sufficiently large scattering at 1275 cm^{-1} for the nanotubes. It should be noted that the second harmonic of this intensity vibration exceeding the magnitude that is usually observed for second-order oscillations is well recorded for EG and nanotubes,

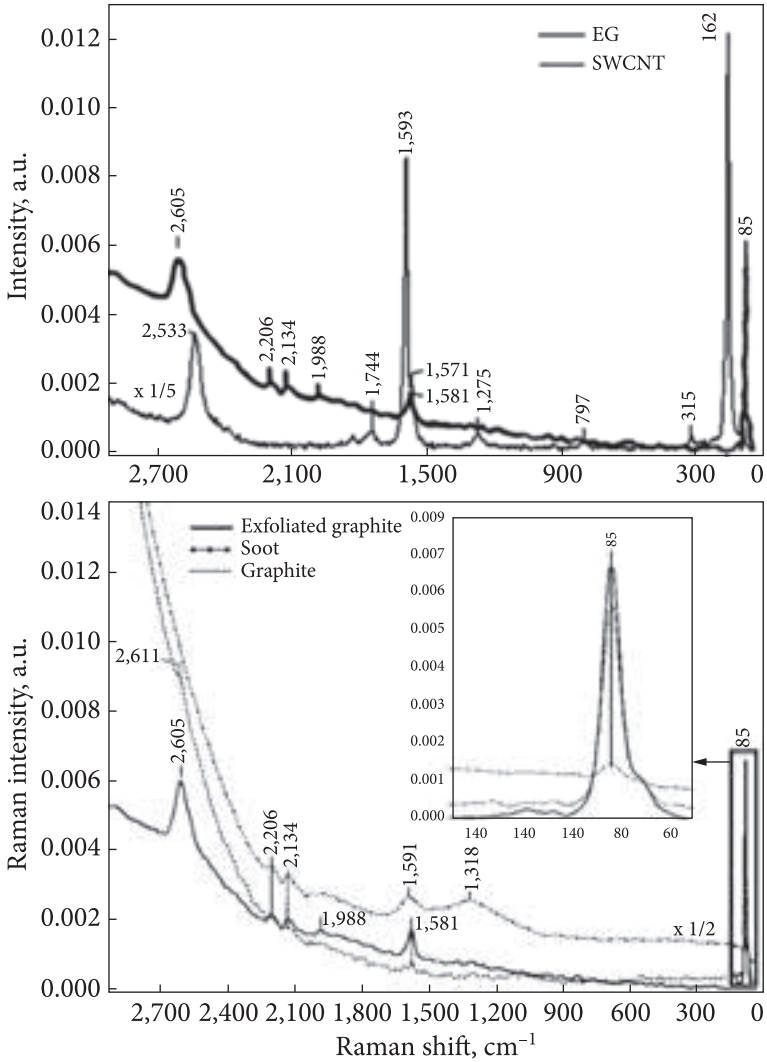

Fig. 6.57. Raman spectra of EG, SWCNT, soot, and crystalline graphite

which may indicate that EG and nanotubes have similar structures leading to strong electron-phonon interaction. The other graphite materials do not show such a feature. Single wall carbon nanotubes have a low-frequency mode of high intensity, which is associated with fluctuations of the tube as a whole [4]. Also, typical for EG is the high intensity of the low-frequency mode with a maximum of 85 cm^{-1}. This abnormally high intensity of this line also confirms the view of a certain structural similarity between EG and nanotubes. Assuming the existence of similar nanostructures in EG with graphite-like parameters of binding and lattice and using the formula that binds the vibration frequency with the

diameter of the structure involved in vibrations [297], then the diameter of the pores or cylindrical cracks can be estimated by the value of ≈2.6 nm. To do this, use the following formula:

$$D^{(\text{nm})} \approx 223{,}75/\omega\ (\text{см}^{-1}). \tag{6.41}$$

It has been noted in Pt. 2.2.3 that these results regarding the porous structure of the EG (nanosized — defects in the form of longitudinal cavities) are well consistent with the results of studies on the EG structure performed by other methods.

The Raman spectra of carbon black were also compared with the Raman spectra of various micro- and nanoscaled carbon materials, and a highly-informative analysis, we suppose, was made in [224] (Fig. 6.58). The deconvolutions into Gauss — Lorentz band shapes of these spectra are also shown there. We see that the Raman spectrum of highly-oriented pyrolytic graphite, HOPG, treated graphite that displays the highest degree of 3D ordering consists of two main bands observed at 1581 and 2687 cm^{-1} (Fig. 6.58, *a*), denoted as the G band and 2D (or G′) band, respectively. As known, these bands correspond to the degenerate in-plane E_{2g} optical mode at the Brillouin zone center, and to the harmonic (second-order Raman scattering) of an in-plane transverse optical (TO) mode close to the zone boundary K point, respectively. The second-order Raman spectrum also contains two weak bands at 2458 and 3246 cm^{-1}, assigned to the combination D + D′′ and to the harmonic 2D′, respectively. The D′′ corresponds to a phonon belonging to the in-plane longitudinal acoustic (LA) branch close to the K point, and D + D′′ corresponds to a phonon of the in-plane longitudinal optical (LO) branch close to the zone center (Γ point).

Several new details appeared in the spectra of multilayer graphene (MLG) and of flake graphite (grade 3775) at 1333 (weak) and 1604 cm^{-1} (very weak) (Fig. 6.58, *b*, *c*). These features were assigned to the D band (i.e., the fundamental of 2D) and to the D D′ band (i.e., the fundamental of 2D D′), respectively. As known, these modes are not Raman active in the first-order Raman scattering of perfect crystals (HOPG), just because they are not zone-center modes, but they become Raman active in defective graphitic materials owing to defect-induced double resonance Raman scattering processes involving the electronic π–π* transitions. Really, the D band involves a defect-induced electron-hole "intervalley" double resonance process which activates a TO phonon close to the zone boundary K point, while the D D′ band is activated by a similar "intra-valley" double resonance process which activates a LO phonon close to the Γ point. Due to the shape of the π–π^* bands, the electronic transitions move inside the (a*, b*) reciprocal plane of the Brillouin zone as a function of the excitation energy. Conversely, the phonons (D or D′) when they are excited with different laser wavelengths describe the dispersion of their respective branches (TO or LO). The TO branch has high dispersion near the K point, so the D band position is

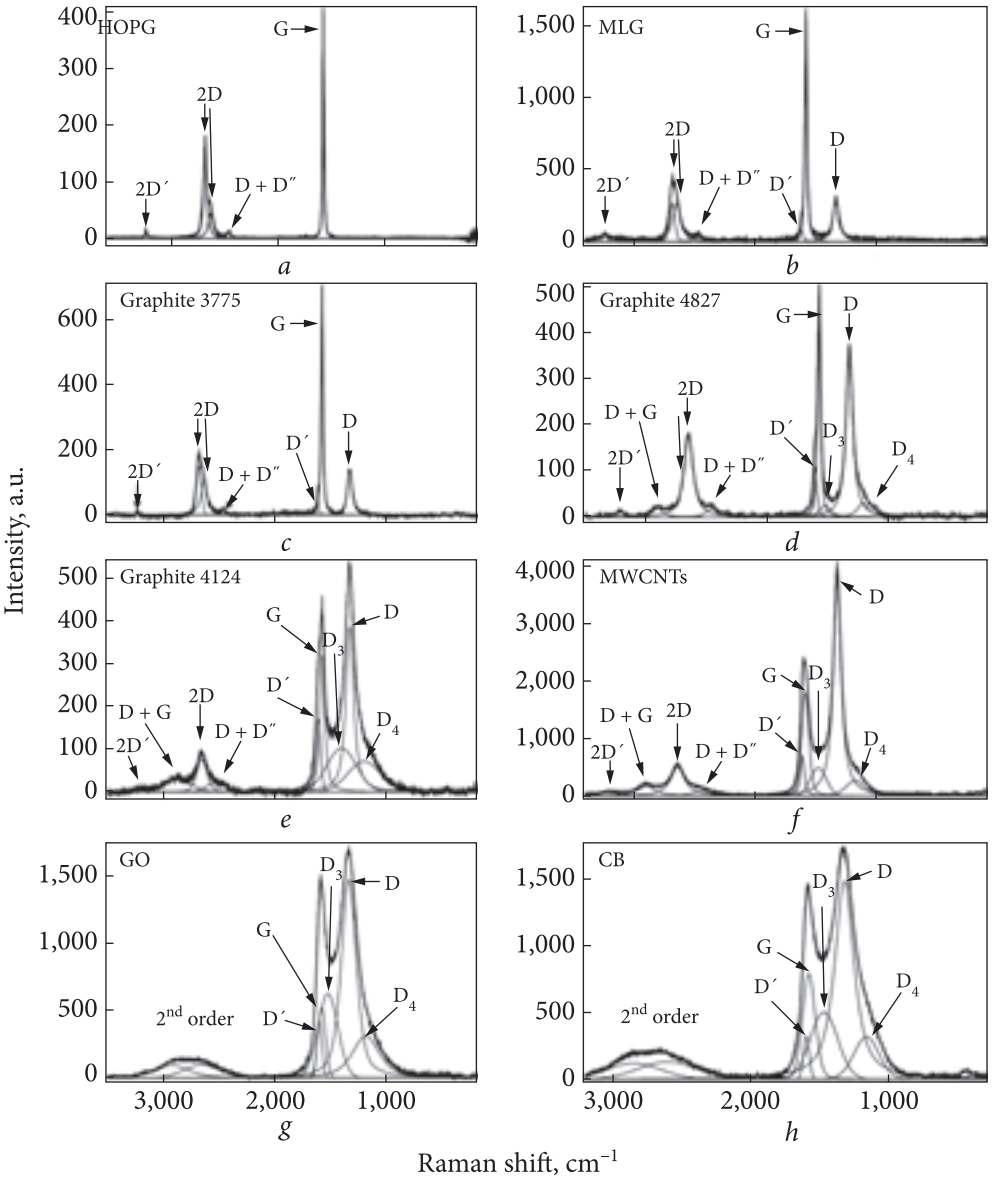

Fig. 6.58. Raman spectra of different carbon materials and their deconvolutions: *a* — highly oriented pyrolitic graphite; *b* — multilayer graphene; *c*, *d* and *e* — graphites of grade 3775, 4827, and 4124, respectively; *f* — multiwall carbon nanotubes; *g* — graphene oxide; *h* — carbon black [224]

blue-shifted as the excitation energy increases, and so is the harmonic 2D. In contrast, the LO branch is quasi-flat near the Γ point, so that no change can be detected in the position of the D′ band (and also of the 2D′ band) if the excitation energy is varied. So, as a consequence of the particular shape and symme-

try of the π and π^* electronic states around the K point of the Brillouin zone, the energy and momentum transfer of the resonant phonons vary according to the slope of the dispersion branches involved in the double resonance process. Described results show the dispersive behaviors consisting of downshifts between 40 and 60 cm^{-1} for the D band and around 100 cm^{-1} for the 2D($G^/$) band with a change in excitation wavelength from 457 to 752 nm [224].

So, the presence of the D band in these materials was assigned to structural defects (probably edge defects in these cases). It was shown that the intensity of the D band relative to that of the G band increases with the degree of disorder, so the intensity ratio I_D/I_G was often used to characterize the average crystal planar domain size *La*. Those values in MLG and graphite (grade 3775) were evaluated to be around 11 and 10.5 nm, respectively.

Also, it is worth noting that the 2D band appears as a doublet for these materials (Fig. 6.58, *a*—*c*). This is due to the splitting of the π and π^* electronic states owing to the interactions between the layer planes. For one-layer (1 L) graphene, the 2D band is a singlet, for 2 L graphene it is a quadruplet and finally for more than five layers, the Raman spectrum is quasi indistinguishable from that of graphite, i.e., the 2D band splitting merges into a doublet. So, taking into account that the 2D band in MLG and graphite 3775 exhibits a doublet structure, we can state that the stacking of the graphene layers along the hexagonal axis remains ordered at least in short or medium ranges [224].

The new observation took place on the Raman spectra of two other graphites (grades 4827 and 4124) which are graphite nano-platelets (GNPs) (Fig. 6.58, *d*, *e*). It can be noticed that in the first-order spectral range an increase in the intensity ratio I_D/I_G together with I_D/I_G. This is a result of the disorder increasing compared to the flake graphite. Indeed, from the intensity ratio I_D/I_G the correlation length La was evaluated to be around 2.7 and 1.8 nm, respectively. Note that this case is near limitation of Tuinstra and Koenig relation validity. It has been also noted that the emergence of two broad features near 1500 and 1200 cm^{-1} was assigned to D3 and D4, respectively [224]. The D4 is a broad low-frequency shoulder of the D band, while the D3 band does not present any apparent maximum on the observed spectra but the addition of them was found necessary to fit correctly the spectral shape between the D and the G bands. The assignment of these modes is not obvious. The authors of the work [224] note that the D4 and D3 bands were present in highly defective carbons like carbon black (CB), and were assigned to the presence of amorphous carbon (D3) and of hydrocarbon or aliphatic moieties connected to graphitic basic structural units (D4).

The second-order spectra were noticably broadened (Fig. 6.58, *d*, *e*). In particular, the 2D band appeared as a singlet due to the presence of some orientation and stacking defects resulting in a broadened "Dirac-like" single 2D band. The presence of a new band at 2900 cm^{-1} whose intensity increases with the

disorder degree was also detected. It was assigned to the combination D + G, which corresponds to the defect-induced double resonance "intervalley" scattering process, or to the combination D + D′, which is allowed through a defect-induced triple resonance process involving both "intervalley" and "intravalley" scattering processes. In the present case, the measured frequency (2901 cm^{-1}) is closer to the calculated one for D + G (2895 cm^{-1}) than that calculated for D + + D′ (2929 cm^{-1}).

Raman scattering was also used for the EG samples characterization in [285, 286], where Raman spectra were recorded at room temperature with a LabRam HR-800 spectrometer using the 488 nm radiation of Ar^+ laser with a power of 0.01 mW. Anodic polarization of the natural purified graphite was used for EG preparation at a stabilized current of 20 mA/cm^2 density with a total electrical charge transfer of 500—3000 C/g. The HNO_3 aqueous solutions of 40%, 60%, and 80% concentrations were used as electrolytes. The samples then were treated with water (20 ml/1 g of initial graphite) and dried in air at 60 °C for 2 h. The samples of the expandable graphite are denoted as "acid concentration charge transfer", i.e the sample synthesized in 60% HNO_3 with 500 Q/g charge transfer is denoted as 60/500. The reference "chemical" EG sample was obtained by water treatment of graphite nitrate of II stage. The EG samples were prepared by the thermal shock of the corresponding EG samples in the air in the temperature range of 400—800 °C. Cylindrical samples (for thermal diffusivity measurements) of 0.2 g/cm^3 density and 12.7 mm diameter were then prepared by EG uniaxial compression.

Thermal shock of synthesized samples results in the formation of worm-like particles. EG macro characteristics, i.e bulk density and carbon yield, are influenced by EG synthesis conditions (Table 6.3). The bulk density of the samples obtained at 400 and 600 °C from 60/2000, 60/3000, and 80/3000 EG is as low as ~1 g/l and slightly depends on the expansion temperature implying GO thermal decomposition as a controlling factor for their expansion. The broad D- and G-lines of similar intensities were detected in the Raman spectra of these EG samples, which is indicative of nanocrystalline graphite and a high concentration of structural defects in the samples. On the contrary, the spectra of EG from 600/500 and the "chemical" sample contain a narrow G-line and they are very close to the natural graphite sample pointing to an almost ideal graphitic microstructure.

In our opinion, multilayered samples of exfoliated graphene are close by structure and composition to the ones described above. They were studied, in particular, in [287], where graphene samples were fabricated from natural flake graphite by micromechanical cleaving with transparent tape followed by application onto a 500 μm thick Si substrate with a 300 nm SiO_2 surface layer. Samples used in the experiments had from 1 to 260 layers and a uniform thickness over a circular area of at least 15 μm in diameter. Samples

with up to seven layers can be distinguished using an optical microscope, due to the optical interference effect. Samples with one to three layers were confirmed using Raman spectroscopy. For the thicker samples, atomic force microscopy was used to determine the number of layers with an accuracy of ±10%. Raman spectra of the thin samples showed no defect-induced D lines. The Si wafer was slightly *n*-doped, however the free electron concentration of $\sim 1 \times 10^{18}\,cm^{-3}$ was sufficiently low to allow for significant transmission at the used probe wavelength.

For each of the graphene/graphite samples, as well as for the bare SiO_2/Si region immediately surrounding it, the time-resolved differential change in reflectivity ($\Delta R/R$) and transmittance ($\Delta T/T$) were measured for up to 35 ps of probe delay. Samples with 0 (bare SiO_2/Si), 1, 2, … 260 layers were measured; a subset of these measurements for the time delay interval 2—15 ps is shown in Fig. 6.59.

The SiO_2/Si time-resolved reflectivity appears to be similar to that studied in [288], although for their probe wavelength of 800 nm, the measured transient optical properties are dominated by interband absorption whereas ours are dominated by free carrier absorption. The non-zero initial value (*i.e.*, before a particular pump pulse arrives) of the reflectivity and transmittance occurs because of some steady-state carrier accumulation effects in the silicon since the recombination time is longer than the inter-pulse separation time of ~12.5 ns.

The results from bulk graphite are also in agreement with well-known data (see Pt. 6.1) after correcting for the difference in probe wavelengths. As the wavelength increases, the optically probed electron and hole states are closer to the band edge and Fermi level, and the apparent relaxation time increases. One can observe that as the number of graphene layers increas-

Table 6.3. **The EG characteristics [286]**

Sample	Expansion temperature, °C	Bd*	CY**, %	Sample	Expansion temperature, °C	Bd *	CY **, %
60/500	400	3.2	84	60/3000	400	1.0	67
	600	2	82		600	0.9	64
	800	1.7	70		800	0.8	58
60/1000	400	3.2	80	40/3000	400	2.5	80
	600	1.8	75		600	1.7	70
	800	1.6	69		800	1.6	65
60/2000	400	1.1	68	80/3000	400	1.2	65
	600	1.0	64		600	1.0	64
	800	1.0	60		800	1.0	57

* Bd, bulk density = EG_{mass}/EG_{volume}; ** CY, carbon yield = $EG_{mass}/EG_{mass} \times 100\%$.

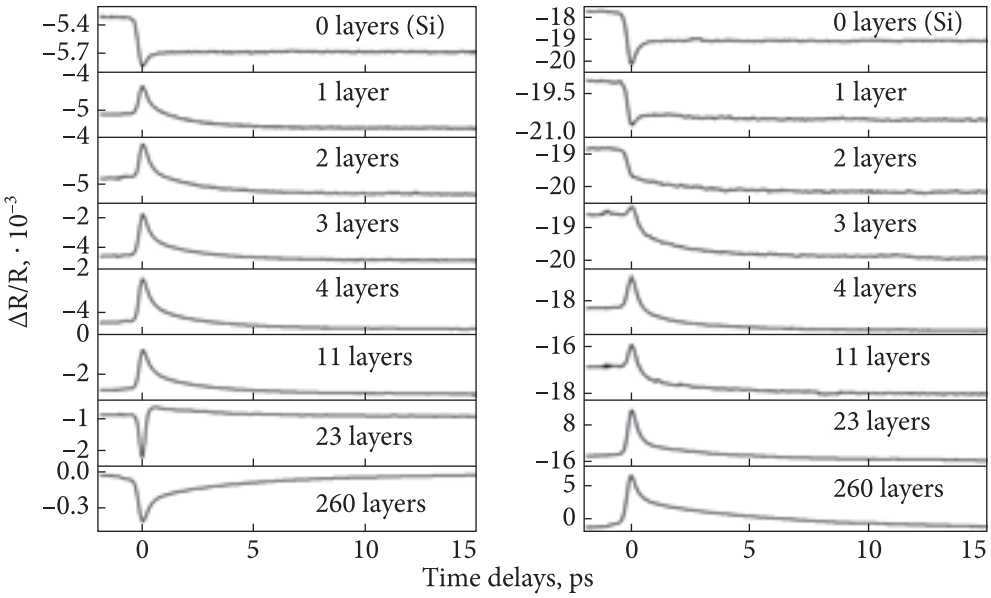

Fig. 6.59. Time-dependent differential reflectivity ΔR/R and transmittance ΔT/T of graphene/graphite samples with the number of carbon layers indicated [287]

es, the signal becomes increasingly different from that of the bare substrate (Fig. 6.59). When the number of layers is more than ~25, the typical behavior of bulk graphite is observed.

The transfer matrix method was used to numerically compute the relative changes in the real and imaginary parts of the optical conductivity, $\Delta\sigma_R/\sigma_R$ and $\Delta\sigma_I/\sigma_I$ from ΔR/R and ΔT/T, respectively. Each of the carbon layers can be represented by a transfer matrix, with $\Delta\sigma_R/\sigma_R$ and $\Delta\sigma_I/\sigma_I$ decreasing into the sample from the illuminated face according to the graphite pump absorption. We take each layer's quiescent optical properties as those of bulk graphite with a thickness of 0.335 nm. When the SiO_2 and Si layers are included, the total reflection and transmission amplitude coefficients can be computed and used to obtain ΔR/R and ΔT/T. At each time delay, the $\Delta\sigma_R/\sigma_R$ and $\Delta\sigma_I/\sigma_I$ values are chosen to obtain the ΔR/R and ΔT/T values observed. For all our samples, the $\Delta\sigma_R/\sigma_R$ shows a similar type of behavior, *i.e.*, a rapid decrease during the pump pulse followed by a non-exponential recovery. However, the $\Delta\sigma_I/\sigma_I$ data sets show different behavior as the number of layers increases. The $\Delta\sigma_I/\sigma_I$ for 1—3 layers, except for some behavior around the pulse overlap time, is very small compared to its value for thicker samples. For the thicker samples, $\Delta\sigma_I/\sigma_I$ shows a magnitude that is clearly non-zero and a non-exponential time dependence similar to that of $\Delta\sigma_R/\sigma$. For the thickest samples, the behaviors of both real and imaginary parts of the optical conductivity are similar to that observed previously

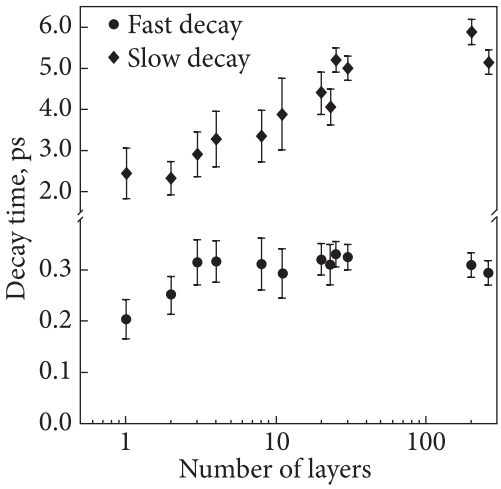

Fig. 6.60. Extracted fast and slow time constants from time-resolved $\Delta\sigma_R/\sigma_R$ for our graphene/graphite samples as a function of the number of layers [288]

for graphite. The non-exponential recovery was modeled in [203] as a double exponential, but in [289] it was modeled as stretched exponential, and both types of behavior were used for all data from [288], although there was a noticeable discrepancy. That is why the authors proceed with fitting data to a double exponential function convolved with the Gaussian pump and probe pulse profiles. The two-time constants extracted from the $\Delta\sigma_R/\sigma_R$ data are shown for samples with up to 260 layers in Fig. 6.60. The fast time constant increases, at best only slightly, from ~200 to ~300 fs over a few layers and thereafter apparently remains constant while the slower time constant increases from 2.5 to 5 ps as the sample thickness increases from 1 to ~30 layers before apparently remaining constant to ~260 layers. Finally, the authors of [288] observed that, at least for our probe photon energies, the properties do not change substantially in proceeding from graphene to few-layer samples. This is perhaps not surprising since graphite is loosely bonded layers of graphene-like planes. Some comparisons with related data in multilayer epitaxially grown graphene have been made, but one should be cautious since the two material systems are different, not only in terms of interlayer stacking but also in defect density, etc.

Simple expressions have been derived elsewhere for the frequency-dependent change in the inter- and intra-band optical conductivity of 2D graphene [290] and 3D graphite [291] following optical excitation. In both cases, after thermalization, $\Delta\sigma_R$ is dominated at near IR wavelengths by the change in the inter-band absorption, determined by the change in the Fermi-Dirac occupancy factor for electrons (e) and holes (h), $f_{e(h),}$ at the optically coupled states. The $\Delta\sigma_I$ is dominated by Kramers — Kronig — related changes to the inter-band absorption and Drude contributions. For 2D materials, this is expected to be weak at visible and near-visible wavelengths, but for 3D materials, the contribution can be non-negligible [291].

The fact that the slow decay time increases gradually with the number of layers indicates the transport of carriers and/or thermal energy across the interface. If one makes the commonly used assumption of no inter-layer interactions and, more importantly, no graphite-SiO_2 interaction, decay times should

not increase after few layers. However, the consideration of ballistic or diffusive transport could explain this trend.

Expanded graphite can be an important step-component material for graphene preparation. That is why the liquid-phase exfoliation method has been considered as one of the most feasible approach for industrial production of graphene due to its scalability and low cost. This approach typically involves sonication of graphite or graphite oxide powders in solvents. Depending on the graphite precursors, liquid-phase exfoliation of graphite has been studied using (1) graphite oxide, (2) natural graphite, and (3) graphite intercalation compound (GIC). Liquid-phase exfoliation of graphite oxide is now one of the most widely used methods for the preparation of graphene. It begins with the intercalation of graphite with strong oxidizing agents followed by expansion of graphite layers via sonication. The reduction of the obtained graphene oxide to graphene is usually conducted by either thermal or chemical approaches [292, 293]. Although this method is capable of high-yield (>50%) production of graphene, the use of a large quantity of acid and oxidizing agents requires time-consuming washing steps and produces hazardous wastes. In addition, the vigorous oxidation of graphite often leads to incomplete restoration of the hybrid sp^2carbon bonds and the presence of residual oxygen functional groups resulting in poor electrical conductance [293].

Liquid-phase exfoliation of GICs for the production of graphene has attracted great interest recently. This method begins with the intercalation of graphite followed by the expansion of graphite via a rapid increase in the vapor pressure of a volatile intercalated substance under microwave or thermal treatment. As non-oxidative agents are applied for intercalation of graphite, and microwave or thermal treatment of GIC leads to a large expansion of graphite, a high-yield production of high-quality graphene can be achieved using this method. E.g., it was reported about solvothermal-assisted exfoliation of EG obtained from GIC in acetonitrile and successful preparation of monolayer and bilayer graphene with 10—12 mass% yield without significant structural defects was performed in [294, 295]. However, these recipes are limited by using either poisonous chemical agents [296] or dangerous chemical reactions [294].

Liquid-phase exfoliation to produce graphene from tetraethylammonium graphite intercalation compound (TEA-GIC) was described in [294]. The process of the graphene preparation consisted of three steps, as shown schematically in Fig. 6.61.

Intercalation of nontoxic TEA was achieved by simple high-power tip-sonication of graphite in TEA aqueous solution. The release of gaseous species due to the decomposition of TEA under microwave irradiation facilitates the expansion of graphite layers. Graphene was obtained by mild sonication of the expanded graphite in NMP. It was characterized by both microscopy and

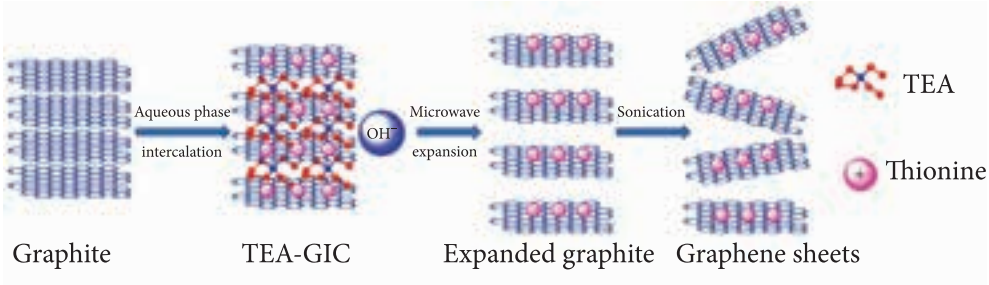

Fig. 6.61. Illustration of experimental procedure for preparation of graphene by liquid phase intercalation and exfoliation of graphite [294]

spectroscopy techniques to clarify the nanoscale structure and mechanisms of formation responsible for the production processes [294].

Natural graphite (2 g, 99.99% purity) was first mixed with an aqueous solution (300 ml) containing TEA tetrafluoroborate (0.8 g), sodium hydroxide (0.15 g), and thionin acetate salt (50 mg). After agitation for 10 min, the suspension was tip sonicated for 6 h (Scientz-II D Ultrasonic Cell Disruptor, 950 W, with 90% amplitude modulation) and then vacuum filtered by a Nylon membrane of 220 nm in pore size. The obtained TEA-GIC was washed with 20 ml deionized water and 20 ml ethanol three times and then vacuum dried at 60 °C for 2 h. After that, the dry graphite powders were microwave irradiated for 5 min (Midea microwave oven, 900 W). The expanded graphite obtained by microwave treatment was then treated ultrasonically in 700 ml NMP for 2 h (Ultrasonic Cleaner, 250 W). The resultant suspension containing graphene was centrifuged at 5000 rpm for 15 min to remove unexfoliated graphite particles. A stable graphene suspension was obtained finally after the supernatant was pipetted off [294].

For graphene films preparation, 100 ml graphene N methyl-2-pyrrolidone (NMP) dispersion with a concentration of 0.14 mg · ml^{-1} was filtered by a Nylon membrane with a 220 nm pore size. The obtained thin graphene paper was dried at 60 °C for 36 h.

Fig. 6.62 shows the SEM images of natural graphite, TEA-GIC, and EG. It can be seen that the surface of natural graphite is smooth and compact while the surface of TEA-GIC is tortuous with lamellar structures clearly visible. EG obtained by further microwave irradiation of TEA-GIC presents a paper-like structure and exhibits a considerable increase in interlayer spacing compared with natural graphite and TEA-GIC. The huge expansion from natural graphite to EG will lead to the destruction of the long-range periodicity associated with the c-axis of graphite.

Powder XRD patterns of natural graphite, TEA-GIC, and EG are displayed in Fig. 6.63, *a*. The peak related to the periodic lamellar structure of graphite at $2\theta = 26.4°$ and two peaks associated with its in-place crystalline structure at

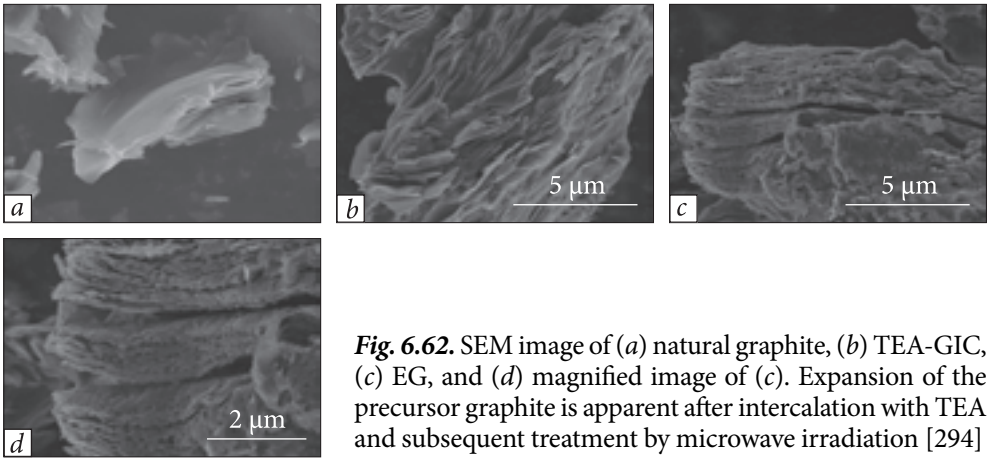

Fig. 6.62. SEM image of (*a*) natural graphite, (*b*) TEA-GIC, (*c*) EG, and (*d*) magnified image of (*c*). Expansion of the precursor graphite is apparent after intercalation with TEA and subsequent treatment by microwave irradiation [294]

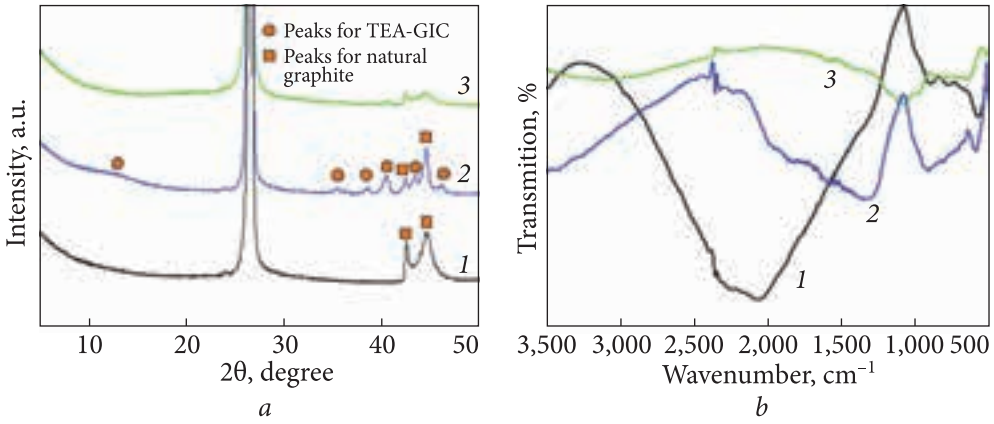

Fig. 6.63. XRD (a) and FTIR (b) spectra of (1) natural graphite, (2) TEA-GIC, and (3) EG. The peaks at 2θ = 12.6°, 35.4°, 38.5°, 40.4°, 43.4°, and 46.1° in the XRD spectrum of TEA-GIC and the decrease of the intensity or disappearance of these peaks in the spectrum of EG along with the peaks at 1363 and 908 cm^{-1} in the FTIR spectrum of TEA-GIC and their disappearance in the spectrum of EG indicate the insertion and decomposition of TEA in the graphite structure [294]

2θ = 42.4 or 44.6° can be seen in all three diffractograms. However, after treatment of natural graphite for aqueous phase intercalation, six additional peaks located at 12.6, 35.4, 38.5, 40.4, 43.4, and 46.1° showed up, suggesting that TEA cations had successfully entered the interlayer space of natural graphite, which resulted in a change of the lamellar structure in the c-axis direction and also changes of the in-plane crystalline structure due to the interaction of TEA with carbon atoms. After microwave treatment of TEA-GIC, the peaks located at 12.6, 43.4, and 46.1° disappeared and the intensities of the peaks located at 35.4, 38.5, and 40.4° decreased significantly.

This result is attributed to the structural changes in which the TEA cations decomposed under microwave irradiation as expected. Fig. 6.63*b* displays the FTIR spectra of natural graphite, TEA-GIC, and EG. The peaks at 1363 and 908 cm^{-1} in the spectrum of TEA-GIC are attributed to the shear vibration of —CH_3 and stretching vibration of C–N, respectively. The occurrence of these two peaks in the spectrum of TEA-GIC and their disappearance in the spectrum of EG further confirmed the insertion and decomposition of TEA in the graphite structure. It was reported that the TEA cations preferred to interact with the hydroxyl groups on the edges of graphite particles as a consequence of dipole-dipole interactions and may enter graphite galleries due to the cation-π electrostatic interactions [297, 298]. Therefore, we believe that under the experimental conditions of this study where intensive sonication was applied to facilitate the vibration of graphite layers, the TEA cations entered successfully the interlayer space of graphite. On the other hand, it was reported that thionin cation was a good stabilizer for graphene dispersion due to its amphiphilic structure, abundance of charge, and strong π-π interaction with graphene [294, 299]. One can see that gaseous species including C_2H_4 and $EtNH_2$ are produced during the decomposition of TEA. The release of them in graphite galleries will lead to a huge expansion of graphite layers. This is why graphene sheets can be obtained by mild sonication of EG in an organic solvent.

We also suppose that these results confirm that graphene-like species are contained in the compositions of the EG samples and, surely, they can be revealed by optical characterization of the EG. No doubt, this conclusion agrees with the following descriptions.

A procedure to produce graphene species based on EG was also used by us. Graphene nanoparticles (GNPs) were prepared using anodic oxidation of EG foil (Ukraine standard TU 26.8-30969031-002-2002) in a low concentrated aqueous KOH solution. As a precursor for EG, intercalated graphite compounds (Ukraine standard TU 14.50.9-30969031-001-2002) obtained by anodic oxidation of natural graphite were used. Such a procedure of two consecutive controlled electrochemical processes allowed us to initially adjust the defective structure of EG as a cluster-assembled nanoscale system, and further, the size and surface state of GNPs [300, 301].

The GNP sizes evaluated by Laser Correlation Spectroscopy (LCS) ("Zeta-Sizer 3" spectrometer (Malvern Instrument, UK) with correlation 7032 and a helium-neon laser LH-111 stated a capacity of 25 mW at $\lambda = 633$ nm). The particle sizes in GNPs stable aqueous dispersions were found to be in the range of tens — to hundreds of nanometers and few — to tens of micrometers and can be regulated within certain limits. GNP films were also made by drying from low-concentrated aqueous suspension on glass substrates [301].

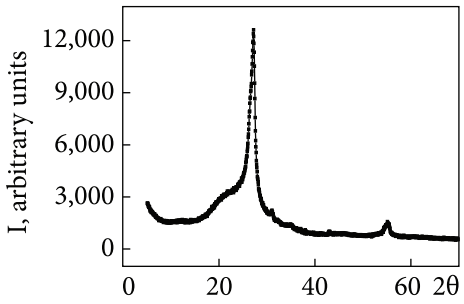

Fig. 6.64. XRD pattern of GNP film [301]

Nanoscale dimensionality of GNPs was detected from macro-Raman spectra (a Brucker RFS 100/s spectrometer, the radiation source was an argon laser, λ = 514.5 nm, diameter of the exciting beam was near 1 mm). The presence of nanoscaled particles was also confirmed by XRD analysis (a diffractometer DRON-4-07, CuKα radiation, Nickel filter in the reflected beam) in Bragg-Brentano geometry. The intensive 2θ peak at 27° related to graphite (002) with a broad shoulder situated at lower 2θ values and a less intensive peak at 55.5°, corresponding to the second order (004), can be seen in the XRD pattern (Fig. 6.64) of the GNPs film obtained after drying aqueous dispersion. These lines indicate the presence of polycrystalline graphite. The widening near the main 2θ peak corresponds to the presence of an amorphous phase, namely GNPs of much lower sizes.

The obtained Raman spectra of GNPs synthesized by us demonstrate the typical Raman shifts for GNPs or graphene multilayers (Fig. 6.65). The G-band (so-called "graphitic" mode of E_{1g} symmetry in Γ-point of Brillouin zone) at 1581 cm^{-1} corresponding to the tangential vibrations of carbon atoms in the rings of graphene sheet [302] is registered. The disorder in the graphene multilayers is characterized by the D-band appearance at 1353 cm^{-1} taking into account the absence of this band in the initial EG [72, 302]. This Raman peak is assigned to the vibration mode of graphene layer rings in the K point of the Brillouin zone. A relative intensity and FWHM of D and G bands reflect the degree of material disorder (broadening of bands corresponds to a larger degree of disorder).

The second-order mode of D-type vibration (2D band) is registered at 2713 cm^{-1} with higher intensity than usually observed for the second-order vibration. This observation can be evidence of the similarity of carbon nanostructures manifesting a strong electron-phonon interaction and strong dispersion dependence of D-mode.

The low-intensity band at 2451 cm^{-1} (D") consists of the sum of D and D_1 modes (D_1 — sp^3 at 1060—1080 cm^{-1}). In the case of GNPs made by us, the position of G-mode at 1581 cm^{-1} does testify to the formation of a good crystalline structure of GNPs (its theoretical value for graphite and graphene is 1580 cm^{-1}); relative intensity I_{2D}/I_G = 1.12. The analysis of fitted data for 2D mode suggests that the obtained GNPs are of good crystalline structure.

The described above approaches can be applied to studies of most micro/nanosized carbon materials (MNCM), and high-brightness luminescent elements can be elaborated on the basis of graphene and graphene oxide [303]. Such

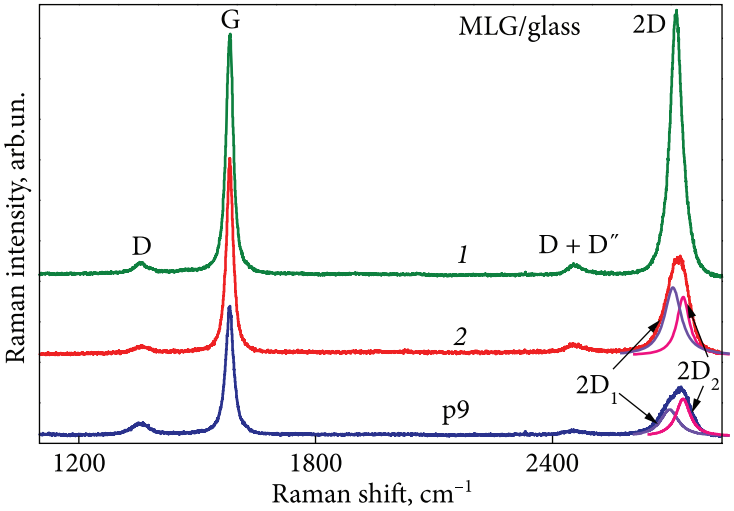

Fig. 6.65. Raman spectra of GNPs on glass substrate measured over different parts of the sample (*1*, *2*, *3*) [301]

elaboration of carbon-based luminescent devices is of high importance because they can overcome known disadvantages of currently used lighting devices (high toxicity of the components, high price of rare-earth elements, low energy efficiency, etc). Two important problems should be solved at the current stage of carbon materials luminescence studying: 1) relatively high price of the large quantity and high-quality MNCM production and 2) low intensity of the MNCM luminescence (increasing the luminescence intensity of MNCM is highly desirable). The first problem attracted great attention, and many methods of carbon nanostructures production have been proposed (mechanical and chemical exfoliation, chemical vapor deposition, arc discharge, etc) [267, 304—310]. The authors of this book also used the electrochemical exfoliation method since it is cost-effective and allows producing of MNCM in large quantities [209, 280, 281].

The new data about intensive PL of carbon nanostructures have been obtained last years and they showed that graphene oxides reveal intensive luminescence and its characteristics depend on the preparation and treatment procedures [311—313].

Despite the fact that a lot of data about the PL properties of various MNCM are evident, the determination of the MNCM luminescence origin requires further studies as we have shown above. Micro/nanosized carbon materials were prepared by us on the EG base using an electrochemical exfoliation method in the form of colloids and thin films similar to those described above. Optical, luminescent, and scanning electron microscopy, Raman scattering spectroscopy, chemical element analysis, and luminescent spectroscopy were applied in order to clarify the

origin of micro/nanosized carbon materials luminescence. That is why two sets of samples were prepared for the study – colloid carbon materials and carbon films on silica substrates. Colloids were prepared by an electrochemical exfoliation method. The thermally expanded graphite was used as a carbon source and the liquid KOH solution was used as an electrolyte. As a result, homogeneous colloids of MNCM particles (flakes) in alkali solution were obtained. Any precipitates of dispersed particles on the bottom of the flasks were not observed for the colloids after 6 months. The starting colloid was taken for study as sample #1 (hereafter C1). Two other samples of the set were obtained by filtering the starting solution through ceramic filters with sizes of pores 100 and 1 μm (denoted as C2 and C3 samples, respectively). Another set of samples consisted of MNCM solid films deposited on a silica substrate by means of small amounts of the mentioned C1, C2, and C3 solutions evaporation. Those samples were denoted hereafter as P1, P2, and P3, respectively. Evaporation took place in ambient air conditions at 60 °C for 16 h. A triple T64000 Horiba Jobin-Yvon spectrometer equipped with a quasi-confocal scanning microscope was used for the Raman scattering spectra measurements. An Ar-Kr Spectra-Physics 2018 laser with the wavelength of incident light λ_{inc} = 488 nm was used for the measurements. An N_2 laser (λ_{ex} = 337.1 nm), two diode-pumped lasers (λ_{ex} = 473 and 532 nm), and an arc Xenon lamp were used as sources of PL excitation. The PL spectra have been studied as a function of the exciting radiation wavelength and were recorded in the wide region of excitation and emission wavelengths (200—800 nm). The sample temperature was near 300 K (RT). A portable microscope allowed us to collect luminescence light with a spatial resolution of the solid sample surface. The sizes of selected areas were in the range of ~20—40 μm.

In the first stage of the study of solid samples, they were characterized by optical microscopy. It was found that each of P1, P2, and P3 films is very inhomogeneous – separated particles are observed in the middle part of the film and self-organized agglomerates of particles are present at the border area of the samples (corresponding images for P1 sample are shown in Fig. 6.66, *a*,*b*). Mentioned inhomogeneity is an opportunity to conditionally select several regions on the film surface, which differ in the size and morphology of the carbon particles.

A more detailed study of the samples surface was performed by scanning electron microscopy. The SEM image of the whole P1 sample is presented in Fig. 6.66, *c*, and its enlarged border part is shown in Fig. 6.66, *d*. Five characteristic regions of different distribution of the MNCM particles were selected for the further study (Figs. 6.66, *c* and 6.66, *d*).

The SEM images of each selected region are shown in Fig. 6.67. The sizes of separated particles and their agglomerates in different parts of the sample are in the range of tens of nanometers up to tens of microns. The border part of the solid samples consists of two slightly different regions (hereafter zones 1 and 2). There

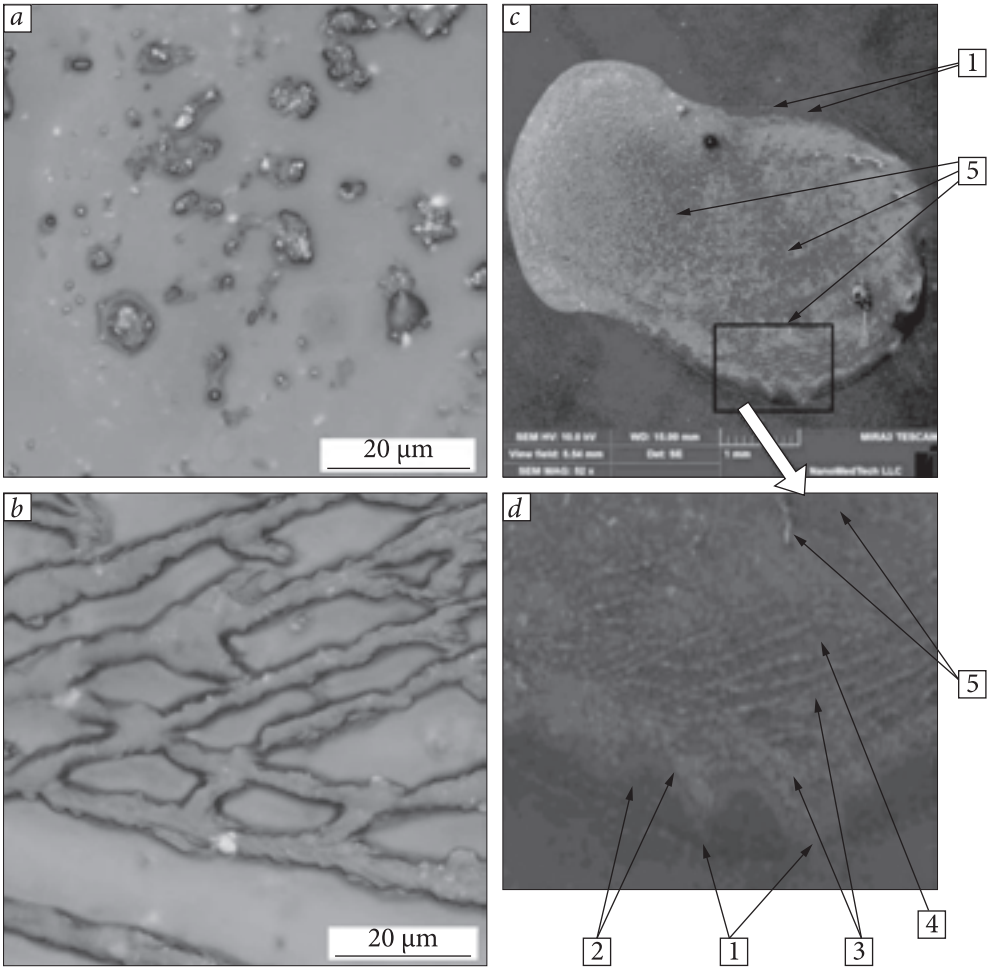

Fig. 6.66. Optical microscopy (*a*, *b*) and SEM images (*c*, *d*) of the P1 sample. The various-type zones (1—5) of the sample are indicated by arrows. Some inclusions are also shown. 1 — border line zone and inclusions; 2 — tide zone and subzones; 3 — dense net zone; 4 — non-compact net zone; 5 — interior zone and inclusions [280]

are particles sizing ≈1—2 μm cling close to each other with some inclusion of larger particles and wires in zone 1 (Fig. 6.67, *a*). Zone 2 is located somewhat closer to the middle of the sample and contains submicron (100—400 nm) particles. The dense net of branch-like particles (width ≈0.5 μ, length >3 μ) is characteristic for zone 3. It is located on the background of carbon layers formed by thin plates. Relatively long (width ≈3 μm, length >10 μm) isolated wires are observed a zone 4. Ensembles of different sizes (50—200 nm) separated particles are characteristic for zone 5 lying in the interior part of the films. Inclusions of larger agglomerates are present somewhere within this zone too. In accordance to the results of opti-

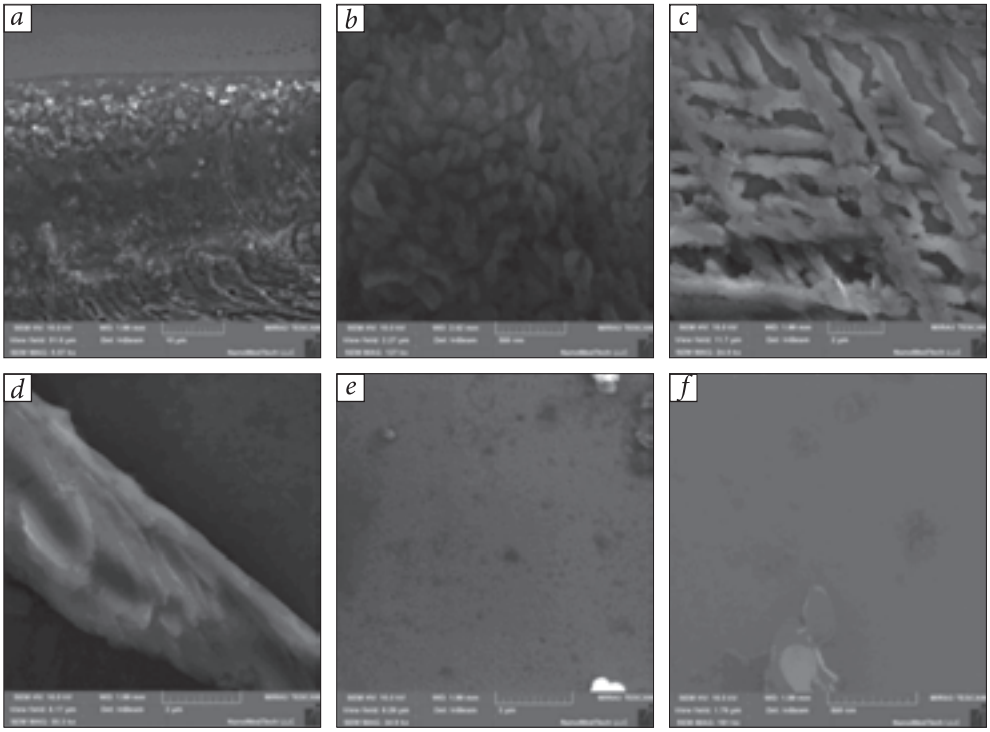

Fig. 6.67. Detailed SEM images of the solid sample P1 in the marked in Fig. 6.40 zones: 1 (*a*), 2 (*b*), 3 (*c*), 4 (*d*), and 5 (*e, f*). Scale divisions: 10 (*a*), 2 μ (*c*, *d*, *e*), and 500 nm (*b, f*) [280]

cal and scanning electron microscopy, mentioned selected regions of the P1 film differ in the density, shapes and sizes of the MNCM particles.

A chemical elements analysis was performed for many specific points of the films using SEM microscope tools. It was found that C, Si, O, and K are the main components of the samples. Below we discuss only the distribution of the chemical elements on the MNCM particles at the selected earlier zones of solid samples. Corresponding results for various points of the P1-P3 samples, containing large and thick particles and their agglomerates, are listed in Table 6.4. Obviously, the higher Si content indicates particles with lower thickness and vice versa. Presented in Table 6.4 data confirm our assumption about the existence of graphite oxide particles in zones 2 and 4. At the same time, there is a low content of oxygen in zone 3, and consequently, no high graphite oxide concentration can be expected. As for zone 5, chemical element analysis indicates the presence of mainly carbon materials, in particular multilayer graphene and graphite flakes.

The Raman spectra of the solid samples are shown in Fig. 6.68. The various regions of the sample surfaces were selected for Raman's monitoring the carbon materials. The region outside of carbon film (zone "out") was also studied in or-

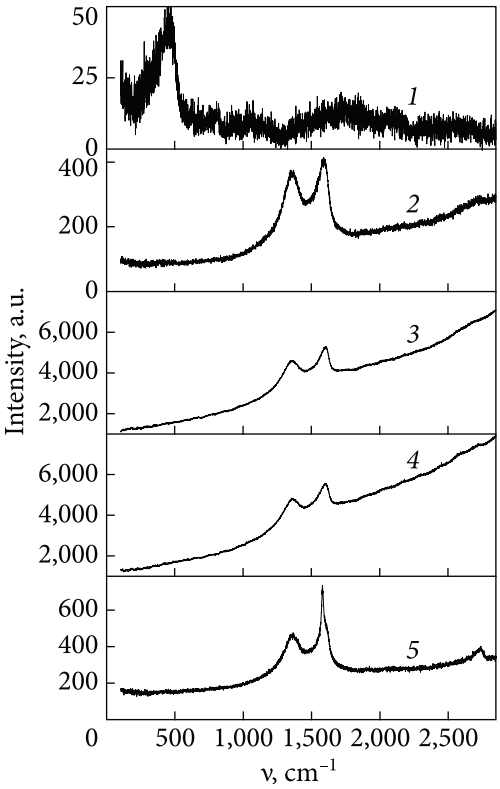

Fig. 6.68. Raman spectra taken from various areas of the P1 sample: *1* — out of the sample; *2* — zone 2; *3* — zone 3, and *4* — zone 4: thick particle areas; *5* — zone 5: thin particle area. The area sizes are near 10 μ. λ_{inc} = 488 nm (2.54 eV); P_{inc} = 100 mW; T = 300 K [280]

der to consider the possible influence of silica substrate on the properties of the solid samples (Fig. 6.67, spectrum 1). Spectra 2—4 in Fig. 6.68 correspond to the regions where carbon layers have a significant thickness (correspond to zones 2—4). Selected regions correspond to various types of MNCM particles' conformation and thickness, which were revealed previously by microscopy studies.

The low-intensity lines were observed in the low frequencies range (<500 cm^{-1}) for a zone "out" the case. These lines correspond to the silicon oxide vibrations. Spectra 2, 3, and 4 are very similar, despite their correspondence to different zones of the sample (zones 2, 3, and 4, respectively). The spectra similarity indicates particles of similar nature. The wide background against which the Raman lines are placed can be caused by the photoluminescence excited by incident light, λ_{inc} = 488 nm, (Fig. 6.70 for comparison). Two intensive lines at 1357 and 1591 cm^{-1}

Table 6.4. **The content of some elements (mass%) accompanied luminescence intensity for different zones of solid samples [280]**

Zone	Si	C	O	K	Luminescence intensity
Zone 1, thick particles	1.27	31.50	36.89	29.75	Noticeable luminescence
Zone 2, small particles	7.11	30.41	31.18	30.25	No luminescence
Zone 3, dense branches	1.07	49.85	8.68	38.27	The same
Zone 4, large particles	0.68	65.00	30.00	4.32	Noticeable luminescence
Zone 5, separated particles	0.96	84.76	7.41	6.86	Background luminescence
Zone 5, agglomerates (~5 μ)	0.65	64.00	12.00	21.60	The same
Zone 5, large particles	0.26	96.20	2.32	1.06	No Luminescence

(their full width at half maximum, FWHM, can be evaluated as 80—180 cm^{-1}) are the so-called disorder-induced D-band and Raman-allowed first-order G-band, respectively [205, 212, 314]. The complex of low intensity band near ~(2700—2730) cm^{-1} is the second-order (2D or G′) band of the zone-boundary phonons of carbon micro/nanostructures [314].

Spectrum 5 somewhat differs from spectra 2—4. It contains most of the peculiarities inherent to the Raman spectra of all studied zones of MNCM films. In particular, the D band has a shape, position, and FWHM similar to those in spectra 2—4. The G′ band has a somewhat higher intensity than zones 2—4, and up to its four components can be distinguished there. The most significant difference between spectra 2—4 and spectrum 5 is seen in the G-band range. The structure-less wide G-band is also present in spectra 2—4, but an additive intensive narrow line (FWHM ~15 cm^{-1}) with a peak at 1580 cm^{-1} is observed there. The FWHM and position of the narrow line are typical for the G band of graphene deposited on SiO_2/Si [330]. This line indicates some amount of graphene in zone 5 of MNCM solid films. The possibility to distinguish four components and the G′ band shape allows assuming the presence of multilayer graphene with four or more layers [316, 317]. At the same time, the similarity of spectrum 5 and spectra 2—4 indicates that some types of MNCM particles are inherent to all of the studied zones.

A more detailed analysis of carbon nanostructures is usually performed by calculation of the I_D/I_G ratio (I_D and I_G are intensities of D- and G-bands, respectively). In the first stage of analysis, the background (luminescent signal) of each Raman spectrum was subtracted. In addition, the narrow band (approximated by Gauss curve with FWHM = 15 cm^{-1} and peak position at 1579.4 cm^{-1}) was subtracted from spectrum 5. The calculated I_D/I_G ratios are 0.91, 0.84, 0.94, and 0.84 for spectra 2, 3, 4, and 5 respectively. The well-known Tuinstra — Koenig relation, $I_D/I_G = C(\lambda)/L_a$ (where $C(\lambda)$ is an incident wavelength-dependent coefficient equal to 4.4 nm for λ_{inc} = 488 nm), allowed us to estimate carbon particles sizes (L_a) [318]. So, we found that zones 2—5 of the P1 sample contain carbon particles. At the same time, according to SEM images, they are of much larger sizes. Thus, we can assume that the large particles are really some agglomerates of MNCM particles of ~5 nm size. It is worth noting that similar Raman spectra were observed for graphene oxide and graphite oxide nanoparticles [293, 319]. We suppose that agglomerates of graphene oxide and graphite oxide nanoparticles are inherent to all zones of studied solid films, while multilayer graphene is present mainly in zone 5 of the films.

The luminescent microscopy and chemical element analysis allowed us to make some conclusions about the composition of luminescent MNCM particles (Table 6.4). Potassium seems to have no influence on the luminescence of studied zones. Really, zone 1 is characterized by noticeable luminescence while zone 2

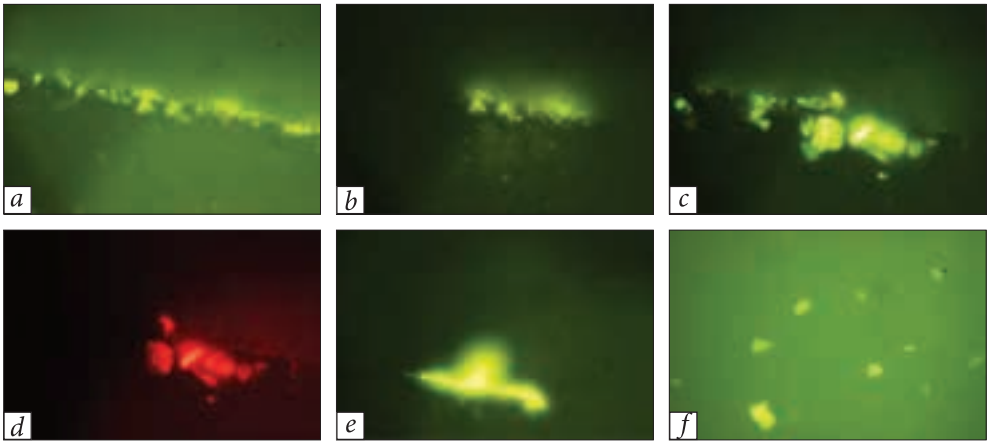

Fig. 6.69. PL images of the P1—P3 types of the samples. The horizontal size of the sample areas is 250 (*a*, *b*) and 25 μ (*c*—e). The *a*—*d* images demonstrate edge areas, while the e and *f* images demonstrate the interior of the samples. Green (*a*—*c*, *e*, *f*) and red (*d*) glass filters were applied under microscopic study [280]

with almost the same potassium content reveals no luminescence. The regions with high content of carbon and low oxygen content reveal only background luminescence. At the same time, the region of thick particles with similar high content of C and O is characterized by intensive luminescence. The absence of luminescence for zone 2 (with the highest Si content, ≈ 7 mass %) can be explained by the assumption that the most of oxygens are related to the silicon oxides of the substrate surface. Thus, intensive luminescence characterizes only those MNCM particles that are relatively large and contain both carbon and oxygen atoms.

Some of the luminescent microscopy images of the solid samples are presented in Fig. 6.69. Emission of the separated particles can be observed for all zones (Fig. 6.69, *a*, *b*). At the same time, it is clearly seen that intensive emission is a property of some relatively large particles (Fig. 6.69, *c*—*f*). Some of these objects reveal very intensive PL (Fig. 6.69, *c*, *e*). The PL spectra are complex and consist of at least two (green and red) components.

So, PL is a property of separated particles and their agglomerates. However, it is weak in the regions where small and thin MNCM pieces are located, and it is much more intensive for large particles and wires.

PL spectroscopy was also applied to all the studied solid samples and starting colloid materials. The PL spectra of MNCM films P1 and P3 are shown in Fig. 6.70. Four different regions of the sample P1, which contains carbon particles of various sizes, were chosen for luminescence monitoring. As Fig. 6.70 shows, the PL properties of sample P1 significantly depend on the region where the luminescence spectrum was registered.

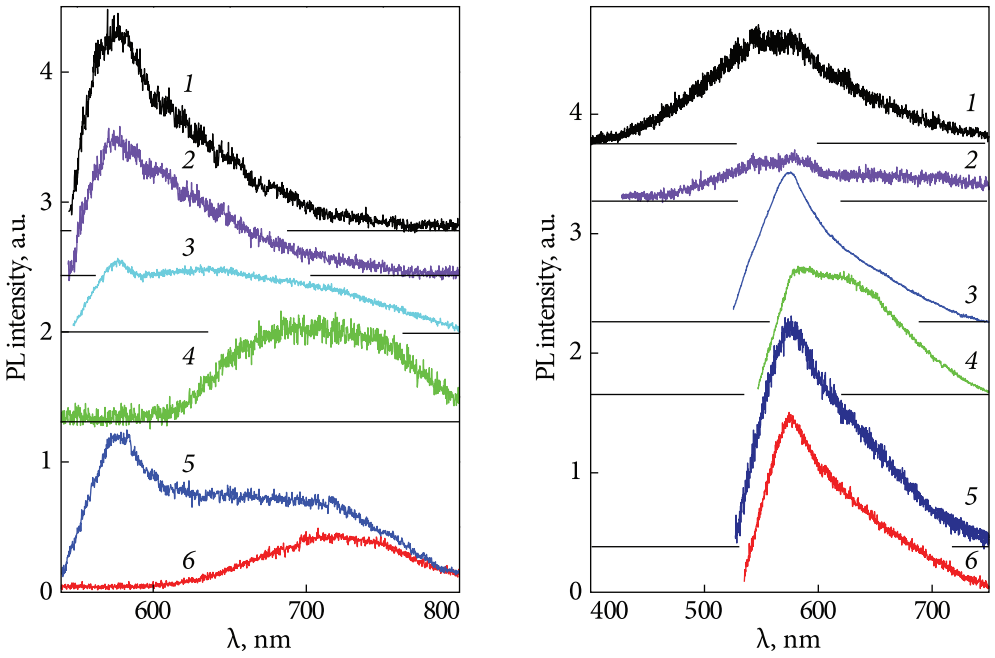

Fig. 6.70. PL spectra of various samples (*##1—4*) of the P1 type: #1P1 (*1*), #2P1 (*2*), #3P1 (*3*), and #4P1 (*4*) and the spectra taken by means of spatial selection of emission from the surface of the P3 type sample (*5*, *6*): emission spectra for the areas with (*5*) and without (*6*) bright fragments. λ_{ex} = 473 nm; T = 300 K. [280]

Fig. 6.71. PL spectra of the C1 (*1—4*), C2 (*5*), and C3 (*6*) samples; λ_{ex} = 337.1 (*1*), 405 (*2*), 473 (*3*, *5*, *6*) and 532 nm (*4*); T = 300 K [280]

There are at least two overlapping PL bands with maxima at $\lambda_{max} \approx 580$ and 710 nm respectively. This observation coincides with the results of luminescent microscopy where green and red luminescence was found for MNCM films. Both green and red luminescence are inherent to sample P3 (Fig. 6.70, curves *5* and *6*) where the particle sizes do not exceed 1 μ. In general, the P3 sample PL spectrum (Fig. 6.70, curve *5*) is similar to those of the P1 film. Regions of high brightness on the sample surface can be distinguished. The PL from these regions was measured using a microscopic portable device, and it was found that the PL spectra consist of only one emission band with a maximum at ~720 nm (or 1.72 eV). Interestingly, this value is very close to the bandgap of graphene oxide cluster (1.7 eV) reported in [320] for saturated (meant high oxygen content) graphene oxide structure with a chemical composition close to $C_8O_2(OH)_2$. The same C to O ratio of 2:1 was obtained from the chemical element analysis for zone 4, where noticeable luminescence was observed. That means that just the presence of the oxygen and/or hydroxyl groups determines the luminescence

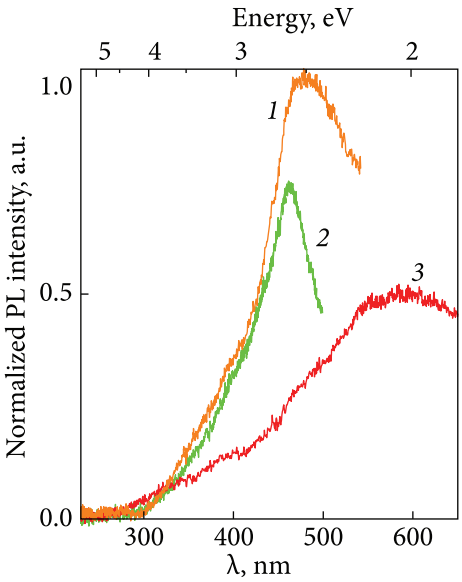

Fig. 6.72. PL excitation spectra for the C1 sample. λ_{reg} = 580 (*1*), 530 (*2*), and 700 nm (*3*). T = 300 K. [280]

of large and thick MNCM particles. The luminescence mechanism, in this case, is related to the radiation transition between the conduction and valence bands of saturated graphite oxide structures. The bright luminescence of zone 1, where the C:O ratio is 1:1, can be explained by the assumption that a substantial part of oxygen is related to the KOH remains.

On the other hand, the bandgap of graphite oxides varies from zero up to several eV depending on the oxidation/reduction level [321, 322], and the green luminescence of studied samples can be related to "unsaturated" graphite oxides. These results are consistent with our data on the chemical elements contained in zone 5, where mostly background luminescence is observed. In fact, the C/O ratios are 6:1 and 12:1 for the regions of zone 5 where only background PL was found (Table 6.4). The conclusion made above is in accordance with [323], where it was shown that the reduction of graphite oxide causes a blue shift of luminescence spectra.

In order to obtain PL excitation spectra for MNCM samples, the starting colloids C1, C2, and C3 were studied. Obviously, due to a higher particle concentration, the luminescence from the colloids is much stronger than that from solid films. The PL spectra of colloids were studied using laser excitations for comparison with solid samples (Fig. 6.71). It is clearly seen from Figs. 6.70 and 6.71 that spectra of both colloid and films are similar for λ_{ex} = 473 nm. Luminescence of low intensity was also observed in the "blue-green" spectral region (420—500 nm) under short wavelength excitation (337.1 and 405 nm). The shape and peak position, λ_{max}, of the PL bands depend on the λ_{ex} as it has been reported for various carbon colloids [311, 324—327].

The PL excitation spectra are shown in Fig. 6.72. The observed red-shift of excitation band maxima with monitoring wavelengths increasing is typical for carbon materials 327]. The difference in band shape indicates that there is a continuous (from the viewpoint of electronic band structure) set of luminescent carbon structures, namely graphite oxide particles with various reduction levels. We suppose that a more detailed description of the PL excitation mechanism in studied structures requires submicron separation of the particles.

So, our colloid carbon systems, made via electrochemical exfoliation from thermally expanded graphite, possess luminescence properties. Their PL spectra are complex, where at least two components, green-yellow and red, can be selected. It is easy to see that the components are similar to those described above for some nanostructural carbon forms. The studied micro/nanocarbon materials consist of different size particles. The larger particles reveal characteristics of graphite oxides while the smallest ones possess some characteristics of multilayer graphene. The small particles show a background luminescence, while the larger ones can reveal intensive PL. The luminescence effectiveness depends on the oxygen group content. The most intensive PL was observed from particles where the\ C/O ratio is equal to 2:1. Importantly, the method applied allows the production of luminescent carbon micro/nanomaterials in large quantities without any additional treatment [280].

Graphene-like carbon micro/nanoparticles can be used to prepare both polymer-based and EG-based composites.

6.2.2. Optical properties of composites with EG as a filler or as a matrix

The incorporation of graphene nanoparticles in polymers leads to changes in the polymer properties (see Chapter 5). There can be a significant increase in the dielectric constant [328], a change in thermodynamic properties of the composite [329], and an increase in the crystallinity degree and resistance to thermal degradation [330]. In addition, the synergetic increase in absorption of electromagnetic radiation provided by an interaction with carbon nanotubes in porous system polydimethylsiloxane [331] and the increase in tensile strength to 21% for bio-thermoplastic materials at low concentrations [332] are also caused by the presence of GNPs. Modification of synthetic polymer fibers by graphene nanoparticles yields some improvements and the appearance of new properties, such as adsorption performance, antibacterial character, hydrophobicity, and conductivity, useful for a wide range of applications [333].

We prepared samples of a polymer-EG composite on a polyamide-12/12 ($PA_{12/12}$) base filled with GNPs up to 0.06 volume fraction using the following procedure. The polymer in the powder form was added to the stable dispersion of GNPs, and then the mixture was dispersed in an ultrasonic bath for 2 min, dried at 350 K, and pressed at 450 K and 5MPa. The fact that the complex dielectric permittivity components, ε' and ε", measured for systems with different volume contents of GNPs at a frequency of 9 GHz (Fig. 6.73), increase with GNPs content increasing and reach the values of ε' = 29.8 and ε" = 13 at φ = 0.06 is an important feature of the composites.

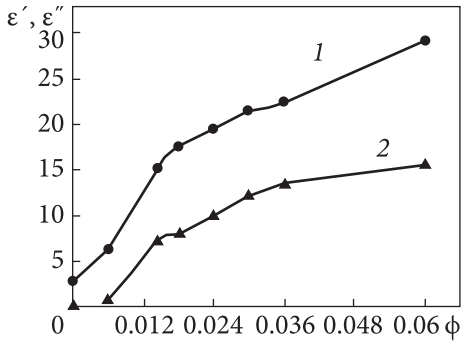

Fig. 6.73. Dependence of real ε' (*1*) and imaginary ε" (*2*) parts of the complex permittivity on the volume content of GNPs at frequency 9 GHz for the PA12/12-GNPs systems [301]

We can state that the increase in the number of dipoles formed from GNPs clusters and the further increase in their size and quantity lead to the formation of a dimensional lattice causing more effective interactions with electromagnetic radiation at a given frequency along with the gradual increase in the dielectric constant values. Another type of polymer-EG composites was described in [333], where epoxy resin was used as a matrix. Epoxy resin (a kind of thermoset polymer) is an organic substance, and EG can be used as an inorganic additive. Epoxy resins are widely used for coatings, adhesives, primers, semiconductor encapsulation, and as matrices for advanced fiber-reinforced composites. A further requirement of current importance is for high flame resistance and imparting flame retardance into epoxy resins. Some studies have demonstrated that EG can improve the flame-retardant property of coatings [335—337]. Due to poor compatibility between polymer matrix and expandable graphite, the performance of flame retardant will be abated. EG was before functionalized by a coupling agent for enhancing the interaction between organic and inorganic phases. The covalent bonds are formed through a sol-gel reaction, which provides thermal stability to composites [334].

EG was supplied with Inter. Carbide Tech. Co. 3–Isocyanatopropyltriethoxysilane (IPTS) as a coupling agent between the epoxy resin and EG was purchased from United Chemical Technologies, Inc., USA. 4,4'-diaminodiphenylmethane (DDM) as a curing agent for epoxy monomer was purchased from the Acros Organics Co. Geel West Zone 2, Janssen Pharmaceuticalaan 3a, 2440 Geel, Belgium. Tetrahydrofuran (THF) was of reagent grade and supplied by the Echo Chemical Co. Ltd., Taiwan. To prepare IPTS-EG, 1 g EG was functionalized with 5 g IPTS in the presence of THF as a solvent, at 60 °C for 4 h. The reaction was monitored by FTIR. IPTS-EG was washed several times with anhydrous THF and then vacuum dried at room temperature overnight. The modified epoxy resin was synthesized as follows: 4g IPTS (equivalent weight 247 g) was added to 10g DGEBA type epoxy resin (equivalent weight 180g) and stirred for 4 h until the characteristic peak of the NCO group disappeared. The IPTS reacted with epoxy to form IPTS-Epoxy. Adequate amounts of IPTS-EG were fed into the THF solution of modified epoxy, and the final solution was stirred at room temperature for 20 min. The products were cast into aluminum

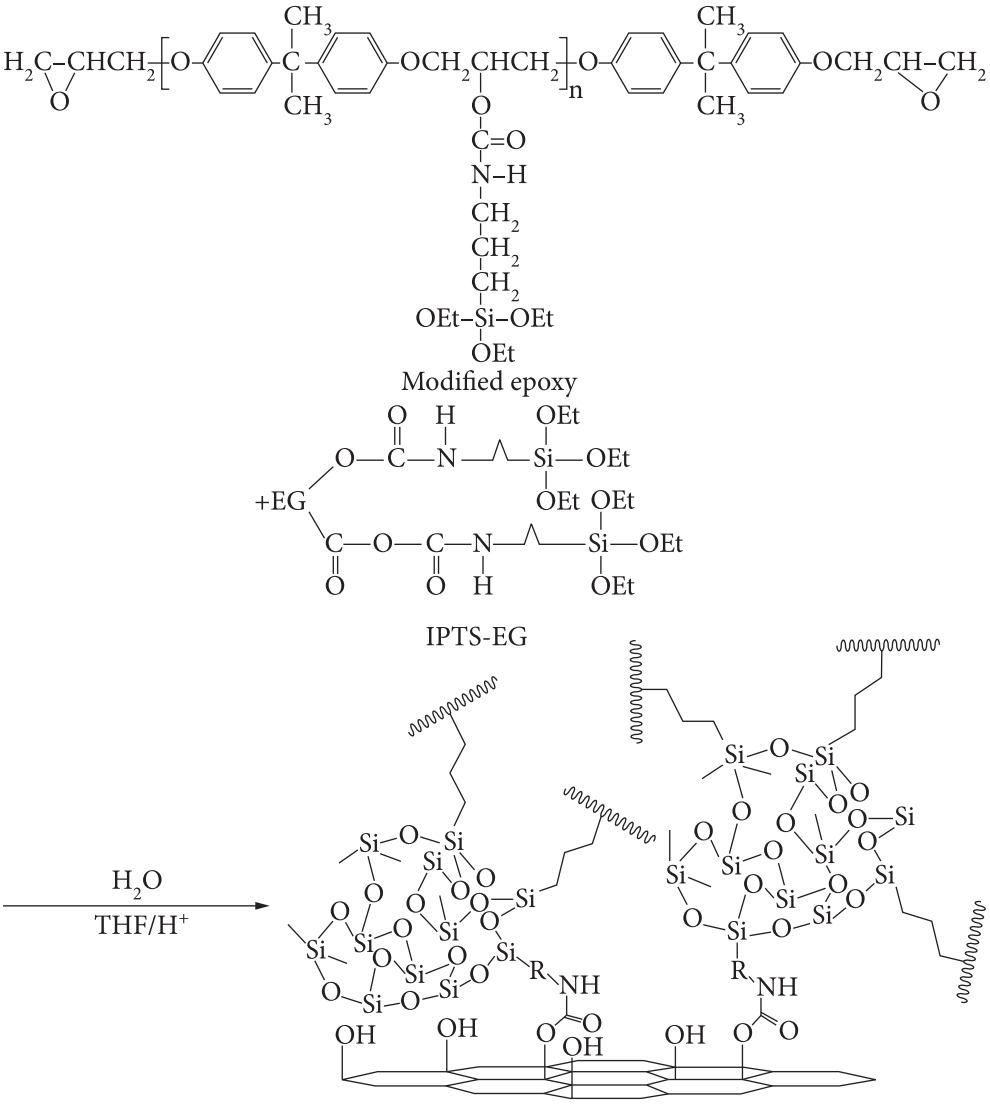

Fig. 6.74. Scheme of IPTS-epoxy and IPTS-EG composites preparation [334]

dishes to gel. The wet gels were aged at room temperature for 24 h and then dried at 100 °C for 5 h in a vacuum oven. The novel composites materials were prepared as described in Fig. 6.74 [334].

The epoxy is composed of monomer and curing agent 4,4'-diaminodiphenylmethane (DDM), which has the —NH functional group to react with the oxirane functional group of the monomer. This chemical reaction can form a 3-D network of the organic matrix. IPTS was used as a coupling agent for organic and inorganic phases to enhance the compatibility through the sol-gel reaction. The

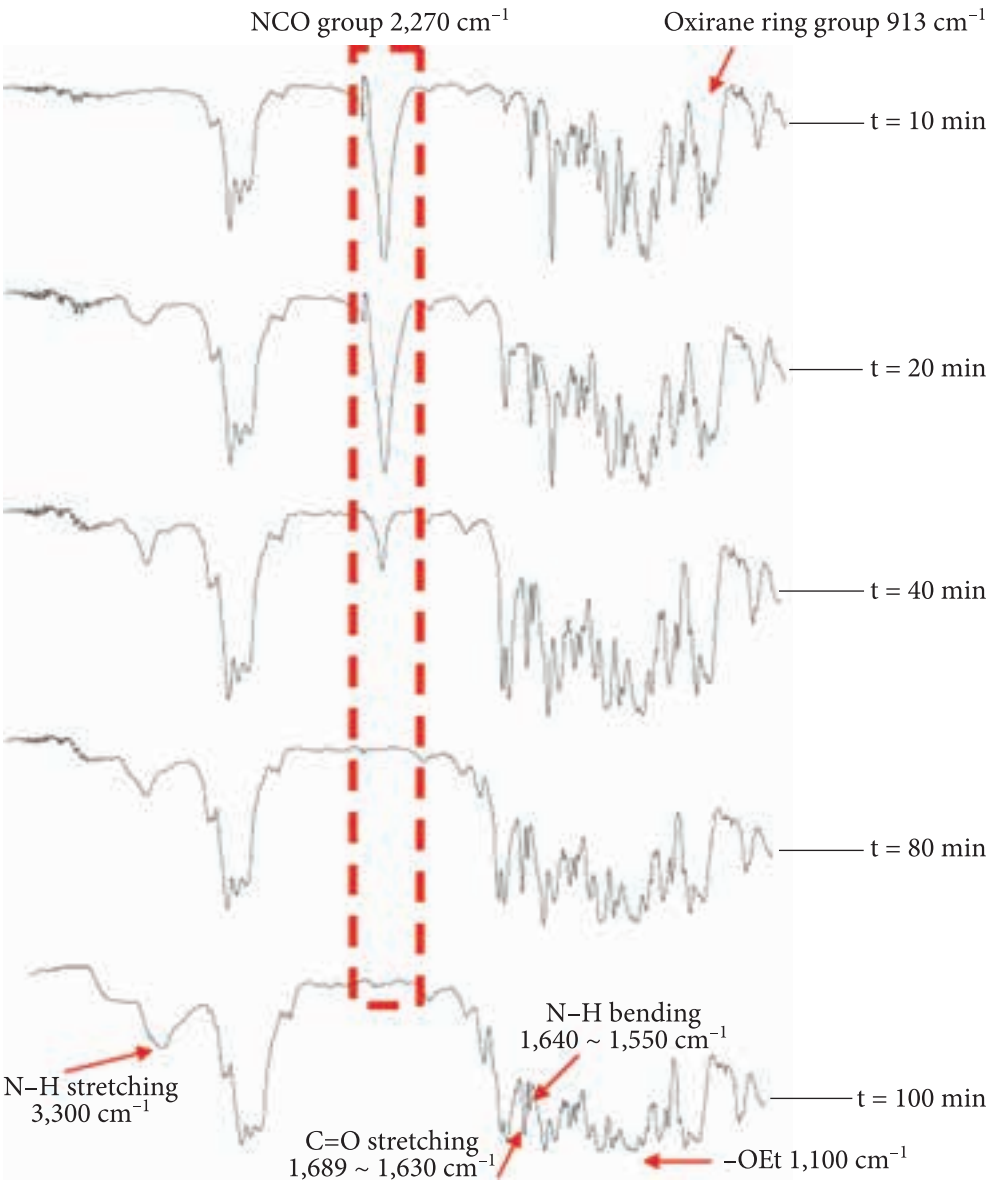

Fig. 6.75. FT-IR spectra of the reaction between epoxy and IPTS [334]

modified epoxy, which has the —OEt functional groups, can react with the grafted EG, which possesses —OEt functional groups, through the sol-gel reaction.

Fig. 6.75 presents FT-IR spectra of the reaction between epoxy and IPTS. It shows the disappearance of the characteristic peak for the IPTS NCO group at 2270 cm^{-1}, while new characteristic peaks at 3400 cm^{-1} and 1700 cm^{-1} are generated. The peaks represent that urethane linkage formed. This phenomenon re-

vealed that the —OH functional group of epoxy had reacted with the —NCO functional group of IPTS. The absorption peak around 1100 cm^{-1} corresponding to the —OEt functional group of IPTS was observed after the reaction with IPTS and epoxy. The absorption peak at 910 cm^{-1}, corresponding to the oxirane group, decreases with increasing the cure reaction time. After the reaction, epoxy resin possesses the functional group —OEt to proceed with a sol-gel reaction. This can enhance the compatibility between organic and inorganic components [334].

The obtained results showed that a functionalized EG can enhance the thermal stability of composites and inorganic components can suppress the production of toxic gases.

We can conclude given the described above results that optical methods, e.g. Raman scattering and FTIR spectroscopy, are important for the characterization of the polymer composite materials containing EG.

The high sorption capacity for many organic substances, extremely low bulk density, high specific surface, high ductility, and ability to be formed with no addition of a binder characterize EG as a material attractive for the creation of new composite materials on its basis. That is, EG can be used not only as a filler but also as a matrix of a composite material.

The results of the creation of polymer-oxide composite materials are well known. They reveal new characteristics and demonstrate prospects for their practical use by using components with different types of chemical bonds (matrix and filler) [338, 339]. Such, by type, composites are EG-oxide filler. Among the fillers, zirconium oxide, ZrO_2 (zirconia), is attracting attention. It has a high catalytic activity and sorption ability and exhibits intense PL [340]. That is, the composites EG + ZrO_2 can be considered optical materials.

These composites can be made by the procedure described in [340]. For intercalation, powdered natural graphite was used there, which within 30—60 min was kept in the intercalant solution, washed to neutral pH, and dried at 110 °C. Intercalation was carried out in a concentrated solution of sulfuric acid (96.5% H_2SO_4) in the presence of oxidizing agents, namely bisulfate and potassium bichromate [340].

The EG-ZrO_2 nanocomposite was prepared by replacing zirconium hydroxide in the solution of zirconium oxychloride with a solution of sodium hydroxide in an aqueous suspension of previously obtained intercalated graphite (IG), followed by thermal decomposition. The IG powder was placed in a 1M $ZrOCl_2$ solution, the mixture was evacuated, and a 0.05M NaOH solution was added during study-state stirring. The resulted precipitate was washed with distilled water, dried at 110 °C, and thermalized. Heat treatment was performed in an electric furnace with a tubular graphite heater in an argon environment (volume fraction of argon was 99.993%). The temperature was controlled by an IR pyrometer Marathon MR1SCSF (Raytek Company, Germany). To obtain a composite of the given form and porosity, heat treatment was carried out in a closed space.

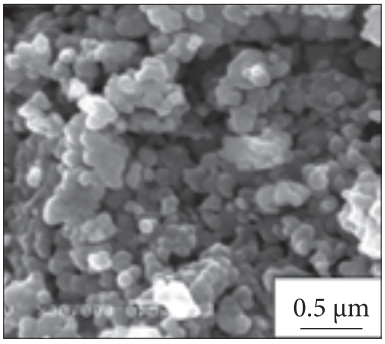

Fig. 6.76. Scanning electron microscopy image of the ZrO_2: $0.005Eu^{3+}$ powder [340]

The comparison of the initial graphite powders and IG samples revealed significant changes in the chemical composition, specific surface area, pycnometric density, and the specific volume of materials.

According to the element analysis, in the case of using the IG–1 sample (the sulfur content was about 4.5 mass%), the amount of zirconium reached 9.5 mass% (mean value 5 mass%) while using the IG-2 sample (7.7 mass% of sulfur) the content of zirconium does not exceed 4.2 mass% (mean value 2 mass%).

Based on the XRD data, it can be concluded that after heat treatment, zirconia is in a crystalline state and, most likely, in a cubic modification (c-ZrO_2). The size of crystallites is about 20 nm. It is noteworthy that the monoclinic modification is stable in the used temperature range, but its XRD peaks were not observed. This may be because the heat treatment of the EG-ZrO_2 composite took place in a reducing atmosphere, leading to defects in the oxygen sub-lattice, which stabilize the cubic modification [341]. A comparison of the SEM data on the size of ZrO_2 crystallites showed that ZrO_2 is agglomerated on the matrix surface in the form of clusters sizing from tens of nanometers to hundreds of microns [341].

The authors of this book also made and studied the EG-ZrO_2 composites, but the procedure for their production differed from that described above. In addition, to fill the EG matrix, they used not "pure", but activated by europium ions Eu^{3+} zirconia, which is of interest due to both luminescence behavior of the ZrO_2 : Eu^{3+} compound and stabilization of the cubic/tetragonal phases of ZrO_2 with Eu^{3+}ions [342]. E.g., a partial stabilization of zirconia nanopowders with tetragonal phase content to 98.5% was observed for Eu_2O_3 concentration ≥3mol% [343]. Fully stabilized zirconia is formed when the amount of europium oxide was much higher (12—27 mol %) [344].

The procedure for the EG-ZrO_2 manufacturing by the authors of this book was as follows. First, EG was obtained by the method described in Chapter 2.

As for nanocrystalline powders of zirconia, they were prepared via a solid-state route using analytically pure zirconyl nitrate ZrO $(NO_3)_2 \times 2H_2O$ and Eu_2O_3 of 0.5 mass% concentration as precursors. To prepare fine powders and to get rid of gaseous co-products, the initial reagent was preheated at 583 K for 4 h and afterward calcined at temperatures 920, 1020, 1120, 1370 K for 15 h for each annealing temperature.

The SEM image of the solid solution ZrO_2: $0.005Eu^3$ is presented in Fig. 6.76. You can see that the product is crystallized in a compact form with a particle size of about 50—150 nm.

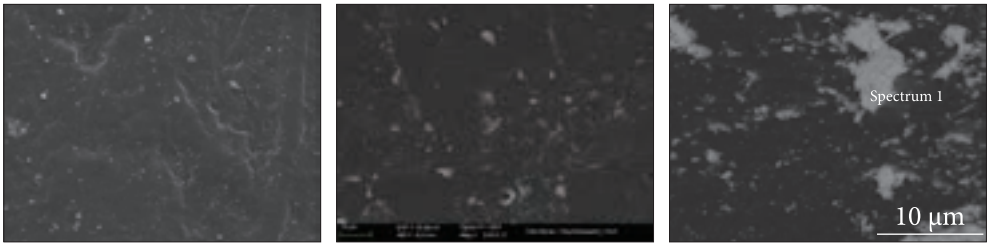

Fig. 6.77. SEM images of EG- ZrO_2: Eu composites with different amounts of ZrO_2: Eu: $1ZrO_2$: Eu on the left, $5ZrO_2$: Eu in the middle, $20ZrO_2$: Eu on the right

To produce composites, 1 g of EG powder was mixed with a certain amount of zirconia powder and manually rubbed in a porcelain mortar for 10 min. The mixture was then moistened with 1 cm^3 ethyl alcohol. The product was again brushed in a mortar for 10 min until a homogeneous material was obtained. Further, this material was drained at 100 °C for 5 min. The mixture was compressed according to the specially selected mode (see Chapter 2) to a maximum pressure of 200 MPa. The obtained samples looked like cylinders with a diameter of ~10 mm and a height of ~8 mm.

Three series of samples with different europium contents were made in such a way: 1 mass% (sample marked as $1ZrO_2$: Eu), 5 mass% ($5ZrO_2$: Eu), and 20 mass% ($20ZrO_2$: Eu).

Note that the surface of all samples had a characteristic metallic luster, which is evidence of rather small roughness.

The SEM images of the ZrO_2 powders coated with gold were\ obtained with a JEOL JSM 6060 LV.

A triple T64000 Horiba Jobin-Yvon spectrometer equipped with a quasi-confocal scanning microscope was used for the micro-Raman scattering spectra measurements. An Ar-Kr Spectra-Physics 2018 laser with a wavelength of incident light of λ_{inc} = 488 nm was used for the measurements.

PL under excitations in the UV and visible regions was studied at room temperature of the samples. An arc Xenon lamp (150 W) with spectrometer MDR–12 (working range 200—650 nm) was used as an excitation source. A diffraction spectrometer MDR-23 (250—700 nm, linear dispersion 1/20 mm/Å) was used for the registration of PL emission and excitation spectra. The optical width of the exiting monochromator slit was in the range of 2—3 nm. The sizes of the incident excitation beam on the sample surface were ~1 × 3 mm. All the PL and the PL excitation spectra were corrected on the system responses.

SEM was used to study the morphology of the surface of composites and the distribution of oxide particles on them (Fig. 6.77). As can be seen from Fig. 6.77, the surface of the samples is a fairly dense package of EG plates (dark background) incorporated with oxide particles (gray details). At low concentra-

tions of oxide (sample EG-1ZrO_2: Eu) small-sized inclusions (100 nm—1 μm) are chaotically distributed over the sample (Fig. 6.77, on the left). A similar picture is realized also for the sample EG-5ZrO_2: Eu, but there, in addition to individual particles up to 100 nm in size, their agglomerates up to 5 μm (Fig. 6.77, in the middle) are present, which, like to nanoparticles, are fairly uniformly distributed over the sample. For a composite containing a significant amount of oxide (sample TPG-20ZrO_2: Eu), nanoparticles can be combined in agglomerates of 1 to 10 μm size, and hence the distribution of the oxide is markedly uneven (Fig. 6.77, on the right). The fact that gray inclusions are particles of zirconia is confirmed by a microelement analysis performed for different areas of the samples using the same electron microscope. In particular, one of the areas is marked in Fig. 6.77, on the right. Areas for the element analysis were selected in places with no apparent presence of inclusions, such as individually located small-sized particles, agglomerates of ~1 μm, and agglomerates of a significant size (~10 μm), as shown in Fig. 6.77.

As a result of the analysis, it was found that the carbon content can reach 99.5 mass% and oxygen content — 0.5 mass% in areas of the first type. There are up to 94 mass% of carbon, up to 2 mass% of zirconium, and up to 4 mass% of oxygen in the areas of the second type, while the contents of the fourth type of areas can be as follows: ~30 mass% carbon, ~20 mass% zirconium, and ~50 mass% oxygen. That is, the analysis results are consistent with the data on composite components determined from the description of the electron microscopy images and with the composition of zirconium oxide: two atoms of oxygen per zirconium atom.

It was reasonable to compare the described above data with the results of the micro-Raman scattering measurements with a scattering cross-section of ~1 μm. Those measurements were made on the same composite samples and in various surface points which differed by composition and EG/zirconia ratio.

Some of the measured Raman spectra are shown in Fig. 6.78. There you can see a spectrum taken far from zirconia particles (1-t type points; curve *1*) and the spectrum taken close to the oxide agglomerate (2-d type points; curve *2*). The spectra are typical for various carbon forms in the spectral range 1000—2000 cm^{-1}, as they show well-distinguished D and G lines, located at 1359 and 1582 cm^{-1} for the 1-st type points and at 1356 and 1583 cm^{-1} for the 2-nd type points.

At the same time, the difference in the intensity ratio for the D and G lines is noticeable. For the 1-t type points, the value of I_D/I_G is about 0.17, while for the 2-d type points $I_D/I_G \approx 0.36$. The data obtained for areas of oxide particles (1-t type points) are close to those characteristic for crystalline graphite and, in some cases, for EG (see the descriptions made above and in [301, 302]). However, unlike the above data, where the EG was not shown due to defects

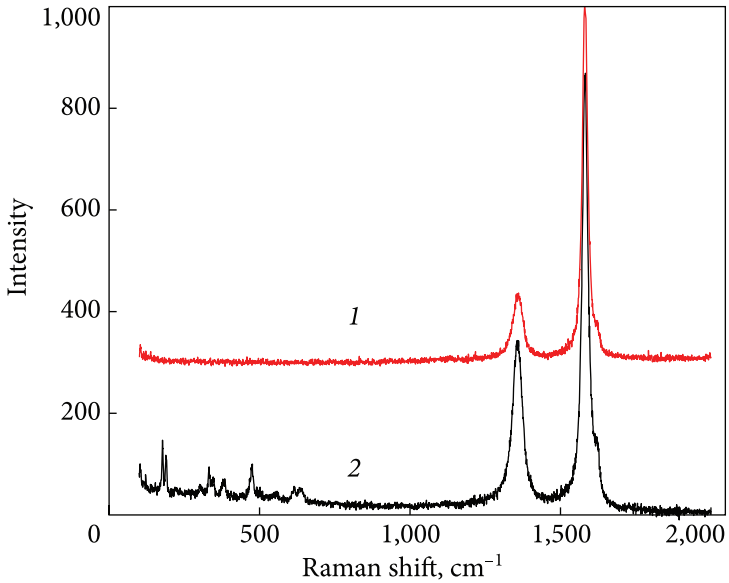

Fig. 6.78. Raman spectra of EG-ZrO_2 : Eu taken in points far from oxide particles (*1*) and in the interface between zirconia particle and carbon matrix (*2*). (Curve *1* is shifted up by 300 units)

and disordered structures of line D, in our samples, this line is quite noticeable, which is apparently due to the destruction of the EG plates-scales due to the mechanical processing and addition of zirconium oxide particles. The effect of the latter is manifested in some shifts of the Raman frequencies (lines in spectra 1 and 2) and more than twice increasing the values of I_D/I_G for the 2-d type points which are interfaces between the EG and oxide particles areas. The fact that these points are such interfaces can be seen from the manifestation in spectrum 2 in the range 100—700 cm^{-1} of not only D and G lines of graphite, but also Raman lines characteristic for ZrO_2 [345].

The effect of the ZrO_2 : Eu filler on the state and structure of the matrix components is revealed in the change in its optical properties. This is quite clearly manifested by the change in the magnitude and spectral dependence of the reflection coefficient in the UV, visible, and near IR ranges (Fig. 6.79).

It is easy to see the similarity of these spectra to those of reflection from graphite, given in Fig. 6.1. The effect of the ZrO_2 : Eu filler is noticeable both on the reflection coefficient, and the form of spectral dependence. We have pointed in Section 6.1 that the range 1.45—5 eV (850—250 nm) corresponds to the intra- and interband transitions related mainly to the π bands. At lower energies, the structure in the reflectance curve near 0.8 eV could be attributed to the onset of transitions between the E_2 and E_3 bands at the point K. The dominant structure in the optical reflectivity of graphite is, however, observed at ~5 eV

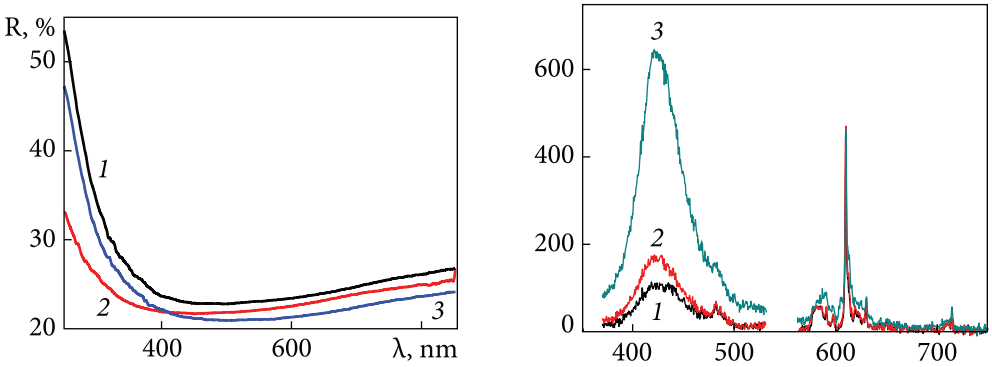

Fig. 6.79. Reflectance spectra of the EG-ZrO_2 : Eu composites with different amounts of ZrO_2 : Eu: 1ZrO_2 : Eu (1), 5ZrO_2 : Eu (2), and 20ZrO_2 : Eu (3)

Fig. 6.80. PL spectra of the EG- ZrO_2 : Eu composites with different amounts of ZrO_2 : 1ZrO_2 : Eu (1), 5ZrO_2 : Eu (2), and 20ZrO_2 : Eu (3)

and associated with interband transitions between π-bands around the M-point in the Brillouin zone.

Thus, the shown in Fig. 6.79 range of reflection spectra of the ZrO_2 : Eu composites manifests both the above-mentioned features and indicates a noticeable effect of the incorporated oxide particles on the carbon matrix electronic structure, especially on the π bond. This may be due to the deformation and possible destruction of the latter. The influence of these two factors is probably different, which may cause different behavior of reflection spectra in the ranges 250—400 and 400—850 nm (Fig. 6.79, curve *2*).

The influence of these factors can be also detected by changes in the luminescence spectra of the composites investigated (Fig. 6.80).

This figure shows two sections of the luminescence spectra in the ZrO_2 : Eu composites upon their excitation with a wavelength of 337.1 nm. The first contains a wide band in the range of 375—525 nm, and the other is a superposition of relatively narrow lines in the range of 565—750 nm. As can be seen, the increase in the oxide concentration, in general, leads to an increase in the band intensity. Thus, the observed luminescence should be associated with the radiation of the composite oxide component. This conclusion, however, is only partially consistent with the known data on the radiation of both EG-matrix and incorporated europium-doped zirconium oxide.

Indeed, we have the opportunity to compare the position and shape of the wide band with the emission of various carbon forms discussed above. It is obvious that in the wide-band spectrum, at least three components with maxima at ~422, 437, and 483 nm can be identified. Similar spectra with a similar set of components were observed in the PL spectra of graphene, graphene quan-

tum dots, and graphite quantum dots (Figs. 6.43, 6.45, 6.50). At the same time, it should be noted that in the same spectral ranges, the own luminescence of zirconium oxide can also be observed [340], an increase in which causes an increase in the composite PL intensity in the range of 375—525 nm. As for PL in the long-wave range, 565—750 nm, it is undoubtedly due to the emission of oxide particles and radiative electronic transitions $^5D_0 \rightarrow {}^7F_J$ (J = 0—4) in the Eu^{3+}shell. We note that the exact correlation of changes in the intensity of two parts of the PL spectra is absent, which is evidence of the mutual effect of the matrix and oxide particles on their electron-vibration states.

Thus, the study of composite materials where EG is a filler and, conversely, composites where EG is a matrix has shown that these materials can be considered optical materials. On their basis, in particular, luminescent light transformers can be created. In addition, the optical methods themselves are an important tool for studying the composition and structure of both EG and composite materials, which include EG.

REFERENCES

1. J.T. McCartney and S. Ergun, *Optical properties of coals and graphite* (U.S. Dept. of the Interior, Bureau of mines, 1967), Bulletin 64.
2. P.E. Trevisanutto, M. Holzmann, M. Côté and V. Olevano. Phys. Rev. B. **81** (12), 121405(R) (2010).
3. R.J. Papoular and R. Papoular, Mon. Not. R. Astron. Soc. **394**, 2175, (2014).
4. M S. Dresselhaus & G. Dresselhaus, Advances in Physics, **51** (1), 1 (2002).
5. Hanlon, L.R., Falardeau, E.R., and Fischer, J.E., Solid St. Commun., **24**, 377 (1977).
6. Hanlon, L.R., Falardeau, E.R., and Fischer, J.E., Mater. Sci. Engng, **31**, 161 (1977).
7. A.B. Djurisic, and E.H. Li.J. Applied Physics. **85** (10), 7404 (1999).
8. E. Taft and H. R. Philipp, Phys. Rev. A. **138**, 197 (1965).
9. H. Venghaus, Phys. Status Solidi B. **71**, 615 (1975).
10. D.L. Greenaway, G. Harbeke, F. Bassani and E. Tossati, Phys. Rev. **178**, 1340 (1969).
11. G. Guizzetti, L. Nosnezo, E. Reguzzoni, and G. Samoggia, Phys. Rev. Lett. **31**, 154 (1973).
12. E. Tossati and F. Bassani, Nuovo Cimento B **65**, 161 (1970).
13. Borghesi and G. Guizzetti, in: *Handbook of Optical Constants of Solids II*, edited by E.D. Palik (Academic, Boston, 1991), pp. 449—460.
14. R. Klucker, M. Skibowski and W. Steinmann, Phys. Status Solidi B **65**, 703 (1974).
15. L.G. Johnson and G. Dresselhaus, Phys. Rev. B **7**, 2275 (1973).
16. R.F. Willis, B. Fitton and G.S. Painter, Phys. Rev. B **9**, 1926 (1973).
17. R. Ahuja, S. Auluck, J. M. Wills, M. Alouani, R. Johansen and O. Erikson, Phys. Rev. B **55**, 4999 (1997).
18. G.S. Painter and D.E. Ellis, Phys. Rev. B **1**, 4747 (1970).
19. W.B. Boyle and P. Nozieres, Phys. Rev. **111**, 782, (1958).
20. S. Ergun, Nature. **213,** 135 (1967).
21. P.L. Walker, Jr. and P.A. Thrower, editors, *Chemistry and Physics of Carbon* (Marcel DeKramers-Kroniger Inc., New York, 1965), vol. 16, pp. 138—161.

22. J.W. McClure and Y. Yafet, in: *Proceedings of the Fifth Conference on Carbon* (Pergamon Press, New York, 1962), vol. 1, p. 22.
23. G. Dresselhaus, M.S. Dresselhaus and J.G. Mavroides, Carbon. **4**, 433 (1966).
24. G. Dresselhaus and M.S. Dresselhaus, Rev. Rev. A. **140**, 401 (1965).
25. G. Dresselhaus and M.S. Dresselhaus, Mater. Sci. Engng, **31**, 235 (1977).
26. J.W. McClure, IBM Jl Res. Dev. **8**, 225 (1964).
27. I.L. Spain, in: *Chemistry and Physics of Carbon*, edited by P. L. Walker (Marcel Dekker, New York, 1973), vol. 8, pp. 105, 110.
28. S. Ergun, in: *Chemistry and Physics of Carbon*, edited by P.L. Walker (Marcel Dekker, L.J. Brillson, E. Burstein, A. A. Maradudin and T. Stark, in: *Proceedings of the International Conference on Semimetals and Narrow Gap Semiconductors*, edited by D.L. Carter and R. T. Bate (Pergamon Press, New York, 1971), p. 187.
29. R.J. Nemanich, G. Lucovsky, and S. A. Solin, Solid St. Commun. **23**, 117 (1977).
30. M.S. Dresselhaus and J.G. Mavroides, IBM Jl Res. Dev., **8**, 262 (1964).
31. H.R. Philipp, Phys. Rev. B. **16**, 2896 (1977).
32. G. Bellodi, A. Borghesi, G. Guizzetti, L. Nosenzo, E. Reguzzoni and G. Samoggia, Phys. Rev. B. **12**, 5951 (1975).
33. K. Nakao, J. Phys. Soc. Japan, **47**, 208 (1979).
34. A. Misu, E. Mendez, and M. S. Dresselhaus, J. Phys. Soc. Japan, **47**, 199 (1979).
35. G. Dresselhaus, Phys. Rev. B. **10**, 3602 (1974).
36. A. Balzarotti and M. Grandolfo, Phys. Rev. Lett., **20**, 9 (1968).
37. S. Ergun, J. B. Yashinsky and J. R. Townsend, Carbon, **5**, 403 (1967).
38. H. Anderegg, B. Feuerbacher and B. Fitton, Phys. Rev. Lett., **26**, 760 (1971).
39. T. Uda, J. Phys. Soc. Japan. **28** (4), 946 (1970).
40. A.B. Kuzmenko, E. van Heumen, F. Carbone and D. van der Marel, Phys. Rev. Lett. **100**, 117401 (2008).
41. B. Draine and H. Lee, Ap. J. **285**, 89 (1984).
42. C. Bohren and D. Huffman, *Absorption and scattering of light by small particles* (John Wiley and Sons, New York, 1983).
43. N.B. Brandt, S.M. Chudinov, and Ya.G. Ponomarev, *Semimetals I: Graphite and its Compounds*, edited by V.M. Agranovich and A.A. Maradudin (North-Holland, Amsterdam, 1988), Modern Problems in Condensed Matter Sciences. vol. 20 (1).
44. F. Bassani, G.P. Parravicini, Nuovo Cimento B. **50** (1), 85 (1967).
45. E. Doni and G.P. Parravicini, Nuovo Cimento B. **64**, 117 (1969).
46. J.G. Carter, R. H. Huebner, R. W. Hamm and R. D. Birkhoff, Phys. Rev. A. **137**, A635 (1965).
47. B. Djurisic, A.B. Rakic and J.M. Elazar, Phys. Rev. E. **55**, 4797 (1997).
48. M. Zanini, L.-Y. Ching and J.E. Fischer, Phys. Rev. B. **18**, 2020 (1978).
49. H. Venghaus, Phys. Stat. Sol. (b). **81**, 221 (1977).
50. U. Buchner, Phys. Stat. Sol. (b). **81**, 227 (1977).
51. A.K. Solanki, A. Kashyap, T. Nautiyal, S. Auluck and M.A. Khan. Sol. St. Commun. **100**, 645 (1996).
52. K. Zeppenfeld, Z. Phys. **211**, 391 (1968).
53. J.B. Yasinsky and S. Ergun, Carbon. **2** (4), 355 (1965).
54. Y. Sato, J. Phys. Soc. Japan **24**, 489 (1968).
55. C. Koike, H. Hasegawa and A. Manabe, Astrophys. Sp. Sc. **67**, 495 (1980).
56. F. Rouleau and P. Martin, ApJ **377**, 526 (1991).

57. J. Robertson, Adv. Phys. **35**, 317 (1986).
58. V. Mennella, L. Colangeli, A Blanco, E. Bussoletti, S. Fonti, P. Palumbo and H. Mertins, A&A **295**, 165 (1995).
59. A. Jones, L. Fanciullo, M. Kohler, L. Verstraete, V. Guillet, M. Bocchio and N. Ysard, A&A **558**, A62 (2013).
60. B. Kwiecinska, D.G. Murchison and E. Scott, J. of Microscopy. **109** (3), 289 (1977).
61. M. Zanini and J.E. Fischer, Mater. Sci. Engng, **31**, 169 (1977).
62. M. Zanini, D. Grubisic and J.E. Fischer, Phys. Stat. Sol., **90**, 151 (1978).
63. M.S. Dresselhaus, G. Dresselhaus, P.C. Eklund and D.D.L. Chung, Mater. Sci. Engng. **31**, 141 (1977).
64. M. Maeda, Y. Kuramoto and C. Horie, J. Phys. Soc. Japan. **47**, 337 (1979).
65. S. Reich and Ch. Thomsen, Phil. Trans. R. Soc. Lond. A. **362**, 2271—2288 (2004).
66. F. Tuinstra and J.F. Koenig, J. Chem. Phys. **53**, 1126 (1970).
67. R.J. Nemanich, G. Lucovsky and S.A. Solin, in: *Proceedings of the International Conference on Lattice Dynamics*, edited by M. Balkanski (Flammarion Press, Paris, 1975), p. 619.
68. R. Nicklow, N. Wakabayashi and H.G. Smith, Phys. Rev. B. **5**, 4951 (1972).
69. J.A. Young and N.U. Koppel, J. Chem. Phys. **42**, 357 (1965).
70. A.P.P. Nicolson, and D.J. Bacon, J. Phys. C. **10**, 2295 (1977).
71. R. Nemanich and S. Solin, Phys. Rev. B. **20** (12), 392 (1979).
72. R.J. Nemanich, and S.A. Solin, Solid St. Commun. **23**, 417 (1977).
73. J. Robertson, Mat. Science and Engineering. R **37**, 129 (2002).
74. D. Guérard, G.M.T. Foley, M. Zanini and J.E. Fischer, Nuovo Cim. B, **38**, 410 (1977).
75. G.R. Hennig, J. Chem. Phys., **43**, 1201 (1965).
76. P. Pfluger, P. Oelhafen, H.U. Künzi, R. Jeker, E. Hauser, K.P. Ackermann, M. Müller and H.-J. Güntherodt, Physica B, **99** (1-4), 395 (1980).
77. S. Basu, C. Zeller, P. Flanders, C. D. Fuerst, W. D. Johnson and J. E. Fischer, Mater. Sci. Engng, **38**, 275 (1979).
78. J.E. Fischer, Mater. Sci. Engng, **31**, 211 (1977); Physics and Chemistry of Materials with Layered Structures, edited by F. Lévy (Dordrecht: Reidel, 1979), vol. 6, p. 481.
79. J. Blinowski, H.H. Nguyen, C. Rigaux, J.P. Vieren, R. Le Toullec, G. Furdin, A. Hérold and, J. Melin, J. Phys. France. **41** (1), 47 (1980).
80. T.E. Thompson, E.R. Falardeau and L.R. Hanlon, Carbon. **15**, 39 (1977).
81. P.C. Eklund, D.S. Smith and V.R.K. Murthy, Synth. Metals. **3**, 111 (1981).
82. J.E. Fischer, T.E. Thompson, G.M.T. Foley, D. Guérard, M. Hoke and F.L. Lederman, Phys. Rev. Lett. **37**, 769 (1976).
83. J. Perrachon, Ph.D. Thesis, University of Pennsylvania, 1978.
84. R.M. Fischer, D.J. Smith, L. A. Freeman, S. J. Pennycook and A. Howie, in: *Extended Abstracts of the 14th Biennial Conference on Carbon* (Pennsylvania State University, 1979,), p. 318.
85. C.C. Shieh, R.L. Schmidt, and J.E. Fischer, Phys. Rev. B. **20**, 3351 (1979).
86. K. Nakao, J. Phys. Soc. Japan. **40**, 761 (1976).
87. A. Avogadro and M. Villa, J. Chem. Phys., **66**, 2359 (1977).
88. D.M. Hwang, M. Utlaut, M.S. Isaacson and S.A. Solin, Physica B. **99**, 435 (1980).
89. G. Ruprecht, D.M. Ginsberg and J.D. Leslie, J. Opt. Soc. Am. **52**, 665 (1962).
90. J.J. Song, D.D.L. Chung, P.C. Eklund and M.S. Dresselhaus, Solid St. Commun. **20**, 1111 (1976).

91. R.J. Nemanich, S.A. Solin and D. Guérard, Phys. Rev. B. **16**, 2965 (1977).
92. S.A. Solin, Mater. Sci. Engng. **31**, 153 (1977).
93. C. Underhill, S.Y. Leung, G. Dresselhaus and M. S. Dresselhaus, Solid St. Commun. **29**, 769 (1979).
94. G.M. Gualberto, C. Underhill, S.Y. Leung and G. Dresselhaus, Phys. Rev. B, **21**, 862 (1980).
95. P.C. Eklund, D.S. Smith, V.R.K. Murthy, and S.Y. Leung, Synth. Metals. **2**, 99 (1980).
96. P.C. Eklund, G. Dresselhaus, M.S. Dresselhaus and J.E. Fischer, Phys. Rev. B. **16**, 3330 (1977).
97. S.A. Solin, Physica B. **99**, 443 (1980).
98. L.Pietronero, S. Strässler, H.R. Zeller and M.J. Rice, Phys. Rev. Lett. **41**, 763 (1978).
99. C.P Eklund, G. Dresselhaus, M.S. Dresselhaus and J.E. Fischer, Phys. Rev. B. **21**, 4705 (1980).
100. D.E. Nixon and G.S. Parry, J. Phys. D. **1**, 291 (1968); J. Phys. C. **2**, 1732 (1969).
101. P. C. Eklund, R. Falardeau and J.E. Fischer, Solid St. Commun. **32**, 631 (1979).
102. M.S. Dresselhaus and G. Dresselhaus, in: *Physics and Chemistry of Materials with Layered Structures,* edited by F. Lévy (Dordrecht: Reidel, 1979), Vol. 6, p. 497.
103. P.C. Eklund, N. Kambe, G. Dresselhaus and M.S. Dresselhaus, Phys. Rev. B. **18**, 7069 (1978).
104. N. Caswell and S.A. Solin, Solid St. Commun. **27**, 961 (1978).
105. B.L. Heflinger, Ph.D. Thesis, MIT, Cambridge, Massachusetts, 1979.
106. L. Pietronero, S. Strässler and H. R. Zeller, Solid St. Commun. **30**, 399 (1979).
107. S.Y. Leung, C. Underhil, G. Dresselhaus and M. S. Dresselhaus, Solid St. Commun. **33**, 285 (1980).
108. E. Mendez, T.C. Chieu, N. Kambe and M.S. Dresselhaus, Solid St. Commun. **33**, 837 (1980).
109. G. Dresselhaus and S.Y. Leung, Solid St. Commun. **35**, 819 (1980).
110. C. Jager, H. Mutschke and T. Henning, Astron Astrophys. **332** (1), 291 (1998).
111. E.T. Arakawa, M.W. Williams and T. Inagaki, J. Appl Phys. **48**(7), 3176 (1977).
112. B.J. Stagg, T.T. Charalampopoulos, Combust. Flame. **94** (4), 381 (1993).
113. A. Grill. Thin Solid Films. **355**–**356**, 189 (1999).
114. N.D. Baydogan, Materials Science and Engineering B. **107,** 70 (2004).
115. R.C. Barklie, Diamond Relat. Mater. **10**, 174 (2001).
116. N. Laidani, R Bartali, G Gottardi, M Anderle and P Cheyssac, J. Phys. Condens. Matter. **20**, 015216 (2008).
117. J. Tauc, R. Grigorovici and A. Vancu, Phys. Status Solidi. **15**, 627 (1966).
118. G.E. Jellison Jr. and F.A. Modine, Appl. Phys. Lett. **69**, 371 (1996).
119. A.R. Forouhi and I. Bloomer Phys. Rev. B. **34**, 7018 (1986).
120. W.A. Mc Gahan, T. Makovicka, J. Hale and J.A. Woollam, Thin Solid Films, **253**, 57 (1994).
121. T. Yamaguchi, Y. Kaneko, A.H. Jayatissa and M. Aoyama, Thin Solid Films. **279**, 174 (1996).
122. S. Waidmann, M. Knupfer, J. Fink, B. Kleinsorge and J. Robertson, J. Appl. Phys. **89**, 3783 (2001).
123. F. Xiong, Y.Y. Chang, R.P.H. Chang, Phys. Rev. B. **48**, 8016 (1993).
124. J. Fink, T. Muller-Heinzerling, J. Pfluger, B. Scheere, B. Dischler, P. Koidl, A. Bubenzer and R.E. Sah, Phys. Rev. B. **30**, 4713 (1984).
125. M.L. Theye, V. Paret and A. Sadki, Diamond Rel. Mater. **10**, 182 (2001).
126. J. Robertson and E.P. O'Reilly, Phys.Rev. B. **35**, 2946 (1987).

127. D.G. McCullosh, D.R. McKenzie and C.M. Goringe, Phys. Rev. B. **61**, 2349 (2000).
128. C.W. Chen and J. Robertson, J. Non Cryst. Solids. **227/228**, 602 (1998).
129. N.M.J. Conway, A.C. Ferrari, A.J. Flewitt, J. Robertson, W.I. Milne, A. Tagliaferro and W. Beyer, Diamond Rel. Mater. **9**, 765 (2000).
130. R.H. Jarman, G.J. Ray and R.W. Stadley, Appl. Phys. Lett. **58**, 1065 (1986).
131. M.A. Tamor, W.C. Vassel and K.R. Carduner, Appl. Phys. Lett. **58**, 592 (1991).
132. M.A. Tamor and W.C. Vassel, J. Appl. Phys. **76**, 3823 (1994).
133. M. Weiler, S. Sattel, T. Giessen, K. Jung, H. Ehrhardt, V.S. Veerasamy and J. Robertson, Phys. Rev. B. **53**, 1594 (1996).
134. M. Chhowalla, J. Robertson, C.W. Chen, S.R.P. Silva, Y. Lifshitz and W.I. Milne, Philos. Mag. B. **76**, 351 (1997).
135. C. Oppedisano and A. Tagliaferro, Appl. Phys.Lett. **75**, 3650 (1999).
136. D. Dasgupta, F. Demichelis, C.F. Pirri and A. Tagliaferro, Phys. Rev. B. **43**, 2131 (1991).
137. G. Fanchini, A. Tagliaferro, D.P. Dowling, K. Donnelly, M.L. McConnell, R. Flood, and G. Lang, Phys. Rev. B. **61**, 5002 (2000).
138. R. Bouzerer, C. Amory, B. Racine and A. Zeinery, J. Non Cryst. Solids. **281**, 171 (2001).
139. V. Paret, A. Sadki, Y. Bounouh, R. Alameh, C. Naud, M. Zarrabian, A. Seignac, G. Turban and M.L. Theye, J. Non Cryst. Solids. **227**, 583 (1998).
140. S.L. Maeng, S. Uchikoga, F.J. Clough, A. Tagliaferro, A.J. Flewitt, J. Robertson and W.I. Milne. Diamond Rel. Mater. **9**, 805 (2000).
141. S. Arena, B. Kleinsorge, J. Robertson, W.I. Milne and M.E. Welland. J. Appl. Phys. **85**, 1609 (1999).
142. J. Robertson, Phys. State Solid B. **186**, 177 (2001).
143. J.S. Lannin. J. Non Cryst. Solids. 97, 39 (1987).
144. A.C. Ferrari and J. Robertson, Phys. Rev. B. **61**, 14095 (2000).
145. A.C. Ferrari, Solid State Commun. **143**(1-2), 47 (2007).
146. A.C. Ferrari and J. Robertson, Phys Rev B. **64**(7), 075414 (2001).
147. P.Y. Yu and M. Cardona, *Fundamentals of Semiconductors. Physics and Materials Properties,* 3rd ed. (Springer, Berlin, 1996).
148. R. Alben, D. Weaire, J.E. Smith and M.H. Brodsky, Phys. Rev. B. **11**, 2271 (1975).
149. N. Wada, P.J. Gaczi and A. Solin. J. Non Cryst. Solids. **35/36**, 543 (1980).
150. R.E. Scroder, R.J. Nemanich and J.T. Glass. Phys. Rev. B. **41**, 3738 (1990).
151. S.R. Salis, D.J. Gardiner, M. Bowden, J. Savage and D. Rodway. Diamond Rel. Mater. **5**, 589 (1996).
152. J. Rao J., K.J. Lawson and J.R. Nicholls, Surface and Coatings Technology. **197** (2—3), 154 (2004).
153. A. Cuesta, P. Dhamelincourt, J. Laureyns, A. Martinezalonso and J.M.D. Tascon, Carbon. **32**(8), 1523 (1994).
154. M. Chhowalla, A.C. Ferrari, J. Robertson and G.A.J Amaratunga. Appl. Phys. Lett. **76**, 1419 (2000).
155. A.C. Ferrari, A. Li Bassi, B.K. Tanner, V. Stolojan, J. Yuan, L.M. Brown, S.E. Rodil, B. Kleinsorge and J. Robertson. Phys. Rev. B. **62**, 11089 (2000).
156. R. Al-Jishi and C. Dresselhaus. Phys. Rev. B. **26**, 4514 (1982).
157. G. Kresse, J. Furthmuller and J. Hafner, Europhys. Lett. **32**, 729 (1995).
158. T. Kohler, T. Frauenheim and G. Jungnickel. Phys. Rev. B. **52**, 11837 (1995).
159. F. Li and J.S. Lanmin. Appl. Phys. Lett. **69**, 3348 (1996).

160. S. Prawer, K.W. Nugent. Y. Lifshitz, G.D. Lempert, E. Grossman, J. Kulik, I. Avigal and R. Kalish. Diamond Rev. Mater. **5**, 433 (1996).
161. K.W.R. Gilkes, H.S. Sands, D.N. Bachelder, J. Robertson and W.I. Milne, Appl. Phys. Lett. **70**, 1980 (1997).
162. V.I. Merkulov, J.S. Lannin, C.H. Munro, S.A. Asher, V.S. Veerasamy and W.I. Milne. Phys. Rev. Lett. **78**, 4869 (1997).
163. K.W.R. Gilkes, S. Prawer, K.W. Nugent, I. Robertson, H.S. Sands, Y. Lifshitz and Z. Shi. J. Appl. Phys. **87**, 7283 (2000).
164. G. Adamopoulos, K.W.R. Gilkes, J. Robertson, N.M.J. Conway, B.Y. Kleinsorge, A. Buckley and D.N. Batchelder, Diamond Rel. Mater. **8**, 541 (1999).
165. J.R. Shi, X. Shi, Z. Sun, S.P. Lau, B.K. Tay and H.S. Tan, Diamond Rel. Mater. **10**, 76 (2001).
166. M. Profeta and F. Mauri, Phys. Rev. B. **63**, 424515 (2001).
167. A.V. Baranov, A.N. Bekhterev, Y.S. Bobocvich and V. I. Petrov. Optical Spectrosc. **62**, 612 (1988).
168. Pocsik, M. Hundhausen, M. Koos, L. Ley. J. Non Cryst. Solids. **227-230**, 1083 (1998).
169. M.J. Matthews, M.A. Pimenta, G. Dresselhaus, M.S. Dresselhaus and M. Endo. Phys. Rev. B. **59**, 6585 (1999).
170. C. Thomsen and S. Reich. Phys. Rev. Lett. **85**, 5214 (2000).
171. M. Ramsteiner and J. Wagner. Appl. Phys. Lett. **51**, 1355 (1987).
172. J. Wagner, M. Ramsteiner, C. Wild and P. Koild. Phys. Rev. B. **40**, 1817 (1989).
173. M. Yoshikawa, C. Katagiri, H. Ishida, A. Ishitani and T. Akamatsu. Solid State Commun. **66**, 1177 (1988).
174. S.V. Chernychov, E.I. Terukov, V.A. Vassilyev and A.S. Volkov. J. Non Cryst. Solids. **134**, 218 (1991).
175. S. Schutte, S. Will, H. Mell and W. Fuhs. Diamond Rel. Mater. **2**, 1360 (1993).
176. Rusli, J. Robertson and G.A.J. Amaratunga. J. Appl. Phys. **80**, 2998 (1996).
177. M. Yoshimi, M. Shimizu, K. Hattori, H. Okamoto and Y. Hamakawa. Optoelectronics. **7**, 69 (1992).
178. J. Wagner and P. Lautenschlager, J. Appl. Phys. **59**, 2044 (1986).
179. M. Koós, I. Póscik and L. Tóth, J. Non Cryst. Solids. **164**, 1151 (1993).
180. Rusli, G.A.J. Amaratunga and J. Robertson. Phys. Rev. B. **53**, 16306 (1996).
181. W. Lomes, M. Hundhausen and L. Ley. J. Non Cryst. Solids. **227**, 570 (1998).
182. M.N. Berberan-Santos, A. Fedorov, J.P. Conde, C. Godet, T. Heitz and J.E. Bouree, Chem. Phys. Lett. **319**, 113 (2000).
183. J. Robertson. Phys. Rev. B. **53**, 16302 (1996).
184. C. Godet and M.N. Berberan-Santos. Diamond Rel. Mater. **10**, 168 (2001).
185. T. Heitz, C. Godet, J.E. Bouree, B. Drevillon and J.P. Conde. Phys. Rev. B. **60**, 6045 (1999).
186. R.A. Street, *Hydrogenated Amorphous Silicon* (Cambridge University Press, Cambridge, 1991).
187. R.A. Street, Adv. Phys. **30**, 593 (1990).
188. B.I. Shklovskii, H. Fritzsche and S.D. Baranovski. Phys. Rev. Lett. **62**, 2989 (1989).
189. B.I. Shklovskii, H. Fritzsche and S.D. Baranovski. J. Non Cryst. Solids. **114**, 325 (1989).
190. W. Siebert, R. Carius, W. Fuhs and K. Jahn, Phys. Stat Solidi B. **140**, 311 (1987).

191. S. Liedtke, K. Jahn, F. Finger and W. Fuhs. J. Non Cryst. Solids. **97**, 1083 (1987).
192. S. Liedtke, K. Lips, K. Jahn and W. Fuhs. J. Non Cryst. Solids. **114**, 522 (1989).
193. R.S. Sussman and R. Ogden, Philos. Mag. B. **44**, 137 (1981).
194. S.R.P. Silva, Rusli, G. Amaratunga, J. Robertson and J. Schwan, Philos. Mag. B. **74**, 369 (1996).
195. S. Xu, M. Hundhausen, J. Ristein, B. Yan and L. Ley, J. Non Cryst. Solids. **164**, 1127 (1993).
196. Ilie, M.N.J. Conway, J. Robertson and W.I. Milne, J. Appl. Phys. **84**, 5575 (1998).
197. Ilie, O. Harel, M.N.J. Conway, T. Yagi, J. Robertson and W.I. Milne, J. Appl. Phys. **87**, 789 (2000).
198. F. Giorgis, F. Giuliani, C.F. Pirri, A. Tagliaferro and E. Tresso, Appl. Phys. Lett. **72**, 2520 (1998).
199. M. Koós, I. Pócsik, J, New York, 1968), vol. 3, p. 45.
200. M. Koós, I. Pócsik, J. Erostyák and A. Buzádi, J. Non Cryst. Solids. **230**, 579 (1998).
201. N.F. Mott and E.A. Davis, *Electronic Processes in Non-Crystalline Materials* (Oxford University Press, Oxford, 1979).
202. S.R. Elliott, *Physics of Amorphous Materials*, 2nd ed. (Longman, London, 1990) p. 283.
203. R.R. Nair, P. Blake, A. N. Grigorenko, K.S. Novoselov, T.J. Booth, T. Stauber, N.M.R. Peres and A.K. Geim, Science. **320** (5881), 1308 (2008).
204. C.F. Chen, C.H. Park, B.W. Boudouris, J. Horng, B.S. Geng, C. Girit, A. Zettl, M.F. Crommie, R.A. Segalman, S.G. Louie and F. Wang, Nature. **471**, 617 (2011).
205. A.C. Ferrari, J.C. Meyer, V. Scardaci, C. Casiraghi, M. Lazzeri, F. Mauri, S. Piscanec, D. Jiang, K.S. Novoselov, S. Roth and A.K. Geim, Phys. Rev. Lett. **97**, 187401 (2006).
206. M.A. Pimenta, G. Dresselhaus, M.S. Dresselhaus, L.G. Cançado, A. Jorio and R. Saito, Phys. Chem. Chem. Phys. **9**, 1276 (2007).
207. A. Das, S. Pisana, B. Chakraborty, S. Piscanec, S.K. Saha, U.V. Waghmare, K.S. Novoselov, H.R. Krishnamurthy, A.K. Geim, A.C. Ferrari and A.K. Sood, Nature Nanotechnol. **3**, 210 (2008).
208. M.S. Dresselhaus, A. Jorio, M. Hofmann, G. Dresselhaus and R. Saito, Nano Lett. **10**, 751 (2010).
209. S. Pisana, M. Lazzeri, C. Casiraghi, K.S. Novoselov, A.K. Geim, A.C. Ferrari and F. Mauri, Nature Mater. **6**, 198 (2007).
210. J. Yan, Y.B. Zhang, P. Kim and A. Pinczuk, Phys. Rev. Lett. **98**, 166802 (2007).
211. K.F. Mak, L. Ju, F.Wang and T.F. Heinz, Sol. St. Commun. **152**, 1341 (2012).
212. L.M. Malard, M.A. Pimenta, G. Dresselhaus and M.S. Dresselhaus, Phys. Rep. Rev. Sect. Phys. Lett. **473**, 51 (2009).
213. W.T. Liu, S.W. Wu, P.J. Schuck, M. Salmeron, Y.R. Shen and F. Wang, Phys. Rev. B. **82**, 081408 (2010).
214. M. Xie, Y. Su, X. Lu, Y. Zhang, Z. Yang and Y. Zhang, Materials Letters. **93**, 161 (2013).
215. S.J. Zhuo, M.W. Shao and S.T. Lee, ACS Nano. **6**, 1059 (2012).
216. S.T. Yang, L. Cao, P.G. Luo, F.S. Lu, X. Wang, H.F. Wang, M.J. Meziani, Y.F. Liu, G. Qi and Y.-P. Sun, J. Am. Chem. Soc. **131**, 11308 (2009).
217. S.N. Baker and G.A. Baker. Angew Chem Int Ed Engl. **49**, 6726 (2010).
218. Z. Yang, R.G. Gao, N.T. Hu, J. Chai, Y.W. Cheng, L.Y. Zhang, H. Wei, E.S.-W. Kong and Y. Zhang, Nano-Micro Lett. **4**, 1 (2012).

219. G. Eda, Y.-Y. Lin, C. Mattevi, H. Yamaguchi, H.-A. Chen, I.-S. Chen, C.-W. Chen and M. Chhowalla, Adv. Mater., **22**, 505 (2010).
220. X. Yan, X. Cui and L.S. Li, J. Am. Chem. Soc. **132**, 5944 (2010).
221. L.Y. Jiao, X.R. Wang, G. Diankov, H.L. Wang and H.J. Dai, Nat Nanotechnol. **5**, 321 (2010).
222. L.Y. Jiao, L. Zhang, X.R. Wang, G. Diankov and H.J. Dai, Nature. **458**, 877 (2009).
223. J. Peng, W. Gao, B.K. Gupta, Z. Liu, R. Romero-Aburto, L. Ge, L. Song, L. B. Alemany, X. Zhan, G. Gao, S.A. Vithayathil, B.A. Kaipparettu, A.A. Marti, T. Hayashi, J.-J. Zhu and P.M. Ajayan, Nano Lett. **12** (2), 844 (2012).
224. L. Bokobza, J.-L. Bruneel and M. Couzi. C — Journal of Carbon Research. **1**, 77 (2015), doi:10.3390/c1010077.
225. C. H. Lui, K.F. Mak, J. Shan and T.F. Heinz. Phys. Rev. Lett. **105**, 127404 (2010).
226. S. Berciaud, M.Y. Han, K.F. Mak, L.E. Brus, P. Kim and T.F. Heinz, Phys. Rev. Lett. **104**, 227401 (2010).
227. M. Freitag, H.-Y. Chiu, M. Steiner, V. Perebeinos and P. Avouris, Nat. Nano. **5**, 497 (2010).
228. T. Gokus, R.R. Nair, A. Bonetti, M. Bohmler, A. Lombardo, K.S. Novoselov, A.K. Geim, A.C. Ferrari and A. Hartschuh, ACS Nano. **3**, 3963 (2009).
229. X.M. Sun, Z. Liu, K. Welsher, J.T. Robinson, A. Goodwin, S. Zaric and H.J. Dai, Nano Res. **1**, 203 (2008).
230. Z.T. Luo, P.M. Vora, E.J. Mele, A.T.C. Johnson and J.M. Kikkawa, Appl. Phys. Lett. **94**, 111909 (2009).
231. T.V. Cuong, V.H. Pham, Q.T. Tran, J.S. Chung, E.W. Shin, J.S. Kim and E.J. Kim, Mat. Lett. **64**, 399 (2010).
232. C. Casiraghi, A. Hartschuh, E. Lidorikis, H. Qian, H. Harutyunyan, T. Gokus, K.S. Novoselov and A. C. Ferrari, Nano Lett. **7** (9), 2711 (2007).
233. Bayer, C. Wiemann, O. Gaier, M. Bauer, and M. Aeschlimann, J. Nanomater., 249514 (2008).
234. F. Rana, Phys. Rev. B. **76**, 155431 (2007).
235. W.-K. Tse, E.H. Hwang, and S. Das Sarma, Appl. Phys. Lett. **93**, 023128 (2008).
236. H. Miyazaki, S. Odaka, T. Sato, S. Tanaka, H. Goto, A. Kanda, K. Tsukagoshi, Y. Ootuka and Y. Aoyagi, Appl. Phys. Express. **1**, 034007 (2008).
237. O. Kashuba and V.I. Fal'ko, Phys. Rev. B. **80**, 241404(R) (2009).
238. S. Park and R.S. Ruoff, Nat. Nanotechnol. **4**, 217 (2009).
239. K. Krishnamoorthy, M. Veerapandian, R. Mohan and S.J. Kim, Appl. Phys. A: Mater. Sci.Process. **106**, 501 (2012).
240. L. Cao, M.J. Meziani, S. Sahu and Y.P. Sun, Accounts of Chemical Research. **46** (1), 171 (2013).
241. K. P. Loh, Q. Bao, G. Eda and M. Chhowalla, Nat. Chem. **2**, 1015 (2010).
242. Q. Mei, K. Zhang, G. Guan, B. Liu, S. Wang and Z. Zhang, Chem. Commun. **46**, 7319 (2010).
243. A. Nourbakhsh, M. Cantoro, T. Vosch, G. Pourtois, F. Clemente, M.H. van der Veen, J. Hofkens, M.M. Heyns, S. De Gendt and B.F. Sels, Nanotechnology. **21**, 435203 (2010).
244. D. Pan, L. Guo, J. Zhang, C. Xi, Q. Xue, H. Huang, J. Li, Z. Zhang, W. Yu, Z. Chen, Z. Li and M. Wu, J. Mater. Chem. **22**, 3314 (2012).
245. J.-L. Chen, X.-P. Yan, K. Meng and S.-F. Wang, Anal. Chem. **83**, 8787 (2011).
246. Y.-P. Sun, B. Zhou, Y. Lin, W. Wang, K.A.S. Fernando, P. Pathak, B.A. Harruff, X. Wang, H. Wang, P. G. Luo, H. Yang, B. Chen, L.M. Veca and S.-Y. Xie, J. Am. Chem. Soc. **128**, 7756 (2006).

247. C. Galande, A.D. Mohite, A.V. Naumov, W. Gao, L. Ci, A. Ajayan, H. Gao, A. Srivastava, R.B. Weisman and P.M. Ajayan, Sci. Rep. **1**, 85 (2011).
248. V. Gupta, N. Chaudhary, R. Srivastava, G.D. Sharma, R. Bhardwaj and S. Chand, J. Am. Chem. Soc. **133**, 9960 (2011).
249. J.-L. Li, H.-C. Bao, X.-L. Hou, L. Sun, X.-G. Wang and M. Gu, Angew Chem Int. Ed Engl. **51**, 1830 (2012).
250. M.L. Mueller, X. Yan, J.A. McGuire and L.S. Li, Nano Lett. **10**, 2679 (2010).
251. S. Zhu, J. Zhang, X. Liu, B. Li, X. Wang, S. Tang, Q. Meng, Y. F. Li, C. Shi, R. Hu and B. Yang, RSC Adv. **2**, 2717 (2012).
252. Y. Liu, C.-Y. Liu and Z.-Y. Zhang, J. Colloid Interface Sci. **356**, 416 (2011).
253. J. Shen, Y. Zhu, C. Chen., X. Yang and C. Li, Chem. Commun. **47**, 2580 (2011).
254. J. Shen, Y. Zhu, X. Yang, J. Zong, J. Zhang and C. Li, New J. Chem. **36**, 97 (2012).
255. L.M. Veca, F. Lu, M.J. Meziani, L. Cao, P. Zhang, G. Qi, L. Qu, M. Shrestha and Y.-P. Sun, Chem. Commun. (18), 2565 (2009).
256. Y. Lin, B. Zhou, K.A.S. Fernando, P. Liu, L.F. Allard and Y.-P. Sun, Macromolecules. **36**, 7199 (2003).
257. Y. Li, Y. Hu, Y. Zhao, G. Shi, L. Deng, Y. Hou and L. Qu, Adv. Mater. **23**, 776 (2011).
258. J.E. Riggs, Z. Guo, D.L. Carroll and Y.-P. Sun, J. Am. Chem. Soc. **122**, 5879 (2000).
259. L. Cao, X. Wang, M.J. Meziani, F. Lu, H. Wang, P.G. Luo, Y. Lin, B. A. Harruff, L.M. Veca, D. Murray, S.-Y. Xie and Y.-P. Sun, J. Am. Chem. Soc. **129**, 11318 (2007).
260. X. Wang, L. Cao, S.T. Yang, F.S. Lu, M.J. Meziani, L.L. Tian, K.W. Sun, M.A. Bloodgood and Y.-P. Sun, Angew Chem Int. Ed Engl. **49**, 5310 (2010).
261. P. Anilkumar, X. Wang, L. Cao, S. Sahu, J.H. Liu, P. Wang, K. Korch, K.N. Tackett II, A. Parenzan and Y.-P. Sun, Nanoscale. **3**, 2023 (2011).
262. X. Wang, L. Cao, C.E. Bunker, M.J. Meziani, F.S. Lu, E.A. Guliants and Y.-P. Sun, J. Phys. Chem. C. **114**, 20941 (2010).
263. D.Y. Pan, J.C. Zhang, Z. Li and M.H. Wu, Adv. Mater. **22**, 734 (2010).
264. J. Lu, P.S.E. Yeo, C.K. Gan, P. Wu and K.P. Loh, Nat. Nanotechnol. **6**, 247 (2011).
265. H. Liu, T.Ye and C. Mao, Angew Chem Int. Ed Engl. **46**, 6473 (2007).
266. Y. Dong, N. Zhou, X. Lin, J. Lin, Y. Chi and G. Chen, Chem. Mater. **22**, 5895 (2010).
267. K.S. Novoselov, A.K. Geim, S.V. Morozov, D. Jiang, Y. Zhang, S.V Dubonos, I.V. Grigorieva, A. A. Firsov, Science. **306**, 666 (2004).
268. V.M. Pereira, J.M.B.L. dos Santos and A.H.C. Neto, Phys. Rev. B. **77**, 115109 (2008).
269. B. O. Dabbousi, J. Rodriguez-Viejo, F.V. Mikulec, J. R. Heine, H. Mattoussi, R. Ober, K.F. Jensen and M. G. Bawendi, J. Phys. Chem. B. **101**, 9463 (1997).
270. Y. Lin, B. Zhou, R.B. Martin, K.B. Henbest, B.A. Harruff, J.E. Riggs, Z. X. Guo, L.F. Allard and Y.-P. Sun, J. Phys. Chem. B. **109**, 14779 (2005).
271. A. B. Bourlinos, A. Stassinopoulos, D. Anglos, R. Zboril, M. Karakassides and E.P. Giannelis, Small. **4**, 455 (2008).
272. H. Peng and J. Travas-Sejdic, Chem. Mater. **21**, 5563 (2009).
273. J. Xu, S. Sahu, L. Cao, P. Anilkumar, K. N. Tackett II, H. J. Qian, C. E. Bunker, E.A. Guliants, A. Parenzan and Y.-P. Sun, Chem Phys Chem. **12**, 3604 (2011).
274. X. Y. Li, H. Q. Wang, Y. Shimizu, A. Pyatenko, K. Kawaguchi and N. Koshizaki, Chem. Commun. **47**, 932 (2011).
275. L. Cao, P. Anilkumar, X. Wang, J.H. Liu, S. Sahu, M.J. Meziani, E. Myers and Y.-P. Sun, Can. J. Chem. **89**, 104 (2011).

276. X. Wang, L. Cao, F.S. Lu, M.J. Meziani, H. Li, G. Qi, B. Zhou, B.A. Harruff, F. Kermarrec and Y.-P. Sun, Chem. Commun. **25**, 3774 (2009).
277. L. Cao, S. Sahu, P. Anilkumar, C.E. Bunker, J. A. Xu, K.A.S. Fernando, P. Wang, E.A. Guliants, K. N. Tackett II, and Y.-P. Sun, J. Am. Chem. Soc. **133**, 4754 (2011).
278. L. Lacerda, G. Pastorin, W. Wu, M. Prato, A. Bianco and K. Kostarelos, Adv. Funct. Mater. **16**, 1839 (2006).
279. B. Zhou, Y. Lin, D.E. Hill, W. Wang, L.M. Veca, L. Qu, P. Pathak, M.J. Meziani, J. Diaz, J.W. Connell, K.A. Watson, L.F. Allard and Y.-P. Sun, Polymer. **47**, 5323 (2006).
280. S.G. Nedilko, S. Revo, V. Chornii, V. Scherbatskyi, K. Ivanenko, M. Nedielko, Y. Sementsov, M. Skoryk, A. Nikolenko and V. Strelchuk, Nanoscale Res Lett. **12**, 28 (2017). doi: 10.1186/s11671-016–1770-5.
281. M. Kartel, Y. Sementsov, S. Makhno, Z. Weijun, Z. Xiaochen, V.G. Li and B. Wang, International Journal of Science, Engineering & Technology. **4** (7), 203 (2017).
282. G.I. Dovbeshko, O.P. Repnystka and Y.V. Shtogun, Chem. Phys. Lett. **372**, 432 (2003).
283. S.Ya. Brichka, H.P. Pryhodko, A.V. Brichka, M.I. Terets, V.A. Pokrovski, G.I. Dovbeshenko and E.P. Repnitskaya, Russian Journal of Physical Chemistry. **78** (1), 121 (2004).
284. Yu.I. Sementsov, G.I. Dovbeshko, S.Ya. Brychka, A.V. Brychka, G.P. Prikhod'ko, in: *Surface Enhanced Infrared Absorption of Graphite-Like Materials: Proc. 12th Intern. Symp. on Intercalation Compounds* (Poznan, Poland, 2003), p. 107.
285. T. Chen, B. Zeng, J.L. Liu, J.H. Dong, X.Q. Liu, Z. Wu, X.Z. Yang and Z.M. Li, J. Phys.: Conf. Ser. **188**, 012051 (2009).
286. I.M. Afanasov, I.V. Makarenko, I.I. Vlasov and G. van Tendeloo, in: *Annual World Conference Proceedings* (American Carbon Society, Clemson, SC, 2010). H.O. Pierson, editor, *Handbook of carbon, graphite, diamond and fullerenes. Properties, Processing and Applications* (Materials Science and Process Technology), 1st Edition, (Noyes Publications, Park Ridge, 1993).
287. R.W. Newson, J. Dean, B. Schmidt and H.M. van Driel, Optics Express. **17** (4), 2326 (2009).
288. A.J. Sabbah and D.M. Riffe, Phys. Rev. B. **66**, 165217 (2002).
289. J.M. Dawlaty, S. Shivaraman, M. Chandrasekhar, F. Rana and M.G. Spencer, Appl. Phys. Lett. **92**, 042116 (2008).
290. F. Rana, IEEE Trans. Nanotechnol. **7**, 91 (2008).
291. K. Seibert, G.C. Cho, W. Kütt, H. Kurz, D.H. Reitze, J.I. Dadap, H. Ahn and M.C. Downer, Phys. Rev. B. **42**, 2842 (1990).
292. Y. Xu, H. Bai, G. Lu, C. Li and G. Shi, J. Am. Chem. Soc. **130**, 5856 (2008).
293. S. Stankovich, D.A. Dikin, R.D. Piner, K.A. Kohlhaas, A. Kleinhammes A, Y.Y. Jia, Y. Wu, S.T. Nguyen and R.S. Ruoff, Carbon, **45**, 1558 (2007).
294. M. Zhou, Tian Tian, X. Li, X. Sun, J. Zhang, P. Cui, J. Tang and L.-C. Qin. Int. J. Electrochem. Sci. **9**, 810 (2014).
295. W. Qian, R. Hao, Y.L. Hou, Y. Tian, C.M. Shen, H.J. Gao and X.L. Liang, Nano Res. **2**, 706 (2009).
296. J.H. Lee, D.W. Shin, V.G. Makotchenko, A.S. Nazarov, V.E. Fedorov, Y.H. Kim, J.Y. Choi, J.M. Kim and J.B. Yoo, Adv. Chem. **21**, 4383 (2009).
297. Z. Liu, Z.M. Wang, X. Yang and K. Ooi, Langmuir. **18**, 4926 (2002).
298. P.K. Ang, S. Wang, Q.L. Bao, J.T. L. Thong and K.P. Loh, ACS Nano. **3**, 3587 (2009).
299. C.Chen, W.T. Zhai, D.D. Lu, H.B. Zhang and W.G. Zheng, Mater. Res. Bull. **46**, 583 (2011).

300. M. Kartel, Yu. Sementsov, G. Dovbeshko, L. Karachevtseva, S. Makhno, T. Aleksyeyeva, Yu. Grebel'na, V. Styopkin, Bo Wang and Yu. Stubrov. Adv. Mat. Let. **8** (3), 212 (2017). DOI: 10.5185/amlett.2017.1428.
301. Yu. Sementsov, S. Mahno, M. Kartel', Bo Wang, G. Dovbeshko, V. Styopkin and S. Nedilko, J. of Innovative Sc., Engin. & Techn. **4** (8), 71 (2017).
302. G.I. Dovbeshko, O.P. Gnatyuk, A.A. Nazarova, Yu.I. Sementsov and E.D. Obraztsova, Fullerenes, nanotubes and carbon nanostructures. **13** (1), 393 (2005).
303. A.C. Ferrari, F. Bonaccorso, V. Fal'ko, K.S. Novoselov, S. Roche, P. Bøggild, S. Borini, F.H.L. Koppens, V. Palermo, N. Pugno, J.A. Garrido, R. Sordan, A. Bianco, L. Ballerini, M. Prato, E. Lidorikis, J. Kivioja, C. Marinelli, T. Ryhänen, A. Morpurgo, J.N. Coleman, V. Nicolosi, L. Colombo, A. Fert, M. Garcia-Hernandez, A. Bachtold, G.F. Schneider, F. Guinea, C. Dekker, M. Barbone, Z. Sun, C. Galiotis, A.N. Grigorenko, G. Konstantatos, A. Kis, M. Katsnelson, L. Vandersypen, A. Loiseau, V. Morandi, D. Neumaier, E. Treossi, V. Pellegrini, M. Polini, A. Tredicucci, G.M. Williams, B.H. Hong, J.-H. Ahn, J.M. Kim, H. Zirath, B.J. van Wees, H. van der Zant, L. Occhipinti, A. Di Matteo, I.A. Kinloch, T. Seyller, E. Quesnel, X. Feng, K. Teo, N. Rupesinghe, P. Hakonen, S.R.T. Neil, Q. Tannock, T. Löfwander and J. Kinaret, Nanoscale. **7** (11), 4598 (2015). https://doi.org/10.1039/C4NR01600A.
304. W.S. Hummers and R.E. Offeman, J. Am. Chem. Soc. **80**, 1339 (1958).
305. D.M. Gattia, A.M. Vittori and R.A.C. Marazzi, Nanotechnology. **18**, 255604 (2007).
306. A.N. Obraztsov, E.A. Obraztsova, A.V. Tyurnina and A.A. Zolotukhin, Carbon. **45**, 2017 (2007).
307. A.S. Tikhomirov, N.E. Sorokina, O.N. Shornikova, V.A. Morozov, G. van Tendeloo and V.V. Avdeev, Carbon. **49**, 147 (2011).
308. A.J. Cooper, N.R. Wilson, I.A. Kinloch and R.A.W. Dryfe, Carbon. **66**, 340 (2014).
309. P. Yu, S.E. Lowe, G.P. Simon and Y.L. Zhong, Curr. Open Colloid Interface Sci. **20**, 329 (2015).
310. I. Rea, M. Casalino, M. Terracciano, L. Sansone, J. Politi, L. de Stefano. Photoluminescence enhancement of graphene oxide emission by infiltration in an aperiodic porous silicon multilayer. Optics express. **24** (21), 24413 (2016)
311. V. Štengl, S. Bakardjieva, J. Henych, K. Lang and M. Kormunda, Carbon. **63**, 537 (2013).
312. N. Fuyuno, D. Kozawa, Y. Miyauchi, S. Mouri, R. Kitaura, H. Shinohara, T. Yasuda, N. Komatsu and K. Matsuda, Adv Optical Mater. **2** (10), 983 (2014).
313. X. Li, M. Rui, J. Song, Z. Shen and H. Zeng, Adv. Funct. Mater. **25**, 4929 (2015).
314. A. Eckmann, A. Felten, A. Mishchenko, L. Britnell, R. Krupke, K.S. Novoselov and C. Casiraghi, Nano Letters. **12** (8), 3925 (2012).
315. Y.Y. Wang, Z.H. Ni, Y. Ting, Z.X. Shen, H.M. Wang, Y.H. Wu, W. Chen and A.T.S. Wee, J. Phys. Chem. C. **112**, 10637 (2008).
316. Y. Zhu, S. Murali, W. Cai, X. Li, J.W. Suk, J.R. Potts and R.S. Ruoff, Adv. Mater. **22**, 3906 (2010).
317. D. Yoon, H. Moon, H. Cheong, J.S. Choi, J.A. Choi and B.H. Park, J. Korean Phys. Soc. **55**, 1299 (2006).
318. A.A.K. King, B.R. Davies, N. Noorbehesht, P. Newman, T.L. Church, A.T. Harris, J.M. Razal and A.I. Minett, Scientific Reports. **6**, 19491 (2016). DOI: 10.1038/srep19491.
319. D. Voiry, J. Yang, J. Kupferberg, R. Fullon, C. Lee, H.Y. Jeong, H.S. Shin and M. Chhowalla, Science. **353** (6306), 1413 (2016).

320. R.J.W.E. Lahaye, H.K. Jeong, C.Y. Park and Y.H. Lee, Phys. Rev. B. **79**, 125435 (2009).
321. J.A. Yan, L. Xian and M.Y. Chou, Phys. Rev. Lett. **103**, 086802 (2009).
322. M. Lundie, Z. Sljivancanin and S. Tomic, J Phys Conf Ser. **526**, 012003 (2014).
323. C.T. Chien, S.S. Li, W.J. Lai, Y.C. Yeh, H.A. Chen, I.S. Chen, L.-C. Chen, K.-H. Chen, T. Nemoto, S. Isoda, M. Chen, T. Fujita, G. Eda, H. Yamaguchi, M. Chhowalla and C.-W. Chen, Angew Chem Int. Ed Engl. **51**, 6662 (2012).
324. S. Zhu, Q. Meng, L. Wang, J. Zhang, Y. Song, H. Jin, K. Zhang, H. Sun, H. Wang and B. Yang, Angew Chem Int. Ed Engl. **52** (14), 3953 (2013).
325. W. Zhang, D. Dai, X. Chen, X. Guo and J. Fan, Appl. Phys. Lett. **104**, 091902 (2014).
326. C.J. Reckmeier, J. Schneider, A.S. Susha and A.L. Rogach, Opt Express. **24**, A312 (2016).
327. J. Shang, L. Ma, J. Li, W. Ai, T. Yu and G.G. Gurzadyan, Sci. Rep. **2**, 792 (2012).
328. M. Tian, Z. Wei, X. Zan, L. Zhang, J. Zhang, Q. Ma, N. Ning and T. Nishi, Composites Science and Technology. **99**, 37 (2014).
329. Ş. İnce, Y. Seki, M.A. Ezan, A. Turgut and A. Erek, Renewable Energy. **75**, 243 (2015).
330. F.-A. He, H.-J. Wu, X.-L. Yang, K.-H. Lam, J.-T. Fan and L.-W. H. Chan, Polymer Testing. **42**, 45 (2015).
331. X. Sun, X. Liu, X. Shen, Y. Wu, Z. Wang and J.-K. Kim, Composites Part A: Applied Science and Manufacturing. **85**, 199 (2016).
332. L. Sisti, J. Belcari, L. Mazzocchetti, G. Totaro, M. Vannini, L. Giorgini, A. Zucchelli and A. Celli, Polymer Testing. **50**, 283 (2016).
333. X. Ji, Y. Xu, W. Zhang, L. Cui and J. Liu, Composites Part A: Applied Science and Manufacturing. **87**, 29 (2016).
334. G.C.-L. Chiang and S.-W. Hsu, Polymer International. **59**(1), 119 (2010).
335. A. Cireli, N. Onar, M.F. Ebeoqluqil, I. Kavatekin, B. Kutlu, O. Culha and E. Celik, J. Appl. Polym. Sci. **105**, 3748 (2007).
336. S. Karatas, Z. Hosqor, Y. Menceloglu, N. Kayaman-Apohan and A. Gungor, J. Appl. Polym. Sci. **102**, 1906 (2006).
337. D.K. Chattopadhyay and K.V.S.N. Raju, Prog. Polym. Sci. **32**, 352 (2007).
338. M. Nedielko, S. Hamamda, O. Alekseev, V. Chornii, M. Dashevskii, M. Lazarenko, K. Kovalov, S.G. Nedilko, S. Tkachov, S. Revo and V. Scherbatskyi, Nanoscale Res Lett. **12**(1), 98 (2017). doi: 10.1186/s11671-017–1862-x.
339. S.G. Nedilko, In: *Nanochemistry, Biotechnology, Nanomaterials, and Their Applications*, edited by O. Fesenko and L. Yatsenko, Springer Proceedings in Physics, (Springer, Cham. 2018), vol. 214., pp. 247—275.
340. V. Chornii, S.G. Nedilko, M. Miroshnichenko, K. Terebilenko, M. Slobodyanik, Materials Research Bulletin. **90**, 237 (2017).
341. A. Orlova, V.V. Sokolov, J.A. Kukushkina, O.V. Almjasheva, Nanosystems: physics, chemistry, mathematics. **3** (5), 138 (2012).
342. R. Marin, G. Sponchia, E. Zucchetta, P. Riello, F. Enrichi, G. De Portu and A. Benedetti, J. Am. Ceram. Soc. **96**, 2628 (2013).
343. I. Prochazka, J. Cizek, O. Melikhova, T.E. Konstantinova and I.A. Danilenko, Acta Polonica A. **125**, 760 (2014).
344. Yu.S. Kuz'minov, E.E. Lomonova and V.V. Osiko, *Cubic zirconia and skull melting* (Cambridge Int. Science Publishing, Cambridge, 2008).
345. C.G. Kontoyannis and M. Orkoula, J. Mat. Sc. **29**, 5316 (1994).

AFTERWORD

Today, one of the most promising areas of nanotechnology is the synthesis and application of carbon nanomaterials. The results of studies described in the monograph allow drawing the following conclusions.

1. The composition Al_2O_3 (Me_xO_y) MoO_3 is complex oxide system of where Me is Fe or Ni. The ratio of metals in this systems is (1…3) Al : Fe (Ni) : (0.04…0.2) Mo. They obtained by co-precipitation from an aqueous solution of Al, Fe, Mo salts in the presence of carboxylic acid and it is a catalyst that provides high structural selectivity in the CNTs synthesis by catalytic precipitation from the gas phase with carbon sources ethylene, propylene, propane-butane in the temperature range of 600…700 °C. Thermal decomposition of Al, Fe, Mo salts of carboxylic acids in an electric furnace (aerosol method, temperature ~ 600 °C, propane-butane burner (T ~ 1000…1200 °C) increases the dispersion of the catalytic phase and CNTs. Synthesis of complex oxide SiO_2 (Fe_xO_y) MoO_3 in a hydrogen burner at a temperature of ~ 1400…1600 °C using chlorides of the corresponding metals as precursors reduces the average CNTs diameter from 20…40 nm to 10…15 nm, thus shifting the average diameter to smaller values.

2. The created fluidized bed of catalyst, due to the reactor rotation in an electric furnace, provides an efficient supply of gas containing sources of carbon, hydrogen, and carrier gas (argon) to the catalyst, which allows synthesizing 0.4—0.5 kg of CNTs of stable quality in the reactor with a volume of 24 dm^3 for 30—60 min. According to the results of the development of CNTs, the technical conditions TU U 24.103291669-009 have been elaborated.

3. A method of deagglomeration of CNTs with obtaining their stable dispersions in liquids and a methodological approach to the homogeneous distribution of CNTs in matrices of different nature have been developed.

4. A new class of low-filled CNTs materials based on matrices of different nature, in particular from thermoplastic and thermosetting polymers, elastomers, thermally expanded graphite, cement paste, cement-sand mixture, and oxide ceramics has been developed. The strength characteristics of such systems as cement paste, sand-cement mixture, and layered samples of fiberglass on epoxy binder filled with CNTs linearly depend on the size of CNTs agglomerates. The strength of hydroxyapatite is determined by its porosity formed by CNTs. For linear polymers filled with nanosized CNTs and pyrogenic silica, the strength characteristics linearly depend on the size of the regions of coherent X-ray scattering.

5. It is experimentally shown that the mechanism of significant change in the properties of different matrices with a low concentration of nanosized fillers is due to the structure-forming ability of CNTs. Thanks to their uniquely large shape factor (length to diameter ratio $\geq 10^3$), they form a continuous nanoscale grid at concentrations of a few tenths of a volume percent. In addition to the fact that a highly modular elastic component (CNTs) is introduced into the elastic-plastic matrix of a polymer, elastomer, or EG, the n-dimensional grid creates a layer of the matrix itself in the nanoscale state, which has significantly better properties than in a normal state. Theoretical calculations confirm the determining role of nanoscale regions of matrices, which are formed by interaction with nanoscale filler, i.e. the matrix response is proportional to the surface area of the interfacial boundary.

6. It is proved that EG is a nanoscale cluster-assembled system. It has long cylindrical, conical, and slit-like defects with average cross-sections from 0.7 nm to more than 20 nm, due to the convolution and inflection of a group or several atomic layers of graphene. Such defects are manifested in the spectra of Raman scattering, electron-positron annihilation, nitrogen adsorption, and transmission electron microscopy images. They determine the elastic-plastic characteristics of the compression deformation of dense materials with EG.

7. The mechanism of the production process of EG, under conditions of rapid heating (in the mode of thermal shock) of hydrolyzed GIC-H_2SO_4, (residual GIC), to high temperatures (1000 °C), is the structural transformation by the type of exfoliation. As a result of this process, the residual GIC-H_2SO_4 at all stages of heat treatment is a heterogeneous system that includes graphite crystals, regions of structural inhomogeneity due to the distribution of intercalant residues with different degrees of order, and phases of intercalant residues of different dispersion. The activation energy, determined from the dependence of the temperature of the structural transition on the pressure, is 70 ± 2 kJ/mol. The structure of the original GIC-H_2SO_4, conditions of hydrolysis, and processing temperature determine the qualitative composition and quantitative ratio of phase formations and determine the state of the surface of the EG. The EG surface has the full range of oxygen-containing centers, characteristic of dis-

persed carbon materials: phenolic, alcohol (C–OH); carbonyl, quinones (C=O); carboxyl, ether (C—OOH); carbonate and/or adsorbed CO, CO_2, however, in contrast to, for example, activated carbon, has a significantly lower oxygen concentration of the order of 1—2% at.

8. The formation of EG into a solid material under pressure (P) occurs in three stages: 1, a linear change in the density (ρ) and a small increase in texture to a density of 0.5 g/cm^3; 2, a nonlinear dependence ρ = f (P), practically invariant texture, up to ρ ≈ 1.3 g/cm^3; 3, plastic deformation with intensive growth of the texture coefficient and formation of a layered structure with the predominant orientation of graphene planes perpendicular to the direction of external load.

9. It is shown that the mechanical characteristics evidence that the structural state of the material is largely determined by the dispersion of the initial graphite, synthesis conditions, and structure of GICs as well as the conditions of their hydrolysis and heat treatment. The strength of extruded EG samples increases with increasing particle size, the Red/Ox potential has a maximum temperature.

10 Experimentally solved problems are as follows: filtration of formed gases, effective electrical contact of dispersed graphite particles, optimized amount of intercalant (concentrated H_2SO_4) for the process of anodic oxidation of dispersed natural graphite. The basic scheme of the process of anodic oxidation of natural graphite (dispersed system) has been developed and the reactor of electrochemical oxidation of continuous action with a production capacity of 10—50 kg/h has been created. Operating modes that provide stable quality of oxidized graphite, satisfactory for obtaining functional products from expanded graphite, have been defined.

11. The problem of compaction of thick (100 cm) and wide (~100 × 100 cm^2) layers of low bulk density (1.5…2.5 g/dm^3) EG by using vertically arranged conveyors with a given surface curvature has been solved. This allowed us: to reduce the stressing rate of rolled products with increasing density, i.e. to increase the time for diffusion yield of gases sorbed by the EG surface, thereby obtaining rolled sheets with a thickness of more than 2 mm; to increase the production capacity of the line compared to the traditional horizontal schemes of their location via reducing the dimensions and metal content of the structure; to design a horizontal type of a gas furnace for the production of EG, which provides separation (stratification) of volatiles (decomposition products of residual GIC) and EG in the initial phase of their formation, which reduces their sorption and thus gives higher purity to the rolled EG materials.

12. It is shown that chemical modification of the EG particle surface, in particular, by thermosetting organic compounds, allows one to strengthen the interparticle interaction. The creation of a continuous distributed carbon structure in the graphite matrix qualitatively changes the physical and mechanical characteristics of CM. A significant increase in the strength characteristics of CM is achi-

eved by introducing a high-modular component — carbon fiber into the system EG-carbon or EG-polymer and creating a system of EG-CNTs without binders.

13. It is proved that the mechanism of the detected effect of direct thermochemical conversion of natural graphite into thermally expanded upon interaction with ferric chloride crystal hydrate ($FeCl_3 \cdot 6H_2O$) consists in successive processes of graphite intercalation with the formation of GIC-$FeCl_2$ and then thermal expansion with the production of GIC-Fe.

14. A process of obtaining graphene nanoparticles with adjustable particle sizes by anodic oxidation of dense EG material in an alkaline electrolyte, which are self-organized in 3D structures on conductive substrates and are an effective filler of polymeric materials, has been elaborated.

The practical significance of the obtained results is as follows.

1. For the first time in Ukraine, the technology for production of EG and sealing materials and products from it was created and realized at the enterprise "TMSpetsmash" Ltd., Kyiv, Ukraine. Such products as gaskets, rings, flat and spirally wound flange gaskets, etc. have been introduced at enterprises of the fuel and energy complex of Ukraine and exported to Belarus, Georgia, and Lithuania. "TMSpetsmash" Ltd. is an official supplier of SE "NNEGC" Energoatom". It meets the needs of seals of nuclear and thermal power engineering, chemical and petrochemical industries, and utilities of Ukraine. Technical conditions of Ukraine (TU U) have been developed for all types of mechanical sealing. Recently, the production of flexible gaskets from CNTs-filled EG has been implemented (temporary technological regulations have been created), which provides an increase in the service life of the seals by almost twice. Analogies of this material are unknown.

2. A new class of CNTs-low-filled materials has been created including thermoplastic polymers, elastomers, expanded graphite, cement paste, oxide ceramics, etc. with significantly improved performance characteristics, which opens up prospects for their industrial application.

Thus, the writing of this monograph is an important and necessary step that can streamline the fundamental and technological aspects in the field of current knowledge about carbon nanoscale materials with a graphite-like structure.

AUTHORS

Yurii I. Sementsov — Doctor of Science (Phys. & Math.), Senior Researcher, Ningbo University of Technology, 201 Fenghua Road, Ningbo, 315211, China
Leading researcher, Chuiko Institute of Surface Chemistry of NAS of Ukraine, Kyiv, Ukraine
Ningbo Sino-Ukrainian, New Materials Industrial Technologies Institute, Kechuang building, N777, Zhongguan road, Zhenhai district, Ningbo, 315211, China
https://orcid.org/0000-0001-5046-811X
Scopus Author ID: 6506011278

Mykola T. Kartel' — Academician of NAS of Ukraine, Doctor of Science (Chem.), professor, Director of Chuiko Institute of Surface Chemistry of NAS of Ukraine, Kyiv, Ukraine; Ningbo University of Technology, 201 Fenghua Road, Ningbo, 315211, China; Ningbo Sino-Ukrainian New Materials Industrial Technologies Institute, Kechuang building, N777, Zhongguan road, Zhenhai district, Ningbo, 315211, China
https://orcid.org/0000-0002-9431-5921
Scopus Author ID: 7004212140

Serhii G. Nedilko — Doctor of Science (Phys. & Math.), Senior Researcher, Head of the S&R laboratory "Spectroscopy of the condensed state of matter" of the Faculty of Physics of Taras Shevchenko Kyiv National University
https://www.scopus.com/authid/detail.
Scopus Author ID: 9633446900

Yurii A. Khyzhnyi — Doctor of Science (Phys. & Math.), Senior Researcher, Senior Researcher of the S&R laboratory "Spectroscopy of the condensed state of matter" of the Faculty of Physics of Taras Shevchenko Kyiv National University, Kyiv, Ukraine
Web of Science ResearcherID: GYA-0449-2022,
https://orcid.org/0000-0003-0111-2920
Scopus Author ID: 6508037897

Kateryna O. Ivanenko — candidate of physical and mathematical sciences, Institute of Macromolecular Chemistry of NAS of Ukraine, Kyiv, Ukraine
Ningbo Sino-Ukrainian New Materials Industrial Technologies Institute, Kechuang building, N777, Zhongguan road, Zhenhai district, Ningbo, 315211, China
https://orcid.org/0000-0002-5637-9633
Scopus Author ID: 14050186500

Розглянуто закономірності формування структури і властивостей sp^2-гібридизованих вуглецевих наноутворень: нанотрубок (ВНТ), термічно розширеного графіту (ТРГ), наночастинок графену і композиційних матеріалів за їх участю з вуглецевими, полімерними і керамічними матрицями, зокрема композит ТРГ-ВНТ, а також механізм впливу низького вмісту нанорозмірних наповнювачів на функціональні й експлуатаційні характеристики створених нанокомпозиційних матеріалів. Експериментально підтверджено, що механізм зміцнення низьконаповнених матриць полягає у створенні сіткою ВНТ прошарків матриці у нанорозмірному стані з покращеними характеристиками. Монографія призначена для фахівців у галузі фізико-хімічного матеріалознавства.

Наукове видання

НАЦІОНАЛЬНА АКАДЕМІЯ НАУК УКРАЇНИ

ІНСТИТУТ ХІМІЇ ПОВЕРХНІ ім. О.О. ЧУЙКА НАН УКРАЇНИ
ІНСТИТУТ ХІМІЇ ВИСОКОМОЛЕКУЛЯРНИХ СПОЛУК НАН УКРАЇНИ
КИЇВСЬКИЙ НАЦІОНАЛЬНИЙ УНІВЕРСИТЕТ імені ТАРАСА ШЕВЧЕНКА

СЕМЕНЦОВ ЮРІЙ ІВАНОВИЧ
КАРТЕЛЬ МИКОЛА ТИМОФІЙОВИЧ
НЕДІЛЬКО СЕРГІЙ ГЕРАСИМОВИЧ
ХИЖНИЙ ЮРІЙ АНАТОЛІЙОВИЧ
ІВАНЕНКО КАТЕРИНА ОЛЕКСІЇВНА

ВУГЛЕЦЕВІ НАНОМАТЕРІАЛИ З ГРАФІТОПОДІБНОЮ СТРУКТУРОЮ ТА ЇХНІ КОМПОЗИТИ: ФІЗИКА, ХІМІЯ ТА ТЕХНОЛОГІЯ

Англійською мовою

Редактор-коректор *Т.М. Ярмола*

Художнє оформлення *О.А. Бурдік*
Технічний редактор *Т.М. Шендерович*
Комп'ютерна верстка *Н.О. Кучеренко*

Підписано до друку 09.12.2022. Формат 70 × 100 / 16. Гарн. Minion Pro.
Ум. друк. арк. 37,05. Обл.-вид. арк. 35,17. Тираж 100 прим. Зам. № 6810.

Видавець і виготовлювач Видавничий дім «Академперіодика» НАН України
01024, Київ, вул. Терещенківська, 4

Свідоцтво про внесення до Державного реєстру суб'єктів
видавничої справи серії ДК № 544 від 27.07.2001